Proceedings

ITISE 2017

International work-conference on Time Series

Granada

September, 18-20 2017

Volumen 1

Proceedings ITISE 2017.

International work-conference on Time Series

Editors and Chairs

Olga Valenzuela
Fernando Rojas
Héctor Pomares
Ignacio Rojas

University of Granada

ISBN: 978-84-17293-01-7

Legal Deposit: GR 1369-2017

Edit and Print: Godel Impresiones Digitales S.L.

Preface

We are proud to present the set of final accepted papers for the fourth edition of the ITISE 2017 conference "International work-conference on Time Series" held in Granada (Spain) during September, 18-20, 2017.

The ITISE 2017 (International work-conference on Time Series) seeks to provide a discussion forum for scientists, engineers, educators and students about the latest ideas and realizations in the foundations, theory, models and applications for interdisciplinary and multidisciplinary research encompassing disciplines of computer science, mathematics, statistics, forecaster, econometric, etc, in the field of time series analysis and forecasting.

The aims of ITISE 2017 is to create a friendly environment that could lead to the establishment or strengthening of scientific collaborations and exchanges among attendees, and therefore, ITISE 2017 solicits high-quality original research papers (including significant work-in-progress) on any aspect time series analysis and forecasting, in order to motivating the generation, and use of knowledge and new computational techniques and methods on forecasting in a wide range of fields.

The list of topics in the successive Call for Papers has also evolved, resulting in the following list for the present edition:

1. **Time Series Analysis and Forecasting**.
    - Nonparametric and functional methods
    - Vector processes
    - Probabilistic Approach to Modeling Macroeconomic Uncertainties
    - Uncertainties in forecasting processes
    - Nonstationarity
    - Forecasting with Many Models. Model integration
    - Forecasting theory and adjustment
    - Ensemble forecasting
    - Forecasting performance evaluation
    - Interval forecasting
    - Econometric models
    - Econometric Forecasting
    - Data preprocessing methods: Data decomposition, Seasonal adjustment, Singular spectrum analysis, Detrending methods, etc.
2. **Advanced method and on-Line Learning in time series**.
    - Adaptivity for stochastic models
    - On-line machine learning for forecasting
    - Aggregation of predictors
    - Hierarchical forecasting
    - Forecasting with Computational Intelligence
    - Time series analysis with computational intelligence

- Integration of system dynamics and forecasting models

3. **High Dimension and Complex/Big Data**.

   - Local Vs Global forecast
   - Techniques for dimension reduction
   - Multiscaling
   - Forecasting Complex/Big data

4. **Forecasting in real problem**.

   - Health forecasting
   - Telecommunication forecasting
   - Modelling and forecasting in power markets
   - Energy forecasting
   - Financial forecasting and risk analysis
   - Forecasting electricity load and prices
   - Forecasting and planning systems
   - Real time macroeconomic monitoring and forecasting
   - Applications in: energy, finance, transportation, networks, meteorology, health, research and environment, etc.

After a careful peer review and evaluation process (each submission was reviewed by at least 2, and on the average 2.9, program committee members or additional reviewer), 121 contributions are presenting in this proceedings (accepted for oral, poster or virtual presentation,according to the recommendations of reviewers and the authors' preferences.

In this edition of ITISE, we are honored to have the following invited speaker:

1. Prof. Dr. Fredj Jawadi , Associate Professor of Economics (MCF-HDR) at the University of Evry, France.

2. Prof. Dr. Joerg Breitung, Professor in the Center of Econometrics and Statistics, University of Cologne, Germany

3. Dr. Travis J. Berge, Senior Economist. Board of Governors of the Federal Reserve System, USA.

4. Dr. Anna Korzeniewska, Faculty, Department of Neurology at Johns Hopkins University School of Medicine, Baltimore MD, USA

5. Dr. Joan Paredes, Senior Scientist, Dr. Joan Paredes, European Central Bank, Frankfurt am Main, Germany.

6. Dr. Pekka Koponen, Senior Scientist, D.Sc.Tech, VTT Technical Research Centre of Finland, Energy Systems, P.O. Box 1000, FI-02044 VTT, Finland

During ITISE 2017 several Special Sessions will be carried out. Special Sessions will be a very useful tool in order to complement the regular program with new and emerging topics of particular interest for the participating community. Special Sessions that emphasize on multi-disciplinary and transversal aspects, as well as cutting-edge topics are especially encouraged and welcome.

This fourth edition of ITISE was organized at the Universidad de Granada, with the help of the Spanish Chapter of the IEEE Computational Intelligence Society and Spanish Network Time Series (RESET). We wish to thank to our main sponsor the institutions Faculty of Science, Dept. Computer Architecture & Computer Technology and CITIC-UGR from the University of Granada for their support. We wish also to thank to the Dr. Veronika Rosteck and Dr. Eva Hiripi, Springer, Associate Editor, for their interest in the future editing a book series of Springer from the best papers of ITISE 2017.

We would also like to express our gratitude to the members of the different committees and to the reviewer for their support, collaboration and good work.

September, 2017
Granada

ITISE Editors and Chairs
Olga Valenzuela
Fernando Rojas
Hector Pomares
Ignacio Rojas

Steering and Local Committee

Amaury Lendasse	University of Iowa
Hector Pomares	University of Granada
Fernando Rojas	University of Granada
Ignacio Rojas	University of Granada
Olga Valenzuela	University of Granada

Program Committee

Adnan Sozen
Ahlame Douzal
Alan Wee-Chung Liew
Alberto Guillén
Alexandra Spitz-Oener
Alexey Koronovskii
Alicia Troncoso
Aman Ullah
Amaury Lendasse
Anke Meyer-Baese
Ansgar Steland
Antonio J. Rivera Rivas
Antonio Montañés
Asesh Roychowdhury
Athanasios Sfetsos
Axel Werwatz
Bormin Huang
C.Germán Castellanos Dominguez
Calvin Wong
Carlos Henrique Ribeiro Lima
Caroline Uhler
Cecilio Tamarit
Chang-Yong Lee
Charilaos Kourogiorgas
Charles Efferson
Chor Foon Tang
Christian Brownlees
Christian Gourieroux
Christoph Winter
Christopher Burke
Chunshien Li
Claudia Villalonga
Dalia Kriksciuniene
Daniel Castillo
Daniel Peña Sanchez
David Giles
Juan María Palomo
Julien Chevallier
Junsoo Lee
K. Muraleedharan
Kalle Saastamoinen
Katerina Tsakiri
Kit Yan Chan
Konstantinos Spiliopoulos
Krzystof Siwek
Lazaros Iliadis
Leonid Sheremetov
Leopold Soegner
Leszek Borzemski
Loli Perez
Luca Faes
Luis Javier Herrera
Manfred Deistler
María Dolores Gadea
María José Del Jesús Díaz
Marc Hallin
Marcel Ausloos
Marco Lippi
Martin Wagner
Matteo Barigozzi
Mehdi Vafakhah
Micael Castanheira
Miquel Montero Torralbo
Mohammed Rezaul Karim
Naoufel Cheikhrouhou
Narayanan Kumarappan
Nicolás Marín Ruiz
Olga Valenzuela
Oresti Banos
P.C. Nayak
Panos Pardalos
Paulo Cortez

Dimitris Varoutas
Dorel Aiordachioaie
Elmar Lang
Erol Egrioglu
Eros Pasero
Ferda Halicioglu
Fernando Pérez de Gracía
Fernando Rojas
Fionn Murtagh
Florian Zimmermann
Francisco Estrada
Francisco Martínez Álvarez
François Schmitt
Fredj Jawadi
Fuxia Cheng
G.S. YIN
Gabriel Pérez Quirós
Gani Aldashev
Georg Görg
Gerhard Rünstler
Germán Gutiérrez Sánchez
Gilney Zebende Zebende
Guy Mélard
Héctor Pomares
Hakan Aladag
Hashem Pesaran
Heather Ruskin
Hisham El-Shishiny
Hooi Hooi Lean
Hui Liu
Ignacio Rojas
Ildar Batyrshin
Ilhan Ozturk
Irina Perfilieva
Isaias Lima
Janusz Kacprzyk
Janusz Miskiewicz
Javier Hualde
Jeff Yao
Jesús Gonzalo
Jianbo Gao
Jing Shi
João Catalão
José L. Aznarte
José María Amigó García
Josep Lluís Carrion-i-Silvestre
Josu Arteche
Juan Manuel Galvez
Paulo Rodrigues
Pei-Chann Chang
Peter Gloesekoetter
Peter M. Robinson
Philipp Sibbertsen
Philippe Weil
Pierpaolo D'Urso
Plamen Ivanov
Popescu Theodor Dan
Ragulskis Minvydas
Rajendra Udyavara Acharya
Rebecca Killick
Ricardo de Andrade Araújo
Rosangela Ballini
Ruqiang Yan
Ryszard Tadeusiewicz
Sajjad Ahmad
Salah Bourennane
Samrad Jafarian-Namin
Shilu Tong
Siem Jan Koopman
Silke Hüttel
Slawek Zadrozny
Suresh Sethi
Tatiana Afanaseva
Thomas Epper
Tin-Chih Toly Chen
Tobias Preis
Tomas Cipra
Toshihisa Funabashi
Tsangyao Chang
Tzung-Pei Hong
Ulrich Foelsche
V. Jothiprakash
Vadlamani Ravi
Vijay P. Singh
Vladas Pipiras
Wei-Chiang Hong
Wei-Xing Zhou
Wieslaw M. Macek
Willem K. M. Brauers
William A. Barnett
Witold Pedrycz
Wolfgang K Härdle
Yixiao Sun
Yucheng Dong
Yukun Bao

PROCEEDINGS ITISE 2017

Advanced in Time Series Forecast

Applications in Time Series

Bio-medical Time Series Analysis

Chaos and Random in Time Series

Computational Intelligence methods for Time Series

Energy Forecasting

Ensemble forecasting

Forecasting Complex/Big data

Future of Mathematical and Logical Structures behind Time Series Analysis and History

Nonstationarity Analysis in Time Series

Recent Developments on Time-Series Modelling

Structural Time Series Models

Alternative Solution for the Adjustment of Defect Liability Period in Construction

Jeong, Kichang[1], Kim Wooram[2] and Lee, Jaeseob[2]

[1] Korea Institute of Construction Management, Seoul, Republic of Korea
[2] Division of Architectural Engineering, Dongguk University, Seoul, Republic of Korea

Abstract. Buildings deteriorate with time. The defects in buildings affect deterioration, but are generally distinguished from natural deterioration. Flaws or defects that do not satisfy normal conditions expected of completed structures are referred to as "defects". Furthermore, such defects are the contractor's liability, and the limited period of this liability is called the 'liability period'.
Practically, it is difficult to adjust the defect liability period of facilities. In particular, if construction is suspended after the facilities are completed or during the assembly phase, the facilities will undergo natural deterioration. This deterioration is accompanied by physical performance degradation, and the contractor would not be willing to bear additional risks incurred by an extension of the defect liability period. However, the employer will demand that the defect liability period should be applied from the actual installation date, despite the effects of natural deterioration. As a result, there is a possibility for conflict.
Even though the delivery date of facilities is delayed due to the suspension of construction, it is, in some cases, possible to adjust the defect liability reasonably through an agreement between the parties, if they adopt a method for recognizing the initial performance maintenance cost.
Therefore, the authors of this study propose an alternative method of contract adjustment, which recognizes the initial performance maintenance cost, in addition to the method of adjusting the defect liability period due to the suspension of construction.

Keywords: defect, liability, delay, power plant, deterioration

1 Introduction

1.1 Background and Purpose

A construction project is a bilateral contract between parties, in which the employer and the contractor sign an agreement through mutual consultation, based on their own will, with each one in an equal position. Furthermore, a construction project undergoes various changes in conditions because it occurs over a long period of time[1], and involves adjustment of the contract amount or construction period according to such changes.

This adjustment is initiated with a claim by one party. A claim for acceleration, delay, or disruption involves a change of the expected time or work method. Each claim requires corresponding evidence. Among them, delay involves an increase of the time required for completing the project that was considered at the time of contract signing, and each party should bear the delay cost for their part. Each must take responsibility for the delay, if there is any.[2]

Delay claim corresponds to a claim for damages, which is included in the delay type. A general characteristic of a delay claim is that the contractor insists that it takes more time to do the required work than they planned, because of the interference and design changes made by the employer, and/or the delayed decision making of the employer or designer. As a result, the contractor must work more than planned, regardless of the performance of the work that they planned or expected at first.[3]

The existing studies on defects include a study that proposes comprehensive improvements on the legitimacy of the defect liability period, rationalization of the responsible entity, and an efficient consumer relief process through a general approach rather than concrete suggestions[4], and a study that proposes the introduction of a performance guarantee system regarding the responsibility for defects.[5] However, no study has been conducted on the method of adjusting the rights and responsibilities for defects. In general, the contract conditions require the contractor to take responsibility for the defects of the construction. However, a 'liability period' is set from the completion date, and there are no terms for adjusting the 'liability period' for delays caused by a reason that is not attributable to the contractor.

In this background, this study analyzes the Conditions of Contract for Construction of the International Federation of Consulting Engineers (FIDIC), which are widely recognized as a standard contract form. It proposes a method of adjusting the defect liability period according to the responsibility for the delay.

1.2 Scope and Method

The subject of this study is limited to the FIDIC's Conditions of Contract for Construction, which is currently recognized as a global standard for conditions of construction contracts, and the delay factors regarding the adjustment of defects are addressed in a limited manner. The study method is as follows:

1. Perform a theoretical discussion related to the defects and contract changes.

2. Analyze the related provisions and problems of contracts prepared under the FIDIC's Conditions of Contract for Construction.

3. Present problems through case analysis.

4. Propose a method of rationally adjusting the responsibility for defects based on these factors.

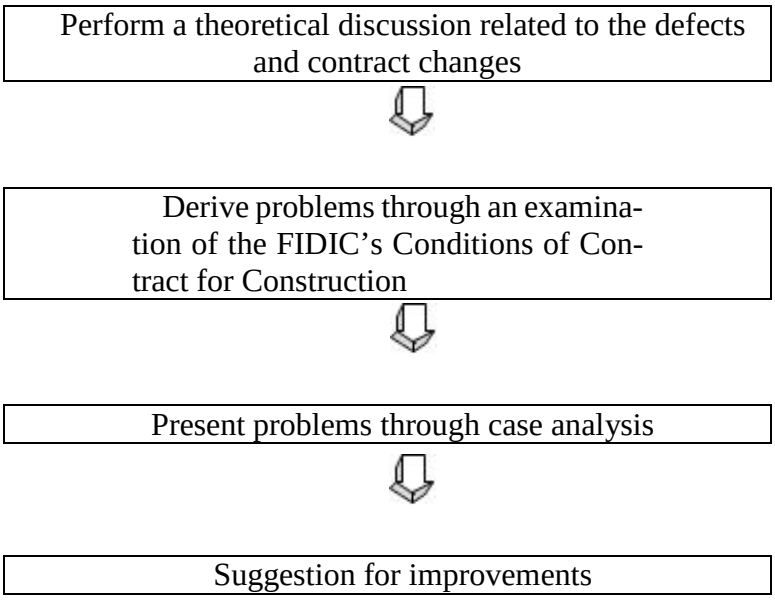

Fig. 1. Flow chart of the study

2 Theoretical Discussion

2.1 Definition of Deterioration and Defect

There is a distinction between general deterioration and a defect. Deterioration occurs when facilities are worn out naturally with time, and their functions are diminished as a result. Jae-Hyeok Park(2009) defined the characteristics of building deterioration by classifying them into physical deterioration, functional and technical deterioration, and socioeconomic deterioration.[6] Further, the dictionary definition of defect is a fault or flaw that does not meet the normal conditions. Furthermore, an architectural defect generally means poor quality that does not meet specifications, functional faults, or incomplete installation resulting from erroneous construction or omission of items in a process that must be performed by the contractor for a building.[7]

Therefore, the natural deterioration of functions due to old facilities or equipment with the flow of time after completion of a building is clearly distinguished conceptually from the defects that occur due to failure to reach a normal state.

2.2 Change of Contract Terms and Conditions

Construction necessarily involves a change of contract terms and conditions because it is a long-term project. A construction project is a bilateral contract between two parties, in which the employer and the contractor sign an agreement through mutual consultation based on their own will, with each in an equal position. Furthermore, a construction project extends over a long period of time, and various changes in conditions can occur. The changed terms and conditions involve an adjustment of the contract amount. A common issue today is the calculation of additional overhead following an extension of construction period.[8]

The adjustment of contract amount starts from a claim by one party. The claims for acceleration, delay, and disruption involve a change of time or work method for the contracted work, and each claim requires evidence. Among them, "delay" involves an increase of the time required to complete the project that was considered at the time of contract. Each party must bear the cost of delay for the part that they are responsible for, if there is any.[9]

Considering that a construction project is a mutual contract where parties take responsibility for their obligations, a contract change due to delays caused by nonfulfillment of obligation should be rationally adjusted considering the increased time and cost.

3 Defect Liability and Contract Change in a FIDIC Agreement

3.1 Outline of the Conditions of Contract for Construction in FIDIC

In this study, the FIDIC's Conditions of Contract for Construction are analyzed to examine defect liability and contract change related to delay. In particular, to investigate the defect liability adjustment for delay, this study focuses on the provisions corresponding to this subject.

FIDIC is an international federation of national member associations of consulting engineers. FIDIC was founded in 1913 by three such associations within Europe. The objectives upon formation were to promote in common the professional interests of the member associations, and to disseminate information of interest to their members. Today, FIDIC membership covers more than 70 countries from all parts of the globe and encompasses most of the private practice of consulting engineers.

This study focuses on the FIDIC because it provides global standard for contract conditions, giving sufficient value to research. Moreover, many studies are being conducted on the Conditions of Contract for Construction, which are the most basic contract terms of FIDIC.

3.2 FIDIC's Terms Related to Defects

Term 11 is related to defects in the FIDIC contract, and it consists of 11 detailed terms, which are outlined in Table 1.

Table 1. Composition of '11. Defects Liability' in the Conditions of Contract for Construction.

11. Defects Liability
11.1 Completion of Outstanding Work and Remedying Defects
11.2 Cost of Remedying Defects
11.3 Extension of Defects Notification Period
11.4 Failure to Remedy Defects
11.5 Removal of Defective Work
11.6 Further Tests
11.7 Right of Access
11.8 Contractor to Search
11.9 Performance Certificate
11.10 Unfulfilled Obligations
11.11 Clearance of Site

To examine the terms in detail, the completion of outstanding work and the defects must be remedied within a reasonable period of time, as specified by the engineer. The employer must notify the contractor in case any defects or damages occur.[10]

It is stated that the contractor must take full responsibility for the defect repair cost.[11] If the main items of construction, partial construction or installation cannot be used for their intended purpose towing to defects or damages even after the takeover, the contractor has a right to extend the defect notification period.

This period cannot be extended for more than two years. However, this term is not applicable if the construction is suspended due to a cause that is not attributable to the contractor.("the Contractor's obligations under this clause shall not apply to any defects or damage occurring more than two years after the defects notification period for the plant and/or materials would otherwise have expired.")[12]

3.3 Terms Related to Delay and Suspension in the FIDIC Contract

Term 8 is related to delay and suspension in the FIDIC contract, and it consists of 12 detailed terms in total. These terms are outlined in Table 2.

Table 2. Composition of '8. Commencement, Delay, and Suspension' in the Conditions of Contract for Construction.

8. Commencement, Delay, and Suspension
8.1 Commencement of works
8.2 Time for Completion
8.3 Programme
8.4 Extension of Time for Completion
8.5 Delays Caused by Authorities
8.6 Rate of Progress
8.7 Delay Damages
8.8 Suspension of Work
8.9 Consequences of Suspension
8.10 Payment for Plant and Materials in Event of Suspension
8.11 Prolonged Suspension
8.12 Resumption of Work

To examine the detailed terms, the contractor has a right to extend the time for completion in case a delay is caused by variations, exceptionally adverse climatic conditions, unforeseeable shortages in the availability of personnel or goods caused by an epidemic or governmental actions, or other miscellaneous reasons that are not attributable to the contractor.[13] The engineer can notify partial or full suspension of the construction to the contractor,[14] and can extend the time for completion and claim compensation in case delay and cost are generated as consequences of such suspension.[15]

Furthermore, the contractor is entitled to payment of the value of the plant and/or materials which have not been delivered to the site if the work on the plant or delivery of the plant and/or materials has been suspended for more than 28 days, and if the contractor has marked the plant and/or materials as the employer's property in accordance with the engineer's instructions.[16] In addition, if the suspension has continued for more than 84 days, the contractor may request the engineer's permission to proceed. If the engineer does not give permission within 28 days after being requested to do so, the contractor may make adjustments according to the terms on variations and adjustments. If the suspension affects the entirety of the work, the contractor may give a notice of termination.[17]

3.4 Terms Related to Variations and Adjustments in the FIDIC Contract

Term 13 is related to variations and adjustments in the FIDIC contract, and it consists of eight detailed terms. They are outlined in Table 3.

Table 3. Composition of '13. Variations and Adjustments' in the Conditions of Contract for Construction

13. Variations and Adjustments
13.1 Right to Vary
13.2 VE
13.3 Variation Procedure
13.4 Payment in Applicable Currencies
13.5 Provisional Sum
13.6 Daywork
13.7 Adjustments for Changes in Legislation
13.8 Adjustments for Changes in Cost

The engineer may initiate variations at any time prior to issuing the takeover certificate of the work. Each variation may include changes to the quantities of any item of work, changes to the quality and other characteristics of any item of work, and changes to the sequence or timing of the execution of the work, among others.[18]

If a variation proposal is requested, the contractor is required to respond via a contractor's proposal for any necessary modifications to the program and to the time for completion.[19]

Furthermore, there is a term on adjustments for changes in cost, according to changes in the appropriate standard prices, which is a simple term for adjusting the change based on price variation.[20]

3.5 Terms for Adjusting Liability Related to Defects in the FIDIC Contract

With regard to defects, the FIDIC clearly states that the defect liability period cannot be extended as a result of a suspension that is due to a reason that is not attributable to the contractor through Term 11.3, Extension of Defects Notification Period. Nevertheless. Therefore, the FIDIC fails to clearly present the concept of an appropriate adjustment method.

4 Presentation of Problem through Case Analysis

As described above, the FIDIC's Conditions of Contract for Construction prescribes that the defect liability period of two years can be extended if the work and plant installation are delayed, but this provision for additional defect liability extension is not applicable in the case where the contractor is not responsible for the delay. In this case, problems may arise because it is difficult to apply this regulation in practice. The authors will explain this practical difficulty through a case study below.

In the Case , which is installation work for boiler equipment, the defect liability period under the contract was one year. The installation was completed on December 31, 2014, but the construction was suspended for one year by an order of the engineer hired by the employer. As a result, the actual completion date of installation was December 31, 2015, one year later.

Table 4. Outline of the Case

Project name	Boiler Installation Work
Defect liability period	1 year
Original installation date (planned)	December 31, 2014
Actual installation date (actual)	December 31, 2015
Work suspension period	1 year

In such cases as the Case example, the following conflict may happen.

Position A. Regarding the equipment of which the delivery was delayed for one year, the defect liability period lasts until December 31, 2015, which is one year from the original installation date. Therefore, the employer cannot demand fulfilment of defect liability from the contractor for defects incurred after the actual installation date.

Position B. Even if delivery of the equipment was delayed for one year, the boiler was maintained and installed in new condition. Therefore, the employer can insist that the defect liability period lasts until December 31, 2016; one year after the actual installation date. In case a suspension of work occurs, the employer will demand the contractor to preserve the site, and the contractor will inevitably incur maintenance costs to maintain the site conditions. It is stipulated that the costs incurred for such maintenance can be claimed.

The issue of the defect liability period can be solved simply through a contract term, but this can be complex in practice. When we look at Case A, we cannot equate the condition of the equipment that has been used for one year to the condition of the equipment that has not been used at all for one year.

5 Alternative Solution

It is practically difficult to adjust the defect liability period for facilities. When the construction work is suspended after the completion or assembly of the facility, the

facility will undergo natural deterioration, which involves physical performance degradation. Therefore, the contractor will not want to bear the additional risks due to the extended defect liability period. However, the employer will demand that the defect liability period should be applied from the actual installation date, despite this natural deterioration. As a result, there is a possibility of a dispute.

However, in case of physical deterioration, the manufacturer of the facility, who has the best expertise on the facility, could maintain the initial performance until the time of delivery if they perform additional technical management to maintain the initial performance until the delayed delivery time. This cost is referred to as initial performance maintenance cost, in this study. If the delivery date of the equipment is delayed due to a suspension of work, the employer may have the contractor submit a plan for the initial performance maintenance cost and compare it with the actual expected cost of defects. If a contract term that allows the evaluation of economic efficiency in this way can be introduced, a rational adjustment of the defect liability could be made by an agreement between the parties.

Therefore, the authors propose a contract adjustment method through the recognition of the initial performance maintenance cost as an alternative to the adjustment of the defect liability period due to a suspension of work.

6 Conclusion

This study was conducted to find an alternative solution to resolve the practical difficulty involved in adjusting the defect liability period. Further, a method of recognizing the initial performance maintenance cost was proposed. An analysis of the contract terms outlined in FIDIC, which are broadly cited as an international standard, revealed that it allows adjustment of the defect liability period. However, a case analysis showed that such an adjustment is not easy in practice. As a solution to this issue, this study proposed a new contract adjustment method for defect liability, through the recognition of the initial performance maintenance cost.

This study suggests a new concept for rational adjustment of defect liability in the event of variation in the construction period, and it is expected to provide a rational solution to the settlement of disputes due to delayed construction. In future studies, this new method must be concretized by additionally reflecting upon the opinions of practitioners and related experts.

References

1. Jeong, kichang., Lee, Jaeseob.: Improvement of the Calculation Standard for Prolongation cost of Domestic Public Construction Project. Korea Journal of Construction Engineering and Management 17(4), 95–102 (2016).
2. Cushman R. F., Carter J. D., Gorman P. J., Coppi D. F. : Proving and Pricing Construction Claims. 3rd edn. Aspen Publishers, New York (2000).
3. Adrian James J.:Construction claims : A Quantitative Approach, Stipes Publishing Company, Illinois (1993)

4. Choi, Min-Soo.: A Study on the Rationalization of Defects Liability in Construction Works. Journal of the architectural institute of korea Structure & Construction 19(1), 137-145(2003)
5. Lee, Hak-ki.: Study on the Problem of Defects Liability System and Introduction on Performance Guarantee System in Domestic. Journal of the Regional Association of Architectural Institute of Korea 2(4), 123-130(2000)
6. Seo, Yuhyeon.: Classification of the Standard Defect Items of Roof and Waterproof Works based on the Defect Litigation Cases of Apartment Buildings. Chungbuk University (2017)
7. Yu, Myeong-Hwa.: The Study on the Causes of Defect & Reduction Measure of the Apartment House. Daegu University (2011)
8. Jeong, kichang., Lee, Jaeseob.: Improvement of the Calculation Standard for Prolongation cost of Domestic Public Construction Project. Korea Journal of Construction Engineering and Management 17(4), 95–102 (2016).
9. Cushman R. F., Carter J. D., Gorman P. J., Coppi D. F. : Proving and Pricing Construction Claims. 3rd edn. Aspen Publishers, New York (2000).
10. '11.1 Completion of Outstanding Work and Remedying Defects' in FIDIC's Conditions of Contract for Construction
11. '11.2 Cost of Remedying Defects' in FIDIC's Conditions of Contract for Construction
12. '11.3 Extension of Defects Notification Period' in FIDIC's Conditions of Contract for Construction
13. '8.4 Extension of Time for Completion, 8.5 Delays Caused By Authorities' in FIDIC's Conditions of Contract for Construction
14. '8.8 Suspension of Work' in FIDIC's Conditions of Contract for Construction
15. '8.9 Consequences of Suspension' in FIDIC's Conditions of Contract for Construction
16. '8.10 Payment for Plant and Materials in Event of Suspension' in FIDIC's Conditions of Contract for Construction
17. '8.11 Prolonged Suspension' in FIDIC's Conditions of Contract for Construction
18. '13.1 Right to Vary' in FIDIC's Conditions of Contract for Construction
19. '13.3 Variation Procedure' in FIDIC's Conditions of Contract for Construction
20. '13.8 Adjustments for Changes in Cost' in FIDIC's Conditions of Contract for Construction

Time Series Anomaly Detection with Discrete Wavelet Transforms and Maximum Likelihood Estimation

Markus Thill[1], Wolfgang Konen[1], and Thomas Bäck[2]

[1] Department of Computer Science, TH Köln – University of Applied Sciences, 51643 Gummersbach, Germany
{markus.thill,wolfgang.konen}@th-koeln.de
[2] Department of Computer Science, Leiden University, LIACS, 2333 CA Leiden, The Netherlands
t.h.w.baeck@liacs.leidenuniv.nl

Abstract. A new algorithm, based on the Discrete Wavelet Transform (DWT), for unsupervised anomaly detection in time series is introduced in this paper. The approach is based on using maximum likelihood estimation (MLE) on the DWT of time series. On a diverse set of 158 time series, the algorithm is compared with three other state-of-the-art anomaly detectors and it is shown to outperform the other approaches on the test set. Thanks to the linear time complexity of the DWT, our new algorithm is also computationally efficient.

Keywords: Time series, anomaly detection, wavelet transform, DWT, maximum likelihood estimation

1 Introduction

Anomaly detection in time series is a key technology in many areas. Industries have more and more devices (predictive maintenance for industry equipment, sensors in the internet of things, or server technologies in cloud services of the internet) which are collecting increasingly large streams of data. Research institutions (e.g. high energy physics or astronomy) are collecting vast amounts of data. To cope with this data, it is of importance to have automated procedures which separate the large amount of normal data from the anomalies, i.e. to have fast and reliable anomaly detection.

An anomaly is however difficult to define. In its most general form it is the absence of normality, but „normality“ depends largely on the context and cannot be expressed in closed form. A further complication is that anomalies can appear on quite different time scales: they can be spikes (short-time events) or broader structures (long-term irregularities). Most anomaly detection algorithms available today have their strength either in shorter or in longer time scales, but not in both.

Wavelets are a well-established technique in signal processing which allow to extract features in a self-similar fashion over a broad range of time scales

(frequencies). This makes them ideally suited to detect anomalies on different time scales where the time scale is a priori unknown.[3]

We present in this paper a new method for detecting anomalies based on wavelet processing and maximum likelihood estimation (MLE). Section 2 explains our method, Sec. 3 describes the experimental setup. Sec. 4 shows results and discusses them. Sec. 5 concludes.

1.1 Related Work

Despite the fact that wavelets are used for decades in signal processing and feature extraction, e. g. for classification of whole time series (machinery data) [12,13], there is only very little work with wavelets being used for anomaly detection, i. e. finding precise time intervals in time series containing anomalies: Kwon et al. [5] use wavelet transforms for the detection of network anomalies in the case of a possible attack by a malicious user. Kanarchos et al. [4] use wavelets in conjunction with neural networks and Hilbert transforms. Their algorithm was only tested on two time series which consisted of synthetic normal data and a synthetic anomaly.

In this work we test our algorithm on two large anomaly benchmarks, one being the well known Numenta Anomaly Benchmark (NAB, 58 time series, most of them real-world) [7] and the other being a subset of the Yahoo's S5 Webscope benchmark [6] (A3, 100 synthetic time series). We compare our algorithm with other state-of-the-art anomaly detectors: Numenta's NuPic, based on Hierarchical Temporal Memory (HTM) [2], our previous algorithm SORAD [10] which is specialized for short-time anomalies, and Twitter's ADVec algorithm [11].

2 DWT-MLEAD Algorithm

In this section we introduce our new unsupervised DWT-MLEAD algorithm which uses **D**iscrete **W**avelet **T**ransform and **M**aximimum **L**ikelihood **E**stimation for **A**nomaly **D**etection in time series.

2.1 Wavelet Transforms

Wavelet transforms [8] allow to represent a time series signal in terms of waves (the so called wavelets) with little local support. While (short-time) Fourier transforms always have a trade-off between accuracy in the frequency domain and accuracy in the time domain, wavelet transforms are used to retrieve accurate time-localized frequency information. The wavelet transform of a time series signal is composed with scaling and shifting functions. They take a mother wavelet and stretch and shrink it (scaling), dilate it along the time axis (shifting), and finally form the scalar product with the time series. Sampling wavelets

[3] We note in passing that the visual or auditory system of higher vertebrates contains information-processing structures similar to wavelets [3], thus underpinning the importance of wavelets for *natural computing*.

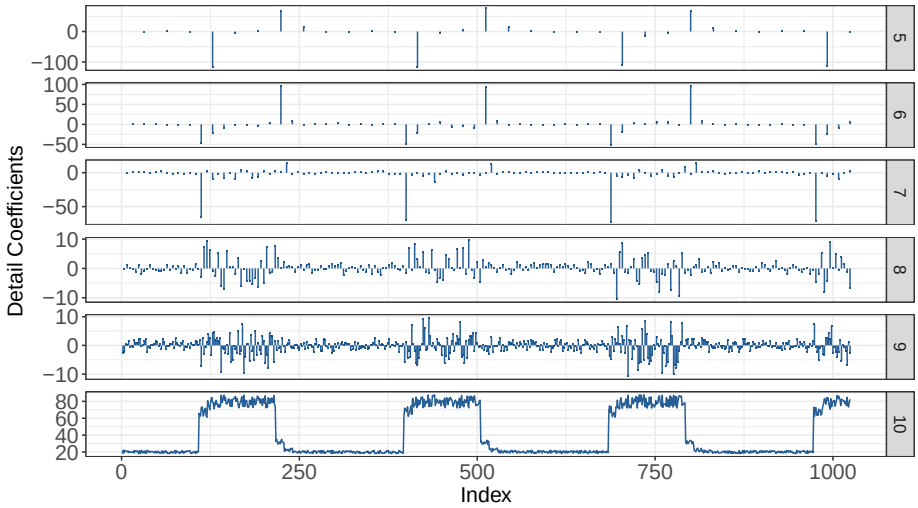

Fig. 1. Example of a decimating DWT using Haar Wavelets for a time series of the NAB data. The original time series is depicted on scale 10. On the scales 5–9 the detail coefficients of the DWT are shown. While we move towards lower scales, the number of coefficients is halved in each step, with 32 coefficients left on scale 5.

in a discrete manner leads to the so called discrete wavelet transform (DWT), which is commonly used in practice and has linear computational complexity. In its current form, DWT-MLEAD performs a decimating DWT using Haar wavelets on each time series. For this purpose, the R-package *wavetresh* [9] is used. Since the package requires the time series to have a length equal to a power of two, we currently artificially extend – where required – a time series of length n to a length $m = 2^{\lceil \log_2(n) \rceil}$, by mirror copying the last segment of the original time series into the extended area. However, we do not consider anomalies which are detected at instances $> n$. DWT-MLEAD utilizes both the detail coefficients $d_{k,\ell}$ and the approximation coefficients $c_{k,\ell}$, computed by the DWT (lines 6–7 in Algorithm 1), where ℓ addresses the level and $k \in 1, \ldots, m$ the time index. The lowest level $\ell = 0$ contains only one coefficient. The highest level $L = \log_2(m)$ has no approximation coefficients but only detail coefficients $d_{k,L}$ which represent the original time series. In Fig. 1 the DWT of a time series from NAB is illustrated.

2.2 Sliding Windows

In order to express temporal relationships, a simple and common approach in many machine learning tasks involving time series is to employ sliding windows of a certain size w (e.g. $w = 10$), which are used to generate fixed-sized input vectors for a model. By stacking the transposed input vectors, we obtain a matrix $\mathbf{X}$ with w columns which can be used to train a model. In the DWT-MLEAD

algorithm (Algorithm 1, lines 9–10), a window of size w_ℓ is slid over the detail and approximation coefficients $d_{k,\ell}$ and $c_{k,\ell}$ at each DWT level $\ell \in \{\ell', \ldots, L\}$ in order to generate the matrices $\mathbf{D}^{(\ell)}$ and $\mathbf{C}^{(\ell)}$. Subsequently, for each matrix a multivariate Gaussian distribution is estimated, as described in the following.

2.3 Gaussian Distributions & Maximum Likelihood Estimation

In order to learn the usual patterns in the time series, DWT-MLEAD estimates multivariate Gaussian distributions for the data generated by the sliding window approach. A Gaussian distribution is fully parametrized by a mean vector $\boldsymbol{\mu}$ and a covariance matrix $\boldsymbol{\Sigma}$. Assuming that an observed data sample was drawn from a specified distribution (a Gaussian), the maximum likelihood estimation (MLE) finds the parameters of this distribution such that these parameters maximize the likelihood of observing the given sample. The function MLE in Algorithm 2 does just this for a given matrix $\mathbf{X}$, where $\mathbf{X} \in \mathbb{R}^{n \times w}$, with $n = m - w + 1$ being the number of input vectors generated by sliding the window over the time series, $\boldsymbol{\mu} \in \mathbb{R}^w$ is a w-dimensional vector, which indicates the center of the distribution, and $\boldsymbol{\Sigma} \in \mathbb{R}^{w \times w}$ describes the covariances between individual dimensions. In Algorithm 1, line 12, DWT-MLEAD estimates the distribution parameters for each $\mathbf{D}^{(\ell)}$ and $\mathbf{C}^{(\ell)}$.

Subsequently, for every entry in $\mathbf{D}^{(\ell)}$ and $\mathbf{C}^{(\ell)}$ we compute the log-likelihood vector $\boldsymbol{p}$ using the previously determined parameters of the Gaussian distribution. This is done in function logProbDensity of Algorithm 2.

2.4 Quantile Boundaries

In order to separate unusual from usual window patterns in $\mathbf{D}^{(\ell)}$ and $\mathbf{C}^{(\ell)}$, one has to find a suitable boundary. The first method we use computes an empirical ϵ-quantile z_ϵ (e.g. the first percentile) for the log-likelihood vector $\boldsymbol{p}$. Another approach we use to estimate the threshold z_ϵ involves a Monte Carlo method, which samples from the estimated Gaussian distribution and determines the $(1-\epsilon)$-quantile for the Mahalanobis distances of the sample to the center of the distribution. After computing z_ϵ in Algorithm 1, line 14, instances are flagged as "unusual" in a binary vector $\boldsymbol{a}$ if their log-likelihood p_i lies beneath z_ϵ (line 15).

2.5 Leaf Counters

For each instance in the original time series the DWT-MLEAD algorithm maintains a leaf counter h_i. If an instance $c_{k,\ell}$ or $d_{k,\ell}$ on a certain level ℓ of the DWT is flagged as unusual (has a flag $a_k = 1$) then an event e – marked as a black node in Fig. 2 – is passed down the DWT tree to all leaf nodes connected with the e node. Each leaf node has a counter h_i (blue rectangles in Fig. 2) which counts all such events (Algorithm 1, line 16). After all events are processed, all counters with a count $h_i < 2$ are deleted (line 17).

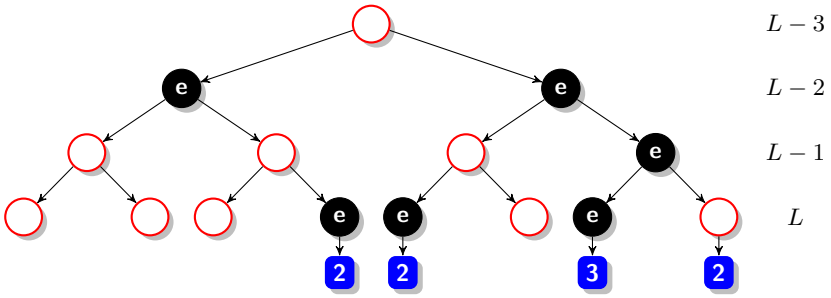

Fig. 2. Detecting anomalies with leaf counters. Along the vertical axis are the DWT levels ℓ, along the horizontal axis are the time indices k. The leftmost event e thus comes from either an unusual $c_{1,L-2}$ or $d_{1,L-2}$. Each event increases the leaf counters (blue rectangles) connected with the e node. Only counters with count ≥ 2 are shown.

2.6 Detecting the Anomalies

Once all the leaf counters are updated, DWT-MLEAD forms clusters C_j of all leaf counters h_i having a neighbor not more than d_{max} apart (Algorithm 1, line 18). Specifically, a cluster C_j is here a set of counters, each counter carrying its leaf position in the original time series and its event count. For each cluster C_j a sum s_j over all event counts is computed. In Fig. 2 for example, all counters form *one* cluster with sum $s_j = 9$. If a sum s_j exceeds the predefined threshold B, then the center of cluster C_j is labeled as anomaly event (line 23). The center $\mu(C_j)$ of cluster C_j is the weighted center of mass of all leaf positions, where the weights are the event counts.

3 Experimental Setup

3.1 The Benchmarks

The Numenta Anomaly Benchmark (NAB) [7] is a publicly available dataset that consists of 58 time series with in total 365,558 data points – the shortest series containing 1,127, the longest containing 22,695 and the average series containing approx. 6,300 instances. The majority of the time series are real-world data coming from application areas such as server monitoring, network utilization, sensor readings from industry and social media statistics [7]; 11 time series were generated artificially, from which 5 are anomaly-free. In total, over all 58 time series, 115 anomalies were labelled, most of which were identified manually. It has to be emphasized that the 58 time series are very diverse. The second benchmark we will investigate is the A3 data from the Webscope S5 benchmark [6]. It consists of 100 synthetic time series, each of length 1500, with in total 850 short-term anomalies. In our setup, the ground truth anomaly labels are not provided to the anomaly detection algorithms, which have to learn to separate anomalies from normal behavior in an unsupervised fashion.

Algorithm 1 DWT-MLEAD, an anomaly detection algorithm using the Discrete Wavelet Transform.

Define: ℓ' as starting level in DWT for analyzing the time series
    ϵ for computation of quantiles (e.g., the 1st percentile)
    d_{max}: maximum distance for same-cluster points
    B: threshold for the counter sum in a cluster that triggers an anomaly
function MLEANOMALY($y = (y_1, y_2, \ldots, y_m)$) ▷ m is a power of 2
    Compute DWT of y for levels $\ell \in \{\ell', \ldots, L\}$, with $L = \log_2(m)$
    Get detail coefficients $d_{k,\ell}$ and approximation coefficients $c_{k,\ell}$ of DWT
    Initialize a leaf counter $h_i = 0$ for each y_i, counting the events it receives
    Set window sizes for each level: $w_\ell = \max\{2, \ell - \ell' + 1\}$
    $\forall \ell \in \{\ell', \ldots, L\}$: Build $\mathbf{D}^{(\ell)}$, $\mathbf{C}^{(\ell)}$ by sliding window of size w_ℓ over $d_{k,\ell}$, $c_{k,\ell}$
    for all $\mathbf{X} \in \{\mathbf{D}^{(\ell)}, \mathbf{C}^{(\ell)} \mid \ell = \ell', \ldots, L-1\} \cup \mathbf{D}^{(L)}$ **do**
        $(\mu, \Sigma) = \text{MLE}(\mathbf{X})$ ▷ Defined in Algorithm 2
        $\boldsymbol{p} = \text{LOGPROBDENSITY}(\mathbf{X}, \boldsymbol{\mu}, \boldsymbol{\Sigma})$ ▷ Defined in Algorithm 2
        Compute ϵ-quantile z_ϵ
        $\boldsymbol{a} = \text{PREDICT}(\boldsymbol{p}, z_\epsilon)$ ▷ Defined in Algorithm 2
        For all $\boldsymbol{a}_i = 1$: Trigger an event moving down the tree to any connected leaf
    When all events are processed: Delete all event counters with count $h_i < 2$
    Form clusters C_j of leaf counters having a neighbor not more than d_{max} apart
    $\mathbf{S} = \{\}$ ▷ Set of detected anomalies
    for all C_j **do**
        s_j = sum of counter values in C_j
        if $s_j > B$ **then**
            $\mathbf{S} = \mathbf{S} \cup \{\mu(C_j)\}$ ▷ Add center $\mu(C_j)$ of C_j to anomaly set
    return S

Algorithm 2 Helper functions for Algorithm 1.

function MLE($\mathbf{X}$)
    $\boldsymbol{\mu} = \frac{1}{n}\sum_{i=1}^{n} \boldsymbol{x}_i$ ▷ Vetor $\boldsymbol{x}_i \in \mathbb{R}^w$ is the ith row of matrix $\mathbf{X} \in \mathbb{R}^{n \times w}$
    $\boldsymbol{\Sigma} = \frac{1}{n-1}\sum_{i=1}^{n} (\boldsymbol{x}_i - \boldsymbol{\mu})(\boldsymbol{x}_i - \boldsymbol{\mu})^T$
    return $(\boldsymbol{\mu}, \boldsymbol{\Sigma})$

function LOGPROBDENSITY($\mathbf{X}, \boldsymbol{\mu}, \boldsymbol{\Sigma}$)
    $\boldsymbol{p} \in \mathbb{R}^n$ ▷ n is the number of rows in $\mathbf{X}$
    for each row $\boldsymbol{x}_i$ of $\mathbf{X}$ **do**
        $\boldsymbol{p}_i = -\frac{1}{2}\log\det(2\pi\boldsymbol{\Sigma}) - \frac{1}{2}(\boldsymbol{x}_i - \boldsymbol{\mu})^T \boldsymbol{\Sigma}^{-1} (\boldsymbol{x}_i - \boldsymbol{\mu})$
    return $\boldsymbol{p}$

function PREDICT($\boldsymbol{p}$, z_ϵ)
    $\boldsymbol{a}$: vector of same size as $\boldsymbol{p}$
    for all $\boldsymbol{a}_i$ **do**
        $a_i = \begin{cases} 1, & \textbf{if } p_i < z_\epsilon \\ 0, & \textbf{otherwise} \end{cases}$ ▷ Binary anomaly flag vector
    return $\boldsymbol{a}$

3.2 Algorithms and their Settings

In the following, we compare DWT-MLEAD with three online anomaly detection algorithms, namely SORAD, NuPic, and ADVec. Although we did not systematically tune the parameters of each algorithm, we empirically determined for each algorithm and each dataset the best parameters from an informal search.

DWT-MLEAD Overall, three main parameters in Algorithm 1 have to be set, which are fixed for the whole dataset: a threshold $\epsilon \in [0, 1]$ for the ϵ-quantiles, which is varied to adjust the tradeoff between precision and recall, a parameter B (threshold for counter sum), and a starting level ℓ'. From Sec. 2.4, we use the empirical quantiles for the NAB data and the Monte Carlo based quantiles for the A3 data. We empirically determined the setting $B = 3.5$, $\ell' = 5$ for the NAB data and $B = 1$, $\ell' = 7$ for the A3 data. The window size w_ℓ is set by Algorithm 1 in a level-dependent fashion. In its current form the DWT-MLEAD algorithm operates offline on each time series, the remaining algorithms investigated in this work are all online.

SORAD In this work we will also report results for a simple online regression anomaly detection (SORAD) algorithm which we recently developed [10]. The algorithm has several parameters which are set as follows for the experiments: We set the forgetting factor of the algorithm to $\lambda = 0.98$, the anomaly threshold ϵ will be varied over a larger range, and the window-size is set to $w = 10$ for the A3 data and to $w = 200$ for the NAB data.

NuPic Numenta's NuPic[4] [2] requires a large number of parameters which cannot be set easily. Although NuPic provides a swarming algorithm [1] that optimizes the parameters, we found that the results for the swarmed parameter search are not significantly different from those for a standard parameter setting, which was also used for the reported results in [7]. Hence, we use the standard parameter setting for all experiments. The only parameter which is adjusted by us is an anomaly threshold that can be varied in the interval [0,1] and – similar to ϵ in SORAD and DWT-MLEAD – trades off precision and recall.

ADVec Twitter's ADVec Algorithm [11], which is available as open-source R package AnomalyDetection from Github[5] is the last algorithm which we will review in this work. The algorithm requires three main parameters, which are as follows: The first parameter α describes the level of statistical significance with which to accept or reject anomalies. As in the other algorithms, this parameter can be interpreted as an anomaly threshold. During our experiments, this parameter will be varied over a large range of values. ADVec requires a second parameter, a period-length, which we fix to the value 40 – which has shown to give

[4] https://github.com/numenta/nupic
[5] http://github.com/twitter/AnomalyDetection

the best results on the investigated data – entirely throughout this work. Finally, we found that the setting of the parameter $\max_{anoms}$ is crucial for the performance of ADVec, especially on the NAB dataset. This parameter determines the maximum number of anomalies that the algorithm will detect as a percentage of the data. We choose $\max_{anoms} = 1\%$ for the A3 data and $\max_{anoms} = 0.1\%$ for the NAB data.

3.3 Algorithmic Performance Measures

Similar to typical classification tasks, for time series anomaly detection problems an algorithm has to classify each time series sample as either anomalous (unusual) or as normal (usual). Commonly, correctly identified anomalies and normal instances are considered as true-positives (TP) and true negatives (TN), respectively. Misclassifications are accordingly referred to as false-positives (FP) and false-negatives (FN). In these cases normal/usual instances are falsely flagged as anomalous (FP) or the algorithm fails to detect real anomalies (FN). Due to the typically large number of TN for anomaly detection tasks, we renounce reporting this score. Based on the three remaining measures additional metrics can be derived, which are useful for comparing the performance of algorithms and will be used in later sections.

$$\text{precision} = \frac{\text{TP}}{\text{TP} + \text{FP}}, \qquad \text{recall} = \frac{\text{TP}}{\text{TP} + \text{FN}} \tag{1}$$

Ideally, one attempts to maximize precision and recall (with a max. value of one). However, since precision and recall are conflicting objectives in practice, the F_1 score – which takes both precision and recall into account – can be used to assess an algorithm's performance. The F_1 score is defined as:

$$F_1 = 2 \cdot \frac{\text{precision} \cdot \text{recall}}{\text{precision} + \text{recall}} \tag{2}$$

Since temporal anomalies can span over larger intervals, we use so-called anomaly windows for the scoring process. For the NAB data the already specified anomaly windows are used and for Yahoo's Webscope S5 data we place windows of size 10 around the labeled anomalies. While each detection outside of an anomaly window will be counted as a FP, multiple detections inside a window are only counted as *one* TP. Conversely, no detection within an anomaly window will be counted as *one* FN as well.

4 Results & Discussion

Table 1 summarizes the results for the four algorithms on the A3 and NAB data. On the A3 data with short-term anomalies, DWT-MLEAD and SORAD both clearly outperform the other algorithms NuPic and ADVec, achieving both, a high precision and recall. NuPic and ADVec produce a large amount of FP and at the same time miss most of the true short-term anomalies. For the NAB data

Table 1. Results for various algorithms on the A3 and NAB dataset. Shown are the sums of TP, FP, FN over all time series and the metrics precision, recall and F_1, cf. Eqs. (1)–(2), derived from these sums. All algorithms have their threshold chosen such that F_1 is maximized (in brackets: F_1 for threshold such that FP $\approx$ FN).

Dataset	Algorithm	Threshold	TP	FP	FN	Precision	Recall	F_1 Score
A3	DWT-MLEAD	0.015	806	8	44	**0.99**	**0.95**	**0.97** (0.95)
	NuPic	0.4	172	267	678	0.39	0.2	0.27 (0.26)
	SORAD	10^{-4}	810	22	40	0.97	**0.95**	0.96 (**0.96**)
	ADVec	20	190	216	660	0.47	0.22	0.3 (0.26)
NAB	DWT-MLEAD	0.02	69	65	46	**0.51**	0.6	**0.55** (**0.55**)
	NuPic	0.55	76	113	39	0.4	**0.66**	0.5 (0.47)
	SORAD	10^{-9}	57	313	58	0.15	0.5	0.24 (0.21)
	ADVec	100	66	164	49	0.29	0.57	0.38 (0.34)

Table 2. Computation times of the algorithms on datasets A3 and NAB. Shown is the average and standard deviation from 20 runs each. The runs were performed on a PC with an i7-3520M CPU and 8 GB of RAM.

	Computation Time (s)			
Dataset	DWT-MLEAD	SORAD	NuPic	ADVec
A3	13.6 ± 0.3	34.6 ± 0.1	810.9 ± 1.3	2.6 ± 0.2
NAB	12.2 ± 0.2	111.6 ± 0.2	1636.4 ± 2.7	5.8 ± 0.5

we observe rather different results: while DWT-MLEAD still outperforms the remaining algorithms according to the overall F_1 score, SORAD now performs the worst according to all metrics. In particular, the precision is rather low for SORAD, due to the large number of FP. NuPic delivers similar results as DWT-MLEAD, with a slight advantage for DWT-MLEAD.

Two example time series from the NAB data with the detections of the individual algorithms are shown in Fig. 3. In the first example it can be clearly seen that SORAD produces many FP at the recurring spikes in the time series. This is due to the fact that SORAD has no long-term memory so that such recurring spikes appear to be anomalous. Only DWT-MLEAD and ADVec detect both anomalies in both examples, although ADVec produces a few more false-positives.

All algorithms examined in this work have a threshold which can be varied in a certain range and which trades off FP and FN (as well as precision and recall) to a certain extent. In Fig. 4 the precision is plotted against the recall for different thresholds. For the A3 data the recorded points of DWT-MLEAD and SORAD clearly dominate those of NuPic and ADVec. For the NAB data the results are more diverse: while SORAD shows the worst performance of all algorithms, DWT-MLEAD and NuPic show the best performance, with NuPic

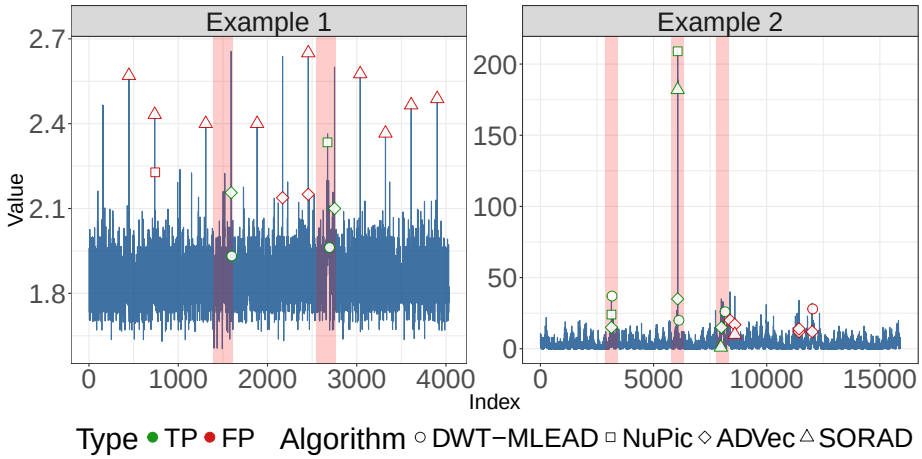

Fig. 3. Example time series taken from the NAB data with the anomalies detected by the algorithms DWT-MLEAD, NuPic, ADVec, and SORAD. The red vertical bars in the plot indicate the true anomaly windows. True-positives are indicated by green colors while False-positives are colored red.

having a slightly higher precision in larger recall ranges (recall > 0.6) and DWT-MLEAD in the lower recall ranges (recall < 0.6).

In Table 2, the computation times for the four algorithms on the A3 and NAB data are shown (mean and standard deviation from 20 runs). Overall, ADVec shows the best results regarding the computation time. On the A3 (NAB) data DWT-MLEAD is faster by a factor of 2.5 (9) than SORAD and 60 (134) than NuPic. However, we assume that an online implementation of DWT-MLEAD might require some additional computation time.

4.1 Discussion

The wavelet transform allows to capture features of the time series on different frequency levels. This is beneficial for detecting both long- and short-term anomalies. It is thus not unexpected that DWT-MLEAD is the only algorithm in our comparison which performs equally well on both benchmarks A3 and NAB. The event pooling mechanism shown in Fig. 2 with a minimum event count of 2 in each leaf counter is effective in shielding against noise which may produce an unusual event in just one frequency level. As expected, SORAD operates only well on short-term anomalies, since it analyzes only a short-term window in the original time series, which is too short for anomalies with a longer range.

The algorithm DWT-MLEAD in its current form has some limitations:

– We did so far only explore Haar wavelets and only modeled a multivariate Gaussian distribution to the data. It may be that other wavelets or other distributions would lead to better results.

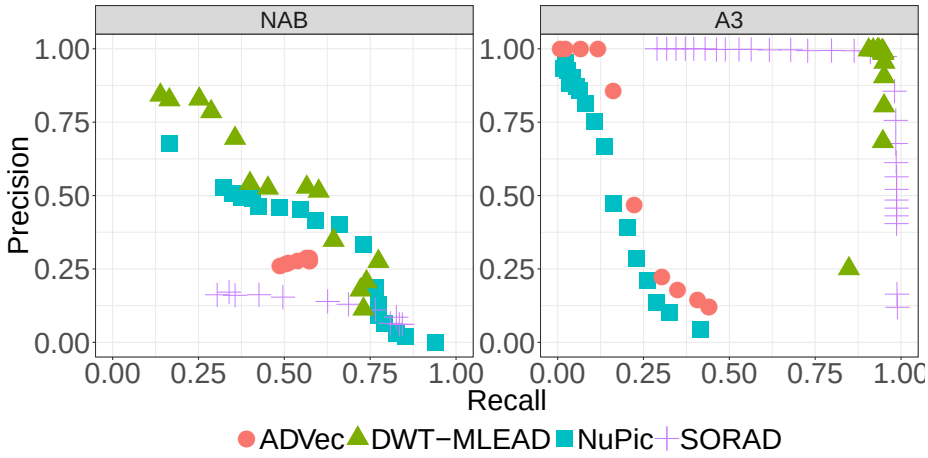

Fig. 4. Multiobjective plot for the NAB and A3 dataset. Precision and recall are computed based on the results of *all* time series of the corresponding data set.

- It is offline, i. e. the anomaly detection is undertaken when the whole time series is available. (It is still unsupervised since no information about prior anomalies is given to the algorithm.) There is however no obstacle to turn it into an semi-online algorithm on longer time series, where the whole algorithm would be repeated after short time intervals (e. g. 100 or 200) on the last 2^m (e. g. 1024 or 2048) time steps of the time series.
- We assume a certain degree of stationarity for the algorithm to work. Trends and change-points cannot be handled well in the offline form. Again, a semi-online version could offer more flexibility in the sense that trends and change-points can be learned by looking at the history of all 2^m-windows.
- If a time series has long-term periodic structures, not all anomalies might be detected correctly. This can happen if the frequency of the long-term periodic structure is lower than the lowest wavelet level ℓ' considered in Algorithm 1. In such cases it might help to extend the algorithm by a periodicity detector and subtract such a periodicity prior to analysing the time series with DWT-MLEAD.

5 Conclusion & Future Work

We have shown that the discrete wavelet transform (DWT) is beneficial for detecting anomalies in time series on various time scales. Specifically, our new algorithm DWT-MLEAD shows consistently good results on two larger benchmarks, one containing short-term anomalies (A3) and the other containing long-term anomalies (NAB). We tested this algorithm against three other state-of-the-art anomaly detectors and found DWT in first place on both benchmarks. It is remarkable that a single algorithmic principle works well over such a diverse

set of time series. Due to the efficient implementation available for DWT, our algorithm is computationally efficient (fast) as well.

5.1 Future Work

DWT-MLEAD works better than the other algorithms tested in this study, but it is not perfect yet, especially not on the NAB benchmark. Future work in this area should focus on improving the first layout of this algorithm, as outlined in Sec. 4.1 (Discussion): other wavelets than Haar wavelets, other than multivariate Gaussian distributions, a semi-online version of the algorithm, automated algorithm parameter tuning, and a periodicity detector.

References

1. Ahmad, S.: Running swarms (May 2017), `http://nupic.docs.numenta.org/0.6.0/guide-swarming.html`
2. George, D., Hawkins, J.: Towards a mathematical theory of cortical micro-circuits. PLoS Comput Biol 5(10), e1000532 (2009)
3. Jones, J., Palmer, L.: An evaluation of the two-dimensional Gabor filter model of simple receptive fields in cat striate cortex. J. Neurophysiol. 2, 1233–1258 (1987)
4. Kanarachos, S., Mathew, J., Chroneos, A., Fitzpatrick, M.: Anomaly detection in time series data using a combination of wavelets, neural networks and Hilbert transform. In: International Conference on Information, Intelligence, Systems and Applications (IISA). pp. 1–6 (2015)
5. Kwon, D., Ko, K., Vannucci, M., Reddy, A.N., Kim, S.: Wavelet methods for the detection of anomalies and their application to network traffic analysis. Quality and Reliability Engineering International 22(8), 953–969 (2006)
6. Laptev, N., Amizadeh, S.: Yahoo anomaly detection dataset S5 (2015), `http://webscope.sandbox.yahoo.com/catalog.php?datatype=s\&did=70`
7. Lavin, A., S. Ahmad, S.: Evaluating real-time anomaly detection algorithms – the Numenta anomaly benchmark. In: IEEE Conference on Machine Learning and Applications (ICMLA2015) (2015), `http://arxiv.org/pdf/1510.03336`
8. Meyer, Y., Salinger, D.: Wavelets and Operators:, Cambridge Studies in Advanced Mathematics, vol. 1. Cambridge University Press (1995)
9. Nason, G.: wavethresh: Wavelets Statistics and Transforms (2016), `https://CRAN.R-project.org/package=wavethresh`, R package version 4.6.8
10. Thill, M., Konen, W., Bäck, T.: Online anomaly detection on the Webscope S5 dataset: A comparative study. In: IEEE Conference on Evolving and Adaptive Intelligent Systems (EAIS 2017). p. 1. Springer (2017)
11. Vallis, O., Hochenbaum, J., Kejariwal, A.: A novel technique for long-term anomaly detection in the cloud. In: 6th USENIX Workshop on Hot Topics in Cloud Computing, Philadelphia, PA (2014)
12. Yen, G.Y., Lin, K.C.: Wavelet packet feature extraction for vibration monitoring. In: IEEE International Conference on Control Applications. vol. 2, pp. 1573–1578 (1999)
13. Zhengjia, H., Jiyuan, Z., Yibin, H., Qingfeng, M.: Wavelet transform and multiresolution signal decomposition for machinery monitoring and diagnosis. In: IEEE International Conference on Industrial Technology (ICIT96). pp. 724–727 (1996)

Robust Multivariate Time Series Analysis in Nonlinear Models with Autoregressive and t-Distributed Errors

Hamza Alkhatib, Boris Kargoll, and Jens-André Paffenholz

Leibniz Universität Hannover, Geodätisches Institut
Nienburger Str. 1, 30167 Hannover, Germany
{alkhatib,kargoll,paffenholz}@gih.uni-hannover.de
https://www.gih.uni-hannover.de

Abstract. We study a time series model which can generally be described as the additive combination of a multivariate, nonlinear deterministic model with multiple univariate, covariance-stationary autoregressive (AR) processes whose white noise components follow independent scaled t-distributions. These distributions allow for the stochastic modeling of heavy tails or multiple outliers and provide the framework for a partially adaptive, robust maximum likelihood (ML) estimation of the deterministic model parameters, of the AR coefficients, of the scale parameters, and of the degrees of freedom of the underlying t-distributions. To obtain the ML estimator, we derive a generalized expectation maximization (GEM) algorithm, which takes the form of linearized, iteratively reweighted least squares. The performance of this estimator is evaluated by means of a Monte Carlo simulation for the observations of a circle in three dimensions, involving different noise models encountered typically in the analysis of global navigation satellite system (GNSS) time series.

Keywords: multivariate time series, nonlinear regression model, AR process, scaled t-distribution, partially adaptive estimation, robust parameter estimation, GEM algorithm, GNSS time series

1 Introduction

Robust estimation is important in many fields of application where the probability density function (pdf) of the random deviations is expected to be heavy-tailed (e.g., as a consequence of multiple outliers). [5] was an early exposition demonstrating the use and usefulness of the scaled (Student) t-distribution in robust maximum likelihood (ML) estimation for regression models. As already indicated by [1], this kind of ML estimation can be expressed in a computationally convenient form as iteratively reweighted least squares, where the weights are used to rescale the variances of the random deviations according to their locations under the pdf. It is possible with this approach to estimate the degree of freedom of the underlying t-distribution, alongside the regression parameters and the scale parameter, turning it into a so-called (partially) adaptive estimator.

In a multivariate regression model, each observable is modeled as a random vector which is explained by a vector-valued (possibly non-linear) deterministic regression function and a vector of random deviations. [6] assumed a multivariate t-distribution with unknown scale factor and unknown degree of freedom for each vector of random deviations and investigated different forms of the expectation maximization (EM) algorithm for the purpose of estimating the unknown model parameters. It was shown earlier in [7] and [10] that the expectation conditional maximization (ECM) and the expectation conditional maximization either (ECME) variants can speed up the convergence of the EM algorithm considerably. To handle models that do not allow for closed form solutions by EM, the optimization principle of generalized expectation maximization (GEM) was proposed by [1]. The idea is to approach the maximum expectation within each EM step rather than trying to reach it fully. GEM algorithms employing Newton-Raphson steps have been applied frequently [9]. A GEM algorithm can in particular be used to handle non-linear regression models. In this situation, an iteratively reweighted least squares algorithm with Gauss-Newton steps was found to be a suitable form of GEM [14, 5].

Besides heavy tails, multivariateness and non-linearity, a further aspect that complicates (partially adaptive) parameter estimation consists in the frequently encountered autocorrelatedness of the random deviations. For instance, many types of sensor data such as inertial sensor data, satellite gravity gradiometry data and GNSS data give measurement results where the random deviations exhibit pronounced colored noise characteristics (see, e.g., [17, 13, 16, 8]). Typically, such datasets contain numerous outliers, so that robust estimation approach is generally desirable. To deal with situation, the aforementioned partially adaptive estimator for regression models based on the scaled t-distribution was extended in [4] to include autoregressive (AR) random deviations, where the white noise components of the AR process are independently and identically t-distributed. A limitation of that method is however that the observables describe only a univariate time series involving a linear regression model.

The purpose of this contribution is to extend the existing univariate, linear model to a multivariate and nonlinear (differentiable) regression model. Concerning the setup of the AR model, we currently limit ourselves to the case where each time series component is associated with a univariate AR process of individual order, independently of the AR processes of the other components. We thus exclude the modeling of cross-correlations, a task which would require the use of vector AR (VAR) processes and which is beyond the scope of the present contribution. The paper is organized as follows.

First, the time series model is described in detail in Sect. 2, and the derivation of a corresponding GEM algorithm is outlined in Sect. 3. Here, it is shown on the one hand how the scaled t-distributions are taken into account within the E step. On the other hand, the linearization of the nonlinear deterministic model is demonstrated in connection with the M step, which is broken up into conditional maximization steps with respect to the different groups of estimated model parameters. In Sect. 4, a time series model for GNSS observations of a

circle in 3D is proposed, and the results of a Monte Carlo simulation as well as real world application based on this observation model are discussed. These findings are used to evaluate the performance of the implemented GEM algorithm in this scenario.

2 The Observation Model

We consider q-dimensional observables $\mathbf{Y}_t = [Y_{1,t} \cdots Y_{N,t}]^T$ measured at equidistant time instances $t = 1, \ldots, n$. The task is to approximate the corresponding measurement results $\mathbf{y}_1, \ldots, \mathbf{y}_n$ by a (vector-valued) nonlinear function $\mathbf{h}_t(\boldsymbol{\xi}) = [h_{1,t}(\boldsymbol{\xi}) \cdots h_{N,t}(\boldsymbol{\xi})]^T$ of unknown parameters $\boldsymbol{\xi} = [\xi_1, \ldots, \xi_m]^T$. We model the uncertainties of the measurement process by means of random deviations $\mathbf{E}_t = [E_{1,t} \cdots E_{N,t}]^T$ between the observables and the functional model, so that the observation equations take the form

$$\mathbf{Y}_t = \mathbf{h}_t(\boldsymbol{\xi}) + \mathbf{E}_t \quad (t = 1, \ldots, n). \tag{1}$$

Here, we assume that each of the N components of the random deviations is subject to autocorrelations in the form of a covariance-stationary autoregressive (AR) model

$$E_{k,t} = \alpha_{k,1} E_{k,t-1} + \ldots + \alpha_{k,p_k} E_{k,t-p_k} + U_{k,t} \quad (k = 1, \ldots, N; t = 1, \ldots, n), \tag{2}$$

in which the random variables $U_{k,1}$, …, $U_{k,n}$ are, for every $k = 1, \ldots, N$, independently and identically t-distributed according to

$$U_{k,t} \sim t_{\nu_k}(0, \sigma_k^2) \quad (k = 1, \ldots, N; t = 1, \ldots, n). \tag{3}$$

Thus, we allow each white noise series $U_{k,1}$, …, $U_{k,n}$ to have an individual fluctuation and tail behavior, as determined by the component-dependent scale parameter σ_k^2 and degree of freedom ν_k. These quantities, alongside the AR coefficients, are considered as additional unknowns to be estimated jointly with the functional parameters $\boldsymbol{\xi}$. The probability density function (pdf) of the scaled t-distributed white noise components $U_{k,t}$ is thus defined by

$$f(u_{k,t}) = \frac{\Gamma\left(\frac{\nu_k+1}{2}\right)}{\sqrt{\nu_k \pi \sigma_k^2}\,\Gamma\left(\frac{\nu_k}{2}\right)} \left[1 + \left(\frac{u_{k,t}}{\sigma_k}\right)^2 / \nu_k\right]^{-\frac{\nu_k+1}{2}} \tag{4}$$

(where Γ represents the gamma function). The preceding assumption of stochastic independence of the white noise components $\mathbf{u}_k = [u_{k,1} \cdots u_{k,n}]^T$ for each $k = 1, \ldots, N$ implies that their joint pdf is given by

$$f(\mathbf{u}_k) = \prod_{t=1}^{n} f(u_{k,t}) = \prod_{t=1}^{n} \frac{\Gamma\left(\frac{\nu_k+1}{2}\right)}{\sqrt{\nu_k \pi \sigma_k^2}\,\Gamma\left(\frac{\nu_k}{2}\right)} \left[1 + \left(\frac{u_{k,t}}{\sigma_k}\right)^2 / \nu_k\right]^{-\frac{\nu_k+1}{2}}. \tag{5}$$

We assume that no stochastic dependencies between the N white noise series exist, so that the joint pdf of the white noise components throughout all series

can be written in the factorized form $f(\mathbf{u}) = f(\mathbf{u}_1)\cdots f(\mathbf{u}_N)$. This implies also that the N colored noise processes (2) can be treated separately. Note that we generally allow these AR processes to have different orders $p_1, \ldots, p_N$. Since we intend to apply the preceding model to rather large time series (with n being at least 100), we deal with the initialization problem of the AR processes in a practical manner, by setting all quantities occurring at time instances $t = 0, -1, \ldots$ equal to 0. Moreover, we assume all AR processes to be invertible, so that we can rewrite them in the form

$$U_{k,t} = E_{k,t} - \alpha_{k,1}E_{k,t-1} - \ldots - \alpha_{k,p_k}E_{k,t-p_k} = \boldsymbol{\alpha}_k(L)E_{k,t}, \tag{6}$$

using the lag operator $L^j E_t := E_{t-j}$ and the lag polynomial $\boldsymbol{\alpha}_k(L) := 1 - \alpha_{k,1}L - \ldots - \alpha_{k,p_k}L^{p_k}$. We can interpret the latter as a digital filter, which decorrelates the colored noise series $e_{k,1}, \ldots, e_{k,n}$ (into the white noise series $u_{k,1}, \ldots, u_{k,n}$).

A maximum likelihood estimation of the unknown model parameters $\boldsymbol{\xi}$, $\boldsymbol{\alpha}_1$, $\ldots$, $\boldsymbol{\alpha}_N$, $\sigma_1^2, \ldots, \sigma_N^2$ and $\nu_1, \ldots, \nu_N$ based on the pdf $f(\mathbf{u})$ or its natural logarithm

$$\log \mathcal{L}(\boldsymbol{\theta}; \mathbf{y}) = \log f(\mathbf{u}) = \log\left[f(\mathbf{u}_1)\cdots f(\mathbf{u}_N)\right] = \sum_{k=1}^{N}\left(n \log\left[\frac{\Gamma\left(\frac{\nu_k+1}{2}\right)}{\sqrt{\nu_k \pi \sigma_k^2}\,\Gamma\left(\frac{\nu_k}{2}\right)}\right] - \frac{\nu_k+1}{2}\sum_{t=1}^{n}\log\left[1 + \left(\frac{\boldsymbol{\alpha}_k(L)(y_{k,t} - h_{k,t}(\boldsymbol{\xi}))}{\sigma_k}\right)^2 / \nu_k\right]\right) \tag{7}$$

and given measurement results $\mathbf{y}$ requires numerical optimization since a closed-form expression of the estimator is unavailable. Following the ideas of [1] and [5], we transform the preceding t-distribution observation model into an easier-to-manage form by introducing latent variables

$$W_{k,t} \,|\, \boldsymbol{\xi}, \sigma_k^2, \boldsymbol{\alpha}_k, \nu_k \sim \frac{\chi^2_{\nu_k}}{\nu_k} = G\left(\frac{\nu_k}{2}, \frac{\nu_k}{2}\right) \qquad (k = 1, \ldots, N; t = 1, \ldots, n), \tag{8}$$

where the gamma distribution is defined by the pdf

$$f(w_{k,t}|\boldsymbol{\theta}) = \begin{cases} \frac{\left(\frac{\nu_k}{2}\right)^{\nu_k/2}}{\Gamma\left(\frac{\nu_k}{2}\right)} \cdot (w_{k,t})^{\nu_k/2-1} \cdot e^{-\nu_k/2 \cdot w_{k,t}} & \text{if } \; w_{k,t} > 0, \\ 0 & \text{if } \; w_{k,t} \le 0 \end{cases} \tag{9}$$

(using $\boldsymbol{\theta}$ for convenience as the vector consisting of all the unknown model parameters). These variables are assumed to be stochastically independent within each series, resulting in the factorization $f(\mathbf{w}_k|\boldsymbol{\theta}) = \prod_{t=1}^{n} f(w_{k,t}|\boldsymbol{\theta})$. The idea is now to define further stochastic properties of the white noise $\mathbf{U}_k = [U_{k,1} \cdots U_{k,n}]^T$ and the latent variables $\mathbf{W}_k = [W_{k,1} \cdots W_{k,n}]^T$ in such a way that the Student pdf (5) is obtained as the marginal distribution from the joint pdf $f(\mathbf{u}_k, \mathbf{w}_k|\boldsymbol{\theta})$ (cf. [9]). This is achieved on the one hand by employing the conditional Gaussian

$$f(u_{k,t}|w_{k,t}, \boldsymbol{\theta}) = \frac{1}{\sqrt{2\pi(\sigma_k/\sqrt{w_{k,t}})^2}} \exp\left\{-\frac{u_{k,t}^2}{2(\sigma_k/\sqrt{w_{k,t}})^2}\right\}. \tag{10}$$

On the other hand, $\mathbf{U}_{k,t}$ is assumed to be independent of the white noise components and latent variables occurring within the series k at the other time instants $1,\ldots,t-1,t+1,\ldots,n$ and within the other series $1,\ldots,k-1,k+1,\ldots,N$ at all time instances, conditional on the values $w_{k,t}$ and $\boldsymbol{\theta}$. This conditional independence assumption allows us to apply for instance the simplification

$$\begin{aligned} &f(u_{k,t}|u_{k,1},w_{k,1}\ldots,u_{k,t-1},w_{k,t-1},u_{k,t+1},w_{k,t+1},\ldots,u_{k,n},w_{k,n},w_{k,t},\boldsymbol{\theta}) \\ &\quad = f(u_{k,t}|w_{k,t},\boldsymbol{\theta}) \end{aligned} \tag{11}$$

in the derivation of the desired joint pdf (similarly to the proof in [2])

$$\begin{aligned} f(\mathbf{u},\mathbf{w}|\boldsymbol{\theta}) &= \prod_{t=1}^{n} f(u_{1,t},w_{1,t}|\boldsymbol{\theta})\cdots\prod_{t=1}^{n} f(u_{N,t},w_{N,t}|\boldsymbol{\theta}) \\ &= \prod_{t=1}^{n} f(w_{1,t}|\boldsymbol{\theta})\, f(u_{1,t}|w_{1,t},\boldsymbol{\theta})\cdots\prod_{t=1}^{n} f(w_{N,t}|\boldsymbol{\theta})\, f(u_{N,t}|w_{N,t},\boldsymbol{\theta}). \end{aligned} \tag{12}$$

We define this be the likelihood function $\mathcal{L}(\boldsymbol{\theta};\mathbf{y},\mathbf{w})$ of the extended observation model. Before proceeding with the corresponding ML estimation, we note that the second factor in $f(w_{k,t},u_{k,t}|\boldsymbol{\theta}) = f(u_{k,t}|\boldsymbol{\theta})\, f(w_{k,t}|u_{k,t}|\boldsymbol{\theta})$ defines the conditional gamma distribution $G(a,b)$ with parameters $a = (\nu_k+1)/2$ and $b = (\nu_k + u_{k,t}^2/\sigma_k^2)/2$, given the value $u_{k,t}$ (applying a proof in analogy to [3]).

3 The Generalized EM Algorithm

In view of (12), (9) and (10), the log-likelihood function takes the form

$$\begin{aligned} \log\mathcal{L}(\boldsymbol{\theta};\mathbf{y},\mathbf{w}) = \text{const.} &- \frac{n}{2}\sum_{k=1}^{N}\log(\sigma_k^2) + \frac{n}{2}\sum_{k=1}^{N}\nu_k\log\left(\frac{\nu_k}{2}\right) - n\sum_{k=1}^{N}\log\Gamma\left(\frac{\nu_k}{2}\right) \\ &- \sum_{k=1}^{N}\sum_{t=1}^{n}\frac{1}{2}\left[\nu_k + \left(\frac{\boldsymbol{\alpha}_k(L)(y_{k,t}-h_k(\boldsymbol{\xi}))}{\sigma_k}\right)^2\right] w_{k,t} + \sum_{k=1}^{N}\sum_{t=1}^{n}\frac{1}{2}(\nu_k-1)\log w_{k,t}. \end{aligned} \tag{13}$$

To set up the generalized EM (GEM) algorithm, we define the Q-function as the conditional expectation of the preceding log-likelihood function (treated now as a random function), given measurement results $\mathbf{y}$ and trial parameter values $\boldsymbol{\theta}^{(i)}$, in the sense of

$$Q(\boldsymbol{\theta}|\boldsymbol{\theta}^{(i)}) = E_{\mathbf{W}|\mathbf{y};\boldsymbol{\theta}^{(i)}}\left\{\log\mathcal{L}\left(\boldsymbol{\theta};\mathbf{y},\mathbf{W}\right)\right\}. \tag{14}$$

3.1 The E Step

Recalling that the likelihood function was defined by (12), we condition directly on the white noise outcome $\mathbf{u}$ and on $\boldsymbol{\theta}^{(i)}$ (which values give $\mathbf{y}$ through the

equations (1) and (2)). Then, (13) yields

$$Q(\boldsymbol{\theta}|\boldsymbol{\theta}^{(i)}) = \text{const.} - \frac{n}{2}\sum_{k=1}^{N}\log(\sigma_k^2) + \frac{n}{2}\sum_{k=1}^{N}\nu_k\log\left(\frac{\nu_k}{2}\right) - n\sum_{k=1}^{N}\log\Gamma\left(\frac{\nu_k}{2}\right)$$
$$- \sum_{k=1}^{N}\sum_{t=1}^{n}\frac{1}{2}\left[\nu_k + \left(\frac{\boldsymbol{\alpha}_k(L)(y_{k,t} - h_{k,t}(\boldsymbol{\xi})}{\sigma_k}\right)^2\right]E_{\mathbf{W}|\mathbf{u};\boldsymbol{\theta}^{(i)}}\{W_{k,t}\}$$
$$+ \sum_{k=1}^{N}\sum_{t=1}^{n}\frac{1}{2}(\nu_k - 1)E_{\mathbf{W}|\mathbf{u};\boldsymbol{\theta}^{(i)}}\{\log W_{k,t}\}. \tag{15}$$

Here, we observe in light of [2] that the two conditional expectations simplify to

$$E_{\mathbf{W}|\mathbf{u};\boldsymbol{\theta}^{(i)}}\{W_{k,t}\} = E_{W_{k,t}|u_{k,t};\boldsymbol{\theta}^{(i)}}\{W_{k,t}\},$$
$$E_{\mathbf{W}|\mathbf{u};\boldsymbol{\theta}^{(i)}}\{\log W_{k,t}\} = E_{W_{k,t}|u_{k,t};\boldsymbol{\theta}^{(i)}}\{\log W_{k,t}\}.$$

Since the latent variable $W_{k,t}$ given the value $u_{k,t}$ follows the gamma distribution $G(a,b)$, the previous two expectations are, respectively, a/b and $\psi(a) - \log(b)$ (where ψ is the digamma function), so that we obtain (cf. [3] for details)

$$w_{k,t}^{(i)} := E_{W_{k,t}|u_{k,t};\boldsymbol{\theta}^{(i)}}\{W_{k,t}\} = \frac{\nu_k^{(i)} + 1}{\nu_k^{(i)} + \left(\frac{\boldsymbol{\alpha}_k^{(i)}(L)(y_{k,t} - h_{k,t}(\boldsymbol{\xi}^{(i)})}{\sigma^{(i)}}\right)^2}, \tag{16}$$

$$E_{W_{k,t}|u_{k,t};\boldsymbol{\theta}^{(i)}}\{\log W_{k,t}\} = \log w_{k,t}^{(i)} + \psi\left(\frac{\nu_k^{(i)} + 1}{2}\right) - \log\left(\frac{\nu_k^{(i)} + 1}{2}\right). \tag{17}$$

Consequently, we may rewrite (15) as

$$Q(\boldsymbol{\theta}|\boldsymbol{\theta}^{(i)}) = \text{const.} - \frac{n}{2}\sum_{k=1}^{N}\log(\sigma_k^2) - \sum_{k=1}^{N}\frac{1}{2\sigma_k^2}\sum_{t=1}^{n}w_{k,t}^{(i)}\left[\boldsymbol{\alpha}_k(L)(y_{k,t} - h_{k,t}(\boldsymbol{\xi}))\right]^2$$
$$+\frac{n}{2}\sum_{k=1}^{N}\nu_k\log\nu_k - n\sum_{k=1}^{N}\log\Gamma\left(\frac{\nu_k}{2}\right)$$
$$+\frac{n}{2}\sum_{k=1}^{N}\nu_k\left[\psi\left(\frac{\nu_k^{(i)} + 1}{2}\right) - \log\left(\nu_k^{(i)} + 1\right) + \frac{1}{n}\sum_{t=1}^{n}\left(\log w_{k,t}^{(i)} - w_{k,t}^{(i)}\right)\right]. \tag{18}$$

We see in light of (16) that the computation of initial weights requires initial parameter values. In cases where these are not given, we choose unit weights $w_{k,t}^{(0)} = 1$ for all $k = 1, \ldots, N$ and all $t = 1, \ldots, n$ for the subsequent M step.

3.2 The M Step

We break up the M step into four conditional maximization (CM) steps (see [10]), one for each of the parameter groups, and substituting the most recent

available estimates whenever needed. Since the regression function $h_{k,t}$ were assumed to be nonlinear functions of $\boldsymbol{\xi}$, it is linearized within the first CM-Step with respect to that parameter group. Choosing for the Taylor point the estimate $\boldsymbol{\xi}^{(i)}$ of the preceding iteration step, we obtain for the partial derivative of the Q-function with respect to ξ_j

$$\begin{aligned}
0 &= \frac{\partial}{\partial \xi_j} Q(\boldsymbol{\theta}|\boldsymbol{\theta}^{(i)}) = -\sum_{k=1}^{N} \frac{1}{2\sigma_k^2} \sum_{t=1}^{n} w_{k,t}^{(i)} \frac{\partial}{\partial \xi_j} \left[\boldsymbol{\alpha}_k(L)(y_{k,t} - h_{k,t}(\boldsymbol{\xi}))\right]^2 \\
&= -\sum_{k=1}^{N} \frac{1}{2\sigma_k^2} \sum_{t=1}^{n} w_{k,t}^{(i)} \frac{\partial}{\partial \xi_j} \left[\boldsymbol{\alpha}_k(L) \left(y_{k,t} - \left[h_{k,t}(\boldsymbol{\xi}^{(i)}) + \frac{\partial h_{k,t}(\boldsymbol{\xi}^{(i)})}{\partial \boldsymbol{\xi}} (\boldsymbol{\xi} - \boldsymbol{\xi}^{(i)}) \right] \right) \right]^2 \\
&= -\sum_{k=1}^{N} \frac{1}{2\sigma_k^2} \sum_{t=1}^{n} w_{k,t}^{(i)} \frac{\partial}{\partial \xi_j} \left[\boldsymbol{\alpha}_k(L) \left(\Delta y_{k,t} - \mathbf{A}_{k,t}^{(i)} \boldsymbol{\Delta\xi} \right) \right]^2,
\end{aligned}$$

where $\Delta y_{k,t} = y_{k,t} - h_{k,t}(\boldsymbol{\xi}^{(i)})$, $\boldsymbol{\Delta\xi} = \boldsymbol{\xi} - \boldsymbol{\xi}^{(i)}$, and $\mathbf{A}_{k,t}^{(i)} = \frac{\partial h_{k,t}(\boldsymbol{\xi}^{(i)})}{\partial \boldsymbol{\xi}}$. Denoting in addition $\mathbf{A}_{k,t,j}^{(i)} = \frac{\partial h_{k,t}(\boldsymbol{\xi}^{(i)})}{\partial \xi_j}$ and forming also the diagonal matrix $\mathbf{W}^{(i)}$ from the values $w_1^{(i)}, \ldots, w_n^{(i)}$, we can derive the system of m equations

$$\mathbf{0} = \sum_{k=1}^{N} \frac{1}{\sigma_k^2} \begin{bmatrix} \boldsymbol{\alpha}_k(L) A_{k,1,1}^{(i)} & \cdots & \boldsymbol{\alpha}_k(L) A_{k,n,1}^{(i)} \\ \vdots & & \vdots \\ \boldsymbol{\alpha}_k(L) A_{k,1,m}^{(i)} & \cdots & \boldsymbol{\alpha}_k(L) A_{k,n,m}^{(i)} \end{bmatrix} \mathbf{W}_k^{(i)} \begin{bmatrix} \boldsymbol{\alpha}_k(L)(\Delta y_{k,1} - \mathbf{A}_{k,1}^{(i)} \boldsymbol{\Delta\xi}) \\ \vdots \\ \boldsymbol{\alpha}_k(L)(\Delta y_{k,n} - \mathbf{A}_{k,n}^{(i)} \boldsymbol{\Delta\xi}) \end{bmatrix}.$$

Fixing now the values of the unknown scale parameters and AR coefficients by taking the estimates from the preceding M step i, we can filter the reduced observations and the Jacobi matrices (for every $k = 1, \ldots, N$ and every $t = 1, \ldots, n$) according to

$$\overline{\Delta y}_{k,t}^{(i)} := \boldsymbol{\alpha}_k^{(i)}(L) \Delta y_{k,t}, \qquad \overline{A}_{k,t,j}^{(i)} := \boldsymbol{\alpha}_k^{(i)}(L) A_{k,t,j}, \qquad \overline{\mathbf{A}}_{k,t}^{(i)} := \boldsymbol{\alpha}_k^{(i)}(L) \mathbf{A}_{k,t} \quad (19)$$

and restate the preceding normal equation system as

$$\begin{aligned}
\mathbf{0} &= \sum_{k=1}^{N} \frac{1}{(\sigma_k^2)^{(i)}} \begin{bmatrix} \overline{A}_{k,1,1}^{(i)} & \cdots & \overline{A}_{k,n,1}^{(i)} \\ \vdots & & \vdots \\ \overline{A}_{k,1,m}^{(i)} & \cdots & \overline{A}_{k,n,m}^{(i)} \end{bmatrix} \mathbf{W}_k^{(i)} \begin{bmatrix} \overline{\Delta y}_{k,1} - \overline{\mathbf{A}}_{k,1} \boldsymbol{\Delta\xi} \\ \vdots \\ \overline{\Delta y}_{k,n} - \overline{\mathbf{A}}_{k,n} \boldsymbol{\Delta\xi} \end{bmatrix} \\
&= \sum_{k=1}^{N} \frac{1}{(\sigma_k^2)^{(i)}} \overline{\mathbf{A}}_k^{(i)} \mathbf{W}_k^{(i)} \left(\overline{\boldsymbol{\Delta \mathbf{y}}}_k - \overline{\mathbf{A}}_k^{(i)} \boldsymbol{\Delta\xi} \right).
\end{aligned}$$

Consequently, the estimate of the update $\boldsymbol{\Delta\xi}$ is given by

$$\boldsymbol{\Delta\xi}^{(i+1)} = \left(\sum_{k=1}^{N} \frac{1}{(\sigma_k^2)^{(i)}} (\overline{\mathbf{A}}_k^{(i)})^T \mathbf{W}_k^{(i)} \overline{\mathbf{A}}_k^{(i)} \right)^{-1} \sum_{k=1}^{N} \frac{1}{(\sigma_k^2)^{(i)}} (\overline{\mathbf{A}}_k^{(i)})^T \mathbf{W}_k^{(i)} \overline{\boldsymbol{\Delta \mathbf{y}}}^{(i)}. \quad (20)$$

This update is added entirely or partially to the trial solution (in the sense of a Gauss-Newton step with step size $\gamma \in (0, 1]$), resulting in

$$\boldsymbol{\xi}^{(i+1)} = \boldsymbol{\xi}^{(i)} + \gamma \boldsymbol{\Delta\xi}^{(i+1)}. \tag{21}$$

In the first iteration step, we would typically use unit weight matrices $\mathbf{W}_k^{(0)} = \mathbf{I}_n$, neutral filters $\boldsymbol{\alpha}_k^{(0)}(L) = 1$ and identity scale factors $(\sigma_k^2)^{(i)} = 1$, corresponding to the initial assumption of normally distributed, uncorrelated and homoskedastic white noise components throughout all time series. For the subsequent CM step with respect to the autoregressive coefficients, the colored noise residuals

$$e_{k,t}^{(i+1)} := y_{k,t} - h_{k,t}(\boldsymbol{\xi}^{(i+1)}) \qquad (k = 1, \ldots, N; t = 1, \ldots, n). \tag{22}$$

will play a central role. We assemble for this purpose the matrices

$$\mathbf{E}_k^{(i+1)} := \begin{bmatrix} e_{k,0}^{(i+1)} & \cdots & e_{k,1-p_k}^{(i+1)} \\ \vdots & & \vdots \\ e_{k,n-1}^{(i+1)} & \cdots & e_{k,n-p_k}^{(i+1)} \end{bmatrix} \qquad (k = 1, \ldots, N), \tag{23}$$

in which we substitute the initial values $e_{k,0}^{(i+1)} = \ldots = e_{k,1-p_k}^{(i+1)} = 0$. Setting now the first partial derivative of (18) with respect to the jth AR coefficient within the Kth time series equal to zero, we have

$$\begin{aligned} 0 &= \frac{\partial}{\partial \alpha_{K,j}} Q(\boldsymbol{\theta}|\boldsymbol{\theta}^{(i)}) = -\frac{\partial}{\partial \alpha_{K,j}} \sum_{k=1}^{N} \frac{1}{2\sigma_k^2} \sum_{t=1}^{n} w_{k,t}^{(i)} \left[\boldsymbol{\alpha}_k(L)(y_{k,t} - h_{k,t}(\boldsymbol{\xi}))\right]^2 \\ &= -\frac{1}{2\sigma_K^2} \sum_{t=1}^{n} w_{K,t}^{(i)} \frac{\partial}{\partial \alpha_{K,j}} \left[\boldsymbol{\alpha}_K(L) e_{K,t}\right]^2. \end{aligned}$$

Substituting for the unknowns $\boldsymbol{\xi}$ within the residual $e_{K,t}$ the already available estimates $\boldsymbol{\xi}^{(i+1)}$ (according to the principle of conditional maximization) and collecting all j partial derivative with respect to the Kth time series in a single equation system, we obtain then for every $K = 1, \ldots, N$ the iteratively reweighted least squares scheme for the estimation of the AR coefficients $\boldsymbol{\alpha}_K$

$$\boldsymbol{\alpha}_K^{(i+1)} = \left((\mathbf{E}_K^{(i+1)})^T \mathbf{W}_K^{(i)} \mathbf{E}_K^{(i+1)} \right)^{-1} (\mathbf{E}_K^{(i+1)})^T \mathbf{W}_K^{(i)} \mathbf{e}_K^{(i+1)}. \tag{24}$$

Since we aim for covariance-stationary and invertible AR processes, it is necessary to determine whether all roots of $\boldsymbol{\alpha}_K^{(i+1)}(z) = 0$ are located within the unit circle. In case this is not true, we stabilize the preceding polynomial by mirroring all roots with magnitude exceeding 1 into the unit circle (cf. [15]), using MATLAB's `polystab` routine. We see from (24) that the individual AR processes can be determined independently, and we use them to filter the colored noise residuals according to (6) through

$$u_{k,t}^{(i+1)} = \boldsymbol{\alpha}_k^{(i+1)}(L) e_{k,t}^{(i+1)} \qquad (k = 1, \ldots, N; t = 1, \ldots, n) \tag{25}$$

in order to obtain the estimated white noise residuals. We are now in a position to estimate within the third CM step each scale factor σ_K^2 via the N independent conditions

$$\begin{aligned} 0 &= \frac{\partial}{\partial \sigma_K^2} Q(\boldsymbol{\theta}|\boldsymbol{\theta}^{(i)}) \\ &= -\frac{n}{2}\frac{\partial}{\partial \sigma_K^2}\log(\sigma_K^2) - \frac{\partial}{\partial \sigma_K^2}\frac{1}{2\sigma_K^2}\sum_{t=1}^{n} w_{K,t}^{(i)}\left[\boldsymbol{\alpha}_K(L)(y_{K,t}-h_{K,t}(\boldsymbol{\xi}))\right]^2, \end{aligned}$$

in which we substitute the current estimates $\boldsymbol{\xi}^{(i+1)}$ and $\boldsymbol{\alpha}_K^{(i+1)}$. Making use of (25), we therefore arrive at the solutions

$$(\sigma_K^2)^{(i+1)} = \frac{1}{n}\sum_{t=1}^{n} w_{K,t}^{(i)}\left(u_{K,t}^{(i+1)}\right)^2 = \frac{(\mathbf{u}_K^{(i+1)})^T \mathbf{W}_K^{(i)} \mathbf{u}_K^{(i+1)}}{n}. \tag{26}$$

It remains for us to compute the solutions for the degrees of freedom of the t-distributions underlying the N time series. Instead of using the Q-function for this purpose, we follow the recommendation of [7] and maximize the log-likelihood function (7) with respect to these parameters (which turns the current ECM algorithm into an ECME algorithm). Using the digamma function ψ, it can be shown that

$$\begin{aligned} 0 = \frac{\partial}{\partial \nu_K}\log\mathcal{L}(\boldsymbol{\theta};\mathbf{y}) &= \frac{n}{2}\psi\left(\frac{\nu_K+1}{2}\right) - \frac{n}{2}\psi\left(\frac{\nu_K}{2}\right) + \frac{n}{2}(\log\nu_K + 1) \\ &\quad -\frac{1}{2}\sum_{t=1}^{n}\log\left[\nu_K + \left(\frac{\boldsymbol{\alpha}_K(L)(y_{K,t}-h_{K,t}(\boldsymbol{\xi}))}{\sigma_K}\right)^2\right] \\ &\quad -\frac{1}{2}(\nu_K+1)\sum_{t=1}^{n}\left[\nu_K + \left(\frac{\boldsymbol{\alpha}_K(L)(y_{K,t}-h_{K,t}(\boldsymbol{\xi}))}{\sigma_K}\right)^2\right]^{-1} \end{aligned}$$

As with the previous three CM steps, we utilize the most up-to-date parameter estimates, now for $\boldsymbol{\xi}$, $\boldsymbol{\alpha}_1$, …, $\boldsymbol{\alpha}_N$, σ_1^2, …, σ_N^2. Denoting furthermore the desired solution by $\nu_K^{(i+1)}$ for every $K = 1, \ldots, N$, where we define $w_{K,t}^{(i+1)}$ in analogy to (16), we can derive the N equations

$$\begin{aligned} 0 &= \log\nu_K^{(i+1)} + 1 - \psi\left(\frac{\nu_K^{(i+1)}}{2}\right) + \psi\left(\frac{\nu_K^{(i+1)}+1}{2}\right) - \log\left(\nu_K^{(i+1)}+1\right) \\ &\quad +\frac{1}{n}\sum_{t=1}^{n}\left(\log w_{K,t}^{(i+1)} - w_{K,t}^{(i+1)}\right). \end{aligned} \tag{27}$$

Thus, the estimates $\nu_1^{(i+1)}$, …, $\nu_N^{(i+1)}$ constitute the zeros of these equations, which are to be found numerically (using for instance MATLAB's `fzero` routine). Note for normally distributed white noise components that these degrees of freedom tend to infinity, in which case the function on the right-hand side

of (27) does not change its sign. This numerical problem with the zero search is circumvented by testing for the existence sign change over a sufficiently large interval, say, over $[10^{-8}, 10^{8}]$; if this does not happen, the estimated degree of freedom should be set to a large value (say, to 10000). We stopped the reiteration in case the maximum number of iteration steps (500) was reached or in case the parameter values of the preceding step i did not change significantly within step $i+1$. We specified two thresholds with respect to largest maximum parameter changes: 10^{-4} for the degrees of freedom, and 10^{-8} for all other parameters.

4 Monte Carlo (MC) Results and Real World Application

4.1 The Framework of the Simulation

We consider in this section a multivariate, non-linear regression model in terms of a circle in $N = 3$ dimensions, having the following six parameters: two for the orientation (azimuth angle $\Phi \in [-\pi, \pi]$ and zenith angle $\theta \in [0, \pi]$) of its unit normal vector, one for the radius (r), and three for the circle center (C_x, C_y, C_z) (see pp. 24-27 in [11]). The observable 3D circle points are described by

$$\begin{pmatrix} X_t \\ Y_t \\ Z_t \end{pmatrix} = \begin{pmatrix} -r\cos(T_t)\sin(\Phi) + r\sin(T_t)\cos(\theta)\cos(\Phi) + C_x \\ r\cos(T_t)\cos(\Phi) + r\sin(T_t)\cos(\theta)\sin(\Phi) + C_y \\ -r\sin(T_t)\sin(\theta) + C_z \end{pmatrix} + \begin{pmatrix} E_{1,t} \\ E_{2,t} \\ E_{3,t} \end{pmatrix} \quad (28)$$

with $t = 1, \ldots, n$. In our current simulation study, $n = 100,000$ time instances in (28) are sampled equidistantly between $T_1 = 0$ and $T_n = 2\pi$ (corresponding to the time interval $[1, 10000]$ sec), and the circle parameters $\boldsymbol{\xi}$ were assumed to take the true values: $r = 0.487$ m, $\Phi = 0$ rad, $\theta = -\pi$ rad, $C_x = -2487.211$ m $C_y = -6053.041$ m and $C_z = -26.293$ m. according to a realistic scenario within the aforementioned application. Concerning the random deviations $\mathbf{E}_t$, we generated three different kinds of time series: (1) a pure white noise process, which may be viewed as an AR(0) process, (2) the AR(1) process

$$E_{k,t} = -0.9E_{k,t-1} + U_{k,t} \qquad (k = 1, \ldots, 3; t = 1, \ldots, n), \quad (29)$$

and (3) the ARMA(3,2) process (used for all $k = 1, \ldots, 3$)

$$E_{k,t} = -0.73E_{k,t-1} - 0.38E_{k,t-2} + 0.14E_{k,t-3} + U_{k,t} - 0.33U_{k,t-1} - 0.35U_{k,t-2}. \quad (30)$$

These models were investigated in the extensive study [8] (see pp. 230) on the stochastic modeling of GNSS data, where the white noise processes $U_{k,1}, \ldots, U_{k,n}$ were assumed to be Gaussian. Besides generating the white noise components $U_{k,1}, \ldots, U_{k,n}$ with the Gaussian sampling distributions

$$U_{1,t}, U_{2,t} \overset{\text{ind}}{\sim} N(0, 0.001^2), \;\; U_{3,t} \overset{\text{ind}}{\sim} N(0, 0.002^2), \quad (31)$$

we sampled also from the scaled t-distributions

$$U_{1,t}, U_{2,t} \overset{\text{ind}}{\sim} t_{2.5}(0, 0.001^2), \;\; U_{3,t} \overset{\text{ind}}{\sim} t_2(0, 0.002^2) \quad (32)$$

and from the contaminated normal distributions

$$U_{1,t}, U_{2,t} \overset{\text{ind}}{\sim} 0.6 \cdot N(0, 0.001^2) + 0.4 \cdot N(0, 0.008^2) \tag{33}$$

$$U_{3,t} \overset{\text{ind}}{\sim} 0.6 \cdot N(0, 0.002^2) + 0.4 \cdot N(0, 0.008^2) \tag{34}$$

to induce heavy tails or outliers. As the Z coordinates measured by GNSS are known to have much larger random fluctuations than the other coordinate components, the true variances in (31), true scale factors in (32) and true variances of the first Gaussian mixture component of (33) – (34) were chosen differently for the X/Y components (corresponding to $k = 1/k = 2$) and the Z component (associated with $k = 3$). Fluctuations due to systematic effects can also be expected to be largest for the Z components, so that the degree of freedom with respect to the variables $U_{3,t}$ in (32) is assumed to be less than for the components $U_{1,t}$ and $U_{2,t}$; thus, we assume the Student white noise in the Z coordinates (vertical coordinates) to be more heavy-tailed than the noise in the other components.

We generated 1000 random samples for the multivariate white noise series $\mathbf{U}_1, \ldots, \mathbf{U}_n$ from each of the distributions, from which we subsequently computed the corresponding noise series $\mathbf{E}_1, \ldots, \mathbf{E}_n$ and then via (28) the simulated observation time series $\mathbf{Y}_1, \ldots, \mathbf{Y}_n$. The proposed GEM algorithm was applied to each of these observation samples in order to estimate the six circle parameters, the coefficients of AR processes (having a suitable, identical order for each coordinate component), and the scale factors as well as degrees of freedom of the three underlying t-distributions. Note that neither the ARMA(3,2) model (30) nor the contaminated normal distributions (33) – (34) constitute special cases of the stochastic model (2) and (4) underlying the applied GEM algorithm.

4.2 Results of the Simulation and Real Data Application

Concerning the functional parameter $\boldsymbol{\xi}$, the Table 1 gives the means of the estimates of the first and third parameter ($\hat{r}$ and $\hat{\theta}$), computed from the 1000 MC runs. The approximation of the true parameter values by these means leads to bias free estimates for the AR(0) and AR(1) model. Only an insignificant bias in $\hat{\theta}$ in case of the ARMA(3,2) model can be detected.

To assess the goodness-of-fit of the AR models, a periodogram-based white noise test (WNT) is applied within each MC run to each of the three decorrelation-filtered residual series $\hat{u}_{k,1}$, $\hat{u}_{k,2}$ and $\hat{u}_{k,3}$. The test statistic determines the maximum cumulated periodogram excess over a cumulated, theoretical white noise periodogram (see [4] for detailed information concerning the computation of the test value). The white noise hypothesis is rejected if this maximum excess is larger than the critical value at a 95% significance level. More specifically, the critical value of the test is determined individually for each sample size n and each probability distribution in such a way that the acceptance rate, throughout all MC runs with generated random deviations e_1, e_2 and e_3 following the AR(0)-white noise model, is identical with the desired significance level 0.95. This critical value is then employed for the current sample size and probability distribution to determine the acceptance rates with respect to the estimated

AR(1) and ARMA(3,2) models. To approximate the ARMA(3,2) model in the applied GEM algorithm we increased the order an AR-processes gradually until the white noise test has been accepted. This results in appropriate model order 30. The WNT results are given in Table 1. Generally, the WNT acceptance rates increase with the AR model and reach 95,0% for AR(0). Apparently, the ARMA(3,2) models (approximated by an AR(30)) are estimated already reasonably well for this large sample size.

The performance of the estimation of the scale factor σ with respect to the $t_\nu(0, \sigma^2)$-distribution underlying the algorithm in Sect. 3 can be assessed only in the two cases that the white noise sampling distribution is (32) or (31), because the latter distributions are special cases of the family of scaled t-distributions. For the AR(0) and AR(1) models the mean value of the MC estimates $\hat{\sigma}$ coincides with the true value 0.001 for X/Y and 0.002 for Z (see Table 1). In contrast, for the ARMA(3,2) model the estimated scale factor is underestimated. In case of sampling by means of the contaminated normal (CN), the estimated scale factor can evidently not capture the effect of the two different variances in the data.

The evaluation of the algorithm's performance in estimating the degree of freedom of the underlying t-distribution is based on the mode of the MC estimates $\hat{\nu}$. As for the scale factor, the sampling distributions (31 and 32) allow for direct comparisons of the mode of the $\hat{\nu}$ with the corresponding true values $\nu = 2/2/2.5$ (with respect to X/Y/Z) and $\nu \to \infty$. The maximum value of an estimated $\hat{\nu}$ is 10000 for numerical reasons, which we therefore take as a sufficient approximation of $\nu \to \infty$. Table 1 shows that the degree of freedom tends to be overestimated for the ARMA(3,2) model.

Finally, the root mean square error (RMSE) measures the estimator's ability to predict the true observations. Since the predicted or adjusted observations are a consequence of the estimation of all four groups parameter groups $\boldsymbol{\xi}$, $\boldsymbol{\alpha}$, σ^2 and ν, the RMSE expresses the overall performance of the proposed GEM algorithm. This error measure includes both the variance and the bias of the estimator, and should therefore approach 0 for different AR models. The RMSE is computed for each MC run, and the resulting mean value is given in the Table 1. It can be seen that the mean of RMSE is substantially reduced with each increase in the AR model orders and for all error models. Only in case of t-distributed errors for the ARMA(3,2) model, one sample from the tail of the distribution occurred, which lead to an extreme estimation result and therefore to an unusually high RMSE value. To accommodate for this sampling effect we computed also the median of the RMSE values, as a robust measure of goodness of fit. As could be expected, the model reproductions based on the t- and the normal sampling distributions are much superior to the contaminated normal.

We also applied the GEM algorithm to approximate a measured and preprocessed 3D GNSS time series (see [12]) by the circle given in (28). One application of this model serves the geo-referencing of terrestrial laser scanner data where the 3D circle describes the circular, horizontal motion of two global navigation satellite system (GNSS) antenna reference points. Dual frequency receivers with individually and absolutely calibrated GNSS antennas were used. The origin of

the coordinates lies in the nearby reference station with a baseline length of approximately 14 m. For further information on the measurement setup (see [12], p. 69). A full rotation consists of 7609 points (acquired with a data rate of 1 Hz) with respect to one antenna. We employed an AR model of order 12 for each time series component. Figure 1 shows the adjusted circle and the observed 3D points. Having obtained an estimated degree of freedom of 10,000 for each component we conclude that given GNSS series are normally distributed.

Table 1. Estimation results based on 1000 MC runs from the generated Student (t), normal (N) and contaminated normal (CN) error models according to (31) - (34). For WNT acceptance rates, Mean($\hat{\sigma}$) and Mode($\hat{\nu}$) results are listed one below the other for the three time series components (X/Y/Z).

	AR(0)			AR(1)			ARMA(3,2)		
Error model	t	N	CN	t	N	CN	t	N	CN
Mean($\hat{r}$)	0.4874	0.4874	0.4874	0.4874	0.4874	0.4874	0.4874	0.4874	0.4874
Mean($\hat{\theta}$)	-3.141593	-3.141592	-3.141585	-3.141592	-3.141592	-3.141589	-3.141593	-3.141592	-3.141573
WNT	0.95	0.95	0.95	0.962	0.972	0.955	0.999	1	1
	0.95	0.95	0.95	0.962	0.972	0.955	0.999	1	1
	0.95	0.95	0.95	0.962	0.972	0.955	0.999	1	1
Mean($\hat{\sigma}$)	0.0010	0.0010	0.0616	0.0010	0.0010	0.0616	0.0006	0.0005	0.0296
	0.0010	0.0010	0.0616	0.0010	0.0010	0.0616	0.0006	0.0005	0.0296
	0.0020	0.0020	0.0663	0.0020	0.0020	0.0663	0.0012	0.0010	0.0318
Mode($\hat{\nu}$)	2.50	10000	10000	2.50	10000	10000	3.00	10000	10000
	2.50	10000	10000	2.50	10000	10000	3.01	10000	10000
	2.00	10000	10000	2.00	10000	10000	2.40	10000	10000
Mean(RMSE) $\times 10^{-6}$	8	6	271	4	3	142	7961	4	191
Median(RMSE) $\times 10^{-6}$	8	6	267	4	3	140	6	4	187

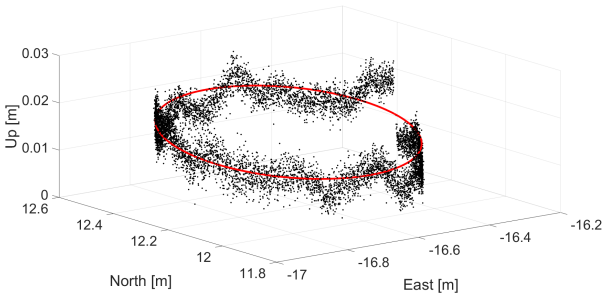

Fig. 1. 3D view of observed (black points) and adjusted circle (red line) for $n = 7827$ real three-dimensional GNSS measurements taken from [12], displayed in a North East Up (NEU) coordinate system.

5 Conclusions

To achieve an adaptive robust adjustment of a multivariate regression time series with outlier-afflicted/heavy-tailed and autocorrelated errors, we described the theory and implementation of a generalized expectation maximization algorithm. Monte Carlo simulations based on different error sampling distributions showed that the bias of the parameter estimates is insignificant when a sufficiently large number of observations (here 100,000) is adjusted. The presented algorithm was also tested in a real-data experiment using GNSS measurements.

References

1. Dempster, A.P., Laird, N.M., Rubin, D.B.: Maximum Likelihood from Incomplete Data via the EM Algorithm. J R Stat Soc (Series B) 39, 1-38 (1977)
2. Gupta, M.R., Chen, Y.: Theory and Use of the EM Algorithm. Foundations and Trends in Signal Processing 4, 223-296 (2011)
3. Koch, K.R., Kargoll, B.: Expectation Maximization Algorithm for the Variance-Inflation Model by Applying the t-Distribution. J Appl Geod 7, 217-225 (2013)
4. Kargoll, B., Omidalizarandi, M., Loth, I., Paffenholz, J.A., Alkhatib, H.: An Iteratively Reweighted Least-Squares Approach to Adaptive Robust Adjustment of Parameters in Linear Regression Models with Autoregressive and t-Distributed Deviations. Journal of Geodesy, https://doi.org/10.1007/s00190-017-1062-6 (2017)
5. Lange, K.L., Little, R.J.A., Taylor, J.M.G.: Robust Statistical Modeling Using the t-Distribution. J Am Stat Ass 84, 881-896 (1989)
6. Liu, C.H.: ML Estimation of the Multivariate t Distribution and the EM Algorithm. J Multivar Anal 63, 296-312 (1997)
7. Liu, C.H., Rubin, D.B.: The ECME Algorithm: A Simple Extension of EM and ECM with Faster Monotone Convergence. Biometrika 81, 633-648 (1994)
8. Luo, X.: GPS Stochastic Modelling: Signal Quality Measures and ARMA Processes. Springer, Berlin, Heidelberg (2013)
9. McLachlan, G.J., Krishnan, T.: The EM Algorithm and Extensions. John Wiley & Sons, Hoboken, New Jersey (2008)
10. Meng, X., Rubin, D.B.: Maximum Likelihood Estimation via the ECM Algorithm: A General Framework. Biometrika 80, 267-278 (1993).
11. Moon, P., Spencer, D.E.: Field Theory Handbook – Including Coordinate Systems, Differential Equations, and Their Solutions. 3rd edition. Springer, New York (1988)
12. Paffenholz, J.A.: Direct Geo-Referencing of 3D Point Clouds with 3D Positioning Sensors. PhD thesis. Deutsche Geodätische Kommission (Series C, 689), Munich, Online available under http://www.dgk.badw.de/fileadmin/docs/c-689.pdf (2013)
13. Park, M., Gao, Y.: Error and Performance Analysis of MEMS-based Inertial Sensors with a Low-cost GPS Receiver. Sensors 8, 2240-2261 (2008)
14. Phillips, R.F.: Least Absolute Deviations Estimation via the EM Algorithm. Statistics and Computing 12:281-285 (2002)
15. Porat, B.: Digital Processing of Random Signals. Dover, Mineola/New York (1994)
16. Schuh, W.D.: The Processing of Band-Limited Measurements; Filtering Techniques in the Least Squares Context and in the Presence of Data Gaps. Space Science Reviews 108, 67-78 (2003)
17. Wang, K., Xiong, S., Li, Y.: Modeling with Noises for Inertial Sensors. In: Position Location and Navigation Symposium (PLANS) 2012, IEEE/ION, 625-632 (2012)

Kurtosis Computations and Black-Scholes Model with GARCH Volatility

Muhammad Sheraz

Department of Mathematical Sciences & Department of Economics and Finance, Institute of Business Administration Karachi, Pakistan, msheraz@iba.edu.pk

Abstract

In Black-Scholes Model (BSM), the pricing of options is based on normality assumption of asset returns. The crucial assumption underlying the BSM model is that the underlying asset return dynamics are captured by the normal distribution with constant volatility. The option price is not a linear function of the underlying asset price, therefore when the portfolio contains options the pricing and modeling in risk management is complicated. Modeling of variance is one of the frequently used method of measuring risk. The time varying variance models such as GARCH models have been used extensively in this regard because these models are capable of describing the unconditional non-normality of the data. In order to allow the skewness and kurtosis the normal distribution model can be modified using various mathematical expansions. The study of stock price models under the GARCH volatility is a new horizon in derivative investment instruments. Duan was the first to provide a solid theoretical foundation for GARCH option pricing. In the recent past a Black-Scholes model with GARCH volatility was introduced. In this article we derive the kurtosis formula for underlying financial time series using BS-Model with GARCH volatility for the case of in the money option. We present the kurtosis formula in terms of the model's parameters. Also we compare our computational results by using another measure of kurtosis for different values of volatilities. We compare performance of GARCH volatility models for underlying financial time series data.

1. Introduction

Fischer Black and Myron Scholes published an option valuation formula in their 1973's article [3] that today is known as Black-Scholes model. The model has some restrictions for example; a constant risk frees interest rate r and a constant volatility σ which do not seem to be realistic. Trading option is risky due to the possibly high random components such as volatility. The concept of non-constant volatility was introduced by Bollerslev's GARCH process [7]. Duan was the first to provide a solid theoretical foundation for GARCH option pricing [9]. Recently a Black-Scholes model with GARCH volatility has been introduced [11]. The volatility measures, the variation of price of financial instrument over time and implied volatility can be derived from the market price of a traded derivative. In financial literature researchers use GARCH models frequently in order to forecast the volatility of underlying stock market [10]. Sheraz and Preda studied the case of at the money options to compute the kurtosis in Black-Scholes model with GARCH volatility [15]. Taylor series approximations have been

adfa, p. 1, 2011.

used extensively in option pricing. In Risk management particularly first and second order Taylor approximations are crucial. Taylor approximations have been also used in Black-Scholes option pricing formula [6,13].

In this article we consider Black-Scholes model with GARCH volatility [11]. In Section 2 Black-Scholes option pricing model and GARCH framework have been discussed. In Section 3 we present our results of kurtosis formula for the case of in the money option (ITM) and kurtosis of formula of a nonlinear time series if volatility process follows AGARCH-(0,1) model. In section 4 we present empirical performance of standard GARCH and Exponential GARCH models. Section 5 concludes our results.

2. Black-Scholes Model and GARCH Processes

Let $(\Omega, \mathcal{F}, P)$ be the probability space then price S of an asset at time t is a Geometric Brownian Motion (GBM).

$$dS_t = rS_t dt + \sigma S_t dW_t \tag{2.1}$$

where $\{W_t\}$ is a standard Brownian motion and $\sigma$is the volatility. We know that according to Black-Scholes option pricing model a European call option for a non-dividend paying stock if Black-Scholes framework is given by

$$C_{BSM} = S\phi(d_1) - Ke^{-r\tau}\phi(d_2) \tag{2.2}$$

where $d_1 = \frac{log\left(\frac{S}{K}\right)+\left(r+\frac{\sigma^2}{2}\right)\tau}{\sigma\sqrt{\tau}}$, $d_2 = d_1 - \sigma\sqrt{\tau}$ and $\phi(.)$ is a cumulative distribution function for standardized Normal random variable and $\tau = T - t$ and S is a price of an asset, $K$is the strike price, r is the interest rate and T denotes the time to expiry.

Definition 1 [3] If S is the stock price, r is risk free interest rate then C is a European call option that, gives its holder the right, but not the obligation to buy the one unit of underlying asset for a predetermined price K at the maturity date T.

When variance of the log of stock returns changes with time i.e. $\sigma = \theta_t$ then a Black-Scholes model with GARCH volatility for a financial time series let say y_t, is given by [11].

$$dS_t = rS_t dt + \theta_t S_t dW_t \tag{2.3}$$

$$y_t = log\left(\frac{S_t}{S_{t-1}}\right) - E\left(log\left(\frac{S_t}{S_{t-1}}\right)\right) = \theta_t Z_t \tag{2.4}$$

where $\{W_t\}$ is a standard Brownian motion and $\{\theta_t\}$ is a volatility process. The call option for the model is given by

$$C_{BSMG} = SE_{\theta_t}\big(\phi(d_1)\big) - Ke^{-r\tau}E_{\theta_t}\big(\phi(d_2)\big) \tag{2.5}$$

where

$$f\big(E(\theta_t^2)\big) = \phi(d_1) = \frac{log\left(\frac{S}{K}\right)+r\tau+\frac{E\left(\theta_t^2\right)}{2}}{\sqrt{E(\theta_t^2)}} \tag{2.6}$$

$$g\left(E(\theta_t^2)\right) = \phi(d_2) = \frac{log\left(\frac{S}{K}\right)+r\tau-\frac{E\left(\theta_t^2\right)}{2}}{\sqrt{E(\theta_t^2)}} \tag{2.7}$$

Definition 2 [7] $\theta_t$is a stationary GARCH process having mean μ_θ and variance σ_θ^2 and GARCH (*p*,*q*) process of Bollerslev (1986) is given by

$$\theta_t^2 = \omega + \sum_{i=1}^{p} \alpha_i \varepsilon_{t-i} + \sum_{j=1}^{q} \beta_j \theta_{t-j}^2 \tag{2.8}$$

$$\varepsilon_t = \theta_t Z_t$$

where, $Z_t \sim N(0, \sigma_\theta^2)$ and $\omega > 0, \alpha_i \geq 0, \beta_j \geq 0$. Option pricing based on GARCH models have been studied under the assumption that the innovations are standard normal (i.e. under normal GARCH).

Theorem 1 [11] For a twice differentiable functions f and g the call price (2.5) can be written as :

$$C_{BSMG} = S\left(f\left(E(\theta_t^2)\right) + \frac{1}{2}\ddot{f}\left(E(\theta_t^2)\right)\left(\frac{1}{3}k^{(y)} - 1\right)E^2(\theta_t^2)\right) - Ke^{-rT}\left(g\left(E(\theta_t^2)\right) + \frac{1}{2}\ddot{g}\left(E(\theta_t^2)\right)\left(\frac{1}{3}k^{(y)} - 1\right)E^2(\theta_t^2)\right) \tag{2.9}$$

where $k^{(y)} = \frac{E(y_t^4)}{E(y_t^2)}$ kurtosis of the observed log-returns y_t and $\ddot{f}\left(E(\theta_t^2)\right), \ddot{g}\left(E(\theta_t^2)\right)$ denote second order derivatives of $f\left(E(\theta_t^2)\right)$ and $g\left(E(\theta_t^2)\right)$ respectively therefore,

$$\ddot{f}\left(E(\theta_t^2)\right) = \frac{1}{\sqrt{2\pi}} e^{\left\{\frac{-\left(2\left(log\left(\frac{S}{K}\right)+rT\right)+E\left(\theta_t^2\right)\right)^2}{8E(\theta_t^2)}\right\}} \cdot \left[\frac{6\left(log\left(\frac{S}{K}\right)+rT\right)-E\left(\theta_t^2\right)}{8E(\theta_t^2)\sqrt{E(\theta_t^2)}} - \left(\frac{E^2(\theta_t^2)-4\left(log\left(\frac{S}{K}\right)+rT\right)^2}{8\left(E(\theta_t^2)\right)^2}\right)\left(\frac{E(\theta_t^2)-2\left(log\left(\frac{S}{K}\right)+rT\right)}{4E(\theta_t^2)\sqrt{E(\theta_t^2)}}\right)\right] \tag{2.10}$$

$$\ddot{g}\left(E(\theta_t^2)\right) = \frac{1}{\sqrt{2\pi}} e^{\left\{\frac{-\left(2\left(log\left(\frac{S}{K}\right)+rT\right)-E\left(\theta_t^2\right)\right)^2}{8E(\theta_t^2)}\right\}} \cdot \left[\frac{6\left(log\left(\frac{S}{K}\right)+rT\right)+E\left(\theta_t^2\right)}{8E^2(\theta_t^2)\sqrt{E(\theta_t^2)}} + \left(\frac{E^2(\theta_t^2)-4\left(log\left(\frac{S}{K}\right)+rT\right)^2}{\left(E(\theta_t^2)\right)^2}\right)\left(\frac{E(\theta_t^2)+2\left(log\left(\frac{S}{K}\right)+rT\right)}{4E(\theta_t^2)\sqrt{E(\theta_t^2)}}\right)\right] \tag{2.11}$$

Then for the case of ATM the value of the kurtosis in terms of the model's parameters for Black-Scholes call option with GARCH volatility is given by

$$k^{(y)} = \frac{768\left(\sqrt{\frac{2\pi}{E(\theta_t^2)}}\frac{C_{BSMG}}{S}-1\right)}{(E(\theta_t^2)+4)(E(\theta_t^2)-8)} + 3 \tag{2.12}$$

where C_{BSMG} is the value of call option for BS-model with GARCH volatility,S is the stock price and θ_t is the GARCH volatility. Consider different values of Call option C_{BSMG} and different stock prices S for BS-model with GARCH volatility proposed in Gong et al. (2010). We consider the kurtosis formula for different values of volatility.

Volatility	Call Price	Kurtosis (k)	Stock Price
		Classical	
0.3	25.33	19.473	400
0.3	20.40	20.848	405
0.3	15.58	22.162	410
0.4	25.33	20.202	400
0.4	20.40	21.382	405
0.4	15.58	22.508	410

3. Kurtosis Computations in Black-Scholes Model with GARCH Volatiltiy

An option is called in the money (ITM) if the strike price *K* and the current spot price *S* of the underlying asset are different. In the following theorem we propose a formula to compute kurtosis when Black-Scholes model follows GARCH volatility.

Theorem 2 For a twice differentiable functions f and g the call price (2.5) can be written as **:**

$$C_{BSMG} = S\big(fE(\theta_t^2)\big) - Ke^{-rT}g\big(E(\theta_t^2)\big) + \frac{1}{2}\Big(\frac{1}{3}k^{(y)} - 1\Big)\Big(S\ddot{f}\left(E(\theta_t^2)\right) - Ke^{-rT}\ddot{g}\left(E(\theta_t^2)\right)\Big)E^2(\theta_t^2) \tag{3.1}$$

Then for the case of ITM options the value of kurtosis is given by

$$k^{(y)} = \frac{6\Big(C_{BSMG} - \mathrm{w}E(\theta_t^2) - \sqrt{2\pi}v\sqrt{E(\theta_t^2)} - 2uv\Big)}{\Big(S\ddot{f}\left(E(\theta_t^2)\right) - Ke^{-rT}\ddot{g}\left(E(\theta_t^2)\right)\Big)E^2(\theta_t^2)} + 3 \tag{3.2}$$

where , $u = log\left(\frac{S}{K}\right) + rT$, $v = S - Ke^{-rT}$, $w = S + Ke^{-rT}$

Proof. Using the property, $d_1 - d_2 = \sqrt{E(\theta_t^2)}$ and expansion

$$\phi\big(E(\theta_t^2)\big) \cong \frac{1}{2} + \frac{1}{\sqrt{2\pi}}\left[E(\theta_t^2) - \frac{E^3(\theta_t^2)}{6} + \frac{E^5(\theta_t^2)}{40} - \dots\right]$$

we find

$$Sf(E(\theta_t^2) - Ke^{-rT}g\big(E(\theta_t^2)\big) = S\left(\frac{1}{2} + \frac{d_1}{\sqrt{2\pi}}\right) - Ke^{-rT}\left(\frac{1}{2} + \frac{d_2}{\sqrt{2\pi}}\right)$$
$$= \frac{S - Ke^{-rT}}{2} + \frac{1}{\sqrt{2\pi}}\left(Sd_1 - Ke^{-rT}\left(d_1 - \sqrt{E(\theta_t^2)}\right)\right)$$

$$= \left(\frac{1}{2} + \frac{d_1}{\sqrt{2\pi}}\right)(S - Ke^{-rT}) + \frac{Ke^{-rT}\sqrt{E(\theta_t^2)}}{\sqrt{2\pi}}$$

$$= \left(\frac{1}{2} + \frac{\log\left(\frac{S}{K}\right) + rT + \frac{E(\theta_t^2)}{2}}{\sqrt{2\pi}\sqrt{E(\theta_t^2)}}\right)(S - Ke^{-rT}) + \frac{Ke^{-rT}\sqrt{E(\theta_t^2)}}{\sqrt{2\pi}}$$

$$= \frac{(S+Ke^{-rT})E(\theta_t^2) + \sqrt{2\pi}(S-Ke^{-rT})\sqrt{E(\theta_t^2)} + 2(\log\left(\frac{S}{K}\right) + rT)(S-Ke^{-rT})}{2\sqrt{2\pi}\sqrt{E(\theta_t^2)}} \quad (3.3)$$

Now equation (3.1) can be written as :

$$\frac{1}{3}k^{(y)} - 1 = \frac{2\left(C_{BSMG} - \left(Sf\left(E(\theta_t^2)\right)\right) - Ke^{-rT}g\left(E(\theta_t^2)\right)\right)}{\left(S\ddot{f}\left(E(\theta_t^2)\right) - Ke^{-rT}\ddot{g}\left(E(\theta_t^2)\right)\right)E^2(\theta_t^2)}$$

$$k^{(y)} = \frac{6\left(C_{BSMG} - \left(Sf\left(E(\theta_t^2)\right)\right) - Ke^{-rT}g\left(E(\theta_t^2)\right)\right)}{\left(S\ddot{f}\left(E(\theta_t^2)\right) - Ke^{-rT}\ddot{g}\left(E(\theta_t^2)\right)\right)E^2(\theta_t^2)} + 3$$

Using equations (2.10), (2.11) and (3.3) we get equation (3.2).In example 3.1 we have considered data used in [11].

Example 3.1 Consider S= 425.33, K = 395, C_{BSMG}= 31.33, T = 24, r = 0.00008 and volatility is 0.1 then we obtain $k^{(y)}$= 39.28. Similarly if S= 425.68, K= 430, C_{BSMG}= 0.15 T = 24, r = 0.00008 and volatility is 0.1 then we obtain $k^{(y)}$= 67.

3.1 Nonlinear Time Series and Kurtosis

Nonlinear time series display features such as time-changing variance, asymmetric cycles, higher-moment structures, thresholds and breaks. Higher kurtosis indicates a peaked return distribution and a greater chance of extremely large deviations from the expected return. Recently, there has been growing development in the use of nonlinear volatility models in financial literature. Black-Scholes option pricing models has some contradictory assumptions, such as constant volatility and normally distributed log returns. In many financial time series, empirical studies reveal some facts such as stock returns and foreign exchange rates that exhibit leptokurtosis and stochastic volatility.

A sequence of random variables $\{y_t\}$ is called an RCA(1) time series if it satisfies the equation

$$y_t = (\phi + b_t)y_{t-1} + \varepsilon_t \quad , t \in \mathbb{Z} \quad (3.4)$$

The two necessary and sufficient conditions for second order stationarity of $\{y_t\}$ are as follows:

i. $\begin{pmatrix} b_t \\ \varepsilon_t \end{pmatrix} \sim \left(\begin{pmatrix} 0 \\ 0 \end{pmatrix}, \begin{pmatrix} \sigma_b^2 & 0 \\ 0 & \sigma_\varepsilon^2 \end{pmatrix}\right)$

ii. $\phi^2 + \sigma_b^2 < 1$

The sequences $\{b_t\}$ and $\{\varepsilon_t\}$ respectively, are the errors in the model. A full description of RCA models and others properties can be found in [1,15,]. Peiris et al [16] have studied a doubly stochastic model of the form given by

$$y_t = (\phi + b_t)y_{t-1} + \varepsilon_t \quad , t \in \mathbb{Z}$$
$$b_{t+1} = ab_t + (1 + b_t)v_{t+1} \quad , t \in \mathbb{Z} \tag{3.5}$$

The above model satisfies the following conditions.

i. $\begin{pmatrix} b_t \\ \varepsilon_t \end{pmatrix} \sim \left(\begin{pmatrix} 0 \\ 0 \end{pmatrix}, \begin{pmatrix} \sigma_b^2 & 0 \\ 0 & \sigma_\varepsilon^2 \end{pmatrix} \right)$

ii. $1 - a^2 - \sigma_v^2 < 1$

iii. $1 - a^2 - 2\sigma_v^2 - \phi^2 + \phi^2 a^2 + \phi^2 \sigma_v^2 < 1$

The asymmetric GARCH (AGARCH) by Engle and Ng and various other nonlinear GARCH extensions have been proposed to capture asymmetric effects [8]. Consider the doubly stochastic volatility process (3.5) with AGARCH (I) – (0,1) errors of the following form [19].

$$\varepsilon_t = \sigma_t Z_t$$
$$\sigma_t^2 = \omega + \alpha(\varepsilon_{t-1} + r)^2 \tag{3.6}$$

We can find using equation (3.5)

$$E(y_t^2) = \frac{(\omega + \alpha r^2)(1 - a^2 - \sigma_v^2)\sigma_z^2}{(1 - \alpha\sigma_z^2)(1 - a^2 - 2\sigma_v^2 - \phi^2 + \phi^2 a^2 + \phi^2 \sigma_v^2)} \tag{3.7}$$

$$E(y_t^4) = \frac{3\sigma_z^4 E(\sigma_t^4) + 6\sigma_z^2 (E(b_t^2) + \phi^2) E(\sigma_t^2) E(y_{t-1}^2)}{(1 - \phi^4 - E(b_t^4) - 6\phi^2 E(b_t^2) - 4\phi E(b_t^3))} \tag{3.8}$$

Then we can find the kurtosis of $\{y_t\}$ is given by

$$k^{(y)} = \frac{E(y_t^4)}{\left(E(y_t^2)\right)^2} \tag{3.9}$$

$$= \frac{\left(3\sigma_z^4 E(\sigma_t^4) + 6\sigma_z^2 (E(b_t^2) + \phi^2) E(\sigma_t^2) E(y_{t-1}^2)\right)\left(\left((1 - \alpha\sigma_z^2)(1 - a^2 - 2\sigma_v^2 - \phi^2 + \phi^2 a^2 + \phi^2 \sigma_v^2)\right)^2\right)}{(1 - \phi^4 - E(b_t^4) - 6\phi^2 E(b_t^2) - 4\phi E(b_t^3))\left(\left((\omega + \alpha r^2)(1 - a^2 - \sigma_v^2)\sigma_z^2\right)^2\right)}$$

4. **GARCH Modeling and Volatility Forecast**

If S_t is the the price of an asset and $t \in [0, T]$, R_t denotes log-return then mathematically $R_t = log\left(\frac{S_t}{S_{t-1}}\right)$ and generally in financial econometrics we write:

$$R_t = \mu + \varepsilon_t \quad , \varepsilon_t / \mathcal{F}_t \sim N(\mu, \sigma^2) \tag{4.1}$$

The distribution of error term ε_t (residuals) is conditional on information set $\mathcal{F}_t$ and assumed to follow a standard Gaussain distribution with mean zero and variance 1. There are various conditional distributions used in GARCH models such as Student-t , generalized error distribution, skewed normal , skewed student-t , skewed generalized error distributions, Johnson reparametrized distribution, generalized hyperbolic distribution and many others.

The generalized hyperbolic distribution reveals the fact that the logarithm of the density function is of hyperbolic shape. On other hand the logarithmic values of the normal distribution are parabolic. The density of the is given by

$$\mathrm{GHYP}(x;\lambda,\alpha,\beta,\delta,\mu) = a(\lambda,\alpha,\beta,\delta)(\delta^2+(x-\mu)^2)^{\frac{\lambda-\frac{1}{2}}{2}} \times K_{\lambda-\frac{1}{2}}\left(\alpha\sqrt{\delta^2+(x-\mu)^2}\right)e^{(\beta(x-\mu))} \quad (4.2)$$

where $\lambda,\mu\in\mathbb{R},\delta>0,0\le|\beta|<\alpha$ and, $a(\lambda,\alpha,\beta,\delta)=\frac{(\alpha^2-\beta^2)^{\lambda/2}}{\sqrt{2\pi}\alpha^{\lambda-\frac{1}{2}}\delta^{\lambda}K_{\lambda}\left(\delta\sqrt{\alpha^2-\beta^2}\right)}$

The parameter λ can be used to define further classes of GHYP distribution, where δ and μ are location and scale parameters respectively.
For $\lambda=1$ we get hyperbolic distribution, a special case of generalized hyperbolic distribution. In other word the parameter λ can be describes as a distribution class selection parameter. If we select $\lambda=-\frac{1}{2}$ we get the Normal inverse Gaussian distribution [5,17].The density function of NIG is given by

$$\mathrm{NIG}(x;\alpha,\beta,\delta,\mu)=\frac{\alpha\delta}{\pi}e^{\left(\delta\sqrt{\alpha^2-\beta^2}+\beta(x-\mu)\right)}\frac{K_1\left(\alpha\sqrt{\delta^2+(x-\mu)^2}\right)}{\sqrt{\delta^2+(x-\mu)^2}} \quad (4.3)$$

where $x,\mu\in\mathbb{R},0\le\delta,0\le|\beta|\le\alpha$. There are various types of GARCH models which have been frequently used in the financial literature. We consider one useful type called exponential GARCH (EGARCH) to model time series of European Brent Crude Oil. Nelson (1991) introduced EGARCH model [14].

$$log\sigma_t^2=\omega+\sum_{i=1}^{p}\alpha_i g(z_{t-i})+\sum_{j=1}^{q}\beta_j log\sigma_{t-j}^2 \quad (4.4)$$
$$g(z_{t-i})=\gamma z_{t-i}+\lambda(|z_{t-i}|-E|z_{t-i}|)$$

where $\omega,\alpha_i,\beta_j\gamma$, and λ are real parameters. The coefficient α_i captures the sign effect and λ the size effect. We used R package Quandl to download the daily prices of crude oil for the period 2008-2015. In Table 1 we present the descriptive statistics for the daily returns of our selected oil prices.

Table 1 Descriptive statistics for daily returns

Data	Min	Max	Mean	Var	SD	Skew	Kurt
2008-2015	16.832	18.129	-0.029	4.498	2.120	0.028	8.576

Model selection is always a crucial problem in any empirical study. The maximum value of likelihood functions (LH) could simply compare the two models when numbers of parameters are same, but for different number of parameters we can use Akaike Information Criterion (AIC for "n" number of parameters of model "m" with N observations. We want to estimate $\omega,\alpha,\beta,\gamma$ from the daily returns series. We fit the model to the data and investigate the output. It is evident that estimates of $\omega,\alpha,\beta,\gamma$ are all highly significant. The Jarque–Bera test suggest that the null hypothesis of joint zero skew and zero kurtosis is easily rejected. We also observe from the Box–Ljung test that the null hypothesis of independence of residuals is easily accepted.

Figure 1 Histogram and Time Series Plot

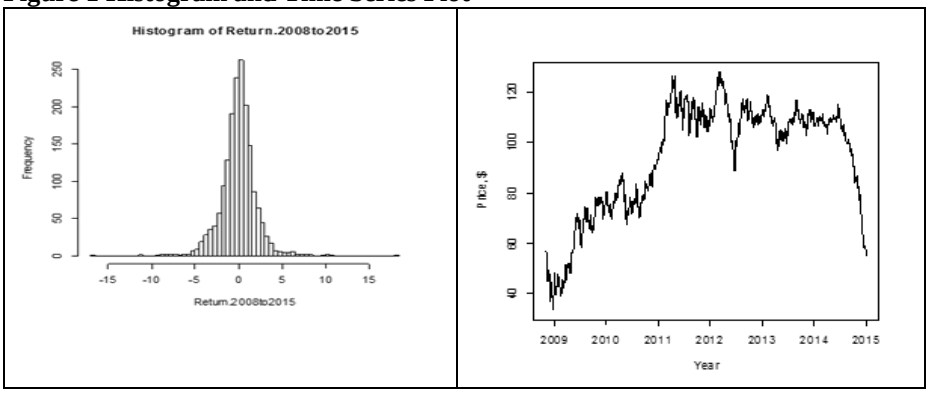

Table 2 Parameter Estimates of GARCH and EGARCH Models

Model	Dist	μ	ω	α	β	γ
GARCH	GHYP	-0.0447	0.0094	0.0452	0.9529	
GARCH	NIG	-0.0458	0.0094	0.0446	0.9535	
EGARCH	GHYP	-0.130	0.0030	-0.060	0.997	0.085
EGARCH	NIG	-0.131	0.0032	-0.061	0.997	0.083

For the returns from 2008-2015 EGARCH with Normal Inverse Gaussian Distribution (NIG) is the best fitted model based on AIC value. In Table 4 series and sigma forecast of underlying data series is given.

Table 3 Model Selection

Data	Model	Distribution	AIC
2008-2015	GARCH	GHYP	3.8860
	GARCH	NIG	3.8861
	EGARCH	GHYP	3.8748
	EGARCH	NIG	3.8738

Table 4 Series and Sigma Forecast EGARCH with Nig Distribution

Forecast	T+1	T+2	T+3	T+4	T+5
Series	-0.0485	0.0626	0.0225	0.0370	0.0317
Sigma	1.8489	1.8517	1.8545	1.8572	1.8599

5. Conclusions

Kurtosis describes the shape of the probability distribution curve. Positive excess kurtosis indicates that distribution has fatter tails than a normal distribution. In practice, return distributions for stocks and most other assets are not symmetric therefore high (low) value of kurtosis shows large(small) deviations from the expected returns. The

proposed kurtosis formula contains the parameters of BS models with GARCH volatility. An extension of GARCH models that is AGARCH-(0,1) has been discussed to obtain kurtosis formula of underlying financial time series. Empirical study results show that kurtosis value is greater than 3 which strongly affirms the non-Gaussian, return distribution.

References

1. Appadoo, S.S.,M. Ghahramani, M., Thavaneswaran,A.: Moment properties of some time series models, The Mathematical Scientist 30(1) (2005) 50–63 (2005)
2. Blest, D.C.: A new measure of kurtosis adjusted for skewness, ANZ Journal of Statistics 45(2), 175-179 (2003)
3. Black, F., Scholes, M.: The pricing of options and corporate liabilities. Journal of Political Economy 81, 637–659 (1973).
4. Black, F.: Studies of stock price volatility changes. In Proceedings of the American Statistical Association, Business and Economics Statistics Section, 177—81(1976)
5. Barndorff, Nielsen, O.: Normal inverse Gaussian distributions and stochastic volatility modelling, Scandinavian Journal of Statistics 24, 1–13 (1997)
6. Butler, J.S.,Schachter, B.:Unbiased estimation of the Black-Scholes formula, Journal of Financial Economics 15(3), 341-357 (1986)
7. Bollerslev,T.: Generalized autoregressive conditional heteroskedasticity, Journal of Econometrics 3(1), 307-327 (1986)
8. Engle, R. F., Ng, V. :(1993) Measuring and testing the impact of news on volatility, Journal of Finance 48, 1749–1777 (1993)
9. Duan, J.C.:The GARCH option pricing model, Mathematical Finanance 5, 3- 32(1992)
10. Fama, E.F.:The behavior of stock-market prices. Journal of Business 38, 1965, 34-105 (1965)
11. Gong,H, A. Thavaneswaean, A., Sing,J.: A Black-Scholes model with GARCH volatility, The Math Scientist 35, 37-42 (2010)
12. George, L.: Computational finance: Numerical methods for pricing financial instruments, Butterworth-Heinemann, Elsevier, (2004)
13. Latane,H.A., Rendleman, R.J., Standard deviation of stock price ratios implied by option premia , Journal of Finance, 31, 369-382 (1976)
14. Nelson, Daniel, B.: Conditional heteroscedasticity in asset pricing: a new approach Econometrica, 59,347–370 (1991)
15. Nicholls, D., Quinn, B.G.: Random Coefficient Autoregressive Models, An Introduction*:* Lector Notes in Statistics, Springer, New York, (1982)
16. Peiris, S., Thavaneswaran ,A., Appadoo,S.S., Doubly stochastic models with GARCH models, Applied Mathematic Letters 24, 1768–1773 (2011)
17. Prause, K.: Modelling finacial data using generalized hyperbolic distributions FDM Preprint. 48, University of Freiburg.(1997)
18. Sheraz, M.:Kurtosis in Black-Scholes model with GARCH volatility, U.P.B. Scientific Bulletin: Series A 78(1), 206-216 (2016)

19. Sheraz, M.: Doubly Stochastic Models with Asymmetric GARCH Errors, Proceedings of the Romanian Academy: Series A 15(2), 107-114 (2014)

Robust estimation of covariance and correlation functions of a stationary multivariate process

Higor Cotta[1,2], Valdério Reisen[1,2], Pascal Bondon[2], and Wolfgang Stummer[3]

[1]NuMEs - DEST/PGGEA - Federal University of Espírito Santo - Brazil
[2]L2S - CNRS - CentraleSupélec - France
[3]Department of Mathematics, University of Erlangen-Nürnberg - Germany
higor.cotta@l2s.centralesupelec.fr
valderio.reisen@ufes.br
pascal.bondon@l2s.centralesupelec.fr

Abstract. In this paper, the effect of additive outliers is considered in the estimation of the covariance and correlation matrix functions of a multivariate stationary process. Robust estimators of these matrices are presented to mitigate the effect of outliers. Some Monte Carlo simulations are carried out to empirically clarify the impact of additive outliers in the standard estimators and to assess the robustness of the proposed estimators. As an illustration, the proposed estimation method is applied to fit a vector autoregressive model to a real data set.

Keywords: Multivariate Time Series; Covariance Matrix; Outliers; Robust Estimation.

1 Introduction

The estimation of the covariance and correlation matrix functions is an important step in the identification and estimation of a multivariate time series model, e.g., for parameter estimation using the Yule-Walker equations. It is well known that outliers in time series affect the correlation structure of the data which may lead to erroneous estimators [1]. How to mitigate this phenomenon is still a challenging problem.

Robust estimation theory has been extensively studied in the statistical community since the 1970s following the seminal works of Huber and Maronna [2, 3]. Several efforts have been done by the time series community to weaken the impact of atypical observations. A concise review of the fundamentals can be found in [4].

In the univariate context, [5] proposed highly robust estimators of the autocovariance (ACOVF) and autocorrelation functions (ACF). The estimators use the so-called $Q_n(.)$ estimator proposed in [6] which has an appealing feature such as being location-free, a high breakdown point (50%) and a bounded influence function. The robustness and efficiency properties of the estimators have also been investigated through analysis of numerical experiments and real data analysis for univariate time series. For further details on these theoretical and

numerical studies, see [7]. For the multivariate context, highly robust estimation of the covariance and correlation matrices for time independent data sets are proposed in [8]. The case for time correlated data is the primary motivation of this work.

In this paper, we extend to a multivariate stationary time series the robust estimator of the autocovariance and the autocorrelation functions of a univariate stationary time series proposed by [5, 8]. We compare the proposed estimator to the sample estimator by means of temporal breakdown point and through Monte Carlo experiments.

This paper is organized as follows. In Section 2, the effect of additive outliers in the covariance and correlation matrix functions of a multivariate time series is shown, and the robust estimators of the covariance and correlation matrix functions are proposed. Section 3 presents some Monte Carlo experiments. A real data example is considered in Section 4 and some concluding remarks are provided in Section 5.

2 Robust estimation of covariance and correlation matrix functions

2.1 Linear Time Series

Let $\boldsymbol{X}_t = [X_{1,t}, X_{2,t}, \ldots, X_{k,t}]'$, $t \in \mathbb{Z}$ be a k-dimensional linear vector process defined by

$$\boldsymbol{X}_t = \boldsymbol{\mu} + \sum_{j=0}^{\infty} \boldsymbol{\Psi}_j \boldsymbol{\varepsilon}_{t-j}, \tag{1}$$

where $\boldsymbol{\mu} = [\mu_1, \ldots, \mu_k]'$ is the mean vector of $\{\boldsymbol{X}_t\}$, $\boldsymbol{\Psi}_0$ is the identity $k \times k$ matrix, $\boldsymbol{\Psi}_j$, $j = 1, \ldots, \infty$ are $k \times k$ matrices of coefficients satisfying $\sum_{j=0}^{\infty} \|\boldsymbol{\Psi}_j\|^2 < \infty$, where $\|A\|$ is the matrix norm of matrix A defined by $\|A\|^2 = \mathrm{Tr}(A'A)$. The process $\boldsymbol{\varepsilon}_t = [\varepsilon_{1,t}, \ldots, \varepsilon_{k,t}]'$ is a zero-mean vector white noise, i.e., $\mathrm{E}(\boldsymbol{\varepsilon}_t) = 0$ and $\mathrm{Cov}(\boldsymbol{\varepsilon}_t, \boldsymbol{\varepsilon}_{t+h}) = \Sigma_{\boldsymbol{\varepsilon}}\, 1_{\{h=0\}}$. Thus, although the elements of $\boldsymbol{\varepsilon}_j$ at different times are uncorrelated, they may be contemporaneously correlated. It results from (1) that

$$\boldsymbol{\gamma}^{\boldsymbol{X}}(h) = \mathrm{Cov}(\boldsymbol{X}_t, \boldsymbol{X}_{t+h}) = \sum_{j=0}^{\infty} \boldsymbol{\Psi}_j \Sigma_{\boldsymbol{\varepsilon}} \boldsymbol{\Psi}'_{j+h}, \quad h \geq 0. \tag{2}$$

The lag-h correlation matrix function of $\{\boldsymbol{X}_t\}$ is defined by

$$\boldsymbol{\rho}^{\boldsymbol{X}}(h) = \boldsymbol{D}^{-1/2} \boldsymbol{\gamma}^{\boldsymbol{X}}(h) \boldsymbol{D}^{-1/2}, \tag{3}$$

where $\boldsymbol{D} = \mathrm{diag}[\gamma_{11}^{\boldsymbol{X}}(0), \ldots, \gamma_{kk}^{\boldsymbol{X}}(0)]$. The (i,j)th element of $\boldsymbol{\rho}^{\boldsymbol{X}}(h)$ is

$$\rho_{ij}^{\boldsymbol{X}}(h) = \frac{\mathrm{Cov}(X_{i,t}, X_{j,(t+h)})}{\sqrt{\mathrm{Var}(X_{i,t})\,\mathrm{Var}(X_{j,t})}} = \frac{\gamma_{ij}^{\boldsymbol{X}}(h)}{\sqrt{\gamma_{ii}^{\boldsymbol{X}}(0)\gamma_{jj}^{\boldsymbol{X}}(0)}}. \tag{4}$$

We denote by $\hat{\boldsymbol{\gamma}}^{\boldsymbol{X}}(h)$ and $\hat{\boldsymbol{\rho}}^{\boldsymbol{X}}(h)$ the sample estimates of $\boldsymbol{\gamma}^{\boldsymbol{X}}(h)$ and $\boldsymbol{\rho}^{\boldsymbol{X}}(h)$, respectively, i.e., the estimate obtained by replacing the unknown covariances in (3) by their sample estimates.

A parametric class of linear time series satisfying (1) is the vector autoregressive moving average (VARMA) model of orders (p, q) defined by the difference equation

$$\boldsymbol{\Phi}(B)(\boldsymbol{X}_t - \boldsymbol{\mu}) = \boldsymbol{\Theta}(B)\boldsymbol{\varepsilon}_t, \tag{5}$$

where B is the backward shift operator ($B\boldsymbol{X}_t = \boldsymbol{X}_{t-1}$), $\boldsymbol{\Phi}(B) = I - \sum_{i=1}^{p} \boldsymbol{\Phi}_i B^i$ and $\boldsymbol{\Theta}(B) = I + \sum_{i=1}^{q} \boldsymbol{\Theta}_i B^i$ where $\boldsymbol{\Phi}_i$ and $\boldsymbol{\Theta}_i$ are $k \times k$ matrices, and $\{\boldsymbol{\varepsilon}_t\}$ is a zero-mean vector white noise process. When the polynomials $\boldsymbol{\Phi}(z)$ and $\boldsymbol{\Theta}(z)$ satisfy $\det(\boldsymbol{\Phi}(z)) \neq 0$ and $\det(\boldsymbol{\Theta}(z)) \neq 0$ for all $z \in \mathbb{C}$ such that $|z| \leq 1$, (5) has a unique stationary causal and invertible solution and the matrices $\boldsymbol{\Psi}_j$ are determined uniquely by $\boldsymbol{\Psi}(z) = \sum_{j=0}^{\infty} \boldsymbol{\Psi}_j z^j = \boldsymbol{\Phi}^{-1}(z)\boldsymbol{\Theta}(z)$ for $|z| \leq 1$.

2.2 Impact of additive outliers in multivariate time series

Outliers can affect the dependence structure of a multivariate time series. In this section, some results related to the effects of outliers on the covariance and correlation structures of a correlated process are derived. We suppose that the observed process $\{\boldsymbol{Z}_t\}$ results from the contamination of $\{\boldsymbol{X}_t\}$ by additive random outliers, i.e.,

$$\boldsymbol{Z}_t = \boldsymbol{X}_t + \boldsymbol{\Omega}\boldsymbol{\delta}_t, \tag{6}$$

where $\boldsymbol{\Omega} = \text{diag}[\omega_1, ..., \omega_k]$ and $\omega_i, i = 1, ..., k$, is the magnitude of the outliers which affects $\{X_{i,t}\}$, $\boldsymbol{\delta}_t = [\delta_{1,t}, ..., \delta_{k,t}]'$ is a random vector indicating the occurrence of an outlier at time t. We assume that $\{\boldsymbol{X}_t\}$ and $\{\boldsymbol{\delta}_t\}$ are uncorrelated processes and that $\mathbb{P}(\delta_{i,t} = -1) = \mathbb{P}(\delta_{i,t} = 1) = p_i/2$, $\mathbb{P}(\delta_{i,t} = 0) = 1 - p_i$ for $i = 1, \ldots, k$ where $0 \leq p_i < 1$. Then $\text{E}(\delta_{i,t}) = 0$ and $\text{Var}(\delta_{i,t}) = p_i$. We assume also that $\text{Cov}(\boldsymbol{\delta}_t, \boldsymbol{\delta}_t) = \Sigma_{\boldsymbol{\delta}} = \text{diag}[p_1, ..., p_k]$ and that $\text{Cov}(\boldsymbol{\delta}_t, \boldsymbol{\delta}_{t+h}) = 0$ when $h \neq 0$.

It follows from (6) that $\text{E}(\boldsymbol{Z}_t) = \text{E}(\boldsymbol{X}_t)$, $\boldsymbol{\gamma}^{\boldsymbol{Z}}(0) = \boldsymbol{\gamma}^{\boldsymbol{X}}(0) + \boldsymbol{\Omega}\Sigma_{\boldsymbol{\delta}}\boldsymbol{\Omega}'$ and $\boldsymbol{\gamma}^{\boldsymbol{Z}}(h) = \boldsymbol{\gamma}^{\boldsymbol{X}}(h)$ when $h \neq 0$. Therefore

$$\rho_{ij}^{\boldsymbol{Z}}(h) = \begin{cases} \frac{\gamma_{ij}^{\boldsymbol{X}}(h)}{\sqrt{(\gamma_{ii}^{\boldsymbol{X}}(0)+p_i\omega_i^2)(\gamma_{jj}^{\boldsymbol{X}}(0)+p_j\omega_j^2)}}, & h \neq 0, \\ \frac{\gamma_{ij}^{\boldsymbol{X}}(0)+p_i\omega_i^2\, 1_{\{i=j\}}}{\sqrt{(\gamma_{ii}^{\boldsymbol{X}}(0)+p_i\omega_i^2)(\gamma_{jj}^{\boldsymbol{X}}(0)+p_j\omega_j^2)}}, & h = 0. \end{cases} \tag{7}$$

We observe that $\rho_{ij}^{\boldsymbol{Z}}(h) \to 0$ as $|\omega_i| \to \infty$ or $|\omega_j| \to \infty$ when $h \neq 0$, these conclusions are deeper analyzed in Proposition 1. The works of [9] and [10] discuss this problem in univariate time series with short and long memory properties.

Proposition 1. *Suppose that $\boldsymbol{Z}_{1,t}, \boldsymbol{Z}_{2,t}, \ldots, \boldsymbol{Z}_{n,t}$ is a set of k-dimensional time series observations satisfying* (6) *and m is the total number of additive outliers affecting these observations. Let $\hat{\rho}_{ij}^{\boldsymbol{Z}}(h) = \hat{\gamma}_{ij}^{\boldsymbol{Z}}(h)/(\sqrt{\hat{\gamma}_{ii}^{\boldsymbol{Z}}(0)\hat{\gamma}_{jj}^{\boldsymbol{Z}}(0)})$, for all $i, j = 1, \ldots, k$.*

a. Assume that $m = 1$, say only one outlier occurring at $\{Z_{i,t}\}$ for a given pair (i, t). Then, for any $j = 1, \ldots, k$ and $h \neq 0$, we have

$$\lim_{n\to\infty} \operatorname*{plim}_{\omega_i\to\infty} \hat{\rho}_{ij}^{\boldsymbol{Z}}(h) = 0.$$

b. Assume that $m = 2$, say only two outliers occurring at $\{Z_{i,t}\}$ and $\{Z_{j,t^*}\}$, where when $t = t^*$, necessarily $i \neq j$, and when $t \neq t^*$, we may have $i = j$ or $i \neq j$. Then, for any $h \neq 0$, we have

$$\lim_{n\to\infty} \operatorname*{plim}_{\substack{\omega_i\to\infty \\ and/or \\ \omega_j\to\infty}} \hat{\rho}_{ij}^{\boldsymbol{Z}}(h) = 0.$$

The proof of Proposition 1 follows the same lines as in [9,10] and is not presented here to save space. Proposition 1 shows that the presence of additive outliers in the process leads to a decreasing of the correlation which is due to the increasing of the variability. This phenomenon is observed as long as one series contains at least one outlier.

2.3 Robust estimation of the covariance and correlation matrix functions

Let $X_1, \ldots, X_n$ be independent and identically distributed univariate random variables with finite variance, and let $\boldsymbol{X} = (X_1, \ldots, X_n)'$. The $Q_n(.)$ estimator of the standard deviation of X_1 is the kth order statistic defined by

$$Q_n(\boldsymbol{X}) = c\,\{|X_i - X_j|; i < j\}_{\{k\}}, \quad i, j = 1, .., n, \tag{8}$$

where c is a constant to guarantee consistency ($c = 2.2191$ when X_1 is Gaussian), $k = \lfloor \binom{n}{2}+2)/4 \rfloor + 1$ and $\lfloor x \rfloor$ is the largest integer smaller than x. The asymptotic breakdown point of $Q_n(\boldsymbol{X})$ is 50%, see [6].

For any univariate second order random variables X and Y, we have

$$\mathrm{Cov}(X, Y) = \frac{\alpha\beta}{4}\big(\mathrm{Var}(X/\alpha + Y/\beta) - \mathrm{Var}(X/\alpha - Y/\beta)\big), \tag{9}$$

for any $\alpha, \beta \in \mathbb{R}$.

Now, let $\{X_t\}$, $t \in \mathbb{Z}$, be a univariate stationary time series with finite variance. Taking $\alpha = \beta$ in (9) and replacing Var(.) by $Q_n^2(.)$, [5] proposed the following highly robust estimate of the autocovariance function of $\{X_t\}$,

$$\hat{\gamma}_{Q_n}(h) = \frac{1}{4}\left(Q_{n-h}^2(\boldsymbol{U} + \boldsymbol{V}) - Q_{n-h}^2(\boldsymbol{U} - \boldsymbol{V})\right), \tag{10}$$

where $\boldsymbol{U} = (X_1, \ldots, X_{n-h})'$ and $\boldsymbol{V} = (X_{h+1}, \ldots, X_n)'$. The autocorrelation function of $\{X_t\}$ can be estimated by

$$\hat{\rho}_{Q_n}(h) = \frac{Q_{n-h}^2(\boldsymbol{U} + \boldsymbol{V}) - Q_{n-h}^2(\boldsymbol{U} - \boldsymbol{V})}{Q_{n-h}^2(\boldsymbol{U} + \boldsymbol{V}) + Q_{n-h}^2(\boldsymbol{U} - \boldsymbol{V})}. \tag{11}$$

The consistency and asymptotic normality of $\hat{\gamma}_{Q_n}(h)$ and $\hat{\rho}_{Q_n}(h)$ are studied in [7] and [11] when $\{X_t\}$ is a short and a long memory process.

In this work, we extend to multivariate time series the estimators (10) and (11). Let $\{\boldsymbol{X}_t\}$ be a k-dimensional stationary vector process with finite variance, we robustly estimate $\boldsymbol{\gamma}^{\boldsymbol{X}}(h)$ by

$$\hat{\boldsymbol{\gamma}}_{Q_n}(h) = [\hat{\gamma}_{Q_{n-h}}^{(X_{i,t},X_{j,t})}(h)]_{i,j=1}^{k} \tag{12}$$

where,

$$\hat{\gamma}_{Q_{n-h}}^{(X_{i,t},X_{j,t})}(h) = \frac{\alpha\beta}{4}\left(Q_{n-h}^2\left(\frac{\boldsymbol{U}}{\alpha}+\frac{\boldsymbol{V}}{\beta}\right) - Q_{n-h}^2\left(\frac{\boldsymbol{U}}{\alpha}-\frac{\boldsymbol{V}}{\beta}\right)\right), \tag{13}$$

$\boldsymbol{U} = (X_{i,1}\ldots, X_{i,n-h})'$, $\boldsymbol{V} = (X_{j,h+1},\ldots,X_{j,n})'$, $\alpha = Q_n(X_{i,t})$ and $\beta = Q_n(X_{j,t})$. The correlation matrix function of $\{\boldsymbol{X}_t\}$ can be estimated by

$$\hat{\boldsymbol{\rho}}_{Q_n}(h) = [\hat{\rho}_{Q_{n-h}}^{(X_{i,t},X_{j,t})}]_{i,j=1}^{k} \tag{14}$$

$$\hat{\rho}_{Q_{n-h}}^{(X_{i,t},X_{j,t})} = \frac{Q_{n-h}^2\left(\frac{\boldsymbol{U}}{\alpha}+\frac{\boldsymbol{V}}{\beta}\right) - Q_{n-h}^2\left(\frac{\boldsymbol{U}}{\alpha}-\frac{\boldsymbol{V}}{\beta}\right)}{Q_{n-h}^2\left(\frac{\boldsymbol{U}}{\alpha}+\frac{\boldsymbol{V}}{\beta}\right) + Q_{n-h}^2\left(\frac{\boldsymbol{U}}{\alpha}-\frac{\boldsymbol{V}}{\beta}\right)}, \tag{15}$$

where $\boldsymbol{U}$, $\boldsymbol{V}$, α and β are defined in (13).

2.4 Temporal breakdown point

The breakdown point of an estimator is the largest proportion of data that may be considered as outliers, and the estimator still gives relevant information about the distribution of the uncontaminated data, see [3]. Contrarily to the case of non-correlated data, the position of atypical observations in a correlated time series leads to different perturbations patterns. Therefore, the concept of breakdown point of an estimator was extended to the time series context by [5] to accommodate the time location of the outliers.

It is known that the sample autocovariance function has a sample breakdown point of zero and its temporal breakdown point is also zero for any lag. As pointed by [5], (10) and (11) have temporal breakdown point of 25%. Now, consider the construction of $\mathbf{U}$ and $\mathbf{V}$ from $\{\boldsymbol{X}_t\}$, as in (13). One may see that the worst scenario happens when both series $\{X_{i,t}\}$ and $\{X_{j,t}\}$ contain outliers spaced by h observations, for a given lag $h \geq 1$. In this scenario, the highly robust estimator of the covariance and correlation matrix functions given by (13) and (15), respectively, have a temporal breakdown point of 25%. That is, as long as the combined number of outliers presented in $\{X_{i,t}\}$ and $\{X_{j,t}\}$ is not superior to 25%, the proposed estimators still provide reliable estimates of the correlation or covariance matrix. To verify this, note the construction of $\mathbf{U}$ and $\mathbf{V}$, where pairs composed by $\{X_{i,t}\}$ and $\{X_{j,t}\}$ are made. Each pair can be seen as one observation, thus leading to (13) and (15), sharing the same robust properties of (10) and (11). This property will be empirically investigated in Section 3.

3 Empirical results

This section reports the results of several Monte Carlo experiments to empirically analyze the impact of additive outliers on the autocorrelation function.

The computational experiments were performed using the R programming language and estimators that we propose are available in the *tsqn* package on "The Comprehensive R Archive Network (CRAN-R)".

The process $\{\boldsymbol{X}_t\}$ is generated as in (5) where $k = 3$, $(p, q) = (1, 0)$, $\boldsymbol{\mu} = 0$,

$$\boldsymbol{\Phi}_1 = \begin{bmatrix} 0.6 & 0.3 & 0.0 \\ 0.1 & 0.2 & 0.0 \\ 0.1 & 0.8 & 0.4 \end{bmatrix}, \tag{16}$$

and $\{\boldsymbol{\varepsilon}_t\}$ is a zero-mean Gaussian white noise process with covariance matrix

$$\boldsymbol{\Sigma}_{\boldsymbol{\varepsilon}} = \begin{bmatrix} 1.00 & 0.70 & 0.70 \\ 0.70 & 1.00 & 0.95 \\ 0.70 & 0.95 & 1.00 \end{bmatrix}. \tag{17}$$

The contaminated process $\{\boldsymbol{Z}_t\}$ is simulated according to (6) where $\omega_i = 4\sqrt{\mathrm{Var}(X_{i,t})}$ and $p_i, i = 1, 2, 3$ are given in the plots and tables. The sample size n is 500 and each experiment is repeated 1000 times. The sample estimate $\hat{\boldsymbol{\rho}}^{\boldsymbol{Z}}(h)$ is defined in the same manner as $\hat{\boldsymbol{\rho}}^{\boldsymbol{X}}(h)$ and $\hat{\boldsymbol{\rho}}^{\boldsymbol{Z}}_{Q_n}(h)$ is obtained by (14) where $\{\boldsymbol{X}_t\}$ is replaced by $\{\boldsymbol{Z}_t\}$. The means of $\hat{\boldsymbol{\rho}}^{\boldsymbol{X}}(h)$, $\hat{\boldsymbol{\rho}}^{\boldsymbol{X}}_{Q_n}(h)$, $\hat{\boldsymbol{\rho}}^{\boldsymbol{Z}}(h)$ and $\hat{\boldsymbol{\rho}}^{\boldsymbol{Z}}_{Q_n}(h)$ are computed over the 1000 replications for each lag h, $0 \leq h \leq 7$.

Figure 1 displays the true value $\rho^{\boldsymbol{X}}_{11}(h)$ and the estimates $\hat{\rho}^{\boldsymbol{X}}_{11}(h)$, $\hat{\rho}^{X_{1,t}}_{Q_{n-h}}(h)$, $\hat{\rho}^{\boldsymbol{Z}}_{11}(h)$ and $\hat{\rho}^{Z_{1,t}}_{Q_{n-h}}(h)$. Figure 2 plots the true value $\rho^{\boldsymbol{X}}_{12}(h)$ and the estimates $\hat{\rho}^{\boldsymbol{X}}_{12}(h)$, $\hat{\rho}^{(X_{1,t},X_{2,t})}_{Q_{n-h}}(h)$, $\hat{\rho}^{\boldsymbol{Z}}_{12}(h)$ and $\hat{\rho}^{(Z_{1,t},Z_{2,t})}_{Q_{n-h}}(h)$. For the other components of $\{\boldsymbol{X}_t\}$ and $\{\boldsymbol{Z}_t\}$, we obtain similar figures. In both figures, the effects of additive outliers appears by comparing the true correlation to the sample estimates $\hat{\boldsymbol{\rho}}^{\boldsymbol{Z}}(h)$ obtained in the contaminated case. Indeed, the values $\hat{\rho}^{\boldsymbol{Z}}_{11}(h)$ and $\hat{\rho}^{\boldsymbol{Z}}_{12}(h)$ are much smaller than $\rho^{\boldsymbol{X}}_{11}(h)$ and $\rho^{\boldsymbol{X}}_{12}(h)$, respectively. These graphical results empirically confirms Proposition 1, and are also in accord with the discussion in [7, 10] for the univariate context. In addition, we observe on both figures that the sample and the robust estimators have similar behaviors in the absence of contamination. Thus, in a practical situation, when the practitioner is uncertain of the presence outliers, (13) and (15) are still reasonable choices. When there are outliers in all components of the vector time series, i.e., $p_i \neq 0$ for all i, the sample estimator is clearly affected by additive outliers while the robust estimator is not much affected when the percentage of contamination is 5%. Therefore (13) and (15) are good alternatives when outliers are present in the data.

In Table 1, we present the root mean squared errors (RMSE) of $\hat{\rho}^{\boldsymbol{X}}_{11}(h)$, $\hat{\rho}^{X_{1,t}}_{Q_{n-h}}(h)$, $\hat{\rho}^{\boldsymbol{Z}}_{11}(h)$ and $\hat{\rho}^{Z_{1,t}}_{Q_{n-h}}(h)$. Table 2, gives the RMSE of $\hat{\rho}^{\boldsymbol{X}}_{12}(h)$, $\hat{\rho}^{(X_{1,t},X_{2,t})}_{Q_{n-h}}(h)$, $\hat{\rho}^{\boldsymbol{Z}}_{12}(h)$ and $\hat{\rho}^{(Z_{1,t},Z_{2,t})}_{Q_{n-h}}(h)$. From both tables, we observe that the sample and the robust estimators have RMSE close to the each other in the absence of contamination while the RMSE of the sample estimate is much larger than the RMSE of the robust estimator when the percentage of contamination is 5%. Moreover, the RMSE of the robust estimator is almost the same in the uncontaminated and the contaminated cases. It is also noted the reduction of the RMSE as the correlations decay to zero.

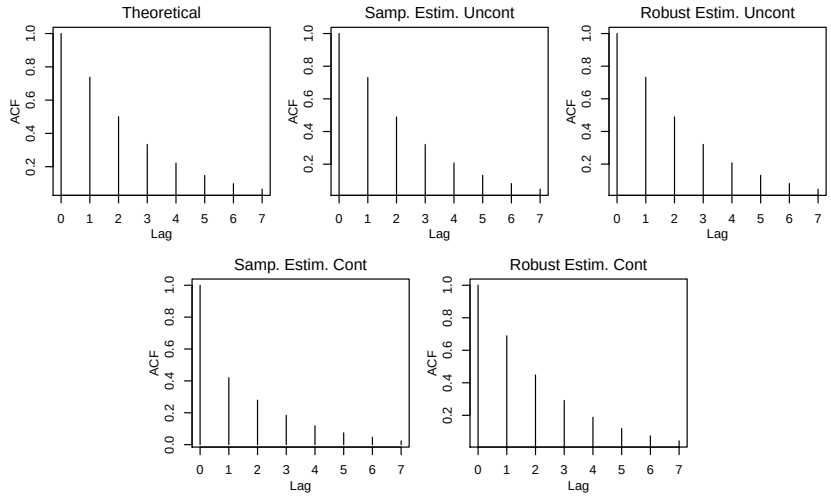

Fig. 1. Autocorrelation function of $\{Z_{1,t}\}$. From left to right and top to bottom, plots are $\rho_{11}^{\boldsymbol{X}}(h)$, $\hat{\rho}_{11}^{\boldsymbol{X}}(h)$, $\hat{\rho}_{Q_{n-h}}^{X_{1,t}}(h)$, and $\hat{\rho}_{11}^{\boldsymbol{Z}}(h)$, $\hat{\rho}_{Q_{n-h}}^{Z_{1,t}}(h)$ when $p_i = 0.05$, $i = 1, 2, 3$.

Table 1. RMSE of $\hat{\rho}_{11}^{\boldsymbol{X}}(h)$, $\hat{\rho}_{Q_{n-h}}^{X_{1,t}}(h)$, $\hat{\rho}_{11}^{\boldsymbol{Z}}(h)$ and $\hat{\rho}_{Q_{n-h}}^{Z_{1,t}}(h)$ when $p_i = 0.05$, $i = 1, 2, 3$.

Lag h	0	1	2	3	4	5	6	7
$\hat{\rho}_{11}^{\boldsymbol{X}}(h)$	0.00000	0.03050	0.05138	0.06391	0.06965	0.07290	0.07506	0.07590
$\hat{\rho}_{Q_{n-h}}^{X_{1,t}}(h)$	0.00000	0.03257	0.05545	0.06855	0.07450	0.07740	0.08050	0.08187
$\hat{\rho}_{11}^{\boldsymbol{Z}}(h)$	0.00000	0.33091	0.23215	0.16371	0.11777	0.09080	0.07516	0.06827
$\hat{\rho}_{Q_{n-h}}^{Z_{1,t}}(h)$	0.00000	0.06132	0.07724	0.07927	0.07782	0.07682	0.07804	0.07806

In order to empirically investigate the breakdown point of the proposed estimator, the RMSE of $\hat{\rho}_{12}^{\boldsymbol{Z}}(h)$ and $\hat{\rho}_{Q_{n-h}}^{(Z_{1,t},Z_{2,t})}(h)$ as the percentage of outliers in $\{\boldsymbol{Z}_t\}$ increases are presented in Tables 3 and 4, respectively. Remark that outliers are present in both $\{Z_{1,t}\}$ and $\{Z_{2,t}\}$. Comparing both tables, note that increasing the percentage of outliers in each series reduces the performance of both estimators. However, not surprisingly, $\hat{\rho}_{Q_{n-h}}^{(Z_{1,t},Z_{2,t})}(h)$ is less affect by the outliers.

4 Real data example

In this real data example, we consider the estimation of the samples correlation function (CF) of the monthly personal consumption expenditure (PCE) and disposable personal income (DSPI) of the United States from January 1959 to March 2012 obtained from the Federal Reserve Bank of St. Louis (FRED Economic Data). This data set has 639 observations and has already been considered as an example in [12]. As pointed out by the author, the original series are

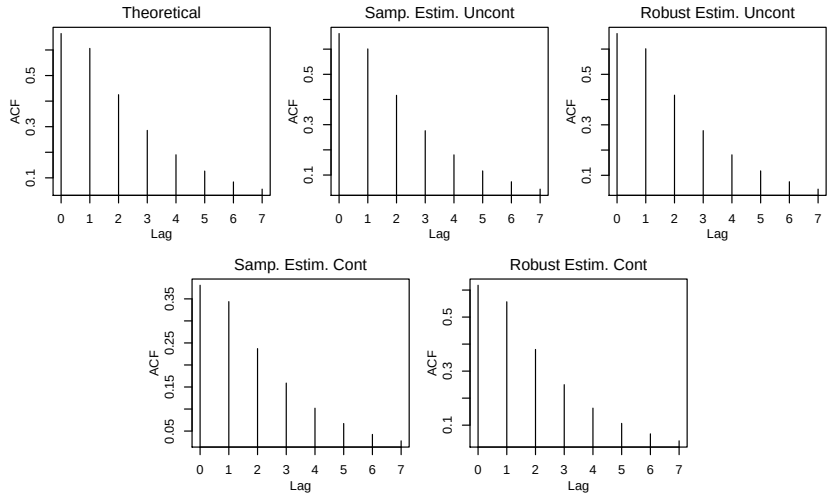

Fig. 2. Correlation function between $\{Z_{1,t}\}$ and $\{Z_{2,t}\}$. From left to right and top to bottom, plots are $\rho_{12}^{\boldsymbol{X}}(h)$, $\hat{\rho}_{12}^{\boldsymbol{X}}(h)$, $\hat{\rho}_{Q_{n-h}}^{(X_{1,t},X_{2,t})}(h)$, and $\hat{\rho}_{12}^{\boldsymbol{Z}}(h)$, $\hat{\rho}_{Q_{n-h}}^{(Z_{1,t},Z_{2,t})}(h)$ when $p_i = 0.05$, $i = 1, 2, 3$.

Table 2. RMSE of $\hat{\rho}_{12}^{\boldsymbol{X}}(h)$, $\hat{\rho}_{Q_{n-h}}^{(X_{1,t},X_{2,t})}(h)$, $\hat{\rho}_{12}^{\boldsymbol{Z}}(h)$ and $\hat{\rho}_{Q_{n-h}}^{(Z_{1,t},Z_{2,t})}(h)$ when $p_i = 0.05$, $i = 1, 2, 3$.

Lag h	0	1	2	3	4	5	6	7
$\hat{\rho}_{12}^{\boldsymbol{X}}(h)$	0.02595	0.03459	0.04592	0.05291	0.05451	0.05496	0.05685	0.05755
$\hat{\rho}_{Q_{n-h}}^{(X_{1,t},X_{2,t})}(h)$	0.02913	0.03804	0.04962	0.05748	0.05939	0.05979	0.06128	0.06269
$\hat{\rho}_{12}^{\boldsymbol{Z}}(h)$	0.28934	0.26774	0.19370	0.13680	0.09784	0.07479	0.06176	0.05521
$\hat{\rho}_{Q_{n-h}}^{(Z_{1,t},Z_{2,t})}(h)$	0.05754	0.06356	0.06710	0.06538	0.06236	0.05965	0.06068	0.06170

not stationary. Thus we work with the differenced observations, in percentages, after applying the log transformation. Figure 3 displays the time series. These plots show the presence of some possible outliers which justifies the comparison between robust and non-robust methods.

In Figures 4 and 5 we present the plots of $\hat{\boldsymbol{\rho}}^{\boldsymbol{X}}(h)$ and $\hat{\boldsymbol{\rho}}_{Q_n}(h)$, respectively. Comparing both plots, notice that vertical scales of both plots are different. Indeed, as a mere evidence, the values of the classical sample autocorrelation are -0.02, -0.03 and -0.02 for lags $h = 1, 2, 3$, respectively, while the robust autocorrelation given by (15) provided 0.32, 0.16, 0.09. Now, for the classical sample cross-correlation between PCE and DSPI the values are 0.25, 0.11, 0.11 and 0.14 for lags $h = 0, 1, 2, 3$, respectively. The robust cross-correlation given by (15) are 0.3, 0.16, 0.22 and 0.25.

Table 3. RMSE of $\hat{\rho}_{12}^{\boldsymbol{Z}}(h)$.

p_i $i=1,2,3$ \ Lag h	0	1	2	3	4	5	6	7
0.05	0.28934	0.26774	0.19370	0.13680	0.09784	0.07479	0.06176	0.05521
0.10	0.39047	0.35826	0.25729	0.17943	0.12558	0.08903	0.06950	0.05666
0.15	0.44192	0.40677	0.28982	0.20084	0.14067	0.09991	0.07345	0.06005
0.20	0.46956	0.43148	0.31149	0.21421	0.14771	0.10663	0.07947	0.06249
0.25	0.48315	0.44506	0.32042	0.22194	0.15276	0.10569	0.07697	0.06118

Table 4. RMSE of $\hat{\rho}_{Q_{n-h}}^{(Z_{1,t},Z_{2,t})}(h)$.

p_i $i=1,2,3$ \ Lag h	0	1	2	3	4	5	6	7
0.05	0.05754	0.06356	0.06710	0.06538	0.06236	0.05965	0.06068	0.06170
0.10	0.10492	0.10795	0.09833	0.08348	0.07124	0.06395	0.06177	0.05992
0.15	0.16088	0.16147	0.13579	0.10610	0.08424	0.07054	0.06293	0.05969
0.20	0.22260	0.21759	0.17829	0.13229	0.09814	0.07742	0.06682	0.05891
0.25	0.28858	0.27794	0.21815	0.15885	0.11540	0.08578	0.06693	0.06026

Now, consider the estimation of the ARMA parameters in (5). We concentrate on VAR(p) models, and the Yule-Walker equations give

$$\Sigma_{\boldsymbol{\varepsilon}} = \boldsymbol{\gamma}^{\boldsymbol{X}}(0) + \sum_{j=1}^{p} \boldsymbol{\Phi}_j \boldsymbol{\gamma}^{\boldsymbol{X}}(-j) \tag{18}$$

and

$$\boldsymbol{\gamma}^{\boldsymbol{X}}(h) = \sum_{j=1}^{p} \boldsymbol{\Phi}_j \boldsymbol{\gamma}^{\boldsymbol{X}}(h-j), \quad h = 1, \ldots, p. \tag{19}$$

Replacing $\boldsymbol{\gamma}^{\boldsymbol{X}}(.)$ in (18) and (19) by $\hat{\boldsymbol{\gamma}}^{\boldsymbol{X}}(.)$ leads to the Yule-Walker estimators whose equation system is solved using the Whittle's algorithm. This estimation procedure can be robustified replacing $\hat{\boldsymbol{\gamma}}^{\boldsymbol{X}}(.)$ by $\hat{\boldsymbol{\gamma}}_{Q_n}(h)$ given by (15).

Returning to the model analysis, based on information criteria, [12] selected a VAR(3) model to adjust the data. Figure 6 presents the standard and the robust correlation matrix function of the residuals of the selected model. In order to save space, only the ACF of PCE and the cross-correlation between PCE and DSPI are shown, the others plots present a similar behavior. Contrasting both plots, we observe that $\hat{\boldsymbol{\rho}}_{Q_n}(h)$ presents higher values of cross-correlations; for example, the cross-correlation between PCE and DSPI at lag $h = 12$ is 0.003 and 0.16, for $\hat{\boldsymbol{\rho}}^{\boldsymbol{X}}(h)$ and $\hat{\boldsymbol{\rho}}_{Q_n}(h)$, respectively. This result is in accordance with Proposition 1 which shows that one outlier is enough to destroy the properties of the sample correlation matrix function, and thus impacting in any other subsequential estimation step.

Now, we robustly estimate the parameters of the model. After, the plots of the sample and robust estimates of the correlation matrix function of the residuals are shown in Figures 7, respectively. Comparing Figures 6 and 7 one may note the reduction in the values. Also, confronting the sample and robust estimates, we note that the values of correlations are more alike; for instance,

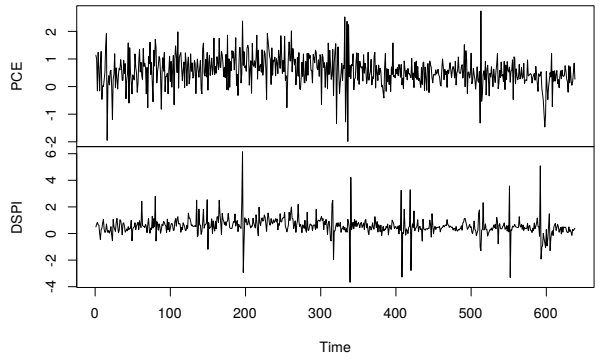

Fig. 3. Time plots of the U.S. personal consumption expenditures and disposable personal income, in percentages.

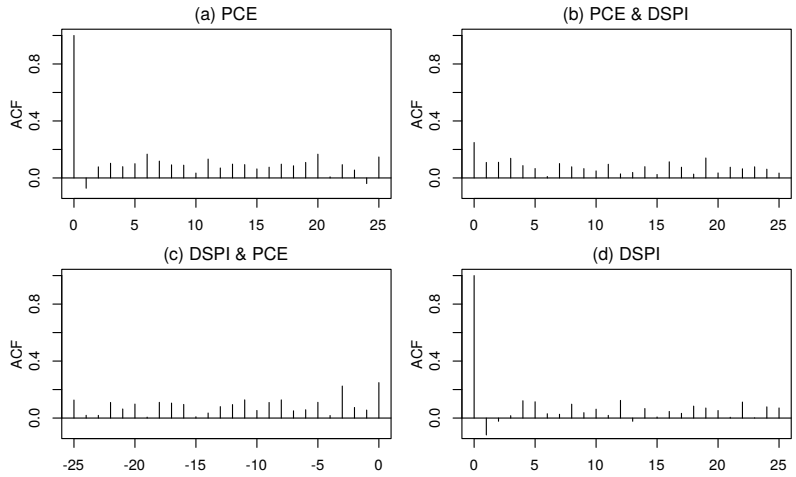

Fig. 4. $\hat{\boldsymbol{\rho}}^{\boldsymbol{X}}(h)$ of PCE and DSPI.

the value obtained by the sample estimate of the cross-correlation between PCE and DSPI at lag $h = 12$ is 0.01, while the robust estimate is 0.03.

5 Conclusions

The effect of additive outliers on the estimation of the covariance and correlation matrix functions of a stationary multivariate discrete time series is addressed. A robust estimation method was proposed as a generalization of existing results in the univariate case. Monte Carlo simulation results illustrated the good behavior in terms of mean square error of the proposed robust estimator even when

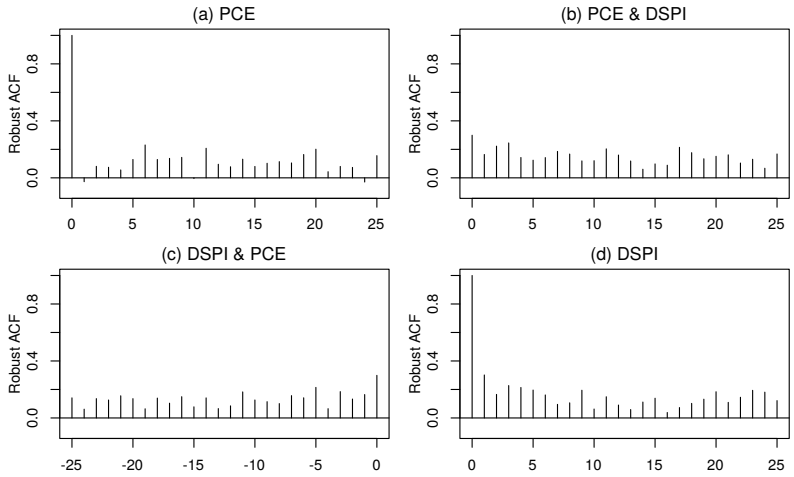

Fig. 5. $\hat{\rho}_{Q_n}(h)$ of PCE and DSPI.

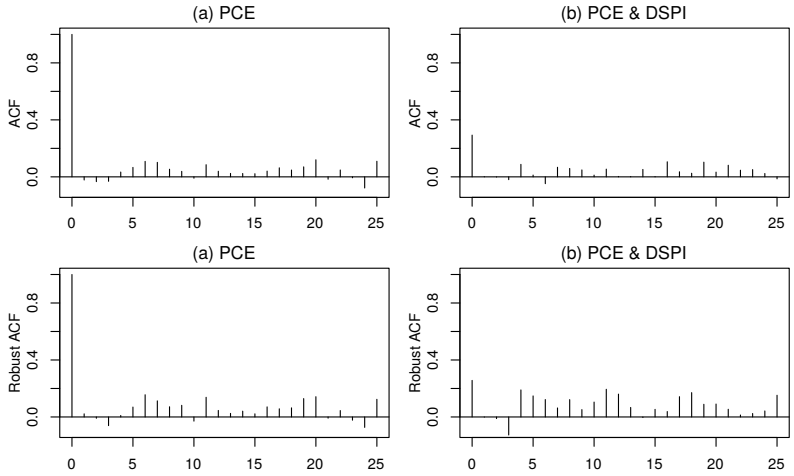

Fig. 6. The sample and the robust estimates of the correlation matrix function of the residuals of the fitted VAR(3) via Yule-Walker.

the data contain a considerate number of atypical observations. A real data set was analyzed where the proposed robust covariance estimator replaced the standard sample covariance estimator in the Yule-Walker equations. Future research will develop the influence function and the asymptotic theory for the proposed estimator.

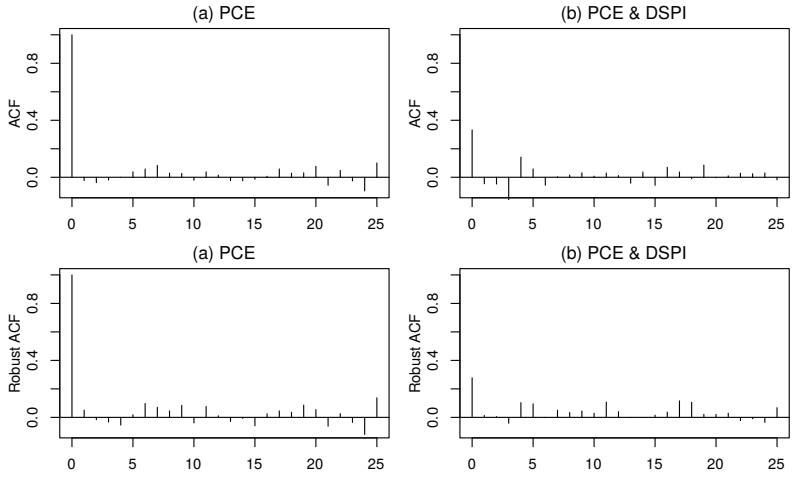

Fig. 7. The sample and the robust estimates of the correlation matrix function of the residuals of fitted VAR(3) via robustified Yule-Walker.

References

1. Tsay, R.S., Peña, D., Pankratz, A.E.: Outliers in multivariate time series. Biometrika **87**(4) (2000) 789–804
2. Huber, P.J.: Robust estimation of a location parameter. The Annals of Mathematical Statistics **35**(1) (1964) 73–101
3. Maronna, R.A.: Robust M-Estimators of multivariate location and scatter. The Annals of Statistics **4**(1) (1976) 51–67
4. Zoubir, A.M., Koivunen, V., Chakhchoukh, Y., Muma, M.: Robust estimation in signal processing: A tutorial-style treatment of fundamental concepts. IEEE Signal Processing Magazine **29**(4) (2012) 61–80
5. Ma, Y., Genton, M.G.: Highly robust estimation of the autocovariance function. Journal of Time Series Analysis **21** (2000) 663–684
6. Rousseeuw, P.J., Croux, C.: Alternatives to the median absolute deviation. Journal of the American Statistical Association **88**(424) (1993) 1273–1283
7. Lévy-Leduc, C., Boistard, H., Moulines, E., Taqqu, M.S., Reisen, V.A.: Robust estimation of the scale and of the autocovariance function of Gaussian short-and long-range dependent processes. Journal of Time Series Analysis **32**(2) (2011) 135–156
8. Ma, Y., Genton, M.G.: Highly robust estimation of dispersion matrices. Journal of Multivariate Analysis **78** (2001) 11–36
9. Chan, W.: A note on time series model specification in the presence of outliers. Journal of Applied Statistics **19**(1) (1992) 117–124
10. Chan, W.: Outliers and financial time series modelling: a cautionary note. Mathematics and Computers in Simulation **39**(3) (1995) 425–430
11. Lévy-Leduc, C., Boistard, H., Moulines, E., Taqqu, M.S., Reisen, V.A.: Large sample behavior of some well-known robust estimators under long-range. Statistics **45**(1) (2011) 59–71
12. Tsay, R.S.: Multivariate Time Series Analysis: with R and financial applications. John Wiley & Sons (2013)

Forecasting German Crash Numbers: The Effect of Meteorological Variables

Kevin Diependaele[1]✉, Heike Martensen[1], Markus Lerner[2], Andreas Schepers[2], Frits Bijleveld[3], Jacques J.F. Commandeur[3,4]

[1]Belgian Road Safety Institute, Brussels, Belgium
kevin.diependaele@bivv.be
[2]Bundesanstalt für Straßenwesen, Bergisch Gladbach, Germany
[3]Stichting Wetenschappelijk Onderzoek Verkeersveiligheid, Den Haag, The Netherlands
[4]Vrije Universiteit, Amsterdam, The Netherlands

Abstract. At the end of each year, the German Federal Highway Research Institute (BASt) publishes the road safety balance of the closing year. They describe the development of accident and casualty numbers disaggregated by road user types, age groups, type of road and the consequences of the accidents. However, at the time of publishing, these series are only available for the first eight or nine months of the year. To make the balance for the whole year, the last three or four months are forecasted. The objective of this study was to improve the accuracy of these forecasts through structural time-series models that include effects of meteorological conditions. The results show that, compared to the earlier heuristic approach, root mean squared errors are reduced by up to 55% and only two out of the 27 different data series yield a modest rise of prediction errors. With the exception of four data series, prediction accuracies also clearly improve incorporating meteorological data in the analysis. We conclude that our approach provides a valid alternative to provide input to policy makers in Germany.

Keywords: Road Safety · Meteorological effects · Structural time-series model

1 Introduction

Reliable accident numbers are essential for monitoring road safety. Obtaining such numbers and analyzing them with respect to short- and long-term trends is, however, not a trivial task. The difficulties that road safety agencies are facing in many countries are both practical and theoretical in nature. Apart from various causes of underreporting, police records are often difficult to obtain directly and/or without serious administrative bottlenecks. Publication of official accident numbers thus typically involves considerable time-delays, which is, of course, detrimental to effective policy making.

In Germany, the Federal Highway Research Institute (Bundesanstalt für Straßenwesen; BASt) collects accident numbers from 1991 (for the whole of Germany) and publishes a yearly report on the balance of national accident numbers. The evolution

is considered on a monthly basis for several subcategories (27 in total), based on road, user and accident variables (e.g., type of road, age, cyclist, fatal, damage only, influenced by alcohol, etc.). The report is prepared and published in December. At that time, however, preliminary accident numbers have only been released up to August of the running year for most subcategories and maximally up to September. At the same time, these numbers are still subject to up- or downward corrections and final numbers are only released in the next year (typically around June).

To deal with this particular situation, BASt has developed heuristics to predict (a) adjustments between provisional and final data from January to August/September and (b) the evolution of accident numbers in the different subcategories from August/September to December. Throughout the years, these heuristics have been refined as the result of a continuous learning process. In particular, the experience with typical responses of accident numbers to weather conditions have had an important impact. This is not surprising, given the variety of countries where correlations between accidents and weather variables have been demonstrated (see e.g., [1]). These correlations arise from complex underlying dynamics. There are, however, two main sources. The first concerns the fact that certain weather conditions have an impact on the risk of accidents. The second type of correlation arises from the impact on risk exposure.

Precipitation like snow and rain increases accident risk because of reduced friction between vehicles and the road surface and because visibility is reduced (precipitation itself, splashing water, frozen/fogged windscreens, etc.). Research shows that, certainly in the case of rain, this increase is not overruled by compensation behaviour such as reduced speed, less frequent overtaking, etc. [2]. The correlation with risk exposure arises from relationships between weather conditions and mobility patterns.

When a substantial amount of snow has fallen, all road users avoid unnecessary trips, while rain, frost and small amounts of snow are thought to reduce mostly the mobility of two-wheelers and pedestrians. The lowering effect on the traffic volume can be so strong, that even with increased accident risk, fewer accidents are observed in bad weather. How specifically the risk- and exposure-related effects combine into a net effect on accident numbers, varies strongly across different weather conditions and road user (e.g., [2,3]).

In the German scenario, it remains hard to make valid predictions about the evolution of accident numbers, even though the pattern of weather conditions is almost entirely known at the time of the analysis. As mentioned above, the weather influence on risk and exposure generates different and sometimes even opposite effects for different accident types, or even for one and the same accident type. Given the inherent correlation of weather variables (e.g., snowfall and temperature) it is also not straightforward to identify the critical variables and their critical values with respect to accident occurrence. Some variables also clearly interact. ‘Warm and dry’ will have a different impact than ‘warm and wet’ or ‘cold and dry’ or ‘cold and wet’. Weather variables also correlate and/or interact with other sources of variation, such as daylight hours, school/public holidays, alcohol consumption, etc..

In the present work we developed a time-series modelling strategy that quantifies the impact of weather conditions on accident numbers in Germany. It must be empha-

sized, however, that it was not the goal of this strategy to disentangle the effect of meteorological conditions on accident risks and occurrences. The sole objective was to develop a tool which would improve the accuracy of the year-end forecasts by BASt, concerning various types of national accident/injury numbers. The main ingredients of our approach are (a) a decomposition of historical data according to structural time-series models with seasonal, trend and weather-regression components and (b) a projection of these models together with known weather values to impute missing accident numbers from August/September to December.

This approach allows to disentangle long-term trends (e.g. casualty reduction due to better occupant protection) from seasonal patterns (e.g. variation in crash-occurrence due to changes in day-light patterns or school holidays). For meteorological variables it moreover allows to specifically include deviations from the typical seasonal pattern and interactions between weather variables. Regional variation of meteorological conditions was taken into account to a limited extent. While the accident data were only available at the national level, weather data were considered at a regional level and weighted by population numbers so as to ensure that the conditions in densely populated areas would have more weight on the predictions.

The results are validated against the consolidated accident numbers of the last years and the predictions based on the earlier BASt heuristics.

2 Methodology

2.1 Accident numbers

The accident numbers are divided into 27 different series with monthly count data since 1991 (see Table 1).

Table 1. Overview of the different monthly accident count series since 1991

1.	total number of police recorded accidents	15.	fatally injured user of motor vehicles (without motorised two wheelers)
2.	total number of injury accidents	16.	fatally injured user of cars
3.	severe accidents with damage only (towe away)	17.	fatally injured user of goods vehicles
4.	total number of casualties	18.	fatally injured user of motor bikes
5.	fatalities total	19.	fatally injured user of mopeds
6.	fatalities inside urban areas	20.	fatally injured user of bicycles
7.	fatalities outside urban areas without motorways	21.	fatally injured pedestrians
8.	fatalities on motorways	22.	injury accidents inside urban areas
9.	fatalities on national roads outside urban areas	23.	injury accidents outside urban areas without motorways
10.	fatalities under 15 years	24.	injury accidents on motorways
11.	fatalaties from 15 to 17 years	25.	injury accidents on national roads outside urban areas
12.	fatalities from 18 to 24 years	26.	injury accidents under the influence of alcohol
13.	fatalities from 25 to 64 years	27.	total number of seriously injured (hospitalized)
14.	fatalities 65 years and older		

For each series there exist a provisional and a final version. The provisional data provide the preliminary counts as they were available for BASt in December of each year. In the majority of these series, the values are systematically missing from August to December. For the first five series in Table 1, the provisional data are available up to September. The final data series provide the completed and adjusted acci-

dent counts for the whole year. For any given year, these data are only released during the next year. Hence, for the current study provisional data were available up to August/September 2016 and final data up to December 2015. This is illustrated in Figure 1 for the total number of police recorded accidents.

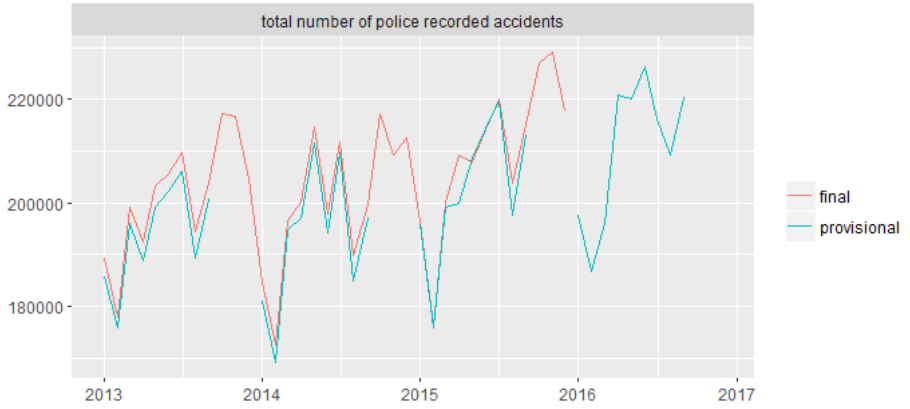

Fig. 1. Illustration of the available data for a given data series. The full series starts in January 1991.

2.2 Weather data

Raw weather data was downloaded from the Deutscher Wetterdienst (DWD). The data represent daily values since January 1st 1991 for the variables shown in Table 2 (see DWD for a more detailed description).

Table 2. Overview of the different weather parameters

Average temperature (°C; 2m above ground level)	LUFTTEMPERATUR
Maximum temperature (°C)	LUFTTEMPERATUR_MAXIMUM
Minimun temperature (°C)	LUFTTEMPERATUR_MINIMUM
Minimum temperature at ground level (°C)	LUFTTEMP_AM_ERDB_MINIMUM
Vapor pressure (hPa)	DAMPFDRUCK
Cloud coverage (1/8)	BEDECKUNGSGRAD
Air pressure (hPa)	LUFTDRUCK_STATIONSHOEHE
Relative humidity (%)	REL_FEUCHTE
Average wind speed (m/s)	WINDGESCHWINDIGKEIT
Maximum wind speed (m/s)	WINDSPITZE_MAXIMUM
Precipitation height (mm)	NIEDERSCHLAGSHOEHE
Precipitation types (yes/no)	NIEDERSCHLAGSHOEHE_IND
- no precipitation	
- rain only	
- snow only	
- rain and snow	
Sunshine duration (h)	SONNENSCHEINDAUER
Snow height (cm)	SCHNEEHOEHE

The data were downloaded from eight weather stations. These stations we identified from a (maximum) surface mapping between (1) fifteen climate zones and their reference weather station (DWD Test Reference Years, TRY, 2004) and (2) the German NUTS 2 regions. This mapping is shown in Table 3. The selected weather stations appear in italics.

The weather data were prepared for the analysis in four steps. First, a number of transformations were applied to reduce the marked skewness in a number of the raw variable distributions (thus, to reduce the influence of atypical values during aggregation). Average wind speed, Maximum wind speed, Precipitation height and Sunshine duration were transformed into their square root. The arcsine square root transformation (i.e., $\sin^{-1}\sqrt{x/\max(x)}$) was applied to Cloud coverage and Relative humidity. Finally, the arcsine square root transformation was also applied to the binary precipitation type variables, but only after calculating the monthly averages ($\sin^{-1}\sqrt{\bar{x}}$).

In the second step, an additional set of variables was created, by expressing the original variables as deviations from the monthly station-level averages. For a given weather variable x, the deviation on day i from the mean for month j at station k was expressed as a z-score, i.e., $z_{x_{ijk}} = (x_{ijk} - \bar{x}_{jk})/\sqrt{Var(x_{jk})}$, with $\bar{x}_{jk}$ the sample mean of variable x in month j at station k since 1991 and $Var(x_{jk})$ the sample variance. The variables that were obtained in this way served as an additional set of input data, quantifying how usual or unusual the daily values are for a given variable at a given weather station, in the light of all other observations since 1991 in the same month and at the same station.

Table 3. Overview of the surface mapping between climate zones and NUTS 2 regions

Climate zone	Reference station	NUTS 2 regions (DE)
Nordseeküste	Bremerhaven	
Ostseeküste	Rostock-Warnemünde	
Nordwestdeutsches Tiefland	*Hamburg-Fuhlsbüttel*	50, 60, 91, 92, 93, 94, F0
Nordostdeutsches Tiefland	*Potsdam*	30, 40, 80, D5, E0
Niederrheinisch-westfälische Bucht & Emsland	*Essen*	A1, A2, A3, A4
Nördliche & westliche Mittelgebirge - Randgebirge	*Bad Marienberg*	A5, B1, B2, C0
Nördliche & westliche Mittelgebirge - Zentrale Bereiche	*Göttingen*	72, 73
Oberharz & Schwarzwald (mittlere Lagen)	Braunlage	
Thüringer Becken & Saechsisches Huegelland	*Chemnitz*	D2, D4, G0
Südöstliche Mittelgebirge <= 1000 m	Hof	
Erzgebirge, Boehmer, & Schwarzwald > 1000 m	Fichtelberg	
Oberrheingraben & unteres Neckartal	*Mannheim*	12, 13, 71, B3
Schwäbisch-fränkisches Stufenland & Alpenvorland	*Passau*	11, 14, 21, 22, 23, 24, 25, 26, 27
Schwäbische Alb & Baar	Stötten	
Alpenrand & -täler	Garmisch-Partenkirchen	

Thirdly, the daily station-level values for each variable were aggregated into monthly national values. The arithmetic mean of each variable was calculated per station, year and month. This mean was then combined into a national value by calculating a weighted mean across the weather stations. The weights in this calculation were proportional to the yearly population size since 1991 in the NUTS regions that were associated with the weather stations (source: Eurostat).

Finally, the matrix of aggregated weather data was transformed into its principal components (PCs). The matrix is characterised by a naturally high degree of multicollinearity, which implies that a small change in the data can drastically change the pattern of estimated coefficients and the associated error distributions. This is not a problem per se, since it was not within the scope of the current study to link specific patterns in accident counts to individual weather variables. However, to avoid overfitting and losing predictive power, the objective is to predict future accident counts, using only those weather variables that have a proven statistically significant relationship with accident counts. Multicollinearity compromises straightforward choices in this respect. The PCs, by definition, provide orthogonal (uncorrelated) dimensions across all weather variables.

2.3 Weather regression models

Predictions were based on independent models of the 27 final accident data series. These models took the form of a log-normal structural time series model with weather PC regression components. Specifically, the linear predictor included a random level, slope, (monthly) seasonal and irregular effect, but also fixed weather PC effects. The generic definition was as follows:

$$y_t = \exp(\mu_t + \sum_{j=1}^{[s/2]} \gamma_{jt} + \sum_{k=1}^{r} \beta_k x_{kt} + \varepsilon_t), \qquad \varepsilon_t \sim \mathcal{NID}(0, \sigma_\varepsilon^2)$$

$$\mu_{t+1} = \mu_t + \nu_t + \eta_t, \qquad \eta_t \sim \mathcal{NID}(0, \sigma_\eta^2)$$

$$\nu_{t+1} = \nu_t + \xi_t, \qquad \xi_t \sim \mathcal{NID}(0, \sigma_\xi^2)$$

$$\gamma_{j,t+1} = \gamma_{jt} \cos\lambda_j + \gamma_{jt}^* \sin\lambda_j + \omega_{jt},$$

$$\gamma_{j,t+1}^* = -\gamma_{jt} \sin\lambda_j + \gamma_{jt}^* \cos\lambda_j + \omega_{jt}^*, \qquad \omega_{jt}, \omega_{jt}^* \sim \mathcal{NID}(0, \sigma_\omega^2)$$

$$\lambda_j = 2\pi j / s$$

with

y_t the observed count at time t for a given series of accident data,

μ_t the trend component, with random disturbance η_{t-1}, slope ν_{t-1} and slope disturbance ξ_{t-1},

γ_{jt} the trigonometric seasonal components with periodicity s = 12 and disturbances ω_{jt} and ω_{jt}^*,

x_{kt} the value of the k-th weather regressor at time t,

β_k the time-invariant coefficient of the k-th weather regressor and

ε_t the additive observation level noise term

All disturbances were modelled as independent stationary Gaussian processes. Models were fit separately for each accident series according to the following procedure. This procedure critically relies on Kalman filtering, mode estimation and importance sampling, as implemented in the R-package KFAS [4].

Initially, observed counts were log-transformed and models were fit using the regular Kalman filter. Importantly, in this step, any zero-counts were replaced with missing values. Models were fit through the Kalman filter with exact diffuse initialization of state vector a_1 and its associated variance-covariance matrix P_1 [5].

$$a_1 = (\mu_1\ \nu_1\ \gamma_{1,1}\ \gamma_{1,1}^*\ \gamma_{2,1}\ \gamma_{2,1}^*\ \dots\ \gamma_{6,1}\ \beta_1\ \dots\ \beta_r)', \qquad \beta_{k,1} = \beta_{k,2} = \dots = \beta_{k,T}$$

$$P_1 = \begin{pmatrix} \sigma_{\mu_1}^2 & \cdots & \sigma_{\mu_1\beta_r} \\ \vdots & \ddots & \vdots \\ \sigma_{\mu_1\beta_r} & \cdots & \sigma_{\beta_r}^2 \end{pmatrix}$$

The Kalman filter provides the equations to calculate

$$a_{t|t} = E(\alpha_t | y_1, \dots, y_t),$$
$$a_{t+1} = E(\alpha_{t+1} | y_1, \dots, y_t),$$
$$P_{t|t} = Var(\alpha_t | y_1, \dots, y_t),$$
$$P_{t+1} = Var(\alpha_{t+1} | y_1, \dots, y_t)$$

recursively from

$$a_t = E(\alpha_t | y_1, \dots, y_{t-1}),$$

$$P_t = Var(\alpha_t | y_1, \ldots, y_{t-1})$$

given the values of the disturbance variance parameters σ_ε^2, σ_η^2, σ_ξ^2 and σ_ω^2. The results of the Kalman filter were used in a backward recursion (the so-called state smoothing recursion) to obtain the expected value of α_t, given the entire series, i.e., $\hat{\alpha}_t = E(\alpha_t | y_1, \ldots, y_n)$ and the corresponding variance $V_t = Var(\alpha_t | y_1, \ldots, y_n)$ (see [6], for details). Models were optimized with respect to the unknown variance disturbance parameters σ_ε^2, σ_η^2, σ_ξ^2 and σ_ω^2 (see [4,7] for details). For each model, optimization was done ten times with a different random set of starting values for the unknown disturbance variance parameters. The fitted model with the highest likelihood value was retained.

For each series, the model was calibrated with respect to the matrix of weather PC regressors. Initially, for each data series, all weather PCs that explained at least 3% of the variance in the aggregated weather data according to the principal components analysis (i.e., the first seven PCs), were included in the model together with their first order interactions. After fitting this model, all interaction terms with a p-value ≥.01 were removed. The model was refit and subsequently, all simple effects of weather PCs with a p-value ≥.10 and which did not occur in any of the interactions were also excluded. The final model thus contains PCs that yield (a) significant (α=.01) first order interaction(s) or a significant (α=.10) main effect.

Finally, to accommodate zero-counts, the calibrated weather regression models were refit in a generalized linear approach using the untransformed counts with a logarithmic link function. The models were fit through the methods of (1) mode estimation, which finds an approximating linear Gaussian state space model, and (2) importance sampling, which corrects for approximation errors (see [6], for details). Starting values for the disturbance variance parameters were taken directly from the best fitting model of the log-transformed counts. The number of simulation runs in the importance sampling procedure was set to 1000.

2.4 Final-provisional models

The weather regression models cannot be applied directly to predict accident counts for the last three/four months of the year, since the accident counts that are available for January-August/September are only provisional. The weather regression models are fit to the final count data. Feeding provisional counts to these models for the first eight/nine months would yield biased results since there are the marked differences between provisional and final counts (see e.g., Figure 1). Before applying the weather regression models to make predictions for September/October-December, the provisional data in each series are therefore adjusted through simple models of the following form:

$$d_t = \mu_t + \sum_{j=1}^{[s/2]} \gamma_{jt} + \varepsilon_t, \qquad \varepsilon_t \sim \mathcal{NID}(0, \sigma_\varepsilon^2)$$

$$\mu_{t+1} = \mu_t + \eta_t, \qquad \eta_t \sim \mathcal{NID}(0, \sigma_\eta^2)$$

$$\gamma_{j,t+1} = \gamma_{jt} \cos\lambda_j + \gamma_{jt}^* \sin\lambda_j + \omega_{jt}, \qquad \omega_{jt}, \omega_{jt}^* \sim \mathcal{NID}(0, \sigma_\omega^2)$$

$$\gamma_{j,t+1}^* = -\gamma_{jt} \sin\lambda_j + \gamma_{jt}^* \cos\lambda_j + \omega_{jt}^*,$$

$$\lambda_j = 2\pi j / s$$

with

- d_t the observed difference between final and provisional count for a given data series at time t, with random disturbance ε_t,
- μ_t the level component, with random disturbance η_{t-1} and
- γ_{jt} the j-th trigonometric seasonal component with periodicity s and disturbances ω_{jt} and ω_{jt}^*

To enable the estimation of a seasonal component, the months for which provisional data are systematically missing were removed from each series, resulting in an adjusted periodicity $s < 12$. Theoretically, this implies, however, that we ignore the increased uncertainty due to these missing values. The parameters were estimated following the same procedure as for log-counts described above. The smoothed state vectors $\left(\hat{\mu}_t\ \hat{\gamma}_{1,t}\ \hat{\gamma}_{1,t}^*\ \ldots\ \hat{\gamma}_{s/2,t}\right)'$ were used to calculate $\hat{d}_t$ for $t = n+1, \ldots, n+s$. In the example shown in Figure 1, $t = n+1$ corresponds to January 2016 and $t = n+s$ corresponds to September 2016. The predicted difference $\hat{d}_t$ is added to the observed provisional data for $t = n+1, \ldots, n+s$, which yields the prediction for the final data in this period.

2.5 Weather PC models

After adjusting the provisional data of each series for the running year, they were merged with the corresponding final data since 1991. These series could be fed into the fitted weather regression models to obtain smoothed predictions for the last three/four months, taking into account the available weather PC values. However, before this was done, one last modelling step took place. The reason was that at the time of reporting in December, when accident predictions are needed, months of weather data are only complete up to November. To accommodate this, we decided to

impute the missing values through a classical structural time series model, fitted independently to each weather PC. Specifically, these models had the following form:

$$y_t = \mu_t + \sum_{j=1}^{[s/2]} \gamma_{jt} + \varepsilon_t, \qquad \varepsilon_t \sim \mathcal{NID}(0, \sigma_\varepsilon^2)$$

$$\mu_{t+1} = \mu_t + \nu_t + \eta_t, \qquad \eta_t \sim \mathcal{NID}(0, \sigma_\eta^2)$$

$$\nu_{t+1} = \nu_t + \xi_t, \qquad \xi_t \sim \mathcal{NID}(0, \sigma_\xi^2)$$

$$\gamma_{j,t+1} = \gamma_{jt} \cos\lambda_j + \gamma_{jt}^* \sin\lambda_j + \omega_{jt}, \qquad \omega_{jt}, \omega_{jt}^* \sim \mathcal{NID}(0, \sigma_\omega^2)$$

$$\gamma_{j,t+1}^* = -\gamma_{jt} \sin\lambda_j + \gamma_{jt}^* \cos\lambda_j + \omega_{jt}^*,$$

$$\lambda_j = 2\pi j / s$$

with

- y_t the observed value for a given weather PC at time t, with random disturbance ε_t
- μ_t the trend component, with random disturbance η_{t-1}, slope ν_{t-1} and slope disturbance ξ_{t-1}
- γ_{jt} the j-th trigonometric seasonal component with periodicity s = 12 and disturbances ω_{jt} and ω_{jt}^*

The parameters were estimated following the same procedure as for log-counts described above. The smoothed state vectors $\left(\hat{\mu}_t\ \hat{\nu}_t\ \hat{\gamma}_{1,t}\ \hat{\gamma}_{1,t}^*\ \ldots\ \hat{\gamma}_{6,t}\right)'$ were used to calculate $\hat{y}_t$, for $t = n+1, \ldots, T$ where n corresponds to November and T to December of the running year.

2.6 Validation

After feeding the fitted weather regression model (see 2.3) with (a) the final and adjusted provisional data (see 2.4) and (b) the observed and imputed weather PC values (see 2.5), the smoothed state vectors $\left(\hat{\mu}_t\ \hat{\nu}_t\ \hat{\gamma}_{1,t}\ \hat{\gamma}_{1,t}^*\ \ldots\ \hat{\gamma}_{6,t}\ \hat{\beta}_1 \ldots \hat{\beta}_r\right)'$ were used to calculate $\hat{y}_t$, for $t = n+1, \ldots, T$, where n corresponds to the last month for which provisional data were available (i.e., August/September).

The main objective of the present study was to investigate whether these predictions would provide a better approximation of the final accident counts as compared to the predictions from the established BASt heuristics. Hence, the following valida-

tion method was applied. For each year between 2000 and 2015 and each accident data series, predictions were generated based on (a) the final data of all previous years, (b) adjusted provisional data for the running year, (c) the observed weather PC values up to November of the running year and (d) the weather PC imputations for December of the running year. The estimated variances of all disturbance parameters were kept constant across all validation years and were taken from each model as fitted to the whole data set. Eventually, the predictions for each month of a given year were summed and compared with the sum of the eventual final data for that year. The same was done for the predictions that were published by BASt at the time. The accuracy of both methods was evaluated by comparing the root mean squared error (RMSE) for each accident data series.

In order to investigate the added value of the weather regression in our approach, we repeated the validation procedure now using the predictions of a log-normal structural time series model without weather PC regression components for the final data.

3 Analysis and Results

In this section we report the results of the validation procedure, as described in the previous section. Table 4 summarizes the results. The first three columns give the RMSEs for each of the accident series, as obtained with (1) the present model-based approach, (2) the earlier heuristic approach of BASt and (3) the same model-based approach, but without weather PC regression components. The two following columns provide the relative gain/loss of accuracies of the present approach. The final column shows the number of weather effects (main effects and interactions) that were retained in the model fitting stage (r). It is beyond the scope of this paper to provide a detailed overview of each of the models and the exact nature of the weather effects therein.

Proceedings ITISE 2017. Granada, 18-20, September, 2017.ISBN: 978-84-17293-01-7

Table 4. Summary of the validation results

	RMSE			% reduction		
Type of crash/victim	Prognose	BASt	Without weather	BASt	Without weather	*r*
Inj. acc. urban	1616	3182	2792	49	42	8
All severely injured	858	1888	1345	55	36	9
Killed rural	57	72	76	21	25	8
All injury acc.	2600	3598	3389	28	23	7
Killed urban	24	32	31	25	23	8
Killed moto	24	26	31	8	23	14
Inj. acc. alcohol	319	475	389	33	18	8
All victims	3754	4843	4529	22	17	10
Killed 65+	32	48	38	33	16	5
Killed 25-64	50	47	59	***-6***	15	6
Killed cyclists	22	24	25	8	12	9
Killed 18-24	23	44	26	48	12	6
Inj. acc. rural	1009	1313	1133	23	11	12
Inj. acc. BS	343	481	385	29	11	10
Killed all	81	75	88	***-8***	8	6
Killed caroccup.	55	62	59	11	7	8
Killed pedstrians	28	34	30	18	7	6
Killed motorveh.	57	62	61	8	7	8
Killed motorway	31	31	32	***0***	3	8
Killed BS	39	40	40	3	3	7
Killed <15	8	9	8	11	***0***	1
Killed goodsveh.	10	10	10	***0***	***0***	3
Killed moped	6	9	6	33	***0***	1
Inj. acc. motorway	329	614	321	46	***-2***	8
Property damage	1366	1383	1309	1	***-4***	11
Killed 15-17	12	14	11	14	***-9***	4
All accidents	16713	31981	15068	48	***-11***	9

The results of our validation study are presented in Table 4. In comparison with the year totals that were previously published by BASt, we see that predictions become more accurate in 23 of the 27 accident data series, with accuracies increasing up to 55 percent. In four cases, there was either no difference or performance dropped slightly. For the number of fatalities on motorways and the fatally injured users of good vehicles, the accuracy did not change. For the total number of killed road users and the number of killed road users between 25 and 64 years old, there were slight drops in performance (i.e., -8% and -6%, respectively).

With respect to the weather PCs, we see that by including these, we obtain higher prediction accuracies in 20 of the 27 data series. The gain in accuracy is largest for injury accidents in an urban environment (42%). The performance did not change with or without weather regressors for (1) the fatalities under 15 years, (2) fatally injured users of goods vehicles and (3) fatally injured users of mopeds. We also see that for these series, few weather effects were retained during model fitting (r = 1, 3 and 1, respectively). Predictions appear to be somewhat better without weather variables in the case of (1) injury accidents on motorways, (2) property damage only accidents, (3) fatalities between 15 and 17 years and (4) the total number of accidents.

Despite this, a reasonable number of weather effects were retained during model fitting.

4 Discussion

Many road safety agencies are confronted with the situation where there are important structural delays in the publication of official national accident counts. Nevertheless, analyses based on recent data are critical for efficient policy making. In this study we have dealt with the task of predicting year totals based on preliminary monthly counts of different accident/injury types, available from January to August/September for the particular case of Germany. The main ingredient of our approach was a structural time series model, trained on all monthly count data since 1991 and including meteorological predictors. In comparison with the earlier heuristic approach used by BASt, the results of our validation study indicate important gains in prediction accuracy, up to 55% in the case of severe injury counts. Only two out of 27 data series showed a modest (-6%, -8%) drop in prediction accuracy. The main conclusion is therefore that our model-based approach is a valid alternative to provide input to policy makers in Germany when only preliminary accident data are available for the running year.

It is important to keep in mind that the present modelling approach was specifically designed with a practical purpose in mind, i.e., a tool to assist BASt in their yearly reporting on the evolutions in accidents and injuries. All modelling and prediction steps were implemented in a stand-alone application, which guided several practical decisions. The treatment of weather effects had to be automated and harmonized across the 27 different data series. It is clear that the performance of each individual model could be improved by a thorough manual checking and analysis of the specific nature of the weather effects.

Nevertheless, our results confirm that the number of accidents has an important association with weather conditions (see, e.g., [1]). Moreover, the results demonstrate that using known weather values as regressors increases the prediction accuracy of accident/injury counts. When weather variables were omitted from the current models, we see an overall drop in prediction performance, with only few exceptions. In four cases we see that there was a slightly better performance without weather variables, despite the fact that several significant relationships with weather variables were identified. The latter seems to indicate that there is still room for improvement in order to capture more complex dynamics in the relationship between weather conditions and road safety. We discuss this in more detail below. Compared to the earlier heuristic approach, however, we see that there is a gain in prediction accuracy, even for those cases where weather regression did not improve the performance.

Unlike in earlier studies, the present methodology does not provide direct insights in the actual nature of weather effects on road safety. Daily weather data from individual weather stations were transformed and scaled. Next, they were aggregated up to the level of monthly national values. Regional population densities were used as weights during this aggregation to exploit the regional variations in weather conditions in predicting accident occurrence at the national level. Through these transfor-

mations, the resulting values cannot easily be traced back to familiar meteorological patterns. Moreover, the current model terms concern the principal components of the transformed weather data. Given the inherent strong correlation between weather variables, principal components allow to obtain coefficients that are robust to new data or small changes in the input data. At the same time, it is straightforward to exclude components which yield no significant relationship with the accident/injury counts and thus avoid over-fitting and poor generalizability. Similar approaches have been applied in regular regression modelling with large quantities of correlated covariates such as in genetics (e.g., [8]).

The use of a principal components regression approach by no means excludes the possibility of interpreting the weather effects. In fact, we believe it is more insightful to identify latent dimensions in the relationship between weather and road safety, instead of focussing on direct physical measures, as the former are better candidates to reveal patterns of meteorological values or 'weather scenarios' that have critical implications for road safety. Performing such an analysis was beyond the scope of the present study, but could provide new theoretical insights and a basis for fine tuning the current approach. With respect to further developments, we believe there is ample room for improvements to capture more complex dynamics in the relationship between weather conditions and road safety. In the current approach we have gone as far as including two-way interactions and, next to absolute values, including expressions of values as month- and station-specific deviations. In this way, it was theoretically possible to capture, for instance, differences in the effect between exceptional rainfall with low and high temperatures.

Although the 'exceptionality' transformation introduced a specific form of non-linearity, prediction accuracies might gain significantly from other forms of non-linear weather effects. A number of authors has pointed out the importance of specific temporal patterns. For instance, after a long dry period, rain can disproportionally increase risk because dust and oil form a slippery film on the road surface (e.g., [9]). It remains challenging, however, to define any non-linear patterns a priori, especially since different types of accidents/injuries might be sensitive to different types of patterns. In addition, the patterns should be relevant at the scale of monthly nationwide aggregations (a heavy local summer thunderstorm might not be).

It is also important to consider the true nature of weather effects. As already mentioned in the introduction, there are two main sources of correlation with road safety. The first concerns the fact that certain weather conditions have an impact on the risk of accident occurrence, e.g., by reducing visibility. The second type of correlation arises from the impact on risk exposure, i.e., by altering the traffic volume for given type(s) of road users (e.g., motorcyclists). In the current framework, there is no distinction between these two types of correlation. This is clearly suboptimal for the quality of predictions when the same weather conditions generate opposite effects on risk and exposure for a given type of accidents/injuries. Such difficulty could be addressed by incorporating weather effects in the latent risk modelling framework [10] where risk and exposure are explicitly treated as different concepts. However, this multivariate approach critically depends on the availability of relevant historical exposure data (e.g., pedestrian counts) which can be linked to historical weather data.

5 Conclusions

Based on the clear gains in prediction accuracies, we conclude that the present structural time-series modelling approach provides a valid alternative to predict the evolution of accident/injury numbers at the end of the year in Germany. Our study also confirms that it is important to view short-term evolutions in crash statistics in the light of weather conditions. Structural time series models with meteorological predictors are a powerful and convenient tool to capture these relationships. The current models could still gain in prediction accuracy by elaborating on more complex dynamics of weather conditions and by including different sets of predictor variables, with proven relationships with road safety, such as economic variables. However, in the present context, additional variables can only be of practical use if their availability does not suffer from serious structural delays.

References

1. Bergel-Hayat, R., M. Debbarha, C. Antoniou, and G. Yannis. Explaining the road accident risk: Weather effects. Accident Analysis and Prevention, 2013, 60: p. 456-465.
2. Focant, N. and H. Martensen. Are there more accidents in the rain? Exploratory analysis of the influence of weather conditions on the number of road accidents in Belgium. 2014: Brussels: Belgian Road Safety Institute.
3. Sabir, M. Weather and travel behaviour, 2011: Amsterdam: Vrije Universiteit Amsterdam
4. Helske, J. KFAS: Exponential Family State Space Models in R. Journal of Statistical Software, 2017, In Press.
5. Koopman, S. J. and J. Durbin, J. Filtering and smoothing of state vector for diffuse state space models. Journal of Time Series Analysis, 2003, 24, p. 85-98.
6. Durbin, J. and S. J. Koopman. Time Series Analysis by State Space Methods, (2nd ed.). 2012: Oxford University Press.
7. Koopman, S. J. Disturbance smoother for state space models. Biometrika, 2003, 80: p. 117-126.
8. Bair, E., T. Hastie, P. Debashis and R. Tibshirani. Prediction by Supervised Principal Components. Journal of the American Statistical Association, 2006, 101: p. 119-137.
9. Eisenberg, D. The mixed effects of precipitation on traffic crashes. Accident Analysis and Prevention, 2004, 36: p. 637-647.
10. Bijleveld, F. D., J. J. F. Commandeur, , P. G.Gould, and S. J. Koopman. Model-based measurement of latent risk in time series with applications. Journal of the Royal Statisitcal Society A, 2008, 171: p. 265-277.

Safety stock calculation based on kernel bandwidth estimates that minimize inventory costs.

Carlos Ruiz-Cañadas[1] and Juan R. Trapero[1]

[1] University of Castilla-La Mancha, Department of Business Administration, 13071 Ciudad Real, Spain

Abstract. Demand forecasting and safety stock levels are employed to mitigate the risk associated to demand uncertainty. Most of the prior work has focused on point demand forecasting, assuming that forecast errors follow a typical normal i.i.d. Nevertheless, the real demand for products is difficult to forecast accurately, which means that---at minimum---the i.i.d. assumption should be questioned. This work analyzes the effects of possible deviations from the i.i.d. assumption and proposes an empirical method based on Kernel Density Estimation (non-parametric) to compute the safety stock. The proposed method estimates the Kernel bandwidth by minimizing both the stockout and holding costs for only certain target cycle service levels.

Keywords: Supply Chain, Safety Stock, Kernel Density Estimation, Forecasting.

1 Calculation of safety stocks

Traditional textbooks [1] illustrate the calculation of safety stocks assuming that the forecasting error is Gaussian independent and identically distributed (i.i.d) with zero mean and constant variance. Under such premises, the safety stock for a determined Cycle Service Level (CSL) is:

$$SS = k \cdot \sigma_L \tag{1}$$

where $k = \Phi^{-1}(1 - CSL)$ is the safety factor; Φ is the accumulated normal distribution; σ_L is the forecast error standard deviation for certain lead time (L), which is assumed to be known and constant. σ_L can be determined from the estimated forecasting model parameters in addition to the forecasting horizon.

Nevertheless, if the forecasting model cannot capture the underlying data generating process, the i.i.d. assumption about the forecasting error is no longer valid [2] and the expression (1) would be flaw. In case forecasting errors are not normal, we can use a non-parametric approach as the Kernel density estimator [3] based on the empirical forecasting errors. In this case, the SS is computed as $SS=Q_L(CSL)$, where $Q_L(CSL)$ is the forecasting error quantile given a CSL target. Such a quantile can be obtained from the kernel density estimator

$$f(x) = \frac{1}{Nh}\sum_{j=1}^{N} K\left(\frac{x-X_j}{h}\right) \quad (2)$$

where N stands for the sample size, $K(\cdot)$ is the Kernel smoothing function and h is the bandwidth [3]. The main contribution of this work is the estimation of h by minimizing the inventory costs, i.e., the stockout and holding costs, for certain quantiles instead of every quantile as it is usually done. Figure 1 shows the total costs (Score) obtained for different benchmarks at certain CSL, where sales data from a manufacturing company specialized in household products have been employed. The costs (score) have been scaled for confidential reasons. The benchmarks employed are: i) A parametric approach based on a Single Exponential Smoothing (SES); ii) The Kernel density estimator whose bandwidth is optimized as described above; iii) the Kernel optimized by default in MATLAB (kernel smoothing function: Epanechnikov, default bandwidth assuming normal distribution); and finally, iv) the empirical percentile obtained from forecasting errors. The results show that the method proposed to optimize the bandwidth provides the lowest cost for higher quantiles (95% and 99%), although for lower quantiles (85 % and 90%) there is a negligible difference between all of them.

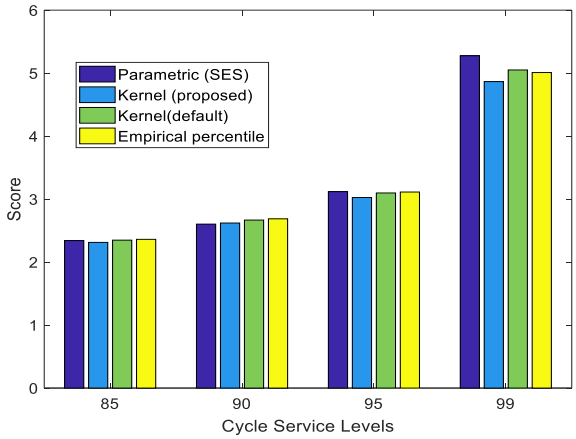

Fig. 1. Scores vs Cycle Service Levels.

References

1. Heizer, J., Render, B.: Principles of Operations Management, Global edition, Pearson (2011).
2. Chatfield, C., Time-series forecasting, CRC Press (2000).
3. Silverman, B.: Density Estimation for Statistics and data analysis, Chapman & Hall/CRC Monographs on Statistics & Applied Probability, Taylor & Francis, Bristol (1986).

Forecasting Diffusion Investments in FinTech Using Diffusion Models

Abstract. FinTech, or Financial Technology, has become an important sector in its own right in the wake of the global financial crisis. Instead of traditional financial services offering packages of services, new innovative FinTech companies offer customized solutions to consumers which are often seen as more efficient and cost-effective. The loss of confidence in banks has allowed for consumers to rethink 'who' the authority of financial services should belong to (Arner, Barberis, & Buckley, 2016; Lee, 2016; Staykova & Damsgaard, 2015)., Technological innovation has created the opportunity for significant widening choice of financial services for consumers. (Deloitte, 2016, p. 4).

The present research models the quarterly evolution of investments, namely the global number of deals in four sectors of FinTech. The analyses is carried out using innovation diffusion models. This research shows that there are different dynamics across sectors. On the one hand Online lending seems to be driven only by imitation and on the other hand heterogeneity propensity of adoption is also different. Nevertheless, all the dynamics are at the level of late majority meaning that they have already achieved the absolute maximum peak of adoption.

1 Introduction

The rise of electronic networks and the information revolution particularly at the beginning of this century have been foreseen as challenging for most of the industrial sectors. Evans and Wurster (2000) in their book Blown to bits, said that some industries, especially those having information as a final product would be submitted to deconstruction transformation. The main reason is that information is the glue that holds value chains, supply chains, consumer franchises and organizations together and for those kinds of industries, "(t)hat glue is melting" (Evans & Wurster, 2000, p. 21). As a result, everyone would be able exchange rich information without any constraints, the hierarchical structure of supply chains, the organization of pyramids, the asymmetries of information, and "the boundary of the corporation will be able to be thrown into question" (p. 37), losing the corresponding competitive advantage. One of those sectors would be corporative and retail banking. In the case of retail banking, the fundamental unit of value is the customer relationship (cf. p. 44) but the deconstruction effect would change the main business focus. The competitive advantage would mainly be determined product by product. Evans and Wurster pointed out at the beginning of this century, that "(t)he deconstruction of the value chain in banking is not distant and futurist as many think" (p. 49). That future is already here now.

The term 'Fintech' is broadly used to refer to this technological evolution caused by the information revolution applied to finance and banking. Broadly speaking this term refer to "the evolving intersection of financial services and technology". Even though it had its first appearance dating back to the late 19th century, the term 'FinTech' has

adfa, p. 1, 2011.

only recently began to gain focused attention by regulators, industry participants and consumers alike.

The aim of this research is to shed some light on the latest FinTech development by focusing on the evolution of investments. We focus on quarterly time series describing the deal activity, namely the number of deals made by equity investments in different sectors of Fintech. The methodology applied growth curves models, specifically innovation diffusion models: Bass-Roger (Mahajan, Muller, & Srivastava, 1990) and Bemmaor (Bemmaor, 1994; Bemmaor & Lee, 2002).

Growth curves have been historically used to describe natural growth of many phenomena such as in physical or social sciences. Another case is the spread of an innovation which is specifically called diffusion. In growth curves, often the aim is not concerned with the underlying natural processes that generate the growth, whereas in diffusion research, the aim is to understand this spread from the perspective of communication and consumer interaction. The spread of diffusion takes place within a social network that is assumed to be fully connected and homogeneous. (Mahajan, Muller, & Bass, 1995; Peres, Muller, & Mahajan, 2010) Therefore, a diffusion model curve is a growth curve but not the other way around. Some scholars may criticize the use of diffusion models in FinTech investment diffusion as it may not look as homogenous and connected than in other innovations situations. (Adomavicius, Bockstedt, Gupta, & Kauffman, 2007). In the literature review, we will try to show that the so-called FinTech ecosystems could be considered as that social network hosting investment activity. Still, if this hypothesis is not accepted, the reader could refer to this curve as a regular growth curve and nevertheless consider the forecasting without making further diffusion-type interpretation.

The paper is structured as follows. The first following section discusses FinTech in general and each of the sectors taken into account in the empirical section and discusses the mathematical models. The second section presents the data and the methodological computational aspect. The fifth is the results followed by the last section which presents the limitations and the future perspectives of this research.

2 Literature review

2.1 Three eras of FinTech innovation

In the banking sector, before the information revolution momentum, some other innovations had been adopted and are marked by the three 'eras' that compose the evolution of FinTech. Since the days of the telegraph, the appearance of credit cards in the US and the fax machine replaced the telex. The launch of the calculator and the first ATM in 1967 marked the end of the first era, namely FinTech 1.0 (from1866 to1967). The following era, FinTech 2.0 (from 1967 to 2008), consisted of the development of traditional Digital Financial Services. Globalization of finance enabled by developments such as SWIFT and NASDAQ (the world's first electronic stock market) followed by events such as the Herstatt crisis of 1974 and Black Monday of 1987 brought with them increased regulatory attention. However, it was the emergence of the internet marked by Wells Fargo's use of the World Wide Web (WWW) to provide online account

checking in 1995, followed by the formation of direct banks without physical branches and the noticeable amounts of money invested in technology by the traditional banks that led to full digitization by the beginning of the 21st century. The Global Financial Crisis of 2008 accompanied by the ever-increasing loss of confidence in banks was seen as a major turning point for the financial industry and the birth of the current day era of the FinTech 'revolution' or FinTech 3.0 which is now a large and rapidly growing industry that represented a total volume of investment of US$12.21 billion in 2014, a 300% increase from the precedent year (Ernst & Young Ltd, 2016).

Technology developers create a favorable environment for FinTech startups to launch innovative services rapidly by providing digital platforms for social media, big data analytics and smartphones to name a few. While big data analytics enables the provision of unique personalized services to customers, "social media facilitates the growth of communities in the crowdfunding and peer-to-peer lending services." (Lee, 2016, p. 59). Nonetheless, this is part of a broader entity, namely the FinTech ecosystem.

"More generally, an ecosystem is defined as a co-opetitive environment in which symbiotic relationships are formed to create mutual value for its stakeholders." (Hedman & Henningsson, 2015, p. 308). The ability to continuously evolve and adapt to changes both inside and outside is one of the key characteristics of an ecosystem and the importance of understanding the ecosystem is critical to developing effective business models (Basole, 2009; Lee, 2016). FinTech ecosystems in Europe and the U.S have "stimulated technological innovation, made financial markets and systems more efficient and improved the overall customer experience." (Strategy& (PwC), 2015).

Five elements of the FinTech ecosystem have been defined as follows, FinTech startups, technology developers, government, financial customers, and traditional financial institutions (Lee, 2016). Another model proposes a FinTech ecosystem development model in four parts, namely the business environment, government/regulatory support, access to capital, and financial expertise (Strategy& (PwC), 2015). Looking closer at the former model, at the centre of the ecosystem lies FinTech startups who are described as mainly entrepreneurial and the drivers of major innovations "in the areas of payment, wealth management, lending, crowdfunding, capital market and insurances by incurring lower operating costs, targeting niche markets and providing more personalized services than traditional firms."

The creation of FinTech startups have been greatly supported by the venture capitalists and private equities whose level of investments have significantly risen over time (Lee, 2016). The aim of the paper is to investigate the dynamic of those investment in the FinTechfour sectors of described below.

Online lending.

The new wave of online lenders mostly focusses on the market segments directly impacted by post-crisis legislation that later became mispriced or neglected by banking and government institutions (Pitchbook Data Inc., 2016a, p. 6). While there are many forms of online lending services (student loans, small business lending), one of the main trends in FinTech in this field is peer-to-peer (P2P). Basically P2P allows individuals to borrow and lend money without the intermediation of a financial institution (Zhang

& Chen, 2017).The efficient structure of P2P lending FinTechs' enables them to offer lower interest rates and improved lending processes for lenders and borrowers (Lee, 2016). The first P2P website was Zopa launched in 2005. These online lending platforms have their own regulatory, analytical and developer costs that must be funded through venture capital which includes a diverse group of investors, namely private equity firms, hedge funds, mutual funds, corporate VC firms and financial services executive-cum-angel investors (Pitchbook Data Inc., 2016a, p. 13). The main differences between P2P and traditional lending market are the following. On the one hand, the majority of the lenders are not professional: there are some empirical evidence showing that decisions are made on irrational basis and based on social mood, such as the physical attractiveness or writing skills of the borrower (Dorfleitner et al., 2016; Jin, Fan, Dai, & Ma, 2017; Zhang & Chen, 2017). On the other hand, sometimes borrowers and lenders are matched anonymously via real time auctions, as with Prosper.com. This does not help an appropriate evaluation of the risk, so Prosper introduced social network features in order to open some more information of members (Freedman & Jin, 2017).

Insurance.

Pricing risk is the core competency of insurance companies and has now become the main focus for competitive advantage in an industry which has become heavily segmented by the disruption of FinTech companies (Pitchbook Data Inc., 2017, p. 7) that employ data analytics to calculate and match risk and are more accurately able to offer personalized products and services to customers. Furthermore, these FinTechs managed to integrate alternative datasets into more accurate pricing models. In comparison to the other FinTech sectors, insurance tech companies did not see a major drop-off of investor interest and reached its plateau in 2015 with $1.5 billion and 90 deals followed by a slight drop in deals in 2016 where numbers were at 74 deals and $1.4 billion consecutively. It is interesting to note that the larger average deal size even since 2014 were 69 deals accounted for only $514 million is an indication of the substantial maturing of the industry (Pitchbook Data Inc., 2017, p. 14).

A*sset Management.*

Economic and regulatory conditions have placed tremendous pressure on fees in the asset management industry and to surpass this hurdle, FinTech has introduced new technologies and business models which are attractive to the millennial generation that represents a large share of the segment's overall investment. As millennials are tech savvy and conscious about fees, they tend to prefer ETFs which offers intraday liquidity and tax efficiency giving the service provider agency over when they can buy and sell and thus control when their capital gains become due (Pitchbook Data Inc., 2016c, pp. 3-5). A steady increase in institutional investor interest since the financial crisis unveiled many flaws in the way money was being managed (Huang, Chen, Wu, Huang, & Shen, 2016) . Private equity (PE) investors' substantial interest in this segment is an indication that the industry is maturing. The strategy of private equity investors is different from venture capitalists in that they tend to purchase mature undervalued companies, add leverage and make operational changes to improve profitability. However, recently PE firms have been involved in more and more growth deals, taking minority

stakes in companies. This shift is reflective in their increased participation in FinTech deals (Pitchbook Data Inc., 2016c, p. 14).

Bitcoin and Blockchain

Blockchain is a technology that allows transactions among potentially unlimited users or possibly devices "seamless, virtually costless, secure, and instantaneous – just as PayPal made it easy for people to buy and sell items on, say eBay" (Anonymous, 2017, p. 86). Those transactions among parties do not need the intermediaries – for example, a bank, a financial institution, or a broker – which also cut out the associated transaction costs (Anonymous, 2017). A blockchain is a text file acting as a public ledger recoding events, i.e. transaction. Although anyone can hold a copy, read and write on the blockchain it is very difficult, near impossible, to commit a fraud due to the use of a cryptographic signature (Mansfield-Devine, 2017, p. 15; Sikorski, Haughton, & Kraft, 2017). Each recorded block includes data of the previous block "which is then cryptographically hashed along with the information about the current transaction" (Mansfield-Devine, 2017, p. 15). A whole avenue of applications is open for this technology (Cheah & Fry, 2015), such as the P2P electricity trading (Anonymous, 2017), internet of things applications, i.e. Radio-Frequency identification and sensor technologies (Pazaitis, De Filippi, & Kostakis, 2017), in e-government like the case in Estonia of the e-resident card (Sullivan & Burger, 2017).

Bitcoin is a decentralized online peer-2-peer digital currency system which does not require any central clearing agency such as bank in the case of traditional electronic cash. The identification problem between two peers in a transaction (i.e. payment) could be solved simply by the availability of a Public Key Encryption but blockchain techniques are necessary when the solvability of the payer has to be verified. Indeed, all the blockchain information "is maintained by a community of participants, known as miners" (Abegg, Agrawala, Crick, & de Montfalcon, 2007; Göbel, Keeler, Krzesinski, & Taylor, 2016, p. 23; Pitchbook Data Inc., 2016b). Practically, when spending bitcoins this verification process could last on average 10 minutes.

In October 2013, the first bitcoin ATM in Vancouver appeared (Yermack, 2013). There are some discussions about the nature of bitcoin as a currency or a commodity. Because of lack of space this cannot be discussed here but some important features are the following. It is not like a currency for the following reasons. Bitcoins cannot be deposited in a bank but can be kept in a system of "digital wallets". Bitcoin does not have a direct link to gold or other precious metals and shows no significant correlation with other currencies such US dollars, Euro, etc.. It cannot be manipulated by anyone, hence in terms of fiat it is better than national currency, because the central bank cannot increase the supply of bitcoins and create inflation (Yermack, 2013). It is like a currency because it can be exchanged to any currency any time but it is a commodity because it also has liquidity limitation. The bitcoin has a finite supply of 21 million which is forecasted to be reached within the next century. It is a hyper-deflationary currency whose purchasing power goes up as the level of adoption goes up. "The increase in adoption explains the meteoric rise in the purchasing power of bitcoins since circulation started in 2009. The first recorded exchange rate of bitcoins for fiat currency was at a rate of 1,309.3BTC for 1USD, offered in October 2009. By April 2014, the exchange rate had

risen to fluctuate around 0.002BTC for 1USD, reflecting roughly a six-hundred-thousand-fold (0r 60,000,000%) increase in the price of a bitcoin in US dollars in four and a half years."(Ammous, 2014). Moreover, bitcoin does not have intrinsic value as gold does (Dyhrberg, 2016). Another interesting empirical result is that the download of cryptocurrency (not only bitcoin) apps have markedly increased in Spain, Italy, somewhat less in Cyprus followed by USA immediately after the Cyprus bailout announcements on march 16, 2013 (Luther & Salter, 2017).

In conclusion, this literature review sheds some light on the latest development of FinTech. Each FinTech sector ecosystem appears to have an internal identity, where the level of homogeneity could change across them. Nevertheless, there are different eco-systems for each sector. The next subsection will describe innovation of diffusion models by presenting the Bass-Rogers and Bemmaor model. The latter allows the estimation of the heterogeneity in the propensity of adoption.

2.2 Innovation diffusion models

The seminal Bass model of diffusion (Bass 1969), an extension of Rogers' (1962) ideas on the diffusion of innovations, quantifying the factors that drive individual and organizational adoption of new products is the starting point of this analysis. Bass considers a differential equation capturing a mixed-influence on diffusion through two main parameters, innovation (p), driven by external channels such as mass communication and imitation (q), driven by intrapersonal communication such as word-of-mouth. Equation 1, below, shows the Bass function (1969) for new product diffusion where N(t) is the cumulative number of adopters at time t, m is the total market adoption, the ceiling level, and the parameters p and q, the coefficients of innovation and imitation respectively,

$$\frac{dN(t)}{dt} = \underbrace{p(m - N(t))}_{\text{adoption due to external influence or independent adoption}} + \underbrace{\frac{q}{m} N(t)(m - N(t))}_{\text{adoption due to internal influence or internal adoption}} \qquad (1)$$

From a marketing perspective, the innovation coefficient p captures the propensity to adopt the new product as driven by external information. The imitation coefficient q, on the contrary, represents the propensity to adopt due to interpersonal communication channels (Mahajan et al., 1990). Eq.1 also contains and generalizes two extreme cases: one that is pure innovation, reducing to a modified exponential function when q=0 and p>0 and one that is pure imitation, represented by a logistic function when p=0 and q>0 (Meade & Islam, 2006). From the mathematical model perspective, q and p

are the shape and scale of the diffusion curves Eq.1 The ratio q/p, defines their shapes of the cumulative diffusion curves: the greater the q/p ratio is, the more prominent the S-shape. In this case, the S-shapes of cumulative adoption curves turn out to be more left-skewed and is therefore leading to a slower penetration rate than with lower values of q/p (Bemmaor & Lee, 2002; Meade & Islam, 2006). Hence, a systematic comparison of the innovation and imitation parameters, p and q, may provide essential information in estimating and forecasting new products' adoption across markets as well as that of different innovations within the same market.

An extension of Bass' distribution curves bridges Rogers' (2003) five adopter categories into the Bass/Rogers or BR model (Mahajan et al., 1990) and the shape of the non-cumulative diffusion curve has a bell shape. The first inflexion point, T1 that separates early adopters from the early majority. The peak of absolute adoption T*, identifies and discriminates between the early majority and the late majority. Finally, the second inflexion point, T2, separates the late majority from laggards (Mahajan et al., 1990, pp. 42-43, Figs. 3 and 4).

The original Bass model assumes a homogenous and fully connected social system within which the diffusion is taking place so that, in this framework, the probability that an individual adopts an innovation is linear with respect to the number of previous adopters, after considering other external factors, such as advertising (Bass, 1969; Mahajan & Muller, 1979).

Bemmaor (1994) proposes a general diffusion model based on heterogeneous individual propensity for adoption. This model includes the Bass model as a special case and assumes that individual-level times for adoption (or first purchase) vary following a shifted Gompertz distribution function (Bemmaor, 1994, p. 207).

The Gamma /Shifted Gompertz (G/SG) aggregate cumulative distribution function has the closed-form expression:

$$F(t) = \left[1 - e^{-bt}\right] / \left[1 + \beta e^{-bt}\right]^{\alpha} \qquad (2)$$

In Eq.2, the parameters b and β can also be expressed in terms of the Bass model parameters, using the two following relationships: b=p+q and β=q/p. For fixed values of b and β, α is the shape parameter of Eq.2 that measures the adopters' population heterogeneity. This parameter solves the models' misrepresentation issue in the cases of "extra-Bass" skew (Bemmaor & Lee, 2002).

If $\alpha \approx 0$, then the shape of Eq.2 is close to an exponential curve, similar to the one would obtain in the Bass model without imitators, when q=0. As α tends to ∞ the G/SG curve resembles a logistic curve, similar to the one would obtain in the Bass model without innovators, when for p=0. If $\alpha \approx 1$ Bemmaor model is equivalent to Bass model.

The presence of a required critical mass for adoption is captured through the lens of the Bass model, via the analysis of the q/p ratio. Therefore, two parametric sets indicate "Extra-Bass" features. On the one hand, q/p ratio and on the other hand, Bemmaor α parameter. This makes multiple interpretations possible. "[…] it is impossible to unambiguously interpret the model parameters of any single diffusion curve as reflecting

social contagion or heterogeneity in the propensity to adopt"(Van den Bulte & Stremersch, 2004, p. 530).

In banking innovation, some studies have been carried out using a diffusion-type interpretation. A qualitative study of German banks has also shown that relative to non-interactive innovations, the diffusion of interactive innovations (i.e. Electronic Funds Transfers and home banking for private customers) was slow to reach critical mass (Mahler & Rogers, 1999). In this case, an S-Shape for non-interactive innovations should be less pronounced, less left skewed, having therefore a smaller q/p ratio than one for interactive innovators. Bass model was used to study 14 alternative investments for disposable income available to US citizen in the early '80s (Srivastava, Mahajan, Ramaswami, & Cherian, 1985). Moreover, a recent study found 41 relevant researches published on "internet banking" and "e-banking" and focused on a cross-country analysis explaining e-banking adoption (Takieddine & Sun, 2015).

In conclusion, the Bemmaor diffusion model completes Bass model by adding heterogeneity of adoption for individuals, however, without identification of the source of heterogeneity. The skewness parameter α of Bemmaor model Eq.2 provides crucial information about heterogeneity and on the "Extra-Bass" shaped diffusion. Therefore, if $\alpha>1$, the Bemmaor model has a left-skewed shape, there is a further indication of the existence of critical mass effects (Meade & Islam, 2008). This paper focuses on the estimation of both the q/p ratios and the shape parameters α in assessing the presence and potential role of critical mass in the adoption processes of four FinTech sectors.

3 Data and methodological aspects

The data belongs to Pitchbook Data Inc. and it consists of quarterly series of the number of deals (deal count) made by investors in four sectors of FinTech. Insurance: the data consists of 16 consolidated observations and one provisional observation from the first quarter of 2013 to the first quarter of 2017 (Pitchbook Data Inc., 2017). Bitcoin and Blockchain: the data consists of 14 consolidated observations and one provisional observation from the first quarter of 2013 to the third quarter of 2016 (Pitchbook Data Inc., 2016b). Asset management: the data consists of 15 consolidated observations and one provisional observation from the first quarter of 2013 to the fourth quarter of 2016 (Pitchbook Data Inc., 2016c). Online lending: the data consists of 26 consolidated observations from the first quarter of 2010 to the second quarter of 2016 (Pitchbook Data Inc., 2016a).

To estimate a Bass, we have customized a routine developed by Michel Leonard of SAS Institute Inc. in 2010. This routine uses the probability density function as shown in Eq.1 (Bass, 1969; Mahajan et al., 1990; Srinivasan & Mason, 1986)
For Bemmaor or G/SG, the estimation uses the closed formula of Eq.2 and for the estimation of T* we refer to Bemmaor and Lee (2002, Appendice). The estimations were done using the SAS routine Proc Model (SAS Institute Inc., 2011).

The values of Adj-R2 are often extremely high (in this case, the lowest estimated value was 0.985 and the highest 0.97) and therefore not very informative. The lack of information of Adj-R2 especially for Bass models have been observed by Van den

Bulte and Joshi (2007). Instead, mean absolute percentage (Root MSE) is reported in table 1. All models suffer from a collinearity effect as in other research such as Scaglione, Giovannetti, and Hamoudia (2015). We acknowledge this limitation.

4 Results

The projected results reported in Table 1 clearly show that the estimates for the shape parameter $\beta=q/p$ differ under the hypotheses of the Bass model for Online lending (q/p=89.9). Online lending is mainly driven by innovation given that p, namely the innovation parameter is not significantly different from 0, this is also true for Bemmaor. The skewness parameter α, indicating the heterogeneity of adoption, is the lowest of the four sectors (α=0.36). Moreover, the corresponding graphs in figure 1 shows a left-skewed shape providing evidence about the existence of critical mass. As it was pointed out in the literature review, it is difficult to isolate which factor is responsible for this "Extra-Bass" shape i.e. the lack of innovation or the heterogeneity in the propensity of adoption.

From the point of view of β (q/p=22.0) Blockchain & Bitcoin (B&B) follows online lending. Nevertheless, the innovation parameter is significantly different from 0. The value of α (1.61), the inspection of the corresponding graphs in figure 1 and the close values of root MSE for the two models show that this diffusion appears to be a Bass diffusion. Another issue is that the value1 for α belongs to the 95% Wald confidence iinterval [0.66,2.57]. In this case, if this hypothesis is accepted it implies that the diffusion of B&B seems to be homogeneous and mainly with the propensity of adoption in the beginning of the diffusion. The peak value is the same for the two models (2014 Q4) reinforcing the coincidence of them.

The Asset management sector has a β value of 11.62 and an α value of 0.66. No reported results show that the confidence interval at 95% of the estimated α is [0.52,0.93] indicating somehow, the lack of coincidence of the two models. Therefore, the propensity of adoption in Asset management is more heterogeneous than the case of B&B.

Finally, insurance is the sector with the lowest β (q/p=8.6) and the highest p (0.023). The α value is 0.42 in line with the conclusion by the observation of the corresponding graphs in figure 1 i.e. the Bass model and Bemmaor model are different. From the point of view of the Bass-Roger categories, each of the sectors have already surpassed the peak T^*, showing that they are in the late majority stage nowadays. Nevertheless, the time to reach this peak date is similar for B&B, Asset management and Insurance (between 8–10 quarters). On the contrary, Online lending needs more than double the time (26 quarters following Bass and 23 following Bemmaor). Figure 2 shows the cumulative distribution and forecasts for both models.

5 Implications, limitations and further research

We have seen that critical mass was most present in Online lending than in the three other cases. The B2C and C2C lending activity is a typical case of an interactive innovation. Although we have no data available of the adoption at that level, empirical evidence referenced in the literature review suggests the existence of critical mass at the C2C level (Mahler & Rogers, 1999) . The fact that investment shows the same pattern could be merely the result of the level of risk connected to the evaluation of the adoption.

Contrary to the former case, the Insurance sector shows the highest p value and may hence be due to the competitive nature and the relevance of high performance price risk evaluation technology for the traditional insurance sector as seen in the literature. As such, investors are also those traditional insurance companies constantly looking to gain the necessary advantage in the field.

Bitcoin -related companies have seen heightened levels of investor interest since the price of bitcoin exceeded $200 in 2013 Q4, an increase in the level of investor interest was seen and could explain the heterogeneity and propensity of early adoption seen in the corresponding graphs in figure 1. However, a decrease in deals over time is expected as the VCs prefer to have more interest in easy-to-define business models (Pitchbook Data Inc., 2016b). This is also line with the corresponding graphs in figure 1 where the peak is shown in 2014 Q4. Nevertheless, this explains only a part of the history, given that that the data also count the deals focussed on Blockchain technology. In the literature review there are some applications in other fields other than banking, such as the electricity market, Internet of things, etc. Therefore, a hyper-cycle could launch in a near future as some new comers will boost the interest in this technology.

Asset management shows that the propensity to adopt is varied among investors which may be linked to the shift of the robo-advisory technology which was focused on created attractive business models for young, tech savvy millennials, to reach other target segments with adapted business models. These varied business models may attract varied investment activity (Pitchbook Data Inc., 2016c) as the corresponding graphs in figure 1 has shown.

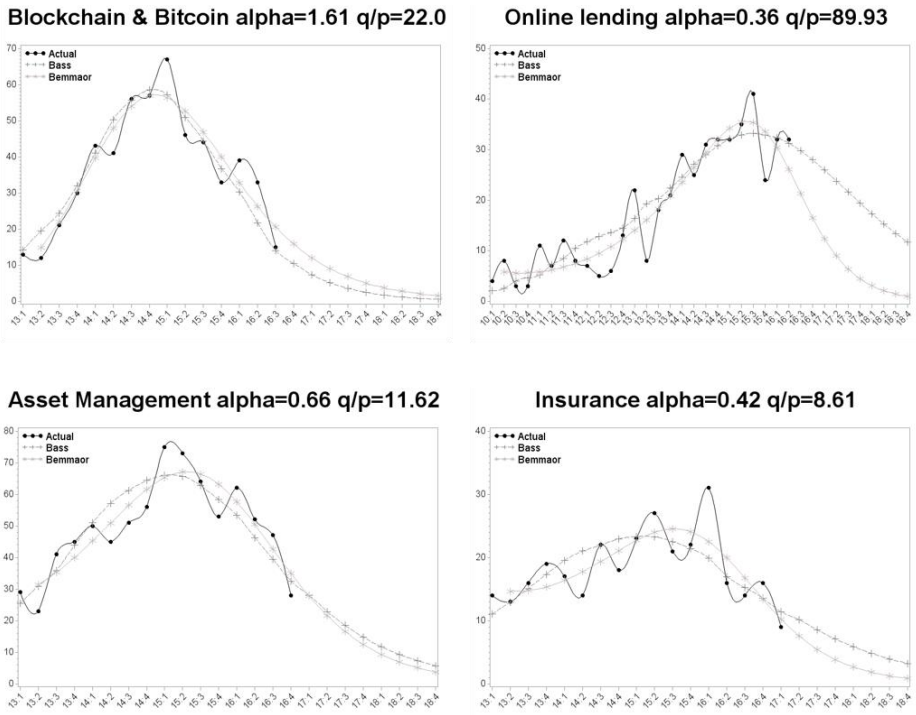

Fig. 1. : Actual,Bass and Bemmaor estimation and forecasting of absolute numbers of deals

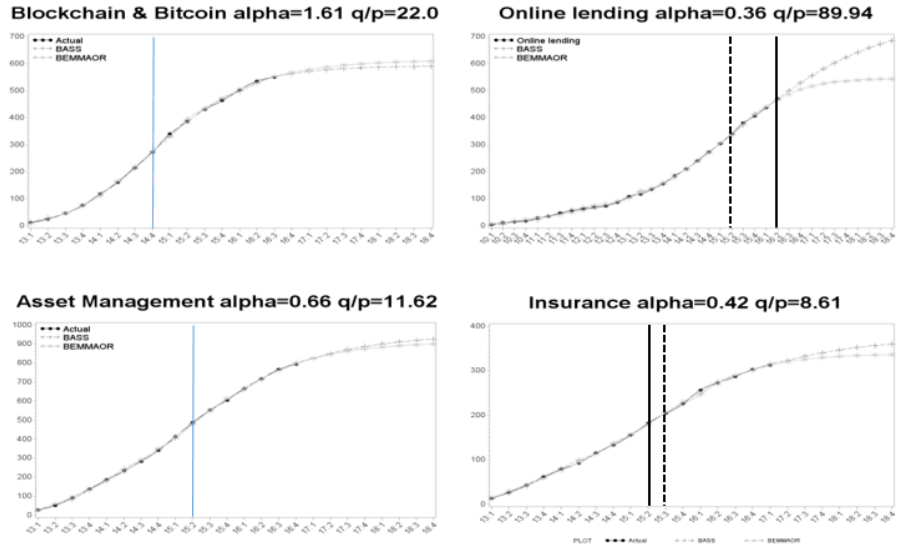

Fig. 2. Actual Bass and Bemmaor estimation and forecasting of absolute numbers of deals. The vertical axis indicates the date T* in the case of Online lending and Insurance, Bemmaor's T* in dotted lines, Bass' in solid lines.

Table 1.

Data	Method	Final market (m)	p	q	alpha	beta=q/p	b=p+q	T*	period	T* (Peak Date)	t1	t1* (Peak Date)	Root MSE
Blockchain & Bitcoin (#Q=15)	Bass	591	0.0165	0.3627		22.0050	0.3792	8.15	2013Q1 to 2016Q3	2014Q4	2.46	2013Q3	5.87
		(15.718)	(0.0059)	(0.0322)		(9.419)	(0.0282)						
	Bemmaor	613	0.0403	0.2709	1.6151	6.7193	0.3112	7.80		2014Q4			4.43
		(15.296)	(0.0181)	(0.0002)	(0.4853)	(4.2416)	(0.0322)						
Online lending (#Q=26)	Bass	760	0.0019	0.1710		89.9393	0.1729	26.02	2010Q1 to 2016Q2	2016Q2	4.53	2011Q1	4.90
		(100.8)	(0.0025)	(0.0243)		(125.7)	(0.0226)						
	Bemmaor	546	0.0000	0.3993	0.3569	17'899	0.399311	21.92		2015Q2			3.75
		(20.59)	(0.00002)	(0.0435)	(0.0416)	(18'366)	(0.0435)						
Asset Mgt (#Q=16)	Bass	949	0.0204	0.2369		11.6169	0.2573	9.53	2013Q1 to 2016Q4	2015Q2	3.40	2013Q3	6.93
		(39.6161)	(0.0048)	(0.0272)		(3.8357)	(0.0239)						
	Bemmaor	910	0.0085	0.3130	0.6578	36.7164	0.3215	9.73		2015Q2			5.45
		(26.883)	(0.0299)	(0.0386)	(0.0901)	(19.3903)	(0.0352)						
Insurance (#Q=17)	Bass	375	0.0232	0.2001		8.6098	0.2233	9.64	2013Q1 to 2017Q1	2015Q2	3.94	2014Q4	3.96
		(25.004)	(0.0075)	(0.0402)		(4.2278)	(0.0350)						
	Bemmaor	338	0.0023	0.3938	0.4199	125.6457	0.3962	10.53		2015Q3			2.45
		(6.8997)	(0.00097)	(0.0368)	(0.0396)	(85.8229)	(0.0359)						

Estimates and root SME for each sector. In bold, estimates significant of 1%, in bold italic at 1%

References

Abegg, B., Agrawala, S., Crick, F., & de Montfalcon, A. (2007). Climate change impacts and adaptation in winter tourism. In S. Agrawala (Ed.), *Climate Change in the European Alps*. Paris: Organisation for Economic Co-operation and Development.

Adomavicius, G., Bockstedt, J. C., Gupta, A., & Kauffman, R. J. (2007). Technology roles and paths of influence in an ecosystem model of technology evolution. *Information Technology and Management, 8*(2), 185-202.

Ammous, S. (2014). Economics beyond Financial Intermediation.

Anonymous. (2017). Blockchain Technology: Will It Make a Difference? *The Electricity Journal, 30*(3), 86-87. doi:http://dx.doi.org/10.1016/j.tej.2017.04.007

Arner, D., Barberis, J., & Buckley, R. (2016). The Evolution of Fintech: A New Post-Crisis Paradigm? *Georgetown Journal of International Law, 47*, 1271-1318.

Basole, R. C. (2009). Visualization of interfirm relations in a converging mobile ecosystem. *Journal of Information Technology, 24*(2), 144-159. doi:10.1057/jit.2008.34

Bass, F. M. (1969). A New Product Growth Model for Consumer Durables. *Management Science, 15*(5), 215-227.

Bemmaor, A. C. (1994). Modeling the diffusion of new durable goods: Word-of-mouth effect versus consumer heterogeneity. In G. Laurent, G. L. Lilien, & B. Pras (Eds.), *Research traditions in marketing* (pp. 201-223). Boston, MA: Kluwer Academic Publish Group.

Bemmaor, A. C., & Lee, J. (2002). The impact of heterogeneity and ill-conditioning on diffusion model parameter estimates. *Marketing Science, 21*(2), 209-220

Cheah, E.-T., & Fry, J. (2015). Speculative bubbles in Bitcoin markets? An empirical investigation into the fundamental value of Bitcoin. *Economics Letters, 130*, 32-36.

Deloitte. (2016). *Connecting Global Fintech: Hub Review 2016*. Retrieved from Available: http://thegfhf.org/wp-content/uploads/2016/10/Connecting-Global-FinTech-Hub-

Review-2016-.pdf: http://thegfhf.org/wp-content/uploads/2016/10/Connecting-Global-FinTech-Hub-Review-2016-.pdf

Dorfleitner, G., Priberny, C., Schuster, S., Stoiber, J., Weber, M., de Castro, I., & Kammler, J. (2016). Description-text related soft information in peer-to-peer lending – Evidence from two leading European platforms. *Journal of Banking & Finance, 64*, 169-187. doi:http://dx.doi.org/10.1016/j.jbankfin.2015.11.009

Dyhrberg, A. H. (2016). Bitcoin, gold and the dollar – A GARCH volatility analysis. *Finance Research Letters, 16*, 85-92. doi:http://dx.doi.org/10.1016/j.frl.2015.10.008

Ernst & Young Ltd. (2016). *Swiss FinTech Report 2016: The Role of Switzerland as a Financial Hub*. Retrieved from Available: http://www.ey.com/Publication/vwLUAssets/EY_Swiss_FinTech_2016_English/%24FILE/EY-Swiss-FinTech-2016-English.pdf: http://www.ey.com/Publication/vwLUAssets/EY_Swiss_FinTech_2016_English/%24FILE/EY-Swiss-FinTech-2016-English.pdf

Evans, P., & Wurster, T. S. (2000). *Blown to bits how the new economics of information transforms strategy*. Boston, Mass.: Harvard Business School Press.

Freedman, S., & Jin, G. Z. (2017). The information value of online social networks: Lessons from peer-to-peer lending. *International Journal of Industrial Organization, 51*, 185-222. doi:http://dx.doi.org/10.1016/j.ijindorg.2016.09.002

Göbel, J., Keeler, H. P., Krzesinski, A. E., & Taylor, P. G. (2016). Bitcoin blockchain dynamics: The selfish-mine strategy in the presence of propagation delay. *Performance Evaluation, 104*, 23-41.

Hedman, J., & Henningsson, S. (2015). The new normal: Market cooperation in the mobile payments ecosystem. *Electronic Commerce Research and Applications, 14*(5), 305-318. doi:http://dx.doi.org/10.1016/j.elerap.2015.03.005

Jin, J., Fan, B., Dai, S., & Ma, Q. (2017). Beauty premium: Event-related potentials evidence of how physical attractiveness matters in online peer-to-peer lending. *Neuroscience Letters, 640*, 130-135. doi:http://dx.doi.org/10.1016/j.neulet.2017.01.037

Lee, I. (2016). Fintech: Ecosystem and Business Models. *Advanced Sciences and Technology Letters, 142*, 57-62. doi:http://dx.doi.org/10.14257/astl.2016.142.10

Luther, W. J., & Salter, A. W. (2017). Bitcoin and the bailout. *The Quarterly Review of Economics and Finance*. doi:http://dx.doi.org/10.1016/j.qref.2017.01.009

Mahajan, V., & Muller, E. (1979). Innovation Diffusion and New Product Growth Models in Marketing *Journal of Marketing, 43*(4), 55-68.

Mahajan, V., Muller, E., & Bass, F. M. (1995). Diffusion of New Products: Empirical Generalizations and Managerial Uses. *Marketing Science, 14*(3), 79-88.

Mahajan, V., Muller, E., & Srivastava, R. (1990). Determination of Adopter Categories by Using Innovation Diffusion Models. *Journal of Marketing Research, XXVII*(February), 37-50.

Mahler, A., & Rogers, E. M. (1999). The diffusion of interactive communication innovations and the critical mass: The adoption of telecommunications services by German banks. *Telecommunications Policy, 23*, 717-740.

Mansfield-Devine, S. (2017). Beyond Bitcoin: using blockchain technology to provide assurance in the commercial world. *Computer Fraud & Security, 2017*(5), 14-18. doi:http://dx.doi.org/10.1016/S1361-3723(17)30042-8

Meade, N., & Islam, T. (2006). Modelling and forecasting the diffusion of innovation-A 25-year review. *International Journal of Forecasting, 22*(3), 519–545.

Meade, N., & Islam, T. (2008). The Effects of Network Externalities on the Diffusion of Cellular Telephones. *Telektronikk: Telecommunications Forecasting, 3*(4), 74-81.

Pazaitis, A., De Filippi, P., & Kostakis, V. (2017). Blockchain and value systems in the sharing economy: The illustrative case of Backfeed. *Technological forecasting and social change*. doi:http://dx.doi.org/10.1016/j.techfore.2017.05.025

Peres, R., Muller, E., & Mahajan, V. (2010). Innovation Diffusion and New Product Growth Models: A Critical Review and Research Directions. *International Journal of Research in Marketing, 27*, 91-106.

Pitchbook Data Inc. (2016a). *Pitchbook Fintech Anaylst Report: Part 1 Online Lending*. Retrieved from https://files.pitchbook.com/pdf/PitchBook_Fintech_Analyst_Report_Part_1_Online_Lending.pdf

Pitchbook Data Inc. (2016b). *Pitchbook Fintech Anaylst Report: Part 2 Bitcoin/Blockchain*. Retrieved from http://www.valuewalk.com/wp-content/uploads/2016/10/PitchBook_Fintech_Analyst_Report_Part_2_Bitcoin_Blockchain.pdf

Pitchbook Data Inc. (2016c). *Pitchbook Fintech Anaylst Report: Part 3 Asset Management*. Retrieved from https://files.pitchbook.com/pdf/PitchBook_Fintech_Analyst_Report_Part_3_Asset_Management.pdf

Pitchbook Data Inc. (2017). *Pitchbook Fintech Anaylst Report: Part IV Insurance*. Retrieved from https://files.pitchbook.com/pdf/PitchBook_Fintech_Analyst_Report_Part_IV_Insurance.pdf

Rogers, E. M. (1962). *Diffusion of Innovations* (1st ed.). New York: The Free Press.

Rogers, E. M. (2003). *Diffusion of Innovations* (5th ed.). New York: The Free Press.

SAS Institute Inc. (2011). *SAS/STAT® 9.22 User's Guide*. Cary, NC: SAS Institute Inc.

Scaglione, M., Giovannetti, E., & Hamoudia, M. (2015). The diffusion of mobile social networking: Exploring adoption externalities in four G7 countries. *International Journal of Forecasting, 31*(4,October–December 2015), 1159–1170. doi:http://dx.doi.org/10.1016/j.ijforecast.2015.03.005

Sikorski, J. J., Haughton, J., & Kraft, M. (2017). Blockchain technology in the chemical industry: Machine-to-machine electricity market. *Applied Energy, 195*, 234-246. doi:http://dx.doi.org/10.1016/j.apenergy.2017.03.039

Srinivasan, V., & Mason, C. H. (1986). Technical Note—Nonlinear Least Squares Estimation of New Product Diffusion Models. *Marketing Science, 5*(2), 169-178. doi:10.1287/mksc.5.2.169

Srivastava, R. K., Mahajan, V., Ramaswami, S. N., & Cherian, J. (1985). A multi-attribute diffusion model for forecasting the adoption of investment alternatives for consumers. *Technological forecasting and social change, 28*(4), 325-333. doi:http://dx.doi.org/10.1016/0040-1625(85)90034-4

Staykova, K. S., & Damsgaard, J. (2015). The race to dominate the mobile payments platform: Entry and expansion strategies. *Electronic Commerce Research and Applications, 14*(5), 319-330. doi:http://dx.doi.org/10.1016/j.elerap.2015.03.004

Strategy& (PwC). (2015). Developing a Fintech Ecosystem in the GCC: Lets Get Ready for Takeoff. Retrieved from https://www.strategyand.pwc.com/media/file/Developing-a-FinTech-ecosystem-in-the-GCC.pdf

Sullivan, C., & Burger, E. (2017). E-residency and blockchain. *Computer Law & Security Review*. doi:http://dx.doi.org/10.1016/j.clsr.2017.03.016

Takieddine, S., & Sun, J. (2015). Internet banking diffusion: A country-level analysis. *Electronic Commerce Research and Applications, 14*(5), 361-371. doi:http://dx.doi.org/10.1016/j.elerap.2015.06.001

Van den Bulte, C., & Joshi, Y. V. (2007). New Product Diffusion with Influentials and Imitators. *Marketing Science, 26*(3), 400-421. doi:10.1287/mksc.1060.0224

Van den Bulte, C., & Stremersch, S. (2004). Social contagion and income heterogeneity in new product diffusion: A meta-analytic test. *Marketing Science, 23*(4), 530-544

Yermack, D. (2013). Is Bitcoin a Real Currency? An economic appraisal. *National Bureau of Economic Research Working Paper Series, No. 19747* (December 2013).

Zhang, K., & Chen, X. (2017). Herding in a P2P lending market: Rational inference OR irrational trust? *Electronic Commerce Research and Applications, 23*, 45-53. doi:http://dx.doi.org/10.1016/j.elerap.2017.04.001

Multiple seasonal Holt-Winters improvement for the special events forecast using Discrete-Interval Multiple Seasonalities

J. Carlos García-Díaz, O.Trull
Departament of Statistics, Applied Operational Research and Quality,
Universitat Politècnica de València
e-mail: juagardi@eio.upv.es

Abstract: Electricity demand prediction based on time series forecasting is an essential task for distribution network operators in charge of electricity distribution and planning. They use information about the observed demand to predict future estimations, both in the short and long term. Forecasting and predictive techniques always have to deal with several irregularities in the time series. The most significant one is the calendar effect because national or local holidays seriously affect the series and, thus, the forecasting process. Many previous studies address this subject by modifying the series and applying dummy variable regressors. We present a new proposal where the calendar effect is included as part of the model rather than as an external modifier. These irregularities are included as new seasonalities using discrete intervals in multiple seasonal Holt-Winters models. This methodology is applied to electricity demand forecasting in Spain, especially to deal with the Easter holidays. Results are shown and discussed.

Keywords: Time series, forecasting, multiple seasonal Holt-Winters models

1 Introduction

Production planning and distribution of electricity in western countries are responsibility of electricity distribution companies, better known as transmission system operators (TSO). They are in charge of the coordination of the real-time production with demand, which affect directly to customer service and prices. This task highly depends on the forecasted demand by the operator since any mismatch between production and demand causes big losses in energy and money. The prediction techniques used by these companies are based on time series forecasting, modelling their own complicated models. The information of the observed demand is thus used to feed those models and lately for making predictions of newer demands and future estimations. However, the behaviour of observed data shows many irregularities the models must deal with: Weather conditions - like summer or winter -and the most important, calendar effect. Literature about weather modelling can be found in [1–4].

adfa, p. 1, 2011.

Regarding the calendar effect, we distinguish between normal days - work days whose pattern always exhibits similar behaviour-, and anomalous days (or special days) – days on witch special conditions modify the regular behaviour, such as holidays, strikes, special events, etc. -. Figure 1 illustrates this irregularity in an Easter week. The treatment of the anomalous days is considered in several works. Most of them include the irregularities as the implementation of a new model or as a part of the model, but modifying it using dummy variables[5,6] or as intervention functions. New recent approaches reveal interesting information, as in the study by Arora et al. [7], where they model with triple seasonal holt-winters, but with rule-based methodologies to deal with special days. Bermudez et al. [8,9] use multivariate time series in which special days are considered as a covariate directly related to the demand. Although all of these methods are efficient and provide good results, we propose a new methodology based on Holt-Winters modelling, which usually provides the most accurate forecasts in terms of demand[10]. A new point of view is proposed where special days are part of the model itself, included as a new seasonal pattern that occurs in discrete time ranges, which allows the model to avoid the use of exogenous variables.

This article is structured as follows. Section 2 presents the new modelling. Section 3 performs the analysis of this method applied to Spanish electricity demand, and, finally, section 4 summarises the conclusions reached.

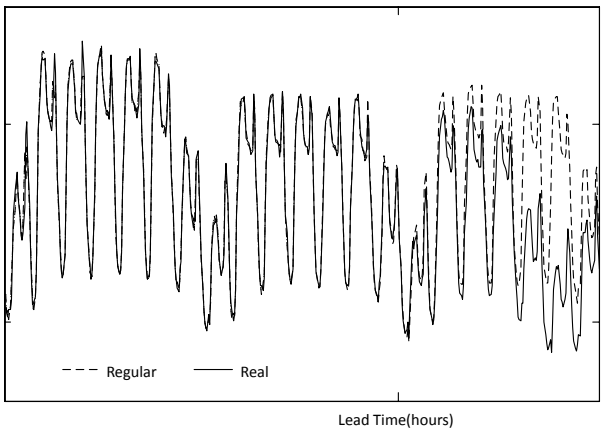

Figure 1. Irregular behaviour of the series due to calendar effect. Dash line represents the behaviour for a regular series. The seasonal pattern is fully accomplished by the series. But the reality – filled line – shows some different behaviour to expected, due to Easter holidays in this case. It may affect several days.

2 Discrete Interval Multiple Seasonal modelling

Multiple seasonal Holt-Winters (nHWT) models were formerly presented by Taylor[1,11]. García-Díaz et al. [12] proposed a generalisation of the method which is shown in (1-4) in the additive trend and multiplicative seasonality form.

$$S_t = \alpha\left(\frac{X_t}{\prod I_{t-s_i}^{(i)}}\right) + (1-\alpha)(S_{t-1} + T_{t-1}) \quad (1)$$

$$T_t = \gamma(S_t - S_{t-1}) + (1-\gamma)T_{t-1} \quad (2)$$

$$I_t^{(i)} = \delta^{(i)}\left(\frac{X_t}{S_t \prod_{j\neq i} I_{t-s_j}^{(j)}}\right) + \left(1-\delta^{(i)}\right)I_{t-s_i}^{(i)} \quad (3)$$

$$\hat{X}_t(k) = (S_t + kT_t)\prod_i I_{t-s_i+k}^{(i)} + \varphi_{AR}^k \varepsilon_t \quad (4)$$

The new proposal discriminates between two kinds of seasonalities. The first one is regular and occurs during the entire time series; once this seasonality starts, it always repeats with a fixed length, leaving no gaps. The second type of seasonality occurs in a discrete interval that may occur one or several times within the other regular seasonalities, and can vary in position over time, but not in length. We refer to this as Discrete-Interval Mobile Seasonalities (DIMS). Additional requirements for DIMS must be fulfilled. A smoothing equation has to model the behaviour of the new seasonality and be updated with each new occurrence in the observed values; thus, it can be integrated within the nHWT model (8). Each repetition in observed values is used to feed the smoothing equation. It also affects the regular seasonality as shown in (7) as well as level (5). This seasonality must only be present in newer expected occurrences as part of the forecast equation (9). The former model is thus expressed as in (5-9).

$$S_t = \alpha\left(\frac{X_t}{\prod I_{t-s_i}^{(i)} \prod D_{t^*-s_j}^{(j)}}\right) + (1-\alpha)(S_{t-1} + T_{t-1}) \quad (5)$$

$$T_t = \gamma(S_t - S_{t-1}) + (1-\gamma)T_{t-1} \quad (6)$$

$$I_t^{(i)} = \delta^{(i)}\left(\frac{X_t}{S_t \prod_{j\neq i} I_{t-s_j}^{(j)} \prod_m D_{t^*-s_m^*}^{(m)}}\right) + \left(1-\delta^{(i)}\right)I_{t-s_i}^{(i)} \quad (7)$$

$$D_{t_h^*}^{(h)} = \delta_D^{(h)}\left(\frac{X_t}{S_t \prod_j I_{t-s_j}^{(j)} \prod_{m\neq h} D_{t_h^*-s_m^*}^{(m)}}\right) + \left(1-\delta_D^{(h)}\right)D_{t_h^*-s_h^*}^{(h)} \quad (8)$$

$$\hat{X}_t(k) = (S_t + kT_t)\prod_i I_{t-s_i+k}^{(i)} \prod_j D_{t^*-s_h^*+k}^{(h)} + \varphi_{AR}^k \varepsilon_t \quad (9)$$

Where S_t, T_t, and $I_t^{(i)}$ are the smoothing equations for level, trend and seasonal indices for each i seasonal pattern of length s_i. $D_{t_h^*}^{(h)}$ are smoothing equations for each DIMS h, of length s_h and defined only in $t_h{}^*$. $\hat{X}_t(k)$ is the k-step ahead forecasting equation where X_t are the observed values. $\alpha, \gamma, \delta^{(i)}$ and $\delta_D^{(h)}$ are the smoothing parameters in each equation. φ_{AR} is the parameter for the first autoregressive error adjustment, and ε_t is the first order error. $t_h{}^*$ must be defined has to be defined so that it only includes the period in which the DIMS occurs. Another aspect that differs DIMS to

regular seasonalities regards the recurrence of the equations. DIMS use information of previous s_h^* observed values, regardless of how many times it occurs.

The way to work with DIMS is illustrated in Figure 2. Initially, the initial values of level, trend and regular seasonalities must be obtained. In a second step, the DIMS initial values obtained and finally, the smoothing parameters must be optimised. After this process, newer forecasts can be stated.

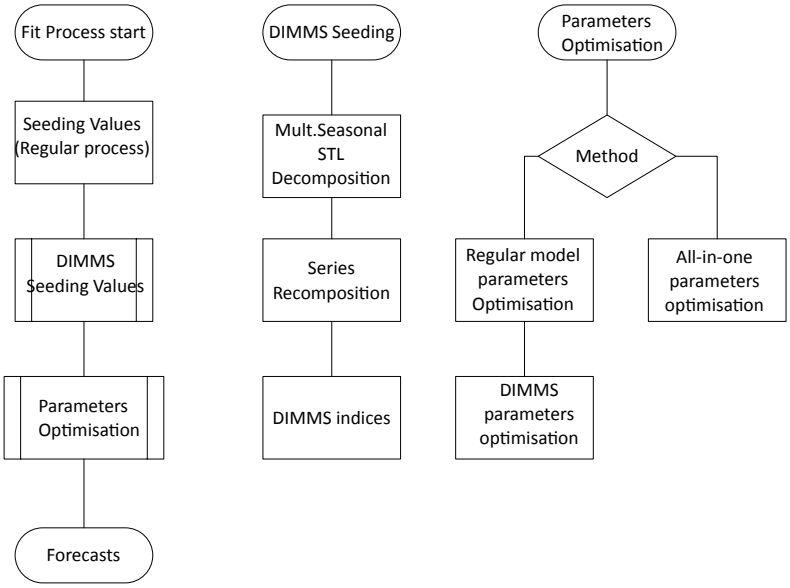

Figure 2. Working procedure to fit model using DIMS and make forecasts.

2.1 DIMS Initialisation procedure

DIMS smoothing equations are recurrent and need to be initialised. The methods used are based on regular seasonal indices techniques, but have to be adapted in order not to disturb main seasonal patterns.

The seeding values can be obtained using the following procedure for each DIMS:

– 1st, a STL decomposition[13] is carried out with all regular seasonal components (10); the series is then recomposed without remainder (11).

$$X_t = T_t + \sum S_t^{(s_i)} + U_t \tag{10}$$

– Where T_t is the trend, and $S_t^{(i)}$ are the seasonal components for period length s_i. U_t stands for the remainder. The recomposition involves only the first parameters, thus

$$R_t = T_t + \sum S_t^{(s_i)} \tag{11}$$

– 2nd, the data is prepared according the DIMS positions and length, with k appearances within the series time range. Each value is divided by the recomposed series values in the same position.

	1	**2**	**3**	**…**	**k**
1	$\frac{X_{p_1}}{R_{p_1}}$	$\frac{X_{p_2}}{R_{p_2}}$	$\frac{X_{p_3}}{R_{p_3}}$	…	$\frac{X_{p_k}}{R_{p_k}}$
2	$\frac{X_{p_1+1}}{R_{p_1+1}}$	$\frac{X_{p_2+1}}{R_{p_2+1}}$	$\frac{X_{p_3+1}}{R_{p_3+1}}$		$\frac{X_{p_k+1}}{R_{p_k+1}}$
…	…	…	…		…
s_m^*	$\frac{X_{p_1+s_m^*-1}}{R_{p_1+s_{m-1}^*}}$	$\frac{X_{p_2+s_m^*-1}}{R_{p_2+s_{m-1}^*}}$	$\frac{X_{p_3+s_m^*-1}}{R_{p_3+s_{m-1}^*}}$		$\frac{X_{p_k+s_m^*-1}}{R_{p_k+s_{m-1}^*}}$

In this table, p_i is the position of each DIMS in the time series, and R_i is the recomposed series value at the i position.

– 3rd, indices are computed as average of all previous values.

$$D_1^{(i)} = \frac{1}{k}\left(\frac{X_{p_1}}{R_{p_1}} + \frac{X_{p_2}}{R_{p_2}} + \frac{X_{p_3}}{R_{p_3}} + \cdots + \frac{X_{p_k}}{R_{p_k}}\right)$$

$$D_2^{(i)} = \frac{1}{k}\left(\frac{X_{p_1+1}}{R_{p_1+1}} + \frac{X_{p_2+1}}{R_{p_2+1}} + \frac{X_{p_3+1}}{R_{p_3+1}} + \cdots + \frac{X_{p_k+1}}{R_{p_k+1}}\right)$$

$$\cdots$$

$$D_{s_m^*} = \frac{1}{k}\left(\frac{X_{p_1+s_m^*-1}}{R_{p_1+s_{m-1}^*}} + \frac{X_{p_2+s_m^*-1}}{R_{p_2+s_{m-1}^*}} + \cdots + \frac{X_{p_k+s_m^*-1}}{R_{p_k+s_{m-1}^*}}\right)$$

2.2 Parameters optimisation

Smoothing parameters are crucial in the model forecasting process, and they must be optimised. This action requires the minimisation of an error measurement indicator in a non-linear problem. The indicator used in this paper for fitting is the root mean squared error (RMSE) as defined in (12).

$$\text{RMSE} = \sqrt{\frac{1}{N}\sum\left(\widehat{X_t} - X_t\right)^2} \tag{12}$$

As shown in Figure 2, there are two possible ways of obtaining them. The first involves the obtaining all parameters simultaneously, as suggested in Chatfield and Taylor[11,14]**;** this is the most common way for regular Holt-Winters methodology. But DIMS are defined only in some discrete time ranges, therefore the proposal of using a two-step process makes sense, in which the regular parameters are obtained first, and then the DIMS smoothing parameter.

3 Spanish electricity data and calendar modelling

In Spain, the TSO is called Red Eléctrica de España (REE). It provides information about the aggregated Spanish hourly electricity demand on its own web page, where the data used in this paper was obtained. The data refer to the period from 1 July 2007 at 02:00 a.m. to 5 April 2015. In this period, some special events took place that can be modelled using DIMS. Although this methodology can be applied to all special events, we concentrated on modelling strikes and Easter in this paper.

The accuracy indicator used to compare the forecasts is the mean average percentage error (MAPE) as defined in (13).

$$\text{MAPE}(\%) = \frac{1}{N} \sum \frac{|\widehat{x_t} - x_t|}{x_t} \times 100 \tag{13}$$

The models used in this work had two seasonal patterns of length $s_1 = 24$ and $s_2 = 168$ hours. Although it was possible the use of a third seasonal pattern, it was discarded, as mentioned in García-Díaz & Trull[12].

An analysis using Easter modelling was carried out. The aim was to model a yearly event that occurs on different weeks each year with a fixed period longer than one day. Easter took place on the dates listed in Table 1. All the regions in Spain have holidays on Holy Thursday and Maundy Friday. The rest of the week has a special behaviour depending on the region and year. Although there is no official holiday, the industrial production level decreases, which has an impact on the demand. The following week includes Easter Monday, and some regions do have holidays on that day. The centre of the graph shows the Easter holidays, when the consumption clearly falls. The surrounding weeks do not show any special behaviour, although our initial suspicions.

Positions and lengths of DIMS are listed in Table 2. The two methods were tested to obtain the parameters: all the parameters together, and the two-steps process. Additionally, several models were tested according to the trend and seasonal methods.

The procedure carried out for the analysis consisted of making 24-hours-ahead forecasts for the Easter periods in 2014 and 2015, and comparing them to the real data measured with MAPE.

Table 1. General Easter period in Spain. It starts with the Palm Sunday and ends with the Resurrection Sunday. This table shows when occur these special days. Not all regions in Spain apply the same Easter period for holidays, but all of them include, at least, the Saint Thursday and Friday.

Year	Palm Sunday	Resurrection Sunday
2008	16 March	23 March
2009	5 April	12 April
2010	28 March	4 April
2011	17 April	24 April
2012	1 April	8 April
2013	24 March	31 March
2014	13 April	20 April
2015	29 March	5 April

Table 2. Analysis framework. Two parameters optimisation methods used, several periods and models.

Analysis Summary		
Parameters Optimisation	All-in-one	Two-Steps
Period	Starting at	Length
1	Monday after Palm Sunday	192 h
2	Thursday Saint	120 h
3	Wednesday	96 h
4	Wednesday	120 h
Models	AMC	AAC

Many models and cases were tested, as described in [12], but only the most interesting ones are summarised in Table 3. The model $AMC_{24,168}$ refers to an additive-trend and multiplicative-seasonality model with two seasonalities (24 hours and 168 hours). The model $AAC_{24,168}$ refers to an additive trend and seasonality model with the same seasonal patterns. Case 0 in both models represent the nHWT results on Easter dates. The model cannot deal with these kinds of irregularities, and MAPE rises to 10%, compared to regular conditions, which show results of about 2% [12]. The rest show lower MAPE - under 5% -, because the inclusion of DIMS improves the results. The comparison of cases 1 and 2 showed that there were no significant differences in terms of DIMS length and position. Therefore, case 2 with the shortest DIMS length, was further developed. In terms of the method used to obtain the parameters, it is not clear that one prevails over the rest; thus, the second method is much faster and will be developed.

Accuracy of forecasts ranges from 1.5% to 3% MAPE, similar to nHWT on regular days. To figure out the effect provided by this new DIMS, Figure 3 shows the comparison between the 24-hours-ahead forecasts made with both methods and the real values. Every day, a 24h forecast was provided by each method, and compared to the real values.

The forecasts are clearly improved by the use of the Easter DIMS. Sundays do not improve much because, although Easter is on Sunday, no special event in terms of demand occurs in this period.

Table 3.24-hours-ahead MAPE on forecasts during Easter. In header columns, you find the day for which the forecast was prepared. Two models are shown here: $AMC_{24,168}$ and $AAC_{24,168}$. Each model has four variants: 0: No DIMS were used; CASE 1: corresponds to period 1 in Table 2. The method used to obtain the parameters show no differences; CASE 2: corresponds to period 2, where M1 used all-in-one parameters estimation, whereas M2 used the two steps procedure.

MODEL		$AMC_{24,168}$				$AAC_{24,168}$			
VARIANT		0	CASE 1	CASE 2, M2	CASE 2, M1	0	CASE 1	CASE 2, M2	CASE 2, M1
Thursday	17/04/2014	13.12	3.05	2.73	2.79	12.25	6.42	5.90	9.18
Friday	18/04/2014	11.38	1.74	2.41	3.06	14.22	1.79	2.39	2.14
Saturday	19/04/2014	10.97	1.68	1.44	1.58	11.34	1.40	1.28	1.09
Sunday	20/04/2014	3.25	1.65	1.88	4.04	5.85	4.33	4.67	4.79
Monday	21/04/2014	4.94	6.25	3.57	7.02	5.80	4.87	5.06	5.87
Thursday	02/04/2015	11.35	2.90	2.79	3.07	12.02	5.47	4.81	8.80
Friday	03/04/2015	10.66	3.44	1.55	2.62	12.82	0.97	1.13	2.44
Saturday	04/04/2015	10.51	1.10	2.58	2.04	10.32	2.64	2.45	2.28
Sunday	05/04/2015	3.60	2.56	1.53	2.47	4.86	3.11	3.44	2.88
Monday	06/04/2015	5.91	1.51	3.93	4.69	7.40	2.84	3.04	2.96

adfa, p. 8, 2011.

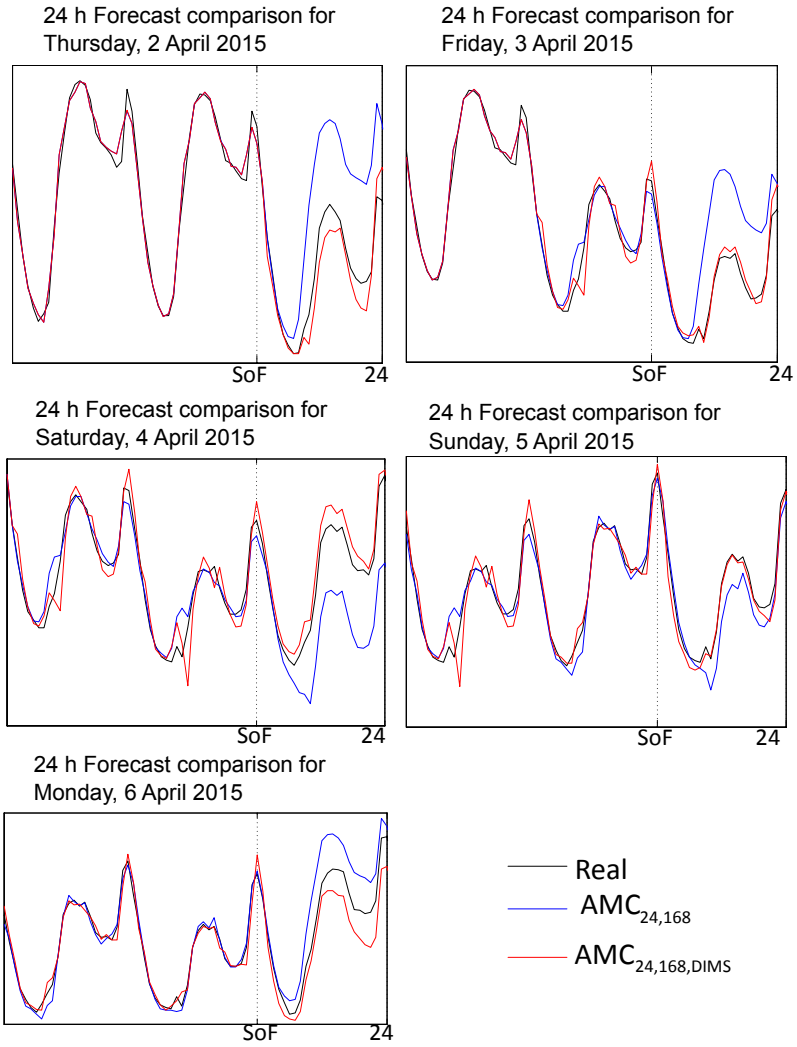

Figure 3. 24 hours ahead forecasts comparison among the regular method, DIMS method and real values. The abscissa represents lead time in hours, from start of forecast (SoF) to 24 hours ahead. The black line represents the real (observed values) to compare with. Blue line is the regular method forecasts, whereas red line uses the new DIMS method.

After checking the very-short-term forecasting with 24-hours-ahead forecasts, the medium term is also analysed. New tests were performed using forecasts of 168h (a week) ahead. In this case, only the $AMC_{24,168}$ model was compared. Results are shown in Table 4. It is clear that, overall, in the Easter period, DIMS improve the forecasts even in the medium term. However, outside this period, the results worsen compared to regular modelling.

adfa, p. 9, 2011.

Table 4. MAPE comparison of 168 hours-ahead forecasting between regular HWTn models and the new proposal using DIMS. The header column lists the day the forecasting was made for.

	REGULAR	**DIMS**
17/4/14	7.67	5.68
18/4/14	9.06	4.60
19/4/14	20.00	5.96
20/4/14	8.04	9.21
21/4/14	6.47	12.29
2/4/15	7.44	5.63
3/4/15	10.48	5.42
4/4/15	21.92	7.30
5/4/15	9.69	10.69
6/4/15	7.57	13.05

4 Conclusions

This paper presents a new way to deal with anomalous patterns in time series. It introduces discrete-intervals mobile seasonalities (DIMS) as part of the multiple seasonal Holt-Winters model. They are fixed-length seasonalities that only occur in some discrete intervals. DIMS are represented by a new smoothing equation that is included as a part of the Holt-Winters model, so that the information from this equation is updated each occurrence. The forecasting equation is also updated by including DIMS indices only in the time interval when a newer occurrence may appear. DIMS initialisation is also presented, along with the procedure to obtain their initial conditions.

DIMS are tested modelling calendar effects as Easters. It is checked the accuracy with events that happen every year, but in a different time position. In this case, several DIMS lengths and position are also tested. Finally, DIMS with length of 192 hours at 00:00 of Holy Thursday are taken. Results highlight a stabilised 24-hours-ahead forecasting MAPE of around 3%, much less than the results obtained with regular method nHWT.

The work with DIMS is not finished. Further developments are needed in order to model all calendar effects and provide better accuracy and stability.

5 References

[1] J.W. Taylor, Triple seasonal methods for short-term electricity demand forecasting, Eur. J. Oper. Res. 204 (2010) 139–152. doi:10.1016/j.ejor.2009.10.003.

[2] O. Hyde, P.F. Hondnett, Modelling the effect of weather in short-term electricity load forecasting, Math. Eng. Ind. 6 (1997) 155–169.

[3] S. Mirasgedis, Y. Sarafidis, E. Georgopopoulou, D. Lalas, M. Moschovits, F. Karagiannis, et al., Models for mid-term electricity demand forecasting incorporating weather influences, Energy. 31 (2006) 208–227. doi:10.1016/j.energy.2005.02.016.

[4] J.W. Taylor, R. Buizza, Using weather ensemble predictions in electricity demand forecasting, Int. J. Forecast. 19 (2003) 57–70. doi:10.1016/S0169-2070(01)00123-6.

[5] J.R. Cancelo, A. Espasa, R. Grafe, Forecasting the electricity load from one day to one week ahead for the Spanish system operator, Int. J. Forecast. 24 (2008) 588–602. doi:http://dx.doi.org/10.1016/j.ijforecast.2008.07.005.

[6] A. Pardo, V. Meneu, E. Valor, Temperature and seasonality influences on Spanish electricity load, Energy Econ. 24 (2002) 55–70. doi:10.1016/S0140-9883(01)00082-2.

[7] S. Arora, J.W. Taylor, Short-term forecasting of anomalous load using rule-based triple seasonal methods, Power Syst. IEEE Trans. 28 (2013) 3235–3242.

[8] J.D. Bermúdez, Exponential smoothing with covariates applied to electricity demand forecast, Eur. J. Ind. Eng. 7 (2013) 333–349.

[9] A. Corberán-Vallet, J.D. Bermúdez, E. Vercher, Forecasting correlated time series with exponential smoothing models, Int. J. Forecast. 27 (2011) 252–265. doi:10.1016/j.ijforecast.2010.06.003.

[10] R. Weron, Electricity price forecasting: A review of the state-of-the-art with a look into the future, Int. J. Forecast. 30 (2014) 1030–1081. doi:10.1016/j.ijforecast.2014.08.008.

[11] J.W. Taylor, Short-term electricity demand forecasting using double seasonal exponential smoothing, J. Oper. Res. Soc. 54 (2003) 799–805.

[12] J.C. García-Díaz, Ó. Trull, Competitive Models for the Spanish Short-Term Electricity Demand Forecasting, in: I. Rojas, H. Pomares (Eds.), Time Ser. Anal. Forecast. Sel. Contrib. from ITISE Conf., Springer International Publishing, Cham, 2016: pp. 217–231. doi:10.1007/978-3-319-28725-6_17.

[13] R.B. Cleveland, W.S. Cleveland, J.E. McRae, I. Terpenning, STL: A seasonal-trend decomposition procedure based on loess, J. Off. Stat. 6 (1990) 3–73.

[14] C. and Y. Chatfield M., Holt-Winters forecasting: some practical issues., Stat. (1988) 129–140.

Chaos Neural Network for Ultra-Long Period Pseudo-Random Number Generator

Hitoaki YOSHIDA[1,*], Yukito KON[1] and Takeshi MURAKAMI[2]

[1]Faculty of Education, Iwate University, Japan
{hitoaki, e0114054}@iwate-u.ac.jp
[2]Technical Division, Iwate University, Japan
mtakeshi@iwate-u.ac.jp

Abstract.
2100 Chaos Neural Networks (CNNs) with modified 32 bits fix-point arithmetic (i-FPA) have generated the ultra-long period pseudo-random number (PRN) series; the period has reached 10^{10494}. The rate of PRN generation using the computer mounted the latest GPU (Tesla P100) has been 1.829 Tbps. CNN with small perturbation as varying external inputs I_D (v-CNN) has changed CNN drastically. 901 v-CNNs have generated the ultra-long period PRN series 10^{11052} at I_D = 0.001275623 with double-precision floating arithmetic. The rate of PRN generation has been 4.383 Tbps. i-FPA and v-CNN are expected to implement a cipher application to protect personal information in a smartphone and other IoT devices.

keywords: chaos time series·GPGPU·pseudo-random number

1 Introduction

Chaotic time series from the chaos neural network (CNN, Fig.1) are useful for a pseudo-random number generator (PRNG) for stream cipher. CNN consists of conventional artificial neurons and generates chaotic outputs [1, 2, 3]. We have studied computer generated chaotic time series from an empirical viewpoint. Theoretical chaotic time series has no period, yet computer generated chaotic time series is *eventually* periodic by the calculation with the finite precision within our knowledge.

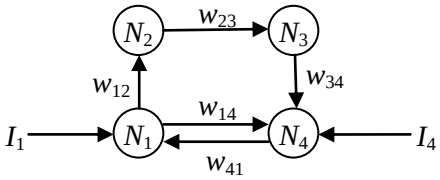

Fig. 1. CNN having cyclic structure (C-4nn).

* Iwate University, Ueda, Morioka, Iwate, 020-8550 Japan.

adfa, p. 1, 2011.

The period of chaotic time series from CNN with double-precision floating-point arithmetic is normally 10^{15}-10^{17}. Outputs of a number of CNNs which have different external inputs compose high dimensional vector, for example 901 CNNs have afforded the far longer period 10^{9774} ($\approx 2^{32469}$) that is estimated with experimental data [4]. The value has been slightly changed by higher-precision approximation compared with the reported value in reference 4. The high dimensional vector has been converted into pseudo-random number series by RNR. The overhead time of RNR is not important more than 100 CNNs [4]. The modified CNN has been featured by far both longer period and higher rate of PRN generation.

In this work we report improved methods for CNN with fix-point arithmetic and double-precision floating-point arithmetic to implement ultra-long-period pseudo-random number (PRN) series. In particular the PRNG has been extremely accelerated by the latest GPU and the modified method. The rate of PRNG has reached the Tbps (10^{12} bit/s) order of magnitude.

2 Time Series of Chaos Neural Network

CNN that composed of 4 neurons in discrete-time system has been used for a chaos generator (Fig. 1). I_j is an external input of jth neuron, and I_1=I_4, I_2=I_3=0 in this work. A total value of inputs in jth neuron at time t is defined as equation 1.

$$u_j(t) = \sum_{i=1}^{n} w_{ij} x_i(t) + I_j \tag{1}$$

$$x_j(t+1) = f(u_j(t)) \tag{2}$$

w_{ij} is a synaptic weight, x_i is an input from ith neuron. An output from jth neuron at time t+1 is defined as equation 2 with the asymmetric piecewise-linear-function (APLF) f (Fig. 2). APLF is useful for avoiding the periodic window corresponds to a non-chaotic periodic orbit, and 7 independent parameters of APLF can be used as secret keys in a cipher system [4,5,7,8].

A period of chaotic time series from CNN changes with a different external input value I. Even if the values of neurons in a CNN coincide with another CNN accidentally, the outputs of the neurons become different owing to a different I. Actually no same period has been observed in our experiments.

The time series generated from CNN can separate into 2 independent subseries; α series and β series (equation 3, 4). The 2 subseries do not mix to each other. The averaged period of the subseries is ca. 10^8, normally 10^7-10^9.

$$\alpha(t) = \begin{bmatrix} \{(x_1(t), x_3(t)) \mid t = 2k, k = 0,1,2,\dots\} \\ \{(x_2(t), x_4(t)) \mid t = 2k+1, k = 0,1,2,\dots\} \end{bmatrix} \tag{3}$$

$$\beta(t) = \begin{bmatrix} \{(x_2(t), x_4(t)) \mid t = 2k, k = 0,1,2,\dots\} \\ \{(x_1(t), x_3(t)) \mid t = 2k+1, k = 0,1,2,\dots\} \end{bmatrix} \tag{4}$$

The whole period of CNN (P) is equivalent to the period of the vector ($\alpha(t)$, $\beta(t)$) which is estimated with L.C.M. (Least Common Multiple) of the periods of α series (p_α) and that of β series (p_β). If the periods of two subseries are different, the whole period of CNN (P) is ca.10^{15}-10^{17}. It is convenient if the periods of two subseries can be controlled as different. In the previous work, different APLFs have been used for the purpose of splitting the period of subseries into two different periods. [4,5]

In the 3rd section we have proposed a very simple and convenient method for generating different periods of subseries.

APLF is shown in Fig.2 with coordinate values of 5 connection points (**A**, **B**, **C**, **D**, **E**). f_1 is a representative APLF for both fix-point arithmetic and double-precision floating-point arithmetic. f_α and f_β are used for improved fix-point arithmetic (i-FPA) in this work (*vide infra*). In cipher system, the coordinates of APLF aren't fixed, because they can be used as secret keys.

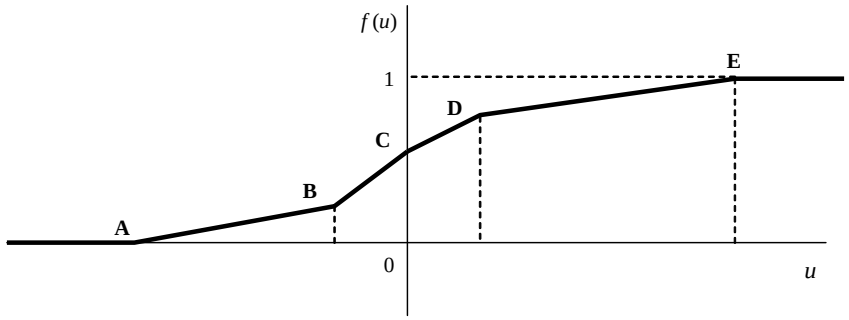

Fig. 2. Asymmetric Piecewise-Linear-Function (APLF).

Table 1. Parameters of APLFs.

APLF	Axis	**A**	**B**	**C**	**D**	**E**
f_1	u	-51.00010	-1.980101	0.000000	1.980101	64.00010
	$f(u)$	0.000000	0.098990	0.499012	0.889100	1.00000
f_α	u	-21.00010	-4.980101	0.000000	4.980101	21.00020
	$f(u)$	-21.00000	-12.98990	0.499012	12.68910	21.00000
f_β	u	-21.00010	-4.981101	0.000100	4.981101	21.00020
	$f(u)$	-21.00100	-12.29999	0.500012	12.69010	21.39999

2.1 Improved method for CNN with fix-point arithmetic (i-FPA)

The 7-bit-rotate-left instruction was used for generation of pseudo-random numbers with fix-point arithmetic (FPA) in reference 5. In this work, the instruction is simplified; 32 bits fix-point arithmetic without a carry using f_α and f_β as APLF has given nearly the same chaotic time series instead of the 7-bit-rotate-left instruction.

The chaotic time series as 4200-dimensional vector (consists of the outputs of 2100 CNNs with different *I*s and their subseries) with the improved method (i-FPA) have reached the longer period. The improved period is 10^{10494}, which is estimated by experimental data. PRN series are extracted by the method mentioned in reference 4 and 5. The randomness of the PRN series is confirmed by NIST SP800-22 tests [6-8].

GPGPU (General-Purpose computing on Graphics Processing Units) is the utilization of GPU to perform computation in applications conventionally handled by CPU [9]. CNN has been implemented with CUDA 8.0 on PC mounted with a GPU (NVIDIA Tesla P100 or K40) in this work. The result is shown in Fig. 3 and Table 2 together with the result of the former study for comparison. Interestingly, PRNG is extremely accelerated by the latest GPU (Tesla P100). The rate is beyond 1 Tbps (10^{12} bit/s); 1792 Gbps by FPA and 1829 Gbps by simplified method i-FPA. The rate of PRN generation is saturated around 10^6 threads (Fig.3). The number of threads is optimized to be the maximum rate: the number of blocks is 65536, the number of threads/blocks is 1024, that is, 6.7108864×10^7 CNNs with different external input *I*s work in parallel on P100.

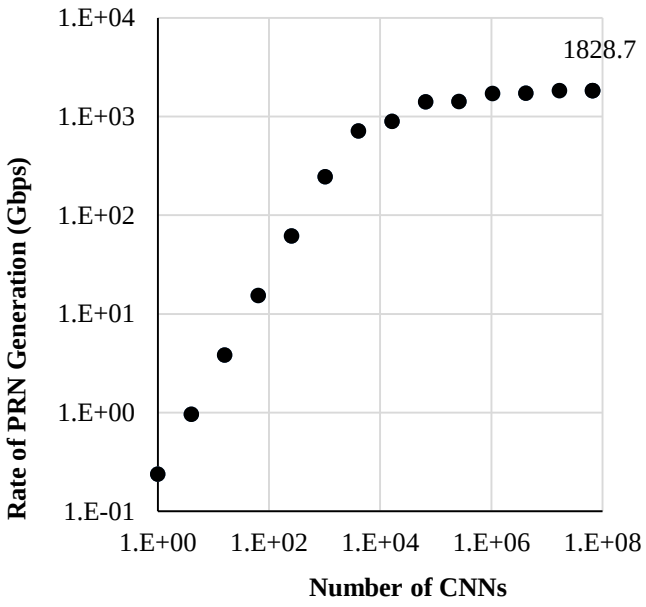

Fig. 3. Rate of PRN generation by modified fix-point arithmetic with P100.

Table 2. Rate of PRNG with fix-point arithmetic (FPA) and the improved method (i-FPA).

GPU	Tesla Accelerator	P100	K40	K10[c)]	C2070
	GPU Architecture	Pascal	Kepler	Kepler	Fermi
CUDA	CUDA Version	8.0	8.0	5.0	5.0
	CUDA Core [a)]	3584	2880	1536	448
Random Number Generation (Gbps)	FPA	1792	818	226[b)]	190[b)]
	i-FPA	1829	860	274	200

a) FP32 (with FMAD, Floating-point Multiple Add). b) Published result in reference 5.
c) Result with a single GPU, although K10 has dual GK104 GPUs.

Large increase in the number of threads (CNNs) on P100 is probably owing to a large number of CUDA core and huge register files (14 MB). The performance of Kepler isn't so bad on FPA and i-FPA, probably because Kepler designed primarily for single precision compute tasks. i-FPA is expected to implement a cipher application on embedded systems to protect personal information in a smartphone with a regular GPU which is designed for fast graphics.

In the next, we propose methods to implement a longer period of PRN series and a higher rate of PRN generation by using double-precision floating-point arithmetic.

3 Chaos Neural Network with Varying External Input (v-CNN)

3.1 A method for the purpose of splitting the periodic orbit of subseries

In this section we have proposed a simple method for the purpose of splitting a periodic orbit into two orbits which have a different period with only one f_1 as APLF. An improved chaos neural network (v-CNN) has an external input I on Neuron 1(N_1) and Neuron 4 (N_4) at even discrete time t = 0, 2, 4..., and has $I+I_D$ at odd discrete time t = 1, 3, 5..., where I_D is a small additional value (perturbation) and I_2=I_3=0.

The perturbation I_D splits the periodic orbit of α and β subseries ($p_\alpha = p_\beta$) into two different periodic orbits ($p_\alpha \neq p_\beta$).

Moreover, the perturbation I_D brings unexpectedly much better effect on the rate of PRN generation and the period of PRN series. Next the periods of v-CNN are studied varying 100 external inputs (Is) to investigate the general distribution of the period of time series from v-CNN; 100 Is are selected from the range [2.6, 2.7) at 0.001 intervals. Distribution of the periods of the time series from CNN (I_D = 0 and the 100 Is) is shown in Fig.4. The abscissa is the number of digits of the period (i.e. common logarithm of P, log P). 63% of the time series has the same-period subseries ($6 \leq \log P \leq 9$) and 37% has the different-period subseries ($11 \leq \log P \leq 18$).

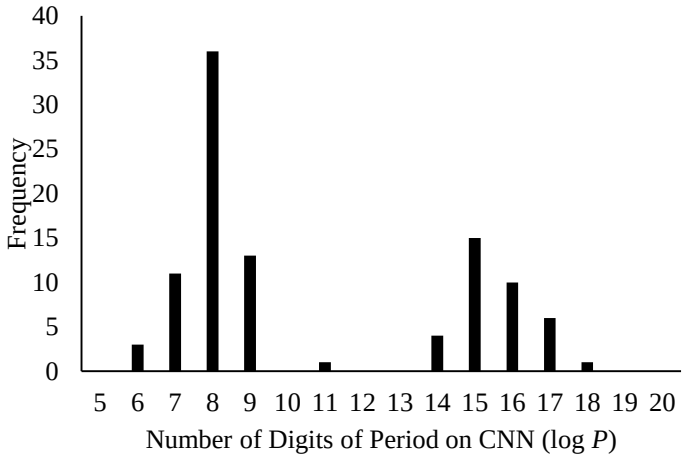

Fig. 4. Distribution of the period on CNN ($I_D = 0$).

Distribution of the periods of the time series from v-CNN ($I_D = 0.127562$ and the 100 *I*s) is shown in Fig.5. 100% of the time series has the different-period subseries ($14 \leq \log P \leq 18$). The perturbation I_D drastically changes the period of the time series. The averaged period of 2300 v-CNNs (23 I_Ds and 100 *I*s) is $\langle \log P \rangle = 16.45$ although the averaged period of 100 CNNs ($I_D = 0$ and 100 *I*s) is only $\langle \log P \rangle = 8.32$.

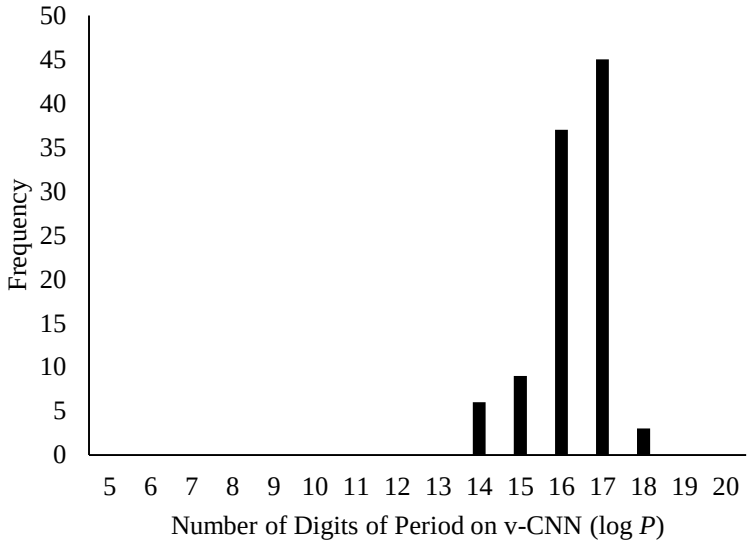

Fig. 5. Distribution of the period of v-CNN ($I_D = 0.127562$).

The transient time for reaching the periodic orbit (q) is also observed. The averaged transient time of 2300 v-CNNs is <log q> = 8.63. The averaged period of subseries of 2300 v-CNN is <log p> = 8.49. <log q> and <log p> are generally very close.

3.2 The perturbation I_D for shifting the bifurcation pattern

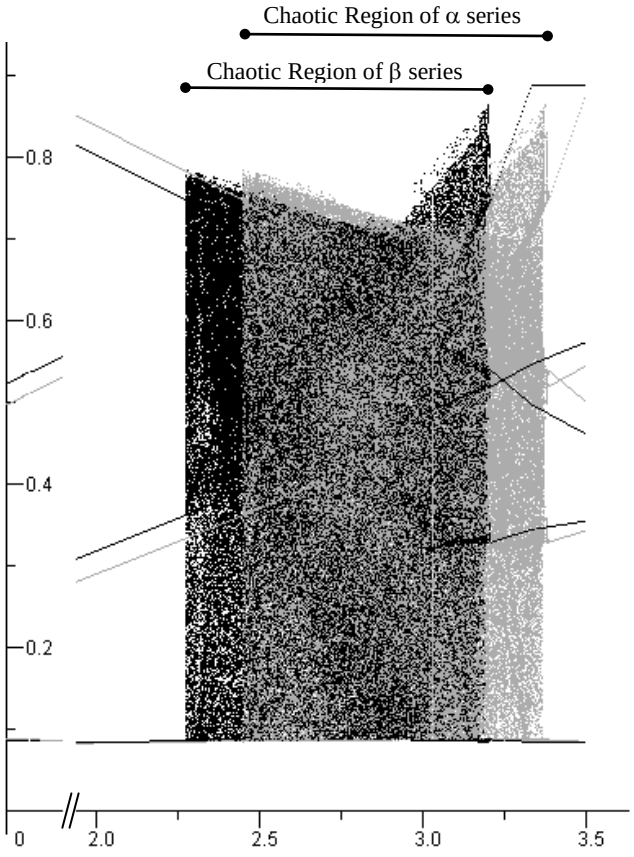

Fig. 6. Bifurcation diagram of v-CNN which consists of 2 subseries.

Interestingly, when $0 < I_D < 0.2$ the perturbation I_D has shifted the bifurcation pattern to the left side for β series (indicated as black dots) and to the right side for α series (indicated as gray dots). When $-0.2 < I_D < 0$ the perturbation I_D has shifted the bifurcation pattern to the opposite side for α and β series, respectively.

Let basic points be the left-edge of the bifurcation pattern (2.45) and be the right-edge of the pattern (3.15) at $I_D = 0$, the shift amount can be predicted by the empiri-

cally obtained equations (the correlation coefficients between I_R (or I_L) and I_D are R = 0.9974-0.9999) as follows:

As for β series, I value of the right-edge of the pattern (I_R) is calculated with the equation 5,

$$I_R = -1.20 \times I_D + 3.15, \quad (5)$$

and similarly that of the left-edge of the pattern (I_L) is calculated with the equation 6,

$$I_L = -1.19 \times I_D + 2.45. \quad (6)$$

As for α series, that of the right-edge of the pattern (I_R) is calculated with the equation 7,

$$I_R = 0.197 \times I_D + 3.15, \quad (7)$$

and similarly that of the left-edge of the pattern (I_L) is calculated with the equation 8,

$$I_L = 0.192 \times I_D + 2.45. \quad (8)$$

The effective range of equation 5-8 is not decided, yet. $-0.2 < I_D < 0.2$ is a minimum range within our research.

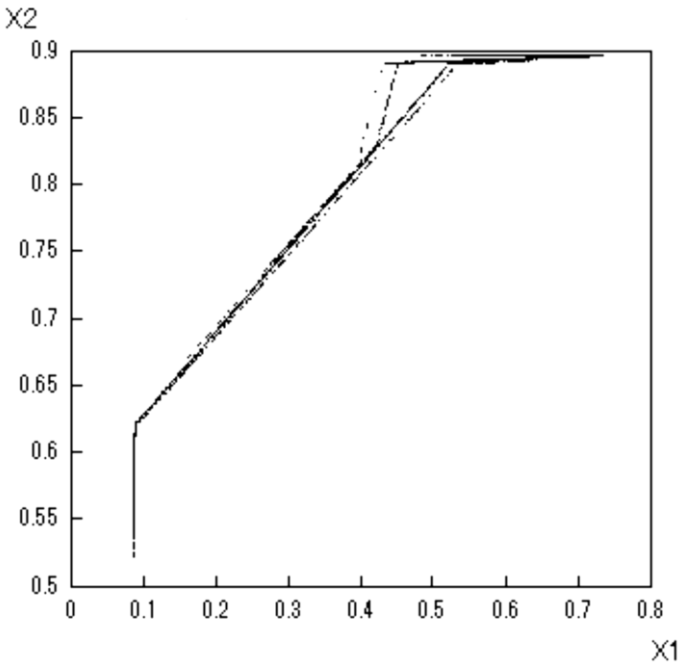

Fig. 7. Attractor of β subseries with I_D = 0.1275623.

All time series are analyzed by the chaos time series analysis [10], and randomness of extracted PRN series are confirmed by NIST SP800-22 tests [6,7] and the method in reference 8. An attractor of chaotic outputs of β series when I_D = 0.1275623 is shown in Figure 7 as a typical example of the strange attractor which has fractal structure by repeated enlargement and folding. The result of the chaos time series analysis is consistent with the feature of chaos (Table 3).

Table 3. Result of Chaos Time Series Analysis.

I_D	Subseries	Correlation Dimension	Lyapunov Spectrum
0.0000000	α, β	1.2	(+0.40, -2.24)
0.1275623	α	1.1	(+0.39, -2.21)
0.1275623	β	1.2	(+0.36, -1.89)

3.3 Acceleration of PRNG with the latest GPU

Result of the comparative study of the normal CNN and the improved CNN (v-CNN) is shown in Table 4 with data in the previous work [4].

Table 4. Rate of PRNG with double-precision arithmetic (CNN) and the improved method (v-CNN).

GPU	Tesla Accelerator	P100	K40	K10	C2070
	GPU Architecture	Pascal	Kepler	Kepler	Fermi
CUDA	CUDA Version	8.0	8.0	5.0	5.0
	CUDA Core [a)]	3584	2880	1536	448
	FP64 FMAD	1792	960	64	224
Random Number Generation (Gbps)	CNN	3827 [c)]	1687	191[b)]	320[b)]
	v-CNN	4383 [d)]	1757	-	-

a) FP32 (FMAD). b) Published result in reference 4. c) Number of CNNs is 8.39×10^6.
d) Number of CNNs is 1.34×10^8.

Also in this case PRNG is extremely accelerated by the latest GPU (Tesla P100), the rate has been 3827 Gbps with CNN and have reached 4383 Gbps (4.383 Tbps) with v-CNN. The number of threads is optimized to be the maximum rate. The rate of PRN generation by v-CNN with the latest GPU (Tesla P100) is shown in Fig.8 as a typical result. v-CNN has been implemented with 1.34217728×10^8 CNNs (or threads), the drastic increase in threads probably owing to simplification of the calculation in v-CNN. Only the small perturbation I_D drastically has changed the performance of CNN. As GPGPU implements low-price and high-performance computing,

the improved method is expected to implement a cipher system for ultrahigh speed network devices to protect personal data superior in excellent cost performance.

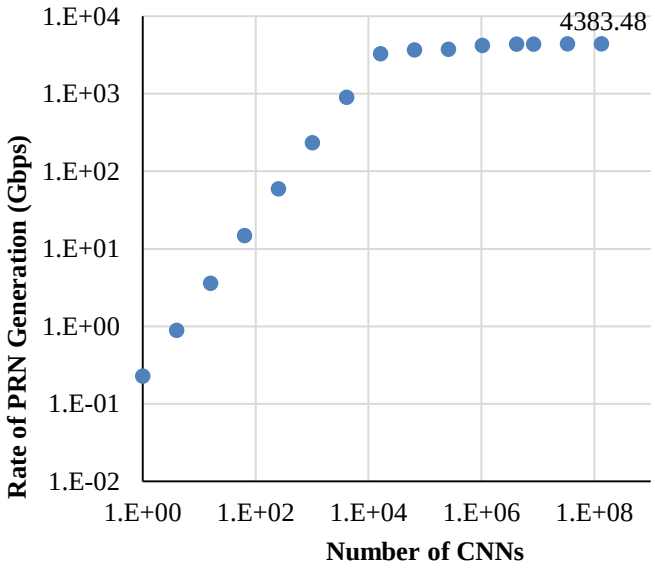

Fig. 8. Rate of PRN generation by v-CNN with P100.

3.4 Further optimization of the period with v-CNN

The averaged period and the averaged transient time are shown in Figure 9. The main ordinate is the averaged whole period of v-CNNs (<log P>) and the secondary ordinate is the averaged period of subseries of v-CNNs (<log p>). The abscissa is I_D.

<log P> has a local maximum in I_D = 0.119725 and <log p> and <log q> also have larger values. The whole period of PRN with 901 v-CNNs at I_D = 0.119725 has been estimated from experimental data under the same condition with 901 CNNs in reference 4. The whole period of 901 CNNs (10^{9774}) has been improved to 10^{10053}. The improved method has increased the period in 10^{279} folds.

The further optimization on external input I and I_D have reached the period 10^{11052} as the whole period of 901 v-CNNs at I_D = 0.001275623. The detailed method on the further optimization will be discussed in a future work.

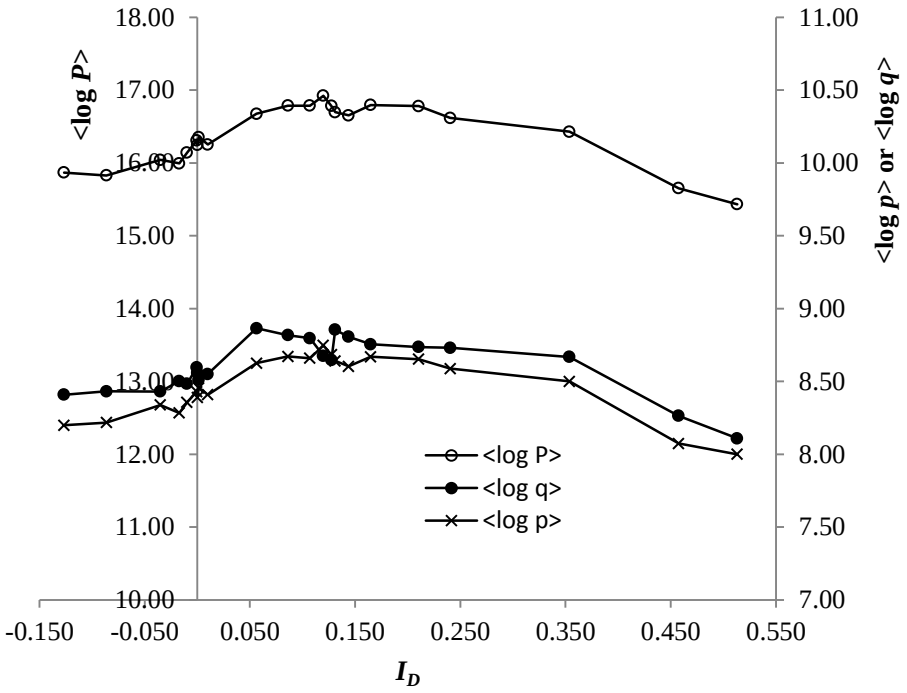

Fig. 9. The averaged period and the averaged transient time of v-CNN.

4 Conclusion and Future Work

2100 CNNs by modified 32 bits fix-point arithmetic (i-FPA) have generated the ultra-long period PRN series, 10^{10494}. The rate of random number generation using the computer mounted the latest GPU (NVIDIA Tesla P100) has reached Tbps (10^{12} bit/s) order of magnitude, that is, 1.829 Tbps. In this case, 6.7108864×10^{7} CNNs with different external input *I*s work in parallel on P100, the period of the CNNs is now under investigation, because it may be far too long.

Chaos neural networks with varying external inputs (v-CNN), actually the small perturbation I_D has changed CNN drastically.

(i) 100% of the time series has the different-period subseries. The averaged period of v-CNNs is $\langle \log P \rangle = 16.45$ although the averaged period of 100 CNNs is only $\langle \log P \rangle = 8.32$.

(ii) When $0 < I_D < 0.2$ the perturbation I_D has shifted the bifurcation pattern to the left side for β series and to the right side for α series. When $-0.2 < I_D < 0$ the perturbation I_D has shifted the bifurcation pattern to the opposite side for α and β series, respectively.

(iii) 901 v-CNNs have generated the ultra-long period PRN series 10^{10053} at I_D = 0.119725 and 10^{11052} at I_D = 0.001275623.

(iv) The rate of PRNG using Tesla P100 has reached 4.383 Tbps.

v-CNN is expected to implement a cipher for ultrahigh speed network devices (e.g. as a backbone router) to protect information security superior in excellent cost performance.

As future work, we will apply i-FPA to a cipher application on embedded systems; for example the system having Cortex (ARM architecture) with GPU to protect personal information in a smartphone and other IoT devices without GPU.

Acknowledgement

Part of the experimental results in this research was obtained using supercomputing resources at Cyberscience Center, Tohoku University. This work was supported by KAKENHI Grant Numbers JP16K00180. Special thanks to the stuff members of Iwate University Super-Computing and Information Sciences Center.

References

1. Yoshida, H., Yoneki, K., Tsunekawa, Y., Miura, M.: Chaos Neural Network. Proceedings of Papers, ISPACS'96, vol. l of 3, pp.16.1.1-5 (1996)
2. Yoshida, H., Nihei, Y., Nakanishi, T.: Comparative Study on Structurally Different Chaos Neural Networks. Proceedings of Papers, ISITA2004, pp.1046-1050 (2004)
3. Nihei, Y., Nakanishi, T., Yoshida, H.: Time Series Analysis for Chaos Neural Network. Technical Reports of IEICE, vol. 104, pp.7-10, (2004)
4. Yoshida, H., Murakami, T., Liu, Z.: High-Speed and Highly Secure Pseudo-Random Number Generator based on Chaos Neural Network. Proceedings of Papers, ICSSE 2015, pp.224-237 (2015)
5. Yoshida, H., Murakami, T., Inao, T., Kawamura, S.: Origin of Randomness on Chaos Neural Network, Trends in Applied Knowledge-Based Systems and Data Science. vol.9799, pp.587-598, (2016)
6. Soto, J., Bassham, L.: Randomness Testing of the Advanced Encryption Standard Finalist Candidates. National Institute of Standards and Technology (NIST) (2000)
7. Rukhin, A., Soto, J., Nechvatal, J., Smid, M., Barker, E., Leigh, S., Levenson, M., Vangel, M., Banks, D., Heckert, A., Dray, J., Vo, S.: A Statistical Test Suite for Random and Pseudorandom Number Generators for Cryptographic Applications, NIST SP800-22 rev.1a, Revised: July 2015 (sts-2.1.1). Lawrence E. Bassham III (2015)
8. Yoshida, H., Murakami, T., Kawamura, S.: Study on Testing for Randomness of Pseudo-Random Number Sequence with NIST SP800-22 rev. la. Technical Reports of IEICE, 110 , pp.13-18 (2012)
9. NVIDIA CUDA ZONE. https://developer.nvidia.com/cuda-zone
10. Aihara, K. ed.: Basics and Application of Chaos Time Series Analysis, Sangyo Tosho, Tokyo (2000)

JOINT MULTIFRACTAL DESCRIPTION OF THE INFLUENCE OF CLIMATIC VARIABLES ON REFERENCE EVAPOTRANSPIRATION TIME SERIES.

Ariza-Villaverde, A.B.[1*] (orcid.org/0000-0002-8549-2774), Pavón-Domíguez, P.[2] (orcid.org/0000-0002-2913-6492), Gómez-López, J.M.[1], Gutiérrez de Rávé, E.[1] (orcid.org/0000-0002-2091-6708), Jiménez-Hornero, F.J.[1] (orcid.org/0000-0003-4498-8797).

[1] University of Córdoba, Córdoba, Spain.
[2]University of Cádiz, Cádiz, Spain.
*g82arvia@uco.es

Abstract. Evapotranspiration (*ET*) is one of the most important components of the hydrological cycle and its estimation is essential for scheduling irrigation system, preparing input data for hydrological water-balance models, computing actual *ET* for a watershed, regional water resources planning and analyzing climate change effect. *ET* is a combination of two separate processes whereby water is lost on the one hand from the soil surface by evaporation and on the other hand from the crop by transpiration and evaporation. Commonly, *ET* is modelled by separating the effects of meteorological conditions from the nature of crop surface and the soil water availability. For this reason, reference evapotranspiration (ET_0) is introduced to quantify evaporative demand of the atmosphere. *ET* is affected by some factors including weather parameters, crop characteristics, management and environmental aspects. However, ET_0 measures the evaporative demand of the atmosphere independently of crop type, crop development and management practices. As water is abundantly available at the reference evapotranspiring surface, soil factors do not affect. Thereby, the only factors affecting ET_0 are climatic parameters. Consequently, ET_0 is a climatic parameter and can be computed from weather data. Hence, ET_0 expresses the evaporating power of the atmosphere at a specific location and time of the year and does not consider the crop characteristics and soil factors.

The most accurate way to quantify ET_0 is by using weighing lysimeters or micrometeorological methods, but these procedures are no practical, as they are time consuming and expensive. To this end, numerous approaches have been proposed to estimate reference evapotranspiration, being grouped in the following categories: i) water budget, ii) combined energy-mass balance methods, iii) temperature based-method, iv) radiation-based methods, v) mass transfer-based-methods and vi) pan evaporation-based models. The use of one method over another is based on the number of atmospheric variables required as input, such as air temperature, wind speed, air relative humidity and solar or net radiation. On the other hand, these approaches have been evaluated under different climate conditions and the

adfa, p. 1, 2011.

results suggest that the ET_0 estimation vary with climatic conditions, except Penman–Monteith (PM) equation, showing its superiority for estimating ET_0 over a wide range of climates. Consequently, the PM equation is recommended as the standard equation for estimating ET_0 by United Nations Food and Agriculture Organization (FAO) and by the American Society of Civil Engineers (ASCE).

Numerous authors have been studied reference evapotranspiration to improve the understanding of its relationship with climatic variables by performing sensitivity analyses. In all the cases, the sensitivity analysis has been examined under a one-at-time perturbation, i.e., one variable was changed while others were kept constant. It is well established in sensitivity studies that significant effects can be produced by a pair of variables acting in concert. Thus, such combined effects can be larger than the sum of the individual effects of the two variables. Nevertheless, the application of the sensitivity analysis in evapotranspiration studies is limited always in the one-at-time case. In the real life, the perturbation of more than one variable is likely to happen at the same time. Thereby, it has been proved that the joint multifractal analysis is able to study the relationship between variables which all of them coexist in the same geometric support. The only condition is that the study variables should have multifractal nature. Several studies have confirmed that ET_0 have self-similarity property, showing multifractal nature. The multifractal formalism known as box-counting has been used as a technique to reveal certain levels of complexities that are overlooked by traditional statistical tools. This formalism proposes that self-similar measures can be represented as a combination of intertwined fractal sets, each of which is characterized by its strength singularity and fractal dimension. This set is called multifractal spectrum and the method of variability characterization, based on the multifractal spectrum, is referred to as a multifractal analysis. The main advantage of this formalism is that its parameters are independent over a range of scales and that no assumption is required about the data following any specific distribution. An extension of this procedure is the joint multifractal theory. This approach analyses the correlations of several multifractal variables which coexist on the same spatial region and, hence for quantifying the relationships between the measures studied. To date, the joint multifractal analysis has been previously applied with success to find out the relationship between two variables (i.e. pollutants time series) although it can be extended to describe the joint behavior of a greater number of variables. Thus, this work explores how the ET_0, calculated by means of PM equation, is affected by the simultaneous action of two of the more relevant climatic variables, such as relative humidity (RH) and air temperature (T), at Córdoba city (southern of Spain, Andalusia).

According to the yielded results, for high T and ET_0 and low RH values it was detected a strong relationship. The strength of this variables association dismisses for high T, RH and ET_0 and high RH and low ET_0 and T. For the rest of sceneries or variables combinations the connection between them was weaker. However, the sceneries that show a strong link between T, RH and ET_0 values are not frequent at Cordoba city. Thus, for high T and ET_0 and low RH values it is found that the singularities distribution exhibits a lower variability having a frequency of occurrence included into a narrow range, between 0.40 and 0.64 (75% of fractal dimensions). Comparing the fractal dimensions for all sceneries, it was ob-

served that the combination of high *RH* and ET_0 and low *T* has the highest frequency of occurrence at Córdoba city, with 75% of fractal dimensions between 0.74 and 0.99.
Results from the joint multifractal analysis suggest that it is a suitable tool for describing the dynamics of a variable (ET_0) linked to others ones (*T* and *RH*), all of them sharing the same geometric support (time series). Considering the singularities distribution has revealed some advantages over statistical parameter such as the mean a variance of a variable.

Keywords: Joint multifractal algorithm· Reference evapotranspiration· Temperature· Relative humidity· Fractals dimensions· Singularities distribution.

Generalized nonparametric method for analyzing economic data inconsistent with the model of single rational representative consumer

Nikolay Klemashev[3] and Alexander Shananin[1,2,3,4]

[1] Moscow Institute Of Physics and Technology, Institutskiy per. 9, Dolgoprudny, Moscow Region, 141701, Russian Federation,
[2] Dorodnicyn Computing Centre, FRC CSC RAS, Vavilov st. 40, Moscow, 119333, Russian Federation,
[3] Moscow State University, Leninskiye Gory 1-52, Moscow, 119991, Russian Federation,
[4] RUDN University, Department of Nonlinear Analysis and Optimization, Miklukho-Maklaya st. 6, Moscow, 117198, Russian Federation

Abstract. We provide a review of methods for studying economic data and building economic indices based on the generalized nonparametric method for computing Konus-Divisia indices, with the focus on the case when the observed behavior is not consistent with the classical Pareto's model of a single rational representative consumer, but may be consistent with the generalized model with two or more rational representative consumers. Computing economic indices allows one to aggregate economic prices and consumption data from the level of individual goods to the level of some general categories of goods.

Keywords: aggregation, demand theory, economic indices, revealed preference

1 Introduction

The standard generalized nonparametric method emerged from the revealed preference theory, which was created in order to address the problem of empirical testing the observed economic data on prices and consumption, which is called trade statistics, for consistency with Pareto's demand model. That model assumes that the aggregate demand may be represented as the outcome of a decision process of a single rational representative consumer who maximizes his or her utility function given his or her budget. The reveled preference theory provides two tests for consistency. One of them checks if the data satisfy Generalized Axiom of Revealed Preference (GARP). If it does, then it is consistent with Pareto's model with nonnegative, nonsatiated, continuous, concave, and monotonic utility function. We call the utility function having all those properties as the general utility function.

The second test checks if the data satisfy Homothetic Axiom of Revealed Preference (HARP). If the data satisfy HARP, then it is consistent with Pareto's

model with general utility function with the additional property of being positive-homogeneous. The nonparametric method and its generalization are based on HARP. The nonparametric method allows one to compute Konus-Divisia economic indices for a group of goods satisfying HARP. The generalized nonparametric method allows one to compute generalized Konus-Divisia indices and is applied when the trade statistics do not satisfy HARP.

2 Arguments in favor of requiring positive-homogeneity of the utility function

We start with the arguments in favor of requiring the positive homogeneity of the representative consumer's utility function. We may consider arbitrary groups of goods for testing for consistency with Pareto's model. We always have aggregate data on consumption, which represents the total consumption of many different economic agents. The number of the agents changes with time. The positive-homogeneity of the utility function implies stability of this group with respect to change of its size. By stability we mean that while the size of the group changes the shares of consumption for individual goods remains the same.

Another argument is that the consistency with Pareto's model implies the existence of a direct relation between prices and consumption for the goods in the group. If we compose the groups of random goods, most probably, the group will not be complete in terms of substitutes and complements and there should be no direct relation between prices and consumption. Therefore, the probability of having a randomly composed group being consistent with the Pareto's model should be low. However, as we show in our numerical experiments in Klemashev and Shananin (2016), a random group of goods has high probability of satisfying GARP. One of the reasons for that is that the total expenditures are growing with time and this makes GARP less restrictive condition. On the contrary, the probability of random group to satisfy HARP is very low at least for relatively small size of the group. The growing total expenditures do not make HARP a less restrictive condition. These features make HARP a more appropriate condition if our goal is to reveal meaningful complete groups of goods.

3 Testing the trade statistics for consistency with Pareto's model with several representative consumers

In this section we turn to the case when we have a single group of goods, which is assumed complete and meaningful, but does not satisfy HARP. One reason is the errors in measurements of price and consumption data. In that case, one should apply the standard generalized nonparametric method, which allows one to compute generalized Konus-Divisia indices and to determine the degree of inconsistency of the trade statistics with HARP.

There may be another reason, however. The observed demand may be the aggregate demand of several social classes with different preferences. In that

case, we say that one cannot aggregate all prices and consumption time series to a single pair of time series of price and consumption indices. Rather, we need to aggregate data to several pairs of consumption and price indices, one for each social class. When we do not know the number of social classes in advance, we proceed from the idea of describing the observed behavior in terms of as few as possible variables and we look for the smallest number of social classes necessary for the data to be consistent with the model with several representative consumers. This minimum number of social classes is given by the class of the differential form of inverse demand functions as shown in Shananin (1989).

This approach faces computational problems. As shown in Nobibon et al. (2013), the problem of testing a single trade statistics for consistency with Pareto's model with two rational representative consumers with general utility functions is NP-complete. There is a partial case of this model, namely the model of temporary dictator. In this model, we have several rational representative consumers and each time period the observed aggregate demand is consistent with the preferences of one of them. R. Deb has shown in Deb (2010) that the problem of testing trade statistics for consistency with this model with general utility functions is also NP-complete. Recently we have proved in Klemashev and Shananin (2015) that if we add the requirement of positively-homogeneous utility functions the problem is still NP-complete.

4 Analysis of budget statistics

The findings in the previous section lead to the conclusion that if one is going to try to reveal the behavior of several social classes with different preferences efficiently, one needs to consider some alternative setups. One such setup is to consider a different type of input data. One example is budget statistics considered in Petrov and Shananin (1997). This is the aggregate data on prices and data on consumption of several individual households. Using this data, we may aggregate consumption data to the level of several small social classes, for examples classes by level of income. We then may try to combine these small social classes into small number of larger classes such that trade statistics for each of these larger classes satisfy HARP. We apply this idea to the data of Family Expenditure Survey in UK from 1975вЂ”1999 in Klemashev and Shananin (2014). We managed to split the households into two social classes – a small number of households with highest income made the first class and a large number of all the rest households made the second class. The trade statistics for both classes satisfy HARP. It is worth noting that the size of the classes is not fixed – the number of households in the first class is increasing with time. Moreover, this class of the richest households appears only stating from 1988. These findings demonstrate the emergence of a new social class of the households with different preferences in the UK during the last quarter of the XX century. This is the result of the changes in the world economy and in social in policies in US and UK.

5 Analysis of stock market crises

Another way to accommodate two social classes with different preferences is to assume that one of the classes is not well represented and its behavior is usually dominated by the other class. However, that class dominates the other class during several periods and only in several goods. This activity leads to major inconsistency of aggregate data with Pareto's model. This approach corresponds to the case when we analyze the statistics of stock market. In that case, the prices are the stock prices and consumption is the trading volumes.

We applied this approach to study Chinese stock market crash in Summer 2015. We consider the aggregate stock market data as the result of actions from the two different classes of investors. The first class consists of major investors. These are agents seeking for stable long-term savings and using long-term, low-risk strategies. The second class is the class of speculators. These are agents, who seek for short-term profit and they use short-term high-risk strategies.

When a stock is transferred from one of the major investors to another, it passes through many intermediate agents, who are speculators. The number of these intermediaries varies. If the number of intermediaries is constant, this does not violate HARP. However, this number varies and the largest changes in this number correspond to the periods of changing preferences of major investors and to higher degree of inconsistency with HARP. There is some base level of this inconsistency, which is assumed normal for the stock market. Periods when the degree of inconsistency rises above this base level correspond to increased activity of speculators and may indicate sudden changes in the preferences of minor investors. With that idea in mind, we developed an algorithm of revealing stocks that are most responsible for the increased inconsistency of aggregate data with Pareto's model. We applied this algorithm to Chinese stock market data and managed to select a single stock out of one hundred stocks in Chinese stock market, which may be said to be responsible for the increased degree of inconsistency with Pareto's model.

6 Conslusions

In conclusion, we point out that although there is no computationally efficient algorithms for testing aggregate economic data for consistency with Pareto's model with two or more rational representative consumers, we still can use some partial cases of this model in order to analyze the economic data when it is not consistent with the classical Pareto's model of a single rational representative consumer.

References

Deb R. (2010): An efficient nonparametric test of the collective household model. Working paper, URL: https://www.economics.utoronto.ca/debrahul/files/Collective_Model.pdf

Klemashev N., Shananin A. (2014): Nonparametric method for analizing budget statistics (in Russian). Proceedings of MIPT **6** 49–56

Klemashev N., Shanain A. (2015): Estimating the complexity of testing the hypothesis about temporar dictator with positively-homogenious utility function (in Russian). Proceedings of MIPT **7** 17–27

Klemashev N., Shananin A. (2016): Inverse problems of demand analysis and their applications to computation of positively-homogeneous Konus-Divisia indices and forecasting. Journal of Inverse and Ill-Posed Problems **24** (2016) 267–391

Nobibon F.T., Cherchye L., Crama Y., Demuynck T., De Rock B., Spieksma F. (2013): Revealed Preference Tests of Collectively Rational Consumption Behavior: Formulations and Algorithms. Working paper, URL: http://papers.ssrn.com/sol3/papers.cfm?abstract_id=2381956

Petrov A., Shananin A. (1997): Integrability Conditions, Income Distribution, and Social Structures. Constructing Scalar-Valued Objective Functions, Springer, 271–278

Shananin A. (1989): On aggregating demand functions (in Russian). Economics and mathematical methods **35** (1989) 1095–1105

Geomagnetic Storms, Earthquakes and their Influence on GNSS Coordinate Time Series

Inese Varna[1], Janis Balodis[1], Diana Haritonova[1]

[1] University of Latvia, Institute of Geodesy and Geoinformatics,
Raina blv. 19, Riga, Latvia
inese.janpaule@lu.lv

Abstract. 10-year GNSS daily solutions for EUPOS-Riga and LATPOS continuously operating GNSS (Global Navigation Satellite Systems) RTK (Real Time Kinematic) reference network stations have been obtained at the University of Latvia, Institute of Geodesy and Geoinformatics using Bernese GNSS software. It is a huge amount of data which enables for deeper investigations of various phenomena affecting the GNSS observation results. The research initiative has been undertaken in order to explain some discrepancies in GNSS observation results. Currently the attention is paid to the Earth magnetic field, geomagnetic storms and earthquakes, also GNSS network 5 minute kinematic solutions were performed for several time periods with high geomagnetic activity.

Keywords: GNSS time series, ionosphere, geomagnetic storms, earthquakes

1 Introduction

The ionosphere plays an important role in GNSS applications because it influences radio wave propagation. The ionosphere delay can be directly measured and mitigated using dual frequency GNSS receivers. However GNSS signal fading due to electron density gradients and irregularities in the ionosphere must be considered.

Total Electron Content (TEC) is the total number of electrons integrated between two points, along a tube of one meter squared cross section. For different wavelengths along the same path, different signal delay can be observed. The TEC depend on magnetic field intensity tied to local time, latitude, longitude, season, geomagnetic conditions, solar cycle, and troposphere conditions. One more parameter which characterizes small-scale and rapid variations of TEC, and is strongly related to scintillation, is the ROTI (Rate of TEC index) [6]. If electron density irregularities cover a big area above receiver, there is a high probability that a receiver can lose several satellite signals simultaneously.

However, the most significant geomagnetic disturbances are in higher latitudes. Here one of the possible causes of GPS disturbances are polar cap patches, which are convecting clouds of enhanced plasma density [5]. The plasma density of polar cap patches is more than twice that of the background. They are either transported across the polar cap from the dense ionospheric plasma at the sunlit side of the Earth or

created by particle precipitation in the cusp. To disturb GPS signals, patches must contain small-scale plasma structures, with scale sizes of decameters to kilometres [4].

A common practice for eliminating ionospheric effect is using ionosphere free linear combination during post-processing. It is a linear combination of observables on two frequencies such as GPS L1 and L2 and it eliminates about 99% of the total ionospheric effect, also called the first order ionospheric effect [2]. The higher – second and third, order ionospheric effects can degrade the accuracy of GNSS solutions and they depend mainly on the level of the solar activity and geomagnetic and ionospheric conditions [3].

2 Daily GNSS network time series

10-year GNSS daily network solutions for EUPOS-Riga and LATPOS (Fig. 4. and 5.) reference network stations in Latvia have been obtained using Bernese GNSS software. EUREF stations BOR1 (Poland), GLSV (Ukraine), JOEN (Finland), LAMA (Poland), MAR6 (Sweden), ONSA (Sweden), PULK (Russian Federation), RIGA (Latvia) and VLNS (Lithuania) have been used as reference stations. The resulting time series were combined with the information of 50 strongest geomagnetic storms and earthquakes with magnitude => 6.0 worldwide [8] and all local earthquakes [7] for each year. As an example, Figure 1 represents station PREI height component time series, geomagnetic storms and earthquakes for year 2015.

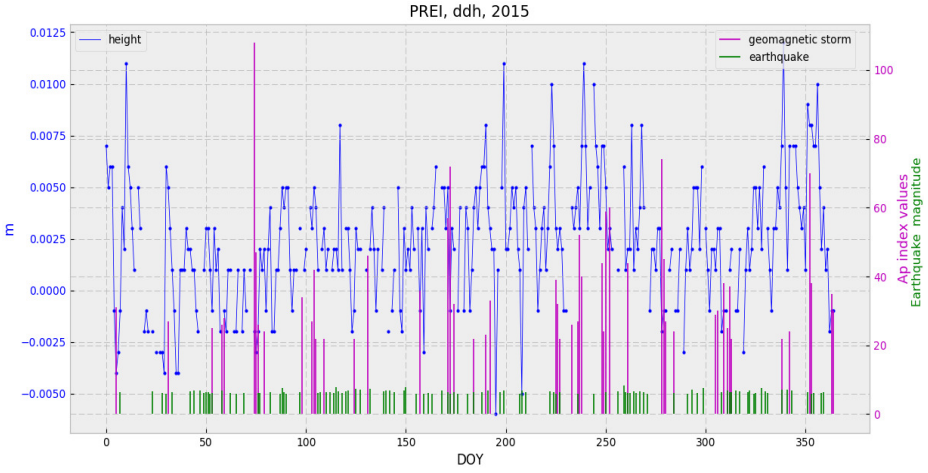

Fig. 1. LATPOS GNSS reference station PREI height component, geomagnetic storms and earthquakes in 2015.

Coordinate time series outliers have been detected using program Find Outliers and Discontinuities in Time Series (FODITS), which is embedded in Bernese GNSS Software v5.2. It automatically analyses and cleans coordinate time series. FODITS

verifies the significance of list of equipment changes and a list of worldwide registered earthquakes, identifies discontinuities and outliers in the time series, and creates the metadata to obtain high accuracy multi–year solutions and cleaned coordinate time series [1].

Event list file was created for 50 strongest geomagnetic storms for each year to detect geomagnetic storm influence on daily GNSS network time series. As it can be seen on Figure 2, there were not detected any correlation between geomagnetic storm occurrence and coordinate time series outliers of GNSS daily network solutions.

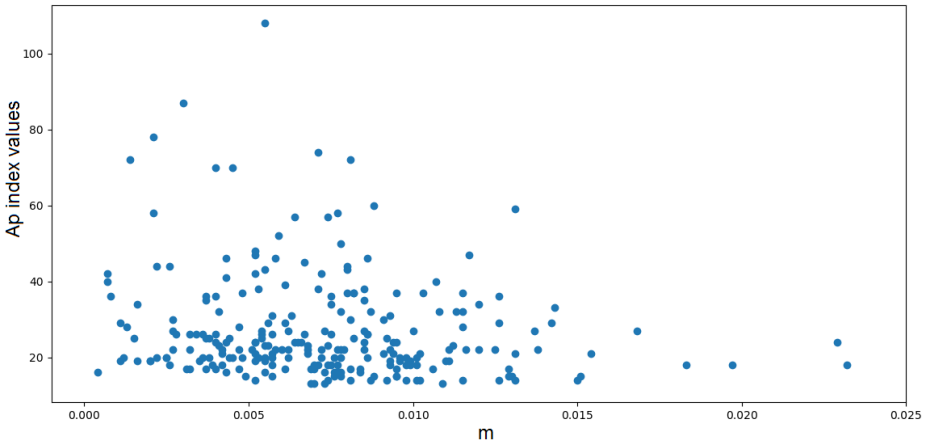

Fig. 2. Correlation between geomagnetic storm Ap indexes and GNSS station IRBE height component outliers, years 2012-2016.

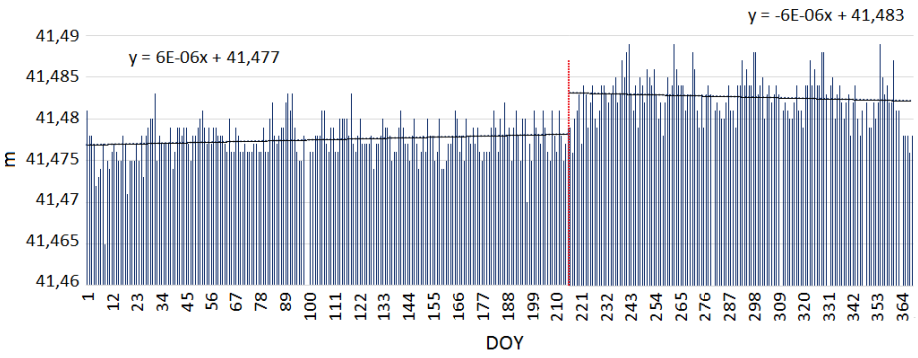

Fig. 3. EUPOS-RIGA GNSS reference station KREI height component jump after days 210. and 211. in year 2015.

Because of coordinate changes at the end of July 2015, a special interest caused earthquakes in Sweden July 29, 2015, magnitude M=3.4, and July 30, 2015, M=4.1, depth 15km.

In order to verify coordinate change, station velocities trends were computed for time periods January 1 – July 28, August 1 – December 31 and January 1 – December 31 in year 2015. The discrepancies were computed by extrapolating the linear trend to August 1 from first of two periods and to August 1 from the linear trend of the second period, correspondingly (Fig. 4., Fig. 5.). The result doesn't mean that this size jumps in coordinates occurred in July 29/30. But it means that velocity trends were broken sharply after the earthquake event in Sweden.

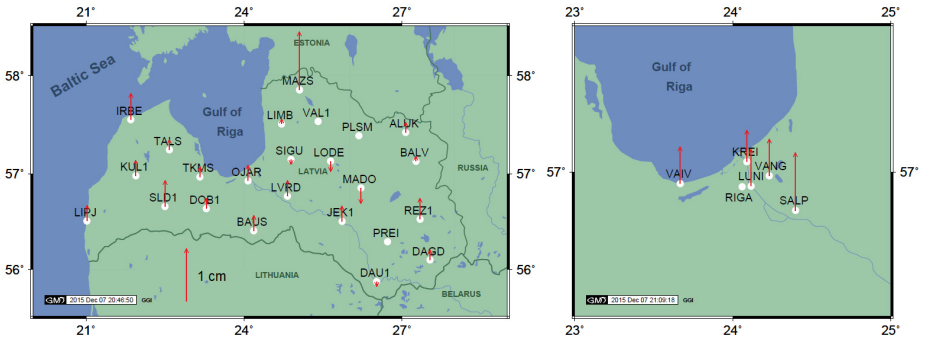

Fig. 4. EUPOS-RIGA (right) and LATPOS (left) GNSS reference station height coordinate discrepancies between trend January 1 – July 28 and August 1 – December 31, 2015, correspondingly.

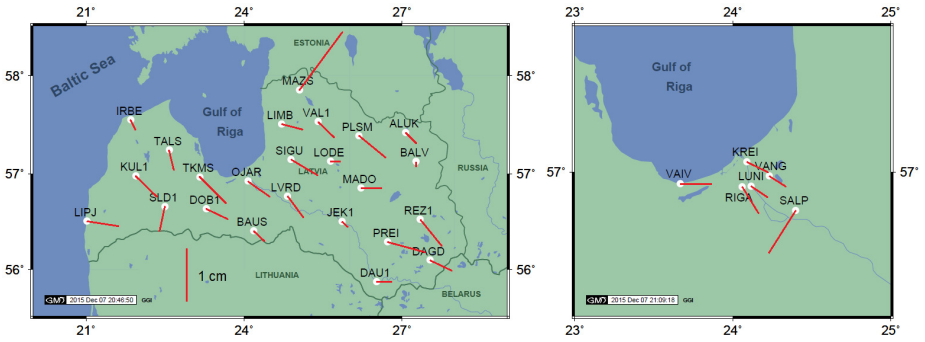

Fig. 5. EUPOS-RIGA (right) and LATPOS (left) GNSS reference station plane coordinate discrepancies between trend January 1 – July 28 and August 1 – December 31, 2015, correspondingly.

Most affected appear coordinate height component for stations IRBE, KREI (Fig. 3.), LUNI, MAZS, SALP, SLD1, VAIV, VANG (Fig. 4.); and coordinate plane components for stations KUL1, LIPJ, MAZS, PLSM, PREI, REZ1, SALP, SIGU,

TKMS, VAIV (Fig. 5.). Also reference station MAR6 in Sweden (Fig. 6) has been affected similarly after days 210. and 211. of year 2015.

The movements in plane are quite a similar in both vector directions and modules (Fig. 5). It is to remind once more that they are not a real movements, but discrepancies obtained by interpolating the coordinate values from one time period forward and from another one backward.

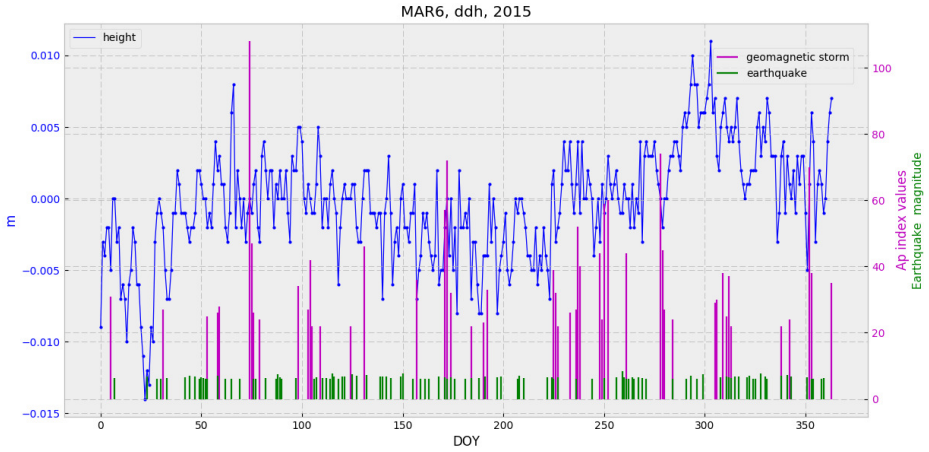

Fig. 6. EUREF GNSS reference station MAR6 height component, geomagnetic storms and earthquakes in 2015.

3 Five-minute kinematic GNSS network time series

Also five-minute kinematic GNSS network solutions were performed for several time periods with high geomagnetic activity. The cases of disturbed coordinates were searched among computed results in six selected periods: the week of St.Patrick's Day storm in March 2015, June and September 2015, January, October and December 2016. Here a significant influence of geomagnetic storms was observed (Fig. 7.). Different stations showed varied behaviour during geomagnetic storms. For example, strong geomagnetic storm on 17 March 2015 created disturbances up to one meter during several hours for LATPOS stations IRBE, JEK1, LIPJ, PREI, REZ1 and VAL1.

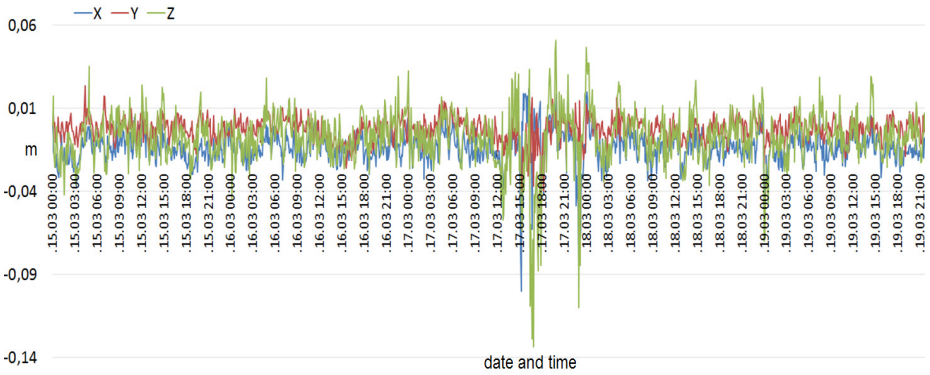

Fig. 7. Coordinate disturbances for GNSS station LIMB kinematic solution during St.Patrick's Day geomagnetic storm on March 17, 2015.

4 Conclusion

There is no correlation between geomagnetic storm occurrence and coordinate time series outliers of GNSS daily network solutions.

A large number of earthquakes every year occur worldwide, most of them do not affect GNSS daily network coordinate time series in Latvia; however a special interest caused earthquakes in Sweden July 29 and July 30, 2015. It was assumed that these earthquakes affected coordinate height component for stations IRBE, KREI, LUNI, MAZS, OJAR, REZ1, SALP, SIGU and VANG; and coordinate plane components for stations KUL1, LIPJ, MAZS, PLSM, PREI, REZ1, SALP, SIGU, TKMS and VAIV.

To obtain conclusions about geomagnetic storm and earthquake influence on daily GNSS time series it is proposed to use time series modelling and intervention analysis. It can be assumed that geomagnetic storms might have a temporary (one day) impact and earthquakes have a permanent impact on daily GNSS time series. Time series modelling gives a possibility to predict time series value for definite days with high geomagnetic activity. Intervention analysis determines how the mean level of a series changes due to an intervention, assuming that the same time series structure for the series holds both before and after the intervention.

It was concluded that the five-minute resolution GNSS observation coordinate results computed in kinematic mode for the ground based continuously operating GNSS reference stations are representing a reasonable contribution for recognition of space weather anomalies.

Acknowledgement

This paper was developed under the contract No.S193-ESS198F-ZF-N-290.

References

1. Dach, R., Lutz, S., Walser, P., Fridez, P. Bernese GNSS Software Version 5.2. Astronomical Institute, University of Bern, Bern, Switzerland, (2015)
2. Elmas Z.G., M.Aquino, H.A.Marques, and J.F.G.Monico. Higher order ionospheric effects in GNSS positioning in the European region. *Ann. Geophys.*, 29, 1383–1399, (2011)
3. Hoque, M.M., N.Jakowski. Estimate of higher order ionospheric errors in GNSS positioning, *Radio Sci.*, 43, RS5008, (2008)
4. Jacobsen K.S., Y.L.Andalsvik. Overview of the 2015 St. Patrick's day storm and its consequences for RTK and PPP positioning in Norway. *J. Space Weather Space Clim.*, 6, A9, (2016)
5. Jin, Y., J.I.Moen, W.J.Miloch. GPS scintillation effects associated with polar cap patches and substorm auroral activity: direct comparison. *J. Space Weather Space Clim.*, 4, A23, (2014)
6. Pi, X., A.J.Mannucci, U.J.Lindqwister, C.M.Ho. Monitoring of global ionospheric irregularities using the worldwide GPS network. *Geophys. Res. Lett.*, 24 (18), 2283–2286, (1997)
7. European-Mediterranean Seismological Centre, https://www.emsc-csem.org/#2
8. Real-time auroral activity and solar activity, https://www.spaceweatherlive.com/en/auroral-activity/top-50-geomagnetic-storms

Forecasting Power Output of Photovoltaic Systems Using Linear, Non-Linear and Enhanced Models

Xanthopoulou Georgia [1], Salamanis Athanasios [2], Kehagias Dionysios [2], Antoniou Ioannis [1], Charalampos Bratsas[1,3], Tzovaras Dimitrios [2]

[1]Aristotle University of Thessaloniki, Department of Mathematics
[2]Centre for Research and Technology Hellas, Information Technologies Institute
[3]Open Knowledge Foundation Greece
georgixv@math.auth.gr

Abstract. Accurate power output forecasting is a critical credibility factor for both conventional and renewable modern power systems. Renewable power systems, like photovoltaic (PV) systems, could be severely affected by alternating weather conditions, and this is an important issue relative to accurate forecasts. In this paper a comparative analysis between modern linear and non-linear methods for energy forecasting is provided. In particular, the Autoregressive Integrated Moving Average (ARIMA) model is used as a linear method and an Artificial Neural Network (ANN) as a non-linear one. Moreover, enhanced models that incorporate, apart from the energy, meteorological variables as explanatory variables in both linear and non-linear models is presented. Preliminary results, through experimentation on real data from a photovoltaic park in Crete, Greece indicate increased forecasting accuracy of the enhanced methods compared to the base models.

Keywords: Autoregressive Integrated Moving Average · Artificial Neural Network · Time Series Forecasting · Photovoltaic Power Output Forecasting · Comparative Analysis

1 Introduction

Nowadays, as the number of global population is increasing, the energy consumption is growing as well. For the purpose of fulfilling the increased need for power demand, renewable power systems are globally deployed, reducing the negative environmental footprint of the conventional power systems. In several places of the planet where the solar energy resources are abundant, the installation of photovoltaic parks is a very common choice. Although solar energy has the greatest energy potential among all renewable energy sources, the solar radiation is severely affected by weather conditions, therefore forecasting the power output of photovoltaic systems becomes a non-trivial task. Several methods have been proposed in the literature regarding the task of forecasting energy PV systems, not taking, however, into account the effect of the alternating weather conditions.

adfa, p. 1, 2017.

In this paper, we present a comparative analysis between linear and non-linear models for energy forecasting in PV systems. In particular, the Autoregressive Integrated Moving Average (ARIMA) family of models from time series analysis are used as linear evaluated models, and Artificial Neural Networks (ANN) with different topologies (i.e. number of neurons at the hidden layer, different activation functions, etc.) as non-linear ones. Both types of models use the produced energy as independent (input) variable. Additionally, a set of both linear and non-linear models that use as independent variables, in addition to energy also various meteorological variables (e.g. irradiance, panel temperature, etc.) are implemented and evaluated.

The rest of the paper is organized as follows. Section II reviews the current state-of-the-art methods associated with the presented work, whereas Section III describes the data used for implementing and evaluating the forecasting models, as well as the preprocessing steps taken to transform the data into a suitable form. Section IV gives a detailed description of the implemented models and the various processing steps followed throughout the analysis. Section V presents the evaluation framework through which the various implemented models were tested, as well as the experimental results. Finally, Section VI concludes the paper reviewing the main contributions and suggesting future directions.

2 Literature Review

Many researchers working on the task of time series forecasting agree that no single method is the best in every situation, due to the current problem complexity. Over the years, several approaches to time series forecasting have been proposed. These approached can be roughly classified into three major categories: linear, non-linear and hybrid methods. Linear methods, such as Autoregressive Moving Average (ARMA) models, ARIMA models, simple linear regression and multiple linear regression analysis are widely used due to their statistical properties. When we refer to non-linear methods, we allude to models originated from the field of Artificial Intelligence, such as ANNs, Support Vector Machines (SVM) and k-Nearest Neighbours (kNN). Also, noticeable research activity has focused on the development of hybrid methods, aiming at consolidating the favourable attributes of both linear and non-linear methods.

Accurate power output forecasting could increase the reliability and performance of the PV systems, and also prevent unnecessary operating costs. Therefore, the implementation of accurate, either linear models or non-linear models, is of paramount importance. This important task is implemented with linear models by several researchers such as Hamid Oudjana et al. [3]. Jiahao et al. [5] used linear regression in their research to study power outputs characteristics. Accurate prediction with multiple linear regression is the aim of Oussama et al. [1] too.

Many researchers working on energy forecasting utilize models based on neural networks because of the non-linearity of the meteorological data (Oussama and Farah [1], Hamid et al. [4] and Mellit et al. [7]). Jiahao et al. [5] investigated ANNs with different topologies in order to make more accurate forecasts, while Anil Rai et al. [8] analyzed ANNs accuracy by comparing different test datasets. Leva et al. [6] ana-

lyzed the sensitivity of the ANNs in power forecasting and Teo et al. [10] apart from the accuracy and the sensitivity of the ANNs, analyzed also the efficiency of different activation functions. Other studies provide comparative results of different models such as ANNs, ARIMA, SVM etc. [1, 4, 9]. Hybrid models are also proposed by several authors indicating increased robustness. [3, 11].

3 Data

In this section we present the dataset used for implementing and evaluating our forecasting models. We also provide details regarding the several preprocessing steps taken, in order to transform the data into a suitable form.

3.1 Data description

In order to implement the various forecasting models and evaluate their forecasting accuracy, we used a dataset containing energy values from several panels of a photovoltaic plant in Crete, Greece during a total period of 7 days (from July 1, 2013, to July 7, 2013). The data granularity is 15 minutes, meaning that for each quarter of each day and photovoltaic panel, an energy value is available. The dataset also contains values of the meteorological variables. In particular, contains values for the solar irradiance (W/m^2), the ambient temperature (°C) and the panel's temperature (°C). The granularity of these variables is the same as the one of the energy. This dataset is very useful because, as it will be presented later, the meteorological variables are strongly correlated with the energy. Figure 1 shows the daily power production in 15-minute interval.

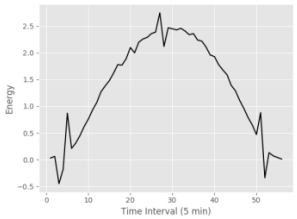

Fig. 1. Daily power output from a panel in the examined photovoltaic park.

3.2 Data Preprocessing

3.2.1 Filling Missing Data

For the purpose of our analysis, it was necessary to process the data by filling the missing data points. As already mentioned, the dataset contains values for several variables for each quarter of an overall period of seven days. For several quarters, the data values were missing and therefore we had to fill them using an interpolation method. Cubic spline interpolation method was used, instead of the more widely used linear interpolation method due to better results.

3.2.2 Outlier Detection

Another important step before starting analyzing the data, was the outlier detection. Identification of outliers is a very important task in the field of time series analysis. An outlier can be defined as a data point in a time series that is significantly different from the rest. In this study, the two-sided median method for cleaning data [2] was used. In this, a neighborhood of points is defined and the median of this neighborhood is calculated. If the absolute value of the difference between the point and the median is greater than a threshold, then the point is considered an outlier and is replaced by the median.

3.2.3 Time series Formulation

After filling the missing data points and removing the outliers, the next step was to construct time series from the original data. As already mentioned, the dataset contained energy data from 6 panels with similar characteristics located in the same photovoltaic park. We constructed one time series of energy values for each panel and day. Each time series has 96 values as the data granularity was 15 minutes. In this way we constructed 42 time series in total for all the panels and examined days. Additionally, we constructed one time series of size 96 for each meteorological variable and examined day. Therefore, we had 21 time series in total for all meteorological variables and examined days.

4 Linear, Non-Linear and Enhanced Forecasting Models

In this section, we thoroughly describe the several implemented methods for power output forecasting in PV systems.

4.1 Linear Forecasting Models

Time series forecasting can be conducted by several approaches. The more traditional, the linear ones, such as moving average models, autoregressive models and simple linear regression models, characterized by simplicity and forecasting accuracy.

4.1.1 Stationarity

A *stationary* time series is one whose statistical properties, such as mean, variance, autocorrelation, etc., are constant over time. The time series forecasting models can be implemented only on stationary time series, and so the non-stationary should be transformed into stationary before implementing the forecasting models. Several methods exist for checking the stationarity of a time series, such as visual inspection, calculation of summary statistics (mean, variance) and statistical tests. There are several statistical tests for checking stationarity such as the *Augmented Dicker-Fuller (ADF)* test, the *Phillips-Perron* test, the *Kwiatkowski–Phillips–Schmidt–Shin (KPSS)*

test, etc. In this work, we used visual inspection, summary statistics calculation and the Augmented Dicker-Fuller statistical test. Through visual inspection, we detected obvious trend in the inputs values of energy, while meteorological variables showed that the mean and the variance remain constant over time from one period to the next.

Moreover, we split the time series into partitions and then we calculated the mean and the variance of each partition. The comparison of the summary statistics verified that the time series are non-stationary. Finally, we used the Augmented Dicker-Fuller test for checking the null hypothesis that our time series (either energy or meteorological) are stationary. As seen in table 1, the statistical test indicates that the time series is non-stationary, for the critical values are smaller than the ADF value and hence the null hypothesis was rejected.

Table 1. Results of Augmented Dicker-Fuller statistical test

	Irradiance	**Temperature**	**Energy**
ADF statistics value	-0.878	-3.406	-2.133
Critical Value: 5%	-2.918	-2.917	-2.923
Critical Value: 10%	-2.597	-2.596	-2.599
Critical Value: 1%	-3.560	-3.558	-3.571

In order to stationarize our time series, we used first and second order differencing. After the differencing we ran the ADF test again, and this time the results indicated that we should accept the null hypothesis.

4.1.2 Model identification

In order to identify which linear model is suitable for forecasting in our time series, we use the Autocorrelation Function (ACF) and the Partial Autocorrelation Function (PACF) plots. In general, if ACF has an exponentially decreasing appearance and PACF becomes zero at specific lag *p*, then an Autoregressive model (AR (*p*)) is suitable for forecasting. On the other hand, if ACF becomes zero in lag *p* and PACF decreases exponentially, a Moving Average (MA (*p*)) should be used. The ACF and PACF plots for energy time series that correspond for a specific photovoltaic panel at July 1, 2013 are shown in Fig. 2. For their form we understand that an AR model with order $p = 1$ (AR(1)) is suitable for representing the data and therefore for forecasting. The same result applies to all time series of our dataset.

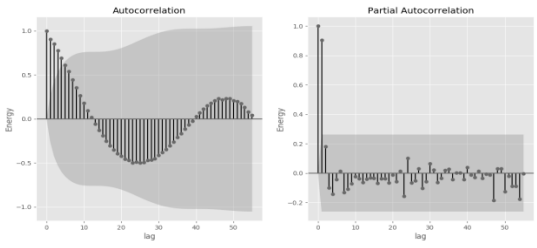

Fig. 2. ACF and PACF plots for model identification.

4.1.3 Autoregressive Integrated Moving Average (ARIMA)

A time series is a sequence of measurements of the same variable(s) made over time. Usually the measurements are made at evenly spaced intervals. In this work, the size of interval is 15 minutes. ARIMA family is the most general class of linear models for forecasting a time series. An ARIMA (*p, d, q*) model consists of three parts. The autoregressive part (AR) with order *p*, the moving average part (MA) with order *q* and the integrated part (I) which describes the number of differencing steps (d) that should be taken in order to stationarize the time series. The model is defined by the following formula.

$$X_t = c + \varepsilon_t + \sum_{i=1}^{p} \varphi_i X_{t-i} + \sum_{i=1}^{q} \theta_i \varepsilon_{t-i} \quad (1)$$

where ε_t are the error terms that follow normal distribution with 0 mean and *c* arbitrary constant.

As already mentioned, one differencing step is taken to stationarize our time series, i.e. $d = 1$. Also, as indicated by the ACF and PACF plots, the ARIMA model that fits more in our time series has strong autoregressive part with order $p = 1$, and no moving average part, i.e. $q = 0$. Consequently, the specific linear model used for power output forecasting in PV systems was ARIMA (1,1,0). We also considered the ARIMA (2,1,0) and ARIMA (3,1,0) models for a more meticulous research and also for detecting if the choice of the order of the autoregressive part through the ACF and PACF was correct. For ARIMA (1,1,0) model equation (1) becomes:

$$X_t = c + X_{t-1} + \varphi_1 (X_{t-1} - X_{t-2}) \quad (2)$$

The training process of an ARIMA model consists of the estimation of the φ and θ parameters. Using the available data, a set of equations like (2) are formulated with unknowns the φ and θ parameters. The number of equations is far greater than the number of the parameters. Therefore, this *overdetermined system* is not solved analytically but in the least-squares way. In this work, we had to estimate 1 parameter for the ARIMA (1,1,0) model and 2 and 3 parameters for the ARIMA (2,1,0) and ARIMA (3,1,0) models. We used the *Singular Value Decomposition (SVD)* method to solve the formulated overdetermined systems and estimate the corresponding parameters.

4.2 Non – linear forecasting methods

Apart from linear methods, extensively studies have been conducted about using non-linear models for time series forecasting. One of the most widely used non-linear models for time series forecasting are the ANNs. In this section we present our implementation of an ANN for power output forecasting in PV systems.

4.2.1 Artificial Neural Networks

ANNs are computational models inspired by the natural neural networks. An *artificial neuron* is essentially a computational node which takes several inputs, combines them using a specific way, and produces an output. Each input is the neuron is multiplied

by a parameter called *weight*, and the partial products are summed and feed as input to a function called *activation function*. This function is, at most times, non-linear towards the inputs (e.g. logistic function, rectifier function, etc.). An ANN consists of a set of artificial neurons interconnected and organized in layers. An ANN usually has one input layer, which receives the inputs, several hidden layers which implement the various data transformations, and one output layer through which the output is derived. An ANN which has only one information flow (from the input to output layer) is called *feed-forward*. A general topology of an ANN is shown in Fig. 3. As mentioned before, the various ANNs utilize various activation functions. One of them is the *sigmoid function* which is a mathematical function having an "S" shaped curve. Often, sigmoid function refers to the special case of the logistic function defined by the formula:

$$f(x) = \frac{1}{1+e^{-x}} \tag{3}$$

Another example is the *identity function* which always returns the same value that was used as its argument. The function is given by the following formula:

$$f(x) = x \tag{4}$$

Finally, there is the *rectifier function* defined as:

$$f(x) = \max(0, x) \tag{5}$$

Usually, the ANNs utilize a supervised learning technique called *backpropagation* for training, i.e. estimating the values of the weights. Backpropagation is a common method of training ANNs and is used in conjunction with optimization methods such as gradient descent. The algorithm repeats a two phase cycle, propagation and weight update.

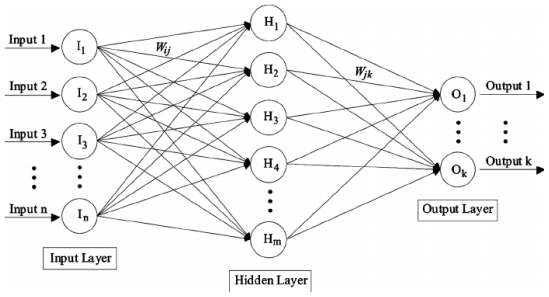

Fig. 3. General topology of an ANN

In this work, we implemented feed-forward ANNs with, one input, one hidden and one output layer for forecasting power output in PV systems. The number of neurons in the input layer was selected equal to the order of the evaluated ARIMA models (i.e. 1, 2 and 3), while in the output layer we had only one neuron. Furthermore, a Wilcoxon test (table 2) showed that we can reject the null hypothesis as the p-values are not greater than 0.05. Hence, in the choice of the number of the neurons in the input layer

there is a significant difference. In order to select the number of neurons in the hidden layer and the appropriate activation function, we ran simulations with different numbers of nodes (from 1 to 100) and different activation functions. The activation functions tested were the logistic sigmoid, the hyperbolic tangent and the rectified linear unit function. At each simulation cycle, we trained a different ANN and used it to make forecasts on a specific test time series. The ANN that yielded the best results in terms of forecasting accuracy was the one with 3 neurons in the hidden layer and the logistic sigmoid function as activation function for all the neurons, apart from the neuron in the output layer for which the identity function was used. Three different variations of this ANN (with 1, 2 and 3 neurons in the input layer) were implemented and compared with the corresponding ARIMA models.

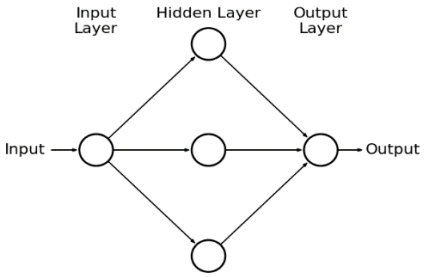

Fig. 4. Topology of an implemented ANN with 1 input, 3 hidden and 1 output neurons.

Table 2. Wilcoxon Statistical Test results

	ANN – 1 neuron	**ANN – 2 neuron**	**ANN – 3 neuron**
Wilcoxon p-value	1.02e-05	5.50e-06	5.36e-06

One very common problem that arises when training ANNs, and especially ANNs with large number of layers and neurons, is *overfitting*. Overfitting is the case where the ANN performs very well on the training data, but poorly on the previous unseen test data, in other words fails to generalize well on new data. There are several ways to overcome overfitting, e.g. increasing the number of training instances or reducing the number of layers and neurons and thus the number of unknown parameters. These methods are not usually adopted reluctantly by the researchers because on one hand the acquisition of more training samples is a costly process, and on the other the reduction of the number of layers and neurons may lead to less powerful networks. Fortunately, there is another way for overcoming overfitting which is called regularization. In this, an extra term, which takes into account the magnitude of the weights of the network, is added to the cost function of the training algorithm. Usually, this term is the sum of the squares of all the weights of the network (excluding the biases) multiplied by a constant called *regularization parameter*. After training the network using the updated cost function, we can see that the effect of the overfitting is reduced. As will be seen at the evaluation framework, in this work we considered only

the test error of our implemented ANN models and not the training error, and therefore we did not examine in depth the possibility of arising the problem of overfitting. We plan to include as future work, an analysis of the generalization capability of our ANN models by comparing the training and test errors and using regularization techniques to improve the generalization capability in the case of overfitting.

4.3 Enhanced models

Renewable energy sources such as solar energy, are weather dependent and it is evident that there is a sort of relationship regarding the forecast. In order to measure the correlation between the meteorological data and the energy production data we calculated *Pearson's correlation coefficient* and *Spearman's correlation coefficient*. Pearson's correlation coefficient is a statistic measuring the linear interdependence between two variables or two sets of data. The value of the coefficient ranges from -1 to 1, with 1 indicating a perfect positive linear relationship, -1 indicating a perfect negative relationship and 0 showing none existing relationship. The formula for calculating the coefficient for two variables *X* and *Y* is the following:

$$\rho = \frac{\mathrm{cov}(X,Y)}{\sigma_x \sigma_y} \tag{6}$$

where *cov(X,Y)* the covariance and σ_x, σ_y the standard deviations of *X* and *Y* respectively.

Spearman's correlation coefficient is a statistical measure of the strength of a monotonic relationship between paired data. The value of the coefficient ranges from -1 to 1, with 1 or -1 indicating that each of the variables is a perfect monotone function of the other. The Spearman correlation coefficient is defined as the Pearson correlation coefficient between the corresponding *ranked* variables.

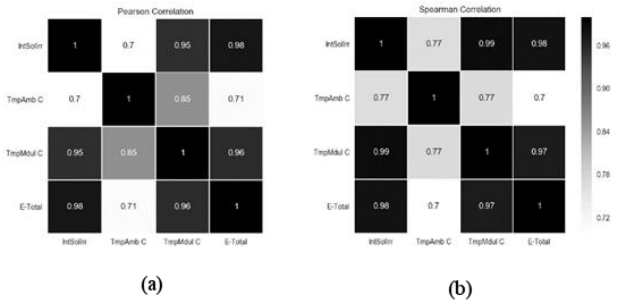

Fig. 5. Pearson's (a) and Spearman's (b) correlation coefficient values between energy (E-Total), solar irradiance (IntSolIrr), ambient temperature (TmpAmb C) and panel's temperature (TmpMdul C).

The Pearson's and Spearman's coefficient values between the energy and the meteorological variables are shown in Fig.1. As shown in the last row of both matrices, the coefficients values between energy and the solar irradiance and panel's tempera-

ture are very close to 1 (0.98 and 0.96 respectively for Pearson's coefficient and 0.98 and 0.97 for Spearman's) and between energy and ambient temperature is approximately 0.7 (0.71 for Pearson's coefficient and 0.7 for Spearman's). These results indicate strong linear correlation between energy and the meteorological variable. Based on this conclusion, we enhanced the implemented forecasting models (both ARIMA and ANN) by adding the environmental variables as explanatory variables of the models. Specifically, we implemented one ARIMA model with explanatory variables the energy and the solar irradiance, one with the energy and the panel's temperature and one with the energy and the ambient temperature. Likewise for the case of the ANN model. Subsequently, we have 6 *enhanced* models in addition to the initial *base* models.

5 Evaluation

In this section, we present the evaluation framework through which the various implemented models were tested, as well as the preliminary experimental results.

5.1 Evaluation Framework

In order to implement and evaluate our models, we split the set of our time series into training and test subsets (80% in the training and 20% in test). We used the training time series to build our models and the test to make forecasts. The forecasts were made for 1 to 4 steps (15-minute intervals) ahead in time. We repeated this process in all possible ways for the purpose of cross-validating the results. We ran all training and test datasets for each implemented model (both base and enhanced) and we compared the results in terms of forecasting accuracy using the *Symmetric Mean Absolute Percentage Error (SMAPE)* metric, which is defined by the following formula:

$$SMAPE = \frac{100\%}{n} \sum_{t=1}^{n} \frac{|F_t - A_t|}{|A_t| + |F_t|} \tag{7}$$

where F_t is the forecasted value and A_t the actual value. We selected SMAPE over other error metrics because it provides a result between 0% and 100% which is more interpretable. The results of the experiments are presented in the following section.

5.2 Experimental Results

Table 3 presents the average forecasting results for all steps ahead of the implemented ARIMA models that use only the energy as explanatory variable. As shown, the ARIMA (1,1,0) model, indicated by the ACF and PACF plots, outperforms its competitors. Similarly, as shown in Table 4, the ANN model with one neuron in the input layer outperforms, in terms of forecasting accuracy, those with 2 and 3 neurons in the input layer, respectively.

Table 3. SMAPE results of different ARIMA models

	ARIMA (1,1,0)	ARIMA (2,1,0)	ARIMA (3,1,0)
SMAPE (%)	11.5	16.87	21.11

Table 4. SMAPE results of different ANN models

	ANN - 1 neuron	ANN - 2 neurons	ANN – 3 neurons
SMAPE (%)	6.38	13.37	18.11

In Fig. 6, the fitting of the all the implemented models (ARIMA and ANNs, base and enhanced) on a test time series is presented. We can see that the forecasting results of all the implemented models fit very well on the real values. Finally, Table 5 presents clearly the forecasting results of all the implemented models. As shown, ANN models have, in general, better forecasting accuracy compared to ARIMA. Also, we can see that the introduction of the meteorological data in the models as explanatory variables (i.e. enhanced models) decrease the forecasting accuracy in the case of the linear models (ARIMA), while it increases the forecasting accuracy in the case of non-linear models.

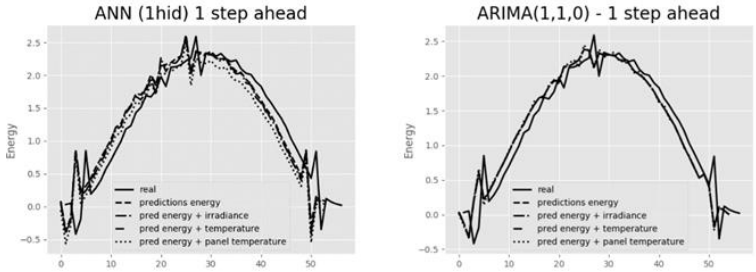

Fig. 6. The ARIMA (b) and ANN (a), base and enhanced, models fitting a test time series.

Table 5. Forecasting results of all implemented models

SMAPE (%)	Energy	En. + Irr.	En. + Amb. Temp.	En. + Panel's Temp.	Average
ARIMA	11.51	14.22	13.31	13.67	13.18
ANN	6.38	6.74	5.91	6.66	6.42

6 Conclusions

In this paper, a set of different models for forecasting power output in PV systems were implemented and evaluated. All steps of time series modelling process were implemented and presented in detail, along with the corresponding steps for building non-linear models. Moreover, the models were enhanced with meteorological data

explanatory variables. Preliminary results, for experiments conducted on real data from a photovoltaic park in Crete, Greece, indicated that the ANN non-linear models outperform the linear ARIMA models in terms of forecasting accuracy. Additionally, the fusion of meteorological data increases the forecasting accuracy of the ANN models. This comprises the major contribution of the applied approach that results in a SMAPE value of 6.38%, which is highly acceptable from the power engineering perspective, as it has a significant practical implication on the reduction of maintenance costs for PV systems, based solely on publicly available meteorological data. The proposed ANN topology that exhibits the best performance is an ANN with one neuron in the input layer, three in the hidden and one in the output layer. Future directions of this work include, the experimentation with more data from different PV systems, the fusion of new data variables in the implemented models and the implementation of a hybrid model that will exploit the best characteristics of the ARIMA and ANN models.

References

1. Ahmia, O., Farah, N., & Mokhtar, B. (2015). Parallel seasonal approach for electrical load forecasting.
2. Basu, S., & Meckesheimer, M. (2007). Automatic outlier detection for time series: An application to sensor data. Knowledge and Information Systems, 11(2), 137–154.
3. Gandelli, A., Grimaccia, F., Leva, S., Mussetta, M., & Ogliari, E. (2014). Hybrid model analysis and validation for PV energy production forecasting. In Proceedings of the International Joint Conference on Neural Networks (pp. 1957–1962).
4. Hamid Oudjana, S., Hellal, a., & Hadj Mahamed, I. (2012). Short term photovoltaic power generation forecasting using neural network. *2012 11th International Conference on Environment and Electrical Engineering*, 706–711.
5. Jiahao, K., Jun, L., Qifan, L., Wanliang, F., Zhenhuan, C., Linlin, L., & Tieying, G. (2013). Photovoltaic power forecasting based on artificial neural network and meteorological data. In TENCON 2013 - 2013 IEEE Region 10 Conference (31194) (pp. 1–4).
6. Leva, S., Dolara, A., Grimaccia, F., Mussetta, M., & Ogliari, E. (2017). Analysis and validation of 24 hours ahead neural network forecasting of photovoltaic output power. Mathematics and Computers in Simulation, 131, 88–100.
7. Mellit, A., Sağlam, S., & Kalogirou, S. A. (2013). Artificial neural network-based model for estimating the produced power of a photovoltaic module. Renewable Energy, 60, 71–78.
8. Rai, A. K., Kaushika, N. D., Singh, B., & Agarwal, N. (2011). Simulation model of ANN based maximum power point tracking controller for solar PV system. Solar Energy Materials and Solar Cells, 95(2), 773–778.
9. Shi, J., Lee, W. J., Liu, Y., Yang, Y., & Wang, P. (2012). Forecasting power output of photovoltaic systems based on weather classification and support vector machines. In IEEE Transactions on Industry Applications (Vol. 48, pp. 1064–1069).
10. Teo, T. T., Logenthiran, T., & Woo, W. L. (2016). Forecasting of photovoltaic power using extreme learning machine. In Proceedings of the 2015 IEEE Innovative Smart Grid Technologies - Asia, ISGT ASIA 2015
11. Zhang, G. P. (2003). Time series forecasting using a hybrid ARIMA and neural network model. Neurocomputing, 50, 159–175.

Extreme value analysis of geomagnetic activity based on the data from Canadian geomagnetic observatories

Lidia Nikitina[1], Larisa Trichtchenko[1], David H. Boteler[1], Callum Heggart[2]

[1] Geomagnetic Laboratory, Natural Resources Canada, Ottawa, Canada
[2] Department of Civil and Environmental Engineering, University of Waterloo, Ontario, Canada
Lidia.Nikitina@canada.ca

Abstract. Extreme space weather events are a natural hazard which can affect different technology. In particular, geomagnetic activity during extreme space weather events could cause damage of power grids transformers and lead to power system collapse as happened in Québec in 1989. The aim of this research is to evaluate extreme levels of geomagnetic activity of different locations across Canada. Hourly ranges of geomagnetic field variations have been used as measures of geomagnetic activity. These geomagnetic indices have been processed to fit one of the extreme value distributions. The likelihood ratio test was applied to the maximum values to determine if the data fit to Gumbel or Fréchet extreme value distribution. The defined distribution was used to evaluate extreme geomagnetic disturbances which could happen once per 50 and once per 100 years with 99% confidence interval. Knowledge of extreme values of geomagnetic disturbances will provide criteria for safe operation of power grids.

Keywords: Extreme value analysis · Space weather · Geomagnetic activity

1 Introduction

Space weather disturbances have a range of impacts on different technologies, including the infrastructure and services that are regarded as critical in modern society i.e. energy supply (power grids and pipelines), communication and navigation. To mitigate these risks it is important to determine the parameters of extreme space weather effects in terms of geomagnetic activity and its consequent effects in critical infrastructure. In this research extreme value statistics has been applied to more than 40 years of magnetic data from the Canadian geomagnetic observatory network. The data were fitted to the generalized extreme valued distribution and the extreme disturbances which could happen once per 50 and once per 100 years were evaluated. These extreme values provide criteria which could be used by power companies and other impacted technologies for design or mitigation purposes.

adfa, p. 1, 2011.

2 Data availability

Natural Resources Canada (NRCan) operates the Canadian geomagnetic observatory network and has archived digital recording of one minute data starting as early as 1972-1975. Data from the most of Canadian observatories cover from 29 to 42 years (Table 1). To describe geomagnetic activity, NRCan historically uses the index of geomagnetic activity which is the difference between the maximum and minimum of the geomagnetic field in each hour [1, 2].

Table 1. Canadian geomagnetic observatories. Data availability.

Geomagnetic observatory	Abbreviation	Number of years of data availability
Victoria	VIC	41 years
Ottawa	OTT	41 years
St. John's	STJ	42 years
Brandon/ Glenlea	BRD/GLN	31 years
Meanook	MEA	42 years
Poste de-la-Baleine/ Sanikiluaq	PBQ/SNK	30 years
Fort Churchill	FCC	41 years
Yellowknife	YKC	39 years
Baker Lake	BLC	40 years
Cambridge Bay	CBB	42 years
Resolute	RES	40 years
Alert	ALE	29 years

3 Methodology

Analysis of extreme geomagnetic activity was made using the generalized extreme value (GEV) distribution with the cumulative probability

$$p(x) = \exp\{-[1 + \gamma(x - \mu)/\sigma]\} \qquad (1)$$

where parameters μ and σ are positive values. In the case when $\gamma>0$ this distribution is known as a Fréchet distribution, for $\gamma<0$ it is a negative Weibull distribution, and in the limiting case with $\gamma\rightarrow0$ it refers to a Gumbel distribution [3,4]. The extreme value statistics were applied to five-day maxima of the geomagnetic data for each observatory. The five day period was selected to satisfy the condition of data independence in extreme value analysis and based on a physical consideration that the duration of a

geomagnetic storm is approximately one or two days. The detailed description of the data processing is provided in [5].

The likelihood ratio test T_{LR} was applied to the processed data to determine if a Gumbel distribution (hypothesis H_0: $\gamma \to 0$) or Fréchet/Weibull distribution (hypothesis H_a: $\gamma \neq 0$) is better fitted to the data,

$$T_{LR} = 2 * ln \frac{\prod_{i \leq n} g_{\overline{\gamma},\overline{\mu},\overline{\sigma}}(X_i)}{\prod_{i \leq n} g_{0,\overline{\mu},\overline{\sigma}}(X_i)} \quad (2)$$

where $g_{\overline{\gamma},\overline{\mu},\overline{\sigma}}(X_i)$ and $g_{0,\overline{\mu},\overline{\sigma}}(X_i)$ are probability distribution functions fitted to the considered data supposing $\gamma \neq 0$ or $\gamma = 0$ [6].

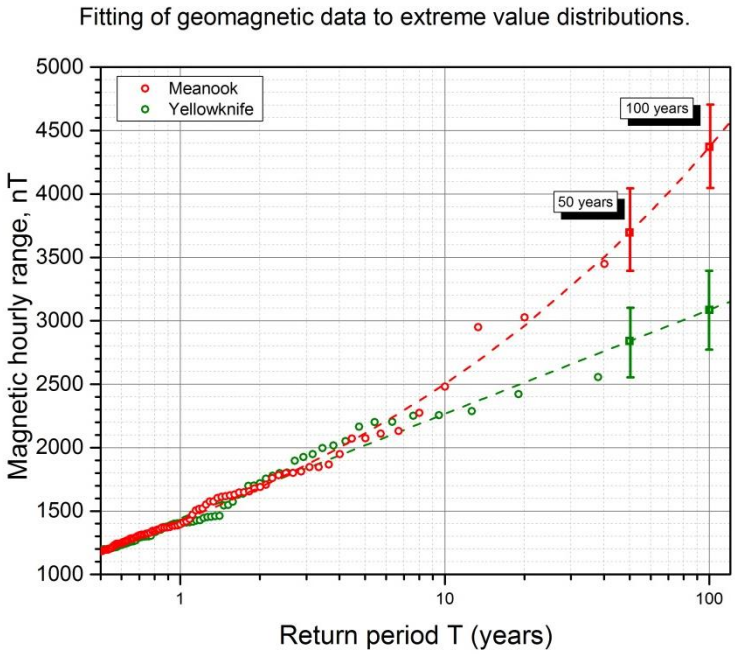

Fig. 1. Fitting of the processed geomagnetic data (circles) to extreme value distribution with the predicted values (squares) which could occur once per 50 years and once per 100 years with 99% confidence intervals. Meanook (red) fits to GEV distribution with γ=0.25 (Fréchet distribution), Yellowknife data (green) fit to GEV distribution with γ→0 (Gumbel distribution)

The above mentioned approach has been applied to the geomagnetic hourly range values for each of the observatories under investigation. The result of the fitting procedure is illustrated by Figure 1 where processed hourly range data from two observatories, Meanook and Yellowknife, and the estimated extreme values are plotted vs the return period T

$$T = \frac{1}{1-p\,(x)}\,. \tag{3}$$

The estimated values are denoted by squares and correspond to the return periods of 50 and 100 years. As is shown in Figure 1, Meanook and Yellowknife have different tails of distributions, Meanook data are fitted by a Fréchet distribution while Yellowknife data have a Gumbel distribution.

4 Results and conclusion

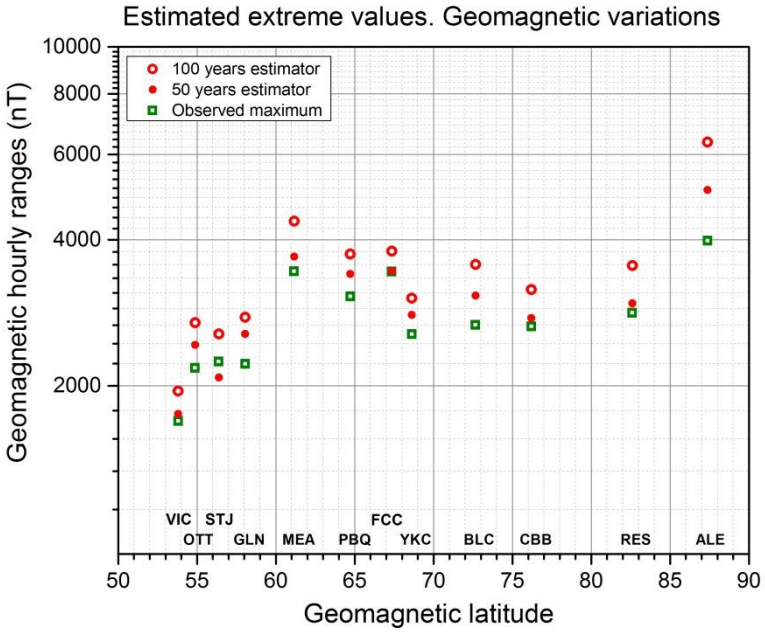

Fig. 2. Measured maximal values (green squares) together with the estimated extreme values geomagnetic variations once per 50 years (solid red circles) and once per 100 years (open red circles)

Extreme value statistical analysis has been employed for estimation of extreme values of the geomagnetic activity to evaluate two extreme scenarios, once in 50 years values and once in 100 years values for geomagnetic activity variations.

The results presented in Figure 2 demonstrate a tendency of increasing of extreme geomagnetic activity for latitudes between 54^0 and 61.2^0 decreasing between 61.2^0 and 72^0 and another increasing to the north of 72^0.

The extreme value analysis demonstrates that for estimation of extreme geomagnetic activity both Gumbel and Fréchet distributions could be used. All observatories

in the geomagnetic latititude range [64^0, 70^0] are well approximated by a Gumbel distribution, while all the observatories to the north of 70^0 are better approximated by a Fréchet distribution.

5 References

1. Boteler, D. H. (2001), Assessment of geomagnetic hazard to power systems in Canada, Nat. Hazards, 23, 101–120.
2. Trichtchenko, L., H.-L. Lam, D.H. Boteler, R. Coles and J. Parmelee, (2009), Canadian Space Weather Forecast Services, Can Aeronaut. Space Journal, 55, 107-113.
3. Gumbel, E.J. (1958), Statistics of extremes. Columbia University Press, New York, 275 pp.
4. Coles, S. (2001), An introduction to statistical modeling of extreme values, Springer Verlag, London, UK, 205 pp.
5. Nikitina, L., L. Trichtchenko, and D. H. Boteler (2016), Assessment of extreme values in geomagnetic and geoelectric field variations for Canada, Space Weather, 14, 481–494, doi:10.1002/2016SW001386.
6. Reiss, R.-D., M. Thomas (2001), Statistical analysis of extreme values with applications to insurance, finance, hydrology and other fields. Birkhauser Verlag AG, 2nd edition.

Estimation of the crustal velocity field in Baza and Galera faults from GPS position time series in 2009-2012

A.J. Gil[1,2,3], A. Sánchez-Alzola[2,4], M.J. Borque[1,2,3], M.C. Lacy[1,2,3], M. Avilés[1,2], J.A. García-Armenteros[1,2], J. Galindo-Zaldívar[5,6],P. Alfaro[7], F.J. García-Tortosa[1,8], A.C. López Garrido[6], C. Sanz de Gadeano[6], P. Ruano[5], F. Martínez[5], A. Pedrera[9]

[1] Centro de Estudios Avanzados en Ciencias de la Tierra (CEACTierra), Univ. de Jaén, Spain
[2] Grupo de Investigación RNM282-Microgeodesia Jaén, Univ. de Jaén, Spain
[3] Departamento de Ingeniería Cartográfica, Geodésica y Fotogrametría, Univ. de Jaén, Spain
[4] Departamento de Estadística e Investigación Operativa, Univ. de Cádiz, Spain
[5] Departamento de Geodinámica, Univ. de Granada, Spain
[6] Instituto Andaluz de Ciencias de la Tierra (CSIC, Univ. de Granada), Spain
[7] Departamento de Ciencias de la Tierra y del Medio Ambiente, Univ.de Alicante, Spain
[8] Departamento de Geología, Univ. de Jaén, Spain
[9] Instituto Geológico y Minero de España (IGME), Spain

Abstract. The active Baza and Galera faults are situated in the Northeast area of Granada province and follow the dynamic of the Betic Cordillera. The goal of our research is to constrain the activity of both faults from high quality geodetic measurements obtaining precise deformation rates. To achieve that in 2008 we installed a network which has been observed since 2009. Here we show the first results computed from four GPS campaigns in the period 2009-2012 and using statistical analysis for signal filtering and outlier detection. These results agree with the general movement of the area due to the tectonic (mean velocities of 18.59 mm/yr East and 15.75 mm/yr North components). Moreover, we have identified differences between the geodynamic of both faults, observing a residual velocity field with values varying from 1-2 mm. The integration of future geologic and seismic information with the deformation measurements will allow a better understanding of the kinematics of these interesting geologic structures.

Keywords: PPP time series, Crustal deformation, Statistical analysis, Baza and Galera faults

1 Geological setting and GPS network

The Galera and Baza fault are two geologic structures located in the central region of the Betic Cordillera. This area has a general extension movement of the main tectonic features highlighted by several geodetic, geologic and geomorphic markers [5], [1], [4], [10]. To observe the dynamic of these faults, a network of seven sites (named 5100-5700) was built in 2008 [5]. The sites were positioned in well-defined areas on both geologic blocks of the faults. They were perfectly fixed over the surface with

concrete on exposed rocks using self-centring mounting. The measurements of the faults cover a total of 4 GPS field campaigns, with 5-day time span, in September 2009, 2010, 2011 and 2012. The main reason of measure in the same month of the year is to avoid seasonality effects in our data that could impact the time series and further analysis.

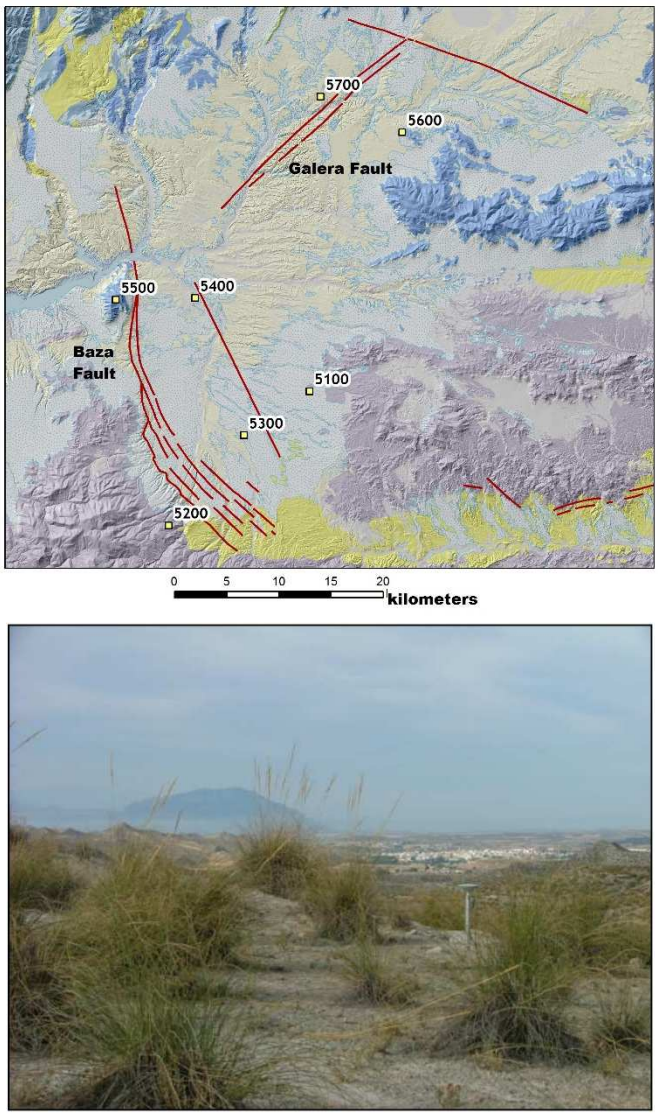

Fig. 1. Top. Spatial distribution of the GPS sites with the trace of the Baza and Galera faults. Bottom. Sismitas site (5700) with the GPS antenna installed during an observation campaign.

Focus on the measurements, the GPS receivers used in 2009 and 2010 campaigns were Leica Geosystem GX1230 receivers with LEIAX1202 antennas whereas newer campaigns in 2011 and 2012 were observed with LEICA Geosystem AR10 receivers and LEIAR10 antennas. Figure 1 shows the spatial distribution of the sites and a picture of Sismitas site (5700) with the GPS antenna installed.

To give the best analysis of the geodynamic, a good estimation of the coordinates of each site is essential. To achieve that, we have used the Precise Point positioning (PPP) methodology using the software developed by the JPL GIPSY-OASIS version 6.4 (https://gipsy-oasis.jpl.nasa.gov/). The main characteristic of this program is the capacity of determinate the position using each site isolated with its own observations. This methodology is a good approach for an accurate crustal deformation analysis and has been applied in many geodetic studies.

The processing strategy followed uses zero-ambiguity resolution strategy [3]. A similar standard procedure for all 4 campaigns was also handle [7]. We have applied JPL final ephemeris and pole products, FES2004 ocean tide loading model [8], hydrostatic and wet components of tropospheric delay and a 10º cut-off angle with calibrated data of antenna phase center. Moreover, to define the processed coordinates, a stable IGS08 reference frame was considered [2]. That is, all the JPL products have been computed in the same IGS08 reference frame, ensuring an unchanged geodetic frame for all the observation campaigns.

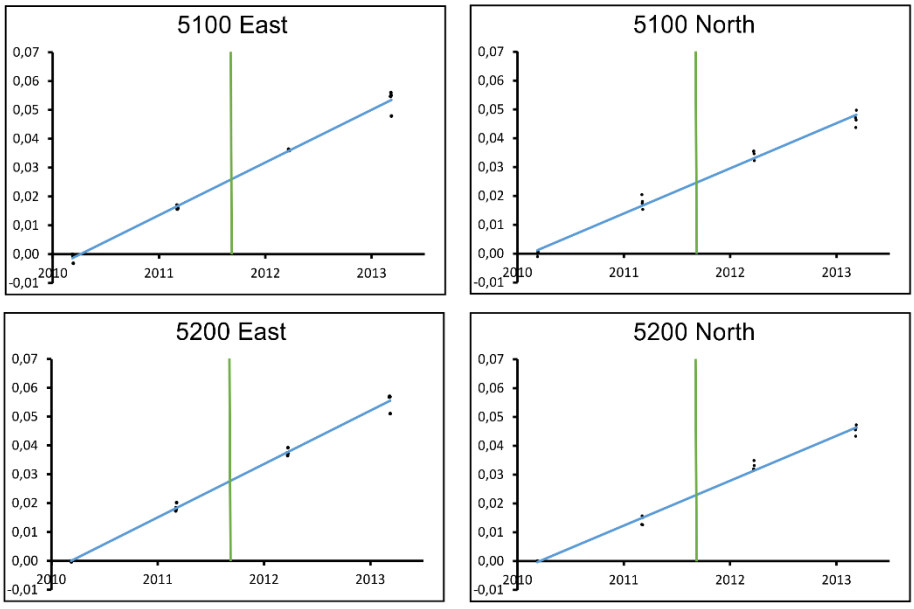

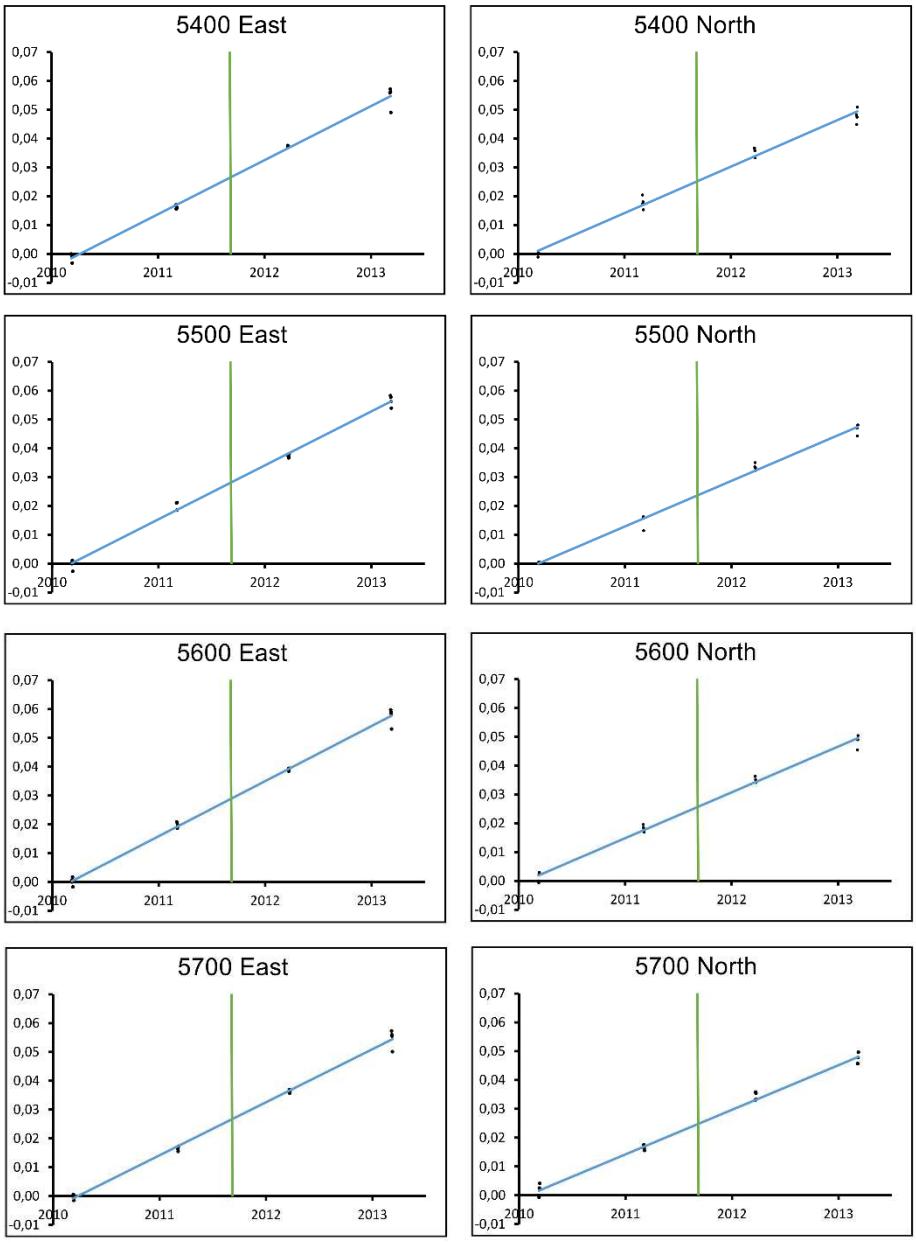

Fig. 2. Position time series in East and North components for all sites of the network

2 GPS time series and statistical analysis

Once the coordinates were processed, we represent all the campaigns using the best trend line fit for each site. Here we also consider the change of antenna between 2011 and 2012 campaigns, which produce a slip in the time series due to the differences in the antenna phase center. For the uncertainties analysis, we have also included the associated formal error from the best-fit trend line derived from the software. This value has been associated to the velocity estimation.

The statistical analysis was focused on several filtering tools which eliminates the outliers due to problems in the GPS processing. Unfortunately, this research has only coordinates during the observation campaigns, so the time series seasonality decomposition has not been possible. Anyway, the trend analysis is enough to give us an estimation of the velocity. We did not consider any change in the position during the campaigns thus the uncertainties observed are attributed to the white noise in acquired observations. Figure 2 shows the position time series in horizontal components (North and East) for all the sites of the network.

The linear trend was computed using MLE algorithms included on CATS Time Series Analysis Software [11]. Basis on the best fit linear regression, the estimation of the likelihood L with noise components and parameters in a set of observations, x, (assuming a Gaussian distribution) is:

$$L(x, C) = \frac{1}{(2\pi)^{\frac{N}{2}} \cdot |C|^{\frac{1}{2}}} e^{(-0.5v^T \cdot C^{-1} \cdot v)}$$

where $|C|^{\frac{1}{2}}$ is the root square of the determinant of the covariance matrix with the assumed noise in the data, N is the number of epochs (points) in our time series and v represents the post-fit residuals to the linear regression with weighted least squares. To a better management, this likelihood could be considered with logarithms. The maximization of $Ln[L(x, C)]$ let a greater numerical stability due to this maximum is unaffected by monotonic transformation. To solve the maximum likelihood problem, CATS software used a variant of the Nelder-Mead uphill simplex choice [9].

Although our study is centered only on the estimation of the linear trend in each GPS point, the CATS Time Series Analysis Software is able to estimate more complex theoretical adjustment models including annual and semiannual periodicities among others. Our uncertainties are computed using partial differential equations based on the linear regression adjustment.

3 First results and analysis

To highlight the local velocities between the sites of the network, once we have filtered the time series, we eliminate the tectonic component using the ITRF08 plate motion model [2]. These accurate measures give us an invaluable information of the geodynamics, standing out the differences between these geologic structures.

The first results indicate a measurable movement between the blocks; for instance, the Galera Fault (mainly 5700 and 5600 sites), showing a sinistral strike slip motion near 1 mm/yr difference. On the other hand, the sites near the Baza Fault present remarkable differences. If we consider the North area (5500 and 5400) the displacements are related probably with the dynamic of the North segment of the Fault, whereas in the South region (5100 and 5200) the residual velocities are fairly similar. Not all of the sites in the network could be considered. During the observation campaigns 5300 site was eliminated of the calculus due to its own motion, which is not explained by the tectonic (this site is located near a rail track slope). Figure 3 shows the absolute velocity field (IGS08 reference frame). Figure 4 includes the velocity field with respect to the Eurasian plate. Table 1 presents the absolute and residual velocities for all the sites and the standard deviations.

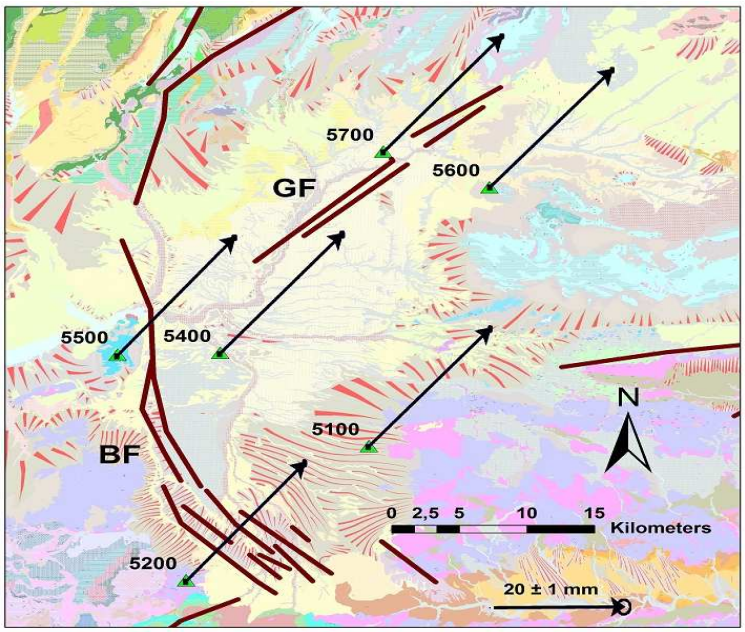

Fig. 3. Absolute velocity field in IGS08 reference frame.

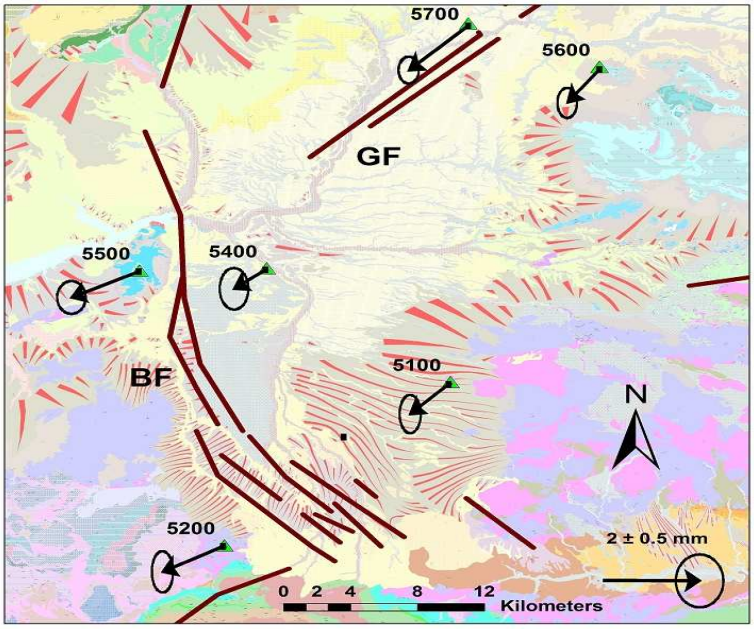

Fig. 4. Residual velocity field (Eurasian plate fixed)

	Absolute East (mm/yr)	Residual East (mm/yr)	Sigma East (mm/yr)	Absolute North (mm/yr)	Residual North (mm/yr)	Sigma North (mm/yr)
5100	18.29	-1.48	0.43	15.66	-1.02	0.49
5200	18.21	-1.56	0.44	15.54	-1.15	0.46
5400	18.76	-0.97	0.44	16.13	-0.55	0.50
5500	18.73	-0.99	0.39	15.82	-0.87	0.39
5600	19.13	-0.60	0.38	15.89	-0.78	0.39
5700	18.42	-1.29	0.40	15.48	-1.20	0.40

Table. 1. Absolute and residual velocities with standard deviations for all the GPS sites.

4 Conclusions

Our research reveals that this statistical methodology and GPS processing technique are able to measure the movements of these two geologic structures from position time series at millimeter level. We obtain absolute velocities in agreement with the general movement of the area due to the tectonic (mean of 18.59 mm/yr East and 15.75 mm/yr North). The differences with the theoretical tectonic plate model allow us to detect a residual velocity field with values varying from 1mm (5600) to close 2mm (5200) showing the deformation pattern of the area. The introduction of longer

time series, with more GPS campaigns and statistical filters, will improve the estimations of velocity and will allow us to confirm these results.

Aknowledgements

This study has been funded by PAIUJA 2017/2018, CEACTierra, and RNM148 and RNM282 research groups of Junta de Andalucía.

References

1. Alfaro, P., Delgado, J., Sanz de Galdeano, C., Galindo-Zaldívar, J., García-Tortosa, F.J., López-Garrido, A.C., López-Casado, C., Marín, C., Gil, A., Borque, M.J., (2008). The Baza Fault: a major active extensional fault in the Central Betic Cordillera (South Spain). *International Journal of Earth Sciences* 97, 1353–1365.

2. Altamimi, Z., Collilieux, X., Métivier, L., (2011). ITRF2008: an improved solution of the international terrestrial reference frame. J. Geod. 858, 457–473. http://dx.doi.org/10.1007/s00190-011-0444-4.

3. Bertiger,W., Desai, S., Haines, B., Harvey, N., Moore, A., Owen, S., Weiss, J., (2010). Single receiver phase ambiguity resolution with GPS data. *J. Geod*. 84 (5), 327–337. http://dx.doi.org/10.1007/s00190-010-0371-9.

4. García Tortosa, F.J., Alfaro, P., Galindo Zaldívar J., Sanz de Galdeano, C. (2011): Glacis geometry as a geomorphic marker of recent tectonics: the Guadix-Baza Basin (South Spain). *Geomorphology* 125, 517-529. doi: 10.1016/j.geomorph.2010.10.021.

5. Gil, A.J., Rodríguez-Caderot, G., Lacy, C., Ruiz, A., Sanz, C., Alfaro, P., (2002). Establishment of a non-permanent GPS network to monitor the deformation in Granada Basin (Betic Cordillera, Southern Spain). *Stud. Geophys. Geod*. 46, 395–410.

6. Gil, A.J.; García Tortosa, F.J.; Alfaro, P.; Galindo, J.; López-Garrrido, A.C.; de Lacy, M.C; Ruano, P.; Pedrera, A.; Sanz, C.; Borque, M.J.; Armenteros, J.A.; Avilés. Geodetic Deformation Monitoring of the Baza Fault from GPS. In proceedings of 7ª Asamblea Hispano-Portuguesa de Geodesia y Geofísica. San Sebastián (2012).

7. Gil, A.J.; Galindo-Zaldívar, J.; Sanz de Galdeano, C.; Borque, M.J.; Sánchez-Alzola, A.; Martínez-Campos, M.; Alfaro, P. (2017). The Padul normal fault ac-

tivity constrained by GPS data: Brittle extension orthogonal to folding in the central Betic Cordillera, *Tectonophysics*, 712–713, 64-71.

8. Lyard, F., Lefevre, F., Letellier, T., Francis, O., (2006). Modelling the global ocean tides: modern insights from FES2004. *Ocean Dyn*. 56, 394–415.

9. Press, W.H., Flannery D.P. Teukolsky, S.A., Vetterling, W.T., (1992). Numerical recipes. Cambridge University Press, New York, 818 pp.

10. Sanz de Galdeano, C., García-Tortosa, F.J., Peláez, J.A., Alfaro, P., Azañón, J.M., GalindoZaldívar, J., López-Casado, C., López-Garrido, A.C., Rodríguez-Fernández, J., Ruano, P., (2012). Main active faults in the Granada and Guadix-Baza Basins (Betic Cordillera). *J. Iber. Geol*. 38, 209–223.

11. Williams, S.D.P., (2008). CATS: GPS coordinate time series analysis software. *GPS Solutions* 12:147-153.

Advanced Symbolic Time Series Analysis in Cyber Physical Systems

Roland Ritt, Paul O'Leary, Christopher Josef Rothschedl, and Matthew Harker

Institute for Automation, University of Leoben, Leoben, Austria
roland.ritt@unileoben.ac.at

Keywords: symbolic time series analysis, single channel lexical analyser, time series, cyber physical system, linear differential operator

This paper presents advanced symbolic time series analysis (ASTSA) for large data sets emanating from cyber physical systems (CPS). The definition of CPS most pertinent to this paper is: *A CPS is a system with a coupling of the cyber aspects of computing and communications with the physical aspects of dynamics and engineering that must abide by the laws of physics. This includes sensor networks, real-time and hybrid systems* [1]. To ensure that the computation results conform to the laws of physics a linear differential operator (LDO) is embedded in the processing channel for each sensor. In this manner the dynamics of the system can be incorporated prior to performing symbolic analysis. A non-linear quantization is used for the intervals corresponding to the symbols. The intervals are based on observed modes of the system, which can be determined either during an exploratory phase or on–line during operation of the system. A complete processing channel (see Fig. 2) is called a single channel lexical analyser; one is made available for each sensor on the machine being observed.

The implementation of LDO in the system is particularly important since it enables the establishment of a causal link between the observations of the dynamic system and their cause. Without causality there can be no semantics and without semantics no knowledge acquisition based on the physical background of the system being observed. Correlation alone is not a guarantee for causality[1]

This work was originally motivated from the observation of large bulk material handling systems, see Fig. 1 for three examples of such systems. Typically, there are $n = 150 \ldots 250$ sensors per machine, and data is collected in a multi rate manner; whereby general sensors are sampled with $f_s = 1\,Hz$ and vibration data being sampled in the kilo-hertz range.

1 Local Linear Differential Operators (LDO)

Although processing the entire 'large' time series is a common practice in exploratory data analysis, reliable local computations (implemented as streaming

[1] Consider an exothermic system with a high activation energy. We must include the exothermic model if we are to establish causality, correlation alone will lead to erroneous interpretation.

Fig. 1. Examples of machines to which the analysis is applied. Image courtesy: Sandvik

algorithms) are preferred in on–line data processing. Since in this work we deal with time series emanating from cyber physical systems new techniques for local computations including the physics of the system (described by differential equations) have to be developed.

An ordinary differential equation (ODE) of the form

$$a_d(t)\,y^{(d)}(t) + a_{d-1}(t)\,y^{(d-1)}(t) + \ldots + a_0(t)\,y^{(0)}(t) = g(t) \tag{1}$$

can be described using a linear differential operator (LDO) D [2] such that $\mathsf{D}^{(i)}y(t) = y^{(i)}(t)$ where y is a function of t, $y^{(i)}$ is the n-th derivative with respect to t and $g(t)$ is the exciting function, in our case the noisy sensor data. This yields to the notation [3]

$$a_d(t)\,\mathsf{D}^{(d)}y^{(d)}(t) + a_{d-1}(t)\,\mathsf{D}^{(d-1)}y^{(d-1)}(t) + \ldots + a_0(t)\,\mathsf{D}^{(0)}y^{(0)}(t) = g(t)\,. \tag{2}$$

Factoring $y(t)$ leads to the compact formulation of the model

$$\mathsf{L}y(t) = g(t)\,, \tag{3}$$

with

$$\mathsf{L} \triangleq a_d(t)\,\mathsf{D}^{(d)} + a_{d-1}(t)\,\mathsf{D}^{(d-1)} + \ldots + a_0(t)\,\mathsf{D}^{(0)}. \tag{4}$$

In the discrete case (3) can be formulated as matrix equation. Solving this equation for y is an inverse problem which can be solved numerically in a discrete sense by

$$\boldsymbol{y} = \mathsf{L}^{+}\boldsymbol{g} + \mathsf{N}_{\mathsf{L}}\boldsymbol{\alpha}, \tag{5}$$

where $\boldsymbol{y}$ is the solution to the inverse problem, L^{+} is the pseudo-inverse of L, N_{L} is an orthonormal basis function set of the null space of L , $\boldsymbol{\alpha}$ is a coefficient vector for the null space (computed by initial- and/or the boundary-values) and $\boldsymbol{g}$ is the noisy time series data vector. Algebraic implementations for the solution of such problems can be found in [4–7].

The LDO, and their inverses, can be implemented as local operators and efficiently computed using a convolutional approach. This is basically a streaming-algorithm and thus suitable for big-data processing.

Furthermore, the covariance of the solution (5) is simply propagated as

$$\Lambda_y = \mathsf{L}^{+}\Lambda_g\left(\mathsf{L}^{+}\right)^{T}. \tag{6}$$

Using Λ_y as an estimate for the covariance in conjunction with the student-t and/or F-distribution permits the estimation of a confidence interval over the complete solution and allows the computation of a prediction interval for future values.

That is, the approach presented here to implementing linear differential operators not only permits the solution of embedded system dynamics but also yields a confidence interval for the predicted values of the dynamics.

2 Symbolic Time Series Analysis

The availability of the sensor signals, their regularized derivative and/or the application of a LDO permits the implementation of an advanced symbolic time series analysis (ASTSA) which includes the modelling of the system dynamics. As a result the time series (TS) can be discretized and compressed using unique symbols for different intervals (the so called alphabet). This step is named lexical analysis. A number of methods for the selection of the symbol intervals based on, e.g. , equal probability, variance or entropy can be found in literature [8–12]. Here, in a new approach, we define the intervals to correspond to the modes of the dynamic system in operation, i.e. each symbol corresponds to a mode or portion of a mode which should be identified. Commonly controllers are designed to operate optimally in a number of specific but distinct modes of the dynamic system.

In a next step, connected sequences with the same symbol can be compressed to a single symbol predicated with its length. The combination of applying a LDO, lexical analysis of the derived signal and compression is called single channel lexical analyser (SCLA), see Fig. 2. Combining the output of multiple SCLA

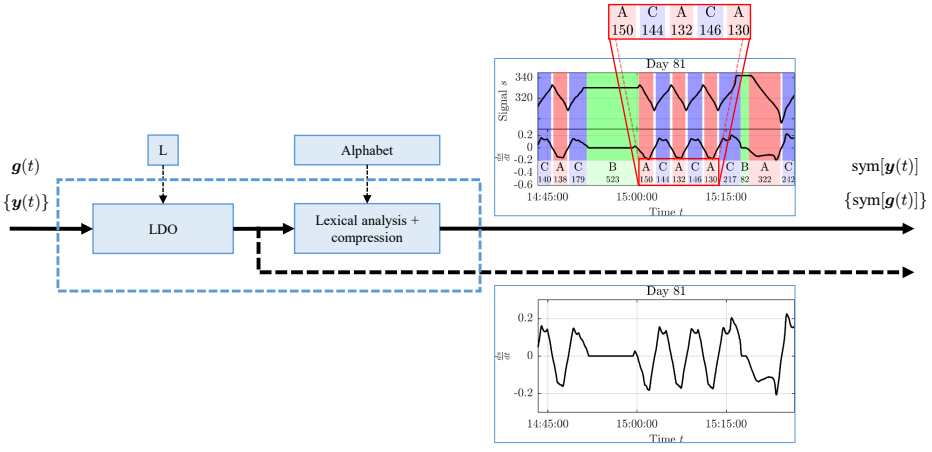

Fig. 2. A single channel lexical analyser (SCLA)

is called multi channel lexical analyser (MCLA). Two examples of symbolic time series analysis using MCLA are demonstrated in Fig. 3 and Fig. 4). For signal 1 and signal 2 the alphabet consists of the three symbols [`u`, `s`, `d`] assigned to the direction of the signal (up, stationary, down). The figures show two operation modes from the same machine. It can be clearly seen, that the operation modes of the machine have a different symbolic representation (visualized as different shaded colours in the plots) and allow a fast intuitive inspection and characterization of the signal. The signal range from the first dashed-blue line to the

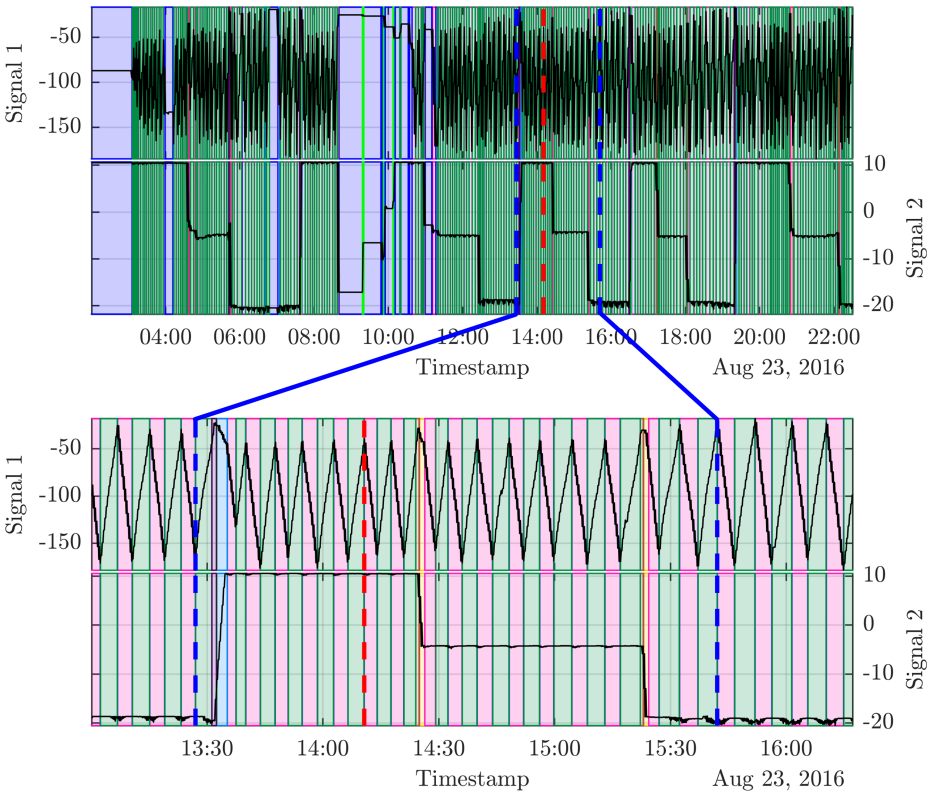

Fig. 3. Operation mode 1; the coloured areas illustrate the output of the MCLA; different colours represent different combinations of symbols from the SCLA of each channel (in this case two channels); the alphabet used for signal 1 and 2 consists of the three symbols [`u`, `s`, `d`]. Top: machine working in operation mode 1 with longer interrupts in-between (light blue area - both signals are stationary); Bottom: snippet of the signal showing the typical repeating pattern of operation mode 1.

dashed-red line (marked in both plots) have the same symbolic representation in both modes, whereas the portion of the signal after the dashed-red line shows a different colour-code for each mode.

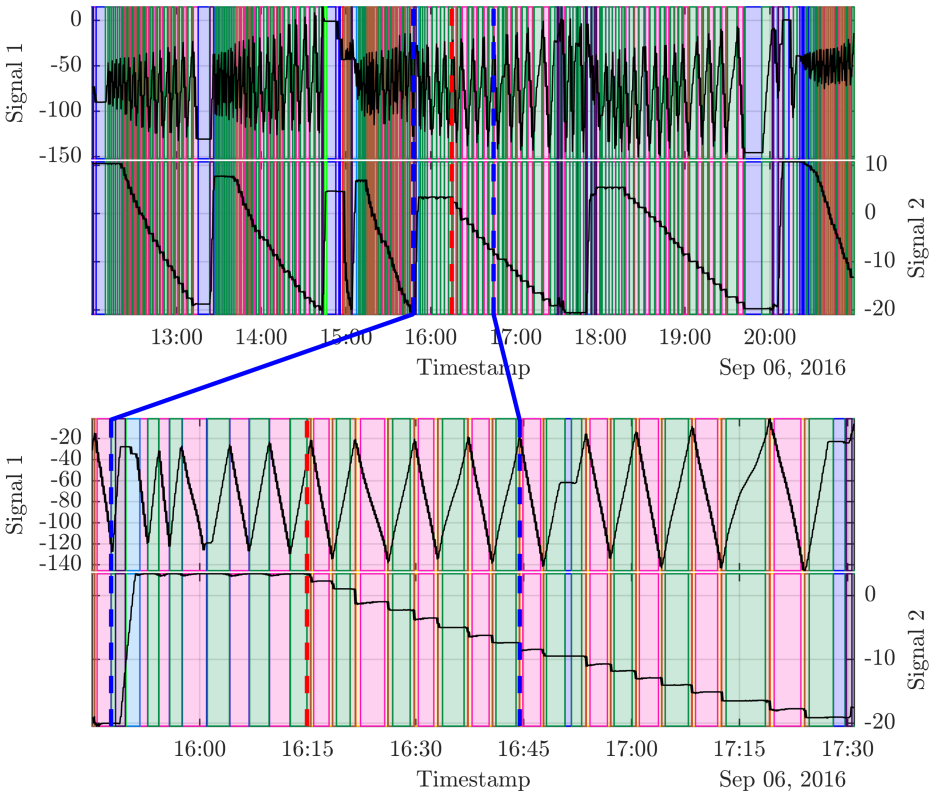

Fig. 4. Operation mode 2; the coloured areas illustrate the output of the MCLA; different colours represent different combinations of symbols from the SCLA of each channel (in this case two channels); the alphabet used for signal 1 and 2 consists of the three symbols [`u`, `s`, `d`]. Top: machine working in operation mode 2 with interrupts in-between (light blue area - both signals are stationary); Bottom: snippet of the signal showing the typical repeating pattern of operation mode 2.

The generated symbolic representation is used for further analyses. Building up histograms for occurring symbol combinations offers an insight in the overall behaviour of the system, see Fig. 5). This allows inter-machine comparison and comparison of different signal portions/ranges as well as classification of the operation mode. On top of Fig. 5 the histograms of the entire signal ranges shown in Fig 3 (top) and Fig 4 (top) are presented. The histograms for the typical repeating snippets, shown in Fig 3 (bottom) and Fig 4 (bottom), are visualized on the bottom. Since the machine is interrupted several times in both operating modes, the bins for the stationary state (`ss`) are more visible for the entire signal sequences (top). Excluding these bins, the statistics (histograms) of the shown snippets can act as representatives (motifs) for the operating modes. It can be seen that the histograms differ whether the machine is operating in

mode 1 (left) or mode 2 (right). Especially the occurrences of `dd` and `ud` reveal the differences. In future investigations the definition of a similarity measure for such histograms is planned to compare them qualitatively and may use this for automatic operation recognition and finding motifs. Note: sorting the histograms in decreasing order of occurrences will yield a classical frequency dictionary.

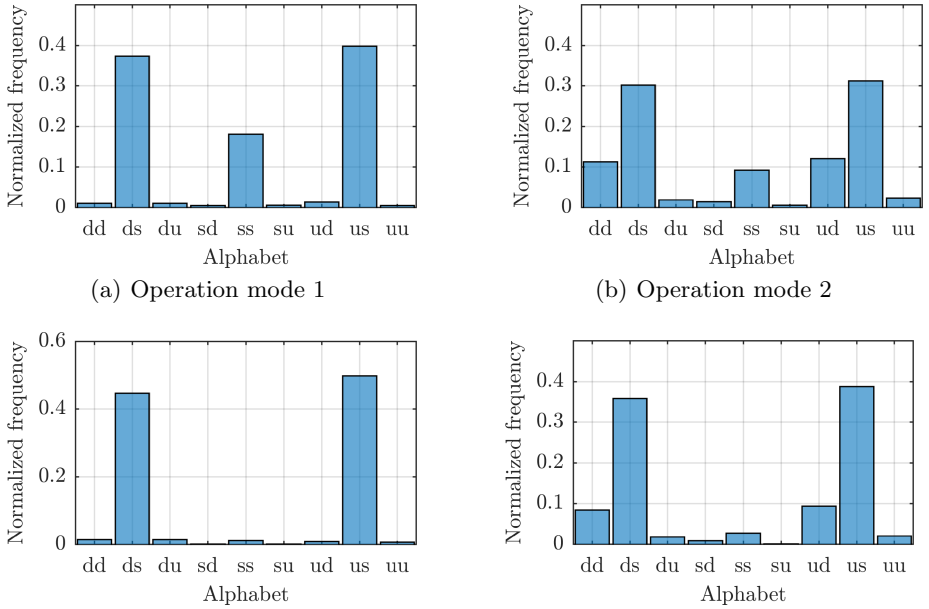

Fig. 5. Histograms of occurring symbol combinations of a machine in two different operation modes. Top: Histograms for the entire time range shown in Fig 3 (top) and Fig 4 (top); Bottom: Histograms for the signal snippets presented in Fig 3 (bottom) and Fig 4 (bottom).

A big advantage of the presented symbolic time series analysis is, that he sequence of symbols - either single or multi channel - can now be addressed with techniques more common to computational linguistics (e.g. *regex*) [13], which is a growing field of research.

3 Conclusion

Successful data analytics in large physical systems must embed the modelling of the individual component and complete system dynamics. This has been addressed by providing for a linear differential operator or its inverse in each and every signal- or derived-data-channel. A multi-variate symbolic time series analysis has

been introduced. It permits a symbolic view of the system and its dynamics. The concept of frequency dictionaries has been applied to automatic operation recognition; this functions for operation types which are characterised by a specific distribution of symbols. A major advantage of the proposed method is its intrinsic multi-scale property. This enables the identification of very short events in very large data sets. Currently, we are performing research on the relationships between the sequences of symbols and the metaphor of language. Initial results indicate that this opens the door to take advantage of new methods emerging in computational linguistics.

References

1. Baheti, R., Gill, H.: Cyber-physical systems. The Impact of Control Technology (2011) 161–166
2. Lanczos, C.: Linear differential operators. SIAM (1961)
3. O'Leary, P., Harker, M., Gugg, C.: An inverse problem approach to approximating sensor data in cyber physical systems. In: 2015 IEEE International Instrumentation and Measurement Technology Conference (I2MTC) Proceedings. Volume 2015-July., IEEE (may 2015) 1717–1722
4. Gugg, C., Harker, M., O'Leary, P., Rath, G.: An Algebraic Framework for the Real-Time Solution of Inverse Problems on Embedded Systems. In: 2015 IEEE 17th International Conference on High Performance Computing and Communications, 2015 IEEE 7th International Symposium on Cyberspace Safety and Security, and 2015 IEEE 12th International Conference on Embedded Software and Systems. Volume V., IEEE (aug 2015) 1097–1102
5. Harker, M., O'Leary, P.: Discrete Orthogonal Polynomial Toolbox - Matlab File Exchange
6. Gugg, C.: An Algebraic Framework for the Solution of Inverse Problems in Cyber-Physical Systems. Phd thesis, Montanuniversitaet Leoben (2015)
7. O'Leary, P., Harker, M.: An algebraic framework for discrete basis functions in computer vision. In: Proceedings - 6th Indian Conference on Computer Vision, Graphics and Image Processing, ICVGIP 2008, IEEE (dec 2008) 150–157
8. Lin, J., Keogh, E., Wei, L., Lonardi, S.: Experiencing SAX: a novel symbolic representation of time series. Data Mining and Knowledge Discovery **15**(2) (aug 2007) 107–144
9. Veenman, C., Reinders, M., Backer, E.: A maximum variance cluster algorithm. IEEE Transactions on Pattern Analysis and Machine Intelligence **24**(9) (sep 2002) 1273–1280
10. Chau, T., Wong, A.: Pattern discovery by residual analysis and recursive partitioning. IEEE Transactions on Knowledge and Data Engineering **11**(6) (1999) 833–852
11. Keogh, E., Lonardi, S., Chiu, B.Y.c.: Finding surprising patterns in a time series database in linear time and space. In: Proceedings of the eighth ACM SIGKDD international conference on Knowledge discovery and data mining - KDD '02, New York, New York, USA, ACM Press (2002) 550
12. Daw, C.S., Finney, C.E.A., Tracy, E.R.: A review of symbolic analysis of experimental data. Review of Scientific Instruments **74**(2) (feb 2003) 915–930
13. Clark, A., Fox, C., Lappin, S.: The Handbook of Computational Linguistics and Natural Language Processing. Volume XXXIII. Wiley-Blackwell (2010)

A Non-stationary Index-flood Model With Local Likelihood Smoothing for Drought Assessment

Filip Strnad, Martin Hanel, Vojtěch Moravec, and Adam Vizina

Faculty of Environmental Sciences, Czech University of Life Sciences, Kamýcká 129, 165 00 Prague, Czech Republic

strnadf@fzp.czu.cz
hanel@fzp.czu.cz
https://www.fzp.czu.cz/en/

Abstract. In this study we evaluate the changes in hydrological drought characteristics for 133 catchments in the Czech Republic over the period 1901-2015. The drought is characterized by deficit volumes, i.e. the volume of runoff continuously bellow a threshold (20th quantile of monthly runoff distribution). It is assumed that the series of annual maximum deficit volumes follow the Generalized extreme value (GEV) distribution. It is further assumed that the distribution of the deficit volumes over a homogeneous region is identical after scaling with a site-specific factor. The model allows for smooth trend in the parameters of the GEV distribution (which are constant over the region). For the smooth variation, the linear trend is fitted in a moving window of neighboring years. Three homogeneous regions representing areas with low, medium and high risk of drought were identified in the Czech Republic. The models with trend in the GEV location parameter performed better than models allowing also for the trend in the GEV scale parameter or the stationary model.

Keywords: drought; deficit volumes; extremes; index-flood model; local likelihood smoothing

1 Introduction

Despite relatively frequent flooding in the Czech Republic in recent decades, drought assessment is receiving more and more public attention. This is partly due to several very dry years (e.g. 2000, 2003 and 2015) with large financial losses (the estimate for 2000 is more than 400 million EUR). This is also reflected in published studies on possible changes in drought characteristics in the area [10, 2] or over Europe [11, 4].

Estimation of the drought characteristics and regionalization of its occurrence is subjected to considerable uncertainty. This uncertainty, in contrast to the extreme rainfall analysis, is strengthened by the fact that drought does not occur every year and more significant droughts occur only in a small fraction of

years. In this study, two strategies are therefore used to reduce the uncertainty of drought estimates.

The first is the use of long time series of precipitation and temperature (1901-2015), which are available in a monthly time step and a spatial resolution of 0.5. These series are corrected for systematic errors and serve as inputs to the BILAN hydrological model [3]. The second strategy is based on the use of regional frequency analysis - the index-flood method [9]. This method assumes that the distribution of scaled extremes (e.g. maximum annual deficit volumes) is the same for all catchments in homogeneous regions. By combining data from different catchments, some uncertainties can be reduced.

Hanel et al. (2009)[5] applied a parametric model to allow for temporal variation in parameters of the regional distribution. The parametric model can, however, be too restrictive (or the proper form of the trend unknown). Ramesh and Davison (2002) [12] describe an extreme value model allowing smooth variation in the parameters of distribution. Their model is nevertheless applied to a single site. The aim of this study is to analyze changes in deficit volumes with an index-flood model allowing for smooth variation in the parameters of regional distribution.

2 Methods and Materials

2.1 Data & Study Area

For the purposes of this study simulated runoff for the period 1901-2015 for 133 catchments in the Czech Republic was used. Sets of parameters for these catchments were derived using conceptual hydrological model BILAN [15] which is widely used in the Czech Republic for regular evaluation of water balance and also for assessment of climate change impacts.

The input data of the model (time series of basin precipitation, temperature and potential evapotranspiration) are based on a combination of HadCRUTS3.21 [6], and gridded observed precipitation and temperature data [14]. Gridded data were fitted to a catchment area using a weighted average (according to the size of the intersection between the river basin and the respective grid boxes). The model was calibrated with focus on the reproduction of drought characteristics.

The deficit volumes were derived with the threshold level method (Hisdal et al., 2004): the drought starts when the discharge drops under predefined threshold and continues until the threshold is exceeded again. In present study the threshold was set to the 80% quantile from the flow exceedance curve.

Observed and simulated deficit volumes were validated by comparing event severity, intensity and length in the period of overlap between observed and simulated data for 53 corresponding catchments. Validation showed that the simulated deficit volumes correspond well to those based on observed data as shown in Fig. 1.

The first step in regional frequency analysis is the identification of regions that can be considered homogeneous. The K-means algorithm [7] was used to find

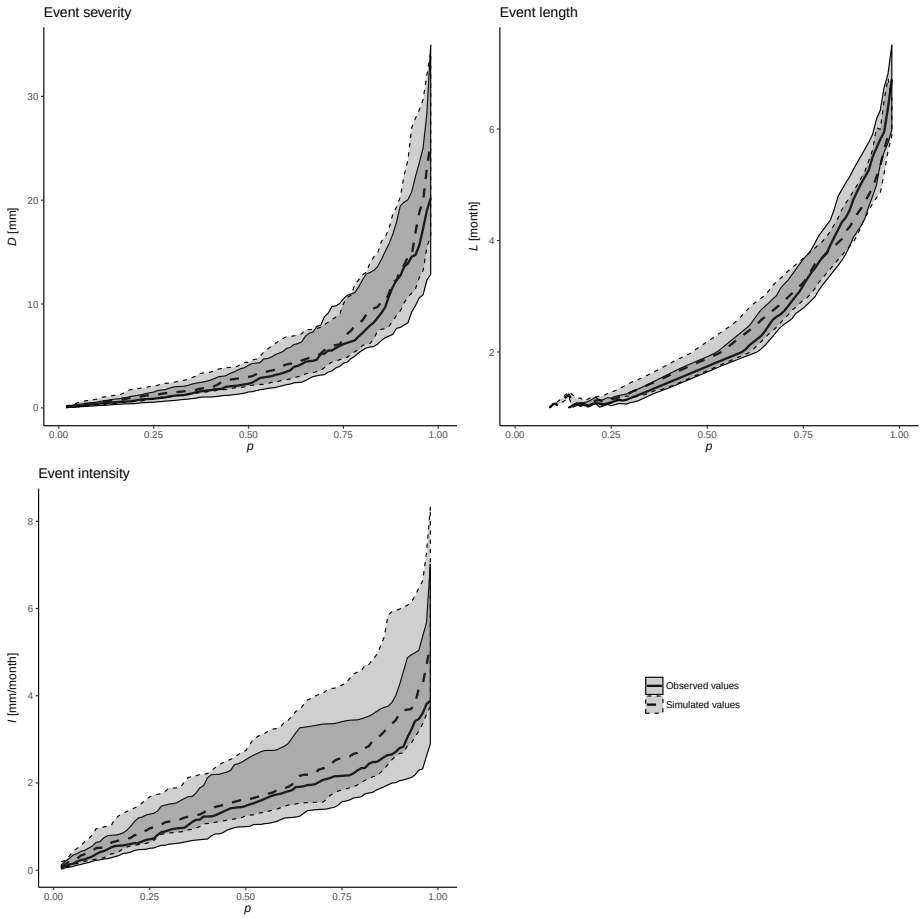

Fig. 1. Comparison of drought characteristics of observed and simulated runoff. On the x axis is the distribution function of the individual characteristics, the y axis shows values of drought characteristics, the polygons correspond to ranges between 1st and 3rd quartile.

clusters of homogeneous regions in the dataset. The K-means algorithm ran with mean runoff and mean potential evapotranspiration for each catchment as inputs, the outputs were three clusters of catchments. The resulting regionalization is shown in Fig. 2. Cluster 1 represents the catchments at high elevations and lot of precipitation. Low land dry catchments with limited precipitation form Cluster 3. The Cluster 2 is a transition between the low drought risk Cluster 1 and high drought risk Cluster 3.

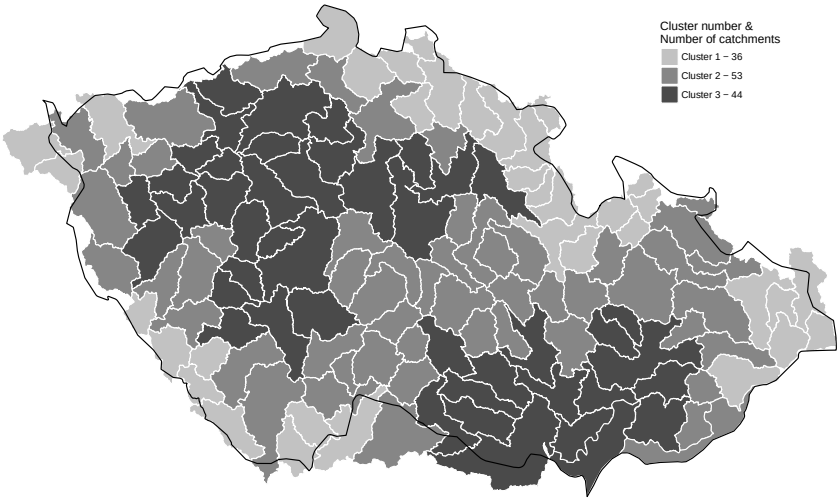

Fig. 2. Resulting regionalization of 133 catchments within Czech Republic.

2.2 Statistical Model

To summarize the changes and differences in the characteristics of the deficit volumes, a statistical model for the annual maximum deficit volume was applied. Note that after extracting the annual maximum deficit volume (note that usually not all the years experienced drought), values were log-transformed in order to be consistent with the GEV distribution.

Following Stedinger et al. (1993) [13] we consider the model with a probability mass concentrated in zero

$$F^*(x) = \begin{cases} p_0 & \text{if} \quad x = 0 \\ p_0 + (1 - p_0)F(x) & \text{if} \quad x > 0 \,. \end{cases} \tag{1}$$

where p_0 is the probability of year without drought. We estimate p_0 as the proportion of zero drought years [1]. Further we describe the model for the distribution of non-zero deficit volumes, $F(x)$.

The at-site annual or seasonal maxima of hydrometeorological variables are often described by the GEV distribution. The three parameters of this distribution, the location (ξ), scale (α) and shape (κ) parameters, control the location, variability and behavior of the tail of the distribution. The parameters can be assumed stationary or can vary in time, e.g. due to climate variability/change. To increase the confidence of the estimates of parameters and quantiles of the GEV distribution, it is often assumed that the maxima over a homogeneous area are identically distributed after scaling with a site-specific factor (both the scaling factor and the method are usually referred to as the index-flood). Hanel et al. (2009) [5] showed that it is convenient to scale the at-site maxima with a GEV location parameter. The quantile function $Q(s,t)$ for each site s and year t is then obtained by upscaling the common regional quantile function (the growth curve) $q(t)$ by the at-site location parameter $\xi(s,t)$, i.e. $Q(s,t) = \xi(s,t)q(t)$.

The parameters can be estimated by maximizing the composite log likelihood

$$L = \sum_{st} l[\theta(s,t); X(s,t)] \; . \tag{2}$$

with $l[\theta(s,t); X(s,t)]$ the log likelihood for seasonal maxima $X(s,t)$ in year t at site s considering the parameters $\theta(s,t) = [\xi(s,t), \gamma, \kappa]$. Hanel et al. (2009) [5] proposed a parametric model relating the GEV parameters to an index of the enhanced greenhouse effect (e.g. temperature, radiative forcing etc.). An alternative that can be used when less prior knowledge on the temporal variation of the GEV parameters is available or in the case when it is difficult to find an appropriate parametric model, is local likelihood smoothing, i.e. assuming that (some of) the GEV parameters vary smoothly in time.

In our study, we assume that the dispersion coefficient and the shape parameter of the GEV model are constant over the area, while the location parameter varies over the area and in time. The location parameter at site s in year t can be described as

$$\xi(s,t) = \xi_0(s)\xi_1(t) \; . \tag{3}$$

with $\xi_1(t)$ estimated as an intercept of a local regression

$$\xi_1(t_j) = \beta_0 + (t_j - t)\beta_1 \; . \tag{4}$$

on a neighborhood of t with $t_j \in (t - dh, t + dh); d$ corresponding to the range of years (i.e. $d = max(t_j) - min(t_j)$) and $h \in (0, 1)$ the bandwidth controlling the amount of smoothing [12]. Please note, that higher-degree polynomials or a constant could be used as a local model for ξ_1.

To estimate the parameters of the GEV model an iterative procedure consisting of three steps was used:

1. the at-site scaling factors $\xi_0(s)$ are estimated for each site s (holding the other parameters fixed on their estimates) by maximizing the log likelihood $\sum_{st} l[\xi_0(s), \widehat{\xi}_1(t), \widehat{\gamma}, \widehat{\kappa}; X(s,t)]$

2. the parameters of the regional growth curve (γ, κ) are estimated similarly by maximizing $\sum_{st} l[\widehat{\xi}_0(s), \widehat{\xi}_1(t), \gamma, \kappa; X(s,t)]$
3. the parameters β_0 and β_1 needed for $\xi_1(t)$ are estimated for each year t by maximizing the local log likelihood $\sum_{js} w_j(t) l[\widehat{\xi}_0(s), \beta_0 + (t_j - t)\beta_1, \widehat{\gamma}, \widehat{\kappa}; X(s,t)]$ with $w_j(t)l(s,t)$ the local log likelihood for station s and neighborhood of t and $w_t(j)$ the kernel function. In our study the Epanechnikov kernel $w(u) = max(1 - u^2, 0)$ is used, and $w_j(t) = w[(t_j - t)/(dh)]$.

The procedure is repeated until the change in composite log likelihood is small. In our case usually only 2-3 iterations were necessary. The parameters are initialized on their L-moments estimates with $\xi_1(t) = 1$. To our experience, the order of the steps does not matter. The bandwidth was chosen subjectively for the purpose of this study.

2.3 Uncertainty and Model Assessment

Using the estimated parameters $\widehat{\theta}(s,t)$ the seasonal maxima $X(s,t)$ transformed according to

$$\widetilde{X}(s.t) = \frac{1}{\widehat{\kappa}} \log \left\{ 1 + \frac{\widehat{\kappa}}{\widehat{\gamma}} \left[\frac{X(s,t)}{\widehat{\xi}(s,t)} - 1 \right] \right\} . \tag{5}$$

should have standard Gumbel distribution if the model is correct. This can be directly checked by the quantile-quantile plots. Further model checking including goodness-of-fit testing considering the Anderson-Darling statistics is possible [5], however, tools for sampling from the null distribution are required to evaluate the critical values of the test. The sampling is not trivial in the case of dependence and presence of zero-drought years. Therefore we limit ourselves to the quantile-quantile plots in the present paper.

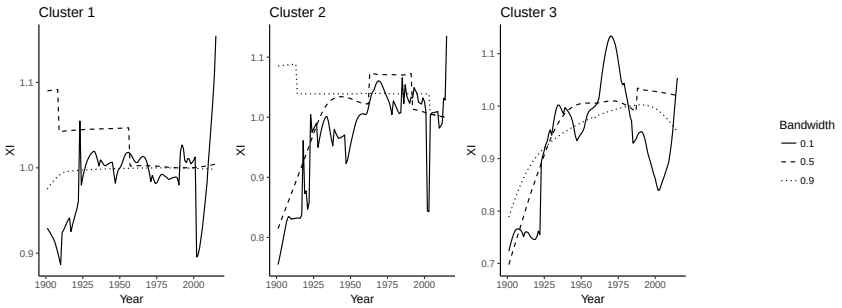

Fig. 3. Estimated trends in the location parameter for all clusters of catchments with three different bandwidths (0.1, 0.5, 0.9).

3 Results and Discussion

Non-stationary models were constructed for each cluster considering bandwidths ranging from 0.1 to 0.9. The estimated trend in the location parameter ξ is shown in Fig. 3. For Cluster 1 (highly elevated catchments) the drought regime is rather stable. Only when small bandwidths are considered the extreme drought event in 2015 is indicated. For other clusters the variability in the location parameter is more pronounced suggesting higher drought risk. The location parameter is in general larger in the second half of the series, for Cluster 3 with bandwidth 0.1 there is an indication of drought period in the beginning of 1970's.

Estimates of the at-site location parameters $\xi_0(s)$ (varying over space) for different bandwidths can be seen in Fig. 4, estimated values of the parameters γ and κ which are constant both in time and space for different bandwidths can be seen in Table 1. Except Cluster 3 the values of $\xi_0(s)$ do not depend considerably on bandwidth. In Cluster 3 the $\xi_0(s)$ is about 30% larger when 0.5 bandwidth is applied than for small or large bandwidths. The large value of $\xi_0(s)$ is compensated by small value of γ for bandwidth 0.5 ($\gamma = 3.1$) when compared to 0.1 and 0.9 bandwidths ($\gamma \sim 3.8$), see Table 1.

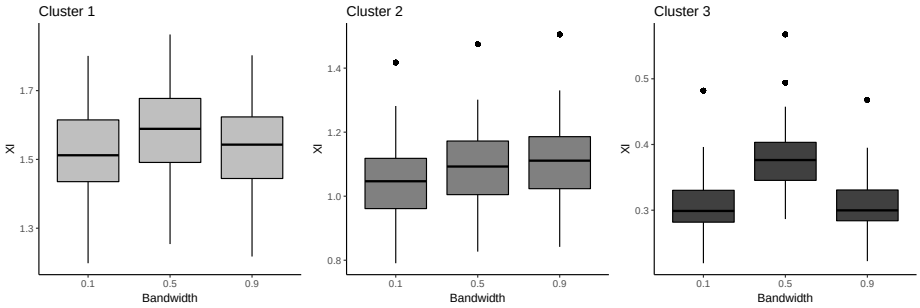

Fig. 4. Estimated at-site $\xi_0(s)$ parameters for all models.

Table 1. Estimated regional parameters for all models.

γ parameter			
Bandwidth	0.1	0.5	0.9
Cluster 1:	0.80	0.80	0.80
Cluster 2:	1.15	1.09	1.16
Cluster 3:	3.76	3.10	3.83

κ parameter			
Bandwidth	0.1	0.5	0.9
Cluster 1:	-0.41	-0.43	-0.42
Cluster 2:	-0.39	-0.39	-0.38
Cluster 3:	-0.30	-0.29	-0.29

The goodness-of-fit was assessed visually with Gumbel plots showing the regional quantile function together with scaled at-site quantile functions (Fig. 5). In general the model seems to be appropriate for the distribution of the deficit

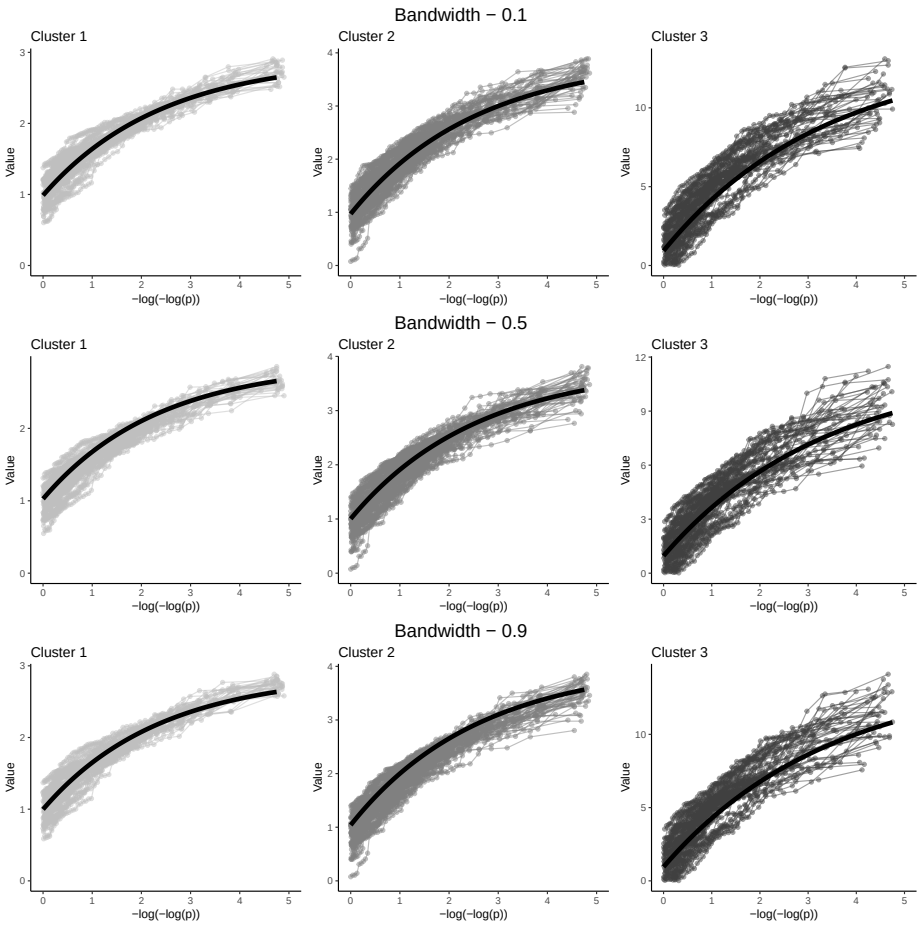

Fig. 5. Regional quantile functions (black line) and scaled quantile functions for all catchments i.e. Gumbel plots for all models. The x axis shows transformed probabilities, the y axis values of deficit volumes.

volumes in the considered catchments. Some deficiencies, however, are present when too small or too large bandwidths are considered. The shape of the regional curve suggest the reverse Weibull distribution with upper limit. This seems to be reasonable since the maximum annual volume below the 20th percentile of monthly runoff is limited.

Fig. 6 shows the quantile-quantile plots for the Gumbel residuals (eq. 5). Again, overall the fit is plausible, but some indication of bias is present for some clusters and bandwidths.

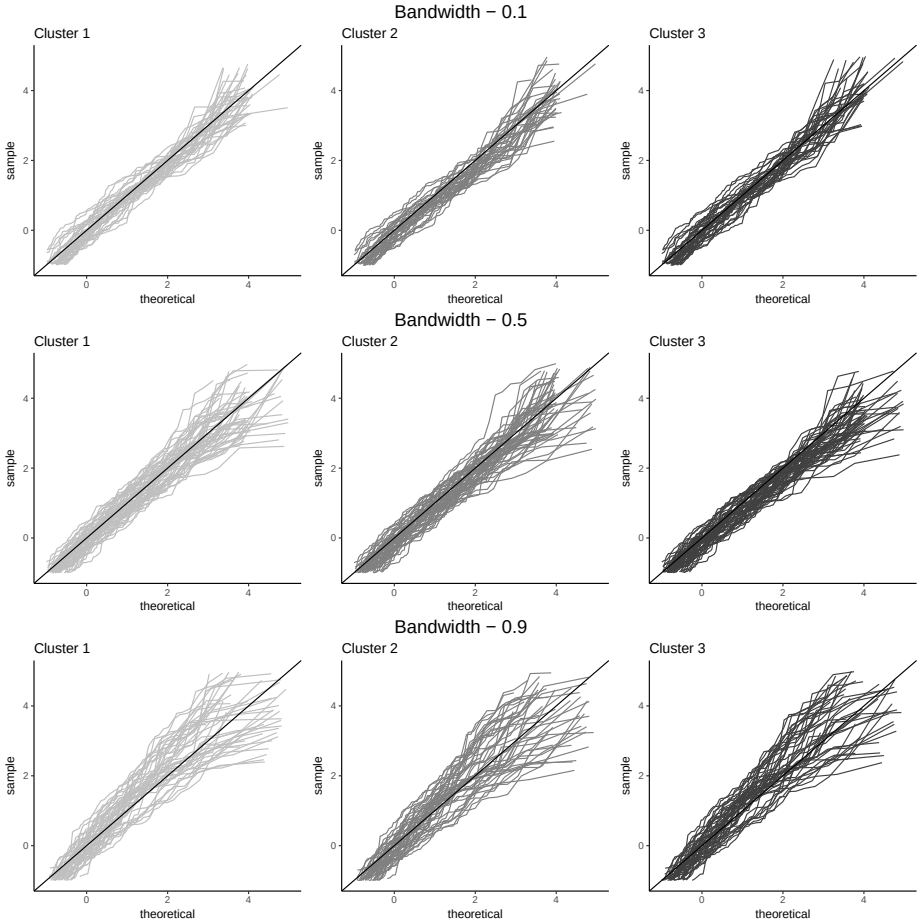

Fig. 6. Quantile-quantile plots for all models, where sample values are quantiles of Gumbel residuals and theoretical values are quantiles of the standard GEV distribution.

4 Conclusions

A regional index-flood model allowing for smooth variation in the parameters of the GEV model was developed and applied to the annual maximum deficit volumes calculated for 133 catchments in the Czech Republic for the period of 1901-2015. It was assumed, that the dispersion coefficient and the shape parameter are constant in time and also over the area, while the location parameter was allowed to vary in time (and over the area).

It was shown that the model provides insight to the temporal evolution and spatial variability of drought characteristics. The main topics for future research include:

- modification of the standard methods used for assessing homogeneity of the regions to the context of our statistical model
- modification of the standard bootstrap procedures to preserve spatial dependence and to allow for zero-drought years
- application of the goodness-of-fit testing methods and when needed revising the regional distribution
- development of objective methods such as cross validation or Akaike information criterion for bandwidth selection

Acknowledgments. The study was supported by the Czech Science Foundation (grant no. 16-16549S) and the Internal Grant Agency of The Faculty of Environmental Sciences (grant no. 20164230).

References

1. Engeland, K., Hisdal, H., Frigessi, A., 2004. Practical extreme valu modelling of hydrological floods and droughts: A case study. Extremes 7, 5-30.
2. Hanel, M., Kašpárek, L., Peláková, M., Beran, A. and Vizina, A., 2013. Evaluation of changes in deficit volumes: support for protection of localities suitable for construction of reservoirs. Considering hydrological change in reservoir planning and management. IAHS Publ, 362, pp.187-192.
3. Hanel, M., Mrkvičková, M., Máca, P., Vizina, A., Pech, P., 2013. Evaluation of simple statistical downscaling methods for monthly regional climate model simulations with respect to the estimated changes in runoff in the Czech Republic. Water Resources Management, 27(15), 5261-5279.
4. Hanel, M., Rakovec, O., Markonis, Y., Máca, P., Samaniego, L., Kumar, R. (2017) Revisiting the recent European droughts in a long-term perspective. submitted.
5. Hanel, M., Buishand, T.A. and Ferro, C.A., 2009. A nonstationary index flood model for precipitation extremes in transient regional climate model simulations. Journal of Geophysical Research: Atmospheres, 114(D15).
6. Harris, I.P.D.J., Jones, P.D., Osborn, T.J. and Lister, D.H., 2014. Updated highresolution grids of monthly climatic observationsthe CRU TS3. 10 Dataset. International Journal of Climatology, 34(3), pp.623-642.
7. Hartigan, J.A. and Wong, M.A., 1979. Algorithm AS 136: A k-means clustering algorithm. Journal of the Royal Statistical Society. Series C (Applied Statistics), 28(1), pp.100-108.

8. Hisdal, H., Tallaksen, L.M., Clausen, B., Peters, E., Gustard, A., 2004. Hydrological Drought Characteristics. In: Tallaksen, L.M., van Lanen, H.A.J. (Eds.), Hydrological Drought Processes and Estimation Methods for Streamflow and Groundwater. Elsevier Science B.V, Developments in Water Science, 48, 139-198.
9. Hosking, J.R.M. and Wallis, J.R., 2005. Regional frequency analysis: an approach based on L-moments. Cambridge University Press.
10. Kašpárek, L., Novický, O. and Peláková, M., 2006. Climate change and water regime in the Czech Republic. TG Masaryk Water Research Institute.
11. Van Lanen, H.A., Laaha, G., Kingston, D.G., Gauster, T., Ionita, M., Vidal, J.P., Vlnas, R., Tallaksen, L.M., Stahl, K., Hannaford, J. and Delus, C., 2016. Hydrology needed to manage droughts: the 2015 European case. Hydrological Processes, 30(17), pp.3097-3104.
12. Ramesh, N.I. and Davison, A.C., 2002. Local models for exploratory analysis of hydrological extremes. Journal of Hydrology, 256(1), pp.106-119.
13. Stedinger, J.R., Vogel, R.M., Foufoula-Georgiou, E., 1993. Frequency Analysis of Extreme Events in Handbook of Hydrology (D.R. Maidment, ed), McGraw-Hill, New York.
14. Stepanek, P., Zahradnicek, P. and Huth, R., 2011. Interpolation techniques used for data quality control and calculation of technical series: an example of a Central European daily time series. Idojaras, 115(1-2), pp.87-98.
15. Tallaksen, L.M. and Van Lanen, H.A., 2004. Hydrological drought: processes and estimation methods for streamflow and groundwater (Vol. 48). Elsevier.

Forecasting of Demand on Raw for Dairy Products

Marina Arkhipova [1[0000-0002-9022-7385]], Viacheslav Sirotin [1[0000-0001-7783-8790]] and Kirill Arkhipov [2]

[1] National Research University Higher School of Economics, Miasnitskaya 20, 101000 Moscow, Russia
[2] Plekhanov Russian University of Economics, Stremyanny lane 36, 117997, Moscow, Russia
vsirotin@hse.ru arhipov.kirill@gmail.com

Abstract. In this paper we analyze problems of predicting the stock of raw materials for dairy products manufacturing. The specific of the industrial process is that plant has low stock of raw and pack materials because of their usually short life time. From one hand, we should avoid the stock excess of raw materials and from the other hand it should be sufficient to prevent the stoppage of the production process. We analyzed the risk factors of the out of stock cases and included them in the forecasting model. A key role in this model belongs to the accuracy of the sales forecast of finished products and we use a set of time series models to ensure the required accuracy. We show that the best choice is the composite model which for each time period takes into account the forecast obtained by each of the available models with a certain weight depending on the accuracy of their forecast at the previous step. Identification of this model is based on time-series data on real sales.

Keywords: Sales Forecasting, Prediction Accuracy, Composite Model.

1 Introduction

Among the problems that have influence on the size of R&P stock, special attention is paid to the accuracy of sales forecast. The accuracy of the sales forecast is very important for stock management and many researchers pay attention to the methods and models that help to improve the forecast accuracy. Concerning new products forecasting we can use the results of the comprehensive review [1]. Special attention is paid to the models used to provide high quality information about future sales. There are many other papers on the forecast quality improvement like [2] where the author uses exponentially weighted quantile regression for forecasting daily sales and [3] where authors concentrate their attention on evaluation of computational intelligence techniques to solve the similar problem. But future sales in the process of industrial production are highly important but not the only aspect of planning. The particular industry feature also does matter.

Specific of the food industry is taken into account in [4] where the dynamics and simulation of a particular food supply chain are considered. Closer to the topic of the research are the papers with the emphasis on the problems of dairy products [5] where

short shelf-life food products are forecasting based on artificial neural networks, and [6] where a multistage stochastic programming model for the New Zealand dairy industry is proposed.

Focus of the research is the improvement of the product planning. All the models present the objective approach to forecasting while the alternative is an expert evaluation. So the results of using the proposed model, from one hand, should be compared with the results that are given by its competitors and, from the other hand, with the results given by experts.

2 The dynamics and peculiarities of dairy production

Improving the accuracy of predictive models of sales of finished dairy products requires an integrated analysis of statistical regularities and the factors affecting the dynamics of the time series.

Trend-seasonal, adaptive and ARIMA models are widely used for sales forecasting [7]. However, forecasting of dairy products sales using basic statistical prediction models can provide low prediction accuracy. Mean relative error for different Danone Russia products is between 18% and 34%, and the forecast bias is about 8%. This is because a basic trend-seasonal model does not take into account the impact of all factors on the time series. For production enterprises operating on the dairy market, where products have a low shelf life, the inaccuracy of the forecast causes the loss of sales or shortage in the market, loss of profit, fines and loss of customer loyalty [8].

To improve forecast accuracy, the following factors should be considered and their influence on time series should be included in the forecasting model [9, 11, 12, 15]:

• the baseline reflects the level of sales to 1% of weighted distribution when fixing the influence of all other factors;

• trend characterizes the long-term tendency of dairy products popularity (as part of a healthy lifestyle) when forecasting sales for aggregated categories (e.g., curd desserts). With respect to predicting a specific dairy product the trend characterizes the product life cycle, which usually is about 2-4 years for dairy product;

• seasonal effect takes into account retrospective data of the sales dynamic under the influence of regularly recurring events. For dairy products the most pronounced is the growth of sales of drinking yoghurt and kefir during the summer period, functional drinks with vitamins (Actimel) in winter, and increased consumption of classical categories (butter, cheese, sour cream) in a pancake week;

• planned promotions and marketing activities have a significant impact on sales dynamics. This group includes TV and Internet advertising, presents for purchasing (e.g. promo codes) and other marketing innovations to support sales and build brand awareness;

• trade marketing activities in the sales channels associated with the planned stock in retailers, like price reductions or red price tags;

• Prices change. Every year for dairy products prices change, which has a significant influence on the level of sales. The period of influence of this factor is restricted to a short period, knowing about upcoming changes, the retailers cannot make a large

supply of products with low shelf life. But it causes an increase in sales in the week before the price increase and decline in the week after;

• the facts of customers service level reducing in the past (for example, due to problems in the production, failures in the distribution system of the product or during transportation);

• other factors;

• the uncertainty of the market, including activities of the competitors.

Visual analysis of the dynamics of the sales of cheese desserts Danissimo (see Fig. 1) shows that there is a fairly steady upward trend of sales, but there is a period of rapid growth (2013 – 2015) and emerging with 2016 the effect of market saturation and a slowdown in sales growth of the category “curd desserts”.

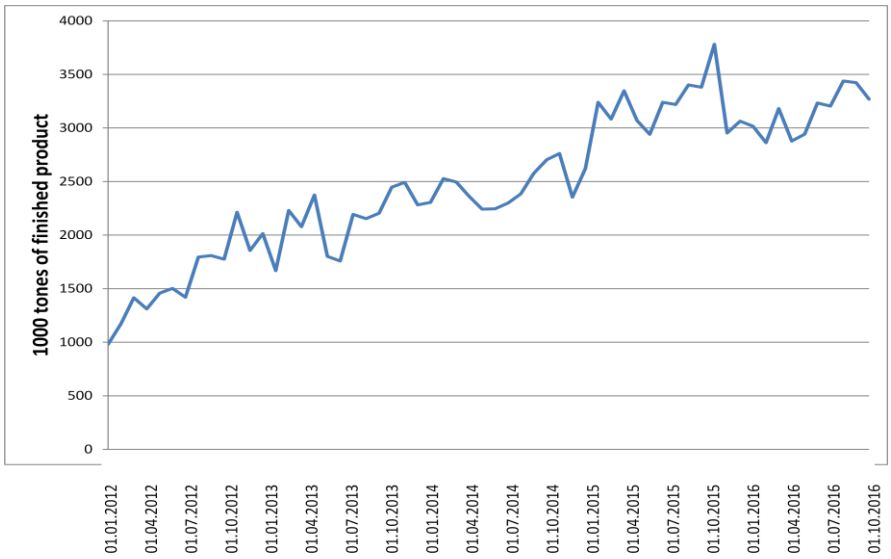

Fig. 1. Sales dynamics of desserts cheese "Danissimo" in 2013 – 2017 (tons of products).

At the first stage of the study a retrospective level of cheese desserts Danissimo sales was adjusted for the customers service level (CSL). Every company has a target (average) CSL which the company can provide with the current operational efficiency – delays in transportation, finished products blockage, etc [20]. For Danone Russia, this value is 95%, so, if in any of the time periods the values of the CSL was below target, that indicates problems in supply chain (failure on the production line, rejection of products, service quality, lack of ingredients or packaging or transport problems, etc.). These issues are not included in the forecast model, as they cannot be foreseen in advance [19], so the absolute value of the shipments was adjusted upward by the amount of sales drop during periods of CSL decrease (see Fig. 2).

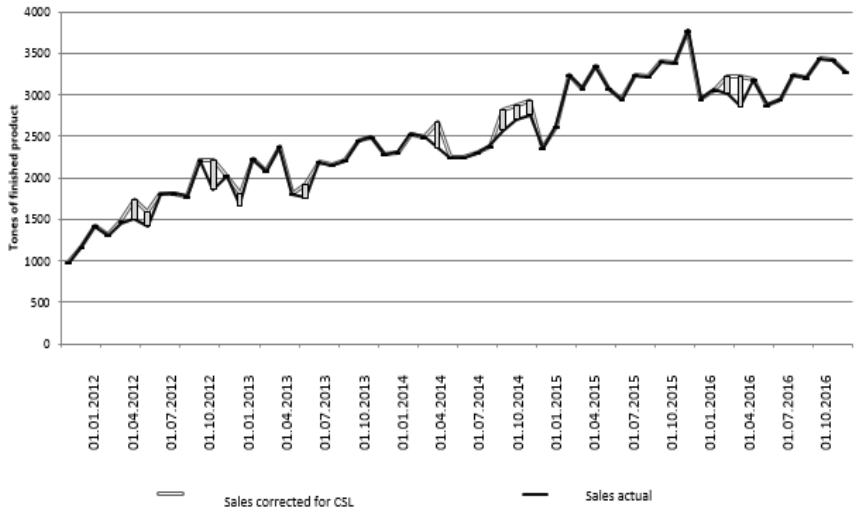

Fig. 2. Correction of the sales level of cheese "Danissimo" in periods of low CSL.

One of the main factors influencing the amount of sales is the weighted percentage of distribution [13, 14]. Its changes can lead to volatility of the aggregate amount of products sales level. Predictive model in the research was built iteratively. At the first stage weighted distribution (WD) was estimated for curd dessert Danissimo. It reflects the volume-weighted sales percentage of retailers where the analyzed product is sold:

$$WD = \frac{\sum_{i=1}^{n} Sales_i}{\sum_{j=1}^{m} Sales_j},$$

where n is the number of retailers where the analyzed product is on shelve;

m is the total number of retailers, which sell products of the analyzed category (dairy food).

Then, for each time period in the past, retrospective data was obtained for the actual values of weighted distribution (WD). The absolute level of sales was recalculated from absolute volume to sales on 1% of WD. So, the retrospective sales data was eliminated by the impact of fluctuations in weighed distribution.

On the next stage, we built a baseline that reflects the level of sales of the product on 1% WD, which would be in the market when excluding the influence of other factors. Analysis of the data shows that sales on 1% of the weighted distribution has not changed during the studied period from 2012 to 2016. Visual analysis of the dynamics shows that during the first two years of the analyzed period sales growth of curd dessert was mainly due to the growth of weighted distribution.

3 Time series models for dairy products

On the next step of the research the retrospective sales data was decomposed into factors: the effect of marketing, television and commercial support. The initial time series of sales of cheese desserts were cleaned from the influence of the factors considered, and the trend-seasonal and adaptive models were built, such as: trend-seasonal model with multiplicative seasonality, harmonic analysis, additive Theil-Wage model, the model with dummy variables. Autocorrelation and autoregressive dependence study in residuals was done for each model. Despite significant improvements in mean relative errors, the calculated forecasted values have still low accuracy, which is very important for stock management of products with low shelf life. For production company, models of safety stock for materials is extremely sensitive to the sales of finished product. If there is a deviation for a long time of actual sales from expected, it can lead to exhaustion of reserves and deficit. Thus, it is important that the forecasting model is able to respond quickly to the trends changes.

For further sales forecast accuracy improvement a combined model was created [7, 17]. In this model sales forecasting estimations obtained by different models are included with a certain weight for each time period depending on the accuracy of their forecast at step t-1. Table 1 gives a summary for comparison of models in terms of accuracy.

Table 1. Characteristics of the adequacy of the sales forecast models of cheese dessert.

Model	Characteristics			Forecast of sales of dairy products,		
Forecast model for trend and seasonality	Mean relative error	Mean absolute error	Average relative displacement	2017 Quarter No	Absolute increase, tons	Growth rate, %
Trend seasonal model with multiplicative seasonality	8,64	141,19	-3,64	1	940	10
				2	471	5
				3	127	1
				4	227	2
Harmonic analysis with AP(1) in residuals	8,77	157,78	2,07	1	1041	11
				2	473	5
				3	139	1
				4	226	2
Additive Theil-Wage model	7,57	136,94	2,70	1	1075	12
				2	478	5
				3	126	1
				4	267	3
Model with dummy variables with AP(1) in residuals	6,59	131,94	-3,59	1	478	5
				2	505	5
				3	216	2
				4	100	1
Combined model with AP(1) in residuals	5,32	126,7	1,83	1	1016	11
				2	461	5
				3	132	1
				4	243	2

The final sales forecast for curd dessert "Danissimo" was combined by the combined model with AR(1) in the residuals (shown in Fig. 3).

As shown in Table 1, all models predict sales growth of curd dessert in 2017, the most optimistic forecast obtained by the additive Theil-Wage model (+5,1%), the most pessimistic model with dummy variables (+3,5%). The highest growth rate of all models is expected for the first quarter (10-12%), with attenuation in the second quarter (5-6%). The rate of growth in the third and fourth quarters is expected to be 1-3%. A significant increase in the first and second quarters are expected mostly due to the influence of marketing and TV supports (according to the forecast, these two supports stimulate increase of sales by 6.8%). In III and IV quarters the commercial support leads to 1% increase with almost constant weighted percentage of distribution. Thus, if during the year, the product will not be supported, growth rate, depending on the model will be 98-103%.

The final sales forecast for curd dessert "Danissimo" was combined by the combined model with AR(1) in the residuals (shown in Fig. 3).

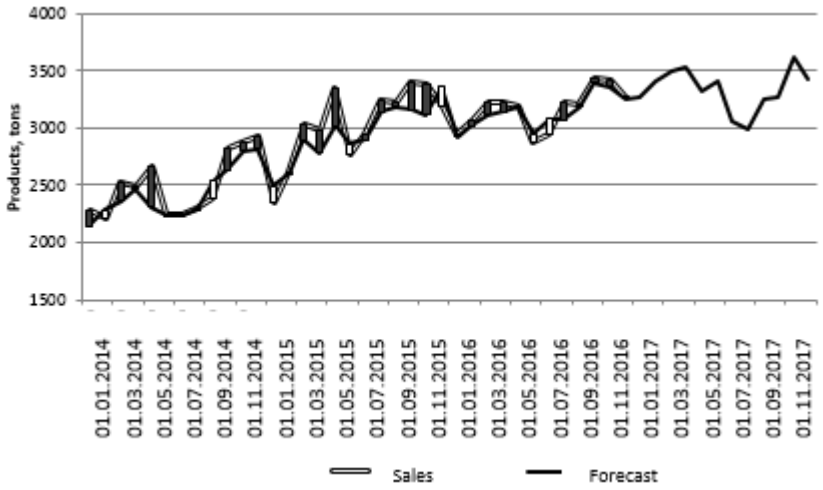

Fig. 3. Actual and forecasted sales volumes of cheese desserts obtained by a combined model for 2017.

After creating the combined model with AR(1) in the residues the correlation at all lags is not statistically significant, the proposal that the residuals follow normal distribution has not been rejected. Thus, the analysis of the characteristics of the combined model suggests that all of the statistically significant dependencies have been taken into account and the model can be used to estimate the sales forecast volumes of dairy finished products. It will improve the stock management and help to create the proper R&P stock policy.

4 Conclusion

Forecast that takes into account the influence of all factors on the dynamics of the market allows production companies to obtain a strong competitive advantage. In the long term horizon accurate products sales forecast allows to leverage investments in production capacity and to etimate an effective system of distribution of finished products. In Mid- and Short-term horizon, an accurate prediction can satisfy the entire market demand with the minimum casts and best customers service level. The combined model based on wide set of various initial models seems to be most promising in planning of dairy production.

5 Acknowledgement

This work was supported by a grant from the Russian Foundation for Humanities №16-02-00561a "Innovation activity in modern Russia: trends and impact on living standards"

References

1. Mas-Machuca, M., Sainz, M., Martinez-Costa, M.: A review of forecasting models for new products. Intangible Capital, 10(1), 1-15 (2014).
2. Taylor, J.: Forecasting daily supermarket sales using exponentially weighted quantile regression. European Journal of Operational Research 178(1), 154-167 (2007).
3. Žylius, G., Simutis, R., Vaitkus V.: Evaluation of computational intelligence techniques for daily product sales forecasting. International Journal of Computing 14(3), 157-164 (2015).
4. Minegishi, S., Thiel, D.: System dynamics modeling and simulation of a particular food supply chain. Simulation Practice and Theory 8(5), 321-339 (2000).
5. Doganis, P., Alexandridis, A., Patrinos, P., Sarimveis, H.: Time series sales forecasting for short shelf-life food products based on artificial neural networks and evolutionary computing. Journal of Food Engineering 75(2), 196-204 (2006).
6. Guan, Z., Philpott, A.B.: A multistage stochastic programming model for the New Zealand dairy industry. International Journal of Production Economics 134(2), 289-299 (2011).
7. Aivazian, S., Mkhitarian, V.: Applied statistics and essentials of econometrics. UNITY, Moscow (2011).
8. Anderson, D., Sweeney, D., Williams, T., Freeman, J., Shoesmith, E.: Statistics For Business and Economics. Cengage Learning EMEA, UK (2009).
9. Arkhipova, M., Akkhipov, K.: Supply process optimization using hubs for materials. In: 9th European Conference on Innovation and Entrepreneurship Proceeding, pp. 43-50. University of Ulster Business School and School of Social Enterprises, Belfast (2014).
10. Ballou, R.: Business Logistic Management, Prentice-Hall International, Inc. (1999).
11. Bowerman, B., O'Connell, R.: Forecasting and Time Series: An Applied Approach, 3rd ed. Brooks, Cole (2000).
12. Box, G., Reinsel, G., Jenkins, G. Time Series Analysis: Forecasting and Control, 3rd ed. Prentice Hall (1994).

13. Coyle,J., Bardi, E., Langley, J.: The management of business logistics. A supply chain perspective. South-Western devise of Thomson Harming (2003).
14. Langley, J., John, J.: Coyle Managing Supply Chains: a logistic approach. Engage Learning, Canada (2008).
15. Makridakis, S., Wheelwright, S., Hyndman, R.: Forecasting: Methods and Applications, 3rd ed. Wiley (1977).
16. Dybskaya, V.: Logistics for practitioners. Effective solutions in warehousing and material handling. UINITI, Moscow (2002).
17. Yiu-Kuen, T.: Nonlife actuarial models. Theory, Methods and Evaluation. Cambridge University press (2009).
18. Global supply chain nonprofit consulting organization Homepage, http:// www.supply-chain.org, last accessed 2017/03/12
19. Informational portal Conncil of Supply Chain Management Professionals Homepage, http:// www.cscmp.com, last accessed 2017/03/12.
20. National trade and marketing research agency Homepage, http:// www.marketcenter.ru, last accessed 2017/03/12.
21. StatSoft Homepage, http://www.statsoft.ru/home/textbook/default.htm, last accessed 2017/03/12.

Spark and Solr: a powerful and ergonomic combination for online search in the Big Data environment (case of the UAE)

K. AOULAD ABDELOUARIT[1,] B. SBIHI[2] and N. AKNIN[3]

[1, 2, 3] TIMS Research Unit, LIROSA Laboratory
Abdelmalek Essaadi University
Tetuan, Morocco
[1] abdelouarit.karim@gmail.com
[2] bsbihi@hotmail.com
[3] aknin_noura@yahoo.fr

Abstract. In this paper, we present a complete, powerful and ergonomic combination for an advanced online search solution in the Big Data environment that will be used by a learner in a context of remote learning or information search, and which will take as sample the students of the UAE (University of Abdelmalek Essaadi). With the aims to evaluate the reliability and the value of the returned information to identify opportunities to improve and organize the results of online search in order to successfully complete the learning process and allow easy consumption of information by the learner. The main challenges of such a solution are the storage and processing of massive and heterogeneous data generated by the Big Data phenomenon. Then, it is necessary to organize these data in order to make them easily exploitable and accessible by the user through the online search interface. It is in this context that we propose to implement a solution based on the combination of two platforms: The Spark system for storage and processing massive data and the Solr Framework for exploring and data searching.

Keywords: big data, online search, spark, solr.

1 Introduction

Nowadays, the potential growth of the amounts of data on the Internet has made it difficult to obtain relevant information by the user and especially for the learner in a context of remote learning or information search. Existing data search algorithms are no longer able to function efficiently because of the huge size of the data to be processed [6]. Although current search engines have been able to develop highly qualified skills and capabilities, the results of data generated are often based on automated algorithms whose suggested queries are often out of context and based on popular search rather than the specific needs for researchers [11]. Thus, the Web pages generated currently by search engines are based on terms requiring sophisticated algorithms and capable of managing a large number of queries in order to generate more relevant results [7].

This paper follows on from our previous work on the study of a complete solution for the processing of massive and heterogeneous data returned by online search engines [7]. It is proposed to develop a methodology based on a tool called “Big-Learn” to integrate multiple type of massive data in one data layer to facilitate access and more optimal relevance search with adequate and consistent results according to the expectations of the learner that uses the online search [13]. Thus, we present the formula of the chosen solution, which consists in using the Spark technology to store and process massive data generated from the Big Data layer. Then, these data are indexed using the Lucene engine. At the end, these indexed data can be easily accessed though a flexible search interface using the Solr Framework [12].

The following paragraph presents the state of the art of using the Spark and Solr systems in the online research process employed by the UAE student (Abdelmalek Essaadi University) in the Big Data environment. Thus, we describe the technique used by Apache Spark to process massive and unstructured data. Next, we expose the mechanism offered by Solr Framework for exploring and data searching; Section 3 presents the technical and application architecture of the solution adopted and its integration with our Big-Learn system [13]. This solution is based on Spark technology and the use of the Solr Framework for the exploration and information search in the Big Data environment. The last paragraph presents a general conclusion outlining a series of perspectives.

2 State of the art

2.1 The Use of Apache Spark to processes massive and unstructured data

Apache Spark is actually the most popular and widely used system for mass data processing [2]. With its Resilient Distributed Dataset (RDD) system, Spark can capture a wide range of processing loads, that previously required separate engines, including SQL, streaming, Machine Learning and graphics processing. The RDDs serve as high-level programming interfaces and also allow transparent management of fault tolerance [2].

Spark's story begins in 2009, when the AMP Lab group at California's Berkeley University began the Spark project to create a unified engine for distributed data processing. Subsequently, this project became open source under the guidance of Apache in 2010 [3]. Spark has been developed for speed of processing and ease of use, it is designed to allow sophisticated analyzes with faster speed, it exceeds Hadoop in the fast processing of massive data, and also in the analysis in real time. It is based on a programming model similar to Hadoop MapReduce but extends to a data sharing abstraction called RDD [4]. The RDDs or resilient distributed data sets are used in Spark to perform various complex operations. These can be stored in memory without using replication. RDDs can support a large number of algorithms and data query operations [5]. Apache Spark has emerged as the next-generation data processing engine, exceeding Hadoop MapReduce which has helped trigger the great data revolution. Spark maintains MapReduce's linear scalability and fault tolerance, but extends it in a few important ways: it's much faster (100 times faster for some applications), much easier to

program because of its rich APIs: Python, Java, Scala, SQL and R, and its basic data analysis, distributed data frame. In addition, this extends well beyond batch applications to support a variety of intensive computational tasks, including interactive queries, flows, machine learning, and graphics processing [1]. These components are designed to work near the kernel and can be used as libraries for application development [8]. Figure 1 shows the Apache Spark ecosystem.

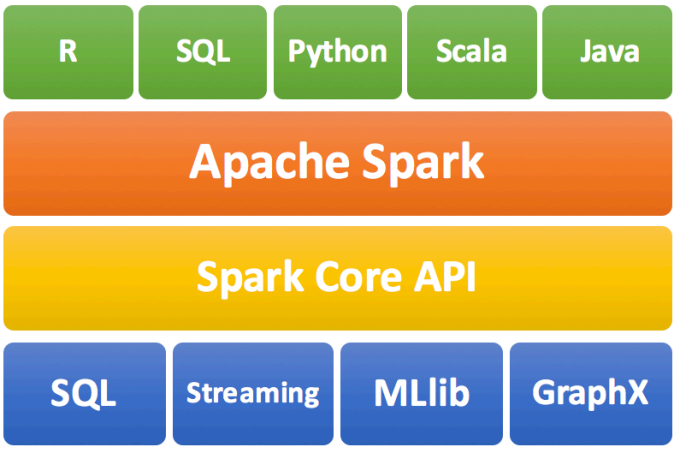

Fig. 1. The Apache Spark Ecosystem.

As shown in this figure, the Apache Spark system allows the development of applications in Java, Scala or Python because it uses a unified API. In addition, it can be used interactively to query data from a Shell. Finally, in addition to the main API, Table 1 shows the Apache Spark components and their description.

Table 1. The components of the Spark ecosystem.

Component	Description
Core	This is the general execution engine of the Spark platform and all the other features are integrated.
SQL	It is a module for the processing of structured data. It can be considered as a distributed SQL query engine.
Streaming	Enables real-time processing of stream data.
MLlib	It is a scalable learning machine library that contains all the classical learning algorithms and utilities
GraphX	It is a graphical calculation engine that allows manipulation and parallel processing of graphics.

Apache Spark can be seen as a more efficient execution engine than MapReduce, but it still uses Hadoop HDFS as a storage system for large datasets. In addition, using memory storage and real-time processing, performance can be faster than other Big

Data technologies. Spark retains intermediate results in memory rather than disk, allowing for faster execution time. Spark tries to store as much memory as possible before moving to disk. Indeed, it allows to work with part of the data in memory, another one on the disk [3]. In addition, Spark uses a batch program to process flows. This technique divides the incoming data and processes small parts one at a time. Unlike MapReduce, Spark supports data reuse and iterations. Spark stores data in memory via iterations with explicit caching. Moreover, Spark performs its operations as acyclic graph planes, which implies that it must plan and execute the same set of instructions in each iteration [9]. The following figure 2 shows the technique used by Apache Spark and its implementation for processing massive data.

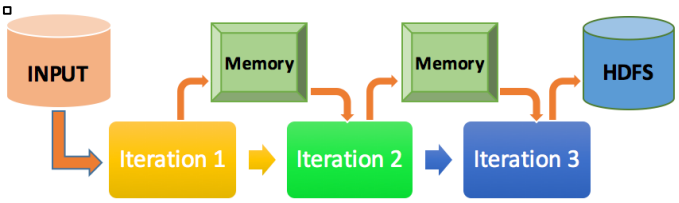

Fig. 2. Processing massive data by Apache Spark.

As described in the figure, Spark performs the operations in memory by copying the data from the distributed storage to the RAM, which is much faster at run time. As a result, the read / write operation time is reduced.

To carry out the data indexing step, we used the Lucene engine which is a tool integrated into the Solr Framework. Finally, these indexed data can be easily accessed thought a flexible search interface offered by the Solr Framework, a search platform that supports information retrieval relying on different features. For example, it tags and stores data into a structured collection in a format suitable that can be easily queried to perform the information retrieval step [14].

2.2 The Use of Solr Framework for Data Search and Exploration in the Big Data Environment

Apache Solr is an open source search platform for searches of data stored in HDFS. Solr includes full-text search, hit highlighting, faceted search, real-time indexing, dynamic clustering, database integration, NoSQL features and rich document handling [16]. Based on the Apache Lucene project, Solr uses Lucene as an indexing engine and full-text search. It enables distributed indexing, replication and load balanced data search, automatic failover and recovery, centralized configuration, and more [7]. The Solr system is coded in Java and can be executed as a standalone full-text search server within a servlet container [17]. Solr uses Lucene library at its core for full-text indexing and search, and has REST-like HTTP/XML and JSON APIs that make it easy to use with many programming languages. The powerful external configuration od Solr Framework allows it to be tailored to any type of application without Java coding, and

it has an extensive plugin architecture when more advanced customization is required [18].

Apache Solr provides a query API (REST API) to create user queries with the Solr language. It also includes a deployment methodology to set up a cluster of Solr servers that combines fault tolerance and high availability. This is referred to as SolrCloud, which offers the ability to run multiple nodes in a cluster and thus provides a highly scalable and highly available cloud environment [10]. Figure 3 shows the technical architecture used by Apache Solr to querying massive data stored in HDFS from the user data request through a web application.

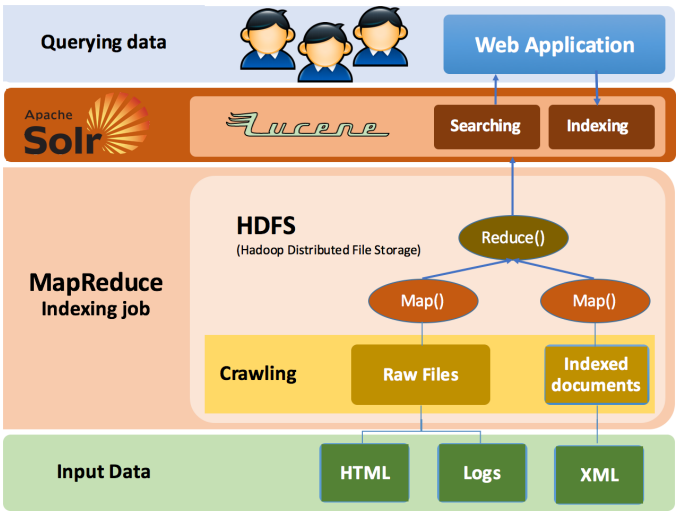

Fig. 3. The technical architecture used by Apache Solr System.

As described in this figure, data coming from Big Data are manifested on different types of files (Web/HTML, Logs, XML Documents, etc.), and are intercepted by Hadoop layer that implements both a distributed file system (HDFS) and an execution layer that supports the MapReduce programming model. Thus, data is loaded and transformed during the map phase, and then combined and saved during the reduce phase to write out Lucene indexes. The Lucene layer reads stored data from HDFS, and stores them using a Lucene Scheme, which in turn saves records as Lucene documents in an index. Once all of the files are indexed at Lucene layer, we can now perform queries against them. At Solr layer, we need to create a schema that matches the index that we are generating from Lucene layer.

The data in Solr are called document. Data indexed by Solr provides a fast response based on query type through Request method on HTTP. In addition, that query results can be instantly listed on the screen, one can also print out in XML, JSON, CSV, etc. formats. Solr uses Lucene library for indexing, analyzing, and searching processes, which involves filtering on existing structures, faceting, caching, and distributed architecture support. While Solr can be used as an API server similar to REST, it can also operate on protocols that are supported by HTTP/XML or JSON coding languages.

Additionally, it supports libraries that work independently in Java and enables specifications [16].

Apache Solr provides a web-based interface to Lucene for both input and output of data. Apache SOLR and Tomcat are Java-based, enabling execution in the vast majority of hardware and software environments. The front-end may be written in any language with support for HTTP- and JSON-based communication [15].

The indexer, Apache Lucene, is also a Java-based application. The indexer opens a port (8983 to be specific) as a query interface. The indexer can then be queried using a standard web browser, specifying query parameters using the GET protocol. Results are returned as XML or JSON type documents [15]. We can access the Solr administration console directly by entering this URL at the browser if your Solr server is installed on your local host: http://localhost:8983/solr/admin.

Since Solr accepts HTTP requests, we can use your web browser to communicate with Solr. And from there, we can run queries against as shown in Figure 4.

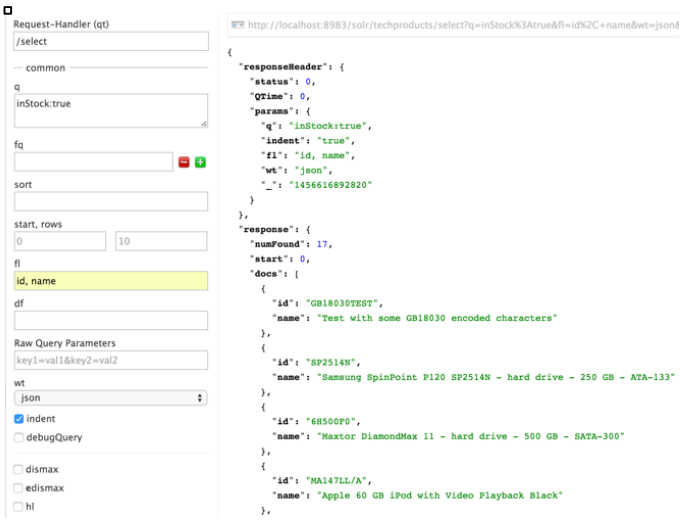

Fig. 4. Executing queries from the Solr admin console.

As shown in this figure, the response returned from Solr console is in JSON format by default, but it allows also the XML format as a result.

3 Towards an efficient and ergonomic combination for online search in the Big Data environment

3.1 The use of the Spark technique with the Solr Framework

As more organizations seek to leverage Spark for big data processing and the real-time analytics, the need for seamless integration between Spark and Solr emerges. The combination of Spark and Solr allows to easily explore a lot of data, and then provide the results quickly via a flexible search interface. Solr supports multiple style queries, we can say that it replaces the NoSQL system for traditional databases, especially when the data size exceeds what is reasonable with a typical RDBMS [7]. Figure 5 presents the integration of the Spark and the Solr systems for processing and searching data in the Big Data environment.

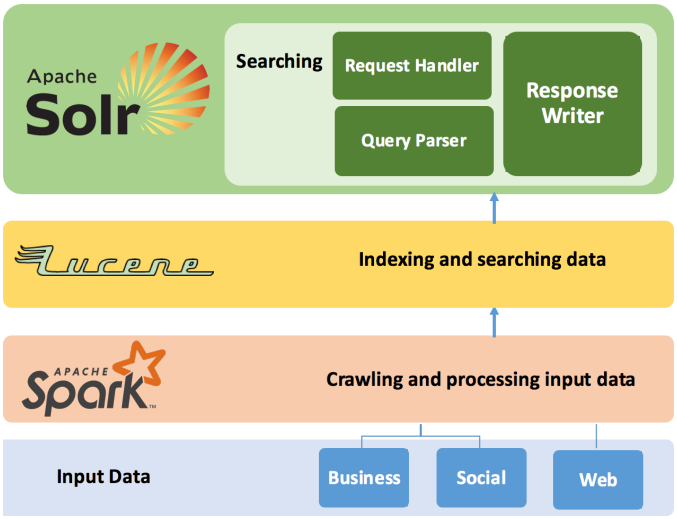

Fig. 5. Using Spark and Solr framework for processing and searching data in the Big Data environment.

As presented in the figure, the data coming from Big Data layer are intercepted by the Apache Spark system and stored at its distributed file system (HDFS). Then, using the MapReduce technique, these data are processed, reduced and indexed to make them easily usable for search.

When a user runs a search query in Solr, this query is processed by the Request Handler (RH), that is a Solr plug-in which defines the logic that should be used when processing a Solr request. So, to process a search query at the Solr, the application manager calls a Query Analyzer (QA), which interprets the terms and parameters of the Solr query. Different query parsers support a different syntax. The default query parser in Solr is known as Query Parser (QP), or more properly the Lucene Query Parser (LQP). The Response Writer component (RW) in Solr is used to return the response and handle the final presentation of the results of the query. Solr includes a variety of Response Writer components including the responses in XML and JSON formats.

3.2 The integration of Spark and Solr in the Big-Learn system

The Big-Learn system was born from the proposal to find a solution to the problem of massiveness and variety of data and especially in an online research or distance training for a learning or documentation purpose. The learner who uses the classical online search platform returns with a mixture of data that do not necessarily respond its expectations and sometimes even prove useless in relation to the needs expressed. It was in this context that it was proposed to develop the Big-learn tool, for processing of the structured and unstructured data set into one, and thus facilitate access and retrieval of information with adequate and consistent results according to the expectations of the learner [13]. Figure 6 shows the Big-Learn processing model of the using online search by the UAE's student in the Big Data environment.

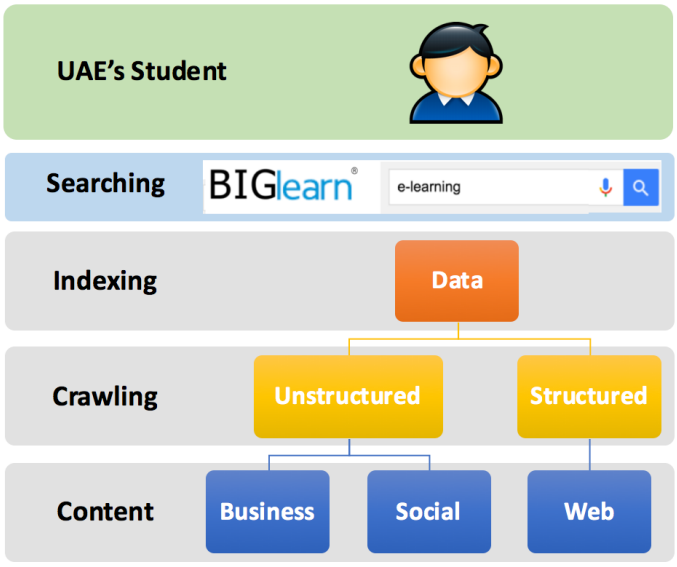

Fig. 6. The application architecture of the Big-Learn System.

As exposed in this figure, the UAE's student accesses the Big-Learn interface in order to launch his search request about his information or documentation needs. Thus, the system searches for data from the Internet. These data come from different sources (social networks, websites, business data, etc.) and come in many forms (structured, semi-structured or unstructured). Then, the system performs indexing of the data to present the results on the user interface. These data results are displayed as pages with links that redirect to the result found.

According to the integration study of the previous technologies, we can deduce the integral architecture of the Big-Learn solution to be adopted in order to meet our needs of improvement of the online search in the Big Data environment. Thus, the best solution is to combine Apache Spark technology for the storage and processing of massive and heterogeneous data, with the Solr framework for search and data exploration, based

itself on the Lucene indexing engine. Figure 7 sets the overall architecture of this solution integrating the various layers of each technique and its role in the integral Big-Learn system.

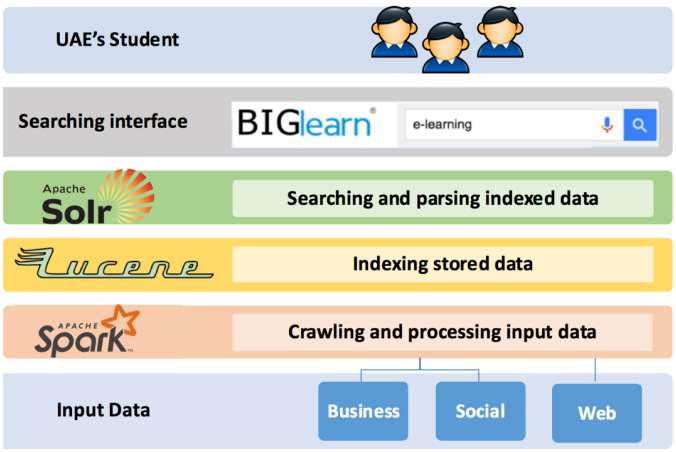

Fig. 7. The technical architecture of the Big-Learn system integrating Spark and Solr Frameworks.

As shown in this figure, data from the Big Data layer is intercepted by the Spark system, which will store this data on the Hadoop distributed file system (HDFS) and then process it using the MapReduce technique. Thus, the data is loaded and processed during the Map() phase, and then combined and stored for the Reduce() phase to create the index with Lucene. The Lucene indexing engine reads the stored HDFS data and stores it using Lucene's schema, which in turn records the records as documents in Lucene index. Once all files are indexed on the Lucene layer, it is now possible to query on their database via the Solr search interface which will be responsible for presenting these results data to the user interface.

4 Conclusion and future work

Few Big Data technologies provide tools for processing massive data in different formats (structured and unstructured). Moreover, search engines available on the Internet do not provide an efficient and comprehensive solution for searching for relevant information in a massive and heterogeneous environment. This article describes the Big-Learn system, a powerful and ergonomic model for an online search solution in the Big Data environment. The formula chosen in this system is based on the combination of two powerful platforms: Spark for massive and heterogeneous data processing, and Solr for indexing, searching and retrieving data. The Big-Learn system will facilitate access

to information and enable a more optimal search results providing adequate and consistent information that meets the user expectations and enables an easy consumption of information especially for the UAE's students.

As perspective of this work, we will study the possibility of integrating our solution to improve teaching and scientific research for learners in the e-learning massive environment. To do this, we will conduct a survey that will consist of using the Big-Learn system for learning or documentation needs, and which will take as a sample the students of the University of Abdelmalek Essaadi. This survey will help us to frame and refine the functional and technical requirements of the Big-Learn solution to finally design a powerful and ergonomic model for massive data processing and exploration.

References

1. SHANAHAN, James et DAI, Liang. Large Scale Distributed Data Science from scratch using Apache Spark 2.0. In : Proceedings of the 26th International Conference on World Wide Web Companion. International World Wide Web Conferences Steering Committee, 2017. p. 955-957.
2. ESSERTEL, Grégory M., TAHBOUB, Ruby Y., DECKER, James M., et al. Flare: Native Compilation for Heterogeneous Workloads in Apache Spark. arXiv preprint arXiv:1703.08219, 2017.
3. Zaharia, M., Xin, R. S., Wendell, P., Das, T., Armbrust, M., Dave, A., ... and Ghodsi, A. 2016. Apache Spark: a unified engine for big data processing. Communications of the ACM, 59(11), 56-65.
4. Lenka, R. K., Barik, R. K., Gupta, N., Ali, S. M., Rath, A., and Dubey, H. 2016. Comparative Analysis of Spatial Hadoop and GeoSpark for Geospatial Big Data Analytics. arXiv preprint arXiv:1612.07433.
5. ARORA, Shefali. Analyzing mobile phone usage using clustering in Spark MLLib and Pig. International Journal, 2017, vol. 8, no 1.
6. Padillo, F., Luna, J. M. and Ventura, S. 2017. Exhaustive search algorithms to mine subgroups on Big Data using Apache Spark. Progress in Artificial Intelligence, 1-14.
7. Aoulad Abdelouarit, K., Sbihi B. and Aknin N., 2016. Towards an approach based on hadoop to improve and organize online search results in big data environment. In Communication, Management and Information Technology: Proceedings of the International Conference on Communication, Management and Information Technology (ICCMIT 2016) (Jul. 2016), 543-550. CRC Press.
8. Mavridis, I., and Karatza, H. 2017. Performance evaluation of cloud-based log file analysis with Apache Hadoop and Apache Spark. Journal of Systems and Software, 125, 133-151.
9. García-Gil, D., Ramírez-Gallego, S., García, S., and Herrera, F., 2017. A comparison on scalability for batch big data processing on Apache Spark and Apache Flink. Big Data Analytics, 2(1), 1.
10. S. Singh, Y. Liu, (2016). A cloud service architecture for analyzing big monitoring data.Tsinghua Science and Technology.[Online]. 21(1), pp. 55-70.
11. C. Leeder, C. Shah (2016). Mesuring the Effect of Virtual Librarian on Student Online Search. The Journal of AcademicLibrariabship. [Online]. 42(1), pp. 2-7.
12. Aoulad Abdelouarit, K., Sbihi B. and Aknin N., 2016. Solr, Lucene and Hadoop: Towards A Complete Solution To Improve Research In Big Data Environment (Case of The UAE) MEDITERRANEAN CONGRESS OF TELECOMMUNICATIONS (CMT'2016), 12-13 May, 2016.

13. Aoulad Abdelouarit, K., Sbihi B. and Aknin N., 2015. Big-Learn: Towards a Tool Based on Big Data to Improve Research in an E-Learning Environment. International Journal of Advanced Computer Science and Applications (IJACSA) 6(10): 59–63.
14. CAVALLINI, Anna, MICIELI, Giuseppe, et QUAGLINI, Silvana. Exploring IBM Watson to Extract Meaningful Information from the List of References of a Clinical Practice Guideline. In : Artificial Intelligence in Medicine: 16th Conference on Artificial Intelligence in Medicine, AIME 2017, Vienna, Austria, June 21-24, 2017, Proceedings. Springer, 2017. p. 193.
15. ROSEN, Paul et PIEGL, Les A. Using data indexing for remote visualization of point cloud data. Computer-Aided Design and Applications, 2017, p. 1-7.
16. AKCA, Mustafa Ali, AYDOĞAN, Tuncay, et İLKUÇAR, Muhammer. An Analysis on the Comparison of the Performance and Configuration Features of Big Data Tools Solr and Elasticsearch. memory, 2016, vol. 74.
17. VENTICINQUE, Alessio, MAZZOCCA, Nicola, VENTICINQUE, Salvatore, et al. Semantic support for log analysis of safety-critical embedded systems. arXiv preprint arXiv:1405.2986, 2014.
18. MANDAL, Sukumar. Use of Search Indexing Tools in Library Automation: A Comparative Analysis. International Research Journal of Multidisciplinary Studies, 2016, vol. 2, no 6.

Dynamical evolution of the community structure of complex network inherent in seismic time series

Norikazu Suzuki

College of Science and Tecnology, Nihon University,
7-24-1 Narashinodai, Funabashi, Chiba, 274-8501, Japan
suzu@phys.ge.cst.nihon-u.ac.jp

Abstract. An earthquake can trigger the next earthquake that can be more than 1000km away[1]. In fact, after the big earthquake M_W 9.0 in Japan six years ago, the seismic wave traveled the whole surface of the earth at least 7 times. This seismic wave actually triggered many subsequent earthquakes in Japan, China, Canada, Mexico and U.S.A.[2]. This fact suggests there exists long-time and long-range correlation between earthquakes even if their distances are very large.
Recently, we have proposed the network representation[3]-[5] of seismicity[6]. The seismic data are mapped to growing random networks[6]. Vertices and edges of such networks correspond to coarse-grained events and event-event correlations, respectively. Yet unknown microscopic dynamics governing event-event correlations and fault-fault interactions is replaced by these edges. Global physical properties of seismicity can then be explored by examining its geometric (e.g., topological etc.), statistical and dynamical properties.
We have shown that it is of the scale-free, and small-world type[6]-[8], hierarchically organized[9], and possesses the assortative mixing property[9]. Combined with other physical properties[10]-[23], these results imply that yet unknown mechanism governing seismicity may be so-called glassy dynamics[24][25], on a growing complex network[3][4][5]. These observations have obvious importance for constructing and improving physical models of seismicity such as the ones exhibiting self-organized criticality.
In this talk, we discuss the dynamical evolution of the structure of earthquake network[26][27]. In particular, we focus our attention on the evolution of the community structure[5], that is, how the whole network is partitioned into sub-networks, in which member vertices are densely interconnected with each other. Since main shocks play the role of hubs, they give an impact on the global structure of the network. In turn, it is expected that the community structure may characterize main shocks in a peculiar manner. We monitor the maximum value of the modularity measure, Q_{max}, of the earthquake networks constructed from the seismic data taken from California and Japan. We report the discovery of a universal behavior in the evolution of Q_{max} around main shocks. Q_{max} stays at a large value before a main shock, suddenly drops to a small

value at the main shock, and then slowly increases to a large value again relatively slowly[27]. This result implies that a main shock absorbs and merges communities to create a larger community. Thus, main shocks are characterized within the network approach in a peculiar manner. We also make a comment on this result in connection with the clustering structure[26] of the earthquake networks.

Keywords: Time series, Earthquake, Complex network, Community structure, Self-organized criticality

References

1. Steeples, D.W., Steeples D.D.: Far-field aftershocks of the 1906 earthquake. Bull. Seismol. Soc. Am. **86** (1996) 921-924
2. Peng, Z., et al., Tectonic tremor beneath Cuba triggered by the M_W 8.8 Maule and M_W 9.0 Tohoku-Oki earthquakes. Bull. Seismol. Soc. Am. **103** (2013) 595-600
3. Watts, D. J., Strogatz, S. H.: Collective dynamics of 'small-world' networks. Nature **393** (1998) 440-442
4. Barabasi, A-L., Albert, R.: Emergence of scaling in random networks. Science **286** (1999) 509-512
5. Newman, M.E.J.,: Networks: An Introduction (Oxford) (2010)
6. Abe, S., Suzuki, N.: Scale-free network of earthquake. Europhys. Lett. **65** (2004) 581-586
7. Abe, S., Suzuki, N.: Small-world structure of earthquake network. Physica A **337** (2004) 357-362
8. Abe, S., Suzuki, N.: Complex-network description of seismicity. Nonlin. Processes Geophys. **13** (2006) 145-150
9. Abe, S., Suzuki, N.: Complex earthquake networks: Hierarchical organization and assortative mixing. Phys. Rev. E **74** (2006) 026113 p1-p5
10. Abe, S., Suzuki, N.: Law for the distance between successive earthquakes. J. Geophys. Res. **108** B2 (2003) 2113-2117.
11. Abe, S., Suzuki, N.: Scale-free statistics of time interval between successive earthquakes. Physica A **350** (2005) 588-596
12. Abe, S., Suzuki, N.: Scale-invariant statistics of period in directed earthquake network. Eur. Phys. J. B **44** (2005) 115-117
13. Abe, S., Suzuki, N.: Universal and nonuniversal distant regional correlations in seismicity: Random matrix approach. ePrint (2009), arXiv:0909.3830
14. Abe, S., Suzuki, N.: Determination of the scale of coarse graining in earthquake networks. EPL **87** (2009) 48008 p1-p5
15. Abe, S., Suzuki, N.: Violation of the scaling relation and non-markovian nature of earthquake aftershocks. Physica A **388** (2009) 1917-1920
16. Abe, S., Suzuki, N.: Scaling relation for earthquake networks. Physica A **388** (2009) 2511-2514
17. Abe, S., Suzuki, N.: Earthquake networks, complex. In: Encyclopedia of Complexity and Systems Science, Springer, New York (2009) 2530-2538 (arXiv:0708.2203)
18. Abe, S., Pasten, D., Suzuki, N.: Finite data-size scaling of clustering in earthquake networks. Phyisca A **390** (2010) 1343-1349
19. Abe, S., Suzuki, N.: Universal law for waiting internal time in seismicity and its implication to earthquake network. EPL **97** (2012) 49002 p1-p5

20. Suzuki, N.: Complex network of earthquakes: Universal law for waiting internal time in seismicity. In: Proceedings of 8th International Conference on Signal Image Technology and Internet Based Systems (IEEE Computer Society) (2012) 707-709
21. Abe, S., Suzuki, N.: Universal clustering structure and $C{\approx}0.85$ scaling in complex earthquake networks. Phyisca A **421** (2014) 343-346
22. Abe, S., Suzuki, N.: Anomalous diffusion of volcanic earthquakes. EPL **110** (2015) 59001-p1-p5
23. Abe, S., Suzuki, N.: Subdiffusion of volcanic earthquakes. Acta Geophys. (2017) doi:10.1007/s11600-017-0029-6
24. Abe, S., Suzuki, N.: Aging and scaling of earthquake aftershocks. Physica A **332** (2004) 533-538
25. Abe, S., Suzuki, N.: Aftershocks in modern perspectives: Complex earthquake network, aging, and non-Markovianity. Acta Geophys. **60** (2012) 547-561
26. Abe, S., Suzuki, N.: Dynamical evolution of clustering in complex network of earthquake. Eur. Phys. J. B **59** (2007) 93-97
27. Abe, S., Suzuki, N.: Dynamical evolution of the community structure of complex earthquake network. EPL **99** (2012) 39001-p1-p4

Quantitative characterization of intracellular calcium signals

Iker Malaina[1], Carlos Bringas[2], Alberto Pérez-Samartín[3], Luis Martinez[1], Ildefonso Martínez de la Fuente[1,4].

[1] Department of Mathematics, University of the Basque Country UPV/EHU, Bilbao, Spain
{iker.malaina, luis.martinez, mtpmadei}@ehu.eus
[2]Department of Cell Biology and Histology, University of the Basque Country UPV/EHU, Bilbao, Spain
carlos.bringas@ehu.eus
[3]Department of Neurosciences, University of the Basque Country UPV/EHU, Bilbao, Spain
a.perez@ehu.eus
[4]Department of Nutrition, CEBAS-CSIC Institute, Espinardo University Campus, Murcia, Spain

Abstract: Unicellular organisms are open metabolic systems that need to process information about their external environment in order to survive. In most types of tissues and organisms**,** cells use calcium signaling to carry information from the extracellular side of the plasma membrane to the different metabolic targets of their internal medium. This information might be encoded in the amplitude, frequency, duration, waveform or timing of the calcium oscillations. Thus**,** specific information coming from extracellular stimuli can be encoded in the calcium signal and decoded again later in different locations within the cell. Despite its cellular importance, little is known about the quantitative informative properties of the calcium concentration dynamics inside the cell. In order to understand some of these informational properties, we have studied experimentally evoked Ca^{2+} series of *Xenopus laevis* oocytes under different external pH stimulus. The data has been analyzed by means of statistical mechanics approaches such as mean square displacement, sample entropy and box counting. Our main result shows that inside all the studied intracellular Ca^{2+} flows a highly organized informational structure emerge, which exhibit superdiffusion lasting in average almost 2 seconds, scale invariance and carry huge amounts of information. The understanding of the informational properties of calcium signals is one of the key elements to elucidate the physiological functional coupling of the cell and the integrative dynamics of cellular life.

Keywords: mean square displacement, box counting, sample entropy, calcium signaling.

Corresponding author: Iker Malaina, Department of Mathematics, University of the Basque Country UPV/EHU, 48080 Bilbao (Spain), email: iker.malaina@ehu.eus.

1 Introduction

Calcium ions play a fundamental role in cell physiology, particularly in signal transduction processes. In fact, calcium signaling represents one of the few universal intracellular messengers that are able to carry information from the extracellular side of the plasma membrane to different metabolic targets in the internal medium [1, 2].

From a biochemical point of view, one of the essential characteristics of Ca^{2+} ion fluxes is their capacity to exert regulatory effects on many enzymes [3, 4], which allows the modulation of the metabolic activity of the cell. As a consequence, calcium signaling participates in a multiplicity of key functions, such as the regulation of cell differentiation [5], cellular migration [6], cell division [7], ROS signaling [8, 9], synaptogenesis [10], apoptosis [11], autophagy [12], exocytosis [13], neuronal plasticity [14], cytoskeleton activity [15], cellular growth [16], dendritic development [17], neurotransmitter release [18], and gene expression [19].

At a molecular level, the mechanisms involved in the generation of calcium signaling essentially result from a complex interplay among extracellular calcium**,** permeable channels and the activation/inactivation of intracellular Ca^{2+} pools, mainly located at the endoplasmic or sarcoplasmic reticulum and mitochondria. These processes are highly regulated by complexly interrelated metabolic reactions [20].

In general, external stimuli are often converted into intracellular Ca^{2+} ion fluxes which encode the input information by means of signal transduction processes, i.e., an extracellular stimulus activates a specific receptor located on either the cell surface or the inside, triggering a biochemical chain of molecular processes, which originates different metabolic responses, a large part of them in the form of intracellular calcium oscillations [21].

In many cells, these molecular processes involve G protein-coupled receptors and the phospholipase C enzymes, located in the cell membrane. Specific phospholipase C can hydrolyse phosphatidylinositol 4,5-bisphosphate (PIP2) into two products: inositol 1,4,5-trisphosphate (IP3) and diacylglycerol (DAG), two classical second messengers.

The level of external stimulation on the cell determines the degree of activation of the receptor and therefore can be directly linked to the intracellular IP3 concentration. IP3 mainly diffuses to the endoplasmic reticulum, and binds to its specific receptor, which is located in an intracellular calcium channel; thus releases Ca^{2+} ions from the endoplasmic reticulum, triggering oscillations in the cytoplasmic calcium concentration [22]. As a result of these complex metabolic processes the temporal behavior of the intracellular Ca^{2+} levels are highly regulated [23].

In spite of its physiological importance, many aspects of the molecular mechanisms involved in the generation of the intracellular calcium concentration dynamics are still poorly understood.

Intracellular Ca^{2+} fluxes can either be localized or invade the whole cell; and depending on the cell type and the stimulus, Ca^{2+} signals are characterized by a rich variety of oscillating patterns, in which the frequency and amplitude can vary practically infinitely [20, 24].

Calcium concentration rhythms represent a genuine manifestation of the dissipative self-organization in the enzymatic activities of the cell. Experimental observations and numerical studies have shown that metabolic processes shape functional structures in which these kinds of molecular rhythms may spontaneously emerge far from thermodynamic equilibrium [25, 26].

It is well established that non-equilibrium states can be a source of order in the sense that metabolic irreversible processes may lead to a new type of dynamic state in which the system becomes ordered in space and time. In fact, the non-linearity associated with irreversible enzymatic reactions seems to be an essential mechanism that may allow dissipative metabolic organization far from thermodynamic equilibrium [27, 28].

Self-organization is based on the concept of dissipative structures, and its theoretical roots can be traced back to the Nobel Prize Laureate in Chemistry Ilya Prigogine [29]. Two main kinds of metabolic dissipative structures exist in cellular conditions: temporal oscillations and spatial biochemical waves [25]. Both kinds of dissipative structures can be observed in Ca^{2+} dynamics. Thus**,** when spatial inhomogeneities develop instabilities in the intracellular medium, in addition to temporal calcium oscillation [30], it may lead to the emergence of spatio-temporal dissipative structures which can take the form of propagating calcium concentration waves [31, 32]. Phase-coupled NAD(P)H waves and calcium oscillations have also been observed [33].

Since the first observations of the calcium rhythmic phenomena, experimental investigation of its molecular mechanism has been accompanied by numerous computational modeling approaches. The use of these numerical studies on Ca^{2+} oscillations can lead to different important conclusions mainly about the nonlinear feedback processes involved in the spontaneous generation of oscillations [34, 35]. For a review on calcium numerical studies, see Dupont et al. [20]. Despite numerous studies on calcium signaling, how information is processed is still insufficiently known.

Different experimental and numerical analysis have shown that the information might be encoded in the amplitude, frequency, duration, waveform or timing of calcium oscillations [36, 37]. Thus, specific information coming from extracellular stimuli can be encoded in the calcium signal and decoded again later in different metabolic targets in the cellular internal medium.

These researches on the calcium information have motivated a number of experimental and theoretical studies. For instance, it has been estimated by means of mathematical simulations the information encoded in a Ca^{2+} series upon hormonal stimulation in hepatocytes [38]. Mutual information has also been used to calculate the amount of information transferred over a calcium signaling channel, using a computational model [39]. Long-term correlations have been observed in calcium-activated potassium channels [40, 41]; other biochemical processes also present long-term correlation**,** for example, the intracellular transport pathway of *Chlamydomonas reinhardtii* [42], the NADPH series of mouse liver cells [43] and the mitochondrial membrane potential of cardiomyocytes [44].

Likewise, the information transfer from the calcium signal to a target enzyme under different physiological conditions has been analyzed using transfer entropy [45] in a computational model, a technique widely used to quantify directed biological interactions [46, 47].

One of the manners to quantify intracellular calcium is by measuring the activity of calcium-activated chloride channels (CaCCs), a key family of chloride channels that regulate the flow of chloride and other monovalent anions across cellular membranes in response to intracellular calcium levels [48]. In fact, this correlation between Ca^{2+} fluctuations and CaCCs has already been observed in several organisms, from *Rana pipens* [49] to *Xenopus laevys* [50].

Here, we have studied experimental intracellular calcium properties by analyzing calcium-activated chloride currents of *Xenopus laevis* oocytes under different external pH stimuli. The data has been analyzed by means of statistical mechanics approaches such as mean square displacement, sample entropy and box counting. Our main result shows that in the intracellular Ca^{2+} flows a highly organized complex informational structure emerges which is characterized by exhibiting super-diffusion lasting in average almost 2 seconds, scale invariance and carrying huge amounts of information.

2 Methodology

2.1 Calcium oscillations in *Xenopus laevis* oocytes

Adult *Xenopus laevis* frogs were obtained from Blades Biological (Cowden, Kent, UK). Oocytes at stage V were plucked from the ovaries and defolliculated by collagenase treatment (type 1, Sigma-Aldrich Quimica, S.A., Madrid, Spain) at 80–630 units/ml in frog Ringer's solution (115 mM NaCl, 2 mM KCl, 1.8 mM CaCl2, 5 mM HEPES at pH 7.0) for 20 min to remove the surrounding follicular and epithelial cell layers. Oocytes were maintained at 18ºC in sterile unsupplemented modified Barth's medium containing (mM): 88 NaCl, 0.2 KCl, 2.4 $NaHCO_3$, 0.33 $Ca(NO_3)_2$, 0.41 $CaCl_2$, 0.82 $MgSO_4$, 0.88 KH_2PO_4, 2.7 Na_2HPO_4, with gentamicin 70 μg ml−1 and adjusted to pH 7.4. Membrane currents were recorded with a standard two-electrode

voltage clamp (Warner Instruments, Oocyte Clamp OC- 725C) and digitized in a PC (Digidata 1200 and Axoscope 8.0 software, Axon Instruments). Oocytes were continually superfused with Ringer's solution (115 NaCl, 2 KCl, 1.8 $CaCl_2$, 5 Hepes) at room temperature (22ºC). The membrane was usually voltage clamped at -60 mV. Fetal Bovine Serum (FBS) (Sigma-Aldrich) diluted 1:1000 Ringer's solution was used for oocytes perfusion to achieve the generation of currents oscillations. Two different pH conditions were considered for the 7 analyzed oocytes, Ringer's solution at pH 5.0 and 7.0. Therefore, we obtained 14 time series, numbered from 1 to 14, where nº1 and nº2 belong to the first oocyte under pH 5.0 and 7.0 respectively; nº3 and nº4 belong to the second oocyte under pH 5.0 and 7.0, and so on. The series were recorded with a sampling frequency of 0.02 for 40 seconds; therefore, our time series had 2,000 time points each.

2.2 Mean square displacement

The MSD calculates the average squared displacements between the values of a time series over increasing time intervals (or scales) [51].

Given a time series $r(t)$, the MSD can be obtained by:

$$MSD(\tau) \equiv \frac{1}{T-\tau}\sum_{t=1}^{T-\tau}(r(t+\tau)-r(t))^2, \text{ for } \tau = 1,\ldots,\tau_{\max},$$

where τ denotes the time interval (or scale). A relevant property of random walks involves scaling in relation to the time of the MSD, with a power law relationship $MSD(\tau) \sim D\tau^{\beta}$, where β characterizes the behavior of diffusive processes. In a typical process, such as a pure uncorrelated Brownian motion, the exponent β is equal to 1. The phenomenon is named super-diffusion if $2>\beta>1$, while if $\beta<1$ it is referred to as sub-diffusion. Here, the diffusion was studied for non-trivial correlations (i.e., while the adjustment R^2 of the regression line with slope β is greater than 0.99) by incrementing time interval $\tau_{\max}$ until the R^2 condition was lost.

2.3 Sample entropy

Sample entropy [52] is a variation of the approximate entropy, with two advantages: data length independence and "trouble free" implementation. In short, given a embedding dimension m, a tolerance r and a number of data points N, Sample entropy (SampEn) can be defined as the negative logarithm of the probability that if the distance of two sets of simultaneous data points of length m is less than r, then two simultaneous data points of length $m+1$ also have a distance $< r$. When a time series has a small SampEn, it means that it contains repetitive patterns, while a higher SampEn corresponds to a less predictive process. To calculate this statistic, we have to fix a positive number r (commonly chosen as $r = 0.2 \cdot SD$, where SD is the standard deviation of the series) and an integer number m (the length of compared runs of data, which in our case was estimated by the method proposed by L.Cao [53] and resulted in $m = 2$).

2.4 Box counting

Box counting [54] is one of the techniques used to estimate the fractal dimension of a time series. Intuitively, this process is similar to zooming in (or out) in order to observe how details change with the scale. When the theoretical fractal dimension exceeds its topological dimension, the set is considered to have fractal geometry. In our case, a fractal dimension close to 2 indicates that the curve convolutes through space nearly like a surface, while a value near to 1 is associated to a less complex behavior, more similar to an ordinary line. This technique is extensively explained in [54].

3 Results

In order to study some of the quantitative properties of calcium currents, we have obtained experimental Ca^{2+}-dependent chloride measurements from seven different *Xenopus laevis* oocytes, each of them under two different external pH stimuli (5.0 and 7.0, i.e., acid and neutral), gathering 14 time series, in which 2,000 data points were considered. In Figure 1, we illustrate two representative experimental calcium flows.

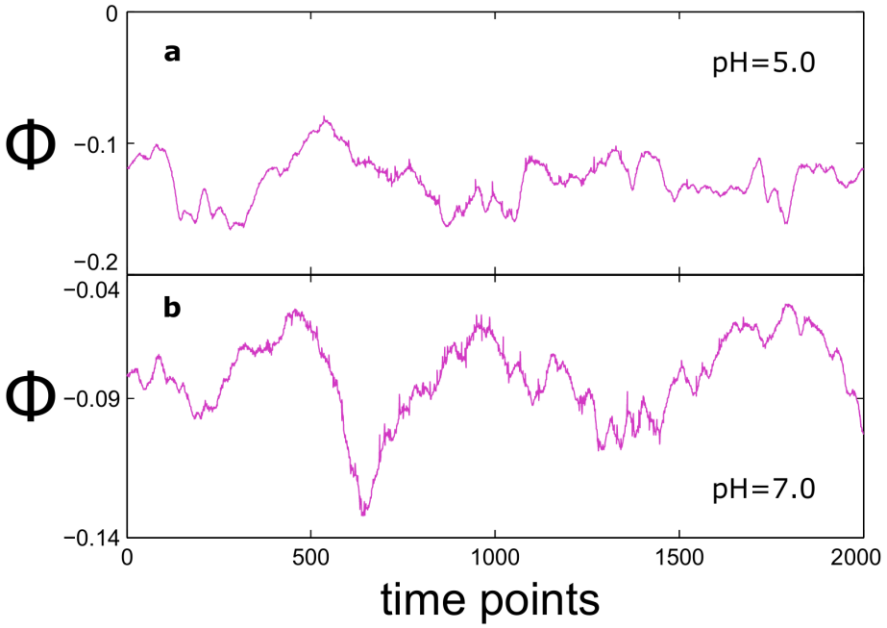

Fig 1. Experimental calcium oscillations in *Xenopus laevis* oocyte. Prototypical calcium time series belonging to the first oocyte, under both acid (**a**), and neutral (**b**) pH conditions. The horizontal axis indicates the time points, while the vertical axis (Φ) corresponds to the electrical potential measured in nanoampers (nA).

First, with the objective of studying the type of diffusion that characterizes our calcium series, we have applied the mean square displacement technique. To estimate

the duration of the diffusion process, we established the criterion of having a R^2>0.99 in the regression adjustment. Thus, we subsequently increased the size of the time interval τ until the criterion was unfulfilled, and reported the values of the slope β and the maximum time interval τ_{max}. The values of the MSD slope were comprehended between 1.13 and 1.67 (being 1.30±0.15 the mean±*SD*), indicating super-diffusion for all the cases. Besides, this behavior was observed for periods ranging between 0.78 and 6.67 seconds, with a mean of 1.9±2.9 seconds (all the values of β and τ_{max} are depicted in Table 1). In figure 2, we illustrate four prototypical slopes of the mean square displacement obtained from calcium series.

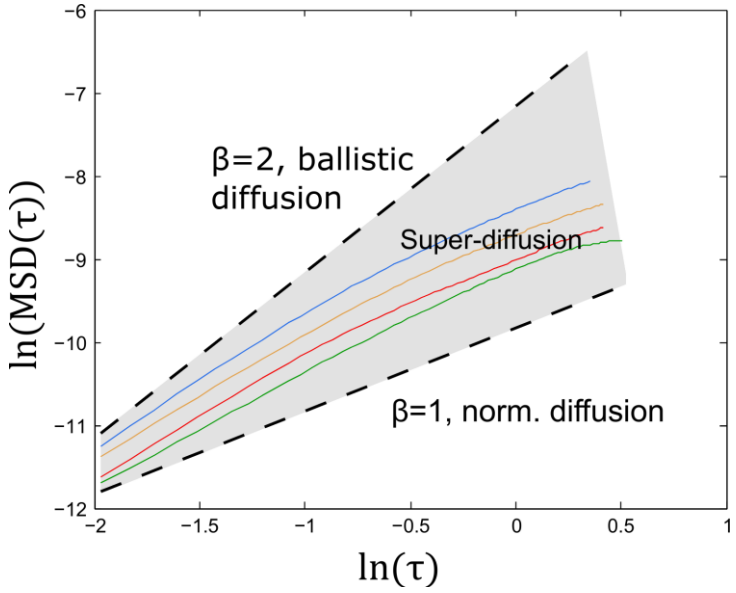

Fig 2. Mean Square Displacement of the calcium time series. Log-log plot of MSD against the time interval τ, for 4 prototypical calcium time series. β=1 indicates normal diffusion while β=2 indicates ballistic diffusion. The grey region defines the area of super-diffusion, in which all experimental slopes are contained.

Then, we analyzed the regularity of our time series by calculating the sample entropy. A time series with predictive patterns would have a sample entropy close to 0, while the entropy of a less repetitive series would be closer to 1. This statistic was calculated for $r = 0.2 \cdot SD$ and $m = 2$ (for more details see the part 2.3 in Methods section). The average entropy of the series was 0.169±0.1, with values ranging from 0.02 to 0.42 (all the SampEn values are given in Table 1).

Table 1. Mean square displacement slope (β), maximum duration (τ_{max}) measured in seconds, sample entropy (SampEn) and fractal dimension (F-dim) of the calcium evoked time series, respectively.

Series	β	τ_{max}	SampEn	F-dim
nº1	1.20	27	1.52	0.20
nº2	1.18	8	1.33	0.18
nº3	1.39	51	1.35	0.21
nº4	1.33	29	1.30	0.13
nº5	1.20	25	1.44	0.42
nº6	1.24	45	1.45	0.18
nº7	1.24	27	1.58	0.24
nº8	1.28	28	1.53	0.18
nº9	1.13	11	1.49	0.30
nº10	1.15	14	1.40	0.13
nº11	1.53	6	1.05	0.03
nº12	1.67	7	1.14	0.02
nº13	1.36	6	1.17	0.04
nº14	1.29	13	1.22	0.10

Next, the fractal dimension of the series was estimated by the box counting technique. If the fractal dimension is near 1, the time series behaves nearly like a regular line, while if it is near 2, it convolutes through space similarly to a surface. The results of our series were comprehended between 1.05 and 1.58, with an average of 1.35 ± 0.16 (all these values are depicted in Table 1).

Finally, we have studied if the results (β, $\tau_{\max}$, SampEn and F-dim) of the series under acid pH were significantly different from those under neutral pH. In order to use the adequate test, first we checked the normality of our variables by the Shapiro-Wilk test. Then, we applied the paired T-test (or Wilcoxon signed rank test when one of the variables was non-normal), obtaining the p-values 0.94, 0.82, 0.42 and 0.12, for β, $\tau_{\max}$, SampEn and F-dim, respectively. These p-values indicate that there were no significant differences between the statistics of both groups.

4 Discussion

Calcium is a key chemical element of the cell which participates in a wide variety of physiological processes and plays a crucial role as a universal messenger in cellular metabolism and signaling.

Here, in order to understand some of the informational properties of the intracellular calcium signals we have studied experimental Ca^{2+} series of *Xenopus laevis* oo-

cytes under different external pH stimulus (acid and neutral) by means of statistical mechanics approaches.

Through the Mean Square Displacement technique, we have observed that all of our calcium series present super-diffusion, which is typical in very complex systems. In contrast with Gaussian series where the immediate future values are only determined by the present, super-diffusive series present a restrictive relationship between past and future values (given rise to long-term correlations and persistence/anti-persistence) [55]. In addition, this property is a manifestation of the sophisticated and intricate regulation ruling the dynamics of intracellular calcium concentrations [56]. Moreover, this is the first time wherein anomalous diffusion (and more specifically, super-diffusion) is observed in intracellular calcium dynamics.

The study of the fractal dimension of the time series by the box counting method has indicated that the calcium time series are scale invariant. In fact, previous studies have observed that this property gives the system important biological advantages, such as adaptability of response to a continuously varying environment [57], which can be a crucial feature for this type of cellular signals.

By estimating the sample entropy of the calcium series, we have corroborated that our series carry quantifiable information. Within the framework of Information Theory, the entropy (and specifically, Shannon entropy) is used to measure the average information content in a system. Here, by approximating Shannon entropy through sample entropy, we have been able to confirm that calcium series are stochastic processes that carry big amounts of molecular information. This property agrees with the widely accepted biochemical theory, in which calcium (acting as a *second messenger*) carries information within the cell in response to extracellular signals.

Finally, we have compared the results of the series under pH 5.0 and 7.0. These analyses have indicated that there were no significant differences between the slopes or the durations of the diffusion processes, the sample entropies or the fractal dimensions. Therefore, we conclude that the aforementioned properties are presented by calcium series regardless of whether the pH stimulus is acid or neutral.

Summarizing, our results show that in the intracellular Ca^{2+} flows, a highly organized complex informational structure emerges which is characterized by exhibiting super-diffusion for almost 2 seconds, presenting scale invariance and carrying high amounts of molecular information.

Understanding the quantitative properties of intracellular calcium signals is one of the key elements to elucidate the physiological functional coupling of the cell and the integrative dynamics of cellular life.

Acknowledgements. Work by the first author was supported by the Basque Government grant PRE-2015-1-585 194, and work by the first and forth authors by the Basque Government grant IT974-16.

References

1. Berridge MJ, Bootman MD, Lipp P (1998) Calcium – a life and death signal. Nature 395: 645–648. doi: 10.1038/27094.
2. Berridge MJ, Bootman MD, Roderick HL (2003) Calcium signalling: dynamics, homeostasis and remodelling. Nature Reviews Molecular Cell Biology 4: 517–529. doi: 10.1038/nrm1155.
3. Vaughan H, Thornton SD, Newsholme EA (1973) The effects of calcium ions on the activities of trehalase, hexokinase, phosphofructokinase, fructose diphosphatase and pyruvate kinase from various muscles. Biochem J 132(3): 527-535.
4. Goldie AH, Sanwal BD (1980) Allosteric control by calcium and mechanism of desensitization of phosphoenolpyruvate carboxykinase of Escherichia coli. J Biol Chem 255: 1399-1405.
5. Bikle DD, Xie Z, Tu CL (2012) Calcium regulation of keratinocyte differentiation. Expert Rev Endocrinol Metab. 7: 461-472. doi: 10.1586/eem.12.34
6. Komuro H, Kumada T (2005) Ca^{2+} transients control CNS neuronal migration. Cell Calcium 37: 387–393. doi: 10.1016/j.ceca.2005.01.006
7. Hepler PK (1994) The role of calcium in cell division. Cell Calcium 16: 322-330. doi: 10.1016/0143-4160(94)90096-5
8. Orrenius S, Gogvadze V, Zhivotovsky B. (2007) Mitochondrial oxidative stress: implications for cell death. Annu Rev Pharmacol Toxicol 47: 143–183. doi: 10.1146/annurev.pharmtox.47.120505.105122
9. Steinhorst L, Kudla J (2013) Calcium and reactive oxygen species rule the waves of signaling. Plant Physiol 163: 471-485. doi: 10.1104/pp.113.222950.
10. Lohmann C, Finski A, Bonhoeffer T (2005) Local calcium transients regulate the spontaneous motility of dendritic filopodia. Nature Neuroscience. 8: 305–312. doi: 10.1038/nn1406
11. Szalai G, Krishnamurthy R, Hajnoczky G (1999) Apoptosis driven by IP3 linked mitochondrial calcium signals. EMBO J. 18: 6349–6361. doi:10.1093/emboj/18.22.
12. Nicolau-Galmés F, Asumendi A, Alonso-Tejerina E, Pérez-Yarza G, Jangi SM, Gardeazabal J, et al (2011) Terfenadine induces apoptosis and autophagy in melanoma cells through ROS-dependent and -independent mechanisms. Apoptosis 16: 1253-1267. doi: 10.1007/s10495-011-0640-y.
13. Barclay JW, Morgan A, Burgoyne RD (2005) Calcium-dependent regulation of exocytosis. Cell Calcium. 38: 343-353. doi: 10.1016/j.ceca.2005.06.012
14. Spitzer NC, Olson E, Gu X (1995) Spontaneous calcium transients regulate neuronal plasticity in developing neurons. J Neurobiol 26: 316–324.
15. Furukawa R, Maselli A, Thomson SA, Lim RW, Stokes JV, Fechheimer M (2003) Calcium regulation of actin crosslinking is important for function of the actin cytoskeleton in Dictyostelium. J Cell Sci. 116: 187-196. doi: 10.1242/jcs.00220
16. Gomes TM, Spitzer NC (1999) In vivo regulation of axon extension and pathfinding by growth-cone calcium transients. Nature 397: 350–355. doi: 10.1038/16927
17. Redmond L, Gosh A (2005) Regulation of dendritic development by calcium signalling. Cell Calcium 37: 411–416. doi: 10.1016/j.ceca.2005.01.009

18. Sudhof TC (2004) The synaptic vesicle cycle. Annu Rev Neurosci. 27: 509–547. doi: 10.1146/annurev.neuro.26.041002.131412
19. Fields RD, Eshete F, Stevens B, Itoh K (1997) Action potential-dependent regulation of gene expression: temporal specificity in Ca2 +, cAMP-responsive element binding proteins, and mitogen-activated protein kinase signaling. J Neurosci 17: 7252–7266.
20. Hayer SN, Bading H (2015) Nuclear Calcium Signaling Induces Expression of the Synaptic Organizers Lrrtm1 and Lrrtm2. J Biol Chem 290: 5523-5532. doi: 10.1074/jbc.M113.532010
21. Dawson AP (1997) Calcium signalling: how do IP3 receptors work? Curr Biol. 7: 544-547. doi: 10.1016/S0960-9822(06)00277-6
22. Krauss G (2007) Biochemistry of Signal Transduction and Regulation. 4th edition. Silverthorn.
23. Brini M, Calì T, Ottolini D, Carafoli E (2013) Intracellular calcium Hhomeostasis and signaling. In: Banci L, Eeditors. Metallomics and the cell. Metal ions in life sciences 12: 120-154. doi: 10.1007/978-94-007-5561-1_5.
24. Dupont G (2014) Modeling the intracellular organization of calcium signaling. Wiley Interdiscip Rev Syst Biol Med 6: 227-237. doi: 10.1002/wsbm.1261.
25. De la Fuente IM (2010) Quantitative analysis of cellular metabolic dissipative, self organized structures. Int J Mol Sci. 11: 3540-3599. doi: 10.3390/ijms11093540.
26. De la Fuente IM (2013) Metabolic Dissipative Structures in Systems Biology of Metabolic and signaling Networks: Energy, Mass and Information Transfer In: Aon MA, Saks V, Schlattner U, Editors. Systems Biology of Metabolic and Signaling Networks. Springer pp 179-211
27. Goldbeter A (2002) Computational approaches to cellular rhythms. Nature 420: 238-245. doi: 10.1038/nature01259.
28. Goldbeter A (2007) Biological rhythms as temporal dissipative structures. In: Special volume in memory of Ilya Prigogine: Adv Chem Phys. 135: 253-295. doi: 10.1002/9780470121917.ch8.
29. Nicolis G, Prigogine I (1977) Self-organization in nonequilibrium systems: From dissipative structures to order through fluctuations. Wiley.
30. Ishii K, Hirose K, Iino M (2006) Ca^{2+} shuttling between endoplasmic reticulum and mitochondria underlying Ca^{2+} oscillations. EMBO 7: 390–396. doi: 1038/sj.embor.7400620
31. Newman EA (2001) Propagation of intercellular calcium waves in retinal astrocytes and Müller cells. J Neurosci 21: 2215-2223.
32. Bernardinelli Y, Magistretti PJ, Chatton JY (2004) Astrocytes generate Na+-mediated metabolic waves. Proc Natl Acad Sci USA 101: 14937–14942. doi: 10.1073/pnas.0405315101
33. Slaby O, Lebiedz D (2009) Oscillatory NAD(P)H waves and calcium oscillations in neutrophils? A modeling study of feasibility. Biophys J 96: 417–428. doi: 10.1016/j.bpj.2008.09.044
34. Goldbeter A, Dupont G, Berridge MJ (1990) Minimal model for signal-induced Ca^{2+} oscillations and for their frequency encoding through protein phosphorylation. Proc Nat Acad Sci 87: 1461–1465
35. Thomas AP, Bird GS, Hajnóczky G, Robb-Gaspers LD, Putney JW (1996) Spatial and temporal aspects of cellular calcium signalling. FASEB J 10: 1505–1517
36. Berridge M. Inositol trisphosphate and calcium signaling (1993) Nature 361: 315–325
37. Larsen AZ, Kummer U (2003) Information Processing in Calcium Signal Transduction. In: Falcke M, Malchow D, editors. Understanding Calcium Dynamics: Experiments and Theory (Lecture Notes in Physics). Berlin: Springer Verlag.

38. Prank K, Gabbiani F, Brabant G (2000) Coding efficiency and information rates in transmembrane signaling. Biosystems 55:15-22.
39. Nakano T, Liu J-Q (2009) Information transfer through calcium signaling In: Schmid A, Goel S, Wang W, Beiu V, Carrara S, editors. Lecture Notes of the Institute for Computer Sciences, Social Informatics and Telecommunications Engineering. Springer. pp 29-33
40. Nogueira RA, Varanda WA, Liebovitch LS (1995) Hurst analysis in the study of ion channel kinetics. Braz J Med Biol Res 28: 491-496.
41. Varanda WA, Liebovitch LS, Figueiroa JN, Nogueira RA (2000) Hurst analysis applied to the study of single calcium-activated potassium channel kinetics. J Theor Biol 206: 343-353.
42. Ludington WB, Wemmer KA, Lechtreck KF, Witman GB, Marshall WF (2013) Avalanche-like behavior in ciliary import. Proc Natl Acad Sci USA 110: 3925-3930. doi: 10.1073/pnas.1217354110.
43. Ramanujan VK, Biener G, Herman B (2006) Scaling behavior in mitochondrial redox fluctuations. Biophys J 90: L70-L72. doi: 10.1529/biophysj.106.083501.
44. Aon MA, Roussel MR, Cortassa S, O'Rourke B, Murray DB, Beckmann M, et al (2008) The scale-free dynamics of eukaryotic cells. Plos One 3:e3624. doi: 10.1371/journal.pone.0003624.
45. Pahle J, Green AK, Dixon CJ, Kummer U (2008) Information transfer in signaling pathways: a study using coupled simulated and experimental data. BMC Bioinformatics 9: 139. doi: 10.1186/1471-2105-9-139.
46. Wibral M, Lizier JT, Vögler S, Priesemann V, Galuske R (2014) Local active information storage as a tool to understand distributed neural information processing. Front Neuroinform 8:1. doi: 10.3389/fninf.2014.00001
47. Wibral M, Pampu N, Priesemann V, Siebenhühner F, Seiwert H, Lindner M, et al (2013) Measuring information-transfer delays. Plos One 8: e55809. doi: 10.1371/journal.pone.0055809
48. Hartzell C, Putzier I, & Arreola J (2005) Calcium-activated chloride channels. Annu. Rev. Physiol, 67: 719-58.
49. Cross NL (1981) Initiation of the activation potential by an increase in intracellular calcium in eggs of the frog, Rana pipiens. Dev Biol 85: 380–384.
50. Miledi R (1982) A calcium-dependent transient outward current in Xenopus laevis oocytes. Proc R Soc Lond B Biol Sci, 215: 491-497.
51. Gorelik R, & Gautreau, A (2014) Quantitative and unbiased analysis of directional persistence in cell migration. Nat. Protoc 9: 1931-1943
52. Richman JS & Moorman JR (2000). Physiological time-series analysis using approximate entropy and sample entropy. American Journal of Physiology-Heart and Circulatory Physiology 278: 2039-2049.
53. Cao L (1997) Practical method for determining the minimum embedding dimension of a scalar time series. Physica D. 110: 43-50.
54. Liu JZ, Zhang LD & Yue GH (2003) Fractal dimension in human cerebellum measured by magnetic resonance imaging. Biophysical Journal 85: 4041-4046.
55. Kilbas AA, Srivastava HM, Trujillo JJ (2006) Theory and Applications of Fractional Differential Equations. Elsevier Science.
56. Raj B, Van de Voorde M, & Mahajan Y (2017) Nanotechnology for Energy Sustainability, 3 Volume Set. John Wiley & Sons.
57. Goldberger AL, Rigney DR, & West BJ (1990) Chaos and Fractals in human physiology. Sci Am. 1990 Feb; 262:42-49.

Real-Time Radioactive Precursor of the April 16, 2016 Mw 7.8 Earthquake in Ecuador

Theofilos Toulkeridis[1⋆], Fernando Mato[1], Katerina Toulkeridis-Estrella[2], Juan Carlos Perez Salinas[3], Santiago Tapia[3], and Walter Fuertes[1]

[1]Universidad de las Fuerzas Armadas ESPE, Sangolquí, Ecuador
[2]Alliance Academy International, Quito, Ecuador
[3]NOVACERO, Lasso, Ecuador
⋆ttoulkeridis@espe.edu.ec

Abstract. On the 16th of April 2016, a Mw 7.8 earthquake impacted coastal Ecuador, being the most devastating registered in northern South America in this century so far. Three hours before, an unusual increase of the environmental radiation level has been registered at 222 km distance from the epicenter. Trough this study, we have been able to achieve an undeniable relation between such type of anomalies of geodynamic origin and the seismic activity in Ecuador, solving thus the uncertainties presented in related studies around this clear earthquake precursor. In this sense, our results demonstrate a full correlation in earthquake detection, reducing also the uncertainty window to less than a few hours.

Keywords: April 16 2016 Mw 7.8 Earthquake in Ecuador, earthquake precursors, environmental radiation, geological radioactivity, Early Warning System

1 Introduction

The deadliest of all natural hazards by death toll are earthquakes [1–5]. There are, at least one dozen of known earthquakes, which claimed more than hundred thousand lives, reaching up to more than 700 thousands in two single events in China [6–10]. Frequencies of seismic events have been studied by a variety of authors [11–14]. However, the most accepted data base is of the National Earthquake Information Center of the United States Geological Survey, where there are annually in average more than 1300 seismic events registered being stronger than magnitudes of 5, more than 130 stronger than magnitudes of 6 or higher, and up to 20 earthquakes with a magnitude of higher than 7. Practically

⋆ We are indebted to the company NOVACERO in Laso, Cotopaxi Province, who generously provided the database for this research. We also thank the Universidad de las Fuerzas Armadas ESPE for logistic and financial support. Fernando Mato acknowledges support from the Prometeo Project of the National Secretariat of Higher Education, Science, Technology and Innovation (SENESCYT), Ecuador.

all earthquakes with magnitudes higher than 6 being close to settlements or cities leave fatalities. There is a high amount of studies, which attempt to predict earthquakes [15–21] and try to be able to identify pre-monitoring signals [22–34]. Such studies may allow the installation of an early warning system, which in turn facilitates in even short time to take actions and protect life, property and certain infrastructure from incoming destructive seismic waves [35–38].

During the reactivation of the Cotopaxi volcano in central Ecuador [39], observations of the radioactivity determination in the environment lead to the idea, that such data may be able to interpret and predict the nearby occurring volcanic eruptions and also seismic events of certain magnitude. The main aim of our research is to establish a mechanism in which we will confirm a relation between the radiation of the environment and the potential prediction of strong seismic events, like the destructive earthquake of the 16th of April 2016 in coastal Ecuador [40].

There are several studies related to radiation as pre-earthquake sign [41–54]. In a particular study, such anomalies were reported for a variety of medium to strong earthquakes such as the M7.9, Bhuj, Gujarat, India in 2001, the M6.8 Boumerdes, North Algeria in 2003, M6.6 Bam Southeastern Iran in 2003 and the M9.0 SumatraAndaman Islands, Northern Sumatra, being a mega trust event in 2004 [54]. The anomalous variation of the radiation has been determined by infrared satellite data and occurred a few days to weeks (4-20 days) prior to the main events [54]. These anomalies are speculated to have been triggered close or within active tectonic faults due to a complex interaction of the existing stress, electrochemical and thermodynamic processes between the lithosphere, hydrosphere and atmosphere as part of electromagnetic phenomena related to earthquake activity [54]. Nevertheless, although the relation between radiation in seismic active areas has been observed in a variety of areas, this is the first time documented on ground data and with a more accurate spatio-temporal earthquake location.

2 Geodynamic Situation of Ecuador and Previous Coastal Earthquakes

Due to its geodynamic situation along the Pacific Rim, the coastal Ecuadorian continental platform is a regularly target of earthquake activity and tsunami impacts [55–57]. The active continental margin and associated subduction zone between the oceanic Nazca Plate with the continental South American and Caribbean Plates, both separated by the Guayaquil-Caracas Mega Shear [58–60] give rise to tsunamis of tectonic as well submarine landslide origin [56, 61–65].

Earthquakes and tsunamis have been credited also to the Galápagos volcanism [66]. The active Galápagos hotspot has produced several voluminous shield-volcanoes, moving towards the ESE, due to the movement of the overlying Nazca oceanic plate [66, 67]. The main Galápagos Islands are located south of the E-W-trending Galápagos Spreading Center, east of the N-S-trending East Pacific Rise and some 1000 km west of the Ecuadorian mainland. Due to the

volcanic activity and the subsequent plate drifting, two aseismic volcanic ridges were created. The first being the Cocos Ridge is moving to the NE while the second, being the Carnegie Ridge, is moving to the East above the Cocos and Nazca Plates respectively [68]. These submarine extinct volcanic ridges are the result of cooling/contraction reactions of magma, as they slowly sunk below the sea surface due to the lack of magma supply, lithospheric movement and strong erosional processes. With time, these submarine volcanic ridges, as well as various microplates, have accreted on the South American continent [69, 70]. Nonetheless, such aseismic ridges like the Carnegie Ridge become and obstacle in the oblique subduction process and may generate within the subduction zone a potential valve of marine quakes, earthquakes and occasionally tsunamis along the Ecuadorian coast [56]. The Carnegie Ridge collides towards the Ecuadorian continental margin with a velocity of as low as 5 cm per year at a latitude between 1N and 2S [71].

From the known record of the last two centuries, the Ecuadorian shoreline has witnessed a dozen times strong earthquakes and marine quakes, some of which generated tsunamis by mainly local origins with various intensities one being of up to 8.8 Mw in 1906 [56, 72–76], while evidences of other events have been recorded by paleo-tsunami deposits [77]. Further prominent examples of earthquakes with subsequent tsunamis along the Ecuador-Colombia subduction zone include tsunamis in 1942 (Mw 7.8), 1958 (Mw 7.7) and 1979 (Mw 8.2) within the 600-km long rupture area of the great 1906 event [78]. While the 1906 event caused the death of up to 1500 persons in Ecuador and Colombia with an unknown financial damage to the existing infrastructure, the 1979 tsunami killed in Colombia at least 807 persons and destroyed approximately 10,000 homes, knocking out electric power and telephone lines [79, 80]. The evaluation of the last marine quakes, which generated tsunamis, suggests that the probability of a major or great earthquake in this margin region is enormous, especially as there must be substantial strain accumulation in this region [56]. Additionally, given into consideration that the last earthquake in 1979 did not release the amount of energy as the 1906 event, there has been a calculated high probability in the near future, that an earthquake within the Ecuadorian-Colombian trench may would generate a tsunami of similar magnitude to that of 1906, which might be even more destructive than the one in the past if it occurs near high tide [56]. The potential of high losses and damage is given by the fact that the infrastructure of the fishing, tourism and other industries and the movement to live along the beaches, have been highly developed within the last decades along the Ecuadorian coasts. Based on historic known impacts of tsunamis in Ecuador in the last two centuries, the probability of a strike in 2015 has been of about 87% [57].

3 The Earthquake of the 16th of April 2016

In the late afternoon of Saturday, at 18:58:36 (UTC-05:00) local time, a devastating earthquake with a magnitude of 7.8 Mw impacted coastal Ecuador [81]. The

seismic event with an epicenter 29 km SSE of Muisne, Province of Esmeraldas (Fig. 1, 2) occurred within a depth of 21 km, killing 663, filling tens of thousands in refuges camps and affecting some two million persons directly. In many aspects, the mentioned earthquake has many similarities with the earthquake of the 14th of May 1942. Nonetheless, the resulting tsunami based most probably on a triggered submarine landslide did not have any remarkable impact [40].

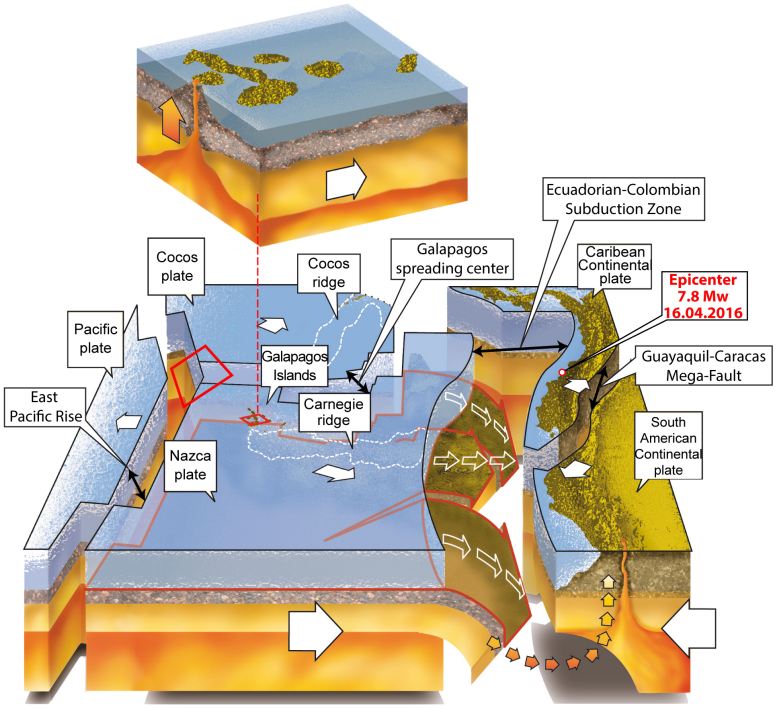

Fig. 1. Geodynamic setting of Ecuador, the Galapagos Islands and the Carnegie Ridge. Adapted from [40] and [57].

The earthquake impacted a large part of a variety of coastal cities destroying a high amount of some close-by villages and cities, Pedernales, Jama, Chone, Portoviejo among others (Fig. 2), in which lines of electricity transmission, infrastructure of water supply, hospitals, schools, private and public buildings, main roads and highways have been severely affected or even completely destroyed. The costs of the damages of the mentioned infrastructure are summing up an approximate loss of some 3.3 billion USD [40, 82].

After the mainshock, 85 aftershocks between 3.8 Mw and 6.8 Mw were recorded by USGS in Ecuador until May 24, last day until we have processed

data. The epicenters were localized within a rectangle of coordinates [79.5 W - 81.5 W, 2 S - 1 N], reaching the highest magnitudes around the rupture zone, and 86.05% of them during the first 10 subsequent days.

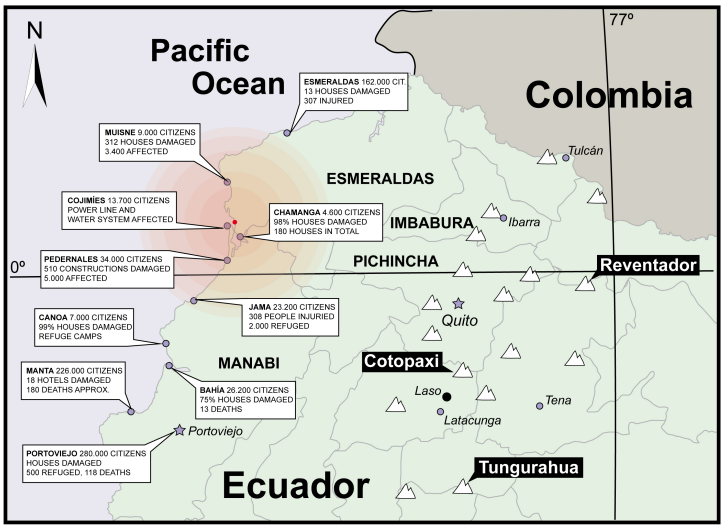

Fig. 2. Epicenter of the 7.8 Mw earthquake (red dot) and a selection of damages in the coastal area. Note location of Reventador, Cotopaxi and Tungurahua volcanoes as well as the station of Laso (black dot), where the radiation of the environment has been determined.

4 Analytical Procedures

A LUDLUM MODEL of the 4525 SERIESTM enabled to determine the occurrences of natural and artificial radioactivity in the environment close to the company NOVACERO, which provides a variety of steel products. In order to detect radioactivity especially in vehicles in a pass-through or drive-through scanning modus, the Model 4525 Radiation Portal Monitor (RPM) has been installed in late 2014, some 22 km SW of the Cotopaxi volcano in central Ecuador. The RPM is a system with sensitive gamma and optional neutron detectors for detecting small amounts of radiation. When no vehicle drives through the scanner, the natural background of radioactivity is measured constantly and simultaneously (one measurement per minute). When a radiation alarm occurs, the Supervisor and any Echo stations will sound an audible alert. The system determines if the alarm is a Naturally Occurring Radioactive Alarm (NORM). NORM consists of materials enriched with radioactive elements found in the environment, such as uranium, thorium, and potassium and any of their decay products such as

radium and radon. These types of alarms are characterized as having a high background over the entire length of the occupancy rather than the "spike" of a typical gamma alarm.

Many factors have to be considered when attempting to do this: (1) Background radiation is not constant. It is continuously changing due to cosmic events, weather (eg. beginning of rainstorms), and other influences. Oilfield pipe, hot water heaters, and industrial piping will sometimes contain scale that is radioactive. Most alarms are the result of NORM; (2) Medical tests that use a radioactive dye or tracer are yet another problem. Patients can be released from the hospital reading several thousand R/hr or less than 100 μSv/hr, and set off RPMs 30 m (100 ft) away; (3) A third problem is that of radiographers and certified welders who use a powerful radiation source to check their material or welds for cracks. This radiation is powerful enough to set off RPMs 3 km away.

5 Results and Discussion

Radiation of the environment in central Ecuador has been determined almost continuously realizing data at every minute of the day since Mid-January of 2015 up to present day. However, most of the time there has been only the regular day-by-day radiation level of the environment defined as background radiation level (Fig. 3d) with 6200 becs per minute. This radiation of the environment appeared with no significant changes since the beginning of the measurements and has been changed only by the appearance of some seismic events, such originating by volcanic nature or fault-triggered.

Therefore, all the main volcanic eruptions of the close-by Cotopaxi volcano during its visible reactivation in spring of 2015 have been registered by the RPM, prior their occurrences. Other temporal eruptive activity and corresponding environmental radiation inside the same time window originating from the Tungurahua and Reventador volcanoes in Ecuador [83, 84], corresponding craters being in a distance of 73 and 132 km from the RPM respectively (Fig. 2), were not registered or identified in our data base, most probably due to their low intensity. Additionally, we have been detected a clear pattern in the determination of the environmental radiation of seismic activity in Ecuador since 2015 for all events registered by USGS with magnitudes above 4.9 Mw.

A few hours before an earthquake generation, from 1 hour (Fig. 3a) to 5 hours (Fig. 3b), an unusual high level of radioactivity has been detected by the RPM, reaching levels between 6800 bec/min (Fig. 3b; 3c) and 7465 bec/min (Fig. 3a). This behaviour is related to almost all of the earthquakes recorded. We have also identified the delay in the generation of the earthquake is in almost all cases inversely proportional to the level of radiation reached and to the duration of such anomalies.

According to the general behaviour of the precursor anomalies identified, on the early hours of the 16th of April in 2016, an unusual radiation level has been registered by the RPM, which we interpret as a clear pre-monitoring signal of a major seismic event resulting to the most devastating Earthquake of northern

South America in this century so far. The alteration of the regular background radioactivity started around 15.30 p.m. and lasted for about almost two hours in which the radiation increased by 650 bec/min, finding a peak level of 6850 bec/min some minutes after the start (Fig. 3c). After reaching this peak level, radiation dropped down to regular level three hours later, sinking down to 6200 bec/min at around 18:45, some minutes prior the Earthquake of 18:58 (Fig. 3c), of which epicenter has been located some 222 km west-northwest of the RPM. This behaviour or pattern prior a seismic event has been previously observed with less intense earthquakes as presented earlier (Fig. 3a; 3b).

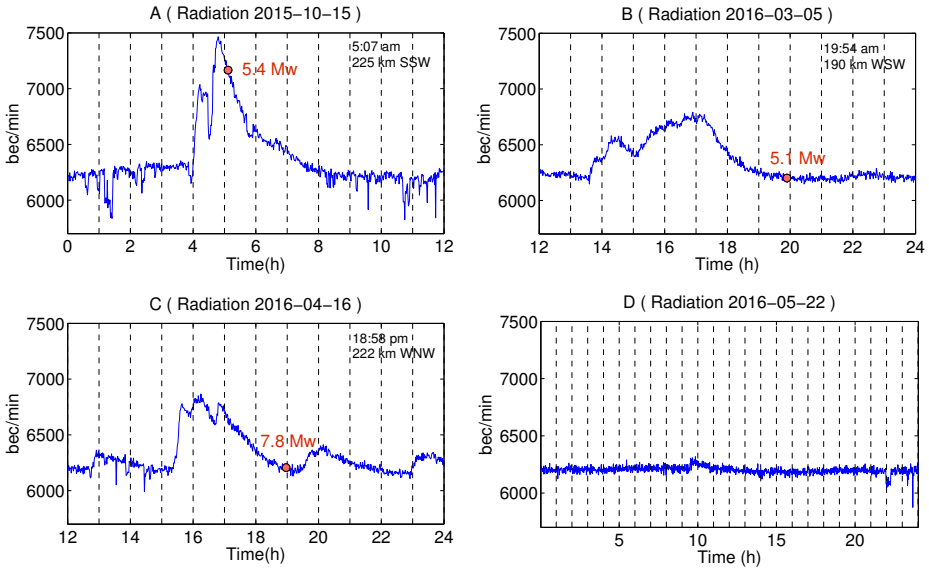

Fig. 3. a) Typical pre-earthquake (5.4 Mw) radiation behaviour of the 15th of October 2015 at 2.50 S, 78.76 W with a depth of 97,1 km (USGS, 2015); b) Typical pre-earthquake (5.1 Mw) radiation behaviour at the 5th of March 2016 at 1.43 S, 80.40 W with a depth of 10 km (USGS, 2016); c) Main 7.8 Mw earthquake of the 16th of April 2016 with different radiation behaviour than regular days. Location of epicenter has been at 0.35 N, 79.93 W at a depth of 21 km (USGS, 2016); d) Regular radiation level of 24 hours of the 22nd of May 2016.

The most plausible origin of such radiation anomalies prior to strong earthquakes might be the result of a complex interaction and coupling behavior of the Lithosphere, Hydrosphere, Atmosphere and Ionosphere [54, 88, 89]. The degree of radiation anomaly certainly depends on the intensity of the earthquake as well as local to regional atmospheric conditions, but will have always a direct link to the magnitude of the earthquake [54]. As such outgoing long wave earth

radiation anomalies and latent increases of temperatures have been noticed prior several strong earthquakes [85–87], some of them which even generated severe tsunamis, the application of an early alert system may be applied in a variety of environments such as active continental rims, like the subduction zones around the Pacific Ocean as well as around transform fault zones, like the Guayaquil-Caracas Mega shear in south America or the San Andres fault in the USA, being able to give enough warning time in order to evacuate people from vulnerable places within an adequate period of time.

6 Conclusions

It has been highlighted the important precursor role of environmental radiation in the precise location of earthquakes in Ecuador. A direct application and benefit of our study may be to achieve an accurate early warning system based on the data presented. The radiation data demonstrate clearly undeniable anomalies, which allow during their development an extremely early warning time towards society and administrators of basic infrastructure to react ahead of a potential catastrophic seismic event. Nonetheless, a more spatial resolution is needed by means of a sensors array, which we propose to be installed based on an efficient and therefore strategic distribution in the entire country of Ecuador. This sensors array will provide then key information for the complex Earthquake Early Warning System, at which we are progressing in Ecuador.

References

1. Kahn, M.E.: The death toll from natural disasters: the role of income, geography, and institutions. Review of economics and statistics. 87(2), 271–284 (2005)
2. Anbarci, N., Escaleras, M. and Register, C.A.: Earthquake fatalities: the interaction of nature and political economy. Journal of Public Economics. 89(9), 1907–1933 (2005)
3. Raschky, P.A.: Institutions and the losses from natural disasters. Natural Hazards and Earth System Science. 8, 627–634 (2008)
4. Marano, K.D., Wald, D.J. and Allen, T.I.: Global earthquake casualties due to secondary effects: a quantitative analysis for improving rapid loss analyses. Natural hazards. 52(2), 319–328 (2010)
5. Holzer, T.L. and Savage, J.C.: Global earthquake fatalities and population. Earthquake Spectra. 29(1), 155–175 (2013)
6. Butler, R., Stewart, G.S. and Kanamori, H.: The July 27, 1976 Tangshan, China earthquakea complex sequence of intraplate events. Bulletin of the Seismological Society of America. 69(1), 207–220 (1979)
7. Chen, Y. ed.: The great Tangshan earthquake of 1976: an anatomy of disaster. Pergamon (1988)
8. Gang, Q.: The Great China Earthquake. Foreign Languages Press, Beijing (1989)
9. Hou, J.J., Han, M.K., Chai, B.L. and Han, H.Y.: Geomorphological observations of active faults in the epicentral region of the Huaxian large earthquake in 1556 in Shaanxi Province, China. Journal of structural geology. 20(5), 549–557 (1998)

10. Gupta, H.K., Rao, N.P., Rastogi, B.K. and Sarkar, D.: The deadliest intraplate earthquake. Science. 291(5511), 2101–2102 (2001)
11. McGuire, R.K.: Probabilistic seismic hazard analysis and design earthquakes: closing the loop. Bulletin of the Seismological Society of America. 85(5), 1275–1284 (1995)
12. Shome, N., Cornell, C.A., Bazzurro, P. and Carballo, J.E.: Earthquakes, records, and nonlinear responses. Earthquake Spectra. 14(3), 469–500 (1998)
13. Ruff, L.J., and Kanamori, H.: Seismicity and the subduction process. Physics of the Earth and Planetary Interiors. 23 (3), 240-252 (1980)
14. McCaffrey, R.: Global frequency of magnitude 9 earthquakes. Geology. 36(3), 263–266 (2008)
15. Scholz, C.H., Sykes, L.R. and Aggarwal, Y.P.: Earthquake prediction: a physical basis. Science. 181(4102), 803–810 (1973)
16. Rikitake, T.: Earthquake prediction. Earth-Science Reviews. 4, 245–282 (1968)
17. Aki, K.: A probabilistic synthesis of precursory phenomena. Earthquake Prediction. 566–574 (1981)
18. Smith, W.D.: Predicting Earthquakes in New-Zealand, Search. 21 (7), 223–226 (1990)
19. Varotsos, P. and Lazaridou, M.: Latest aspects of earthquake prediction in Greece based on seismic electric signals. Tectonophysics. 188(3), 321–347 (1991)
20. Keilis-Borok, V.: Earthquake prediction: State-of-the-art and emerging possibilities. Annual review of earth and planetary sciences. 30(1), 1–33 (2002)
21. Johnston, M.J.S., Borcherdt, R.D., Linde, A.T. and Gladwin, M.T.: Continuous borehole strain and pore pressure in the near field of the 28 September 2004 M 6.0 Parkfield, California, earthquake: Implications for nucleation, fault response, earthquake prediction, and tremor. Bulletin of the Seismological Society of America. 96(4B), S56–S72 (2006)
22. Allegre, C.J., Le Mouel, J.L. and Provost, A.: Scaling rules in rock fracture and possible implications for earthquake prediction. Nature. 297(5861), 47–49 (1982)
23. Asteriadis, G. and Livieratos, E.: Pre-seismic responses of underground water level and temperature concerning a 4.8 magnitude earthquake in Greece on October 20, 1988. Tectonophysics. 170(1), 165–169 (1989)
24. Smith, W.D.: Resolution and significance assessment of precursory changes in mean earthquake magnitudes, Geophys. J. Int. 135 (2), 515–522 (1998)
25. Sidorin, A.Y.: Search for earthquake precursors in multidisciplinary data monitoring of geophysical and biological parameters. Natural Hazards and Earth System Science. 3(3/4), 153–158 (2003)
26. Freund, F.T.: Pre-earthquake signals? Part I: Deviatoric stresses turn rocks into a source of electric currents. Natural Hazards and Earth System Science. 7(5), 535–541 (2007)
27. Cicerone, R. D., Ebel, J. E. and Britton, J.: A systematic compilation of earthquake precursors. Tectonophysics. 476(3), 371–396 (2009)
28. Freund, F.T., Kulahci, I.G., Cyr, G., Ling, J., Winnick, M., Tregloan-Reed, J. and Freund, M.M.: Air ionization at rock surfaces and pre-earthquake signals. Journal of Atmospheric and Solar-Terrestrial Physics. 71(17), 1824–1834 (2009)
29. Akhoondzadeh, M., Parrot, M. and Saradjian, M.R.: Electron and ion density variations before strong earthquakes (M¿ 6.0) using DEMETER and GPS data. Natural Hazards and Earth System Science. 10(1), 7–18 (2010)
30. Pulinets, S. and Ouzounov, D.: LithosphereAtmosphereIonosphere Coupling (LAIC) modelAn unified concept for earthquake precursors validation. Journal of Asian Earth Sciences. 41(4), 371–382 (2011)

31. Vigny, C., Socquet, A., Peyrat, S., Ruegg, J.C., Mtois, M., Madariaga, R., Morvan, S., Lancieri, M., Lacassin, R., Campos, J. and Carrizo, D.: The 2010 Mw 8.8 Maule megathrust earthquake of Central Chile, monitored by GPS. Science. 332(6036), 1417–1421 (2011)
32. Yao, Y., Chen, P., Wu, H., Zhang, S. and Peng, W.: Analysis of ionospheric anomalies before the 2011 M w 9.0 Japan earthquake. Chinese Science Bulletin. 57(5), 500–510 (2012)
33. Tramutoli, V., Aliano, C., Corrado, R., Filizzola, C., Genzano, N., Lisi, M., Martinelli, G., Pergola, N.: On the possible origin of thermal infrared radiation (TIR) anomalies in earthquake-prone areas observed using robust satellite techniques (RST). Chem. Geol. 339, 157-168 (2013)
34. Eleftheriou, A., Filizzola, C., Genzano, N., Lacava, T., Lisi, M., Paciello, R., Pergola, N., Vallianatos, F. and Tramutoli, V.: Long-Term RST Analysis of Anomalous TIR Sequences in Relation with Earthquakes Occurred in Greece in the Period 20042013. Pure and Applied Geophysics. 173(1), 285–303 (2016)
35. Suárez, G., Novelo, D. and Mansilla, E.: Performance evaluation of the seismic alert system (SAS) in Mexico City: a seismological and a social perspective. Seismological Research Letters. 80(5), 707–716 (2009)
36. Rainieri, C., Fabbrocino, G. and Cosenza, E.: Integrated seismic early warning and structural health monitoring of critical civil infrastructures in seismically prone areas. Structural Health Monitoring. 10(3), 291–308 (2011)
37. Satriano, C., Wu, Y.M., Zollo, A. and Kanamori, H.: Earthquake early warning: Concepts, methods and physical grounds. Soil Dynamics and Earthquake Engineering. 31(2), 106–118 (2011)
38. Oliveira, C.S., de S, F.M., Lopes, M., Ferreira, M.A. and Pais, I.: Early Warning Systems: Feasibility and End-Users' Point of View. Pure and Applied Geophysics. 172(9), 2353–2370 (2015)
39. Toulkeridis, T., Arroyo, C.R., Cruz D'Howitt, M., Debut, A., Vaca, A.V., Cumbal, L., Mato, F. and Aguilera, E.: Evaluation of the initial stage of the reactivated Cotopaxi volcano - Analysis of the first ejected fine-grained material. Natural Hazards and Earth System Sciences. 3(11), 6947–6976 (2015)
40. Toulkeridis, T., Chunga, K., Rentería, W., Rodriguez, F., Mato, F., Nikolaou, S., Cruz D'Howitt, M., Besenzon, D., Ruiz, H., Parra, H. and Vera-Grunaer, X.: The 7.8 Mw Earthquake and Tsunami of the 16th April 2016 in Ecuador - Seismic evaluation, geological field survey and economic implications. J. Tsunami Soc. Int, in press. (2017)
41. Madariaga, R.: High-frequency radiation from crack (stress drop) models of earthquake faulting. Geophysical Journal International. 51(3), 625–651 (1977)
42. Gokhberg, M.B., Morgounov, V.A., Yoshino, T. and Tomizawa, I.: Experimental measurement of electromagnetic emissions possibly related to earthquakes in Japan. Journal of Geophysical Research: Solid Earth. 87(B9), 7824–7828 (1982)
43. Dea, J.Y., Richman, C.I. and Boerner, W.M.: Observations of seismo-electromagnetic earthquake precursor radiation signatures along Southern Californian fault zones: evidence of long-distance precursor ultra-low frequency signals observed before a moderate Southern California earthquake episode. Canadian journal of physics. 69(8-9), 1138–1145 (1991)
44. Serebryakova, O.N., Bilichenko, S.V., Chmyrev, V.M., Parrot, M., Rauch, J.L., Lefeuvre, F. and Pokhotelov, O.A.: Electromagnetic ELF radiation from earthquake regions as observed by lowaltitude satellites. Geophysical Research Letters. 19(2), 91–94 (1992)

45. Virk, H.S. and Singh, B.: Radon anomalies in soil-gas and groundwater as earthquake precursor phenomena. Tectonophysics. 227(1), 215–224 (1993)
46. Zeng, Y., Aki, K. and Teng, T.L.: Mapping of the highfrequency source radiation for the Loma Prieta earthquake, California. Journal of Geophysical Research: Solid Earth. 98(B7), 11981–11993 (1993)
47. Hartzell, S., Liu, P. and Mendoza, C.: The 1994 Northridge, California, earthquake: Investigation of rupture velocity, risetime, and highfrequency radiation. Journal of Geophysical Research: Solid Earth. 101(B9), 20091–20108 (1996)
48. Maeda, K. and Tokimasa, N.: Decametric radiation at the time of the Hyogoken Nanbu Earthquake near Kobe in 1995. Geophysical research letters. 23(18), 2433–2436 (1996)
49. Ouzounov, D. and Freund, F.: Mid-infrared emission prior to strong earthquakes analyzed by remote sensing data. Advances in Space Research. 33(3), 268–273 (2004)
50. Tronin, A.A., Hayakawa, M. and Molchanov, O.A.: Thermal IR satellite data application for earthquake research in Japan and China. Journal of Geodynamics. 33(4), 519–534 (2002)
51. Pulinets, S.A. and Dunajecka, M.A.: Specific variations of air temperature and relative humidity around the time of Michoacan earthquake M8. 1 Sept. 19, 1985 as a possible indicator of interaction between tectonic plates. Tectonophysics. 431(1), 221–230 (2007)
52. Ni, S., Kanamori, H. and Helmberger, D.: Seismology: energy radiation from the Sumatra earthquake. Nature. 434(7033), 582–582 (2005)
53. Pulinets, S.A., Ouzounov, D., Karelin, A.V., Boyarchuk, K.A. and Pokhmelnykh, L.A.: The physical nature of thermal anomalies observed before strong earthquakes. Physics and Chemistry of the Earth. Parts A/B/C, 31(4), 143–153 (2006)
54. Ouzounov, D., Liu, D., Chunli, K., Cervone, G., Kafatos, M. and Taylor, P.: Outgoing long wave radiation variability from IR satellite data prior to major earthquakes. Tectonophysics. 431(1), 211–220 (2007)
55. Gusiakov, V.K.: Tsunami generation potential of different tsunamigenic regions in the Pacific. Marine Geology. 215(1-2), 3–9 (2005)
56. Pararas-Carayannis, G.: Potential of tsunami generation along the Colombia/Ecuador subduction margin and the Dolores-Guayaquil Mega-Thrust. Science of Tsunami Hazards. 31(3), 209–230 (2012)
57. Rodriguez, F., D'Howitt, M.C., Toulkeridis, T., Salazar, R., Romero, G.E.R., Moya, V.A.R. and Padilla, O.: Journal of Tsunami Society International. Journal of Tsunami Society International. 35(1), 18–33 (2016)
58. Kellogg, J.N. and Vega, V.: Tectonic development of Panama, Costa Rica and the Colombian Andes: Constraints from Global Positioning System geodetic studies and gravity. Geol. Soc. Am. Special Paper 295, 75-90 (1995)
59. Gutscher, M.A., Malavieille, J.S.L. and Collot, J.-Y.: Tectonic segmentation of the North Andean margin: impact of the Carnegie ridge collision. Earth Planet. Sci. Lett. 168, 255-270 (1999)
60. Egbue, O. and Kellogg, J.: Pleistocene to Present North Andean escape. Tectonophysics. 489, 248–257 (2010)
61. Shepperd, G.L. and Moberly, R.: Coastal structure of the continental margin, northwest Peru and southwest Ecuador. Geological Society of America Memoirs. 154, 351–392 (1981)
62. Pontoise, B. and Monfret, T.: Shallow seismogenic zone detected from an offshore-onshore temporary seismic network in the Esmeraldas area (northern Ecuador). Geochemistry, Geophysics, Geosystems. 5(2), (2004)

63. Ratzov, G., Sosson, M., Collot, J. Y., Migeon, S., Michaud, F., Lopez, E. and Le Gonidec, Y.: Submarine landslides along the North EcuadorSouth Colombia convergent margin: possible tectonic control. In Submarine Mass Movements and Their Consequences. Springer Netherlands. 47–55 (2007)
64. Ratzov, G., Collot, J. Y., Sosson, M. and Migeon, S.: Mass-transport deposits in the northern Ecuador subduction trench: Result of frontal erosion over multiple seismic cycles. Earth and Planetary Science Letters. 296(1), 89–102 (2010)
65. Ioualalen, M., Ratzov, G., Collot, J. Y. and Sanclemente, E.: The tsunami signature on a submerged promontory: the case study of the Atacames Promontory, Ecuador. Geophysical Journal International. 184(2), 680–688 (2011)
66. Toulkeridis, T.: Volcanic Galápagos Volcánico. Ediecuatorial, Quito, Ecuador (2011)
67. Holden, J. C. and Dietz, R. S.: Galapagos gore, NazCoPac triple junction and Carnegie/Cocos ridges. Nature. 235, 266–269 (1972)
68. Harpp, K. S., Fornari, D. J., Geist, D. J. and Kurz, M. D.: Genovesa Submarine Ridge: A manifestation of plumeridge interaction in the northern Galpagos Islands. Geochemistry, Geophysics, Geosystems. 4(9), (2003)
69. Reynaud, C., Jaillard, ., Lapierre, H., Mamberti, M. and Mascle, G. H.: Oceanic plateau and island arcs of southwestern Ecuador: their place in the geodynamic evolution of northwestern South America. Tectonophysics. 307(3), 235–254 (1999)
70. Harpp, K. S. and White, W. M.: Tracing a mantle plume: Isotopic and trace element variations of Galpagos seamounts. Geochemistry, Geophysics, Geosystems. 2(6), (2001)
71. Pilger, R. H.: Kinematics of the South American subduction zone from global plate reconstructions. Geodynamics of the eastern Pacific region, Caribbean and Scotia arcs. 113–125 (1983)
72. Rudolph E. and Szirtes S.: Das kolumbianische Erdbeben am 31 Januar 1906, Gerlands Beitr. z. Geophysik. 2, 132–275 (1911)
73. Kelleher, J.A.: Ruptures zones of large South American earthquakes and some predictions. Journal of Geophysical Research. 77(11), 2087–2103 (1972)
74. Beck, S.L. and Ruff, L.J.: The rupture process of the great 1979 Colombia earthquake: evidence for the asperity model. J.Geophys. Res. 89, 9281-9291 (1984)
75. Kanamori, H. and McNally, K.C.: Variable rupture mode of the subduction zone along the EcuadorColombia coast. Bull. Seismol. Soc. Am. 72(4), 1241-1253 (1982)
76. Swenson, J.L. and Beck, S.L.: Historical 1942 Ecuador and 1942 Peru subduction earthquakes, and earthquake cycles along ColombiaEcuador and Peru subduction segments. Pure Appl. Geophys. 146(1), 67-101 (1996)
77. Chunga, K. and Toulkeridis, T.: First evidence of paleo-tsunami deposits of a major historic event in Ecuador. Science of Tsunami Hazards. 33, 55–69 (2014)
78. Collot, J.Y., Marcaillou, B., Sage, F., Michaud, F., Agudelo, W., Charvis, P., Graindorge, D., Gutscher, M.A. and Spence, G.: Are rupture zone limits of great subduction earthquakes controlled by upper plate structures? Evidence from multichannel seismic reflection data acquired across the northern Ecuadorsouthwest Colombia margin. Journal of Geophysical Research: Solid Earth. 109(B11), (2004)
79. Pararas-Carayannis, G.: The Earthquake and Tsunami of December 12, 1979, in Colombia. Intern. Tsunami Information Center Report. Abstracted article in Tsunami Newsletter. 13(1), (1980)
80. USGS (United States Geological Service): Historic Earthquakes, 1906 January 31st. (2016)
81. USGS (United States Geological Service): M7.8 - 29km SSE of Muisne, Ecuador. (2016)

82. El Telegrafo.: http://www.eltelegrafo.com.ec/noticias/ecuador/3/manana-se-daran-a-conocer-cifras-oficiales-del-costo-del-terremoto. (2016)
83. Global Volcanism Program. Report on Tungurahua (Ecuador). In: Sennert, S K (ed.), Weekly Volcanic Activity Report, 24 February-1 March 2016. Smithsonian Institution and US Geological Survey. (2016)
84. Global Volcanism Program. Report on Reventador (Ecuador). In: Sennert, S K (ed.), Weekly Volcanic Activity Report, 9 March-15 March 2016. Smithsonian Institution and US Geological Survey. (2016)
85. Cervone, G., Singh, R.P., Kafatos, M., Yu, C. Wavelet maxima curves of surface latent heat flux anomalies associated with Indian earthquakes. Natural Hazards and Earth System Sciences 5 (27), 8799. (2005)
86. Pulinets, S., Ouzounov, D., Ciraolo, L., Singh, R., Cervone, G., Leyva, A., Dunajecka, M., Karelin, Boyarchuk, K. Thermal, atmospheric and ionospheric anomalies around the time of Colima M7.8 Earthquake of January 21, 2003. Annales Geophysicae 24, 835849. (2006)
87. Dey, S., Sarkar, S., Singh, R.P. Anomalous changes in column water vapor after Gujarat earthquake. Advances in Space Research 33 (3), 274278. (2004)
88. Pulinets, S.A., Boyarchuk, K.A., Hegai, V.V., Kim, V.P., Lomonosov, A.M. Quasi-electrostatic model of atmospherethermo- sphereionosphere coupling. Advances in Space Research 26 (8), 12091218. (2000)
89. Hayakawa, M., Molchanov, O.A. (Eds.). Seismo Electromagnetic Lithosphere Atmosphere coupling. Terra Scientific Publishing Company (TERRAPUB), Tokyo. (2002)

Local selection of learning data for neural networks in prediction of PM10 pollution

Krzysztof SIWEK[1]
Stanislaw OSOWSKI[1,2]
[1]Warsaw University of Technology
[2]Military University of Technology
Warsaw, POLAND

Abstract. The paper presents the new, local selection of learning data to the learning problem in prediction of daily average PM10 using neural networks. The learning stage of networks is performed for each testing vector separately. The actual testing vector is compared to the learning data base and the set of its vectors closest to the actual testing vector is selected and then used in learning. Thanks to such approach the actual predictor is trained on the data set representative for the particular task. The numerical experiments performed on the real data of the PM10 pollution in Warsaw using few types of neural networks have shown that developed computerized system generates prediction of the significantly increased accuracy.

Keywords: PM10 forecasting; neural networks; local selection of data; computational intelligence

1 Introduction

The precise prediction of air pollution for the next day belongs to difficult problems due its high changes from day to day [1]. Special attention is given to the particulate matter PM10 (PM of diameter up to 10μm), which is very dangerous for the health of people [2]. Therefore, the forecasting of its level for the next day is needed to allow counteracting it.

Many papers deal with this problem. Actually the best results have been obtained by applying artificial neural networks. The proposed solutions exploit such networks as multilayer perceptron (MLP) [1],[3],[4],[5] radial basis function (RBF) [6],[7], Elman network [6], principal component analysis [8] as well as Support Vector Machine [9]. The success in prediction depends on the selection of diagnostic features used as input attributes, type of applied network as well as organization of learning procedure.

It was found that the predicted atmospheric variables (temperature, wind, humidity, etc.) related to the day under prediction are of great importance in preparing the diagnostic features, because these variables form the platform on the basis of which the pollution is created. In our climate the season of the year (spring, summer, autumn, winter) influences also the pollution due to the need of heating houses in cold seasons of the year. The last but not least is the type of the day, since the transport vehicles of the street, especially their intensity, depend on the day type and represent a significant source of dust.

The traditional approach to learning is to split the data set into two parts: the learning and testing subsets. The network is adapted using the learning part and then tested on the testing data. We propose here different approach. The learning phase of the network is done separately for each testing vector and is performed on the specially selected learning subset, chosen for the individual testing vectors. Instead of one learning phase of the network we apply as many learning stages as is the number of testing vectors. The learning set is formed from only the data vectors which are closest to the actually applied testing vector. Thanks to this the network in learning phase is supplied only by the data similar to the actual testing vector. The learning problem is easier and specializes in specific forms of testing data. Thanks to this the accuracy of prediction can be increased in a significant way.

The numerical experiments performed for the daily average PM10 pollution data measured within 4 years in Warsaw, Poland have confirmed the superiority of this approach. All quality measures: mean absolute error, root mean square error, mean absolute percentage error, correlation of the prediction and target data as well as index of agreement have been improved.

2 Proposed solution

2.1 Feature generation

The first problem that should be solved is selection of the most important diagnostic features, which will be applied as the input attributes to the predicting networks. These features are created on the basis of the atmospheric parameters (temperature,

humidity, wind, insolation), season of the year, type of the day and the past (known) history of pollution changes in the previous day. On the basis of these variables different descriptors of the process (potential diagnostic features) are created by using different mathematical operations, such as derivative, gradient, estimation of trend of their change, extreme values, etc.

On the basis of our experience in this field the potential diagnostic features have been defined in the following way. The first subset is formed from the environmental parameters forecasted for the next day by the responsible agenda of the country. They include the 24-hour average value of temperature in the particular place, wind speed, wind direction, humidity, pressure and insolation. The next subset is formed from the known past day parameters. They include the average, maximum and minimum values of temperature and pressure, the average and maximum pollution corresponding to the previous day, linear trend of changing the hourly pollution of the previous day, the prediction of the average pollution for the forecasted day made on the basis of this linear trend and the elements coding the season of the year (2-element binary code representing winter, spring, summer and autumn) and day type of the week (one binary code representing working and weekend days). The last subset of features is created by the pollution level for all hours of the previous day. As a result the set of 55 potential features has been generated [9]. This set was subject to normalization, implemented by dividing the real values of the particular feature by their mean in all observations.

2.2 Feature selection

In the process of the problem analysis the set of 55 descriptors has been obtained. Not all of them are of equal prognostic ability. Therefore the stage of their selection should be applied. To diversify the view on the forecasting task we have applied 2 different procedures: the stepwise fit and genetic algorithm. Thanks to the application of different selection mechanisms we expect different contents of the selected sets. They will present the input attributes to the predicting system.

The stepwise fit belongs to popular methods and relies on adding and removing particular features from the already established set [10],[11]. It starts from an empty feature set and adds sequentially the individual features not yet chosen (so called forward selection). In the next step the procedure checks whether some feature should be removed from the set (so called backward elimination). The adding and removing process is based on comparing the performance of the system at the actual contents of the feature set. Each candidate feature subset is checked in 10-fold cross-validation by repeating the prediction with different training and testing subsets of observations. Both forward and backward operations interlace each other.

After adding the new variable, a test is made to check if some variables from the actual set may be removed without increasing the error of regression. The stepwise fit tries to find the optimal set of features for which the quality measure of the prediction model is maximized. The process is controlled by two parameters: *penter* and *premove* [11]. The former specifies the maximum *p*-value for a variable to be recommended for adding to the model. The latter one defines the minimum *p*-value for a variable to be removed from the actual set. The *p*-value is the probability for a given model that, when the null hypothesis is true, the mean error would be the same as or

more extreme than the actual observed results. The stepwise fit was applied at the values of *penter*=0.06 and *premove*=0.08, chosen after some introductory experiments. They have been performed on the available data base.

As a result of this process 17 features have been selected. To such features belonged: the values prognosed for the next day by the Interdisciplinary Centre for Mathematical and Computational Modelling (ICM) in Warsaw: average temperature, minimum temperature, maximum temperature, average humidity, minimum humidity, mean insolation, minimum wind speed in x coordinate, maximum wind speed in x coordinate, minimum wind speed in y coordinate, maximum wind speed in y coordinate. The next subset was composed of the past known values: the 24-hour average pollution of the previous day , minimum pollution of the previous day, the particular pollution values corresponding to 2 hours of the previous day: at 1 o'clock and 23 o'clock, the binary code of the season of the year (winter – 11, spring – 10, summer – 01 and autumn – 00) and the code of the type of the day (working day – 1 and weekend day – 0).

The genetic selection is based on presenting the real features by their binary (0 or 1) representation in chromosomes [11],[12]. The value 1 means inclusion of the feature in the input vector **x** to regression system and zero – its elimination. The SVM of Gaussian kernel in regression mode was used as the predictor in this genetic process. The genetic population applied in the experiments was equal 100 chromosomes, crossover rate 80% and mutation rate 1%. The genetic operations: crossover, mutation and selection applied to the pollution data lead to the minimum of the error of classification for the validation data. The elements of value 1 in the best chromosome indicate the optimal set of features.

As a result of these operation the set of 19 best features has been selected. This set is slightly different from the previous one and includes the following variables prognosed for the next day: average temperature, minimum temperature, maximum temperature, maximum humidity, mean insolation, minimum wind speed in x coordinate, maximum wind speed in x coordinate, average wind speed in y coordinate, minimum wind speed in y coordinate, maximum wind speed in y coordinate. The other features are related to the previous day values: the 24-hour average pollution, maximum pollution, minimum pollution, the predicted value of the average humidity for the next day following from this trend, the particular pollution values corresponding to 2 hours of the previous day: at 1 o'clock and 23 o'clock. The last three elements were related to the binary code of the season of the year and the code of the type of the day, the same as in the previous selection.

2.3 Predicting networks

Three types of neural predictors have been checked in experiments. They include multilayer perceptron (MLP), radial basis function network (RBF) and support vector machine (SVM) [13][14]. All of them represent the universal approximation ability, frequently applied in regression problems. Their signal processing methods as well as learning principles differ a lot, therefore, they produce the output signals created in an independent way.

The classical approach to learning neural networks uses the whole learning data set selected randomly from the available base. After learning stage the parameters of

the networks are fixed and their generalization ability is tested on the separate testing set left from the data base for this purpose.

Our approach to the learning problem of these networks is different. The separate learning stage of the network is performed individually for each testing vector. First, the learning base of vectors is searched for extracting the limited set of vectors $\mathbf{x}_l$ which are nearest to the actual testing vector $\mathbf{x}_t$. The distance between vectors $\|\mathbf{x}_t - \mathbf{x}_l\|$ is taken into account in this process. Different types of the norm can be used in such calculations. We have used L1 norm.

After selecting the set of learning vectors the adaptation process of the network is performed using any learning algorithm. The parameters of the adapted network are fixed and the testing vector applied to its input. The generated output signal presents the prediction of the pollution level for the tested input vector.

Application of the next testing vector means the repetition of these stages. As a result the learning process of neural predictors is repeated as many times as is the number of testing vectors. Implementing this process for the next day forecast means only one learning experiments. Therefore, this process is not tedious in practical application.

3 Results of numerical experiments

3.1 Data base

The numerical experiments have been performed using the PM10 data collected by the Regional Inspectorate for Environmental Protection of Warsaw, Poland. All of them have been registered in the meteorological stations located in the suburb of Warsaw within 4 years (1445 data samples together). The measurements have been registered every hour and then averaged for each day. Fig. 1 presents the changes of the hourly averaged values for the days representing 4 seasons of one chosen year.

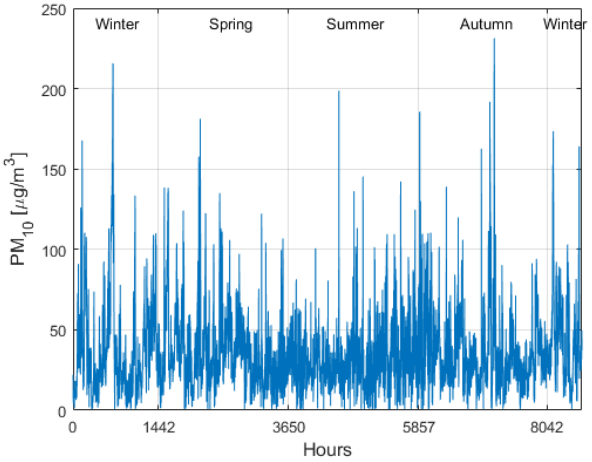

Fig. 1. The distribution of hourly average values of PM10 pollution in four seasons of one year.

The highest peaks of pollution correspond to the winter autumn, while the smallest one to summer. The variability of the level of pollution is well illustrated by the mean values (mean) and standard deviations (std) for the particular seasons of the year. They are depicted in Table 1

Table 1. The variability of the level of pollution in different seasons of the year (in $\mu g / m^3$).

Season	Mean	Std	Std/mean
Winter	39.16	29.44	0.75
Spring	36.70	24.14	0.66
Summer	30.60	17.74	0.58
Autumn	35.62	24.79	0.70

3.2 Results of experiments

The numerical experiments have been performed by applying different types of neural networks, including MLP, RBF and SVM. The aim was to check the possibility of improving forecasting quality of the daily average pollution by applying locally selected learning data. At the same time we study, how different neural structures are sensitive to such approach, especially the limitation of the number of learning samples taking part in adaptation process of predictors.

The introductory experiments were conducted to estimate the optimal structures and parameters of these networks. The optimal MLP structure contained 2 hidden layers of 6 and 4 sigmoidal neurons, respectively, and one output linear neuron generating the forecasted daily average value of PM10 pollution for the next day. The RBF structure used one hidden layer of 30 Gaussian neurons of the centers adapted using the K-means algorithm and one linear output neuron adapted by using pseudoinverse. In learning regression the SVM of the Gaussian kernel and of width parameter σ=0.1 was used. The tolerance ε=0.01 and the regularization constant C=100. All parameter values have been found after some introductory experiments performed on the small selected set of the learning data.

Because of two different selection methods resulting in different contents of the input attributes the experiments have been conducted separately for both of them. As a result 6 different neural structures have been checked in experiments. For comparative reasons the additional experiments have been performed at application of the classical approach to learning, using the same learning and testing data as in the local approach.

Different quality measures have been applied to assess the quality of solution. They include the following measures:

- mean absolute error (MAE)

$$MAE = \frac{1}{p}(\sum_{i=1}^{p}|t_i - y_i|) \quad (1)$$

- root mean squared error (RMSE)

$$RMSE = \sqrt{\frac{1}{p}\sum_{i=1}^{p}|t_i - y_i|^2} \tag{2}$$

- mean absolute percentage error (MAPE)

$$MAPE = \frac{1}{p}\left(\sum_{i=1}^{p}\frac{|t_i - y_i|}{d_i}\right)\cdot 100\% \tag{3}$$

- correlation coefficient (R) of the observed and predicted data

$$R = \frac{R_{yt}}{std(y)std(t)} \tag{4}$$

- index of agreement (IA)

$$IA = 1 - \frac{\sum_{i=1}^{p}(t_i - y_i)^2}{\sum_{i=1}^{p}\left(|t_i - \bar{t}| + |y_i - \bar{t}|\right)^2} \tag{5}$$

In these equations p is the number of data points, $y_i = \hat{P}_i$ is the predicted value, t_i – the really observed value, $\bar{t}$ the average of really observed data, R_{yt} is the covariance value between the really observed and predicted data points of PM_{10} concentration, and *std* standard deviation of the appropriate variable.

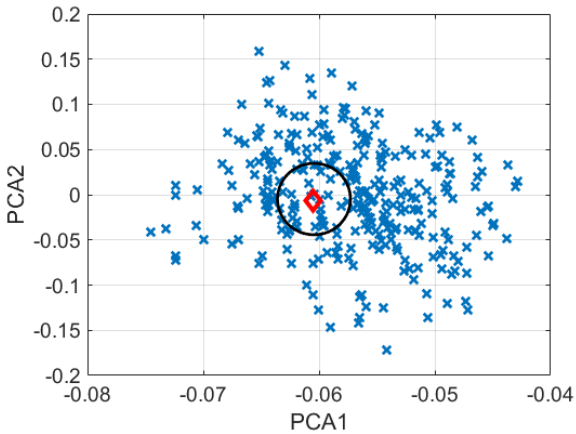

Fig. 2. The distribution of learning data closest to the testing sample. The multidimensional data have been mapped into 2-coordinate system using PCA.

The first experiments were directed to find the optimal number of the input samples from the learning set suited for the actual testing vector, which will result in the best statistical performance of the predictors. This is a crucial element of process, since too

high number will include the learning samples far from the testing vector and too small number will reduce the generalization ability of the neural networks. This problem is illustrated in Fig. 2, presenting two different populations of learning data closest to the testing sample mapped into 2-dimensional system using principal component analysis (PCA) [13]. The circle area presents the data closest to the testing vector denoted by the diamond mark.

At high number of learning samples some data points are far from the testing sample and might be treated as the outliers in this particular case. The distribution of small size learning data is better concentrated around the testing sample and provides good perspective for proper local learning results.

The searching procedure for the optimal size of learning data should take into account the whole population of the testing data. The MAE error calculated for the whole testing set has been chosen as the discriminating quality factor. Table 2 presents the MAE values for the number of learning data changing from 50 to 500. The best results are depicted in bold.

Table 2. The dependence of MAE value (in $\mu g / m^3$) for different arrangement of predictors with size of the learning samples selected for the testing data.

Size of learning data	Genetic feature selection			Stepwise fit for feature selection		
	SVM	MLP	RBF	SVM	MLP	RBF
50	5.93	7.43	6.44	6.02	7.67	6.32
100	**5.48**	7.05	6.29	5.95	7.15	6.25
200	5.55	**6.65**	**5.92**	**5.81**	**6.82**	**6.11**
300	5.59	6.99	6.12	5.84	7.13	6.22
400	5.78	7.38	7.12	6.05	7.28	7.01
500	5.98	7.51	7.41	6.08	7.56	7.43

Fig. 3 presents the graphical illustration of the results of these experiments. As it is seen the optimal size of the learning set depends on the particular arrangement of the predictor. The best results have been achieved for RBF+genetic selection at application of 100 learning vectors selected from the whole learning set.

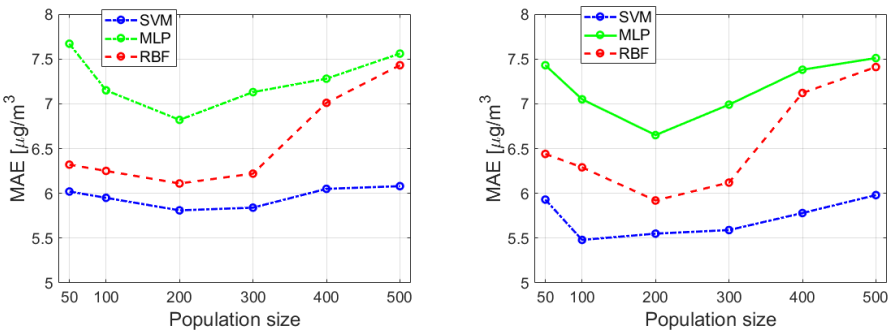

Fig. 3. The dependence of MAE with the change of the population size of learning vector: a) genetic feature selection b) stepwise fit for feature selection.

Each predictor has its own optimal value of learning size. These numbers were used in the next experiments of forecasting. Table 3 presents the numerical results of these experiments in the form of five quality measures estimated for the testing data.

Table 3. The obtained quality measures of PM10 forecast for different arrangement of predictors and application of the optimal number of learning samples.

Quality measures	Genetic feature selection			Stepwise fit for feature selection		
	SVM	MLP	RBF	SVM	MLP	RBF
MAE [$\mu g / m^3$]	5.48	6.65	5.92	5.81	6.82	6.11
RMSE [$\mu g / m^3$]	9.24	10.03	9.41	9.54	10.69	9.98
MAPE [%]	19.58	22.10	20.17	19.62	21.33	22.64
R	0.90	0.83	0.89	0.89	0.80	0.79
IA	0.96	0.91	0.95	0.95	0.92	0.90

For comparative analysis we have checked the classical approach to prediction problem using the same split of learning and testing subsets as in the previous case. This time all learning samples have been used in adaptation stage of all predictors. The testing stage was performed on the same set as in the previous experiments. The results are presented in Table 4.

Table 4. The quality measures of PM10 forecast for different arrangement of predictors at application of all learning samples used in adaptation stage (classical approach).

Quality measures	Genetic feature selection			Stepwise fit for feature selection		
	SVM	MLP	RBF	SVM	MLP	RBF
MAE [$\mu g / m^3$]	8.75	10.00	10.60	8.81	10.44	10.97
RMSE [$\mu g / m^3$]	15.00	16.03	22.41	14.67	16.86	23.21
MAPE [%]	26.75	33.41	33.47	26.66	33.78	34.09
R	0.71	0.66	0.61	0.70	0.64	0.59
IA	0.79	0.76	0.73	0.78	0.75	0.70

These results confirm the superiority of the presented local approach to learning over the traditional one. All quality measures are much better and their relative improvement is in the range from 10% to 30%. Table 5 presents the detailed comparative results corresponding to the best arrangement of predicting systems in the proposed local approach and the classical method, both at application of SVM predictor combined with genetic selection.

Table 5. The detailed comparison of quality measures of PM10 forecast for the proposed local approach and classical method of learning.

	MAE [$\mu g / m^3$]	RMSE [$\mu g / m^3$]	MAPE [%]	R	IA
Local approach	5.48	9.24	19.58	0.90	0.96
Classical approach	8.75	15.00	26.75	0.71	0.79

Fig. 4a presents the graphical results of fitting the true distribution of PM10 levels used in testing stage. The continuous line represents the true values and the dashed line its forecast made by the best network arrangement (SVM+genetic selection) at application of local approach. Fig. 4b illustrates the error of prediction, as the difference of both curves.

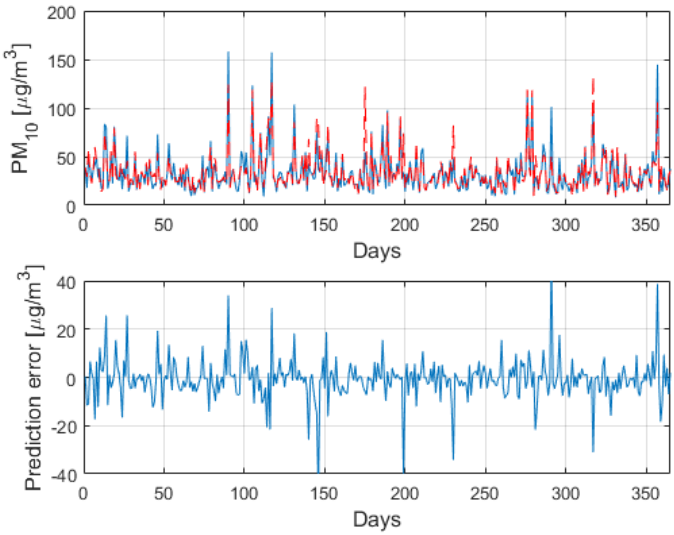

Fig. 4. The graphical results of prediction for the testing data: a) distribution of true (blue solid line) and forecasted (red dashed line) PM10 values, b) the error of forecasting.

4 Conclusions

The paper has proposed and tested novel approach to learning the neural networks in forecasting the daily average values of PM10 pollution. The novelty of the proposed approach using the specialized neural networks learned for each individual testing vector. In adaptation procedure we use only small portion of learning samples which is closest to the actual testing vector. The learning set is chosen on the basis of distance of the actual testing vector to the learning samples. The vector norm L1 was used in this step, as the measure presenting the difference between the particular elements in both vectors in the most faithfully way.

The numerical experiments performed by using the PM10 data registered within 4 years in Warsaw have shown high efficiency of the proposed method. Irrespective of the applied neural network structure (MLP, RBF, SVM) the quality measures of prediction have been significantly improved with respect to classical approach to the problem.

The important advantage of the proposed method is that it does not require very exhaustive information about air pollutant, reaction mechanisms, meteorological pollutant sources. The system allows to model the nonlinear relationships between very different predictor variables in a successful way. Good quality of the results make them attractive in predictive application of PM10 concentration.

References:

1. Hooyberghs, J., Mensink, C., Dumont, G., Fierens, F., Brasseur, O.: A neural network forecast for daily average PM10 concentrations in Belgium. *Atmospheric Environment*, 39, 3279-3289 (2005).

2. Martuzzi M., Mitis F., Iavarone I., Serinelli M.: Health impact of PM_{10} and ozon in 13 Italian cities *WHP report* (2005).
3. Paschalidou A., Karakitsios S., Kleanthous S., Kassomenos P.: Forecasting hourly PM_{10} concentration in Cyprus through artificial neural networks and multiple regression models: implications to local environmental management, *Environ. Sci. Pollut. Res.* DOI 10.1007/s11356-010-0375-2, 2010.
4. Gennaro G., Trizio L., Gilio A., Pey J., Pérez N., Cusack M., Alastuey A., Querol X.: Neural network model for the prediction of PM10 daily concentrations in two sites in the Western Mediterranean, *Science of The Total Environment,* 463, 875–883 (2013).
5. Ul-Saufie A. Z., Yahya S, Ramli N.A.: Comparison between multiple linear regression and feed forward back propagation neural network models for predicting PM10 concentration level based on gaseous and metorological parameters, *Intern. J. of Applied Science and Technology*, 1(4), 42-49 (2011).
6. Taheri Shahraiyni H., Sodoudi S.: Statistical modeling approaches for PM10 prediction in urban areas; A review of 21st-century studies, Atmosphere, 7(*2*), 1-24, doi:10.3390/atmos7020015 (2016).
7. Feng Q., Wu S., Y. Du, Xue H., Xiao F, Ban X., : Improving Neural Network Prediction Accuracy for PM10 Individual Air Quality Index Pollution Levels, Environ Eng Sci. 30(12), 725–732 (2013).
8. Taşpınar F.: Improving artificial neural network model predictions of daily average PM10 concentrations by applying principle component analysis and implementing seasonal model, *Journal of the Air & Waste Management Association*, 65, 800-809 (2015).
9. Siwek K., Osowski, S.:Data mining methods for prediction of air pollution, International *Journal of Applied Mathematics and Computer Science*, 26(2), 467–478 (2016),
10. Guyon, I., Elisseeff, A.: An introduction to variable and feature selection. *Journal of Machine Learning Research*, 3, 1158 – 1182 (2003).
11. Matlab - user manual. *MathWorks*, Natick, USA (2016).
12. Haupt R.L., Haupt S.E.: *Practical Genetic Algorithms*, Wiley, New York (2004).
13. Tan P.N., Steinbach M., Kumar ,V.: Introduction to data mining. Pearson Education Inc., Boston (2006).
14. Schölkopf B., Smola A.: *Learning with Kernels.* MIT Press, Cambridge MA. (2002)..
15. Wilks D. S.: *Statistical Methods in the Atmospheric Sciences,* Academic Press, San Diego, USA, (1995).
16. Nikias L., Petropulu A.: *Higher order spectral analysis,* Prentice Hall, New York, (1993).

Intelligent approach to vehicle routes planning base on artificial neural networks prediction model

Daniel Kubek[1], and Paweł Więcek[2]

[1]Cracow University of Technology, Kraków, Poland
dkubek@pk.edu.pl
[2]Cracow University of Technology, Kraków, Poland
pwiecek@pk.edu.pl

Abstract. The aim of the article it to present an approach to robust optimization of vehicles routes within urban area, based on the driving times short-term predictions in the selected area of urban road network. The forecasted values of the travel times were determined by the use of artificial neural network prediction model, taking into account the certain degree of forecast uncertainty, expressed by a given prediction error. The effectiveness of the proposed in the work solution has been verified on the basis of the results obtained by the classic optimization process wherein the optimization parameters are certain and accurate. The received simulation results indicate that use of forecasting techniques with robust optimization models has a positive impact on the quality of final solutions.

Keywords: Short-term forecasting, Artificial neural networks, Robust vehicle routing problem with time windows

1 Introduction

The basic and natural feature of the transport system is dynamism of phenomena and processes. The dynamism is a consequence of the transport system properties: high level of complexity (large-scale system), large number of users (diverse transport interactions and behaviours), occurrence of complex and random traffic phenomena and susceptibility to external factors (weather, reliability of technical and road infrastructure) [1, 22]. High dynamism and randomness of processes and phenomena in the city transport system does influence the quality of obtained data and information which describe this system. Such quality can be expressed, inter alia, by means of so-called uncertainty and indeterminacy of data. The uncertainty of traffic information can be understood as impossibility to foresee in advance the detailed traffic parameters, which would not have any errors. For example, using historical data to plan future, real processes will always have a certain forecast error. Such error forms an uncertainty set for the described process. The uncertain data are often supplemented by mathematical models which have estimation errors, just like in case of forecasting methods. Hence, the second basic source of uncertainty of traffic information is forecasting models used to estimate future traffic parameters. The other source of uncer-

adfa, p. 1, 2011.

tainty of traffic information is the accuracy of implementation of a solution in practical conditions [3].

These premises indicate that the correct approach to describe the actual objects is methods which allow to define the uncertain parameters, i.e. the parameters which can assume values from a given range. There are a few such approaches in the literature now. These are, inter alia, stochastic optimization, optimization in which the variables are expressed by fuzzy sets [28], and the robust optimization. The first two are rather popular methods to cope with uncertain data, but their basic shortcoming in application to actual problems is the assumption that the randomness is implemented on the basis of known probability distribution [12]. In case of urban traffic, sudden changes in travel time are natural, but it is not possible to indicate the probability distribution which could describe such changes. Examples would be random traffic accidents, traffic incidents, roadworks, breakdown of the control system. These are so-called non-recurrent incidents which are difficult or even impossible for foresee.

The third approach – robust optimization – is a method to account for data uncertainty, however here the variability is not described with a single, specific probability distribution [4, 12, 10, 31]. This solution is resistant to the fluctuations of model parameters when - for many parameter value scenarios - the obtained solution is at least acceptable and meets all the model conditions (model limitations) with high probability. The cost of such solution is the least of the worst possible variants.

On the basis of aforementioned issues, it seems justified to develop and analyze the models describing the transport processes where the model parameters can change their values. Further in the paper, presented is the issue of short-term traffic forecasts – a key issue for the turban traffic control and management. Then, we deal with the subject of determining the optimum routes for logistics vehicles in the urban network using the robust optimization on the basis of forecast travel times in chosen sections, estimated by neural networks. The obtained data (results) have been compared with classic approach wherein it is assumed that the optimization parameters are certain and accurate (e.g. deterministic data). The advantages and the characteristics are exemplified in the actual Krakow road network.

2 Short-term traffic forecasting methods

2.1 Review of methods

The issue of short-term traffic forecasting in urban areas has become in the last decades a crucial subject of research in the transport engineering and the urban logistics systems. The interest is stirred mainly by the need to develop intelligent traffic control methods, create advanced passenger information systems and applications which facilitate the deliveries of goods in the municipal road network. The other reasons include growing traffic in urban areas and the development of data acquisition and processing technologies [2, 17, 32, 34]. Short-term traffic forecasting, as an integral part of the Intelligent Transportation Systems, relates mostly to predicting future values of parameters such as traffic volume, density, speed or travel time in sections of

the urban road network. Such prediction has the time horizon spanning from a few seconds to maximum a few hours. The values are estimated usually on the basis of current and historical traffic information. Transport and logistics companies nowadays very often need to have an accurate traffic forecasts to provide increasingly reliable transport services. Making traffic forecasts on the urban road network level is still a challenge, mainly due to difficulties to install sensors in an adequate portion of the streets and to find optimum locations for these sensors. Such problem is discussed at length in [13, 18]. Additional aspects that make traffic prediction process in a city difficult are constantly increasing traffic volume, changing travel patterns, driver's behaviors as well as traffic incidents and weather conditions.

The review of literature on short-term traffic forecasting shows a multiplicity of available methods and tools. Commonly the approaches used in short-term traffic forecast can be classified into four categories: naive, parametric, non-parametric, and hybrid. Naive approaches refer to models that perform simple estimate of traffic in the future, e.g., historic averages. Parametric approaches refer to models based on techniques which require a set of fixed parameter values as part of the mathematical or statistical equations, while a non-parametric approaches regards mostly data-driven and empirical algorithms to determine the predictions. Other short-term traffic prediction models present hybrid methods as a combination of the above-mentioned approaches. The most of the studies on short-term traffic forecast were concentrated on using standard statistical techniques such as simple smoothing, complex time series analysis and filtering methods. These include approaches based on regression models [7, 29], Autoregressive Integrated Moving Average – ARIMA [21, 37]. A variation of the ARIMA model, which is Seasonal ARIMA (SARIMA) models, has also been implemented in many studies [26, 27]. Various smoothing and filtering techniques are also frequently applied, for example Kalman filter models [15, 16, 38]. Large randomness and indeterminacy in the urban traffic result in popularity of approaches using Bayesian networks based on the probability theory [11, 14]. These methods belong to the group of statistical analysis of time series which yield good results when the modeled phenomenon does not show sudden changes in time. However when the traffic flow data reveals strongly nonlinear characteristics the classic methods may not be able to recognize this nonlinearity. To deal with this limitation an artificial neural networks have been often used for short term traffic forecasting [19, 20, 25, 33]. To improve the effectiveness of prediction process and make forecasts more accurate and resistant to sudden changes in traffic, a hybrid approaches have been applied using both neural models, fuzzy reasoning systems and genetic algorithms. Examples of such solutions are presented with more detail in [6, 8, 35, 36, 39, 40].

2.2 Application of artificial neural network for short term travel times prediction

The main components of each time series include trend, constant level of variable, a cyclic component and a random component. This also applies to time series which describe the traffic data. In reality, by analyzing data from individual sections of road

network, in addition to random disturbances, a certain cyclist and nonlinearity can be observed (rush hours, specific days of the week or month, weekends, etc.). To provide an effective and reliable process of vehicles routes optimization for logistics companies a travel times predictions have been made using time delay neural network. The model uses non- linear autoregressive technique (NAR) to construct a function f of unknown shape with the form:

$$Y^P(t) = f(Y_{t-1}, Y_{t-2,\ldots,} Y_{t-p}) \quad (1)$$

where:
$Y^P(t)$ – forecasted variable in t period of time
$Y_{t-1}, Y_{t-2,\ldots,} Y_{t-p}$) – values of forecasted variable in t-1, t-2,…t-p time periods.

The applied in the studies network consist of three layers: input, hidden, and output. Input neurons represent the values of the forecasted variable delayed in time. The hidden neurons are responsible for transferring a signal between input and output layer. Each neuron takes the output from many other neurons and its actual output is calculated using transfer function. In this work a sigmoid transfer function has been used because it produces a continuous values what is necessary in supervised training process of the network. To increase the effectiveness of prediction process the optimal number of neurons in input and hidden layer was selected by the use of iterative optimization procedure shown on Fig. 1.

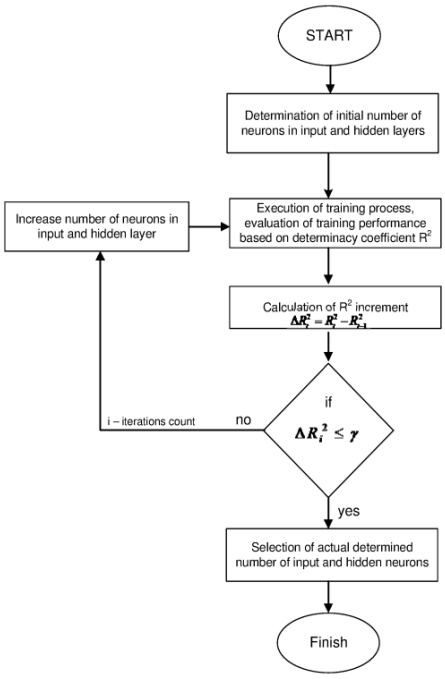

Fig. 1. Iterative optimization procedure for the optimal number of neurons in input and hidden layers (Source: own elaboration)

At the beginning an initial number of input and hidden neurons were chosen. After training process based on Lavenberg Marquardt algorithm a performance level of training was evaluated by the use of determination coefficient R^2 for test data set. In each iteration the increase of ΔR^2 was measured. If the ΔR^2 was greater than threshold value γ=0.01 the number of neurons in input and hidden layer was increased. The best results were obtained for network structure: 10 input neurons, 22 hidden neurons and one output neuron. The example of the results of neural network training for selected road sections shows Fig. 3.

3 Robust vehicle routing problem with time windows based on forecasts

3.1 Applied approach

Proposed methodology based on an integration of robust shortest path R-SPP with the vehicle routing problem with time windows - VRP-TW which is approximation of robust vehicle routing problem with time windows - R-VRP-TW. More precisely the approach was described in [9] and in previous authors works [22-24]. The main concept is presented on Fig. 2.

Proposed approach based on external data such current traffic at urban road network, specification of demand to be served, transportation company data and finally, the most important, the prediction values of travel times and its corresponding estimation errors. The model assumed that each section of the network is characterised by interval travel times and the values are different and dependent on a given number of time intervals. The given arrival time defined by customers time windows, the length of time windows, the prediction errors for this time window and predicted value of travel time related to interval time-dependent model of time are used to define the uncertainty sets for travel time to each road section. E.g. uncertainty set for travel time between i-th customer and j-th customers is created on: predicted travel time in road network during related time windows for i-th customer and related estimation error for this time interval. That pre-processed data are used to compute the robust paths between all pair of customers and it is determinate by bi-criteria robust path problem. The procedure simplifies the computable complexity of problem and creates new virtual graph with robust cost and paths. The criteria are minimizing of the travel time and minimizing the distance. Using two criteria is crucial, especially in robust approach applied to urban traffic environment, because when only single criterion is used, it is possible to obtain solution with good robustness of travel time, but the distance may be unnecessarily large [23]. The output of first stage of proposed methodology is virtual complete graph defining virtual connection between customers and depot. The attributes of edges are set of robust paths and robust travelling times.

In the second stage of approach the classical model of VRP-TW is used. Based on obtained solution and first stage output the robust solution for robust vehicle routing problem with time windows is computed.

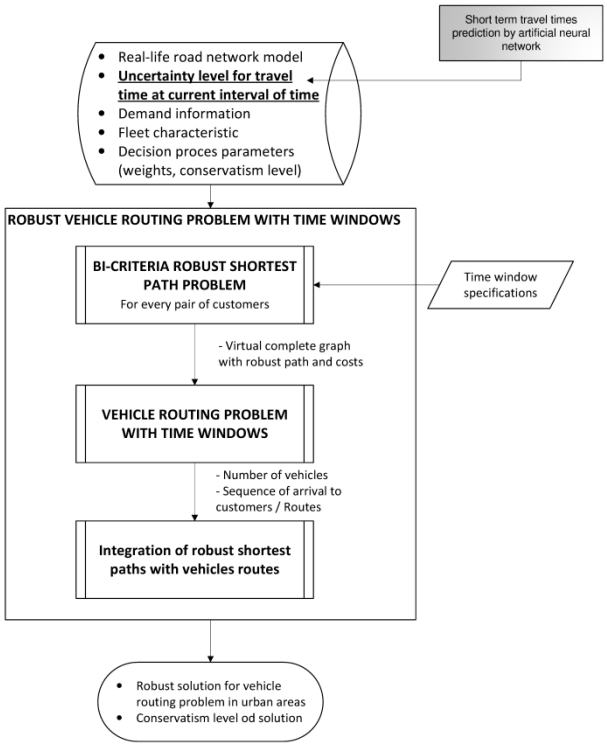

Fig. 2. The integration approach for robust vehicle routing problem with time windows (Source: [23])

3.2 Mathematical formulation

Bi-criteria robust shortest path problem

The Robust Shortest Path Problem (RSPP) model was developed on the basis of [5] and previous research in [22, 23]. The RSPP can be presented using the graph theory, where it is assumed that: there is a directed graph **G** = (**V,A**), where **V** = {1,2,…,n} is the set of vertices, and **A** = {(i,j): i∧j∈ V, i≠j} is the set of directed graph arcs. To each arc (i,j) from the set **A** assigned were weights: travel time **T** and the arc length **D**. It is assumed that the travel time can take values from the set **T** = $\{T_{ij} \in [T_{ij}^{med}-T_{ij}^{dev}, T_{ij}^{med}+T_{ij}^{dev}], \forall(i,j) \in \mathbf{A}\}$, where T_{ij}^{med} means the expected travel time, and T_{ij}^{dev} means the possible deviation from the expected travel time. It is assumed that values are interval time-dependent, such as $T_{ij}^{med}(\tau)$, where τ is indices of time interval, but to keep clearance of notation, the additional indexes are omitted. The problem is to find the optimum connection between two points in the network: {org,des}⊆**V**, in terms of the used criterion, taking into account some degree of data uncertainty. The criterion comprises two aspects: path length expressed as the travel time, and the distance travelled. The goal is to find the path in the network which has the shortest time and length.

There are the following variables in the model: x_{ij} means whether the arc (i,j) is in the path; y_{ij} additional variable which corresponds to the optimal solution of the original problem (uncertain model); α_{ij} additional dual variable, resulting from the linearization of the SPP uncertain model and θ additional dual variable, resulting from the linearization of the SPP uncertain model.

The criterion function of the RSPP model consists of two elements: minimization of travelling time and minimization of distance, and can take the following form:

$$(RSPP): \ min_{F_1,F_2}\left[W \cdot \frac{F_1 - F_1^{min}}{F_1^{max} - F_1^{min}} + (1-W) \cdot \frac{F_2 - F_2^{min}}{F_2^{max} - F_2^{min}}\right] \quad (2)$$

$$F_1 \geq \sum_{(i,j)\in A} x_{ij} \cdot T_{ij} + \theta \cdot \Gamma + \sum_{(i,j)\in A} \alpha_{ij} \quad (3)$$

$$F_2 \geq \sum_{(i,j)\in A} x_{ij} \cdot D_{ij} \quad (4)$$

$$\sum_{\{j:(i,j)\in A\}} x_{ij} - \sum_{\{j:(j,i)\in A\}} x_{ji} = \begin{cases} 1, & for\ i = org \\ -1, & for\ i = des \\ 0, & i.o.c. \end{cases} \quad (5)$$

$$\theta + \alpha_{ij} \geq T_{ij}^{dev} \cdot y_{ij}, \ \forall (i,j) \in \boldsymbol{A} \quad (6)$$

$$-y_{ij} \leq x_{ij} \leq y_{ij}, \ \forall (i,j) \in \mathbf{A} \quad (7)$$

$$x_{ij} = \{0,1\}, \ \forall (i,j) \in \mathbf{A}; \quad y_{ij} \geq 0, \ \forall (i,j) \in \mathbf{A}; \quad \alpha_{ij} \geq 0, \ \forall (i,j) \in \mathbf{A}; \quad \theta \geq 0 \quad (8)$$

The criterion function (2) has been written in the normalized form. The normalization has been introduced due to the fact of adding two different criteria with varying units of measure. Parameters F_1^{min}, F_1^{max} mean respectively the minimum/ maximum travel time in a given network, and parameters F_2^{min}, F_2^{max} - respectively the minimum/ maximum length of path in a given network where the distance was the criterion. The additional parameter W was introduced in order to be able to assign appropriate weights to a given member of the criterion. The limitation (3) corresponds to the criterion of time in which the travel time uncertainty was accounted for. In addition to dual variable, the inequality also includes a new parameter Γ which in the literature on the subject matter is interpreted as level of conservatism of the obtained solution. In practice, it determines the number of coefficients of criterion function costs matrix for which there are deviations from the average value. If Γ=|V|, then min-max approach is applied, such as Soyster model [30]. The expression (4) is the second model criterion – minimization of the total path length. Limitations (5) ensure the proper flow in graph. Constraints (6) and (7) relate to the dual variables which guarantee the correctness of the robust solution of the original problem. The last limitations (8) result from determination of the type of variables.

Vehicle routing problem with time windows

The RSPP can be presented using the graph theory, where it is assumed that: there is a directed complete graph $\mathbf{G^{VRP}} = (\mathbf{V^{VRP}}, \mathbf{A^{VRP}})$, where $\mathbf{V^{VRP}} = \{1,2,\ldots,n\}$ is the set of vertices, and $\mathbf{A^{VRP}} = \{(i,j): i \wedge j \in V, i \neq j\}$ is the set of directed graph arcs. The set

$\mathbf{C} \subset \mathbf{V}^{\mathbf{VRP}}$ is the set if customers indices, $\mathbf{C}=\{2,3,...,n)$. Depot is V_1. To each arc (i,j) from the set $\mathbf{A}^{\mathbf{VRP}}$ assigned travel time T_{ij}^{VRP} obtained from R-SPP. The problem is to find the optimum solution minimizing the total duration of traveling times. Every customer form **C** has assigned the demand $d_i > 0$, service time $s_i > 0$ and time windows for start time of transportation services, $tw_i = [a_i,b_i]$. The depot has m number of vehicles, $\mathbf{K}=\{1,2,...,m\}$ and capacity of each is defined by Q.

There are the following variables in the model: X_{ij}^{VRP} means whether the arc (i,j) is in the path; Y_i additional variable which corresponds to arrival time to i-th customer; D_{ij} additional variable related to goods flow between (i,j) pair of customers

The aim of VRP-TW optimization model is to determine the optimal solution of vehicle routes by minimizing the travelling time:

$$(VRP-TW): \ \min_{X} \sum_{(i,j)\in A} X_{ij} \cdot T_{ij}^{VRP} \tag{9}$$

$$\sum_{j\in V^{VRP}} X_{ij} = 1, \ \forall i \in C \tag{10}$$

$$\sum_{j\in V^{VRP}} X_{ji} = 1, \ \forall i \in C \tag{11}$$

$$\sum_{j\in C} X_{0j} \leq m \tag{12}$$

$$\sum_{j\in V^{VRP}} D_{ij} - \sum_{j\in V^{VRP}} D_{ji} = d_i, \ \forall i \in C \tag{13}$$

$$D_{ij} \leq Q \cdot X_{ij}, \ \forall (i,j) \in A^{VRP} \tag{14}$$

$$Y_i - Y_j + \max\{b_i + T_{ij}^{VRP} + s_i - a_j; 0\} \cdot X_{ij} \leq b_i - a_j, \ \forall (i,j) \in A^{VRP} \tag{15}$$

$$a_i \leq Y_i \leq b_i, \ , \ \forall i \in V^{VRP} \tag{16}$$

$$Y_i \geq 0, \ \forall i \in V^{VRP}; \ D_{ij} \geq 0, \ \forall (i,j) \in A^{VRP}; \ X_{ij}^{VRP} = \{0;1\}, \ \forall (i,j) \in A^{VRP} \tag{17}$$

The criterion function is minimization of total travel time (9). The limitations (10) and (11) correspond to flow constraints in graph. The expression (12) ensures that at least *m* number of vehicle will be used. The proper goods flow is guaranteed by constraints (13) and (14). The time windows constraints are defined by (15) and (16). The last limitations (17) result from determination of the type of variables.

4 Case study

4.1 Assumptions and data

The models presented in previous sections of the paper have been used to check what advantages and disadvantages can be obtained by using robust models in determining the routes in a city combined with prediction form artificial neural networks. The analysis was performed for the real road network in Krakow, Poland. Analyzed road network was converted to graph representation, which consists 251 vertices and 548 directed arcs. The traveling time for analyzed network were achieved by functionality

of Google Maps Distance Matrix API. The travel time values were prepared for one week with 10 minutes of sampling.

To shown the efficiency of artificial neural network prediction the illustrative example was computed for selected sections. The forecasting horizon was equal 20 minutes ahead and covered time period equals 2 days. The prediction model was updated every 20 minutes as soon as latest traffic data was available. The accuracy of forecasts was evaluated by Mean Absolute Percentage Error (MAPE) and Root Mean Square Error. For all population of prediction errors values of quartiles (Q0.25; Q0.5; Q0.75) have been calculated (see Table 1). The accuracy of predictions shows Fig. 3.

Table 1. Quartiles for MAPE and RMSE error for travel time prediction based on artificial neural network for selected road sections.

		ID's section										
	Quartiles	**1**	**3**	**4**	**6**	**7**	**9**	**10**	**11**	**12**	**15**	**16**
MAPE [%]	**Q 0.25**	6.5	3.1	4.5	11.2	5.1	3.8	5.6	5.7	3.4	6.0	7.6
	Q 0.50	12.0	5.9	8.4	21.9	8.6	7.1	11.1	14.1	7.3	11.3	14.6
	Q 0.75	23.6	11.6	15.6	34.3	13.7	13.9	20.3	28.5	15.1	23.0	26.1
RMSE [s]	**Q 0.25**	4.7	3.2	5.8	5.9	2.2	3.4	5.0	4.7	2.7	4.2	5.2
	Q 0.50	10.3	6.1	11.7	13.8	4.0	7.3	10.8	13.7	6.6	8.3	10.4
	Q 0.75	23.7	15.7	26.6	34.7	6.3	19.7	36.8	37.7	15.1	19.2	23.5

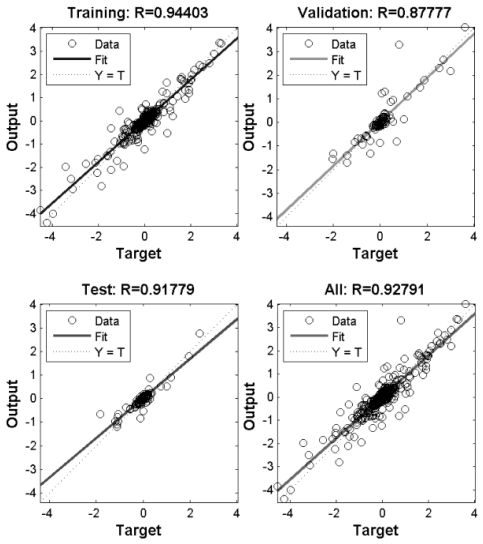

Fig. 3. The accuracy of predictions for travelling time (Source: own elaboration)

The data for robust vehicle routing problem were defined based on quartiles of MAPE errors of prediction process. For vehicle routing planning horizon (1 day) the

prediction ware made and the output with MAPE errors from previous prediction process were used to create uncertainty sets for R-SPP procedure (Fig. 4). Additionally the samples of travel times were aggregated to 1 hour interval, hence the uncertainty set covered one hour of possible travel time changeability.

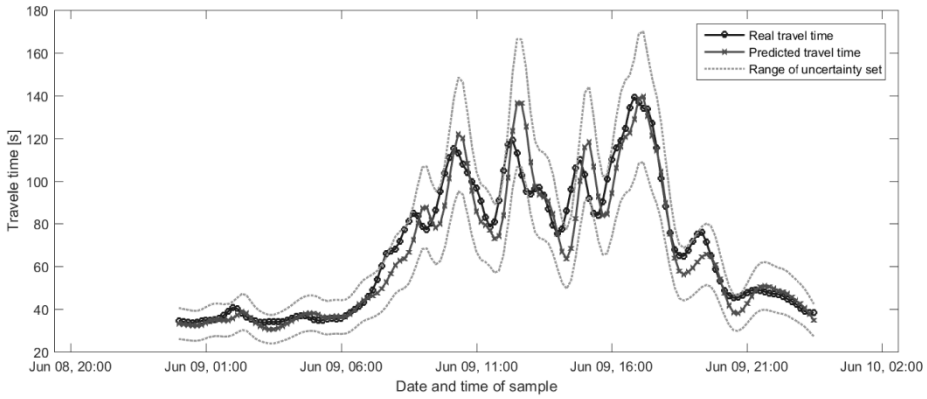

Fig. 4. Real travel times, predicted travel times and range for uncertainty set for selected section (Source: own elaboration)

The approach was implemented in MATLAB software and optimization was processed with CPLEX 12.5 engine. Criterion of convergence of optimization algorithm was set to 1% for absolute GAP parameter. Any heuristic optimization method was not applied due to ensure noise-free results of proposed optimizations approaches (exact optimization method were used).

4.2 Simulation Results

In order to present the obtainable effects of using robust optimization of VRP-TW based on prediction methods, the 3 instances of demand were created: 50, 60 and 70 customers. For each instances two optimization procedures were used - the deterministic and the robust. The deterministic procedure assumes that there is any errors form prediction module and predicted travel times are certain (no possible changeability of values). The robust procedure assume that travel times can take values from uncertainty set, which were created based on mean MAPE errors for each road section and current interval of time.

In both cases the weight of sub-criteria in R-SPP was 60/40% for the time and the path length, respectively. This ratio was indicated by one of the leading transport companies which provide global transport and logistics services. The level of conservatism was set to $\Gamma=0$ and $\Gamma=20$, for deterministic and robust approach, respectively. Additionally, to compare obtained solutions, the five comparing variants were created. Each variant consist 100 scenarios of travel time changeability in designed fashion (variable $T_{ij}^{(e)}$ refer to real value of travel time at specific interval of time):

- Variant 1 - the travel times was randomly generated from range: $[T_{ij}^{(e)}; T_{ij}^{(e)}+\xi \cdot MAPE_{ij} \cdot T_{ij}^{(e)}]$, where ξ is randomly generated numbers from range [0.2; 0.5],
- Variant 2 - $[T_{ij}^{(e)}; T_{ij}^{(e)}+ \xi \cdot MAPE_{ij} \cdot T_{ij}^{(e)}]$, where ξ is randomly generated numbers from range [0.5; 1.0],
- Variant 3 - $[T_{ij}^{(e)}; T_{ij}^{(e)}+ \xi \cdot MAPE_{ij} \cdot T_{ij}^{(e)}]$ where ξ is randomly generated numbers from range [0.7; 1.5],
- Variant 4 - $[T_{ij}^{(e)}; T_{ij}^{(e)}+ \xi \cdot MAPE_{ij} \cdot T_{ij}^{(e)}]$ where ξ is randomly generated numbers from range [1.0; 2.0].

The generated comparing data were used to evaluate the quality of solutions for both optimization approaches. The obtained results are presented in Table 1 - value represents the mean value for whole set of all 100 scenarios within the variant.

The calculations are to show that despite using advanced forecasting methods such, the differences in paths routing significantly affect the final costs. Please note that the presented simulations do not account for the dynamism of the transport system and non-recurrent situations, i.e. the road incidents. Main advantages of using the proposed approach are the reduction of total travel time, up to 9%, and high reduction of late arrival to the customers. The so-called "price of robustness" of obtain solution is the increase the waiting time, but what is most important, the size of growth of the wait time is not equivalent size of growth of decrease of late time (the parameters do not compensate each other). Only one instances, n=60, the increasing of distance was noted - meanly up to 2.7%.

Table 2. Simulation results for deterministic approach for VRP-TW based on forecasting values.

Deterministic scenario		Travel time [s]	Total travel time [s]	Waiting time [s]	Late time [s]	Distance [m]	No. of routes [-]
n=50	**Variant 1**	152.9	557.9	0.0	30.2	52 517.0	4
	Variant 2	185.1	590.1	0.0	60.6		
	Variant 3	233.1	638.1	0.0	135.1		
	Variant 4	275.8	680.8	0.0	245.0		
	Mean	211.7	616.7	0.0	117.7	-	-
n=60	**Variant 1**	129.7	625.7	0.0	49.5	48 579.9	3
	Variant 2	154.6	650.6	0.0	104.8		
	Variant 3	192.6	688.6	0.0	220.8		
	Variant 4	227.4	723.4	0.0	330.5		
	Mean	176.1	672.1	0.0	176.4	-	-
n=70	**Variant 1**	134.1	675.1	0.0	20.3	54 239.5	3
	Variant 2	158.9	699.9	0.0	86.5		
	Variant 3	197.9	738.9	0.0	266.4		
	Variant 4	229.5	770.5	0.0	463.4		
	Mean	180.1	721.1	0.0	209.2	-	-

Table 3. Simulation results for robust approach for VRP-TW based on forecasting values and prediction errors.

Robust scenario		Travel time [s]	Total travel time [s]	Waiting time [s]	Late time [s]	Distance [m]	No. of routes [-]
n=50	Variant 1	139.9	544.9	75.8	0.0	48 568.1	3
	Variant 2	169.9	574.9	9.1	0.0		
	Variant 3	213.1	618.1	0.0	16.9		
	Variant 4	252.4	657.4	0.0	103.9		
	Mean	193.8	598.8	21.2	30.2	-	-
n=60	Variant 1	123.5	619.5	40.2	0.0	49 919.2	3
	Variant 2	145.9	641.9	10.5	0.0		
	Variant 3	178.9	674.9	0.0	11.9		
	Variant 4	213.2	709.2	0.0	74.4		
	Mean	165.4	661.4	12.7	21.6	-	-
n=70	Variant 1	132.6	673.6	61.2	0.0	54 032.0	3
	Variant 2	157.2	698.2	19.1	0.0		
	Variant 3	193.7	734.7	0.0	8.0		
	Variant 4	228,3	769,3	0,0	53,6		
	Mean	178,0	719,0	20,1	15,4	-	-

5 Summary

The research presents two important issues: application of artificial neural network to forecast the travel times in urban road network and advanced use the characteristic any forecast method to vehicle routing problem. Despite many advanced methods of short-term urban traffic forecasting, there is a clear need for using robust models to determine the routes of vehicles which provide transport services inside cities. High variability and indeterminacy is a natural feature of traffic, particularly in urbanized areas. Hence, in order to obtain more effective and reliable data it makes sense to account for uncertainty of forecast data while planning the routes for urban logistics vehicles. The results obtained in the calculation example indicate that use of forecasting techniques with robust optimization models has a positive impact on the quality of final solutions. The approach presented in the paper can be used with success in practical operation of transport and logistics companies.

References

1. Adamski A. (2003) Inteligentne systemy transportowe: sterowanie, nadzór i zarządzanie. Wydawnictwo AGH, Kraków
2. Barceló J, et al. (2010) Travel time forecasting and dynamic origin-destination estimation for freeways based on bluetooth traffic monitoring. Transp.Res. Rec.: J. Transp. Res. Board. vol. 2175 (1), pp 19–27
3. Ben-Tal A, El Ghaoui L, Nemirovski A. (2009) Robust optimization. New Princeton University Press, Jersey
4. Bertsimas D, Brown DB, Caramanis C (2008) Theory and Applications of Robust Optimization. SIAM Review, vol. 53(3)

5. Bertsimas D, Sim M (2003) Robust discrete optimization and network flows. Mathematical Programming, vol. 98, pp 49–71
6. Chan KY, Dillon TS, Singh J, Chang E (2012) Neural-network-based models for short-term traffic flow forecasting using a hybrid exponential smoothing using a hybrid exponential smoothing and levenberg-marquardt algorithm. IEEE Transactions on Intelligent Transportation Systems, vol. 13 (2), pp 644–654
7. Clark, Stephen (2003) Traffic prediction using multivariate nonparametric regression. Journal of Transportation Engineering, vol. 129 (2), pp 161–168
8. Dimitriou, L, Tsekeris T, Stathopoulos A (2008) Adaptive hybrid fuzzy rule-based system approach for modeling and predicting urban traffic flow. Transportation Research Part C: Emerging Technologies, vol. 16 (5), pp. 554–573
9. Donati AV, Montemanni R, Gambardella LM, Rizzoli AE (2003) Integration of a robust shortest path algorithm with a time dependent vehicle routing model and applications. International Symposium on Computational Intelligence for Measurement Systems and Applications, CIMSA, pp. 26 - 31
10. El Ghaoui L. (2003) Uniwersytet w Berkeley. Robust Optimization and Applications. http://rutcor.rutgers.edu/
11. Fei X, Lu CC, Liu KA (2011) Bayesian dynamic linear model approach for real-time short-term freeway travel time prediction. Transportation Research Part C: Emerging Technologies, vol. 19 (6), pp 1306–1318
12. Gabrela V, Murata C, Thiele A (2014) Recent advances in robust optimization: An overview. European Journal of Operational Research, vol. 235(3), pp 471–483
13. Gentili M, Mirchandani PB (2012) Locating sensors on traffic networks: models, challenges and research opportunities. Transportation Research Part C: Emerging Technologies, vol. 24, pp 227–255
14. Ghosh B, Basu B, O'mahony M (2007) Bayesian time-series model for short-term traffic flow forecasting. Journal of Transportation Engineering, vol. 133 (3), pp 180–189
15. Guo J, Huang W, Williams BM (2014) Adaptive Kalman filter approach for stochastic short-term traffic flow rate prediction and uncertainty quantification. Transportation Research Part C: Emerging Technologies, vol. 43, pp 50–64
16. Guo J, Williams BM (2010) Real-time short-term traffic speed level forecasting and uncertainty quantification using layered Kalman filters. Transportation Research Record. vol. 2175, pp 28–37
17. Herrera Juan C, et al. (2010) Evaluation of traffic data obtained via GPS-enabled mobile phones: The Mobile Century field experiment. Transportation Research Part C: Emerg. Technol., vol. 18 (4), pp 568–583
18. Hu ShR, Peeta S, Chun-Hsiao Chu (2009) Identification of vehicle sensor locations for link-based network traffic applications. Transportation Research Part B: Methodological, vol. 43 (8–9), pp 873–894
19. Ishak S, Alecsandru C (2004) Optimizing traffic prediction performance of neural networks under various topological input and traffic condition settings. Journal Transportation Engineering, vol. 130(4), pp 452–465
20. Ishak S, Kotha P, Alecsandru C (2003) Optimization of dynamic neural network performance for short-term traffic prediction. Transp Res Record, vol. 1836, pp 45–56
21. Kamarianakis Y, Prastacos P (2005) Space–time modeling of traffic flow. Comput. Geosci, vol. 31 (2), pp 119–133
22. Kubek D (2016) Charakterystyka problemu wyznaczania tras dla pojazdów z oknami czasowymi w warunkach niepewności. In: Selected aspects of logistics management. Vol. 4, Feliks J (eds), AGH, Kraków, pp 78-93

23. Kubek D (2016) Optymalizacja typu "robust" tras przewozu ładunków na obszarach miejskich, Doctoral Thesis, Politechnika Krakowska
24. Kubek D, Więcek P, Chwastek K (2016) The Impact of Short Term Traffic Forecasting on the Effectiveness of Vehicles Routes Planning in Urban Areas. Transportation Research Procedia, vol. 18, pp 172-179. doi: 10.1016/j.trpro.2016.12.024
25. Li CS, Chen MC (2013) Identifying important variables for predicting travel time of freeway with non-recurrent congestion with neural networks. Neural Comput & Applic. vol. 23, pp 1611–1629
26. Lin L, Wang Q, Sadek A (2013) Short-term forecasting of traffic volume evaluating models based on multiple data sets and data diagnosis measures. Transp. Res. Rec., vol. 2392, pp 40–47
27. Lippi M, Bertini M, Frasconi P, (2013) Short-term traffic flow forecasting: an experimental comparison of time-series analysis and supervised learning. Intell. Transp. Syst. IEEE Trans. vol. 14, pp 871–882
28. Peng J, Shang G, Liu H, (2006) A Hybrid Intelligent Algorithm for Vehicle Routing Models with Fuzzy Travel Times. Computational Intelligence, Lecture Notes in Computer Science, vol. 4114, pp 965-976
29. Smith Brian L, Williams Billy M., Oswald R Keith (2002) Comparison of parametric and nonparametric models for traffic flow forecasting. Transportation Research Part C: Emerging Technologies, vol. 10 (4), pp 303–321
30. Soyster A (1973) Convex programming with set-inclusive constraints and application to inexact linear programming. Operation Research, vol. 21, pp 1154-1157
31. Stavros A, Zenios (2009) Robust Optimization. Encyclopedia of Optimization. Springer US
32. Treiber M, Kesting A. (2012) Validation of traffic flow models with respect to the spatio-temporal evolution of congested traffic patterns. Transportation Research Part C: Emerging Technologies, vol. 21 (1), pp 31–41
33. Vanajakshi L, Rilett LR (2004) A comparison of the performance of artificial neural networks and support vector machines for the prediction of traffic speed. IEEE Intell Veh Symp, pp 194–199
34. Vlahogianni EI, Golias JC, Karlaftis MG (2004) Short-term traffic forecasting: overview of objectives and methods. Transportation Reviews, vol. 24 (5), pp 533–557
35. Vlahogianni EI, Karlaftis MG (2013) Testing and comparing neural network and statistical approaches for predicting transportation time series. Transportation Research Record Journal of the Transportation Research Board, vol. 2399
36. Wang J, Shi Q (2013) Short-term traffic speed forecasting hybrid model based on Chaos-Wavelet analysis-support vector machine theory. Transportation Research Part C: Emerging Technologies, vol. 27, pp 219–232
37. Williams BM (2001) Multivariate vehicular traffic flow prediction: evaluation of ARIMAX modeling. Transportation Research Record Journal of the Transportation Research Board, vol. 1776 (1), pp 194–200
38. Xie Y, Yuanchang Zhang Y, Ye Z (2007) Short-term traffic volume forecasting using Kalman filter with discrete wavelet decomposition. Comput.- Aid. Civ. Infrastruct. Eng, vol. 22 (5), pp 326–334
39. Yin H., et al. (2002) Urban traffic flow prediction using a fuzzy-neural approach. Transportation Research: Part C, vol. 10 (2), pp 85–98
40. Zhang Y, Zhang Y, Haghani A (2014) A hybrid short-term traffic flow forecasting method based on spectral analysis and statistical volatility model. Transportation Research. Part C., vol. 43, pp 554–573

Electricity price forecasting using a hybrid time series model

Büşra Taş[1] and Ceylan Yozgatlıgil[1]

[1] Middle East Technical University, Statistics, Ankara 06800, Turkey
busratas@metu.edu.tr

Abstract

Electricity price forecasting is very important in a competitive market. Decision makers highly benefit from accurate forecasting. Shocks to demand or supply affect the electricity prices since electricity cannot be stored. As a result, electricity prices show high volatility. Additionally, it may have multiple levels of seasonality such as our case. Thus it makes forecasting very difficult with conventional methods.

In this study, a hybrid model is constructed with SARIMA and NARX models for analysis of hourly electricity prices in Turkey. Time series can contain both linear and nonlinear patterns. Thus, using a hybrid model can give better results in forecasting. Both linear and nonlinear parts of the time series can be modeled by this approach. In this study, electricity prices and electricity demand variables are used. Seasonal Autoregressive Integrated Moving Average (SARIMA) model is used to capture the linear behavior of the electricity price series. However, nonlinear patterns cannot be modeled by SARIMA models. Neural Network is used to model the nonlinearity in the series. After that, residuals of this SARIMA model is used as output variable in the Nonlinear Autoregressive Model with Exogenous Inputs (NARX). Electricity demand is used as exogenous variable in NARX model. Number of hidden neurons and number of delays are determined according to have a well performed network. Linear modeling is implemented in R and NARX model is built using Neural Network Time Series Tool in MATLAB.

Keywords: Electricity price forecasting, Hybrid method, Neural Network.

1 Introduction

1.1 Data Description

The data set used in this study is hourly electricity demand (in MWh) and price (in TL/MWh) of Turkey. Series is from 1st January 2012 to 11 June 2014. This time period equivalent to 21342 hours. There is multiple seasonality (daily, weekly, monthly) in the price.

1.2 Methodology

In ARIMA modeling linear structure is assumed. So, nonlinear behaviors cannot be captured. On the other hand, artificial neural networks (ANNs) can be used for nonlinear modeling. Time series generally have both linear and nonlinear patterns.
Zhang [1] proposed a hybrid methodology which combines linear and nonlinear components as follows:

$$y_t = L_t + N_t \tag{1}$$

where y_t shows the time series, L_t shows the linear component and N_t shows the nonlinear component.

Price forecasts are obtained by using this hybrid methodology. Since there are multiple levels of seasonality, a model with dummy variables is fitted to handle the weekly seasonality.

Algorithm that is used for electricity price forecasting as follows:
Step 1. A model with dummy variables are constructed to eliminate weekly seasonality.
Step 2. SARIMA model is constructed with the residuals of the model in step 1.
Step 3. NARX neural network model is used for modeling the residuals of the model in step 2 and demand is used as input variable.
Step 4. Forecasts for demand is obtained.
Step 5. Forecasts are combined using the hybrid model.

We are expecting to have more accurate forecasts with hybrid methodology than using only SARIMA or only neural network models. Additionally, fitting SARIMA model to the series can solve the overfitting problem which is caused by neural network model. Therefore, we propose a three stage hybrid SARIMA and NARX neural network model for forecasting hourly electricity price.

References

1. Zhang, G.P.: Time series forecasting using a hybrid ARIMA and neural network model. Neurocomputing (50), 159-175 (2003).
2. Aladag, C.H., Egrioglu, E., Kadilar, C.: Forecasting nonlinear time series with a hybrid methodology. Applied Mathematic Letters (22), 1467-1470 (2009).
3. Khashei, M., Bijari, M.: A novel hybridization of artificial neural networks and ARIMA models for time series forecasting. Applied Soft Computing (11), 2664-2675 (2011).
4. Weron, R.: Electricity price forecasting: A review of the state-of-the-art with a look into the future. International Journal of Forecasting (30), 1030-1081 (2014).

Forecasting Intraday Risk Measures using Multiplicative Component GARCH Model and Multimodal Distributions

Aymeric Thibault and Pascal Bondon

Laboratoire des Signaux et Systèmes
CNRS - CentraleSupélec - Université Paris-Sud, France.

Abstract. Forecasting intraday risk measures such as Value-at-Risk (VaR) and Expected Shortfall (ES) for high-frequency financial data has gained increasing interest since the volume of high-frequency trading stepped up over the two last decades. This paper proposes an autoregressive moving average multiplicative component generalized autoregressive conditional heteroskedastic (ARMA-mcsGARCH) model with innovations following a multimodal extension of the Exponential Power Distribution (EPD), called the Orthogonal Polynomial Exponential Power Distribution (OPEPD). An application to risk measurement for high-frequency data is presented. An ARMA-mcsGARCH model is fitted to Financial Times Stock Exchange (FTSE) 100 intraday returns. Performances for VaR and ES estimation are evaluated. We show that the OPEPD outperforms commonly used distributions in risk measurement.

Keywords: Multimodality, Asymmetric distributions, Expected shortfall, Value-at-Risk, mcsGARCH model

1 Introduction

Over the two last decades, the rise of high-frequency trading and the availability of intraday data for financial assets led market participants to focus on intraday volatility. Modelling and forecasting high-frequency volatility is a subject of great importance in estimation of risk measures such as VaR and ES. Conventional GARCH models [1], [2] were run on high-frequency data and the resulting model parameters were not consistent between different intraday frequencies, mostly due to the noticeable diurnal patterns of volatility [3]. Recently, [3] developed the mcsGARCH model based on [4]. It decomposes the volatility of price returns into three multiplicative components, namely daily, diurnal and stochastic. Fitting a mcsGARCH model requires two steps. First, we are interested in the estimation of the daily component which is a daily determined forecast volatility. To do so, a large literature exists and GARCH-based models are efficient for daily data [5]. For daily data, a special attention shall be paid to the innovations of the GARCH models: their distribution exhibit high kurtosis and left-skewness highly impacting estimation of risk measures and therefore portfolio optimization. Once the daily component is obtained, a mcsGARCH model

is fitted to the corresponding intraday data. The interrelated innovations show extreme kurtosis and skewness and they are fitted with an OPEPD distribution.

Recently, Polynomial-Normal [9] and Polynomial-t-Student distributions [10] were used to fit the innovation of GARCH models for financial series. It is shown that such polynomial-distributions improve performance in risk measurement compared to their non-polynomial counterparts. In this paper, we propose an OPEPD which presents two different moment parameters controlling the skewness and kurtosis. A polynomial-like component is multiplied to manage multimodality.

The paper is organized as follows. Section 2 proposes a new OPEPD and its main characteristics are exposed. Section 3 is dedicated to an application of the OPEPD to risk measurement for the FTSE 100 index over a period of two months covering "Brexit" referendum in June 2016. An ARMA-GARCH model with OPEPD innovations is derived for mcsGARCH daily component estimation. Then, an ARMA-mcsGARCH model with OPEPD innovations is used to forecast risk for high-frequency data. Backtesting and comparison of performances for VaR and ES estimation under different innovation distributions are presented. Concluding remarks can be found in Section 4.

2 An Orthogonal Polynomial Exponential Power Distribution

The generalized error distribution class, initially proposed by [11], is called Exponential Power Distribution (EPD) by [12]. The corresponding density function is

$$f_{\text{EPD}}(x|\alpha,\mu,\sigma) = \frac{1}{\sigma} f_\alpha\left[\frac{x-\mu}{\sigma}\right],$$

where $f_\alpha(x) = c_\alpha \exp(-|x|^\alpha)$, $\alpha > 0$ is the shape parameter, $c_\alpha^{-1} = 2\Gamma(1+1/\alpha)$ and Γ is the Gamma function, $\mu \in \mathbb{R}$ is the location parameter and $\sigma > 0$ is the scale parameter. The OPEPD is an polynomial extension of the EPD and presents two different shape parameters a and b controlling respectively the skewness and kurtosis of the distribution. Both parameters have a clear interpretation and are directly related to the $3th$ and $4th$ moment of the OPEPD. The singularity of the OPEPD is the presence of a multimodal component through the use of orthogonal polynomials. Following the work of [13], we derive a special case of orthogonal polynomials. The sequence of monic polynomials of degree n, $p_n(x), n \in \mathbb{N}$ is said to be orthogonal for the measure μ if $\int_{\mathbb{R}} |x|^k d\mu(x) < \infty$ for all integer k and

$$\langle p_n \mid p_m \rangle = \int_{\mathbb{R}} p_n(x)p_m(x)d\mu(x) = \delta_{nm} \int_{\mathbb{R}} x^n p_n(x)d\mu(x) = \delta_{nm}\gamma_n\,, \qquad (1)$$

where $\delta_{mn} = 1$ if $m = n$ and 0 otherwise. Setting $p_0(x) = 1$, the sequence $p_n(x)$ is uniquely defined by (1) and can be obtained by the Gram-Schmidt process. We have

$$\gamma_n = \frac{\det(Q_{n+1})}{\det(Q_n)}\,, \qquad (2)$$

where Q_n denotes the submatrix resulting from the deletion of the $(n+1)th$ row and the $(n+1)th$ column of $M_{n+1}(x)$ defined by

$$M_{n+1}(x) = \begin{bmatrix} m_0 & m_1 & \dots & m_n \\ \vdots & \vdots & \vdots & \vdots \\ m_{n-1} & m_n & \dots & m_{2n-1} \\ 1 & x & \dots & x^n \end{bmatrix},$$

and $m_k = \int_{\mathbb{R}} x^k d\mu(x) < \infty$. Furthermore,

$$p_n(x) = \frac{\det(M_{n+1}(x))}{\det(Q_n)}\,. \tag{3}$$

We consider here the polynomial $q(x, a, b, \alpha) = 1 + \frac{a}{\gamma_3} p_3(x, \alpha) + \frac{b}{\gamma_4} p_4(x, \alpha)$ where $p_n(x, \alpha)$ is the n^{th} orthogonal polynomial of the EPD density with $(\mu, \sigma) = (0, 1)$. Finally, the OPEPD density function is given as follows

$$f_{\text{OPEPD}}(x, \eta) = q(\frac{x-\mu}{\sigma}, a, b, \alpha) f_{\text{EPD}}(x|\alpha, \mu, \sigma)\,, \tag{4}$$

where $\eta = (\mu, \sigma, a, b, \alpha)$. The non-negativeness of OPEPD is investigated and the set Ξ of admissible values of (a, b), α being fixed, for $f_{\text{OPEPD}}(x, \eta)$ to be well-defined, can be given. The set Ξ provides the equations of the frontier and the maximum absolute values for (a, b) are respectively called $\max_a$ and $\max_b$. When $\alpha = \frac{1}{2}$, we have $\max_a = 41.2$ and $\max_b = 12476$, where $\max_a$ and $\max_b$ represent, respectively, the maximum skewness and kurtosis that the OPEPD can reach.

3 Real Data Example

This section aims to evaluate the performance of risk measure estimation under unstable periods of time. Especially, we analyze the VaR and ES estimation with high-frequency FTSE data during the "Brexit" period. An ARMA-mcsGARCH model is fitted and this method requires two steps. First, we consider FTSE daily log-return (Y_t^d) from January 1, 2013 to May 14, 2016, totalling $T^d = 850$ daily observations. An ARMA-GARCH model with OPEPD innovations is fitted to the in-sample data and one-day-ahead daily volatility forecast $\hat{\sigma}_t^d$ are computed over the out-of-sample period from May 15, 2016 to July 15, 2016 ($F^d = 44$ forecasts). Second, 1-minute FTSE returns ($Y_{t,i}^{\text{HF}}$) follow an ARMA-mcsGARCH model for the in-sample period ($T^{\text{HF}} = 840$ observations for each of the $N^{\text{HF}} = 24$ days from May 15, 2016 to June 19, 2016). One minute-ahead VaR and ES are then estimated over the period from June 20, 2016 to July 15, 2016 covering the "Brexit" referendum.

[3] proposes a GARCH model for high-frequency intraday financial returns called mcsGARCH. The conditional variance is specified to be a multiplicative product of daily, diurnal, and stochastic intraday volatility. Days are here indexed

by $t = 1, ..., N^{\text{HF}}$ and 1-minute intervals by $i = 1, ..., T^{\text{HF}}$. Under this indexation, we note $(t, i)+j$ the jth data point following the one at indexed time (t, i). $(Y_{t,i}^{\text{HF}})$ is described by the following process:

$$\begin{aligned} Y_{t,i}^{\text{HF}} &= \sum_{j=1}^{l} \phi_j^{\text{HF}} Y_{(t,i)-j}^{\text{HF}} + X_{t,i}^{\text{HF}} + \sum_{j=1}^{m} \theta_j^{\text{HF}} X_{(t,i)-j}^{\text{HF}} \,, \\ X_{t,i}^{\text{HF}} &= \sigma_t^d s_i q_{t,i} \varepsilon_{t,i}^{\text{HF}} \,, \\ (q_{t,i})^2 &= a_0 + \sum_{j=1}^{u} a_j (X_{(t,i)-j}^{\text{HF}})^2 + \sum_{j=1}^{v} b_j (q_{(t,i)-j})^2 \,, \end{aligned} \tag{5}$$

where σ_t^d is the daily volatility and is estimated by its forecast $\hat{\sigma}_t^d$ from (Y_t^d) (assumed to follow an ARMA-GARCH model with OPEPD innovations), s_i is the diurnal volatility pattern, $q_{t,i}$ is the intraday volatility component with $E(q_{t,i}^2) = 1$ and $\varepsilon_{t,i}^{\text{HF}}$ is an error term. $\varepsilon_{t,i}^{\text{HF}}$ follows a standardized OPEPD distribution obtained by taking $\mu = 0$ and $\sigma = 1$. The parameters are estimated

Table 1. Statistical characteristics of $\hat{\varepsilon}_{t,i}^{\text{HF}}$.

Signal	Mean	Standard Deviation	Min	Max	Skewness	Excess Kurtosis
$\varepsilon_{t,i}^{\text{HF}}$	0.01	3.53	-595.43	126.17	-88.23	15062.31

with maximum likelihood estimation (MLE). Then, we have access to an estimate $\hat{\varepsilon}_{t,i}^{\text{HF}}$ of the innovations $\varepsilon_{t,i}^{\text{HF}}$ of the mcsGARCH model. The main statistical characteristics of $\hat{\varepsilon}_{t,i}^{\text{HF}}$ are presented in Tab. 1. This Table points out the need for distributions that can reach extreme values of skewness and kurtosis. The above-mentioned maximum value $\max_a$ and $\max_b$ shows that the OPEPD is a good candidate for modelling such innovations while classical distributions can't be used for intraday financial data. Backtesting procedures are applied for both VaR and ES. We show that the OPEPD outperforms commonly used distributions in risk measurement when applied to high-frequency financial data.

4 Conclusion

This paper proposes an ARMA-mcsGARCH model with innovations following the OPEPD. An application to risk measurement for high-frequency data is given and time series analysis through the mcsGARCH model exhibit good performance.

References

1. Engle, R.F.: Autoregressive conditional heteroscedasticity with estimates of the variance of United Kingdom inflation. Econometrica **50**(4) (1982) 987–1007
2. Bollerslev, T.: Generalized autoregressive conditional heteroskedasticity. J. Econometrics **31**(3) (1986) 307–327
3. Engle, R.F., Sokalska, M.E.: Forecasting intraday volatility in the us equity market. multiplicative component garch. Journal of Financial Econometrics **10**(1) (2012) 54–83
4. Andersen, T.G., Bollerslev, T.: Intraday periodicity and volatility persistence in financial markets. Journal of Empirical Finance **4**(2–3) (1997) 115 – 158
5. Tsay, R.S.: Analysis of financial time series. Wiley series in probability and statistics. Wiley-Interscience, Hoboken (N.J.) (2005)
6. Huang, C.K., Chinhamu, K., Huang, C.S., Hammujuddy, J.: Generalized hyperbolic distributions and value-at-risk estimation for the south african mining index. International Business and Economics Research Journal (IBER) **13**(2) (2014)
7. Komunjer, I.: Asymmetric power distribution: theory and applications to risk measurement. J. Appl. Econometrics **22**(5) (2007) 891–921
8. Zhu, D., Zinde-Walsh, V.: Properties and estimation of asymmetric exponential power distribution. Journal of Econometrics **148**(1) (2009) 86 – 99
9. Li, H., Melnikov, A.: Polynomial extensions of distributions and their applications in actuarial and financial modeling. Insurance: Mathematics and Economics **55** (2014) 250 – 260
10. Li, H., Melnikov, A.: On polynomial extension of t-distribution and its financial applications. Risk and Decision Analysis **4**(4) (2013) 255 – 266
11. Subbotin, M.T.: On the law of frequency of error. Mat. Sb. **31**(2) (1923) 296–301
12. Box, G.E.P., Tiao, G.C.: Bayesian inference in statistical analysis. Addison-Wesley, Reading MA (1973)
13. Bagnato, L., Potì, V., Zoia, M.: The role of orthogonal polynomials in adjusting hyperpolic secant and logistic distributions to analyse financial asset returns. Statistical Papers **56**(4) (2015) 1205–1234

Astronomical Time Delay Estimations

Mariko Kimura[1], Hyungsuk Tak[2], and Taichi Kato[1]

[1]Department of Astronomy, Graduate School of Science, Kyoto University, Oiwakecho, Kitashirakawa, Sakyo-ku, Kyoto 606-8502, Japan
[2]Statistical and Applied Mathematical Sciences Institute, Durham, NC, USA
mkimura@kusastro.kyoto-u.ac.jp

Abstract. Estimating time lags between astronomical time series data of brightness is known to be challenging due to their sparse observations. We propose a Bayesian method based on a state-space model to estimate the time delays between these irregularly sampled time series data. This method can be applied to many kinds of black-hole systems in which accretion-type light variations are observed. We apply this method to the multi-wavelength observational data of V404 Cyg, a black-hole binary, and estimate time delays on timescales of several tens of seconds with high accuracy.

Keywords: Bayesian inference, state-space model, accretion, black holes physics

1 Introduction

Astronomical time series data of brightness, called light curves that exhibit light variations of stars with time, are sparsely observed for several reasons. We can observe stars only at night with ground-based telescopes. Bad weather conditions also deter us to obtain evenly-spaced time series. Even if we observe stars through astronomical satellites, the observation becomes impossible for a specific period of time due to the star position in the sky and/or the position of the satellites. Consequently, astronomers obtain unevenly-spaced time series with possibly large gaps between observations. In addition, measurement errors are heteroskedastic.

Astronomers often observe the same target in different wavelengths (optical, ultraviolet, X-ray, radio wavelengths, and so on) with different telescopes and/or detecters. In this case, it is difficult to achieve completely simultaneous multi-wavelength light curves because light curves in different wavelengths would appear different. Moreover, each of them is an irregularly-sampled and sparse data set as described above. A realistic data set displayed in Fig. 1 shows these features.

If these multi-wavelength light curves are correlated with each other, their time delay estimate gives astronomers important information about the state of our universe, the structure of astronomical objects and the origin of radiation from them. However, the time delay estimation is challenging mainly due to

the sparse samplings of the astronomical time series. In astronomy, for example, a grid-based cross-correlation function has been widely used despite its limited applicability to almost evenly-sampled and completely simultaneous high-quality data. Also, astronomers usually interpolate the light curves to use the cross-correlation function method without any physical modeling. Additionally, many simultaneous multi-wavelength sparse light curves have not been used in the time delay estimation although recent developments of astronomical surveys and telescopes will provide enormous amount of multi-wavelength light curves in the near future.

Thus, the development of the sophisticated time delay estimation method is necessary and we solve all these difficulties by adopting a Bayesian approach. In this paper, we introduce our approach to the time delay estimation between multi-wavelength sparse light curves with a Bayesian state-space model.

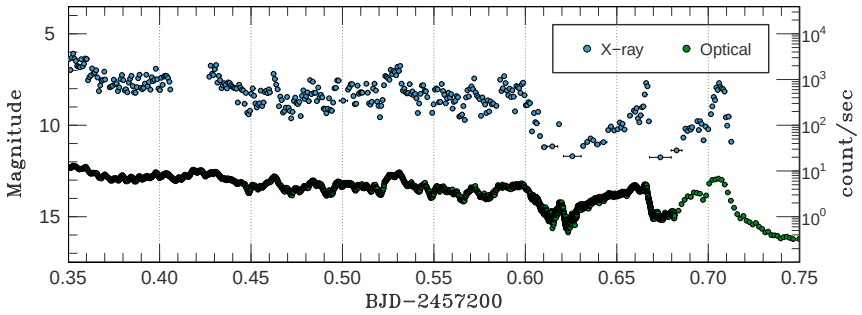

Fig. 1. An example of two astronomical time series in different wavelengths. They are light variations during the 2015 June outburst in V404 Cyg, a black-hole X-ray transient. The vertical axis represents brightness of the object in units of magnitudes (an astronomical logarithmic measure of brightness) and the horizontal axis indicates the observation time in units of barycentric Julian dates minus 2457200. The blue and green circles denote the light curves in the X-ray 25–60 keV band (taken by the *INTEGRAL* satellite) and the optical V band (taken by ground-based telescopes).

2 Importance of Time Delay Estimation in Astronomy

Analyses on the time delays between several correlated light curves are crucial in astronomical probes. Here we focus on accretion-type light variations[1] and introduce three areas where the time delay estimation plays an important role.

[1] When gas accreted onto a compact abject (a white dwarf, a neutron star and a black hole), the gravitational energy of the gas is released outside as light rays.

2.1 Gravitationally Lensed Quasars

A strong gravity of a massive object bends light rays from another object behind the massive object. This phenomenon is called "gravitational lensing". For instance, when a massive galaxy intervenes between a quasar[2] and the earth, light rays from the quasar are bent by the gravitational field of the massive intervening galaxy. The bent light rays pass through some different routes and form multiple images in slightly different locations in the sky. Reconstructing light curves from each of the gravitational lensed images, we will find that the fluctuation pattern of one light curve is lagging behind in time. Also, one light curve is offset in brightness to the other due to their different trajectories from the quasar to Earth and differing degrees of lensing magnification. Moreover, each of the images can exhibit an extrinsic variability of brightness since each of light paths is subject to various microlensing effects[3] [1].

Estimating the time delay between gravitationally lensed quasar light curves provides valuable information in cosmology [2]. It has been used to determine the Hubble constant, the current expansion rate of the Universe [3]. This is because the time delay is inversely proportional to the Hubble constant [4]. In addition, investigating the gravitational lensing effect is related to the probe of dark matter.[4] Moreover, an accurate time delay estimation could also constrain the matter density and the dark energy equation of state [5].

2.2 Reverberation Mapping in Active Galactic Nuclei

Active galactic nuclei including quasars are enormous and luminous central region of galaxies. They have supermassive black holes at the center and accretion disks are formed around them, which are surrounded with broad-line regions, lumps of moving gas. The optical or ultraviolet continuum radiation from accretion disks shows stochastic variability, and photoionizes gas around them and drives broad emission lines after a light travel time. The emission-line variations are considered to be scaled and smoothed according to the size and movement of the broad-line region.

Although the central engine is believed to be accretion of matter onto supermassive black holes, it is difficult to study the small angular scales involved in the accretion process. A delay of the emission-line variability to the continuum one has been utilized to investigate the structure around the central black holes. We can deduce the structure of the broad-line regions from the estimation of time delay between the continuum and emission-line variations. This method is known as "reverberation mapping" [6]. We can also estimate the black hole mass with the time delay and the velocity dispersion of the responding emission-line gas [7].

[2] Quasars are the most luminous active galaxies having supermassive black holes at the center. They become bright when the central black holes absorb gas around them.

[3] Microlensing is magnification of light brightness when the light ray passes close to moving stars within the intervening galaxy.

[4] Dark matter fills with galaxies, but is invisible because of no radiation.

2.3 Origin of Short-term Variability in X-ray Transients

X-ray transients are binary systems composed of a black hole or a neutron star and a low-mass star. As in active galactic nuclei, an accretion disk is formed around the central compact object (see Fig. 2). They go through sporadic outbursts which are sudden increase of the luminosity of the accretion disk in multi-wavelengths. The outbursts are believed to be caused by the disk instability due to partial ionization of Hydrogen [8].

The global trend of their outbursts can be explained by the disk instability model. However, the origin of short-term variability which has been sometimes observed in their outbursts is not clearly known. To investigate the origin of the short-term variability, the time delay estimations between optical and X-ray light variations has been performed because the time delay depends on the radiation process and the disk structure to some extent (see Fig. 3). For instance, optical delays on timescales of several tens of seconds represent X-ray reprocessing[5] [9, 10]. This phenomenon is similar to the reverberation in the field of active galactic nuclei. Since the disk has some width in the radial direction, the time delay becomes wide in the time direction in general. On the other hand, very short time lags close to zero suggest the synchrotron emission [11, 12]. Additionally, large time delays in optical more than ten minutes would be produced by the adiabatically expanding jet ejections from the vicinity of the central object [13, 14].

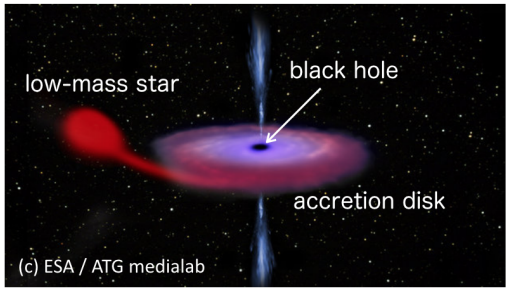

Fig. 2. Schematic figure of an X-ray transient.

3 Our Bayesian Approach

We introduce our Bayesian approach in the context of X-ray transients described in Sec. 2.3. We estimate time delays between multi-wavelength light curves of

[5] A part of radiated X-rays from the inner disk are absorbed at the outer disk and optical lights are re-emitted from the warm outer disk.

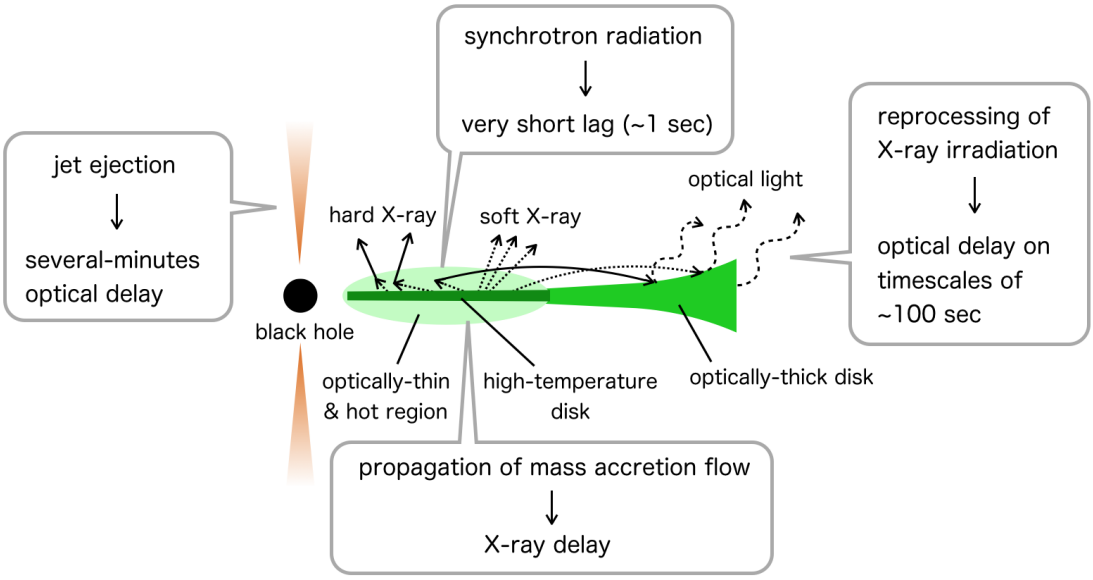

Fig. 3. Schematic picture of the structure of X-ray transient and related radiation processes producing different time lags.

V404 Cyg, a black-hole binary with a Bayesian method that was originally proposed for gravitational lensed systems [17]. This Bayesian method models the observational light curves using a state-space model and produces the posterior distribution of the time delay. We describe the formulation of our method in Sec. 3.1 and analyze the realistic data of V404 Cyg using the method in Sec. 3.2.

3.1 Bayesian State-space Model for Time Delay Estimation

Our method is specified in [17], and we briefly introduce its overview here. First, we introduce the observation equation of a state-space model. We denote n observed magnitudes of one light curve by $\boldsymbol{x} = \{x_1, x_2, \ldots, x_n\}$ that are measured at irregularly-sampled observation times $t_{x_1}, t_{x_2}, \ldots, t_{x_n}$. Similarly, we denote m observed magnitudes of the other light curve by $\boldsymbol{y} = \{y_1, y_2, \ldots, y_m\}$ that are observed at irregularly-sampled observation times $t_{y_1}, t_{y_2}, \ldots, t_{y_m}$. These magnitudes are observed up to their heteroskedastic measurement errors and we denote the known measurement standard deviations by δ_i for x_i and η_j for y_j. The measurement errors are Gaussian, and thus the observed magnitudes follow Gaussian distributions centered at the unknown latent magnitudes with standard deviations of the measurement errors, i.e.,

$$\begin{aligned} x_i \mid X(t_{x_i}) &\sim \mathrm{N}\big(X(t_{x_i}),\ \delta_i^2\big) \ \text{ for } i = 1, 2, \ldots, n, \\ y_j \mid Y(t_{y_j}) &\sim \mathrm{N}\big(Y(t_{y_j}),\ \eta_j^2\big) \ \text{ for } j = 1, 2, \ldots, m. \end{aligned} \tag{1}$$

where $X(t_{x_i})$ represents the latent magnitude corresponding to x_i and $Y(t_{y_j})$ indicates that corresponding to y_j.

We assume that one of the continuous-time latent light curves is a shifted version of the other by the time delay Δ in the horizontal axis and by the magnitude offset β in the vertical axis, i.e., $Y(t) = X(t-\Delta)+\beta$ for $t \in \mathbf{R}$. This curve-shifting assumption [18] enables representing all the observed magnitudes by a single latent light curve $X(t)$, e.g., equation (1) can be expressed as

$$y_j \mid X(t_{y_j}-\Delta), \Delta, \beta \sim \mathrm{N}\big(X(t_{y_j}-\Delta)+\beta,\ \eta_j^2\big) \text{ for } j = 1, 2, \ldots, m. \quad (2)$$

Fig. 4 displays a diagram describing this data generation procedure.

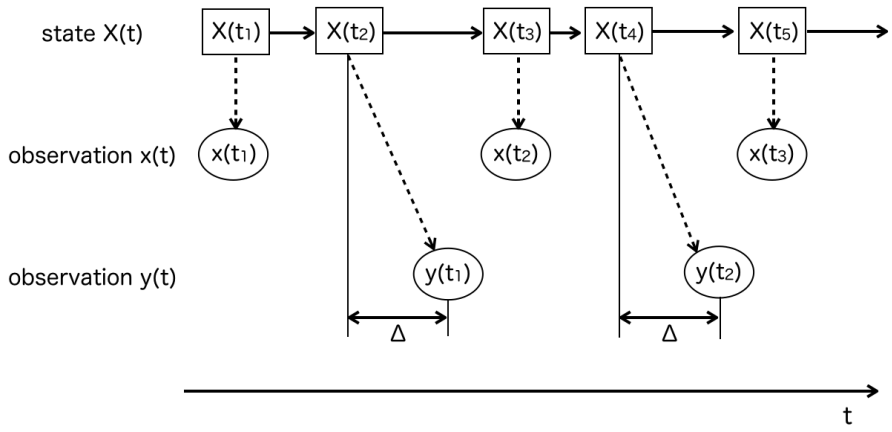

Fig. 4. Flowchart of a state-space model. Here, $X(t_i)$, $x(t_j)$ and $y(t_k)$ represent the latent magnitude, the observational magnitude at time t_j and the observational magnitude at time t_k, respectively. Each observation is assumed to be a realization of the latent magnitude up to a heteroskedastic measurement error; see equations (1) and (1) for details.

We assume that the latent light curve, $X(t)$, is a realization of an Ornstein-Uhlenbeck (O-U) process (also called a damped random walk (DRW) process among astronomers) [15]. The O-U process is suitable for modeling accretion-type light variations in both active galactic nuclei and black-hole binaries because of their power-law type power spectral density. This process is defined by the following stochastic differential equation including three parameters,

$$dX(t) = -\frac{1}{\tau}(X(t)-\mu)dt + \sigma dB(t). \quad (3)$$

Here μ and σ denote the overall mean and short-term variation of the underlying O-U process on the magnitude scale, respectively, τ is a timescale of the process

in days, and $B(t)$ is a standard Brownian motion. The solution of this equation gives us a Gaussian conditional distributions among the unknown magnitudes as follows:

$$X(t_1^{\Delta}) \sim \mathrm{N}\left(\mu,\ \frac{\tau\sigma^2}{2}\right),\ \text{and for } i = 2, 3, \ldots, n+m,$$
$$X(t_i^{\Delta}) \mid X(t_{i-1}^{\Delta}) \sim \mathrm{N}\left(\mu + a_i\big(X(t_{i-1}^{\Delta}) - \mu\big),\ \frac{\tau\sigma^2}{2}(1-a_i^2)\right) \tag{4}$$

where $a_i = \exp(-(t_i^{\Delta} - t_{i-1}^{\Delta})/\tau)$ and $\boldsymbol{t}^{\Delta} = (t_1^{\Delta}, \ldots, t_{n+m}^{\Delta})$ denote the sorted vector of $n+m$ observation times among the n observation times, $t_{x_1}, \ldots, t_{x_n}$, and the m time-delay-shifted observation times, $t_{y_1} - \Delta, \ldots, t_{y_m} - \Delta$. We collectively denote all the latent magnitudes by $\boldsymbol{X}(\boldsymbol{t}^{\Delta})$. These conditional distributions define the relationship between a pair of adjoining latent magnitudes in the state equation of a state-space model.

We set up scientifically motivated independent prior distributions for the five unknown parameters, Δ, β, μ, σ, and τ, as follows.

$$\begin{aligned}
\Delta &\sim \mathrm{Uniform}(w_1,\ w_2)\\
\beta &\sim \mathrm{N}(0,\ 10^5)\\
\mu &\sim \mathrm{Uniform}(-30,\ 30)\\
\sigma^2 &\sim \text{inverse Gamma}(1,\ 1)\\
\tau^2 &\sim \text{inverse Gamma}(1,\ 2\times 10^{-7}).
\end{aligned} \tag{5}$$

We may obtain the information about the minimum and maximum values of the time delay, w_1 and w_2, from the results of past analyses and astronomical probes using a physical model. The scales of the prior distributions of σ and τ are chosen to reflect on the large amplitude and the small timescale of the variability. See Sec. 2.4 and 2.5 of [17] for details and motivation for the choice of these prior distributions.

The resulting full posterior density of the unknown parameters is $\pi(\Delta, \beta, \mu, \sigma, \tau, \boldsymbol{X}(\boldsymbol{t}^{\Delta}))$ and is proportional to the multiplication of the probability density functions whose distributions are specified in equations (1), (2), (4) and (5). To sample the posterior distributions, we use a Metropolis-Hastings within Gibbs sampler [19] (see Sec. 3 of [17] for details of the sampling method).

3.2 Application to a Black-hole Binary

V404 Cyg, a black-hole X-ray transient, underwent an outburst in June, 2015. During the outburst, this system showed rapid and violent optical variability whose origin is under debate [16]. This object also underwent another outburst in December, 2015 and we performed optical photometry of the outburst through the VSNET (Variable Star Network) team. Comparing our optical data and the X-ray light curves of the *INTEGRAL* Imager on Board the Integral Satellite/CdTe array monitoring[6], we found two intervals, labeled as intervals (1)

[6] <http://www.isdc.unige.ch/integral/analysis#QLAsources>

and (2) during which X-ray and optical large-amplitude and stochastic variations were correlated in the outburst. However, the observational data were too sparse to apply the conventional method such as cross-correlation functions; see the upper panels of Fig. 5 for details of the data. Thus we apply the Bayesian approach specified in Sec. 3.1 to these data.

Before using the Bayesian time delay estimation method, we confirmed that the power density spectra of the X-ray light variations including the intervals (1) and (2) were well expressed by a power law. In addition, we derived more dense X-ray light curves with compact time bins whose sizes are all equal to five seconds from the *INTEGRAL* IBIS/ISGRI archived data. Moreover, we scaled the X-ray light curves to the amplitudes of optical variations since our data do not completely meet the curve-shifting assumption as described in Sec. 3.1. For this work, we used the results of the logarithmic regression between the X-ray and optical luminosity (see Sec. 3.2 of [20] for detailes). The data sets after the scaling are displayed in the middle panels of Fig. 5.

To implement the time delay estimations for the intervals (1) and (2), we used an R package, `timedelay`, which is publicly available at CRAN[7]. For preparation, we computed the profile likelihood of the time delay and detected their dominant modes in each interval. We initialized three Markov chains near the dominating mode for each time interval, running for 150,000 iterations; we discard the first 50,000 as burn-in iterations. To improve the convergence of the MCMC for Δ in the presence of multimodality, we adopted a repelling-attracting Metropolis algorithm [21]. The Gelman-Rubin convergence diagnostic statistics [22] of the three chains were 1.0004 and 1.0009 in intervals (1) and (2), respectively, close enough to unity. The posterior distributions of the estimated time delays are displayed in the bottom panels of Fig. 5. We found that the X-rays came later than the optical emission by $\sim$30–50 sec in the two intervals.

As for the origin of the short-term variability, X-ray reprocessing and synchrotron radiation as explained in Sec. 2.3 and Fig. 3 have been well considered for a long time. However, the estimated X-ray delay is not expected by these mechanisms. This is because X-ray reprocessing and synchrotron radiation will produce optical delays on timescales of several tens of seconds and very short time lags. Therefore, our time delay estimates indicate that fluctuations of mass accretion flow possibly propagate from the outer disk to the inner disk (see Sec. 4 in [20] for detailes).

4 Discussion and Future Study

In the field of gravitational lensed systems, several model-based methods have been developed during a blind competition called the Time Delay Challenge [23]. The competition was to prepare for the upcoming large-scale astronomical survey with the Large Synoptic Survey Telescope and lasted from October 2013 to July 2014. In the field of reverberation mapping in active galactic nuclei, a

[7] <https://cran.r-pro ject.org/package=timedelay>

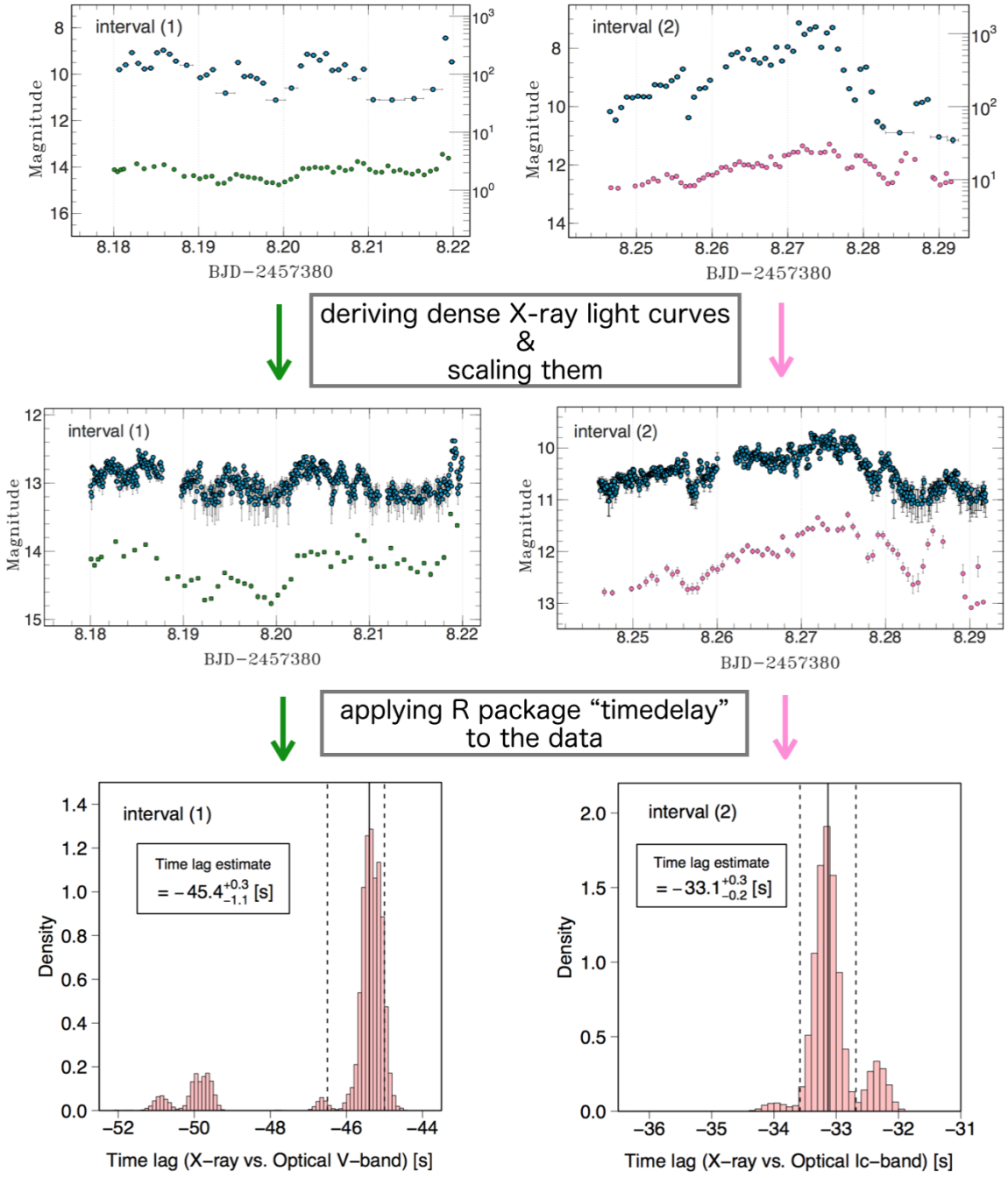

Fig. 5. Process of time delay estimations. Upper: Simultaneous optical and X-ray light curves during two intervals in the December outburst in V404 Cyg. The length of each interval is about an hour. The blue, green and pink circles represent the *INTEGRAL* X-ray light curves in the 25–60 keV energy band, the optical V-band data and the optical I_C-band data. Middle: optical light curves and more dense X-ray light curves after scaling for intervals (1) and (2). Lower: Posterior distributions of the time delays of the optical variations to the X-ray ones for intervals (1) and (2). The solid line indicates the posterior median of the time delay and the dashed lines represent the 68% quantile-based interval. The time delay estimate shown in each figure is the posterior median with 68% quantile-based interval. There are invisibly small modes near −30.5 and −25.8 seconds in the posterior distribution for interval (1) and near −48.1 seconds in that for interval (2), but we displayed only major modes. The data were the same in Figures 2, 4 and 5 in [20].

Gaussian process model with an exponential covariance matrix was introduced to reconstruct irregularly sampled observational light curves [24]. In the field of X-ray transients, however, a fully Bayesian method for time delay estimations between accretion-type light curves was adopted for the first time in our work [20]; statistically elegant methods other than cross-correlation function or its analogues had not been used before. The advantages of our Bayesian approach is to estimate time delays without any interpolations and to compute their errors. In addition, we can obtain the posterior distributions with high accuracy compared to conventional cross-correlation-based methods. For example, we also tried computing discrete correlation functions and the resulting errors are more than 40 times larger than those obtained by our Bayesian method.

Our approach is originally developed for the time delay estimations between gravitational lensed light curves, but has a great possibility to be extended for other fields in astronomy. For example, a light curve can be expressed by the convolution of the other light curve and a transfer function as follows:

$$Y(t) = \int \Psi(\Delta) X(t - \Delta) d\Delta, \tag{6}$$

where $\Psi(\Delta)$ is a transfer function. Although the transfer function is a delta function of the time delay in [17], introducing the triangular or rectangular or gaussian function as a transfer function will enable us to apply the method to reverberation mapping in active galactic nuclei. Also in the field of X-ray transients, this expansion is meaningful because we can estimate the disk size from the width of the time delay, taking advantage of X-ray reprocessing.

One challenging issue in using a transfer function other than a delta function is that the transfer function involves some unknown parameters. We cannot perform the imaging of X-ray transients and active galactic nuclei because they are too far away from us and thus may appear to be small point souces. Instead we can obtain light variations of them, which would include some valuable information on the structure of these objects. For instance, the shape of smoothing optical light curves produced by X-ray reprocessing could vary with the structure of the outer disk. The inference on the transfer function could tell us a detailed circumstance of the disk. In the near future, enormous observational data will be collected by the rapid progress of astronomical surveys and big telescopes. If we obtain rich data, a Bayesian inference on the transfer function might be possible.

5 Conclusions

Astronomical light curves usually have irregularly-sampled and sparse observation times. Moreover, we rarely obtain completely simultaneous multi-wavelength light curves. It is, therefore, necessary to devise the method for time lag estimations between such sparse multi-wavelength light curves. We estimated time lags between X-ray and optical light curves in a black-hole binary, V404 Cyg, with high accuracy by using a fully-Bayesian method including state-space model.

From the obtained X-ray delays, we suggested the disk structure was different in the 2016 outburst from that in the previous outburst. The method that we used assumes O-U process expresses stochastic light variations, which originate in the accretion to the central compact object, and could be applied to many light variations in various black-hole systems by changing the transfer function. Progress of astronomical study with the method is greatly expected in the near future.

Acknowledgments. We are thankful to many amateur observers in the VSNET (Variable Star Network) team for providing a lot of data used in this research. We also thank the *INTEGRAL* groups for making the products of the ToO data publicly available online at the *INTEGRAL* Science Data Centre. This work was financially supported by the Grant-in-Aid for JSPS Fellows for young researchers (MK) and by the Grant-in-Aid "Initiative for High-Dimensional Data-Driven Science through Deepening of Sparse Modeling" from the Ministry of Education, Culture, Sports, Science and Technology (MEXT) of Japan (25120007, TK). Hyungsuk Tak acknowledges partial support from the United States National Science Foundation under Grant DMS 1127914 to the Statistical and Applied Mathematical Sciences Institute.

References

1. Refsdal, S., Stabell, R., Pelt, J. and Schild, R., Constraints on source and lens parameters from microlensing variability in QSO 0957+561 A,B, A&A, 360, pp. 10–14 (2000)
2. Treu, T. and Marshall, P. J., Time delay cosmography, A&AR, 24, 11 (2016)
3. Refsdal, S., On the possibility of determining Hubble's parameter and the masses of galaxies from the gravitational lens effect, MNRAS, 128, 307 (1964)
4. Blandford, R. D. and Narayan, R., Cosmological applications of gravitational lensing, ARA&A, 30, pp. 311–358 (1992)
5. Linder, E. V., Lensing time delays and cosmological complementarity, Phys. Rev. D., 84, 12 (2011)
6. Blandford, R. D. and McKee, C. F., Reverberation mapping of the emission line regions of Seyfert galaxies and quasars, ApJ, 225, pp. 419–439 (1982)
7. Peterson, B. M. and Bentz, M. C., Black hole masses from reverberation mapping, NewAR, 50, pp. 796–799 (2006)
8. Tanaka, Y. and Shibazaki, N., X-ray Novae, ARA&A, 34, pp. 607–644
9. van Paradijs, J. and McClintock, J. E., Absolute visual magnitudes of low-mass X-ray binaries., A&A, 290 (1994)
10. Hynes, R. I., O'Brien, K., Horne, K., Chen, W. and Haswell, C. A., Echoes from an irradiated disc in GRO J1655-40, MNRAS, 299, 37 (1998)
11. Merloni, A., Di Matteo, T. and Fabian, A. C., Magnetic flares and the optical variability of the X-ray transient XTE J1118+480, MNRAS, 318, L15 (2000)
12. Kanbach, G., Straubmeier, C., Spruit, H. C. and Belloni, T., Correlated fast X-ray and optical variability in the black-hole candidate XTE J1118+480, Nature, 414, pp. 180–182 (2001)

13. van der Laan, H., A Model for Variable Extragalactic Radio Sources, Nature, 211, pp. 1131–1133 (1966)
14. Mirabel, I. F., Dhawan, V., Chaty, S., Rodriguez, L. F., Marti, J., Robinson, C. R., Swank, J. and Geballe, T., Accretion instabilities and jet formation in GRS 1915+105, A&A, 330, pp. L9–L12 (1998)
15. Kelly, B. C., Bechtold, J. and Siemiginowska, A., Are the Variations in Quasar Optical Flux Driven by Thermal Fluctuations?, ApJ, 698, pp. 895–910 (2009)
16. Kimura et al., Repetitive patterns in rapid optical variations in the nearby black-hole binary V404 Cygni, Nature, 529, pp. 54–58 (2016)
17. Tak, H., Mandel, K., van Dyk, D. A., Kashyap, V. L., Meng, X.-L. and Siemiginowska, A., Bayesian Estimates of Astronomical Time Delays between Gravitationally Lensed Stochastic Light Curves, preprint, (arXiv:1602.01462) (2016)
18. Pelt, J. and Hoff, W. and Kayser, R. and Refsdal, S. and Schramm, T., Time delay controversy on QSO 0957+561 not yet decided, A&A, 286, pp. 775–785 (1994)
19. Tierney, Luke, Markov Chains for Exploring Posterior Distributions, The Annals of Statistics, 22, pp. 1701–1728 (1994)
20. Kimura et al., Rapid Optical Variations Correlated with X-rays in the 2015 Second Outburst of V404 Cygni (GS 2023+338), MNRAS, accepted (2017), DOI: 10.1093/mnras/stx1555
21. Tak, H. and Meng, X.-L. and van Dyk, D. A., preprint, (arXiv:1601.05633) (2016)
22. Gelman, A. and Rubin, D. B., Inference from Iterative Simulation Using Multiple Sequences., Statistical Science., pp. 457–472 (1992)
23. Liao et al., Strong Lens Time Delay Challenge. II. Results of TDC1, ApJ, 800, 11 (2015)
24. Zu, Y., Kochanek, C. S. and Peterson, B. M., An Alternative Approach to Measuring Reverberation Lags in Active Galactic Nuclei, 735, 80 (2011)

Period Analysis in Astronomy by using Lasso

Keisuke Isogai[1], Taichi Kato[1], and Makoto Uemura[2]

[1]Department of Astronomy, Graduate School of Science, Kyoto University, Oiwakecho, Kitashirakawa, Sakyo-ku, Kyoto 606-8502, Japan
[2]Astrophysical Science Center, Hiroshima University, Kagamiyama 1-3-1, Higashi-Hiroshima, Hiroshima 739-8526
isogai@kusastro.kyoto-u.ac.jp

Abstract. Period analysis of brightness variations of astronomical objects is important in understanding the astrophysics. However, there are some difficulties. The time seriese data in astronomy is not uniformly sampled because the data is often obtained by several observation equipments and there are observational gap due to the whethear, sun light and so on. We introduced least absolute shrinkage and seletion operator (Lasso) for such data. As the results of our research, it is confirmed that the obtained signal is very sharp compared with descrete Fourier Transfer. We present three applications to the actual time-series data.

Keywords: period analysis, sparse modeling, Lasso, astronomy, variable stars

1 Introduction

Some astronomical objects called "variable stars" (e.g. pulsating stars and dwarf novae) show various periodic modulations of brightness. We cannot directly observe the structures of such objects because they are too far away. Thus it is important to obtain time-series data of brightness called "light curves" and analyze periods accurately. These periods help us to understand the structure or physical mechanism of such objects.

When analyzing light curves, astronomers often suffer from some problems. The light curves are obtained by several observational equipments, then the time intervals are irregular. Furthermore, we cannot always observe the target due to the wethear, sun, moon, or seasonal reason. As a result, light curves are basically sparse data. It is difficult to simply apply a Fast Fourier Transform (FFT) or descrete Fourier Transform (DFT) to such data. The window function for unevenly spaced data is complicated profile, then power spectrum by Fourier often shows many aliases. Thus it is needed to develop a new method to distinguish the closely separated signals in sparse data.

Compressed sensing can deals with a class of problems in restoring or estimating sparsely scattered, finite number of parameters in a huge dimension. We know that light curves of some variable stars are composed of finite number of frequencies. Thus we can apply the method of compressed sensing to period analysis of variable stars. In this paper, we present the new method of period analysis and the three applications to the actual time-series data.

2 Method

We assume a time-series data $Y(t_{\rm i})$ which is subtracted for their average and the mean of Y is zero. The observation can be expressed as a sum of signal $Y_{\rm s}$ and random errors n [5]:

$$Y_{\rm i} = Y(t_{\rm i}) = Y_{\rm s}(t_{\rm i}) + n(t_{\rm i}) \tag{1}$$

We assume a simply formulation with the combination of a large set of sine and cosine functins. Then $Y_{\rm s}$ can be expressed as

$$Y_{\rm s}(t_{\rm i}) = \sum_{,mj} a_{\rm j} \cos(\omega_{\rm j} t_{\rm i}) + \sum_{\rm j} b_{\rm j} \sin(\omega_{\rm j} t_{\rm i}) \tag{2}$$

where ω are frequencies and a and b are amplitiudes. The problem can be set to estimate a and b from Y.

Basically, the number of ω is too large to solve. Thus we introduced least absolute shrinkage and seletion operator (Lasso) [4] for period analysis of variable stars [1]. By using L1 regularization, we can solve such ill-posed problems. For the sample code, see the appendix in [1].

3 Results

3.1 Application to V1504 Cyg: evenly spaced and high density time-series data

We review the result of [2]. We were able to obtain evenly spaced and high density time-series data by Kepler Space Telescope. V1504 Cyg is a dwarf nova which shows "outbursts" with small periodic variations. Figure 1 shows two-dimensional discrete Fourier power spectrum and lasso one. In comparison to discrete Fourier, lasso yields very sharp signals, thus we succeeded in resolving the complex light curve into two or three periodic variations.

3.2 Application to EZ Lyn: unevenly spaced and sparse time-series data

We review the result of [3]. EZ Lyn is a pulsating star which has multiple periodic modulations. Figure 2 represents the two-dimensional lasso power spectrum. In spite of the noisy and unevenly spaced light curve, we can see very closely separated multiple signals.

3.3 Application to OV Boo: sinusoidal-like and non-sinusoidal variations

We will introduce the recent research of the eclipsing binary system "OV Boo" (Ohnishi et al. in prep.). Two-dimensional lasso power spectrum revealed that the light curve is composed of two periodic variations (figure 3). Note that one variation has a sinusoidal-like profile but the other has a profile very different from sinusoidal.

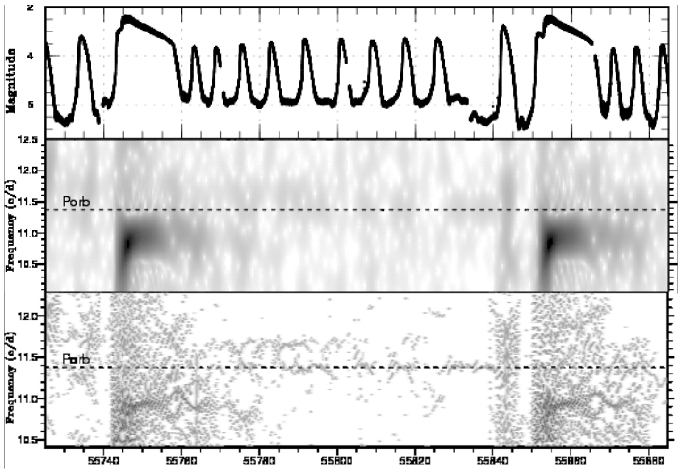

Fig. 1. Upper: Kepler light curve of V1504 Cyg, Middle: two-dimensional discrete Fourier power spectrum, Lower: two-dimensional lasso power spectrum. The sliding window and the time step used are 5d and 0.5 d, respectively.

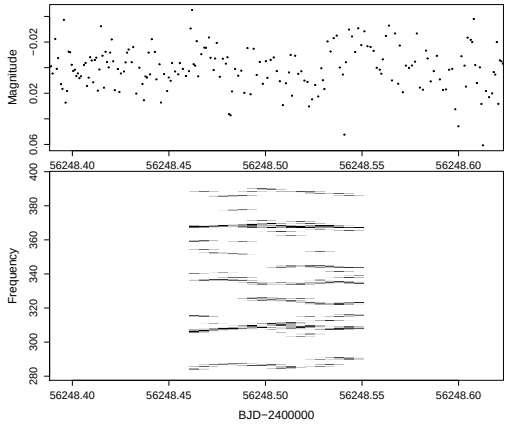

Fig. 2. Upper: light curve of EZ Lyn, Lower: two-dimensional lasso power spectrum. The sliding window and the time step used are 0.15 d and 0.005 d, respectively.

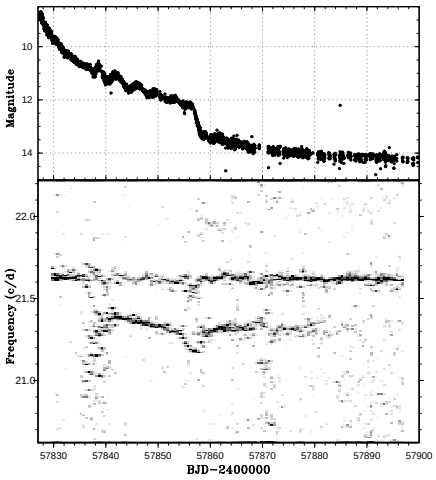

Fig. 3. Upper: light curve of OV Boo, Lower: two-dimensional lasso power spectrum. The sliding window and the time step used are 5 d and 0.5 d, respectively.

4 Summary

I'm so sorry for my incompleted paper. If accepted, I would revise this manuscript as soon as possible.

References

1. Kato, T., Uemura, M.: Period Analysis using the Least Absolute Shrinkage and Selection Operator (Lasso), PASJ, 64, 122 (2012)
2. Osaki, Y., Kato, T.: A Further Study of Superoutbursts and Superhumps in SU UMa Stars by the Kepler Light Curves of V1504 Cygni and V344 Lyrae, PASJ, 66, 15 (2014)
3. Pavlenko, E., Kato, T., Sosnovskij, A. A., Andreev, M. V., Ohshima, T., Sklyanov, A. S., Bikmaev, I. F., Galeev, A.I.: Dwarf Nova EZ Lyncis Second Visit to Instability Strip, PASJ, 66, 133 (2014)
4. Tibshirani, R.: Regression shrinkage and selection via the lasso, J. R. Statistical Soc. Ser. B, 58, 267 (1996)
5. Tanaka, T.: Mathematics of Compressed Sensing, IEICE Fundamentals Review, 4, 39 (2010)

Analyzing Spatial Dissimilarities via Effective-Time Series

Madalina Olteanu and Julien Randon-Furling

SAMM (EA 4543) Université Paris 1 Panthéon Sorbonne
90 rue de Tolbiac, 75013 Paris, France
{madalina.olteanu,julien.randon-furling}@univ-paris1.fr
http://samm.univ-paris1.fr

Abstract. We introduce a novel method to explore dissimilarities between N spatial units on a grid. Given a variable (that can be an average number over the unit, quantiles of a statistical distribution, a full distribution etc.), we associate to each unit the values of this variable computed on the set of its n-nearest neighbouring units (itself included), with $1 \leq n \leq N$.
Treating n as an effective time yields a set of time series. These will converge to the same final value but following different trajectories. Analyzing and comparing the differences, *eg* via clustering algorithms, allows one to quantify spatial dissimilarities on the grid with respect to the given variable.
We illustrate our method with an example drawn from urban geography.

Keywords: spatial patterns, dissimilarity, effective time, clustering

1 Introduction

In diverse areas of human and social sciences, and chiefly in geography, land and urban economy, one usually has to work with data available at a given spatial level – for example census blocks in the USA [1] or output areas in the UK [2]. Aggregating such blocks leads to various statistical difficulties, the most famous of which is the so-called "modifiable areal unit problem" first identified by S. Openshaw [3, 4]. Also, in most instances, elementary spatial units will exhibit dissimilarities. Indeed, if the data gives the number of medical practitioners, or quantiles of the income distribution within the unit, then generally units will differ from one another [5]. Such dissimilarities may or may not present spatial patterns. If they do, the geographical system may be said to exhibit spatial segregation, especially if the variables considered correspond to the relative proportions of different population groups [6–16].

In this paper we explore how modifiable areal units may actually prove to be a valuable tool to quantify segregation and spatial patterns of dissimilarities. Our idea is that instead of only comparing individual units [17], one may gain greater insight into relative spatial differences by taking into account the broader picture: that is, by considering ever larger neighbourhoods around a unit. Enlarging the

area all the way up to the whole city will give the same picture for every unit, that is, the same values for the variables under consideration. But the path followed from values at the unit level to values at the metropolitan level will depend on the starting unit. And these paths will be all the more different as units (and groups of units) differ from one area of the city to another.

Although intuitively relatively easy to describe, such a procedure presents a number of difficulties from a statistical point of view. We address some of them in this paper, therefore introducing a general framework for the definition of effective-time series (Section 2) associated with each of the smallest spatial units for various types of data (Section 3): raw numbers, fractions and averages, quantiles of distributions and full distributions. Finally, we illustrate this new method using available public data on the city of Paris (Section 4).

2 Effective-Time Series

Consider a grid comprising N fundamental spatial units. For a given unit, define $G_n(i)$, the cluster formed by itself and its $n-1$ nearest neighbouring units. Thus, $G_1(i)$ is just the i-th unit on its own, while $G_N(i)$ is the whole grid (whichever i from which one starts).

Now suppose one has a statistical variable ξ defined on each element of

$$\mathcal{G} = \{G_n(i),\, 1 \leq i, n \leq N\} \ .$$

Then, define for each areal unit i a function f_i such that $f_i(n)$ gives the value of ξ computed on $G_n(i)$.

Interpreting n as an effective time, one has for each areal unit i a time series representing the trajectory that takes ξ from its value on unit i to its value on the whole grid.

Analyzing these N time series, one then seeks to:

1. identify units that exhibit similar trajectories – this may be done for instance using clustering algorithms;

2. detect the crossing over between two regimes: the local one and the global one – in the former, ξ takes values significantly distinct from the one on the whole grid; in the latter, it takes very similar values.

3 Constructing datasets defined on $\mathcal{G}$

One of the statistical subtleties arises upon building datasets so that they are defined on $\mathcal{G}$.

Consider indeed the following standard situation: data is available in the form of a size factor s_i (*eg* a number of inhabitants) for each spatial unit, as well as the value of a possibly multi- or even infinite dimensional variable ξ.

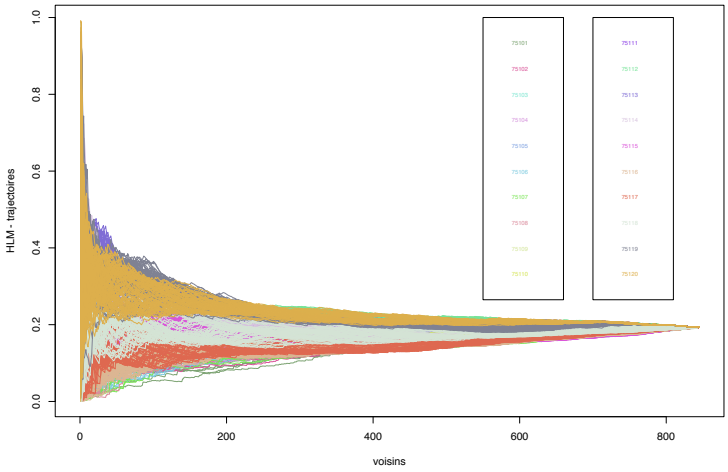

Fig. 1. Trajectories for the social housing rate, starting from each of 845 statistical units (so-called IRIS) in Paris. (Colours correspond to larger administrative districts called *Arrondissements*.)

This could be the number of offices or services of such and such type available in the unit, the social housing rate, an average income, a local density of public transportation, quantiles of a distribution...

When grouping n units, one needs to compute the value of the variable on the new aggregate. This is done easily in the case when ξ is simply a number:

$$\xi(G_n(i)) = \Sigma_{j \in G_n(i)} \, \xi(j) \; . \tag{1}$$

Similarly, $\xi(G_n(i))$ is readily computed when $\xi(i)$ is a rate or an average:

$$\xi(G_n(i)) = \frac{\Sigma_{j \in G_n(i)} \, s_j \xi(j)}{\Sigma_{j \in G_n(i)} \, s_j} \; , \tag{2}$$

with s_i the population of unit i (or another relevant size factor).

When ξ is a distribution that is known entirely (*eg* one knows the income of every single household in any of the units), one simply aggregates the individual datasets to obtain the dataset for a group of spatial units, and the corresponding empirical distribution is obtained readily.

A more difficult case, alas very frequent, is that when ξ retains only certain percentiles of a distribution. For instance:

$$\xi(i) = \{2354; 4684; 6546; 8138; 10542; 13622; 17058; 22202; 30862\} \, , \tag{3}$$

are the deciles of the income distribution (in euros per year) for a given spatial unit in the northern part of Paris.

In this case, one is led to either (or both) rely on an Ansatz for the shape of the underlying distribution (eg assume that it is log-normal, or exponential or other) or simulate the full dataset (with assumptions on the intradecile distributions) [18–23].

An example is given in Section 4, as we are faced with this problem when we consider income data for the city of Paris, available only in the form of quantiles for each census block.

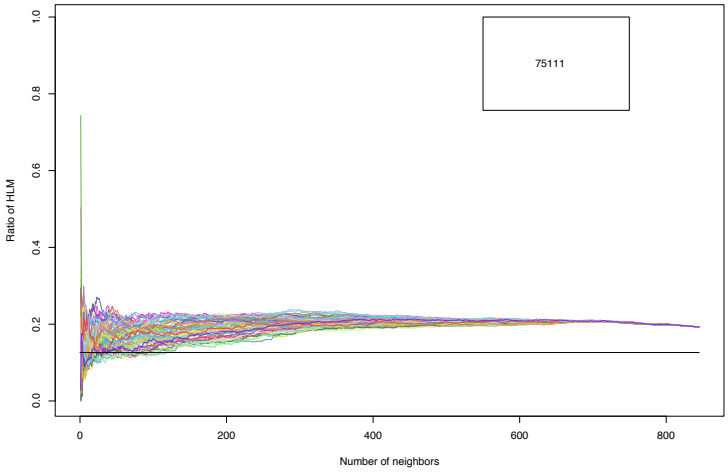

Fig. 2. Trajectories for the social housing ("HLM") rate, starting from each statistical IRIS (census block) in Paris's 11th district. The solid flat line gives the district's average social housing rate. (Colours correspond to the different IRIS taken as starting points for the effective-time series.)

4 Example: dissimilarities in Paris

As an illustration of how our method works in practice on real data, let us work with two types of data in Paris, available from France's census bureau, called INSEE ("Institut national de la statistique et des études économiques").

4.1 Social housing rate

For each basic statistical unit, named IRIS (*Îlot regroupé pour l'information statistique*), the rate of social housing among all housing in the IRIS is published. One is then in a situation where computing the corresponding rate for groups of

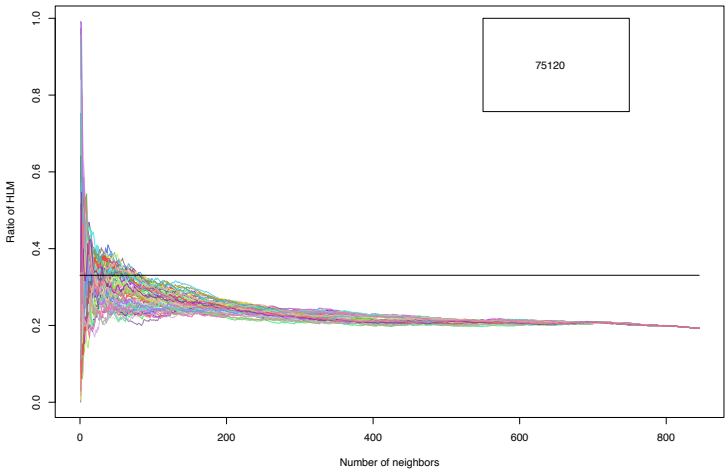

Fig. 3. Trajectories for the social housing ("HLM") rate, starting from each statistical IRIS (census block) in Paris's 20th district. The solid flat line gives the district's average social housing rate. (Colours correspond to the different IRIS taken as starting points for the effective-time series.)

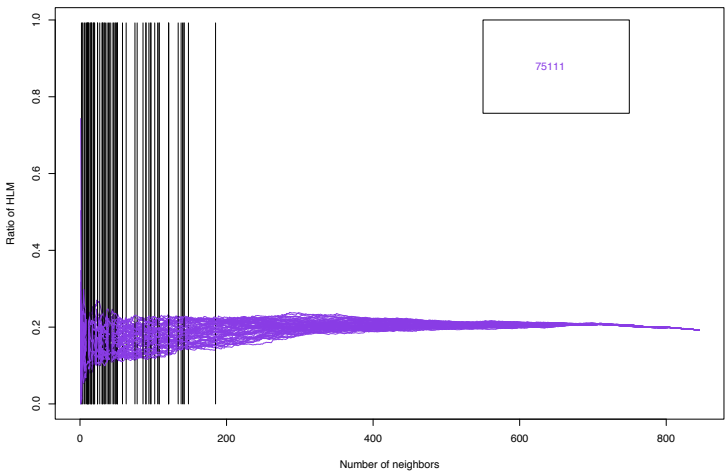

Fig. 4. Times of convergence within ± 0.05 of the city's mean, for the social housing ("HLM") rate, starting from each statistical IRIS (census block) in Paris's 11th district. Solid vertical lines correspond to convergence times on each path.

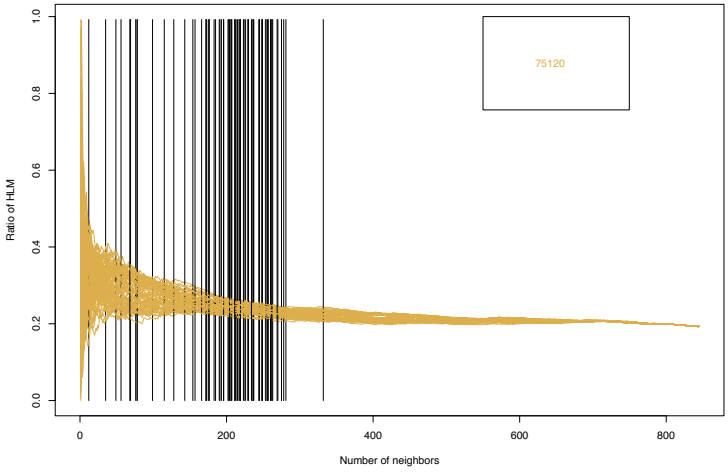

Fig. 5. Times of convergence within ± 0.05 of the city's mean, for the social housing ("HLM") rate, starting from each statistical IRIS (census block) in Paris's 20th district. Solid vertical lines correspond to convergence times on each path.

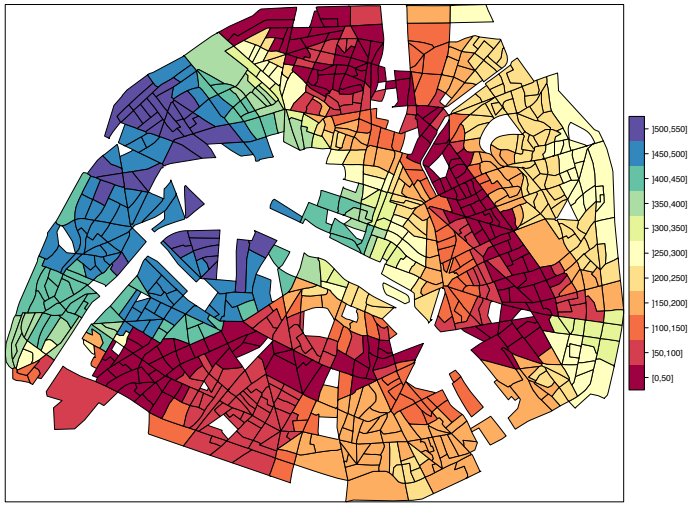

Fig. 6. IRIS areas coloured according to their (effective) time of convergence to the global mean. (White areas correspond to parks, riverbanks and IRIS where data is not available.)

IRIS is easy, and the effective-times series defined in Section 2 can be computed. These are shown in Figure 1.

One observes groups of paths that tend to start higher or lower than the metropolitan average, and converge to it more or less quickly, obviously with a strong spatial dependency as far as the initial units are concerned. Zooming in on some of the large administrative districts called *arrondissements*, one may for instance distinguish two traits:

- districts with bundles of paths that concentrate in about 200 effective-time steps;
- districts with bundles of paths that require a longer scale (*eg* 400 time steps) to come together.

This is very telling about the relative inner homogeneity of different districts. For example the north-eastern 20th arrondissement is, in terms of social housing rate, more homogeneous than the 11th (neighbouring the 20th, but closer to the city center) – see Figures 2 and 3.

We also look at the points when each path enters into a given interval (*eg* ± 0.05) within the city's average value. This reveals different patterns of convergence to the global mean, from one district to another and, inside each district, from one IRIS to another, as can be seen in Figures 4 and 5.

One may also classify IRIS blocks according to their "times of convergence" to the global mean and represent them accordingly on a geographical map of Paris (Fig. 6). Of course there are boundary effects. However, one notes that these are not predominant as peripheral western and north-eastern parts of the city, for instance, do not exhibit the same times of convergence to the city's average. In fact, boundaries, by forcing the aggregation of IRIS blocks closer to the city centre and beyond (rather than neighbouring IRIS blocks just outside the city) tend to smooth patterns rather than exacerbate them.

A particularly interesting feature that our method reveals is that the western (W) part of the city is "further away" from the whole city than the north-eastern (NE) part. Both parts correspond to extreme points for the variable in question, with a concentration of social housing in the NE part and a substantially lower than average rate in the W part. Starting from these extremal points above and below the city's average, but with symmetrical geographical position in the city, the W and NE parts could have had similar times of convergence to the city's mean. However, this is clearly not the case, thus revealing a higher level of singularity, as far as social housing is concerned, in the W part of the city than in the NE part.

Conversely, one observes a quasi ring of IRIS blocks with relatively short effective times of convergence to the city's mean. These are the historically socially mixed areas along the *boulevards*, the former *faubourgs* that used to be just outside the city's walls before these were transformed into *boulevards*. Our method thus reveals a lasting imprint visible in terms of distance to the city's average for a variable, the social housing rate, that may be taken as a proxy to social diversity.

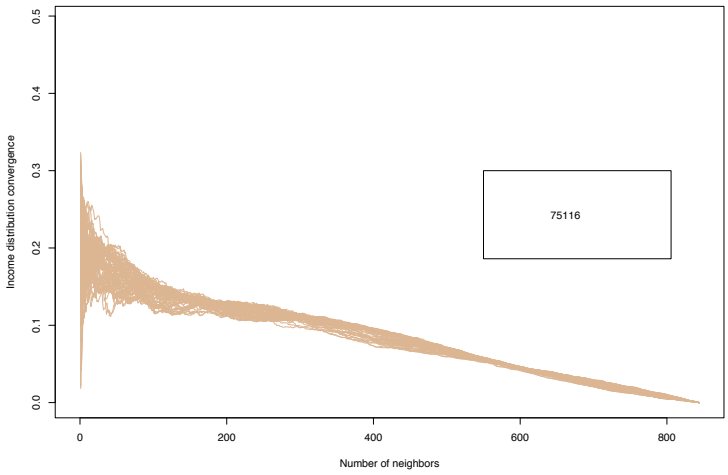

Fig. 7. Trajectories for the income distribution, starting from each statistical IRIS (census block) in Paris's 16th district. Ordinates correspond to the Kolmogorov-Smirnov distance between a group of blocks' income distribution and the whole city's income distribution.

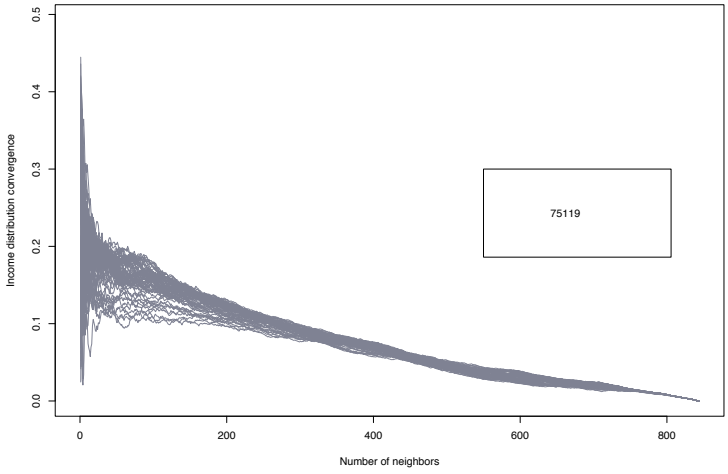

Fig. 8. Trajectories for the income distribution, starting from each statistical IRIS (census block) in Paris's 19th district. Ordinates correspond to the Kolmogorov-Smirnov distance between a group of blocks' income distribution and the whole city's income distribution.

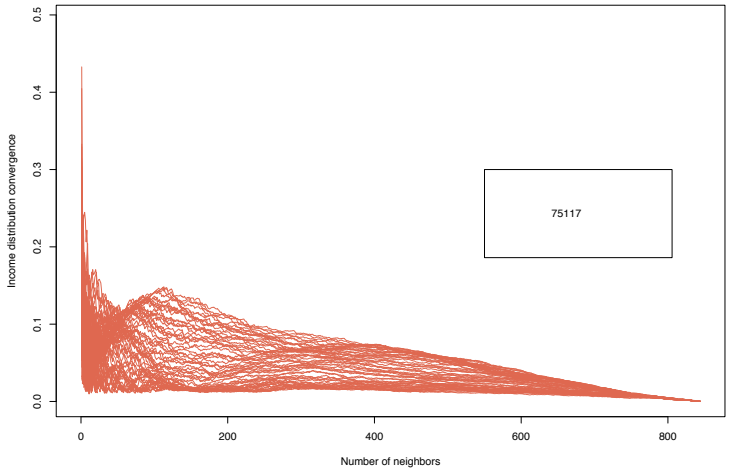

Fig. 9. Trajectories for the income distribution, starting from each statistical IRIS (census block) in Paris's 17th district. Ordinates correspond to the Kolmogorov-Smirnov distance between a group of blocks' income distribution and the whole city's income distribution.

4.2 Income distribution

We now consider a second example, and build effective-time series for the income distribution in Parisian census blocks.

As explained in section 2, when working with distributions available only through their quantiles, computing points for each group of blocks is a slightly more involved task. In this case, we chose to estimate the parameters of the best-fitting distribution (which happened to be log-normal) given a block's quantiles. Then, from this distribution, we simulated data corresponding to the number of households in the block. Thus we obtained a full ensemble of simulated households for every possible group of neighbouring blocks, from one block only to the whole city.

We show only some preliminary results here, in the form of trajectories for IRIS blocks in three Parisian districts of comparable sizes and population numbers: the 16th, 17th and 19th *arrondissements* – see Figures 7, 8 and 9. The first one corresponds to the western peripheral part of the city, the second one to the north-western part and the third one to the north-eastern part.

Focusing on the 16th and 19th districts, one observes again that, also in terms of income distribution, the 16th tends to be further away from the full city's picture, as it takes generally longer for its blocks to converge to the city's distribution than for blocks in the 19th district for instance.

The 17th district exhibits a totally different behaviour, with trajectories that first come close to the city's mean but then bounce up again further from it. This

can be understood as follows: some IRIS blocks in the 17th district belong to relatively well mixed neighbourhoods, but the aggregation process around them leads to incorporate at an early stage (very) wealthy blocks from the neighbouring 16th or 8th districts, which sends trajectories away from the city's distribution. A similar effect may (and does) take place for neighbourhoods relatively close to blocks that are much poorer than the city as a whole.

5 Conclusion

In the literature, aggregation of spatial data units has been so far generally considered as a difficulty to circumvene rather than an opportunity to analyze spatial dissimilarities. The new method introduced in this paper uses aggregation as a means to extract information on the relative singularity of each spatial unit within the city as a whole. Aggregation procedures may indeed reveal features that are not so easily seized from other perspectives. Another example is the recent use of aggregation to explore the behaviour (and more specifically the scaling laws) of various statistical variables across a phase space corresponding to almost all possible city boundaries' definitions in England and Wales [24].

We have chosen here to represent the aggregation procedure as an effective-time series, mostly in order to allow for standard analyses and vocabulary to be used. Also, viewing aggregation paths as time series helps understand the singular nature of each path, and its strong dependency on the initial block.

However, one may choose other representations. In particular, in the time-series framework, we have called *time of convergence* the number of aggregated neighbouring blocks needed around a starting block to get close enough to the city's value of the variable under consideration. But it may be more telling geographically to call this number the local urban *radius*, *distance* or *metric*. Indeed it is a proxy for the area one needs to explore locally to obtain a reasonably good perception of the city as a whole.

Note also that one does not have to be working in the discrete framework of statistical blocks. For certain variables, such as access to public transport networks, one may work directly in terms of a local density, and therefore compute surface areas (or equivalently radii) for which, around a given point, one obtains the same density per inhabitant as in the whole city.

In future work, we will seek to examine further the properties of such local urban metrics. This should allow us to extend the illustrative examples presented here into a proper study of the Parisian metropolitan area, before carrying the same analysis on other metropolitan areas, *eg* Greater London, for comparison purposes.

References

1. US Census Bureau. Geographic areas reference manual, 1994.
2. Office for National Statistics. Census geography. `https://www.ons.gov.uk/methodology/geography/ukgeographies/censusgeography`. Accessed 2017-07-21.
3. Stan Openshaw. *The modifiable areal unit problem*. University of East Anglia, 1984.
4. Stan Openshaw and Peter J Taylor. A million or so correlation coefficients: three experiments on the modifiable areal unit problem. *Statistical applications in the spatial sciences*, 21:127–144, 1979.
5. Edward L Glaeser, Jed Kolko, and Albert Saiz. Consumer city. *Journal of economic geography*, 1(1):27–50, 2001.
6. Donald O Cowgill and Mary S Cowgill. An index of segregation based on block statistics. *American Sociological Review*, 16(6):825–831, 1951.
7. Otis Dudley Duncan and Beverly Duncan. A methodological analysis of segregation indexes. *American sociological review*, 20(2):210–217, 1955.
8. Reynolds Farley and Karl E Taeuber. Population trends and residential segregation since 1960. *Science*, 159(3818):953–956, 1968.
9. Charles F Cortese, R Frank Falk, and Jack K Cohen. Further considerations on the methodological analysis of segregation indices. *American sociological review*, pages 630–637, 1976.
10. Joseph Schwartz and Christopher Winship. The welfare approach to measuring inequality. *Sociological methodology*, 11:1–36, 1980.
11. Michael J White. The measurement of spatial segregation. *American journal of sociology*, 88(5):1008–1018, 1983.
12. David R James and Karl E Taeuber. Measures of segregation. *Sociological methodology*, 15:1–32, 1985.
13. Sean F Reardon and Glenn Firebaugh. 2. Measures of Multigroup Segregation. *Sociological methodology*, 32(1):33–67, 2002.
14. Lawrence A Brown and Su-Yeul Chung. Spatial segregation, segregation indices and the geographical perspective. *Population, space and place*, 12(2):125–143, 2006.
15. I. Caridi, J.P. Pinasco, N. Saintier, and P. Schiaffino. Characterizing segregation in the SchellingVoter model. *Physica A: Statistical Mechanics and its Applications*, 487:125 – 142, 2017.
16. Marie Cottrell, Aurélien Hazan, Madalina Olteanu, and Julien Randon-Furling. Multidimensional urban segregation: an exploratory case study. In *12th International Workshop on Self-Organizing Maps and Learning Vector Quantization (WSOM+)*. IEEE eXplore, 2017.
17. Sanjoy Chakravorty. A measurement of spatial disparity: The case of income inequality. *Urban Studies*, 33(9):1671–1686, 1996.
18. Thomas M Stoker. Completeness, distribution restrictions, and the form of aggregate functions. *Econometrica: Journal of the Econometric Society*, pages 887–907, 1984.
19. Christian Genest and James V Zidek. Combining probability distributions: A critique and an annotated bibliography. *Statistical Science*, pages 114–135, 1986.
20. A Stewart Fotheringham and David WS Wong. The modifiable areal unit problem in multivariate statistical analysis. *Environment and planning A*, 23(7):1025–1044, 1991.
21. Christian Genest. Vincentization revisited. *The Annals of Statistics*, pages 1137–1142, 1992.

22. Dennis E Jelinski and Jianguo Wu. The modifiable areal unit problem and implications for landscape ecology. *Landscape ecology*, 11(3):129–140, 1996.
23. Fabio Busetti. Quantile aggregation of density forecasts. *Oxford Bulletin of Economics and Statistics*, 2014.
24. Elsa Arcaute, Erez Hatna, Peter Ferguson, Hyejin Youn, Anders Johansson, and Michael Batty. Constructing cities, deconstructing scaling laws. *Journal of The Royal Society Interface*, 12(102):20140745, 2015.

Sequential motor unit number estimation (MUNE)

Gareth Ridall, Andrew Titman

Lancaster University, UK.
g.ridall@lancs.ac.uk

Abstract. In the field of neurology there is interest in determining the number of units supplying a muscle group. As increasing stimulus is applied at the nerve, each motor unit of the axon bundle is activated with increasing probability and the observed response is recorded. A variable dimension state space model is used where the observed responses are assumed Gaussian, conditional on binary indicators determining whether a unit is firing. The set of all feasible trajectories of binary states are stored in a particle system summarised by sufficient statistics with weights calculated from the marginal likelihood. We use a type of auxiliary particle filter, formulating an efficient proposal mechanism for the potential binary states for the current observation. We compare our algorithm with RJMCMC [1], and discuss some of the new algorithm's advantages.

Keywords: MUNE, Sequential Monte Carlo, The Kalman Filter, the Static Particle Filter, Marginalisation

1 Introduction

A universally accepted method of motor unit number estimation (MUNE) is needed to provide a reliable and meaningful endpoint in clinical trials on drugs designed to slow down the onset of neuro-degenerative diseases such as A.L.S or motor neurone disease. Despite a long history of research that span over 50 years, no universally accepted method of MUNE has emerged, [2]. [3] developed a complex statistical model based on a set of assumptions with a basis in accepted neurological science. Markov Chain Monte-Carlo (MCMC) was used for estimation and the BIC for model selection. [1] used a similar model but improved the model selection method through the use of reversible jump Markov Chain Monte Carlo (RJMCMC). This method has proved useful for conducting MUNE with low to moderate numbers of units and has been used in the studies of [4] [5]. However it is computationally demanding [6] and furthermore relies on a judgment of convergence of a complex Markov chain. Our new sequential method cuts down the computational burden substantially. In addition it also offers extensions not possible with MCMC such as the online resolution of design issues.

Rather than conditioning on nuisance parameters, as is done in RJMCMC, we propose a state space model that relies on the sequential marginalisation of

states and parameters. This marginalisation provides the evidence for a particular binary firing combination. Although the evidence for a combination may not be strong initially evidence for it may strengthen later as more observations are collected. Thus at any one time there may be many multiple firing histories each with their own cumulative evidence. The measurement process is Gaussian and Bayesian estimates of the posterior and marginal likelihood are available in closed form. However the state process is binary so we must resort to approximations. The particle filter provides a general solution to the nonlinear, non-Gaussian filtering problem with arbitrarily accuracy. A general review can be found in [7] and a review of particle filters with parameters can be found at [8].

The history of firing combinations, the evidence for them and the sufficient (or approximately sufficient) statistics become the components of a particle filter. The current trajectory of states is summarised by a set of sufficient and approximately sufficient statistics. These are used to propose the next firing combination. This proposal needs to be exhaustive but when the number of units firing stochastically is large the set of proposals must be thinned down to a manageable size. We use the trick similar to that of [9] and propose according to the approximate predictive. For this we use an approximation as the true predictive involves numerical integration and is computationally demanding For each feasible combination we augment the sufficient statistics of identical particles to encompass the new combination and adjust the cumulative weight. Despite the initial thinning step the size of the set of trajectories will eventually become unmanageable and a resampling step needs to be carried out to prune out particles with low cumulative evidence. In constructing our particle filter, we attempt to minimise the Monte Carlo variation and use deterministic methods where possible. The pruning of unlikely trajectories also needs to be treated carefully because a firing combination may only have a low predictive probability initially. In this paper we explain and apply our method to simulated data only. Real data is presented just for illustrative purposes.

2 The context

An experiment is carried out to determine the number of motor neurones in a subgroup of muscles supplied by a nerve. A stimulus of magnitude S_t is applied at the nerve and the response (measured by force or compound muscle action potential (CMAP)) is recorded and denoted by y_t.

As the stimulus is increased a motor unit moves from inactive ($k \in \mathcal{I}_t$) to firing stochastically ($k \in \mathcal{S}_t$)(or some of the time) to firing all of the time ($k \in \mathcal{A}_t$). Figure (1) shows how these categories change as the stimulus is increased.

$$\text{inactive } (\mathcal{I}_t) \longrightarrow \text{stochastic } (\mathcal{S}_t) \longrightarrow \text{always } (\mathcal{A}_t). \tag{1}$$

These categories are created by putting a threshold on the predictive probability of firing and is explained in Section (4.1).

When considering possible firing combinations at the next observation, only the units $k \in \mathcal{S}_t$ need to be considered but we must also include the possibly that an inactive unit fires for the first time.

3 The model

In this section we describe the model for the firing combinations or state process and then conditional likelihood or the probability of the observations given the firing process. We then formulate the likelihood for the complete data followed by priors for all the parameters.

3.1 The firing process

Let N_t denote the number of units firing at the current instance in time.T he probability of each unit $k = 0, 1, \ldots, N_t$ firing at time $t = 1, 2, \ldots$ is modelled as Bernoulli with a logistic link to stimuli.

$$\begin{aligned} Z_{k,t} \mid m_k, \delta_k &\sim \text{Bernoulli}\,(p_{k,t}) \\ \text{logit}\ \ (\text{p}_{\text{k,t}}) &= \delta_k(S_t - m_k). \end{aligned} \tag{2}$$

We denote the hidden binary combination as $\mathbf{z}_t$ where

$$\mathbf{z}_t = \left(1,\, z_{1,t},\, z_{2,t},\, z_{3,t},\, \ldots,\, z_{N_t,t}\ \right).$$

These combinations are shown on Figure (2) to the right of the observation where it first occurs.

The mean threshold of a unit, m_k, is the stimulus for which a motor unit has a 50% probability of firing. The precision of the threshold, δ_k^2, determines the steepness of the corresponding excitability curves and the range over which the unit displays stochastic firing.

For the parameters governing the firing process $\boldsymbol{\omega}_k = \{m_k, \delta_k\}$ we allocate a normal prior,

$$\boldsymbol{\omega_k} \sim \text{Normal}\,(\boldsymbol{\omega_{k0}}, \boldsymbol{\Sigma}_{k,0}), \quad k = 1, 2, \ldots N_t. \tag{3}$$

A geometric prior for the number of units, N_t, can be used:

$$p(N_t = n) = \theta(1-\theta)^n, \quad n = 1, 2, \ldots \tag{4}$$

where $0 < \theta < 1$.

3.2 The conditional likelihood

The observations y_t are assumed conditionally independent (given the firing patterns $\mathbf{z}_t$) and are distributed about the expected value as shown by

$$y_t \mid \mathbf{z}_t, \boldsymbol{\mu}_t, \sigma \sim \text{Normal}\left(\mathbf{z}_t\boldsymbol{\mu}_t, \sigma^2\right), \tag{5}$$

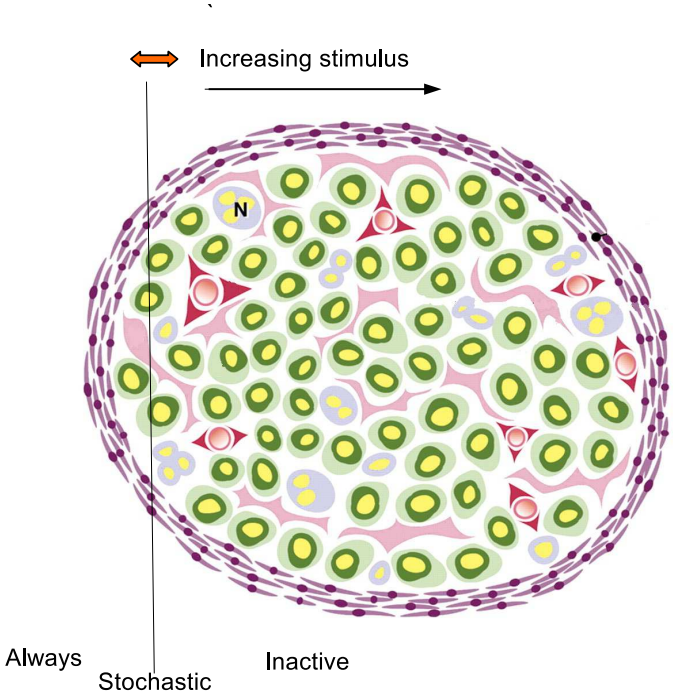

Fig. 1. The diagram shows an axon bundle. A stimulus is applied from the left hand side. The boundary of the influence of the stimulus is shown by a vertical line. As the stimulus increases the boundary moves to the right and an increasing number of axons are activated. Axons to the right have not been activated yet whereas units on the left are always firing. Axons near the boundary are firing some of the time.

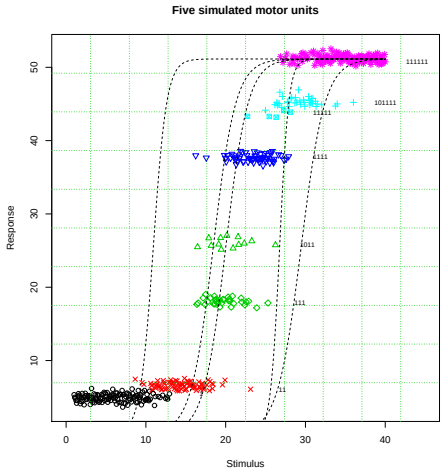

Fig. 2. The diagram shows data simulated from a five unit model. The colors depict the number of units firing. The symbols depict the different firing combinations. The firing combinations are shown to the right of the points. We show the hidden binary response at time t on right of the first occurrence of that combination.

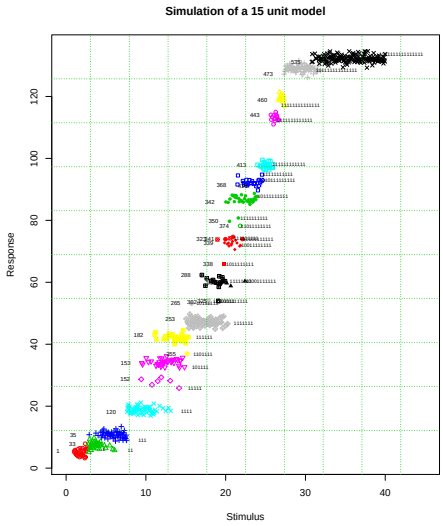

Fig. 3. The diagram shows data simulated from a fifteen unit model. The colors depict the number of units firing. The symbols depict the different firing combinations. The firing combinations are shown to the right of the points. We show the hidden binary response at time t on right of the first occurrence of that combination and the stimulus number shown to the left of the same point.

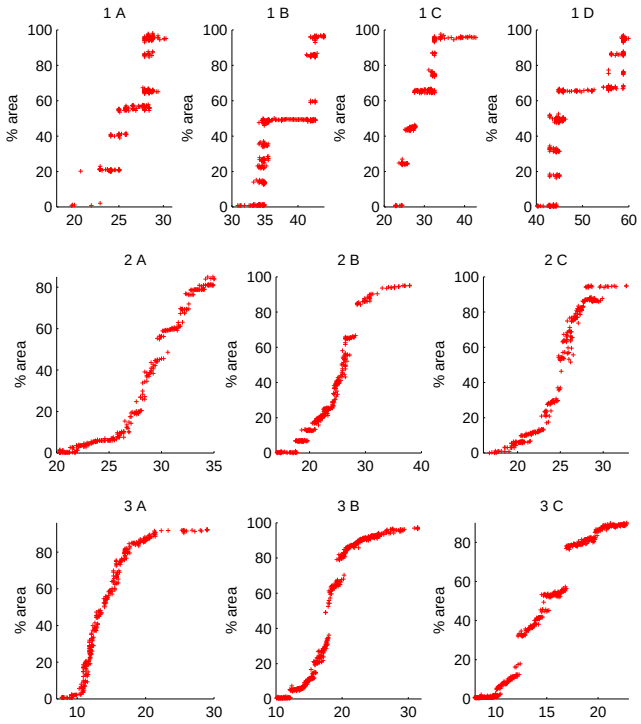

Fig. 4. Replicate studies carried out on three patients. The data collection is repeated with the electrodes removed and repositioned for each repeat study. The disease progression is extremely advanced for the patient in the top frame. This is less so for the second, and with the third the disease has only just been diagnosed so it has not progressed far.

where σ^2 is the variance of the observations and the vector $\boldsymbol{\mu}_t$ represents the motor unit sizes denoted by $\boldsymbol{\mu}_t = \left(\mu_0, \mu_1, \mu_2, \mu_3, \ldots, \mu_{N_t}\right)^T$, where μ_0 is the mean of the baseline signal.

This model assumes that all observations have the same variance but this assumption can be generalised in a straight-forward manner. Fully conjugate priors for the measurement parameters, $\boldsymbol{\mu}$ and σ^2 can be depicted as:

$$\begin{aligned} \boldsymbol{\mu}_{\mathbf{1:}\boldsymbol{N_t}} &\sim \text{Normal}\left(\boldsymbol{\mu_0}, \sigma^2\mathbf{C_0}\right) \\ 1/\sigma^2 &\sim \text{Gamma}\left(a_0, b_0\right). \end{aligned} \tag{6}$$

These priors ensure that the posterior parameters and the predictive distributions are available in closed form.

3.3 The probability model

Equations (2),(3),(4),(5) and (6) can be combined to give the full probability model,

$$\begin{aligned} p(y_t, \mathbf{z}_t, \sigma_t, \boldsymbol{\omega}_{1:N_t}, \boldsymbol{\mu}_{1:N_t}, N_t) = {} & p(y_t \mid \mathbf{z}_t, \boldsymbol{\mu}_{1:N_t}, \sigma^2) \\ & \times \prod_{k=1}^{N_t} p_{k,t}^{z_{k,t}} (1 - p_{k,t})^{1 - z_{k,t}} \\ & \times p(\boldsymbol{\mu}_{1:N_t}, 1/\sigma_t^2 \mid N_t, a_0, b_0, C_0, \boldsymbol{\mu}_0) \\ & \times \prod_{k=1}^{N_t} p(\boldsymbol{\omega}_k \mid \boldsymbol{\omega}_0, \boldsymbol{\Sigma}_0) \\ & \times \theta(1 - \theta)^{N_t}. \end{aligned}$$

4 Sequential inference

It is important to understand that the identification of the correct firing states is critical for our method to work. If the firing combinations are known then all of the parameters can be calculated very simply using a weighted least squares estimate for the parameters of the measurement process and iteratively weighted least squares for the parameters of the state process. Often at any time point there is more than one possible firing combination and it is not immediately obvious which is the best. It is therefore necessary to keep each of these combinations until one can eventually be excluded for comparative lack of cumulative evidence. We define a particle representation of the set of possibilities.

Each particle has

1. A history of firing combinations for each of the previous stimuli.
2. A set of sufficient statistics for the measurement process. These statistics will increase in dimension as more units are activated.

3. A set of sufficient statistics for the firing process. Some of these will be firing all the time which means they do not need to be sequentially updated. Some are stochastic which do need to be updated with each observation and finally inactive units where the sufficient statistic is just the prior.
4. A cumulative weight representing the evidence for the trajectory of firing combinations.

We let the set of particles at time t be represented by

$$\left\{ \underbrace{\boldsymbol{\mu}_t^{(p)}, \mathbf{C}_t^{(p)}, a_t^{(p)}, b_t^{(p)}}_{\text{Measurement process}}, \mathbf{z}_{1:t}^{(p)}, \underbrace{\boldsymbol{\omega}_{k\in\mathcal{A}_t}^{(p)} \boldsymbol{\omega}_{k\in\mathcal{S}_t}^{(p)}, \boldsymbol{\Sigma}_{k\in\mathcal{A}_t}^{(p)} \boldsymbol{\Sigma}_{k\in\mathcal{S}_t}^{(p)}}_{\text{Firing process}} \right\}_{p=1}^{P_t} \tag{7}$$

with associated weights of evidence $\left\{ w_t^{(p)} \right\}_{p=1}^{P_t}$, normalised weights, $\left\{ W_t^{(p)} \right\}_{p=1}^{P_t}$.

Our method of inference has a structure similar to that of the auxiliary particle filter [9] and summarise our particle filter in the following steps:

1. **From all possible firing combinations select good proposals.** For each current particle, propose all possible combinations and then using the predictive probability select the best firing pattern.
2. **Extend and update sufficient statistics.** For each proposal from a parent particle, update the child particle.
3. **Reweight the cumulative evidence for the current trajectory** by assimilating the evidence for the current firing combination.
4. **Prune or resample the particles if necessary.** Remove the particles with very low cumulative evidence.

We now explain the above steps more carefully.

4.1 Propose and thin

Firstly we propose a set of feasible firing patterns for the most recent observation. The number of possible firing combinations depends on the number of units firing stochastic and incorporates the additional possibility that a new unit fires for the first time. Because of the large number of possibilities, $(2^{|\mathcal{S}_t|+1})$, combinations with very low predictive probability are discarded.

We denote the set of firing combinations of same dimension as $\left[\mathbf{z}_{t+1}^{(c)} \right]_{c=1}^{2^{|\mathcal{S}_t|}}$, and sample from this set proportional to the predictive probability which is given by

$$\begin{aligned} q(\mathbf{z}_{t+1}^{(c)}) &\propto p(y_t \mid \mathbf{z}_{t+1}^{(c)}, \boldsymbol{\mu}_t) p(\mathbf{z}_{t+1}^{(c)} \mid \boldsymbol{\omega}_{1:N_t}, S_{t+1}) \\ &\propto p(y_t \mid \mathbf{z}_{t+1}^{(c)}, \boldsymbol{\mu}_t) \prod_{z_{k,t+1} \in \mathbf{z}_{t+1}^{(c)}} \tilde{p}_{k,t+1}^{z_{k,t+1}} (1 - \tilde{p}_{k,t+1})^{1 - z_{k,t+1}}. \end{aligned} \tag{8}$$

where we use $\tilde{p}_{k,t+1}$) to denote the predictive probability of a unit firing: $\tilde{p}_{k,t+1} = \int p(\mathbf{z}_{k,t+1} = 1 \mid \omega_k) p(\omega_k) d\omega_k$. The approximate predictive has the effect of shrinking the probability toward 0.5 according to the amount of uncertainty in this parameter. This is particularly important in this application where we use this probability to classify the activity status of the motor unit. [1]

We denote the set of proposals where the dimension is increased by one as $\left[\mathbf{z}_{t+1}^{(c)+}\right]_{c=1}^{2^{|\mathcal{S}_t|}}$. Proposing sensible firing combinations is more difficult because the parameters of the new motor unit are not known. The dimension of the sufficient statistics for the measurement process must be increased. We denote the new covariance matrix $\mathbf{C}_t^{(c)+}$ and the mean vector as $\boldsymbol{\mu}_t^{(c)+}$.

$$\boldsymbol{\mu}_t^{(p)+} \leftarrow \begin{bmatrix} \boldsymbol{\mu}_t \\ \mu_0 \end{bmatrix} \quad \mathbf{C}_t^{(c)+} \leftarrow \begin{bmatrix} \mathbf{C}_t^{(c)} & \mathbf{0} \\ \mathbf{0}^T & C_0 \end{bmatrix}$$

$$\boldsymbol{\mu}_{t+1}^{(c)+} \leftarrow \boldsymbol{\mu}_t^{(c)+} + \frac{\mathbf{C}_{t+1}^{(c)+} \mathbf{z}_{t+1}^{(c)+T}}{1 + \mathbf{z}_{t+1}^{(c)+} \mathbf{C}_{t+1}^{(c)+} \mathbf{z}_{t+1}^{(c)+T}} \times (\mathbf{y}_{t+1} - \mathbf{z}_{t+1}^{(c)+} \boldsymbol{\mu}_t^{(c)+}).$$

In addition, a new particle for the firing process must be constructed from the prior and the current observation.

Each of the proposals for the firing combination $\mathbf{c}$ are augmented by the new state and indexed as before by $c = 1, 2, \ldots, 2^{|N_t|}$ are made from

$$q(\mathbf{z}_{t+1}^{(c)+}) \propto p(y_{t+1} \mid \mathbf{z}_{t+1}^{(c)+}, \boldsymbol{\mu}_{t+1}^{(c)+}) \prod_{z_{k,t+1} \in \mathbf{z}_{c,t+1}^{+}} \left[\tilde{p}_{k,t+1}^{z_{k,t+1}} (1 - \tilde{p}_{k,t+1})^{1 - z_{k,t+1}}\right] p(z_{k+1,t+1}^{f}) \tag{9}$$

where $p(z_{k+1,t+1}^{f})$ is an estimate of a motor unit $k+1$ firing for the first time at time $t+1$.

We then normalise the $2^{|\mathcal{S}_t|+1}$ set of proposals discarding all proposals that are below a threshold. We denote the set of thinned proposals as $\{\mathbf{z}_{t+1}^{(p)}\}_{p=1}^{P_t}$ and $\{\mathbf{z}_{t+1}^{(p)+}\}_{p=1}^{P_t^+}$ and their proposal probabilities as $q(\mathbf{z}_{t+1}^{(p)})$ and $q(\mathbf{z}_{t+1}^{(p)+})$. A number of identical children particles are created for each candidate.

4.2 Update for the measurement process

For each of the children the sufficient statistic for the measurement process is updated.

[1] We approximate the predictive probability by,

$$\tilde{p}_{k,t+1} = \text{logit}^{-1}\left[\left(1 + \frac{\pi s_{t+1}^2}{8}\right)^{-\frac{1}{2}} \times \boldsymbol{\delta}_k (S_{t+1} - m_k)\right]$$

where

$$s_{t+1}^2 = \begin{bmatrix} S_{t+1} - m_k \\ -\delta_k \end{bmatrix}^T \boldsymbol{\Sigma}_t \begin{bmatrix} S_{t+1} - m_k \\ -\delta_k \end{bmatrix}$$

and $\text{logit}^{-1}(x) = (1 + e^{-x})^{-1}$ [10].

Assuming that we have a proposal of the same dimension, $\mathbf{z}_{t+1} \in \{\mathbf{z}_{t+1}^{(p)}\}_{p=1}^{P_t}$, then the normal-gamma updates can be used to update the sufficient statistics of the measurement process. In the next section we drop the reference to to the particles (p) that we are considering for reasons of simple exposition.

$$\boldsymbol{\mu}_{t+1} \leftarrow \boldsymbol{\mu}_t + \frac{\mathbf{C}_t \mathbf{z}_{t+1}^T}{1 + \mathbf{z}_{t+1}\mathbf{C}_t\mathbf{z}_{t+1}^T} \times (\mathbf{y}_{t+1} - \mathbf{z}_{t+1}\boldsymbol{\mu}_t)$$

$$\mathbf{C}_{t+1} \leftarrow \left(\mathbf{z}_{t+1}^T\mathbf{z}_{t+1} + \mathbf{C}_t^{-1}\right)^{-1} = \mathbf{C}_t - \mathbf{C}_t\mathbf{z}_{t+1}^T\left(1 + \mathbf{z}_{t+1}\mathbf{C}_t\mathbf{z}_{t+1}^T\right)^{-1}\ \mathbf{z}_{t+1}\mathbf{C}_t$$

$$a_{t+1} \leftarrow a_t + \frac{1}{2}$$

$$b_{t+1} \leftarrow b_t + \frac{1}{2}(\mathbf{y}_{t+1} - \mathbf{z}_{t+1}\boldsymbol{\mu}_{t+1})^T\left(1 + \mathbf{z}_{t+1}\mathbf{C}_{t+1}\mathbf{z}_{t+1}^T\right)^{-1}(\mathbf{y}_{t+1} - \mathbf{z}_{t+1}\boldsymbol{\mu}_{t+1}).$$

The predictive distribution, used to calculate the evidence for the proposed state using the parameters before the update is

$$y_{t+1} \mid \mathbf{z}_{t+1} \sim \mathrm{T}(\mathbf{z}_{\mathrm{t}+1}\boldsymbol{\mu}_{\mathrm{t}}, (\mathbf{z}_{\mathrm{t}+1}\mathrm{C}_{\mathrm{t}}\mathbf{z}_{\mathrm{t}+1})\frac{\mathrm{b_t}}{\mathrm{a_t}}, 2\mathrm{a_t}), \tag{10}$$

and we denote this conditional likelihood as $\tilde{L}(\mathbf{z}_{t+1} \mid y_{t+1})$.

If the proposal of firing indicators has an extra dimension, $\mathbf{z}_{t+1}^+ \in \{\mathbf{z}_{t+1}^{(p)+}\}_{p=1}^{P_t}$ then in the normal-gamma updates we must augment the mean and covariance matrices first, $\mathbf{C}_t \rightarrow \mathbf{C}_t^+$ and $\boldsymbol{\mu}_t \rightarrow \boldsymbol{\mu}_{t+1}^+$, as shown in previous section. Subsequently

$$\boldsymbol{\mu}_{t+1} \leftarrow \boldsymbol{\mu}_t^+ + \frac{\mathbf{C}_t^+\mathbf{z}_{t+1}^{+T}}{1 + \mathbf{z}_{t+1}^+\mathbf{C}_t^+\mathbf{z}_{t+1}^{+T}} \times (\mathbf{y}_{t+1} - \mathbf{z}_{t+1}^+\boldsymbol{\mu}_t^+)$$

$$\mathbf{C}_{t+1} \leftarrow \left(\mathbf{z}_{t+1}^{+T}\mathbf{z}_{t+1}^+ + \mathbf{C}_{\mathbf{t}}^{+\mathbf{-1}}\right)^{-1} = \mathbf{C}_{\mathbf{t}}^+ - \mathbf{C}_{\mathbf{t}}^+\mathbf{z}_{\mathbf{t+1}}^{+\mathbf{T}}\left(\mathbf{1} + \mathbf{z}_{\mathbf{t+1}}^+\mathbf{C}_{\mathbf{t}}^+\mathbf{z}_{\mathbf{t+1}}^{+\mathbf{T}}\right)^{\mathbf{-1}}\ \mathbf{z}_{\mathbf{t+1}}^+\mathbf{C}_{\mathbf{t}}^+$$

$$a_{t+1} \leftarrow a_t + \frac{1}{2}$$

$$b_{t+1} \leftarrow b_t + \frac{1}{2}(\mathbf{y}_{t+1} - \mathbf{z}_{t+1}^+\boldsymbol{\mu}_{t+1}^+)^T\left(1 + \mathbf{z}_{t+1}^+\mathbf{C}_{t+1}^+\mathbf{z}_{t+1}^{+T}\right)^{-1}(\mathbf{y}_{t+1} - \mathbf{z}_{t+1}^+\boldsymbol{\mu}_{t+1}^+)$$

The predictive distribution of the observations given the states and the parameters before updating

$$y_{t+1} \mid \mathbf{z}_{t+1}^+ \sim \mathrm{T}(\mathbf{z}_{\mathrm{t}+1}^+\boldsymbol{\mu}_{\mathrm{t}}^+, (\mathbf{z}_{\mathrm{t}+1}^+\mathrm{C}_{\mathrm{t}}^+\mathbf{z}_{\mathrm{t}+1}^+)\frac{\mathrm{b_t}}{\mathrm{a_t}}, 2\mathrm{a_t}), \tag{11}$$

and we denote this conditional likelihood as $\tilde{L}(\mathbf{z}_{t+1}^+ \mid y_{t+1})$.

4.3 Update the parameters of the firing process

[11] show how the approximate the sufficient statistics for the states of the firing process can be updated sequentially. For each of the potential firing combinations denoted by $\mathbf{z}_{t+1}^{(p)}$ only the particles representing the motor units that are

stochastic ($k \in \mathcal{S}_t$) or are projected to be firing for the first time need to be considered.

First we denote the probability of the next motor unit firing as $p_{k,t+1} = \text{logit}^{-1}\left[\delta_{\text{k}}(\text{S}_{\text{t+1}} - \text{m}_{\text{k}})\right]$. The score and the approximate expected Fisher information can be calculated by

$$D_{k,t+1} \leftarrow (z_{k,t+1} - p_{k,t+1}) \begin{bmatrix} -\delta_k \\ S_{t+1} - m_k \end{bmatrix}$$
$$\mathcal{I}_{k,t+1} \leftarrow \mathcal{I}_{k,t} + p_{k,t+1}(1 - p_{k,t+1}) \begin{bmatrix} \delta_k^2 & \delta_k(m_k - S_{t+1}) \\ \delta_k(m_k - S_{t+1}) & (S_{t+1} - m_k)^2 \end{bmatrix}$$

and one step of the Fisher scoring method can be applied:

$$\boldsymbol{\omega}_{k,t+1} \leftarrow \boldsymbol{\omega}_{k,t} + \mathcal{I}_{k,t+1}^{-1} D_{k,t+1}.$$

Moreover the sufficient statistics for the covariance, $\boldsymbol{\Sigma}_{k,t+1} = \mathcal{I}_{k,t+1}^{-1}$ and the mean $\boldsymbol{\mu}_{k,t+1}$ are also updated for each $k \in \mathcal{S}_t$.

The evidence or marginal likelihood for each of combinations of the firing states can be found by integrating numerically over all stochastically firing units (and possibly a new unit). For each combination

$$\tilde{L}(\mathbf{z}_{t+1} \mid S_{t+1}) = \prod_{k \in \mathcal{S}_t, \mathcal{S}_t^+} \tilde{L}(z_{k,t+1} \mid S_{t+1}) \tag{12}$$

where $\tilde{L}_z(z_{k,t+1} \mid S_{t+1})$ denotes the evidence of the firing state of a single motor unit.

4.4 Re-weighting the particle

In this section we show how the cumulative weights of the particle for Equation (7) are updated. For updating particles of the same dimension $\mathbf{z}_{t+1}^{(p)} \in \{\mathbf{z}_{t+1}^{(p)}\}_{p=1}^{P_t:}$

$$w_{t+1}^{(p)} = w_t^{(p)} \times \frac{\tilde{L}(\mathbf{z}_{t+1}^{(p)} \mid S_{t+1}) \tilde{L}(\mathbf{z}_{t+1}^{(p)} \mid y_{t+1})}{q(\mathbf{z}_{t+1}^{(p)})},$$

where $q(\mathbf{z}_{t+1}^{(p)})$ described in Equation (8). $\tilde{L}(\mathbf{z}_{t+1}^{(p)} \mid S_{t+1})$ is given by Equation(12) and $L_c(\mathbf{z}_{t+1}^{(p)} \mid y_{t+1})$ is given by Equation (10).

When increasing the dimension by one $\mathbf{z}_{t+1}^{(p)+} \in \{\mathbf{z}_{t+1}^{(p)+}\}_{p=1}^{P_t^+}$ we use

$$w_{t+1}^{(p)} = w_t^{(p)} \times \frac{\tilde{L}_z({\mathbf{z}_{t+1}^+}^{(p)} \mid S_{t+1}) \tilde{L}_c({\mathbf{z}_{t+1}^+}^{(p)} \mid y_{t+1})(1-\theta)}{q({\mathbf{z}_{t+1}^+}^{(p)})}.$$

4.5 The resampling step

Despite the initial thinning step cuts down the number of particles will have to be cut down to a manageable size from time to time. For this purpose we used systematic resampling [12].

5 Testing and Analysis

At the time of writing this paper we have not had time to analyse real data. Neither have we been able to carry out large scale systematic comparisons between our method and RJMCMC. However all indications are that it will be a big improvement. We have started testing our model on two simulated data sets. The first, Figure (2) shows a five unit model. The new binary combinations are shown to the right of where it occurs for the first time. In this case only one particle was needed as the proposal mechanism was able to correctly identify the new combination in every case using the approximation (assuming all the states were correctly identified up to that point). The second data set shown in Figure (3) shows 28 different firing combinations. In all cases thresholds for defining an active units as $k \in \mathcal{S}_t \iff 0.99 > \tilde{p}(s_{k,t}) > 0.01$ was sufficient to keep the correct trajectory within the particles containing those trajectories under consideration. If the correct combination is eliminated from those under consideration then the model will be bound to fail from that point on. In this case we used 51 particles. We hope to carry out more comprehensive testing with real and simulated data over the next few months. We have included some real data to illustrate the problem

6 Summary and conclusion

Our motivation for developing this algorithm was to provide a scheme that is less computationally demanding than the method of [1] and thus be more useful for the medical practitioners throughout the world. Our particle filter moves through model space rather than parameter space in a typical model. We have cut down the number of possible states by considering only those units that are stochastic at a given time. The proposal mechanism for dimension changes is far better than that of [1]. For RJMCMC, an acceptance probability of 1/50 is thought to be good. With our sequential method, we are achieving at least 9/10. We have also demonstrated that the particle filter can work successfully with a large number of parameters. Our simulated second model has 50 parameters and the state space of binary possibilities is enormous. We achieve this by dynamical marginalisation. Marginalisation over parameters from the measurement process is easy but marginalisation of parameters from the state process requires a numerical integration (itself computationally costly) over a potentially enormous number of possibilities. We restrict the number of integrations that need to be carried out numerically by introducing an initial proposal step where the number of candidate models are greatly thinned down based on the evidence supplied by an approximations to the predictive.

The use of the particle filter comes with advantages in addition to speed. Drift in the observation process is very common in scans of the nature described in this paper. Although parameter drift in the measurement model was not investigated in our paper it is easily incorporated within the Kalman filter. Parameter drift was not dealt with in the method of [1] despite its ability to lead to an overestimate of motor unit numbers. A second issue concerns that of design. Data

collection methods are often extremely inefficient. Little thought has gone in to selecting stimuli that provide increase the accuracy of MUNE with the minimum number of observations. If the range of possible stimuli changes is restricted to a small number of possibilities then there is no reason why online experimental design cannot be carried out dynamically and on line thus shortening the time needed for a useful estimate of motor unit numbers.

References

1. Ridall, P. G., Pettitt, A. N., Friel, N., , Henderson, R., and McCombe, P. Motor unit number estimation using reversible jump Markov chain Monte Carlo (with discussion) . *J. Royal Statist. Soc. C* , 56:235–269. (2007)
2. Shefner, J. Motor unit number estimation in human neurological diseases and animal models. *Clin Neurophysiol.*, 112:955–64. (2001)
3. Ridall, P. G., Pettitt, A. N., Henderson, R., and McCombe, P. Motor unit number estimation: A Bayesian approach. *Biometrics*, 62:1235–1250. (2006)
4. Ngo, S. T., Baumann, F., Ridall, P., Pettitt, A.N., H., R.D., Bellingham, M., and McCombe, P. The relationship between bayesian motor unit number estimation and histological measurements of motor neurons in wild-type and $sod1^{G93A}$ mice. *J. Clin. Neurophysiol.*, 123:2080–2091. (2012)
5. Baumann, F., Henderson, R., Ridall, P., Pettitt, A. N., and McCombe, P. L. Use of Bayesian MUNE to show differing rate of loss of motor units in subgroups of ALS. *J. Clin. Neurophysiol.*, 12:2446–53. (2012)
6. Gooch, C., T.J., D., Chan, K., Bromberg, M., Lewis, R., Stashuk, D., Berger, M., Andary, M., and Daube, J. Motor unit number estimation: a technology and literature review. *Muscle and Nerve*, 50:884–93. (2014)
7. Doucet, A. and Johansen, A. A tutorial on particle filtering and smoothing : fifteen years later. In Crisan, D. and Rozovskii, B., editors, *Oxford Handbook of Nonlinear Filtering*. Oxford University Press. (2011)
8. Kantas, N., S. S., Maciejowski, J., and Chopin, N. On particle methods for parameter estimation in state-space models. *Statistical Science*, 30:328–351. (2015)
9. Pitt, M. and Shephard, N. Filtering via simulation: Auxiliary particle filters. *J.A.S.A.*, 94:590–591. (1999)
10. McKay, D. The evidence framework applied to classification networks. *Neural computation*, 4:720–736. (1992)
11. McCormick, T., Raftery, A., Madigan, D., and Burd, R. Dynamic logistic regression and dynamic model averaging for binary classification. *Biometrics*, 66:1162–1173. (2011)
12. Douc, R., Cappe, O., and Moulines, E. Comparison of resampling schemes for particle filtering. In *Proceedings of the 4th International Symposium on Image and Signal Processing and Analysis*. (2005)

The electricity consumption in selected sectors of the Polish economy

Marek Kott

Wroclaw University of Science and Technology, Wroclaw, Poland
marek.kott@pwr.edu.pl

Abstract. Energy has one of the most important roles in the life of society development. It is also essential and necessary factor in the implementation of any business. The most prized form of energy is electricity. The biggest of advantage of electricity is the ability to convert it to any other form of energy (eg mechanical, heat).
Constantly increasing energy needs of state economies, dwindling fossil fuel resources and environmental degradation caused by the extraction of raw materials and stimulate the production of electricity force us to pay special attention to problems of energy policy, and thus on energy security.
The paper presents econometric models of electricity consumption for the most important sectors of the Polish economy.

Keywords: Electricity consumption, Analysis, Econometric models.

1 Introduction

Efficient political and economic activities should be based on gaining information about sectors. The gathered data effectively used in the process of forecasting and simulation can contribute to formulation of appropriate legal regulations. It is therefore essential to develop and then introduce sustainable energy policy which is one of the most important tasks faced by states.

Most European economies can be divided into the following sectors: industry, transport, agriculture, services and households. From the point of view of electricity, the most important sectors for the Polish economy are: industry and households in which since the beginning of the 21st century electricity consumption has increased by 16% and 32% respectively. Figure 1 presents electricity consumption in the Polish economy against the background of selected countries.

adfa, p. 1, 2011.

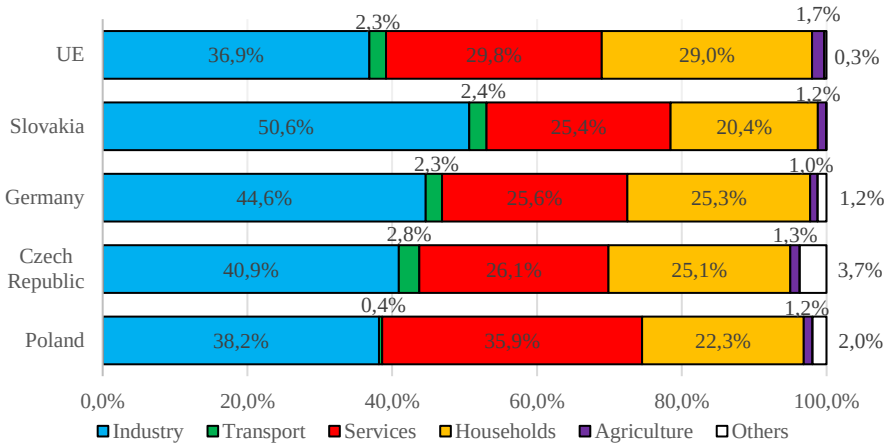

Fig. 1. Electricity consumption in selected countries by sectors [2,4]

2 Industry

Industry can be defined as economic activities carried out in buildings and facilities (plants) especially adjusted for the purpose, equipped with appropriate machines and devices, where a qualified work force using factory production methods and organization provides (extracts) and processes objects of work into finished products fulfilling production and human consumption needs. Industry is characterized by:

- strong influence on spatial management and natural environment, e.g. coal industry,
- increasing influence of industrial production on the course, organization and technical equipment of work processes in non-industrial activities, e.g. electromechanical industry,
- multilateral supply and production relations with other branches of the national economy,
- numerous relations with the development of science and technology, e.g. chemical industry,
- multilateral links with the economic and social development of the country and the development of foreign trade.

The structure of industry, which has been subject to studies, is presented on Figure 2 and it takes the specificity of Polish industry into account. In accordance with the European Classification of Economic Activities Rev. 2 (NACE Rev. 2) the industry sector has been divided into three divisions, within which ten industry branches were specified. In the analysis presented below, Polish industry was compared to the industry sector of other countries in Central Europe: Czech Republic, Slovakia and Germany.

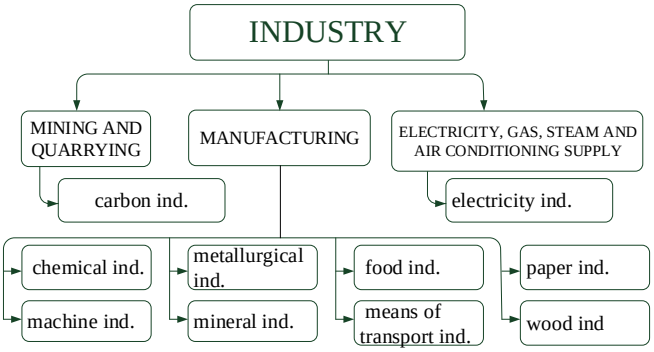

Fig. 2. Intra-industry structure of the domestic industry

Employment in the Polish industry is generally decreasing, mainly in the sector of services (nearly 22% of professionally active people work in the industry sector). In Table 1 the percentage of employment in three industry divisions was compared. The largest differences in employment can be observed in mining, in which less than 1.5% of people employed in industry work, while the EU average is 1.02%. It is the result of a strongly developed industry related to coal and brown coal mining. This fact significantly contributes to Poland's negative attitude to the assumptions of the document titled Energy Roadmap 2050. While, in the case of Electricity generation and supply overemployment can be observed. The EU average is 0.89% of people generally employed in this industry and it is 0.25% less than employment in this division in Poland. In manufacturing the employment index in Poland and other Member States is at a similar level. Despite the reduction of employment in the majority of sectors, a slight increase in the number of enterprises employing more than 49 people took place. Since the beginning of the 90s an increase in the number of industrial plants could be observed, however it ceased after 2000. Bad economic conditions in this period resulted in closing of plants mainly in the food, machinery and mineral industry. Currently, the number of economic entities employing more than 49 people is approx. 4,800. [1,2,3]

Table 1. Numbers of employees in industry in thousands [2,4]

Country	Mining And Quarrying		Manufacturing		Electricity, Gas, Steam And Air Conditioning Supply	
	in thousands	% of all employees	in thousands	% of all employees	In thousands	% of all employees
European Union	-	1,02%	-	18,71%	-	0,89%
Czech Republic	47,9	0,98%	1236	25,30%	56,8	1,16%
Germany	95,8	0,25%	7747	20,00%	350	0,90%
Poland	230	1,44%	2961	18,55%	182	1,14%
Slovakia	13,9	0,60%	530	22,86%	31	1,34%

Another significant indicator which helps define the place of Polish industry in Europe is the industrial productivity index calculated in gross value added per person

(Table 2). Comparing the value of this index in Poland and in the states with a similar level of economic development (Czech Republic, Slovakia), it can be stated that the values do not vary significantly. However, comparing the results in Poland with highly developed countries (Germany), we can observe that in most sectors the values of the industrial productivity index are more than twice as low.

Table 2. Labour productivity in industry (gross value added per person) [1,2,4]

Country	mining ind.	food ind.	paper ind.	chemical ind.	mineral ind.	metallurgical ind	machine ind.	means of transport ind.	wood ind.	electricity ind.,
European Union	45,3	40,8	64,5	95,0	49,0	63,0	66,1	68,9	27,8	175,0
Czech Republic	62,8	20,1	28	42,5	29,8	27,6	25,9	38,8	13,1	181,4
Germany	70,4	36,2	65,9	110,7	60,3	76,1	74,6	97,8	46,1	188,6
Poland	41,7	19,4	33	44,1	28	30,8	24,1	32,9	13,1	75,4
Slovakia	-	19,1	40,4	34,7	24,6	30,9	22	31,1	14,8	136,6

Table 3. Electricity consumption rate in the industry [1,2,4]

Country	electricity ind.	food ind.	paper ind.	chemical ind.	mineral ind.	metallurgical ind	machine ind.	means of transport ind.	wood ind.
European Union	1,5%	10,9%	12,2%	18,6%	6,3%	11,7%	12,1%	5,1%	2,1%
Czech Republic	1,6%	7,0%	7,4%	16,5%	0,9%	11,3%	14,8%	11,9%	2,3%
Germany	0,8%	7,9%	10,5%	23,1%	5,6%	11,9%	16,1%	7,9%	1,9%
Poland	4,8%	12,0%	8,4%	19,1%	4,4%	14,0%	8,7%	4,5%	4,2%
Slovakia	0,3%	4,3%	8,4%	11,8%	20,8%	21,8%	9,4%	7,9%	1,3%

From the energy perspective, the industry sector can be assessed, comparing the percentage share of the studied industrial branches in electricity consumption for the sector. In Poland more than 80% of electricity used in industry is used for the needs of the analysed industrial branches. From Table 3 it can be concluded that metallurgical and mining industries are characterized by excessive energy consumption. It can be also stated that energy consumption in Polish industry is distributed similarly to other Member States.

Summarizing, Polish industry is still characterized by excessive energy consumption which is caused among others by:

- thermodynamic imperfection of production processes,
- improper use of production and utility equipment,
- excessive energy consumption of production processes,
- excessive share of energy-intensive products in production and export,
- insufficient use of secondary raw materials,

- insufficient efficiency of energy receivers,
- insufficient use of waste energy.

3 Households

In Poland there are more than 14 million households, 50% of which are characterized by a cubature of up to 200 m^3 and a surface area not exceeding 60 m^2, in which most often 2-3 people live (average: 2.8 people). In the last decade, a systematic increase in the surface area and cubature of dwellings and a decrease in the average number of people per household can be observed. A statistical household in Poland uses approx. 2,000 kWh of electricity per year and this value is twice as low as the average in EU countries [2,4]. In the table 4 Polish households are compared with households in EU countries.

Table 4. Basic information about the countries [2,4]

Country	Population		Number of households		Final consumption of electricity	
	mln	%	mln	%	TWh	%
European Union	506,1	100,00%	211,2	100,00%	2706,3	100,00%
Czech Republic	10,5	2,08%	4,7	2,21%	56,2	2,08%
Germany	80,4	15,89%	40,7	19,25%	512,8	18,95%
Poland	38,5	7,61%	14,6	6,93%	125,9	4,65%
Slovakia	5,4	1,07%	1,8	0,86%	24,2	0,89%

Characteristics of households from the perspective of electricity consumption were prepared based on guidelines described in the document published by Eurostat - *Manual for statistics on energy consumption in households (MESH)* and on data of the Central Statistical Office of Poland. Electricity receivers were divided into six groups:

- dwelling heating equipment,
- water heaters,
- food cooking equipment,
- room cooling equipment,
- lighting, household appliances and electronics,
- other, not listed in other groups.

Only 5.3% of dwellings are equipped with the first group of devices. Due to significant costs and a large range of other cheap carriers being available (in particular coal), electric heating is not used on a large scale. Electric heating appliances are mainly used as supplementary heat sources or are used in places where no other type of heating can be used [1,2].

In 23.5% households electric water heaters (heating elements, boilers) are installed. The number of such devices has been maintained at a constant level in recent years. The average age of such devices is 9 years which shows that the devices are not technically outdated [1,2].

Gas cookers with an electric oven can be found in every second household, while fully electric cookers (hobs with an oven) in every tenth. It should be also mentioned that more than 50% of households are equipped with a microwave oven [1,2].

Less than 0.5% of households are equipped with air conditioning, however this number has grown significantly in recent years due to newly built apartments with a higher finish standard. Mostly they are devices intended to cool individual rooms. Only 0.04% apartments have central air conditioning [1,2,6].

Household appliances, electronics and lighting constitute the largest group of electricity receivers. Nearly every household has a fridge, a washing machine and a TV set. The average power of installed light bulbs (including energy saving fluorescent lamps and LED sources) in a household is estimated to be at 550W, while power of installed light bulbs per unit area is 7.21 W/m^2 [1,2,6].

In the table 5 electricity consumption according to previously discussed groups of devices for Poland and for the average of 27 UE countries was compared. The largest differences can be observed in the percentage share in electricity consumption for the group of heating appliances and household appliances. In the case of the first group of appliances, this fact can be interpreted as the lack of profitability of investing in electric heating of rooms in Poland. Excessive electricity consumption by household appliances in Poland can be caused among others by the advanced age of household appliances, and therefore household appliances in Poland are characterized by lower energy classes than the same household appliances in highly developed EU countries.

Table 5. Electricity consumption in the household sector by devices [6]

Country		Percentage consumption of electricity in the household					
	TWh	dwelling heating equipment	water heaters	food cooking equipment	household appliances and electronics	lighting	room cooling equipment
European Union	785,1	20,3%	10,8%	10,1%	49,2%	9,7%	-
Czech Republic	14,1	17,6%	20,2%	19,7%	37,2%	5,2%	-
Germany	129,6	6,4%	13,9%	16,6%	53,8%	9,3%	-
Poland	28,1	8,0%	8,0%	11,0%	66,0%	7,0%	-
Slovakia	4,9	9,0%	5,2%	1,2%	77,2%	7,4%	-

One of the main long-term goals of the European Commission in the field of limiting electricity consumption in households is to promote energy certificates and labels for household appliances, lighting, buildings and passenger vehicles. EU energy labels are to provide consumers with legible information about household appliances they purchase concerning energy consumption, water consumption or other performance parameters. Based on them, the consumer is able to identify the actual energy efficiency of a device and assess its saving potential in bills for electricity. From the data quoted recently, in Poland there is still a need to promote visibility concerning certification and energy labelling of household appliances among consumers.

4 Econometric modelling of electricity consumption in selected sectors of the national economy

Econometric modelling of electricity consumption in selected sectors of the national economy is a multifaceted and complex process. One of the manners to define the main factors affecting energy consumption in selected sectors is the application of econometric modelling. A variable explained in such a model is the electricity consumption index in the examined sector.

There are two different ways to determine the factors that affect the consumption of electricity in the selected sectors. For the industry sector has chosen a characteristic variable - the energy intensity of the industry. It was assumed that the rate of energy intensity in industry is the ratio of electricity consumption to 100 PLN (polish national currency) sales in a specific industry and is expressed by the equation:

$$e = \frac{E_w}{f} \tag{1}$$

where:
e – energy intensity of industry branch,
E_W – direct energy consumption in the industry branch [kWh],
f – effect - volume of production sold in the industry branch [PLN].

For households sector the factors were divided into three groups: energy and technical factors, financial and economic factors and social factors. In econometric modelling factors should fulfil substantive criteria: capture the most important properties of the analysed phenomena, be precisely defined, allow mutual control through knowledge of statistical and substantive relationships that occur between them and be characterized by consistency of proportions between the number of variables representing a given aspect of the phenomenon and their substantive significance.

Factors fulfilling the above listed criteria can play the role of explanatory variables in the econometric model. The linear econometric model with numerous explanatory variables has the following form:

$$Y = a_0 + \sum_{k=1}^{K} \left(a_k X_k \right) + \varepsilon \tag{2}$$

where:
Y – variable explained,
X_k – k - explanatory variable for $k = 1, 2 \ldots K$,
a_0, a_k – structural parameters of the model for $k = 1, 2 \ldots K$,
ε – random component.

To define individual parameters of the econometric model, the classic least squares method was used. The subsequent steps in the econometric analysis are shown in Figure 3.

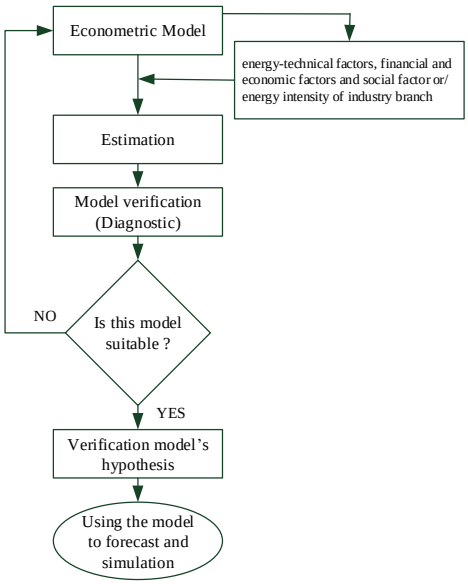

Fig. 3. The Diagram of Econometric analysis [5]

To verify the econometric model, numerous statistical tests were used, which was made possible thanks to the use of *GRETL* software. Diagnostics involved: assessment of the variation coefficient, assessment of the significance of structural parameters (Student's t-test, Snedecor's f-test), assessment of the model adjustment degree (R^2 determinant), assessment of normal distribution (Jarque-Bera test), evaluation of linearity of the model analytical form (White test) and assessment of the linearity of the explained variables. [5]

The structural parameters of the constructed econometric models are presented in Tables 6 and 7. Statistical data concerning electricity consumption in selected sectors and results obtained using econometric models were compared in the figure 4.

Table 6. Structural parameters of the electricity consumption model in industry sector

Parameter	Value	Description	Unit
a_0	14,2	constant	-
a_1	1,13	energy intensity - electricity ind.	$\frac{kWh}{100PLN}$
a_2	-0,17	energy intensity - mining ind.	$\frac{kWh}{100PLN}$
a_3	-1,95	energy intensity - chemical ind.	$\frac{kWh}{100PLN}$
a_4	-1,19	energy intensity - machine ind.	$\frac{kWh}{100PLN}$
a_5	2,42	energy intensity -metallurgical ind	$\frac{kWh}{100PLN}$
a_6	2,1	Price of electricity for midle size cpmpany	previous year=100%

Table 7. Structural parameters of the electricity consumption model in households sector

Parameter	Value	Description	Unit
a_0	44683,8	constant	-
a_1	209,3	Average monthly expenses on 1 person for energy carriers	PLN
a_2	-173,6	Average monthly expenses on 1 person for household equipment	PLN
a_3	-1523,5	Share of expenditure on the use of housing and energy carriers in total expenditure	%
a_4	-27381,6	Price of electricity for households	PLN/kWh
a_5	-173,9	Household appliances in dishwashers	% of all households

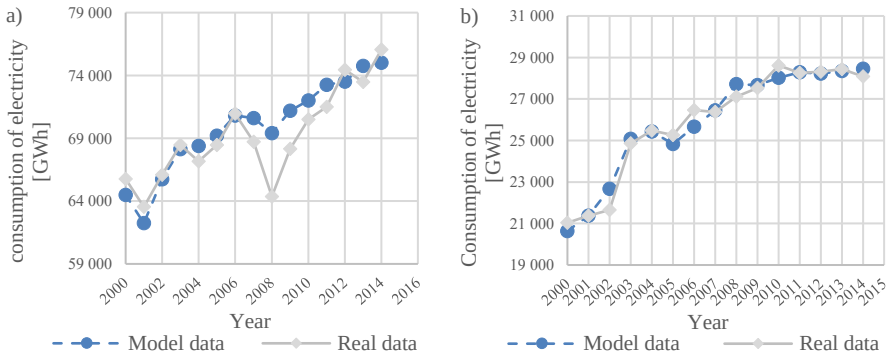

Fig. 4. The electricity consumption in a) industry sector b) households sector

5 Summary

The Polish economy is still undergoing a transformation which commenced in 1989. The analysis indicated that the key factor affecting the consumption of electricity in Poland is its price. The most energy intensity industries has the greatest impact on Electricity consumption in industry . Restructuring and modernization of important industries will enable the implementation of state energy policy in line with its objectives. Such further decrease in energy consumption must be caused mainly by investments in new energy efficient technologies, and not by limiting the volume of production of heavy or mining industries as this is currently happening. The state should promote energy saving through appropriate legal acts [3].

The presented comparative analysis of the domestic household sector in comparison to selected EU countries in the context of climate and energy policy indicated that there are still differences between Poland and highly developed countries of Western Europe. The largest differences concern the mix of used energy carriers, the manner of its use and the quality of electric equipment.

Based on the presented econometric model, we can conclude that mainly financial and economic factors impact electricity consumption by the household sector in Poland. In the coming years we can expect an increase in the number of electric devices in domestic households. To prevent an increase in energy consumption in the sector of households with the increase in the number of mainly small electric devices, numerous tools affecting improvement of energy efficiency in this sector of economy must be applied, i.e.:

- universal and broad access to information on energy labelling of lighting equipment, household appliances and electronics, implemented among others by media information campaigns and Internet services,
- implementing a system of common education consisting of trainings affecting increased social awareness related to rational energy use in the household sector,
- introducing a system of professional trainings (for installers and sellers) increasing qualifications and skills in consulting, selection and use of energy efficient technologies intended for individual recipients,
- introducing numerous legal regulations aimed at promoting effective energy use by the end users, taking particularly individual recipients into account,
- creating a complex system of financing ventures concerning the potential of effective energy use and use of renewable energy sources in multi-family and single-family buildings with public funds; making it possible for households to become a prosumer on the market of electricity.

References

1. Central Statistical Office *Statistical Yearbook of Industry 200-2015*, Warsaw 2001-2016
2. Central Statistical Office Yearbook: International Statistics 2015, Warsaw 2015
3. European Commission, *Energy Roadmap 2050*. Brussels, 2011 Available: http://ec.europa.eu/energy/energy2020/roadmap/index_en.htm
4. Eurostat online database Available: http://epp.eurostat.ec.europa.eu/po rtal/page/portal/statistics/search_database
5. *Gretl User's Guide*, Cottrell A., Lucchetti R. Available: https://sourceforge.net/projects/gretl/files/manual/
6. Odyssee-Mure database, Available: http://www.indicators.odyssee-mure.eu/energy-efficiency-database.html

A GIS-based Model for Cholera Forecast

Ngoc Anh Thi Le[1] and Xuan Dau Hoang[2]

[1] Hanoi Medical University, Hanoi 10000, Vietnam
[2] Posts and Telecommunications Institute of Technology, Hanoi 10000, Vietnam
dauhx@ptit.edu.vn

Abstract. The spread of infectious diseases has a close relationship with temporal and spatial localities due to it is more likely to occur if individuals are in near disease sources in terms of specific space and time. Therefore, it is important to take both temporal and spatial factors in the epidemic data analysis. The basic principle is to examine the dependent relationship among observations on both space and time dimensions. In order to meet these requirements, Geographic Information System (GIS) has the advantage over traditional non-space methods. GIS can be used to determine the location and create the map of disease cases. It can also be used for researching causes of disease outbreaks and for simulating and forecasting the disease spread. This paper proposed a GIS-based model for cholera forecast for Hanoi city, Vietnam, which took the impact of the city's climate changes into consideration. Experimental results showed that GIS can be effectively used for the cholera epidemic analysis of the research area. The research pointed out hot spots of cholera disease as well as it well explained the relationship between spatial distribution variables, including climate, water area and population, and the temporal distribution variable of the cholera case number.

Keywords: Spatial analysis; epidemic forecast; forecast model; GIS-based cholera forecast.

1 Introduction

Cholera first appeared in the world in 1817 and quickly became one of the main causes of mass death worldwide, especially in developing countries in the tropics in Africa, Asia and South America. Historically, cholera outbreaks had been considered as disasters because of the high mortality rate, fast spreading, wide region of influence and difficult to control [1,2]. Vibrio cholera virus can easily spread, or spread through humans and animals, especially in regions lacking clean water, poor sanitation facilities and heavy pollution. Many studies have shown a causal relationship between factors, including human behaviour, ecology and infectious factors, and disease outbreaks. Therefore, the analysis of the spatial model and factors that affect cholera plays a very important role in research on the nature of the disease spreading. This paper first investigates some cholera forecasting models in the world and in the region that have used GIS technology and then proposes a GIS-based model for cholera fore-

cast for the city of Hanoi, Vietnam. The rest of the paper is organized as follows: Section 2 presents the related works; Section 3 describes the experimental data sets and the proposed forecast model. The experimental results and discussion are presented in Section 4 and Section 5 is the conclusion of the paper.

2 Related Works

In recent years, GIS has been widely used as the support tool for the decision making process in economic, social and defense activities of many countries in the world [3,4]. GIS provides tools for statistical analysis, spatial modelling and researching on the relationship between natural and environmental factors, and the health and diseases of people [5]. GIS can also be used for monitoring and forecasting the disease development, which thereby helps different levels of management make appropriate decisions for each point of time. As a broad range of applications, there have been many different approaches to GIS-based data analysis, such as Inverse Distance Weighting (IDW), Hot Spot Analysis, Geographically Weighted Regression (GWR)...[6]. Hot Spot Analysis is a method of spatial grouping. It applies Getis-Ord Gi* [6] statistical computation for each object in the spatial data set. This method calculates the results by considering each object in context with the surrounding objects. An object of a high value is not necessarily a meaningful hot spot statistically. To become a hot spot in terms of statistics, an object must have a high value and is surrounded by other high value objects. The local statistical method, such as GWR considers the heterogeneity of the spatial relationships. In other words, it models relationships that are vary across different spatial locations.

In 2008, Osei and Duker have used spatial regression models (including spatial error model and spatial lag model) to explore the dependence of the incidence of cholera to a local environmental factor, such as open landfills in Kumasi, Ghana [7]. The study results showed that areas with the higher density of open landfills had higher cholera incidence than that of areas with the lower open landfills. Moreover, areas near an open landfill have a higher cholera incidence than that of areas far the open landfill [7]. Further research in 2012 by Osei and his colleagues produced more positive results when using spatial regression models to explore the spatial dependence of cholera to water bodies potentially contaminated [8].

In 2014, Rasam et al. [9] conducted a study to integrate GIS and a technical analysis of the cholera epidemiological analysis of the spatial model in the district of Sabah, Malaysia. Results showed that cholera tends to concentrate around the region where there are infected people around 1,500 meters. The cholera outbreak usually occurs in crowded areas with unsanitary environments and close to the contaminated water sources. In addition, cholera has a close relationship with the coastal areas. It can be concluded that GIS plays a very important role as a spatial technology to determine distribution models and to clarify the hypotheses of disease development.

In Vietnam, cholera is a serious infectious disease to humans and it still exists in some localities. To actively prevent the recurrent of cholera epidemic affecting people's health, the deployment of GIS applications for the control and prediction of

cholera epidemic is seen as a feasible solution highly complementary to the professional medical measures. It also helps the health sector and governments at all levels carry out the most appropriate intervention to improve the effectiveness of the prevention and control of cholera [5, 8]. Currently in Vietnam, GIS analysis applications in the medical field are very limited. Most of GIS-based medical applications stop at the creation of maps of the disease occurring positions, the number of cases and the GIS-based database management of disease. To the best of our knowledge, we have not found any published works of GIS analysis applications that found out the cause and the distribution pattern of disease cases in the outbreak, as well as predicted the possibility of future cases. Therefore, the objective of this study is to build a predictive cholera model for the city of Hanoi, which takes the impact of variables of the climate, the water surface area and the population to the number of cholera cases using GIS-based spatial regression analysis model.

3 Proposed Model for Cholera Forecast

3.1 Experimental data sets

Experimental data include numbers of cholera cases collected by the Hanoi's Preventive Health Centre. Climate and hydrology data in Hanoi were from the National Meteorological Research Centre. The data sets used for experiments of this study are described in Table 1.

Table 1. Input data sets for the research.

Data Sets	Description
Administrative map at 1: 50,000	Represents the boundaries of 29 districts of Hanoi city.
Hydrogeological map at 1: 50,000	Represents the network of rivers, streams, lakes in Hanoi city.
Population data	Represents the size of population of each district of Hanoi city in years of the period 2007-2010.
Meteorological data	Collected for the period 2001-2011 by measuring stations in Hanoi, namely Ba Vi, Ha Dong, Hoai Duc, Lang and Son Tay. Data include rainfall, air temperature; relative air humidity; number of hours of sunshine; daily wind speed.
Cholera data	Represents archived data of cholera cases by dates of the period 2001-2011 in Hanoi city.

3.2 Proposed Model for Cholera Forecast

Fig. 1 shows the proposed GIS-based model for cholera forecast for the city of Hanoi. Input data include the administrative map, hydrogeological map, population data, meteorological data by dates (R - rainfall; Sh - sunshine hours; T - air temperature, U - relative air humidity; V - wind speed) and numbers of cholera cases by dates in the period 2001-2011.

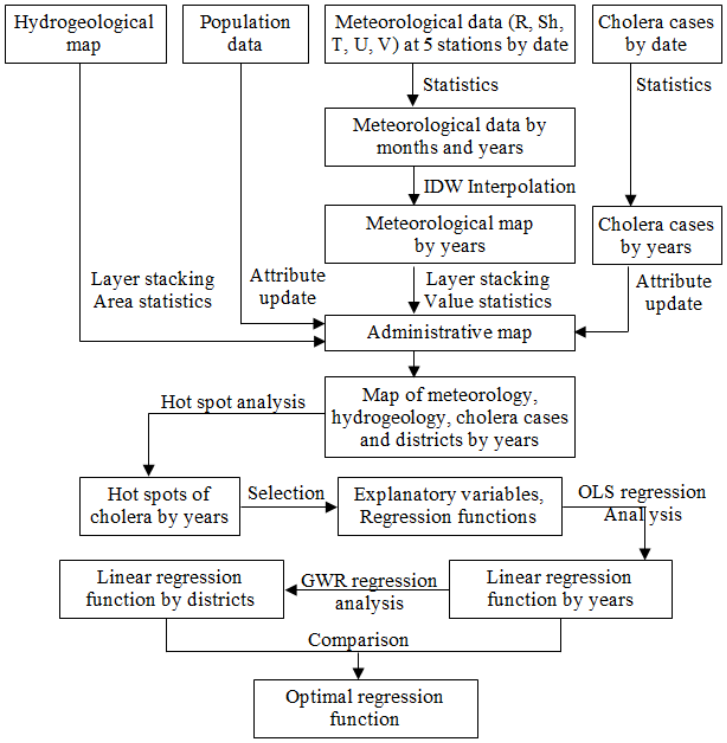

Fig. 1. The proposed GIS-based model for cholera forecast.

The proposed GIS-based model presented in Fig. 1 consists of the following processing steps:

- Step 1: Collect input data including administrative and hydrogeological maps, population data, meteorological data by dates (R - rainfall; Sh - sunshine hours; T - air temperature, U - relative air humidity; V - wind speed) and number of cholera cases by dates of the period 2001-2011 in Hanoi city.
- Step 2: Integrate the hydrogeological map into the administrative map of each district; Get the water surface areas (including surface areas of rivers, ponds and lakes) of each district.
- Step 3: Integrate the population data into the administrative map of each district by years.
- Step 4: Using meteorological data collected by 5 stations by dates, create meteorological data by months (monthly average for R, Sh, T, U, V) and by years (yearly average for R, Sh, T, U, V) for each meteorological station.
- Step 5: Using the IDW interpolation method, construct the meteorological map for the whole city of Hanoi by months and years. Then, integrate the meteorological map into the administrative map of each district. And then, create monthly and yearly average of each factor of the meteorological data for each district.

- Step 6: Using the collected data of cholera cases by dates, create the total number of cholera cases by months and by years for each district of Hanoi.
- Step 7: The aggregated result of steps 2, 3, 4, 5, 6 is the administrative map of each district with integrated data layers of water surface areas, population, meteorological factors and number of cholera cases by months and by years.
- Step 8: Carry out the hotspot analysis of cholera epidemic using the Getis-Ord Gi* statistical method for the whole city of Hanoi in order to figure out areas where cholera cases appear frequently. The result of this step is the input for the selection of explanatory variables in the cholera epidemic regression model.
- Step 9: Select explanatory variables (water surface areas, population, R, Sh, T, U, V) and the form of the regression function (logarithm) for OLS (Ordinary Least Square) linear regression analysis.
- Step 10: Carry out OLS analysis and construct the simulation function to forecast cholera cases by months and years.
- Step 11: Using the result of OLS analysis, conduct the GWR (Geographically Weighted Regression) analysis to construct suitable linear function for each district.
- Step 12: Compare the OLS and GWR analysis results using the AIC (Akaite's Information Criterion) and R^2 (Adjusted R_squared) to get the optimal regression model for cholera forecast.

4 Experiments and Results

4.1 Description of Experiments

Based on the proposed cholera forecast model described in Fig. 1, we carried out the data pre-processing and the following experiments:

1. Hot spot analysis of cholera epidemic: The goal of this experiment is to find hot spots of the cholera outbreak, and the relationship between the outbreak and spatial factors, including meteorology and hydrology and population density;
2. Experiment of multi-variable regression models for cholera epidemic forecast. This experiment is done using the results of the analysis of cholera epidemic hot spots. It consists of three stages: (i) Selection of explanatory variables for cholera outbreak, (ii) Linear regression analysis – OLS [6] and (iii) Geographically weighted regression – GWR [6]. These stages are sequentially conducted because the result of the previous stage is the input for next step.

4.2 Hot Spot Analysis of Cholera Epidemic

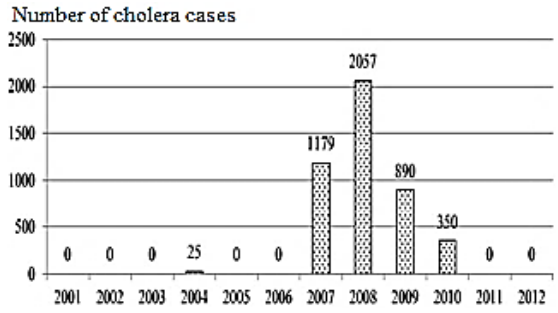

Fig. 2. Number of cholera cases in the period 2001-2012.

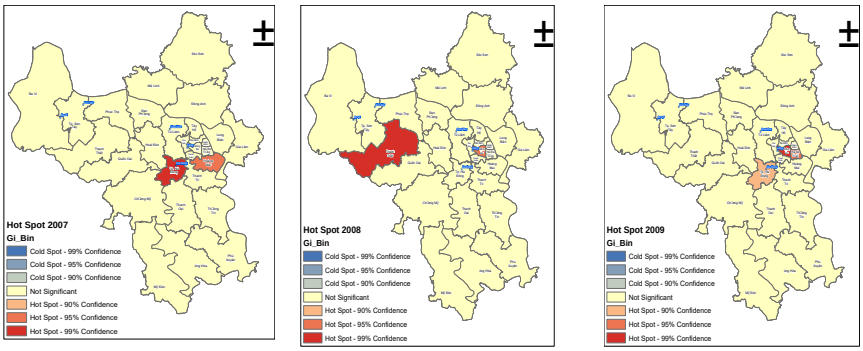

Fig. 3. Hotpot analysis of number of cholera cases in 2007, 2008 and 2009

From annual statistical data of cholera cases in the period 2001 - 2012 represented in Fig. 2, we can see that cholera was initially recorded in Hanoi with only 25 cases in 2004. Then, cholera outbreak had been occurred continuously from 2007 to 2010, with the peak of 2008. However, in terms of space, the question is in which areas were cholera cases usually occur? Was the distribution of cases clustered or scattered throughout the region? To answer these questions, the hotspot analysis was conducted for each year using Getis-Ord Gi * statistical method in the whole Hanoi city to identify areas, in which cholera cases frequently appeared. The result of this step is used for the selection of explanatory variables in the regression models of disease. Hotspot analysis results for 2007, 2008 and 2009 are shown in Fig. 3. It can be seen from the results that hot spots of numbers of cholera cases are vary according to each year. However, they are generally concentrated around urban areas, including Ba Dinh, Hai Ba Trung, Thanh Xuan, Dong Da, Hoang Mai and Cau Giay districts. These districts are densely populated areas, adjacent to Nhue, Kim Nguu and To Lich rivers. These are highly polluted rivers flowing through the city of Hanoi.

4.3 Experiments of Multi-variable Regression Models for Cholera Forecast

Selection of explanatory variables of cholera epidemic. Analysis results of cholera case hotspots by year show that the hotspots are concentrated in the densely populated area and are located close to the polluted rivers. Based on the above statement and previous cholera research results, this study selected explanatory variables for the cholera outbreak in Hanoi city as follows: climate (R, Sh, T, U, V: annual average), water surface area (km^2) and population (thousands of people). Due to the numbers of cholera cases are unevenly distributed over the years (in other words, the data do not follow standard distribution rules), this study selected the following regression function to explain the number of cholera cases (y) as follows:

$$\text{Log}(y) = \alpha + \beta_1 * R + \beta_2 * Sh + \beta_3 * T + \beta_4 * U + \beta_5 * V + \beta_6 * \textit{Water surface area} + \beta_7 * \textit{Population} + \varepsilon \quad (1)$$

Where, Log(y) is the logarithm of the number of cholera cases; α is the blocking ratio; $\beta_1, \beta_2, \beta_3, \beta_4, \beta_5, \beta_6, \beta_7$ are regression ratios; ε is the random error.

The purpose of the selection of the logarithmic regression function is to transform the data into the standard distribution. Climate, water surface area, population variables are considered independent, while the variable of the number of cholera cases is considered dependent. Regression models will predict the incidence of cholera cases in Hanoi based on the climate, water surface area and population data.

Linear regression analysis – OLS. The linear regression analysis - OLS is conducted to build the simulation and forecasting function of cholera cases over the years for the entire area of Hanoi. Overall results of OLS linear regression analysis for the years of 2007, 2008, 2009 and 2010 are shown in Table 2. The standard deviation of the residuals (the actual number of cases – simulation cases) for each year is shown in Fig. 4. The study uses the adjusted determination coefficient metrics (Adjusted R_squared or R^2) for describing the impact level of the climate, water surface area and population variables to the number of cholera cases. This adjusted determination coefficient indicates the explanatory variables in the model to explain how much of the variation of the dependent variable.

Table 2. R^2 in OLS linear regression analysis by years in Hanoi.

Year	Explanatory variables	Adjusted R_squared (R^2)	Statistical value (*p_value)
2007	Constant, Water surface, Climate	0.258771	< 0.01
2008	Constant, Water surface, Population	0.424545	< 0.01
2009	Constant, Water surface, Climate, Population	0.704000	< 0.01
2010	Constant, Water surface, Climate, Population	0.637462	< 0.01

From the analysis results shown in Table 2, we can draw the following remarks: In 2007, the combination of climate and water surface factors can explain 25.87% of the cases across the region. In 2008, the combination of population and water surface

factors can explain 42.45% of the cases across the region. In 2009 and 2010, the combination of climate, population and water surface can explain 70.40% and 63.74% of the cases across the region, respectively. The current trend shows that the climate is having profound changes due to the negative impacts by human and natural activities. These changes have a significant impact on the human health.

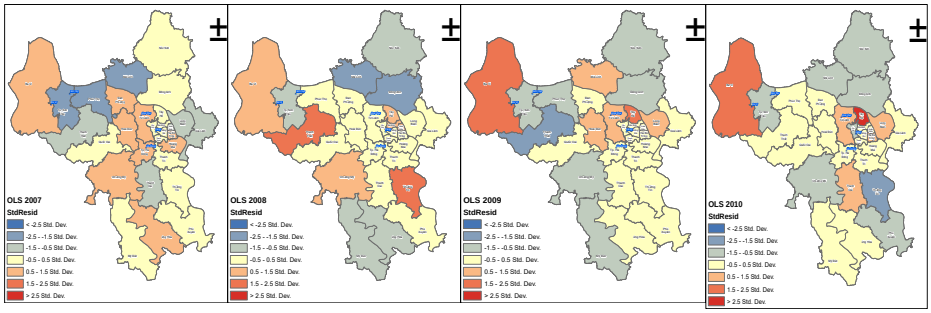

Fig. 4. Standard deviation of the residuals (the actual cases – simulation cases) for 2007, 2008, 2009 and 2010

Geographically weighted regression - GWR. The global statistical model using OLS linear regression assumes spatial homogeneity of the relationship between the dependent variable and the explanatory variables. This hypothesis can bring misleading results when OLS is used for data in spatial context. To overcome the above issue, the local statistical method of geographically weighted regression was born. This method considers the heterogeneity of the spatial relationships. In other words, it models relationships vary across different spatial locations. Based on the results of OLS regression analysis for the whole region by year, we build the geographically weighted regression model to improve its explanatory capability as well as to establish a linear function suitable for each district. The study uses the AIC information (Akaite's Information Criterion) standard method [10] to compare the two models. Accordingly, the model that has a lower AIC value will be more accurate than the model that has the higher AIC value. The results of AIC comparison and the adjusted determination coefficient (R^2) between OLS and GWR models for each year are presented in Table 3. The results show that the GWR model is better than the OLS model in 3 years of 2008, 2009 and 2010.

Table 3. Comparison of OLS and GWR models by years.

Items	2007		2008		2009		2010	
	OLS	GWR	OLS	GWR	OLS	GWR	OLS	GWR
AIC	101.10	101.10	105.38	104.65	81.83	73.51	81.81	78.94
R^2	0.26	0.26	0.42	0.46	0.70	0.84	0.64	0.69

Fig. 5 shows the values of the adjusted determination coefficient (R^2) of the GWR model varies locally by districts. This indicates that the spatial variation of the rela-

tionship between the explanatory variables and the number of cholera cases in the year. Specifically, values of the adjusted determination coefficient R^2 can be divided into two groups of low and high values. Accordingly, for 2007, there is an increase in the value of R^2 from West to East. For the years after (2008, 2009 and 2010), the increase in the value of R^2 turns into the direction from North to South.

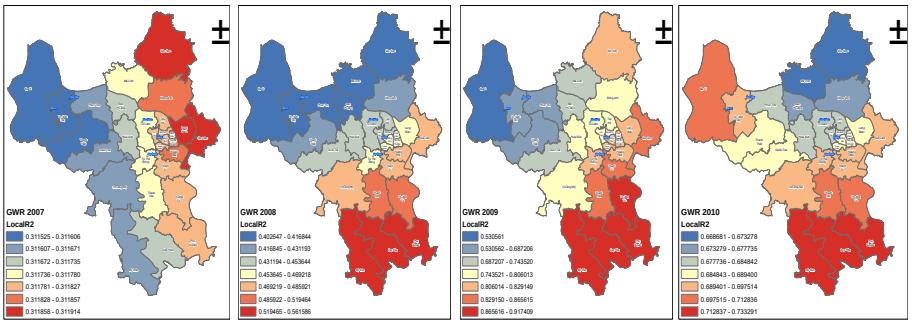

Fig. 5. R^2 of the GWR model for 2007, 2008, 2009 and 2010

The advantage of GWR model is the ability to visually show the estimated coefficients of each explanatory variable for each space unit that is the district. This makes it easier to explore complex relationships.

4.4 Discussion

Some comments are drawn from the results of OLS and GWR regression analytics as follows:

- On the annual basis, clear impact of climate to cholera cases in the years 2007, 2009, 2010 is found, while the remaining year 2008 this effect is negligible. On the other hand, the impact of water surface to cholera cases is clearly found for all years from 2007 to 2010. Population factor has clear impact to cholera cases in two years of 2008 and 2010. The analytical results of the study show water surface factor plays an important role in forecasting models.
- In terms of space, the predicted number of cases in urban areas is generally smaller than the actual number of cases. Meanwhile, in North and South suburb districts the predicted number is often greater. Further research is needed to understand the interaction of space in the impact to the cholera cases to provide the best forecasting models.
- In terms of models, both OLS and GWR models can explain the number of cholera cases. However, GWR model produces better results by years over OLS model thank to its ability to estimate the space-dependent coefficients of the model.

5 Conclusion

This research has identified the hot spots of the cholera disease, which are often formed into clusters around the metropolitan area, where the population are very crowded and adjacent to the polluted rivers. The study also experiments OLS and GWR regression models to generalized forecast the cholera in Hanoi city by years based on climate variables, population and water surface area in the period 2001 - 2011. The experimental results have shown that GIS can be effectively used for the cholera epidemic analysis of the research area. The research pointed out the hot spots of cholera disease as well as it explained the relationship between spatial distribution variables, including climate, water area and population, and the temporal distribution variable of the number of cholera cases. That contributes to support for the management of the disease over space and time. At the same time, the research results have created important bases for further studies on the simulation and forecasting the cholera in the city of Hanoi.

In addition to these achievements, there are some issues that need further research to improve as: (1) the monitoring period of cholera cases was relatively short, in which cholera cases only appeared in five years (2004, 2007, 2008, 2009 and 2010) in the whole period of 2001-2011. Besides, the number of cholera cases appeared in each year is small. Furthermore, the data of cholera cases from 2001 to 2011 was unbalanced. Therefore, in order to see the clearer impact of the climate, water surface and population to the cholera epidemic, the monitoring of the cholera epidemic should be continued in the coming years; (2) the spatial accuracy of the research is limited due to the fact that it analyses epidemic at the district level. Therefore, further analysis should be conducted at the level of wards to improve the spatial accuracy. In addition, in the collection of cholera cases, detailed information should be recorded for each case, such as the address and GPS coordinates to give more detailed input to the GIS analysis.

References

1. Plowright, R.K., Cross, P.C., Tabor, G.M., Almberg, E., Bienen, L. and Hudson, P.J.: Climate Change and Infectious Disease Dynamics. New Directions in Conservation Medicine: Applied Cases of Ecological Health. Oxford University Press, pp.111–121 (2012).
2. Leckebusch, G.C. and Abdussalam, A.F.: Climate and socioeconomic influences on interannual variability of cholera in Nigeria. Health & Place, [online] 34, pp.107–117 (2015). Available at: http://linkinghub.elsevier.com/retrieve/pii/S1353829215000660.
3. Heywood, I., Cornelius, S. and Carver, S.: Introduction to Geographic Information Systems. Pearson Publication (2002).
4. Nguyen Kim Loi and Tran Thong Nhat: Geographic Information System – ArcView 3.3. Ho Chi Minh city: Argriculture Publisher (2007).
5. Cromley, E.K., McLafferty, S.L.: GIS and Public Health, 2nd ed., New York, USA, The Guilford Press (2011).

6. Auchincloss, A.H., Gebreab, S.Y., Mair, C., Roux, A.V.D.: A Review of Spatial Methods in Epidemiology, 2000–2010. The Annual Review of Public Health is online at publhealth.annualreviews.org (2012).
7. Frank B Osei, Alfred A Duker: Spatial dependency of V. cholera prevalence on open space refuse dumps in Kumasi, Ghana: a spatial statistical modelling. International Journal of Health Geographics (2008).
8. Frank B Osei, Alfred A Duker, and Alfred Stein: Cholera and Spatial Epidemiology, Cholera, Dr. Sivakumar Gowder (Ed.), ISBN: 978-953-51-0415-5, InTech, Available from: http://www.intechopen.com/books/cholera/cholera-and-spatial-epidemiology (2012).
9. Rasam, A.R.A., Ghazali, R., Noor, A.M.M., Mohd, W.M.N.W., Hamid, J.R.A., Bazlan, M.J. and Ahmad, N.: Spatial epidemiological techniques in cholera mapping and analysis towards a local scale predictive modelling. IOP Conference Series: Earth and Environmental Science (2014). Available at: http://stacks.iop.org/1755-1315/18/i=1/a=012095?key=crossref.018d453478b90fd70bf231feaecdaab6.
10. Nkeki, F.N. and Osirike, A.B.: GIS-based local spatial statistical model of cholera occurrence: using geographically weighted regression. Journal of Geographic Information System, 5, pp.531–542 (2013).

Correlation Dimension Estimation from EEG Time Series for Alzheimer Disease Diagnostics

Martin Dlask* and Jaromir Kukal

Czech Technical University in Prague,
Trojanova 12, Prague, Czech Republic
{martin.dlask,jaromir.kukal}@fjfi.cvut.cz

Abstract. Biomedical data often carry chaotic character that can be investigated with the tools of fractal geometry. Correlation dimension is a suitable measure that can be used for the analysis of EEG signal in order to discover Alzheimer disease (AD). However, its estimation is often biased and inaccurate. We present rotational spectrum method that estimates the correlation dimension without bias for arbitrary set in Euclidean space and apply it to the EEG. Using multiple testing we discovered channels with significant difference of fractal dimension between CN and AD patients. Using space reconstruction theorem it was possible to prove that the left occipital and temporal part of human brain carries

Topic of article

Fractal behaviour of time series with chaotic character can be investigated in many ways. The dependency of the time series can be measured by fractal dimension or Hurst exponent. In this paper we focus on the estimation of the correlation dimension D_2 that belongs to the family of entropy-based fractal dimensions. The traditional approach of estimating the correlation dimension is called correlation sum method. However it was proven that this method provides biased estimates and therefore is unsuitable for data classification.

The more exact method of correlation dimension estimation that utilizes the power spectrum of investigated set. The method employs the Fourier transform of an n-dimensional set $F \subset \mathbb{R}^n$ that is defined as

$$F(\boldsymbol{\omega}) = \mathrm{E}_{\boldsymbol{x}\sim \mathrm{U}(F)} \, \exp(-\mathrm{i}\boldsymbol{\omega}\cdot\boldsymbol{x}) \tag{1}$$

for angular frequency $\boldsymbol{\omega} \in \mathbb{R}^n$ and for $\boldsymbol{x}$ uniformly distributed on F. The rotational spectrum is defined using the factorisation of angular frequency $\boldsymbol{\omega} = \Omega \cdot \boldsymbol{\psi}$ for $\Omega \in \mathbb{R}_0^+$ and normalisation vector $\boldsymbol{\psi} \in \mathcal{S}_{n-1}$ from $n-$dimensional sphere as

$$S(\Omega) = \mathrm{E}_{R\in \mathrm{SO}_{(n)}} \quad \mathrm{E}_{\boldsymbol{\psi}\in S_{n-1}} \quad \mathrm{E}_{\boldsymbol{x},\boldsymbol{y}\sim \mathrm{U}(F)} \quad \exp(-\mathrm{i}\Omega\boldsymbol{\psi}R(\boldsymbol{x}-\boldsymbol{y})), \tag{2}$$

*

for any rotation $R \in \mathrm{SO}(n)$ from the group of all rotations in $\mathbb{R}^n$ around the origin. The resulting characteristics has suitable properties, because it can be expressed analytically as

$$S(\Omega) = \mathrm{E}_{\boldsymbol{x},\boldsymbol{y}\sim \mathrm{U}(F)} H_n(\Omega \, \|\boldsymbol{x} - \boldsymbol{y}\|), \tag{3}$$

for the kernel function H_n

$$H_n(q) = \frac{2^{\frac{n-2}{2}} \cdot \Gamma\left(\frac{n}{2}\right)}{q^{\frac{n-2}{2}}} J_{\frac{n-2}{2}}(q), \tag{4}$$

where J is noninteger Bessel function. Due to the relationship between correlation dimension and the rotational spectrum, the correlation dimension can be calculated as following

$$\lim_{\Omega\to\infty} \frac{\ln S(\Omega)}{\ln \Omega} = -D_2. \tag{5}$$

The rotational spectrum can be estimated from any set by means of Monte Carlo simulation and due to the linear dependance for high parameter ω in log-log plot, the correlation dimension can be calculated using model

$$\ln S(\Omega) = A - D_2 \cdot \ln \ \Omega + \epsilon \tag{6}$$

for parameters D_2, A using maximum likelihood method. The new method was proven to be useful for the analysis of any sets in Euclidean space, including the trajectories of time series. The aim of our work is to analyse EEG signals from patients that are suffering from Alzheimer disease (AD) and control normal (CN) patients. Based on the estimation of correlation dimension and statistical testing it is possible to distinguish between these two groups of patients. The subject of the analysis is 146 EEG samples of CN and 28 samples of AD patients. Every sample contains 19 time series of the signal development in time from 19 electrodes located on the patient head. The EEG signal will be analysed in three different ways.

The first possibility of EEG signal analysis considers the signal as a vector process in 19-dimensional space and estimates the correlation dimension for each patient. We call this approach as global channel based analysis.

The second possibility of the investigation is to use state space reconstruction. Considering the time series is a dynamic process, we can employ the Whitney embedding theorem for the estimation of attractor dimension. The structure of the state series is the same as the structure of the attractor, therefore their correlation dimension is the same.

The last approach for the EEG analysis is to estimate the correlation dimension of the graph. EEG time series graph is a set in two dimensional space, therefore the correlation dimension can vary between one and two.

We performed 39 tests with the null hypothesis

$$H_0 : \mu_{\mathrm{AD}} = \mu_{\mathrm{CN}} \tag{7}$$

where the μ_{AD} is the expected value of correlation dimension of AD patients and μ_{CN} is the expected value of CN patients. The aim is to find the channels where the difference between the dimension estimates is highest. Since in this case multiple testing is presented, we need to diminish the significance level based on Hochberg false discovery rate theorem.

The estimates of correlation dimension were proven to have normal distribution along the both groups, therefore we use the two-sample t-test for the hypothesis testing. Table 1 provides the results of the correlation dimension estimation together with the p-value for those channels, where the null hypothesis was rejected. The $\widehat{D}_{\mathrm{CN}}$ and $\widehat{D}_{\mathrm{AD}}$ are the mean values of correlation dimension in case of CN and AD patients, respectively, whereas std is their standard deviation. The abbreviation SR denotes the space reconstruction method and G abbreviation denotes the EEG graph method.

channel	method	$\widehat{D}_{\mathrm{CN}}$	$\mathrm{std}_{\mathrm{CN}}$	$\widehat{D}_{\mathrm{AD}}$	$\mathrm{std}_{\mathrm{AD}}$	p-value
17	SR	5.5412	0.93852	4.8159	0.7146	0.0001
18	SR	5.5004	0.94848	4.8259	0.97334	0.0007
8	SR	5.4573	0.9181	4.8029	1.2555	0.0014
13	G	1.7776	0.27605	1.6051	0.12824	0.00151
13	SR	5.4947	0.8995	4.9561	0.8167	0.0037
14	SR	5.6979	1.1058	5.1039	0.6296	0.0065

Table 1. Correlation dimension of EEG signal.

The most significant changes were recorded on the channels in the left occipital and the left temporal part of human brain where the null hypothesis about the equality of mean values of correlation dimension was rejected. The more suitable for the EEG analysis is the state space reconstruction that was performed in our case in 15-dimensional space that brought significant differences between the two groups of patients.

References

1. Dlask, M., Kukal J.: Application of rotational spectrum for correlation dimension estimation. Chaos, Solitons and Fractals 99, 256-262 (2017)
2. Grassberger, P., Procaccia, I.: Measuring the strangeness of strange attractors. Physica D: Nonlinear Phenomena 9, 189–208 (1983)
3. Grassberger P., Procaccia, I.: Characterization of strange attractors. Phys. Rev. Lett. 50, 346–349 (1983)
4. Jeong, J. . EEG Dynamics in patients with Alzheimers disease. Clinical Neurophysiology 115, 490-505 (2004)
5. Vysata, O., Prochazka A. et. al.:Change in the characteristics of EEG color noise in Alzheimers disease. Clinical EEG Neuroscience 45, 147–151 (2014).

An application of the GAM-PCA-VAR model to respiratory disease and air pollution data

Márton Ispány, Juliana Bottoni de Souza, Valdério A. Reisen, Glaura C. Franco, Pascal Bondon, and Jane Meri Santos

Faculty of Informatics, University of Debrecen, Hungary
ispany.marton@inf.unideb.hu
Programa de Pós-Graduação em Engenharia Ambiental, CT-UFES, Brazil
juliana_bottoni@yahoo.com.br jmerisantos@yahoo.com.br
Departamento de Estatística, CCE-UFES, Brazil
valderioanselmoreisen@gmail.com
Departamento de Estatística, UFMG, Brazil
glaura@est.ufmg.br
Laboratoire des Signaux et Systèmes, CentraleSupélec, Gif sur Yvette, France
pascal.bondon@l2s.centralesupelec.fr

Abstract. The hybrid GAM-PCA-VAR model, which is the combination of the principal component analysis (PCA) and the generalized additive model (GAM) along with a vector autoregressive (VAR) process, is proposed for studying the health effects of air pollution. The model is applied to a real data set with the aim of quantifying the association between the number of hospital admissions for respiratory diseases as response variable and air pollution concentrations, especially, PM_{10}, SO_2, NO_2, CO and O_3, as covariates.

Keywords: Generalized additive model; Multicollinearity; Principal component analysis; Relative risk; Serial correlation; Vector autoregressive model.

The generalized additive model (GAM) with a Poisson marginal distribution as the standard statistical methodology is frequently applied in environmental epidemiological studies about the health effects of air pollution. In spite of its widespread use, many authors claim that care is needed when applying the GAM to multiple time series as covariates, see e.g. [1]. The problems identified by these authors may be due to the fact that the pollutant variables not only possess serial dependence, but also present interdependence amongst themselves. In a forthcoming paper, see [2], we propose the hybrid GAM-PCA-VAR model to handle these problems. The PCA is used to eliminate the multicollinearity between the pollutants while the VAR model is used to handle the serial correlation of the data in order to produce white noise processes as covariates in the GAM.

The mathematical definition of the GAM-PCA-VAR model is the following. Let the response $\{Y_t\} \equiv \{Y_t\}_{t\in\mathbb{Z}}$ be a count time series and the conditional distribution of Y_t, given the past $\mathcal{F}_{t-1}$ which contains the available information

up to time $t-1$, have Poisson distribution with mean μ_t which depends on the covariates and the parameters. It is supposed that the multivariate covariates of pollutants $\boldsymbol{X}_t = (X_{1t}, \ldots, X_{qt})^\top$ follows a VAR(1) process with autoregressive coefficient matrix Φ and variance matrix $\Sigma_{\boldsymbol{\varepsilon}}$ of the white noise innovation $\{\boldsymbol{\varepsilon}_t\}$. The principal components (PCs) $Z_{1t}, \ldots, Z_{rt}$, $r \leq q$, are defined by

$$Z_{it} = \boldsymbol{a}_i^\top \boldsymbol{\varepsilon}_t = \boldsymbol{a}_i^\top (\boldsymbol{X}_t - \Phi \boldsymbol{X}_{t-1}), \qquad i = 1, \ldots, r,$$

where $(\lambda_i, \boldsymbol{a}_i)$, $i = 1, \ldots, r$, denote the first r-th eigenvalues/eigenvectors of the variance matrix $\Sigma_{\boldsymbol{\varepsilon}}$. Therefore, the PC vector $\boldsymbol{Z}_t = (Z_{1t}, \ldots, Z_{rt})^\top$ has uncorrelated components, and the process $\{Z_{it}\}$ is a white noise with variance λ_i. The PCs are the explanatory covariates in the standard GAM using the standard link function

$$\mu_t = \exp\left\{ \sum_{i=0}^{r} \upsilon_i Z_{it} + \sum_{j=q+1}^{p} f_j(X_{jt}) \right\}$$

where X_{jt}, $j = q+1, \ldots, p$, denote the confounding variables (for example, the temperature and the humidity).

Under the assumption that the distribution of the innovation vector is multivariate normal, the conditional log-likelihood of the GAM-PCA-VAR model, given a sample $(\boldsymbol{X}_1, Y_1), \ldots, (\boldsymbol{X}_n, Y_n)$, is derived as:

$$\sum_{t=2}^{n} (Y_t \ln \mu_t - \mu_t) - \frac{1}{2} \sum_{t=2}^{n} (\boldsymbol{X}_t - \Phi \boldsymbol{X}_{t-1})^\top A \Lambda^{-1} A^\top (\boldsymbol{X}_t - \Phi \boldsymbol{X}_{t-1}) - \frac{n-1}{2} \ln \det \Lambda,$$

where A is the (q, r) matrix whose ith column is $\boldsymbol{a}_i$ and $\Lambda = \operatorname{diag}(\lambda_1, \ldots, \lambda_r)$. Since the maximization of this log-likelihood is computationally intensive, the following three-stage estimation method is proposed. First, a VAR(1) model is fitted to the pollutant covariates by applying standard time series techniques. We denote by $\hat{\Phi}$ the corresponding estimate of Φ and by $\hat{\varepsilon}_t = \boldsymbol{X}_t - \hat{\Phi} \boldsymbol{X}_{t-1}$ the estimated residuals. Next, the first r PCs $\hat{Z}_{it}$ of $\hat{\varepsilon}_t$ are computed using PCA. Lastly, a GAM model is fitted by maximizing the Poisson part of the log-likelihood where Z_{it} is replaced by $\hat{Z}_{it}$.

The empirical results show that the GAM-PCA-VAR model is able to remove the autocorrelations from the principal components. In addition, this method produces an estimate of the relative risk for each pollutant, which is not affected by the serial correlation present in the data.

References

1. Dionisio, K. L., Chang, H. H. and Baxter, L. K.: A simulation study to quantify the impacts of exposure measurement error on air pollution healh risk estimates in copollutant time-series models. Environmental Health 15:114 (2016).
2. de Souza, J. B., Reisen, V. A., Franco, G. C., Ispány, M., Bondon, P., Santos, J. M.: Generalized additive model with principal component analysis: An application to time series of respiratory disease and air pollution data. J. Roy. Statist. Soc. Ser. C, accepted for publication.

Cryptanalysis of a Random Number Generator Based on a Chaotic Ring Oscillator

Salih Ergün

TÜBİTAK-Informatics and Information Security Research Center
PO Box 74, 41470, Gebze, Kocaeli, Turkey
salih.ergun@tubitak.gov.tr

Abstract. This paper introduces cryptanalysis of a random number generator (RNG) based on a chaotic ring oscillator. An attack system is proposed to discover the security weaknesses of the chaos-based RNG. Convergence of the attack system is proved using master-slave synchronization scheme. Future evaluation of the RNG is obtained from a scalar time series where the only information available are the structure of the RNG and a scalar time series observed from the chaotic ring oscillator. Simulation and numerical results verifying the feasibility of the attack system are given. It is verified that deterministic chaos itself cannot be pointed out as the source of randomness.

1 Introduction

Over the last decades there has been an increasing emphasis on using tools of information secrecy. Certainly, random number generators (RNGs) have more prominently positioned into the focal point of research as the core component of the secure systems. Although many people are even unaware that they are using them, we use RNGs in our daily business. If we ever obtained money from a bank's cash dispenser, ordered goods over the internet with a credit card, or watched pay TV we have used RNGs. Public/private key-pairs for asymmetric algorithms, keys for symmetric and hybrid crypto-systems, one-time pad, nonces and padding bytes are created by using RNGs [1].

Being aware of any knowledge on the design of the RNG should not provide a useful prediction about the output bit sequence. Even so, fulfilling the requirements for secrecy of cryptographic applications using the RNG dictate three secrecy criteria as a "must": 1. The output bit sequence of the RNG must pass all the statistical tests of randomness [2]; 2. The previous and the next random bit must be unpredictable [3] and; 3. The same output bit sequence of the RNG must not be able to be reproduced [4].

An important principle of modern cryptography is the Kerckhoff's assumption [2], states that the overall security of any cryptographic system entirely depends on the security of the key, and assumes that all the other parameters of the system are publicly known. Cryptanalysis is the complementary of cryptography. Interaction between these two branches of cryptology form modern

cryptography which has become strong only because of security analysis revealing weaknesses in existing cryptographic systems.

There are four fundamental techniques for random number generation: 1. Amplification of a noise source [5, 7]; 2. Jittered oscillator sampling [1, 6]; 3. Discrete-time chaotic maps [8–10] and; 4. Continuous-time chaotic oscillators [11, 12]. Although the use of discrete-time chaotic maps in the realization of RNG has been widely accepted for a long period of time [8], it has been shown during the last decade that continuous-time chaotic oscillators can also be used to realize RNGs [11, 12]. In particular, a "true" RNG based on a chaotic ring oscillator has been proposed in [11]. In this paper we target the RNG reported in [11] and further propose an attack system to discover the security weaknesses of the targeted system.

The strength of a cryptographic system almost depends on the strength of the key used or in other words on the difficulty for an attacker to predict the key. On the contrary to recent RNG design [12], where the effect of noise generated by circuit components was analyzed to address security issue, the target random number generation system [11] pointed out the deterministic chaos itself as the source of randomness.

The organization of the paper is as follows. In Section 2 the target RNG system is described in detail; In Section 3 an attack system is proposed to cryptanalyze the target system and its convergence is proved; Section 4 illustrates the numerical results with simulations which is followed by concluding remarks.

2 Target System

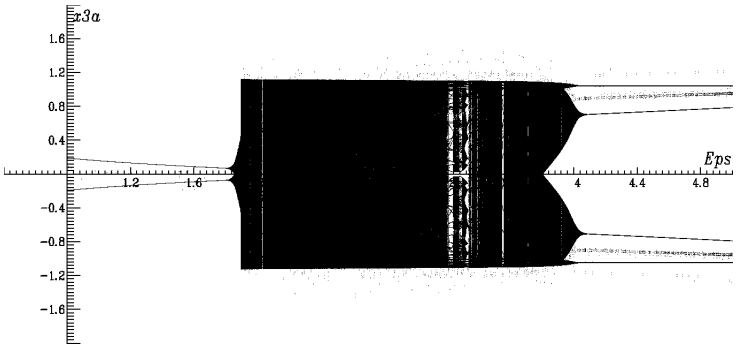

Fig. 1. Bifurcation diagram against the parameter ε.

Chaotic systems are categorized into two groups: discrete-time or continuous-time, respectively regarding on the evolution of the dynamical systems. In target random number generation system [11], a simple continuous-time chaotic circuit is utilized as the core of the RNG. This chaotic system is derived from two ring oscillators coupled by diodes [11].

Using the normalized quantities: $x_n = v_n/V_{th}$, $y_d = i_d R_d/V_{th}$, $t = T/RC$, $\alpha = G_m R$, $\beta = C/(C+C_1)$, $\gamma = R/R_1$, $\delta = R/R_d$, and $\varepsilon = R/R_2$, the equations of the chaotic circuit transform into the following equation Eqn. 1:

$$\begin{aligned}
\dot{x_{1a1}} &= -x_{1a1} - \alpha x_{3a1} \\
\dot{x_{2a1}} &= -x_{2a1} - \alpha x_{1a1} \\
\dot{x_{3a1}} &= -\beta(\gamma+1)x_{3a1} - \alpha\beta x_{2a1} - \beta\delta y_d \\
\dot{x_{1b1}} &= -x_{1b1} - \alpha x_{3b1} \\
\dot{x_{2b1}} &= -x_{2b1} - \alpha x_{1b1} \\
\dot{x_{3b1}} &= -(\varepsilon+1)x_{3b1} - \alpha x_{2b1} + \delta y_d
\end{aligned} \tag{1}$$

where

$$y_d = \begin{cases} x_{3a1} - x_{3b1} - 1 & for\ x_{3a1} - x_{3b1} > 1 \\ 0 & for\ |x_{3a1} - x_{3b1}| \leq 1 \\ x_{3a1} - x_{3b1} + 1 & for\ x_{3a1} - x_{3b1} < -1 \end{cases}$$

The equations in 1 generate chaos for different sets of parameters. Bifurcation diagram against the parameter $\varepsilon = R/R_2$ is constructed. As shown in Fig.1, the given system generates chaos for the parameter ε over a wide range ($1.81 < \varepsilon < 3.13$) which points out that the non-ideal effect on the performance of the chaotic system is not critical. The chaotic attractor ($Horizontal : x_{3b1}$, $Vertical : x_{2b1}$) given in Fig.2 is obtained from the numerical analysis of the system with $\alpha = 3.7$, $\beta = 0.1$, $\gamma = 1$, $\delta = 100$ and $\varepsilon = 2.5$.

Target random number generation mechanism is described in [11] where bit generation method is based on jittered oscillator sampling technique. As depicted in [11] output of a fast oscillator is sampled on the rising edge of a jittered slower clock using a D flip-flop where the jittered slow clock is realized by a chaotic ring oscillator circuit.

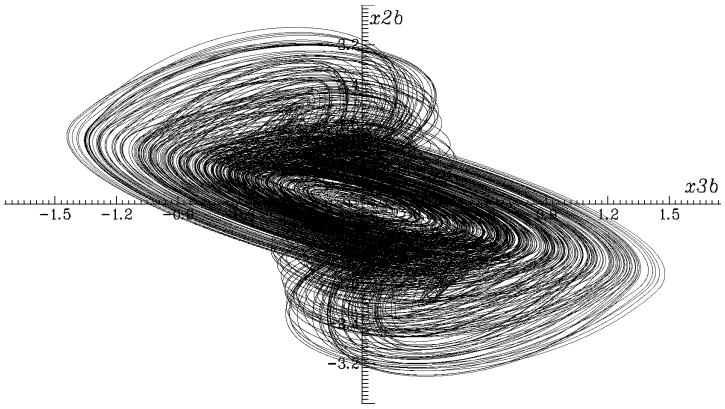

Fig. 2. Numerical analysis results of the chaotic system for $\alpha = 3.7$, $\beta = 0.1$, $\gamma = 1$, $\delta = 100$ and $\varepsilon = 2.5$.

In this design, if the fast and the slower clock frequencies are known as well as the starting phase difference ΔT, the output of the fast oscillator, sampled at the rising edge of the jittered slower clock, can be predicted. It can be shown that the output bit sequence $S_{(bit)i}$ is the inverse of least significant bit of the ratio between the total periods of the jittered slower clock and period of the fast clock:

$$S_{(bit)i} = (\frac{\lfloor \frac{(\sum_{j=1}^{i} T_{slow\ j}) - \Delta T}{T_{fast}/2} \rfloor mod2}{(2d_{fast})})' \tag{2}$$

where $T_{fast} = \frac{1}{f_{fast}}$, f_{fast}, d_{fast} are the period, frequency and the duty cycle of the fast clock, respectively, and the periods of the jittered slower clock $T_{slow\ j}$ are obtained at times t satisfying:

$$s(t) = x_{3a1}(t) = Q\ with\ \frac{ds}{dt} > 0 \tag{3}$$

where $x_{3a1}(t)$ is the chaotic signal, and Q is the logic threshold of the D flip-flop. We have numerically verified that, for high $\frac{f_{fast}}{f_{slow\ center}}$ ratios, the effect of ΔT becomes negligible and the mean value (m_{output}) of the output sequence S_{bit} approaches the fast clock duty cycle d_{fast} where frequency of the chaotic signal, corresponding to mean frequency of the jittered slower clock $f_{slow\ center}$, determines the throughput data rate (f_{rng}). It should be noted that, anyone who knows the chaotic signal output can reproduce the same output bit sequence.

The authors of [11] have preferred to use NIST 800-22 [13] statistical test suite in order to analyze output randomness of their RNG design. However, Big Crush [14] and Diehard [15] statistical test suites which are available at the publication date of target paper weren't applied to output bit stream of the RNG. It should be noted that, the target random number generation system [11] doesn't satisfy the first secrecy criteria, which states that "RNG must pass all the statistical tests of randomness."

3 Attack System

After the seminal work on chaotic systems by Pecora and Carroll [17], synchronization of chaotic systems has been an increasingly active area of research [18]. In this paper, convergence of attack and target systems is numerically demonstrated using master-slave synchronization scheme [18]. In order to provide cryptanalysis of the target random number generation system an attack system is proposed which is given by the following Eqn. 4:

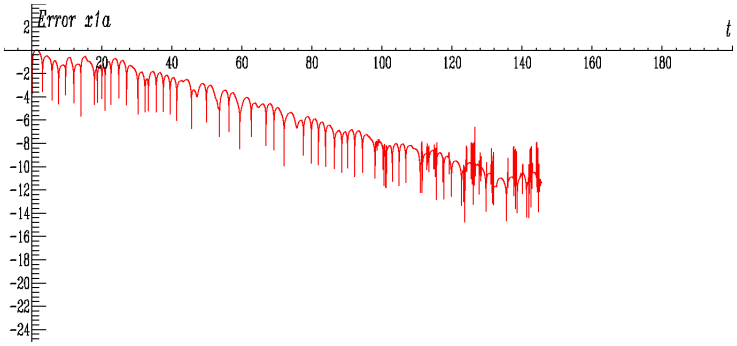

Fig. 3. Synchronization error Log $|e_{x1a}(t)|$.

$$
\begin{aligned}
\dot{x_{1a2}} &= -x_{1a2} - \alpha x_{3a2} \\
\dot{x_{2a2}} &= -x_{2a2} - \alpha x_{1a2} + c(x_{2a1} - x_{2a2}) \\
\dot{x_{3a2}} &= -\beta(\gamma+1)x_{3a2} - \alpha\beta x_{2a2} - \beta\delta y_d \\
\dot{x_{1b2}} &= -x_{1b2} - \alpha x_{3b2} \\
\dot{x_{2b2}} &= -x_{2b2} - \alpha x_{1b2} \\
\dot{x_{3b2}} &= -(\varepsilon+1)x_{3b2} - \alpha x_{2b2} + \delta y_d
\end{aligned}
\tag{4}
$$

where

$$
y_d = \begin{cases} x_{3a2} - x_{3b2} - 1 & for\ x_{3a2} - x_{3b2} > 1 \\ 0 & for\ |x_{3a2} - x_{3b2}| \leq 1 \\ x_{3a2} - x_{3b2} + 1 & for\ x_{3a2} - x_{3b2} < -1 \end{cases}
$$

where c is the coupling strength between the target and attack systems. The only information available are the structure of the target random number generation system and a scalar time series observed from x_{2a1}.

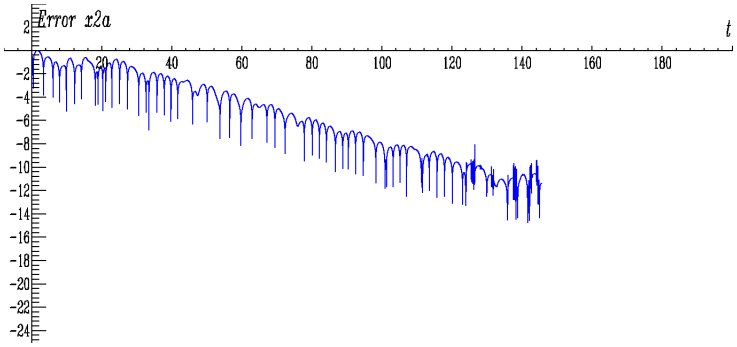

Fig. 4. Synchronization error Log $|e_{x2a}(t)|$.

In this paper, we construct the attack system expressed by the Eqn. 4 that synchronizes ($x_{2a2} \rightarrow x_{2a1}$ for $t \rightarrow \infty$) where t is the normalized time. We define the error signals as $e_{x1a} = x_{1a1} - x_{1a2}$, $e_{x2a} = x_{2a1} - x_{2a2}$, and $e_{x3a} = x_{3a1} - x_{3a2}$ where the aim of the attack is to design the coupling strength such that $|e(t)| \rightarrow 0$ as $t \rightarrow \infty$.

The master-slave synchronization of attack and target systems is verified by the conditional Lyapunov Exponents (CLEs), and as firstly reported in [17], is achievable if the largest CLE is negative. Largest CLEs are calculated for different values of coupling strength c while a scalar time series is observable from x_{2a1}. When c is greater than 0.42 then the largest CLE is negative and hence identical synchronization of target and attack systems starting with different initial conditions is achieved and stable [17]. (Largest conditional Lyapunov Exponent is -0.0108588 for $c = 0.5$). However for c is less than 0.42, largest CLE is positive and identical synchronization is unstable.

Log $|e_{x1a}(t)|$, Log $|e_{x2a}(t)|$, and Log $|e_{x3a}(t)|$ are shown in Fig.3, Fig.4 and Fig.5 respectively, for $c = 3$, where the synchronization effect is better than that of $c = 0.5$. As shown in the given figures, the attack system converges to target system and master-slave synchronization is achieved in less than $145t$.

4 Numerical Results

We numerically demonstrate the proposed attack system using a 4^{th}-order Runge-Kutta algorithm with fixed step size and its convergence is illustrated in Fig.3, Fig.4 and Fig.5, respectively. Numerical results of $x_{1a1} - x_{1a2}$, $x_{2a1} - x_{2a2}$, and $x_{3a1} - x_{3a2}$ are also given in Fig. 6, Fig. 7, and Fig. 8, respectively illustrating the unsynchronized behavior and the synchronization of target and attack systems.

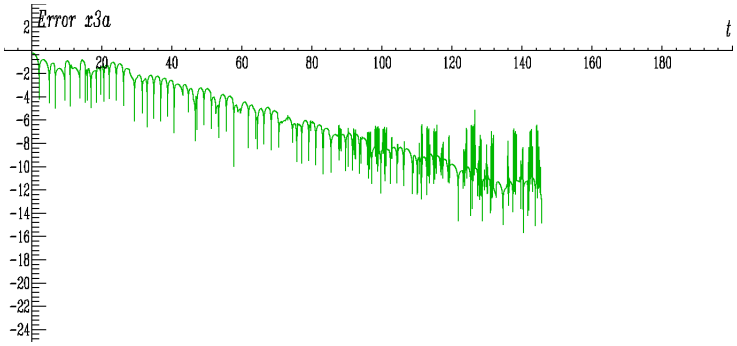

Fig. 5. Synchronization error Log $|e_{x3a}(t)|$.

It is observed from the given figures that, master-slave synchronization is achieved and stable. As shown by black lines in these figures, no synchronous

phenomenon is observed before $145t$. In time, the proposed attack system converges to the target system and identical synchronization is achieved where colored lines depict synchronized behaviors of chaotic states in Fig. 6, Fig. 7, and Fig. 8, respectively.

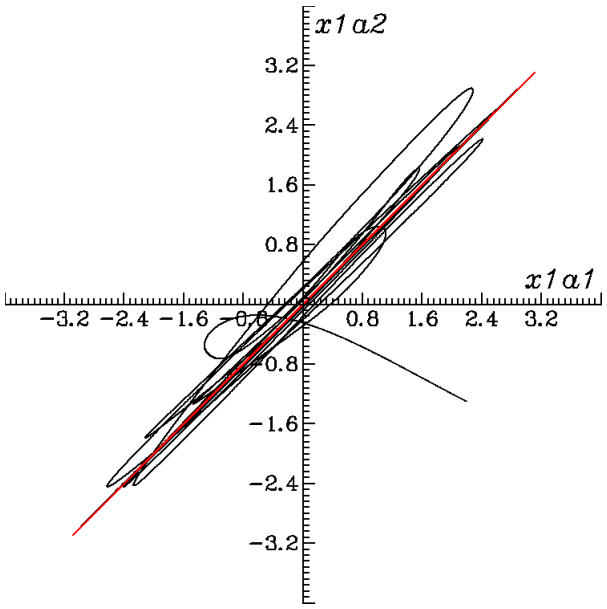

Fig. 6. Unsynchronized behavior and the synchronization of target and attack systems: $Horizontal : x_{1a1}$, $Vertical : x_{1a2}$.

Since the identical synchronization of attack and target systems is achieved ($x_{2a2} \rightarrow x_{2a1}$) in $145t$, the estimated values of x_{3a1} and $S_{(bit)i}$ bit which is generated according to the procedure explained in Section 2 converge to their corresponding fixed values. As a result, it is obvious that identical synchronization of chaotic systems is achieved and hence output bit streams of target and attack systems are synchronized.

It is clearly shown master-slave synchronization of proposed attack system is achieved. Hence, output bit sequences of target and attack systems are synchronized. In conclusion, cryptanalysis of the target random number generation system not only predicts the previous and the next random bit but also demonstrates that the same output bit sequence of the target random number generation system can be reproduced. As a result, the target random number generation system [11] satisfies neither the second, nor the third secrecy criteria that a RNG must satisfy. It should be noted that, deterministic chaos itself cannot be pointed out as the source of randomness.

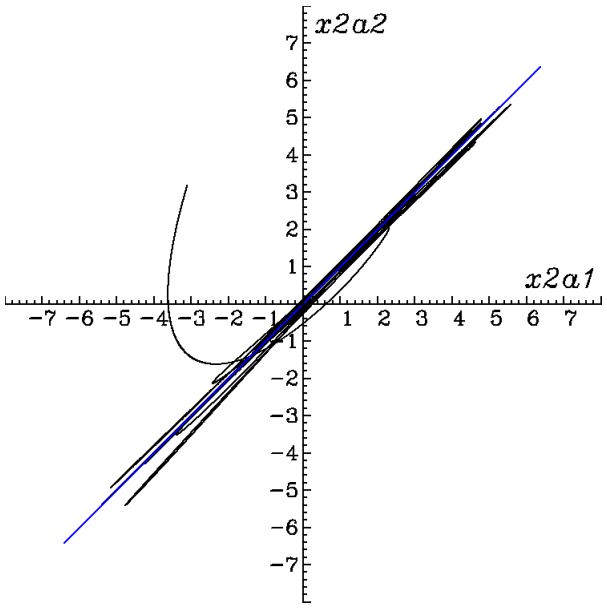

Fig. 7. Unsynchronized behavior and the synchronization of target and attack systems: $Horizontal : x_{2a1}$, $Vertical : x_{2a2}$.

5 Conclusions

In this paper, we propose a cryptanalysis method for a chaos based random number generator (RNG). An attack system is introduced to discover the security weaknesses of the chaos-based RNG and its convergence is proved using master-slave synchronization scheme. Although the only information available are the structure of the target RNG and a scalar time series observed from the target chaotic system, identical synchronization of target and attack systems is achieved and hence output bit streams are synchronized. The target RNG does not fulfill Big Crush and Diehard statistical test suites, the previous and the next bit can be predicted, while the same output bit sequence of the RNG can be reproduced. Simulation results presented in this paper not only verify the feasibility of the proposed method but also encourage its use for the cryptanalysis of the other chaos based RNG designs. Proposed attack, renders generated bit streams predictable, thereby qualifying the target RNG to be used as a not true but pseudo random source.

References

1. Jun, B. and Kocher, P., "The Intel Random Number Generator," Cryptography Research, Inc. white paper prepared for Inter Corp. Apr. 1999 http://www.cryptography.com/resources/whitepapers/IntelRNG.pdf.

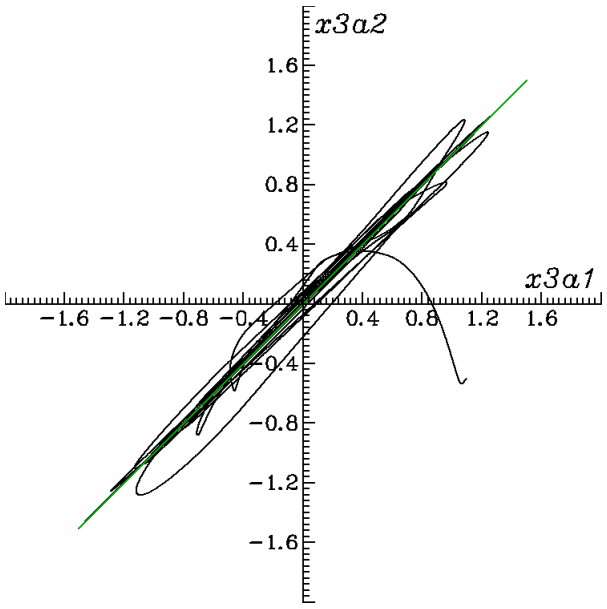

Fig. 8. Unsynchronized behavior and the synchronization of target and attack systems: $Horizontal : x_{3a1}$, $Vertical : x_{3a2}$.

2. Menezes, A., Oorschot, P.van, Vanstone, S.: Handbook of Applied Cryptology. CRC Press (1996)
3. Schrift, A. W., Shamir, A.: On the Universality of the Next Bit Test. Proceeding of the CRYPTO. (1990) 394-408.
4. Schneier, B.: Applied Cryptography. 2. edn. John Wiley & Sons (1996)
5. C.S. Petrie and J.A. Connelly, "A Noise-Based IC Random Number Generator for Applications in Cryptography," IEEE Trans. Circuits and Systems I, vol. 47, no. 5, pp. 615-621, May 2000.
6. M. Bucci, L. Germani, R. Luzzi, A. Trifiletti, and M. Varanonuovo, "A High Speed Oscillator-based Truly Random Number Source for Cryptographic Applications on a SmartCard IC", IEEE Trans. on Computers, vol. 52, pp. 403-409, Apr. 2003.
7. Göv, N.C., Mıhçak, M.K. and Ergün, S.: True Random Number Generation Via Sampling From Flat Band-Limited Gaussian Processes. IEEE Trans. Circuits and Systems I, Vol. 58. 5 (2011) 1044-1051
8. Stojanovski, T., Kocarev, L. "Chaos-Based Random Number Generators-Part I: Analysis", IEEE Trans. Circuits and Systems I, Vol. 48, 3 (2001) 281-288
9. Callegari, S., Rovatti, R., Setti, G."Embeddable ADC-Based True Random Number Generator for Cryptographic Applications Exploiting Nonlinear Signal Processing and Chaos", IEEE Transactions on Signal Processing, Vol. 53, 2 (2005) 793-805
10. T. Stojanovski, J. Pihl, and L. Kocarev, "Chaos-Based Random Number Generators-Part II: Practical Realization," IEEE Transactions on Circuits and Systems I, vol. 48, no. 3, pp. 382-385, Mar. 2001.

11. İ. Çicek, G. Dündar, “A hardware efficient chaotic ring oscillator based true random number generator,” Proc. IEEE International Conference on Electronics, Circuits and Systems, (2011) 430 - 433
12. Ergün, S., Güler, Ü., and Asada, K., “A High Speed IC Truly Random Number Generator Based on Chaotic Sampling of Regular Waveform” IEICE Transactions on Fundamentals of Electronics, Communications and Computer Sciences, Vol. E94-A, no.1, (2011) 180-190
13. National Institute of Standard and Technology, FIPS PUB 140-2, Security Requirements for Cryptographic Modules, NIST, Gaithersburg, MD 20899, (2001)
14. P. L’Ecuyer, Universit’e de Montr’eal., “Empirical Testing of Random Number Generators”, 2002, Available at http://www.iro.umontreal.ca/ lecuyer/
15. G. Marsalgia, “Diehard: A Battery of Tests of Randomness”, 1997, Available at http://stat.fsu.edu/∼geo/diehard.htm
16. National Institute of Standard and Technology, “A Statistical Test Suite for Random and Pseudo Random Number Generators for Cryptographic Applications”, Available at http://csrc.nist.gov/groups/ST/toolkit/rng
17. Pecora, L.M., Carroll, T.L., “Synchronization in chaotic systems,” Physical Review Letters, vol. 64, no. 8, (1990) 821-824
18. Hasler, M., “Synchronization principles and applications,” Tutorials IEEE International Symposium on Circuits and Systems (ISCAS ’94), C. Toumazou, Ed., London, England, (1994) 314-327

Factors Affecting Randomness in Pseudo-Random Number Series Extracted from Chaotic Time Series of Logistic Map and Chaos Neural Network

Hitoaki YOSHIDA[1,*], Masatomo SASAKI[1], Takeshi MURAKAMI[2], Shogo SHIMONO[1] and Satoshi KAWAMURA[3]

[1]Faculty of Education, Iwate University, Japan
{hitoaki, e0114070, e0112088}@iwate-u.ac.jp
[2]Technical Division, Iwate University, Japan
mtakeshi@iwate-u.ac.jp
[3]Super-Computing and Information Sciences Center, Iwate University, Japan
kawamura@iwate-u.ac.jp

Abstract. The time series of the logistic map and the chaos neural network have been studied from an empirical view point. The pseudo-random number series are extracted from the chaotic time series by our own method. A *pseudo-complexity* is proposed on the basis of the staying time of the transient orbit and the period of the chaotic orbit. The results of the NIST SP800-22 tests suggest that the *pseudo-complexity* may be useful as necessary conditions to pseudo-random numbers for cryptographic applications. We have studied also the property of pseudo-random numbers extracted from periodic chaos and the related chaotic time series, *tombolo chaos* that is not periodic chaos but outlines of islands still remain. The findings are useful to evaluate chaotic time series for a pseudo-random number generator (PRNG) applied to a cipher system.

Keywords: chaotic time series·chaos neural network·pseudo-random number

1 Introduction

We have widely studied on the chaos neural network (CNN) that consists of conventional artificial neurons and generates chaotic outputs [1-3]. We have studied computer generated chaotic time series from an empirical view point. Theoretical chaotic time series has no period and its orbit is infinite, computer generated chaotic time series, however, is eventually periodic by the calculation of the finite precision. We have reported the estimation method of the period of chaotic time series, because which is too long to observe directly in some case [4-5]. Empirical chaotic time series from CNN are useful for extracting pseudo-random numbers (PRNs) which are applied to stream cipher, and have been commercialized as security systems [9]. The extraction method of PRN from chaotic time series is shown in Fig.1 [6, 8, 10].

* Iwate University, Ueda, Morioka, Iwate, 020-8550 Japan.

adfa, p. 1, 2011.

All PRNs extracted form chaotic time series by the method are not always useful for a PRNG empirically, because there are some limitations to use practically. For example, an error originated from binarization [6], the properties of the chaotic time series [7], and so on. In this work we report some other factors affecting randomness in chaotic time series of the logistic map and CNN. In particular, *pseudo-complexity* of time series is proposed to study necessary conditions (minimum requirement) to pseudo-random numbers for cryptographic applications. As for the properties of the chaotic time series we have reported preliminary result on periodic chaos which consists of 2 islands [6, 14]. In this work we report the further finding on periodic chaos which consists of more number of islands and on related chaotic time series.

2 Extraction of Pseudo-Random Number Series from Chaotic Time Series

The iteration of CNN is computed by double-precision arithmetic, and a pseudo-random number is extracted from a chaotic output of CNN by the method shown in Fig.1. The lowest 3 bits of the mantissa are discarded because they contain statistical deviation. The lower 24 bits in the remaining mantissa part are extracted as a pseudo-random number, and following iterations afford pseudo-random number series [9-10, 13].

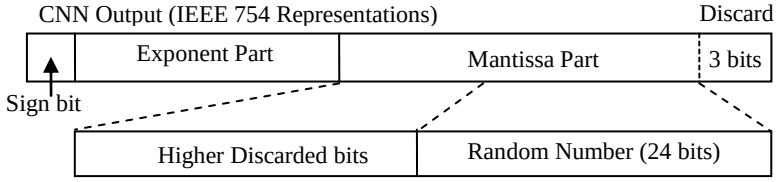

Fig. 1. The method for extraction of a random number from a CNN output.

In this work the time series of the well-known logistic map (equation 1) are studied for a comparable study [14]. Pseudo-random number series have extracted from the chaotic time series of the logistic map by the same method that shown in Fig.1. Obtained pseudo-random number series are tested by NIST SP800-22 test suite (version: sts-2.1.2) which corrects problems of a non-overlapping template matching test and an overlapping template matching test [11]. Maurer's "universal statistical" test has been improved according to Coron's approximation [12]. In our work a test fail rate is estimated by repeated NIST tests and an overall result is judged by the test fail rate: less than 1.0% for normal test, less than 2.7% for UN test [10, 12].

$$x_{n+1} = \mu x_n (1 - x_n) \tag{1}$$

3 Kolmogorov Complexity and Pseudo-Complexity

The Kolmogorov complexity of an object is the minimal length (or the limit of the size of a compressed representation of the object) of a binary program that produces the object as output [15].

As for a pseudo-random number series the Kolmogorov complexity may vary whether the algorithm and parameters are known or not, practically. In this work we have proposed a *pseudo-complexity* for a pseudo-random number series extracted from a chaotic time series by the method shown in Fig. 1. A *pseudo-complexity* (*Pc*) is defined as the maximal bits of a pseudo-random number series that has not a period. The targeted pseudo-random number series should pass the following tests with high probability (< 10%) before calculation of a *pseudo-complexity*:

(a) The frequency test and the run test which are the minimum requirements for NIST SP800-22 tests.

(b) The serial test and the approximate entropy test which are the test for uniformity and compressibility.

The threshold of the probability may choose a smaller value (e.g. < 1 %), but practically 10% is adopted expecting to obtain more information on a boundary region.

Examples: (i) If a binary pseudo-random number is "10101110001", a pseudo-complexity is $Pc = \log_2 11 \approx 3.46$. (ii) If a period of a pseudo-random number block (24 bits for each block) is 786239, a pseudo-complexity is $Pc = \log_2 (786239 \times 24) \approx 24.17$. (iii) A pseudo-complexity is not applicable to the original time series of the logistic map, because the distribution is not uniform and consecutive numbers have correlation.

4 Pseudo-Complexity of Logistic Map

Periods of the logistic map (p) are empirically obtained as shown in Table 1. The period depends on an initial value (x_0). As for μ = 4.00, 3.95, 3.94, 3.93, 3.92, 3.91, 3.90, 1000 initial values between 0-1 are respectively studied with double-precision floating-point arithmetic. In general the period of the logistic map under the condition is ca.10^3-10^7. About 4×10^5 bits of pseudo-random number need for 1 sequence of NIST tests and about 4×10^8 bits (1000 sequences of 400 kbits) need for 1 set of NIST tests, because necessary length of binary bits is more than 387840 bits for UN test. Staying time of a transient orbit (q) before a periodic orbit also depends on the initial value (x_0). Because a 24-bit-pseudo-random-number sequence is generated by the method of Fig.1 for iteration, a pseudo-complexity (*Pc*) is calculated by p and q as follows:

$$Pc = \log_2 24(p+q) \tag{2}$$

As for the pseudo-random number of the chaos neural network (*vide infra*), a pseudo-complexity is calculated using equation 2 also by a period and staying time of a transient orbit of CNN.

Table 1. Empirically obtained periods of the logistic map. [a)]

$\mu = 4.00$		$\mu = 3.95$		$\mu = 3.90$	
period	**frequency**	**period**	**frequency** [b)]	**period**	**frequency** [b)]
2441806	9	64386	7	1589143	3
2625633	11	1257374	4	7724511	31
5638349	708	1709862	19	9840432	99
10210156	9	3061880	8	18143091	93
14632801	106	3371345	25	60858285	773
		21929348	164		
		64068460	772		

a) The specification of workstation. CPU: Intel Xeon E5-2609 2.40GHz, compiler: gcc 4.3.4 and OS: SUSE Linux.

b) The column do not include 1 initial value which converged to a fix point.

Representative results on *the examination of the proportion of sequences passing a test* (hereinafter, called "the examination of the proportion") in the NIST tests are summarized in Table 2. x_0 is the initial value of the logistic map and $\mu = 4.0$ in equation 1.

The result is sorted by the pseudo-complexity. The test fail rate is an average of repeated 48 times of the NIST tests. In this case the test fail rates of UN, OT and AE test are sometimes over the permissible range. The passed series in the overall tests is very few compared with C-4nn under appropriate conditions.

Overall result is decided by the examination of the proportion and the examination of uniform distribution of P-values in the NIST tests, and the test fail rate of the examinations in our work. The passed series in the overall tests is not found when *Pc* is less than 26.5, but as *Pc* increases the number of the passed series increases. It suggests that $Pc > 26.5$ is the necessary condition of suitable pseudo-number series. The result is also true for $\mu = 3.90, 3.91, 3.92, 3.95, 4.00$.

In the next, correlation between *Pc* and the test fail rate is studied. The selected correlation coefficient between the pseudo-complexity (*Pc*) and the test fail rate is shown in Table 3 on the logistic map ($\mu = 4.0$). It suggests the negative correlation of the pseudo-complexity (*Pc*) only with the fail rate of NT test (the non-overlapping template matching test) on the examination of the proportion. The correlation coefficients corresponding to other μ are shown in Table 4. All data suggests same negative correlation. The necessary condition ($Pc > 26.5$) may originate from NT test, because the test fail rate of NT test is above 1% when $Pc < 26.5$.

The purpose of NT test is to detect generators that produce too many occurrences of a given non-periodic (aperiodic) pattern [11]. The correlation may be caused by the repetition originated from relatively short periods. The details are expected in further study.

Table 2. Result of NIST SP800-22 tests and the *pseudo-randomness* on the logistic map.

x_0	time [a]		Selected Test Fail Rate (%) [b]								*Pc*	overall result
	period	transient	RK	NT	OT	UN	AE	RE	SE	LC		
0.798	2625633	864946	0.0	2.3	2.1	4.2	0.0	0.3	0.0	2.1	26.3	
0.060	2625633	1963946	0.0	1.7	14.6	2.1	0.0	0.5	0.0	0.0	26.7	
0.164	2625633	2481946	0.0	1.6	8.3	0.0	0.0	0.3	0.0	2.1	26.9	
0.988	2441806	2725760	0.0	1.4	2.1	2.1	6.3	0.3	0.0	0.0	26.9	
0.958	2441806	3208760	2.1	0.6	4.2	10.4	0.0	0.0	0.0	0.0	27.0	
0.171	5638349	254718	0.0	0.8	0.0	0.0	8.3	0.5	3.1	0.0	27.1	
0.025	2625633	3841579	2.1	1.7	2.1	10.4	0.0	0.0	0.0	0.0	27.2	
0.581	2625633	5868212	0.0	0.9	0.0	0.0	0.0	0.5	0.0	0.0	27.6	pass
0.433	5638349	4027718	0.0	0.4	0.0	2.1	8.3	0.3	0.0	0.0	27.8	
0.489	2625633	7223212	0.0	0.6	0.0	4.2	0.0	0.5	0.0	0.0	27.8	
0.034	2441806	7414372	0.0	0.5	0.0	0.0	0.0	0.5	0.0	0.0	27.8	
0.393	2441806	7563372	0.0	0.5	0.0	2.1	0.0	1.6	0.0	0.0	27.8	
0.238	10210156	151440	0.0	0.5	0.0	14.6	0.0	0.5	0.0	0.0	27.9	
0.624	2441806	8718372	0.0	0.6	0.0	0.0	0.0	0.5	1.0	0.0	28.0	pass
0.376	2441806	8718372	0.0	0.6	0.0	0.0	0.0	0.5	1.0	0.0	28.0	pass
0.679	10210156	1539440	0.0	0.5	0.0	22.9	0.0	0.5	0.0	0.0	28.1	
0.431	5638349	8519067	0.0	0.3	0.0	0.0	6.3	0.3	0.0	0.0	28.3	
0.198	14632801	513393	0.0	0.1	0.0	12.5	0.0	0.5	0.0	0.0	28.4	
0.163	14632801	768393	0.0	0.1	0.0	6.3	0.0	0.5	0.0	0.0	28.5	
0.714	10210156	5240440	0.0	0.2	0.0	16.7	0.0	0.5	0.0	0.0	28.5	
0.249	10210156	8242596	0.0	0.2	0.0	22.9	0.0	0.3	0.0	0.0	28.7	
0.024	14632801	5782393	0.0	0.2	0.0	10.4	0.0	0.8	0.0	0.0	28.9	
0.937	10210156	11159596	0.0	0.2	0.0	8.3	0.0	0.0	0.0	2.1	28.9	
0.204	10210156	11760596	0.0	0.2	0.0	2.1	0.0	0.8	0.0	0.0	29.0	pass
0.350	14632801	14758194	0.0	0.2	0.0	2.1	0.0	0.5	0.0	0.0	29.4	pass
0.023	14632801	18212194	0.0	0.1	0.0	2.1	0.0	0.8	0.0	0.0	29.6	pass
0.847	14632801	20759194	0.0	0.1	0.0	4.2	0.0	1.0	0.0	0.0	29.7	
0.432	5638349	64797557	0.0	0.2	0.0	6.3	0.0	0.3	0.0	0.0	30.7	
0.753	5638349	71333906	0.0	0.3	0.0	2.1	0.0	0.3	0.0	0.0	30.8	pass
0.002	5638349	90090302	0.0	0.1	2.1	0.0	0.0	0.8	0.0	0.0	31.1	

a) 1 simulation time corresponds to an iteration of the map.

b) Abbreviations of test names: RK: Binary Matrix Rank Test, NT: Non-overlapping Template Matching Test, OT: Overlapping Template Matching Test, UN: Maurer's "Universal Statistical" test, AE: Approximate Entropy Test, RE: Random Excursions Test, RV: Random Excursions Variant Test, LC: Linear Complexity Test.

Table 3. Selected correlation coefficients between *Pc* and the test fail rate.

tests	RK	NT	OT	UN	AE	RE	RV	LC
R	-0.269	-0.746	-0.410	0.010	-0.261	0.227	-0.150	-0.262

Table 4. Correlation coefficients between *Pc* and the test fail rate of NT test.

μ	3.90	3.91	3.92	3.93	3.94	3.95	4.00
R	-0.683	-0.707	-0.670	-0.680	-0.698	-0.776	-0.746

5 Maps in Chaos Neural Network

CNN that composed of 4 neurons in discrete-time system has been used for a chaos generator (Fig. 2) [6, 8, 13].

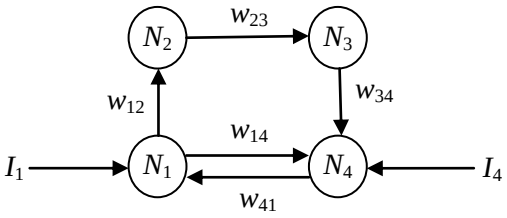

Fig. 2. CNN having cyclic structure (C-4nn).

A total value of inputs in *j*th neuron at time *t* is defined as equation 3. w_{ij} is a synaptic weight, x_i is an input from *i*th neuron and I_j is an external input of *j*th neuron. An output from *j*th neuron at time *t*+1 is defined as equation 4 with the asymmetric piecewise-linear-function (APLF) [5, 6-9].

$$u_j(t) = \sum_{i=1}^{n} w_{ij} x_i(t) + I_j \tag{3}$$

$$x_j(t+1) = f(u_j(t)) \tag{4}$$

The input-output characteristics of C-4nn are shown in Fig.3, which is corresponding to a bifurcation diagram of the logistic map. Of course a bifurcation is observed in CNN, the mixing among neurons also occurs. Therefore it is not a simple bifurcation diagram.

The input-output characteristics in Fig.3 may not be suitable for pseudo-random number generation, because periodic chaos and periodic windows exist. We dare to select the condition for studying factors affecting randomness in chaotic time series. The input-output characteristics of CNN are easily controlled with the parameters, synaptic weights, connection between neurons, and initial values of neurons. Appropriate examples of PRNG for cipher have already reported [5-6, 8, 10].

The range of the external inputs (I) corresponding to chaotic outputs is about [3.79, 4.63] in Fig.3. The range of I which is corresponding to periodic chaos is [4.03, 4.06] (region B) and [4.52, 4.59] (region D). Let the islands of periodic chaos be S_1, S_2, ..., S_{10} that is also a set of real numbers.

If I = 4.0560, a range of outputs corresponding to each island of periodic chaos is obtained as follows:

$$S_1 = \{x \in \mathbb{R} | 0.79190 < x < 0.80770\}, \quad S_2 = \{x \in \mathbb{R} | 0.59296 < x < 0.60074\}$$

$$S_3 = \{x \in \mathbb{R} | 0.49048 < x < 0.49479\}, \quad S_4 = \{x \in \mathbb{R} | 0.18468 < x < 0.19364\}$$

$$S_5 = \{x \in \mathbb{R} | 0.08790 < x < 0.08804\}, \quad S_6 = \{x \in \mathbb{R} | 0.08412 < x < 0.08440\}$$

$$S_7 = \{x \in \mathbb{R} | 0.06765 < x < 0.06849\}, \quad S_8 = \{x \in \mathbb{R} | 0.06699 < x < 0.06700\}$$

$$S_9 = \{x \in \mathbb{R} | 0.06675 < x < 0.06677\}, \quad S_{10} = \{x \in \mathbb{R} | 0.06630 < x < 0.06633\}$$

The order of cyclic access of the islands is with strict regularity, S_1, S_{10}, S_6, S_2, S_9, S_5, S_3, S_8, S_4, S_7, S_1 and the same order shall apply hereinafter. The island cannot divide more islands, because the access frequencies of islands are all the same and because the order of cyclic access of islands is unique.

If I = 4.5600, a range of outputs corresponding to each island is obtained as follows:

$$S_1 = \{x \in \mathbb{R} | 0.48723 < x < 0.50375\}, \quad S_2 = \{x \in \mathbb{R} | 0.43539 < x < 0.45007\}$$

$$S_3 = \{x \in \mathbb{R} | 0.19590 < x < 0.20489\}, \quad S_4 = \{x \in \mathbb{R} | 0.16818 < x < 0.17821\}$$

$$S_5 = \{x \in \mathbb{R} | 0.08748 < x < 0.08782\}, \quad S_6 = \{x \in \mathbb{R} | 0.08657 < x < 0.08688\}$$

$$S_7 = \{x \in \mathbb{R} | 0.06857 < x < 0.06943\}, \quad S_8 = \{x \in \mathbb{R} | 0.06851 < x < 0.06853\}$$

$$S_9 = \{x \in \mathbb{R} | 0.06796 < x < 0.06880\}, \quad S_{10} = \{x \in \mathbb{R} | 0.06785 < x < 0.06789\}$$

The order of cyclic access of the islands is S_1, S_{10}, S_6, S_3, S_7, S_2, S_9, S_5, S_4, S_8, S_1 and the same order shall apply hereinafter. The island cannot divide more islands because of as the same reason as mentioned above.

The normal periodic chaos which originates from bifurcation consists of 2^n (n = 1, 2, 3...) islands. Yet, in this work the number of islands is 10 ($\neq 2^n$). It is not strange because not only a bifurcation but also the mixing among the outputs of the neurons occurs. The chaotic region between two periodic-chaos region [4.06, 4.52] (region C in Fig.3) is not periodic chaos but outlines of islands still remain. Since it seems to be a tombolo (a spit of sand linking an island to another island), we call it *tombolo chaos* (Fig.4).

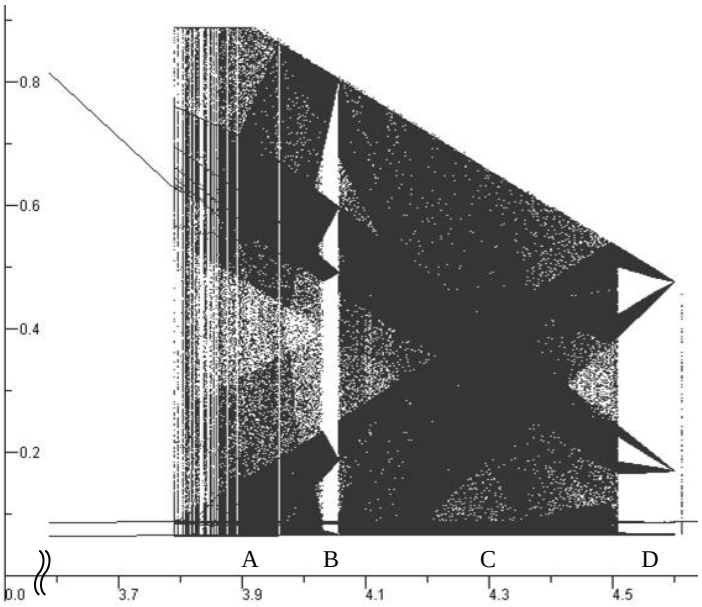

Fig. 3. Input-output Characteristics of Neuron 1 (N_1) in C-4nn.

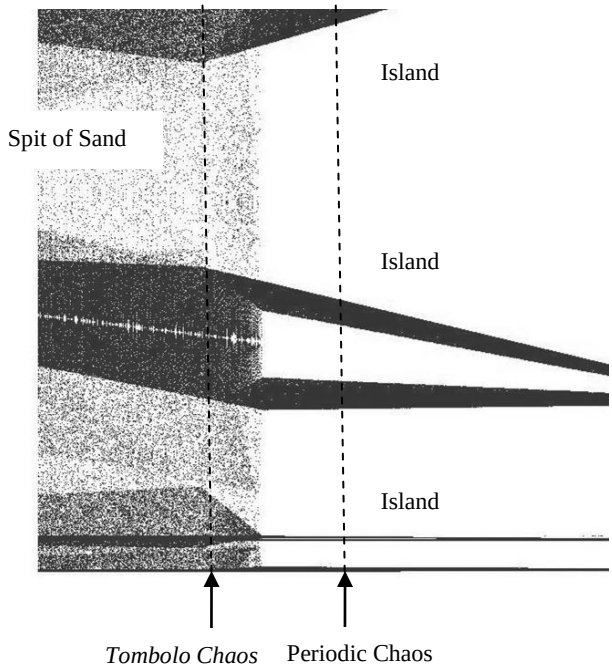

Fig. 4. Periodic Chaos and *Tombolo Chaos* (enlarged view of Fig.3).

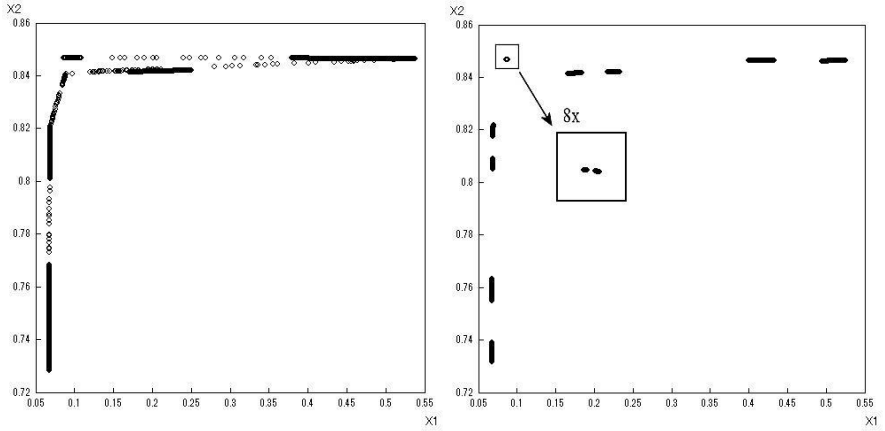

(a) *Tombolo Chaos* (I = 4.503566). (b) Periodic Chaos (I = 4.523918).

Fig. 5. Attractor of periodic chaos and *tombolo chaos.*

The boundary line between tombolo chaos and periodic chaos is about 4.52 in Fig.3 and Fig.4.

Region A in Fig.3 is not covered by this work, because region A may consist of not only *tombolo chaos* but also periodic windows which don't afford pseudo-random number series.

Attracter of C-4nn outputs is shown in Fig.5, 2500 outputs are plotted as circles. Fig.5b shows the attractor of periodic chaos (I = 4.523918) that consists of 10 islands enlarging the small islands into 8×. The chaos time series analysis affords the correlation dimension D_2 = 0.95 and the maximum Lyapunov exponent λ_{max} = 0.25. Fig.5a shows the attractor of *tombolo chaos* (I = 4.503566), and the chaos time series analysis affords the correlation dimension D_2 = 1.05 and the maximum Lyapunov exponent λ_{max} = 0.20.

Representative result on the examination of the proportion is summarized in Table 5. I is an external input of C-4nn, and I_{bn} represents the external input value corresponding to periodic chaos or *tombolo chaos*: I_{b5} = 4.155010, I_{b1} = 4.436959 and I_{b2} = 4.503566 for *tombolo chaos*, I_{b3} = 4.523918 and I_{b4} = 4.570233 for periodic chaos. The NIST recommended size of random numbers 10^9 bits (1000 sequences of 1000 kbits) is used for 1set of NIST tests. A 48-bit-pseudo-random-number sequence is generated for each iteration.

All results don't have the correlation of the pseudo-complexity (Pc) with the test fail rate on the examination of the proportion. It suggests that the obtained pseudo-complexity is above necessary condition (Pc > 26.5).

The result of NIST tests suggests that the property of chaos also affects randomness of the pseudo-random number series. The pseudo-random number series from periodic chaos and *tombolo chaos* don't always satisfy the permissible range of the test fail rate. The result suggests that both time series are not suitable for application

to a cipher system. Periodic chaos and *tombolo chaos* are visually detectable with the input-output characteristics.

Table 5. Result of NIST SP800-22 tests and the *pseudo-randomness* on C-4nn.

I	chaos type	N	Selected Test Fail Rate (%) [a)]								Pc	overall result
			RK	NT	OT	UN	AE	RE	SE	LC		
I_{b4}	periodic	2	0.0	0.3	4.0	0.0	0.0	0.1	0.0	1.0	32.1	
I_{b4}	periodic	3	0.0	0.3	2.0	7.0	0.0	0.6	0.0	0.0	32.1	
I_{b4}	periodic	1	0.0	0.4	0.0	0.0	0.0	0.4	0.0	0.0	32.1	pass
I_{b4}	periodic	4	0.0	0.7	0.0	0.0	0.0	0.4	0.0	0.0	32.1	
I_{b1}	tombolo	2	0.0	0.1	0.0	2.0	0.0	0.5	0.0	1.0	33.4	pass
I_{b1}	tombolo	3	0.0	0.1	0.0	2.0	0.0	0.3	0.0	0.0	33.4	pass
I_{b1}	tombolo	1	0.0	0.1	4.0	0.0	1.0	0.3	0.5	0.0	33.4	
I_{b1}	tombolo	4	1.0	0.2	0.0	0.0	0.0	0.3	0.0	0.0	33.4	pass
I_{b3}	periodic	2	0.0	0.2	0.0	0.0	0.0	0.3	0.5	0.0	33.5	pass
I_{b3}	periodic	3	0.0	0.3	0.0	2.0	0.0	0.4	0.5	0.0	33.5	pass
I_{b3}	periodic	1	0.0	0.2	2.0	1.0	0.0	0.4	0.0	0.0	33.5	pass
I_{b3}	periodic	4	0.0	0.1	0.0	3.0	0.0	0.4	0.0	1.0	33.5	
I_{b2}	tombolo	2	1.0	0.2	5.0	1.0	0.0	0.1	0.0	1.0	33.5	
I_{b2}	tombolo	3	0.0	0.1	1.0	0.0	0.0	0.6	0.5	0.0	33.5	pass
I_{b2}	tombolo	1	0.0	0.2	0.0	1.0	0.0	0.4	0.0	0.0	33.5	pass
I_{b2}	tombolo	4	1.0	0.1	0.0	0.0	0.0	0.3	0.0	0.0	33.5	pass
I_{b5}	tombolo	2	0.0	0.2	0.0	0.0	0.0	0.3	0.5	0.0	33.6	pass
I_{b5}	tombolo	3	0.0	0.1	1.0	2.0	0.0	0.5	0.0	0.0	33.6	pass
I_{b5}	tombolo	1	0.0	0.3	2.0	0.0	0.0	0.4	0.0	0.0	33.6	
I_{b5}	tombolo	4	0.0	0.3	1.0	0.0	0.0	0.3	0.0	0.0	33.6	pass

a) Result of the examination of proportion in the NIST tests. The test fail rate is averaged by repeated 100 times of the NIST tests.

6 Randomness of Periodic Chaos and Tombolo Chaos

Normal periodic chaos which originates from bifurcation consists of 2^n islands [2]. Periodic chaos consists of 10 ($\neq 2^n$) islands in this work, probably because it originates not only from bifurcation but also from a mix of chaotic time series. Periodic chaos is known to be ergodic but not *mixing* [16]. The ergodic property can be evaluated through UN test, because UN test is designed to be able to detect any one of the very

general class of statistical defects that can be modeled by an ergodic stationary source. There is no contradiction on ergodicity of chaotic maps.

Yet, periodic chaos sometimes shows the higher test fail rate of UN test and OT test, but not always high. Tombolo chaos also shows same tendency, but the fail rate of the test is lower than periodic chaos.

The ergodic property is probably theoretically true, but is it also empirically true? If the number of iterations isn't large enough, the outputs may be unevenly distributed even in the lower bits of the output.

7 Conclusion

The time series of the logistic map and the chaos neural network have been studied from an empirical view point. The pseudo-random number series have been extracted from the chaotic time series by our own method. The pseudo-complexity is proposed on the basis of the staying time of the transient orbit and the period of the chaotic orbit. The results of the NIST SP800-22 tests suggest that the pseudo-complexity may be useful as necessary conditions ($Pc > 26.5$) to pseudo-random numbers for cryptographic applications. The result also suggests that the negative correlation of the pseudo-complexity (Pc) with the fail rate of the non-overlapping template matching test (Table 4).

The pseudo-random number series have been studied as for periodic chaos and *tombolo chaos*. The result suggests that the pseudo-random number series from periodic chaos and *tombolo chaos* don't always satisfy the permissible range of the test fail rate, therefore both time series are not suitable for application to a cipher system. Periodic chaos and *tombolo chaos* are easily excluded in practical use, because they are visually detectable with the input-output characteristics.

The generality of the pseudo-complexity should be checked in the future work. The detail properties of *tombolo chaos* will be studied in future work, and the relation between ergodicity and periodic chaos has remained an unsolved problem.

Acknowledgement

Part of the experimental results in this research was obtained using supercomputing resources at Cyberscience Center, Tohoku University. This work was supported by KAKENHI Grant Numbers JP16K00180. Special thanks to Mr. Mitsuaki SASAKI and the stuff members of Iwate University Super-Computing and Information Sciences Center.

References

1. Yoshida, H., Yoneki, K., Tsunekawa, Y., Miura, M.: Chaos Neural Network. Proceedings of Papers, ISPACS'96, vol. l of 3, pp.16.1.1-5 (1996)
2. Yoshida, H., Nihei, Y., Nakanishi, T.: Comparative Study on Structurally Different Chaos Neural Networks. Proceedings of Papers, ISITA2004, pp.1046-1050 (2004)
3. Nihei, Y., Nakanishi, T., Yoshida, H.: Time Series Analysis for Chaos Neural Network. Technical Reports of IEICE, vol. 104, pp.7-10, (2004)
4. Murakami, T., Satoshi, K., Yoshida, H.: Prediction of Periods on Chaos Time Series: Dependence on Precision of Chaos Neural Network Outputs. Technical Reports of IEICE, vol. 107, pp.21-26, (2008)
5. Komori, T., Yi, H., Nakanishi, T., Murakami, T., Yoshida, H.: Behavior Analysis of Chaos Neural Network with Simplification of Nonlinear Function. Technical Reports of IEICE, vol. 109, pp.53-58, (2009)
6. Yoshida, H., Murakami, T., Inao, T., Kawamura, S.: Origin of Randomness on Chaos Neural Network, Trends in Applied Knowledge-Based Systems and Data Science. vol.9799, pp.587-598, (2016)
7. Yoshida, H., Sasaki, M., Murakami, T., Kawamura S.: Study on Properties of Periodic Chaos and Controlling Method of Islands in Chaos Neural Network Outputs, Proceedings of The 34th JSTE Tohoku Section Conference, pp.59-60, (2016)
8. Yoshida, H., Murakami, T., Liu, Z.: High-Speed and Highly Secure Pseudo-Random Number Generator based on Chaos Neural Network. Proceedings of Papers, ICSSE 2015, pp.224-237 (2015)
9. Yoshida, H., Murakami, T.: Japan patent JP5504501B (2014)
10. Yoshida, H., Murakami, T., Kawamura, S.: Study on Testing for Randomness of Pseudo-Random Number Sequence with NIST SP800-22 rev. la. Technical Reports of IEICE, 110 , pp.13-18 (2012)
11. Rukhin, A., Soto, J., Nechvatal, J., Smid, M., Barker, E., Leigh, S., Levenson, M., Vangel, M., Banks, D., Heckert, A., Dray, J., Vo, S.: A Statistical Test Suite for Random and Pseudorandom Number Generators for Cryptographic Applications, NIST SP800-22 rev.1a, Revised: july 2015 (sts-2.1.1). Lawrence E. Bassham III (2015)
12. Coron, J.-S., Naccache, D.: An Accurate Evaluation of Maurer's Universal Test. Proceedings of SAC '98, Berlin: Springer-Verlag Lecture Notes in Computer Science, No.1556, pp.57-71 (1998)
13. Kawamura, S., Yoshida, H., Miura, M., Abe, M.: Implementation of Uniform Pseudo Random Number Generator and Application to Stream Cipher based on Chaos Neural Network. Proceedings of Papers, ICFS2002, R-18, pp.4-9 (2002)
14. May, R.: Simple mathematical models with very complicated dynamics, Nature, vol.261, pp.459-467, (1976)
15. Kolmogorov, A.: On Tables of Random Numbers. Sankhyā Ser. A. 25, pp.369-375, (1963).
16. Thompson, J.M., Stewart, H.B.: Nonlinear dynamics and chaos: geometrical methods for engineers and scientists, Wiley, (1986)

Exploring a century of Savoy history using hidden-Markov models with Beta-inflated distributions

Julien Alerini[1] and Madalina Olteanu[2]

[1] IHMC-PIREH, UMR 8589, Université Paris 1 Panthéon-Sorbonne, France
julien.alerini@univ-paris1.fr
[2] SAMM, EA 4543, Université Paris 1 Panthéon-Sorbonne, France
madalina.olteanu@univ-paris1.fr

Abstract. This manuscript aims at illustrating the interest of hidden Markov models mixing zero Beta-inflated distributions or one Beta-inflated distributions for studying specific time series, involving continuous proportions in the interval $[0, 1]$. More specifically, we are interested in segmenting a time series of historical data stemming from the XVIth and the XVIIth centuries, in order to bring to light the behavior of the Savoy Duchy and the transitions which marked deep political changes in the State functioning.

1 Introduction

Studying time series of continuous proportions or continuous ratios is of interest in various fields of research such as economy, biology or history. But this data may often have some specific features which make traditional time series or regression models unfitted. One such common feature is an excess mass of zeros and/or ones, combined with a behavior subject to changes in regime.

For regime switches, models based on hidden Markov models, [1], [2], were long proved to be a good option for exploring and explaining data. For the excess zeros and/or ones, one solution consists in using "inflated" distributions and, more specifically for proportions, Beta-inflated distributions, [3], [4].

The starting point of the present manuscript and of the interest in hidden Markov models with inflated Beta distributions lies in the study of a bivariate time series of historical data, related to the legislative activity of the Duchy of Savoy during the XVIth and the XVIIth centuries. The historian wished to know whether there was a synchrony between the periods of conflict experienced by the State and an intense legislative output or, on the contrary, whether the two were not completely correlated.

In our first work on this data [5], the time series containing the counts of legislative texts related to military logistics only was considered. The results were very promising and showed, according to the fitted model, various temporalities of the State, one of which enhanced the link between the diplomatic situation and the military preparedness, although it dispelled their synchrony.

The next step of our study was to include in the analysis a second series containing the entire legislative output and focus on the ratio between the documents on military logistics and the whole legislation. In this case, the data is no longer a time series of counts with excess zeros, but of continuous proportions with excess zeros and ones. For this specific data, we proposed a hidden Markov model with zero-and-one Beta inflated distributions [6]. Although the results were mainly consistent with our previous findings, they were less convincing in terms of persistency of the states. One reason for this could be the fact of having considered inflated distributions both in zero and in one. In the present manuscript, we propose a restriction of the model to zero **or** one Beta inflated distributions. As it will be shown later, the scale or the time-step used for exploring the data is crucial for the analysis, hence, according to it and according to the composition of the time series, different models will be trained.

In the next section we recall the definitions and notations for the zero or one Beta inflated distributions, and next we introduce the hidden-Markov models that will be used hereafter. Some simulated examples illustrate the empirical convergence of the EM algorithm. Section 3 contains an analysis of the historical data and a conclusion follows in Section 4.

2 Zero-or-one Beta-inflated hidden Markov models

Two distinct HMM models will be used in this manuscript: on the one hand, we shall introduce a two-state model mixing a zero-inflated distribution with a one-inflated one. On the other hand, we shall use a hidden Markov model with zero Beta-inflated distributions only. The latter is not new in the literature and has been already studied in the recent paper [7]. For this reason, we shall describe the entire estimation procedure for the first model, together with some simulated examples, and only recall the formulae of the estimated updates for the second. The estimation procedure is very similar to that of the previously introduced ZOIB-HMM model [6].

2.1 Zero or one Beta-inflated distributions

Before introducing the hidden-Markov model, let us briefly recall the zero or one Beta-inflated distributions. Transforming a regular Beta distribution into an inflated one is achieved by mixing it with a Dirac mass either in 0, or in 1, such that support of the density is either $[0, 1[$, or $]0, 1]$. For a complete review on Beta inflated distributions, the reader may refer to [8].

Let us recall that if $X \sim \mathcal{B}(\alpha, \beta)$ is a random variable Beta-distributed, with $\alpha, \beta > 0$ and probability density $f_B(\bullet; \alpha, \beta)$, and with the notations $\mu = \frac{\alpha}{\alpha+\beta}$, $\phi = \alpha + \beta$, the expectation and the variance of X may be expressed as :

$$\mathbb{E}(X) = \mu \ ; \ \mathbb{V}(X) = \frac{\mu(1-\mu)}{\phi+1}. \tag{1}$$

Besides its support reduced to the interval $]0, 1[$, the interest of using a Beta distribution for statistical modeling also resides in the large variety of shapes

for its density, which makes it quite appealing for applications. The zero Beta-inflated distribution may then be defined as a mixture between a regular $\mathcal{B}(\alpha, \beta)$ distribution and a Dirac mass in 0, such as its density writes

$$f_0(x; \eta, \alpha, \beta) = \eta^{\mathbb{1}_{x=0}}((1-\eta) f_B(x; \alpha, \beta))^{\mathbb{1}_{x\in]0,1[}}, \tag{2}$$

while the one Beta-inflated distribution may be expressed in a similar manner, but using a Dirac mass in 1:

$$f_1(x; \eta, \alpha, \beta) = \eta^{\mathbb{1}_{x=1}}((1-\eta) f_B(x; \alpha, \beta))^{\mathbb{1}_{x\in]0,1[}}. \tag{3}$$

Here, η is the parameter of the mixture and α, β are the parameters of the Beta distribution. Throughout the rest of the paper, let $\xi = (\eta, \alpha, \beta)$ be the three-dimensional parameter of a Beta-inflated distribution.

2.2 Estimation procedure for the zero or one Beta-inflated hidden-Markov model

Let us now describe the hidden-Markov models having zero or one-inflated Beta distributions as emission probability distributions. Consider $(X_t)_{t\in\mathbb{Z}}$ the observed time series, valued in $[0, 1]$, and $(S_t)_{t\in\mathbb{N}}$ the unobserved process, controlling the parameters of the distribution of X_t. Throughout the rest of the paper, S_t is supposed to be a homogeneous Markov chain, irreducible, recurrent and aperiodic, with two possible states $E = \{e_1, e_2\}$ and defined by its transition matrix $\Pi = (\pi_{ij})_{i,j=1,2}$, $\pi_{ij} = \mathbb{P}(S_t = e_j | S_{t-1} = e_i)$, with $\pi_{ij} > 0$, $\sum_{j=1}^{2} \pi_{ij} = 1$, and by its initial probability distribution π^0, $\pi_i^0 = \mathbb{P}(S_1 = e_i)$, $\forall i = 1, 2$.
Furthermore, let us suppose that X_t are independent conditionally to S_t, and that X_t conditionally to $S_t = e_1$ is distributed according to a zero Beta-inflated distribution, while X_t conditionally to $S_t = e_2$ is distributed according to a one Beta-inflated distribution. With the notation $\xi_i = (\eta_i, \alpha_i, \beta_i) \in]0, 1[\times]0, +\infty[^2$, the set of possible values for the parameters is

$$\Theta = \left\{ \theta = ((\xi_i)_{i=1,2}, \Pi) \in (]0, 1[\times]0, +\infty[^2)^2 \times]0, 1[^4, \forall i \in \{1, 2\}, \sum_{j=1}^{2} \pi_{ij} = 1 \right\} \tag{4}$$

The usual procedure for training hidden Markov models, the EM algorithm [1], [9], is used here, with a slight modification for the updates of the parameters in the Beta distribution. With the previous assumptions, and with the notations $X_1^T = (X_1, ..., X_T)$, $S_1^T = (S_1, ..., S_T)$, the complete likelihood is given by:

$$\mathcal{L}(X_1^T, S_1^T; \theta) = \prod_{t=1}^{T} \prod_{i=1}^{2} f(X_t | S_t = e_i; \xi_i)^{\mathbb{1}_{\{S_t = e_i\}}} \prod_{t=2}^{T} \prod_{i,j=1}^{2} \pi_{ij}^{\mathbb{1}_{\{S_{t-1}=e_i, S_t=e_j\}}} \times C \ , \tag{5}$$

where $f(X_t | S_t = e_1; \xi_1)$ is the zero Beta-inflated density, defined in Equation 2, $f(X_t | S_t = e_2; \xi_2)$ is the one Beta-inflated density, defined in Equation 3, and $C = \prod_{i=1}^{2} \left(\pi_i^0\right)^{\mathbb{1}_{\{S_t=e_i\}}}$ is the likelihood of the initial state of the Markov chain.

When replacing the Beta-inflated densities by their analytical expressions, the complete likelihood may further be written as:

$$\mathcal{L}(X_1^T, S_1^T; \theta) = \prod_{t=1}^{T} \Big[\eta_1^{\mathbb{1}_{\{X_t=0, S_t=e_1\}}} (1-\eta_1)^{\mathbb{1}_{\{X_t\in]0,1[, S_t=e_1\}}} \eta_2^{\mathbb{1}_{\{X_t=1, S_t=e_2\}}} \times (1-\eta_2)^{\mathbb{1}_{\{X_t\in]0,1[, S_t=e_2\}}} \Big] \times \prod_{t=1}^{T}\prod_{i=1}^{2} \left(f_B\left(X_t, \alpha_i, \beta_i\right)\right)^{\mathbb{1}_{\{X_t\in]0,1[, S_t=e_i\}}} \times \prod_{t=2}^{T}\prod_{i,j=1}^{2} \pi_{ij}^{\mathbb{1}_{\{S_{t-1}=e_i, S_t=e_j\}}} \times C$$
$$= \mathcal{L}_1(X_1^T, S_1^T; \boldsymbol{\eta}) \mathcal{L}_2(X_1^T, S_1^T; \boldsymbol{\alpha}, \boldsymbol{\beta}) \mathcal{L}_3(X_1^T, S_1^T; \Pi), \quad (6)$$

where $\boldsymbol{\eta} = (\eta_1, \eta_2)$, $\boldsymbol{\alpha} = (\alpha_1, \alpha_2)$ and $\boldsymbol{\beta} = (\beta_1, \beta_2)$. The EM algorithm consists in iteratively maximizing the expected value of the complete likelihood $\mathcal{L}(X_1^T, S_1^T; \theta)$ with respect to θ, and conditionally to the observed data set X_1^T and a fixed value of the parameter $\theta^\star$, and then updating $\theta^\star$ at each step.

E-Step. The E-step is given by the computation of the expected value of the complete likelihood, conditionally to the observed data,

$$Q(\theta|\theta^\star) = \mathbb{E}_{\theta^\star}\left[\ln \mathcal{L}(X_1^T, S_1^T; \theta) | X_1^T\right]. \quad (7)$$

According to Equation 6, $Q(\theta|\theta^\star)$ can be split into :

$$Q(\theta|\theta^\star) = Q_1(\boldsymbol{\eta}|\theta^\star) + Q_2(\boldsymbol{\alpha}, \boldsymbol{\beta}|\theta^\star) + Q_3(\Pi|\theta^\star)\ , \quad (8)$$

where

$$Q_1(\boldsymbol{\eta}|\theta^\star) = \mathbb{E}_{\theta^\star}\left[\ln \mathcal{L}_1(X_1^T, S_1^T; \boldsymbol{\eta}) | X_1^T\right]$$
$$= \sum_{i=1}^{2} \sum_{X_t\in]0,1[} \omega_t(e_i) \ln(1-\eta_i) + \sum_{X_t=0} \omega_t(e_1) \ln \eta_1 + \sum_{X_t=1} \omega_t(e_2) \ln \eta_2\ , \quad (9)$$

with $\omega_t(e_i) = \mathbb{P}_{\theta^\star}(S_t = e_i | X_1^T)$;

$$Q_2(\boldsymbol{\alpha}, \boldsymbol{\beta}|\theta^\star) = \mathbb{E}_{\theta^\star}\left[\ln \mathcal{L}_2(X_1^T, S_1^T; \boldsymbol{\alpha}, \boldsymbol{\beta}) | X_1^T\right]$$
$$= \sum_{i=1}^{2} \sum_{X_t\in]0,1[} \omega_t(e_i) \ln\left(f_B\left(X_t, \alpha_i, \beta_i\right)\right); \quad (10)$$

$$Q_3(\Pi|\theta^\star) = \mathbb{E}_{\theta^\star}\left[\ln \mathcal{L}_3(X_1^T, S_1^T; \Pi) | X_1^T\right] = \sum_{i,j=1}^{2} \sum_{t=2}^{T} \omega_t(e_i, e_j) \ln \pi_{ij}\ , \quad (11)$$

with $\omega_t(e_i, e_j) = \mathbb{P}_{\theta^\star}(S_{t-1} = e_i, S_t = e_j | X_1^T)$. The probabilities $\omega_t(e_i)$ and $\omega_t(e_i, e_j)$ may be easily computed using the forward-backward procedure,

typical for the EM algorithm [10].

M-Step. The three terms of $Q(\theta|\theta^\star)$ may be independently maximized in each of the parameters, $\boldsymbol{\eta}$ for Q_1, $\boldsymbol{\alpha}$ and $\boldsymbol{\beta}$ for Q_2 and, respectively, $\mathit{\Pi}$ for Q_3. For η_i and π_{ij}, the analytical expressions of the updates may be straightforwardly computed:

$$\hat{\eta}_1 = \frac{\sum_{X_t=0} \omega_t(e_1)}{\sum_{X_t\in[0,1[} \omega_t(e_1)} \ , \ \hat{\eta}_2 = \frac{\sum_{X_t=1} \omega_t(e_2)}{\sum_{X_t\in]0,1]} \omega_t(e_2)} \ ,$$
$$\text{and } \hat{\pi}_{ij} = \frac{\sum_{t=2}^{T} \omega_t(e_i, e_j)}{\sum_{t=1}^{T} \omega_t(e_i)} \ . \tag{12}$$

Regarding α_i and β_i, there are no analytical expressions of the estimates, directly tractable from $Q_2(\boldsymbol{\alpha}, \boldsymbol{\beta}|\theta^\star)$. Rather than numerically optimizing this function and slowing down the algorithm which would also probably become numerically unstable, we prefer the use of moment estimates, which appear as good substitues for the MLE:

$$\tilde{\alpha}_i = \tilde{\mu}_i\tilde{\phi}_i \ , \ \tilde{\beta}_i = (1-\tilde{\mu}_i)\tilde{\phi}_i, \tag{13}$$

where

$$\tilde{\mu}_i = \frac{\sum_{X_t\in]0,1[} \omega_t(e_i)X_t}{\sum_{X_t\in]0,1[} \omega_t(e_i)} \ , \ \tilde{\phi}_i = \frac{\tilde{\mu}_i(1-\tilde{\mu}_i)}{s_i^2} - 1,$$
$$s_i^2 = \frac{\sum_{X_t\in]0,1[} \omega_t(e_i)\left(X_t - \tilde{\mu}_i\right)^2}{\sum_{X_t\in]0,1[} \omega_t(e_i)}. \tag{14}$$

Experimental results For each of the following scenarios and for sample sizes ranging from 500 to 5 000, 100 trajectories of the model were simulated. The values of the parameters used for the simulations are the following:

$$\mathit{\Pi} = \begin{pmatrix} 0.9 & 0.1 \\ 0.1 & 0.9 \end{pmatrix} \ , \ (\alpha_1, \alpha_2) = (1; 0.5) \ , \ (\beta_1, \beta_2) = (1; 2) \ ,$$

$\eta_1 \in \{0.5, 0.7\}$ and $\eta_2 = 0.5$. The results are detailed in Tables 1 and 2 below. In each case are reported the mean values of the estimates, as well as their standard errors and medians. We also provide the ratio of errors in the a posteriori identification of the hidden regimes (mean-values, standard errors and medians). The parameters are generally correctly estimated, even for short time series. The fact of having replaced the maximum likelihood estimates with moment estimates for the α_i's and β_i's does not affect the quality of the estimation procedure and the convergence of the algorithm.

2.3 Some remarks on zero Beta-inflated hidden-Markov models

As mentioned previously, zero Beta-inflated hidden-Markov models were already introduced in the literature a couple of years ago [7]. They are of particular

	$T = 500$		$T = 1000$		$T = 5000$	
$\hat{\Pi}$	0.87(*0.10*)	0.13(*0.10*)	0.87(*0.09*)	0.13(*0.09*)	0.87(*0.09*)	0.13(*0.09*)
	0.90	**0.10**	**0.90**	**0.10**	**0.90**	**0.10**
	0.13(*0.09*)	0.87(*0.09*)	0.12(*0.07*)	0.88(*0.07*)	0.13(*0.11*)	0.87(*0.11*)
	0.11	**0.89**	**0.10**	**0.90**	**0.10**	**0.90**
$\hat{\eta}_1, \hat{\eta}_2$	0.53(*0.11*)	0.50(*0.10*)	0.52(*0.08*)	0.50(*0.06*)	0.51 (*0.11*)	0.52(*0.11*)
	0.51	**0.50**	**0.50**	**0.50**	**0.50**	**0.50**
$\hat{\alpha}_1, \hat{\alpha}_2$	1.00(*0.19*)	0.52(*0.13*)	0.98(*0.17*)	0.52(*0.10*)	0.95(*0.17*)	0.51(*0.07*)
	1.00	**0.51**	**0.99**	**0.52**	**1.00**	**0.50**
$\hat{\beta}_1, \hat{\beta}_2$	1.03(*0.16*)	1.91(*0.50*)	1.01(*0.15*)	1.99(*0.38*)	0.98(*0.11*)	1.92(*0.28*)
	1.04	**1.90**	**1.00**	**1.99**	**1.00**	**2.00**
$\%ERR$	6.72(*6.82*)		5.97(*5.73*)		6.59(*6.43*)	
	4.40		**4.40**		**4.31**	

Table 1. Simulation results for $\eta_1 = 0.5$, $\eta_2 = 0.5$ and 100 time-series of length T. Mean, standard error (italics) and median (bold) of the estimates.

	$T = 500$		$T = 1000$		$T = 5000$	
$\hat{\Pi}$	0.88(*0.06*)	0.12(*0.06*)	0.89(*0.03*)	0.11(*0.03*)	0.89(*0.03*)	0.11(*0.03*)
	0.90	**0.10**	**0.90**	**0.10**	**0.90**	**0.10**
	0.12(*0.08*)	0.88(*0.08*)	0.12(*0.08*)	0.88(*0.08*)	0.14(*0.12*)	0.86(*0.12*)
	0.11	**0.89**	**0.10**	**0.90**	**0.10**	**0.90**
$\hat{\eta}_1, \hat{\eta}_2$	0.70(*0.08*)	0.51(*0.09*)	0.69(*0.06*)	0.52(*0.09*)	0.68 (*0.07*)	0.55(*0.14*)
	0.70	**0.50**	**0.70**	**0.51**	**0.70**	**0.50**
$\hat{\alpha}_1, \hat{\alpha}_2$	1.04(*0.24*)	0.52(*0.10*)	1.04(*0.20*)	0.50(*0.06*)	0.96(*0.17*)	0.51(*0.10*)
	1.00	**0.51**	**1.01**	**0.50**	**0.99**	**0.50**
$\hat{\beta}_1, \hat{\beta}_2$	1.03(*0.19*)	2.06(*0.50*)	1.06(*0.17*)	1.99(*0.33*)	1.02(*0.08*)	2.00(*0.34*)
	1.02	**1.99**	**1.05**	**1.97**	**1.02**	**2.00**
$\%ERR$	4.58(*4.82*)		4.14(*4.88*)		5.16(*5.70*)	
	3.40		**2.95**		**2.96**	

Table 2. Simulation results for $\eta_1 = 0.7$, $\eta_2 = 0.5$ and 100 time-series of length T. Mean, standard error (italics) and median (bold) of the estimates.

interest for time series of proportions with excess zeros and (almost) no ones. In this case, the emission probability distribution in each state of the Markov chain is a zero-inflated Beta distribution. This can be written similarly to Section 2.2 and the updates for the estimates are identical to those in Equations 12, 13 and 14, except for the mixture parameters which become:

$$\hat{\eta}_i = \frac{\sum_{X_t=0} \omega_t(e_i)}{\sum_{X_t \in [0,1[} \omega_t(e_i)} \ , \ i = 1, 2.$$

3 Segmenting a century of historical data

In order to attempt to bring some answers to the historian questioning on the temporality of the Savoy State and on the synchrony between the diplomatic

situation and the legislative activity of the Duchy, we used a bivariate time series stemming from the XVIth and the XVIIth centuries. The corpus comes from the massive work of F-A. Duboin [11]. The opus was aimed at the restauration of the Sabaudian law, following the Napoleonic age, and contains all documents stored in the Piedmontese institutions. According to [12], the edition would be exhaustive and few texts would be missing. The historian resumed the corpus of data in a bivariate monthly representation, one component storing the whole number of legislative texts issued during each month, and the other the number of texts linked to military logistics. [3]

As mentioned in the introduction, our first work considered the series of texts related to military logistics [5] only. The results were very promising, since they allowed to highlight two temporalities of the State, one of them more related to the diplomatic situation and the military preparedness, and the other to the inner structure of the State. These historical insights were close to the Braudelian architecture of time, and, furthermore, they allowed to understand the path from the event to the trend.

Naturally, the next step of our work was then to use the bivariate data and more specifically the ratio between the two series, which gives the importance of military logistics in the legislative activity. We wanted to investigate the legislative behavior of the State and the variations of the importance of military logistics. Two levels of representations were finally studied: a monthly series of ratios and an aggregate quarterly series of ratios. More than a half of the monthly series (illustrated in Figure 1) elements are equal to zero, while the mean value is 0.09 and the standard deviation is 0.17. The quarterly series (illustrated in Figure 2) contains less zeros and is more homogeneous, with a median equal to 0.07, a mean value equal to 0.09 and a standard deviation of 0.10. The two series, and more particularly the quarterly one, appear to change their behavior during the second half, which contains less zeros and also less spikes, and during which the activity of the State seems to be more regular. This hypothesis is to be confirmed by the hidden-Markov models.

3.1 A zero-or-one Beta-inflated HMM for monthly data

The monthly series of the ratios has already been investigated in a previous work [6], using a zero-and-one Beta-inflated hidden Markov model. Although the results were globally consistent with our previous findings, the transition matrix showed that regimes were not very persistent and the numerous switches from one state to the other made the interpretation of the results difficult to achieve.

Since one of the hypothesis supporting the hidden Markov chain approach is the possible existence of two regimes, a "sparse" one in terms of legislative

[3] In the first version of this proposal, which was submitted as an extended abstract, we also mentioned an illustration of the proposed models on another time series, related to the proportion of rainy days recorded by a weather station in the Netherlands. Due to the limited number of pages, these results will not be presented here, but they are available upon request.

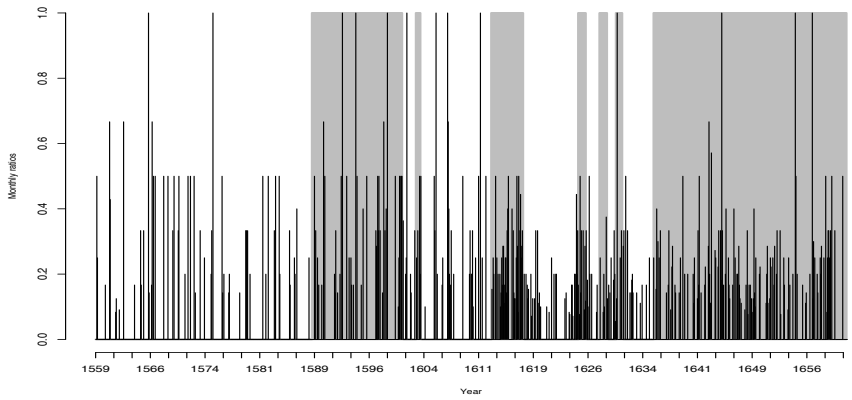

Fig. 1. Ratio of texts on military logistics among the entire production of law (monthly representation). The periods of war for the Duchy are in grey.

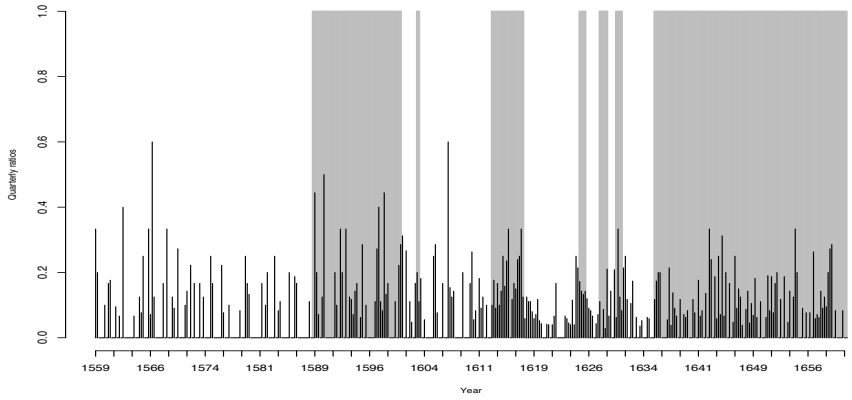

Fig. 2. Ratio of texts on military logistics among the entire production of law (quarterly representation). The periods of war for the Duchy are in grey.

activity, with plenty of zeros, and a more intense one, with a maximum value of one reached by the ratios, we trained the more constrained model proposed in Section 2.2. The parameters estimated for the monthly data are:

$$\hat{\Pi} = \begin{pmatrix} 0.79 & 0.21 \\ 0.62 & 0.38 \end{pmatrix} \ , \ (\hat{\alpha}_1, \hat{\alpha}_2) = (25.19; 4.36) \ , \ (\hat{\beta}_1, \hat{\beta}_2) = (24.49; 15.96),$$

and $(\hat{\eta}_1, \hat{\eta}_2) = (0.94, 0.04)$, with a BIC equal to 1191.05. The estimated Beta components of the distributions are illustrated in Figure 3. According to these results, one may easily notice that the first regime is essentially containing zeros, more than 90% in average, and that the Beta component is having a probability mass concentrated around large values of the ratios (between 0.4 and 0.7), while the second regime captures the maximum values of the ratios (4% of ones in average), whereas, at the same time, the probability mass of the Beta distribution is more related to the smaller values of the ratios (between 0 and 0.4).

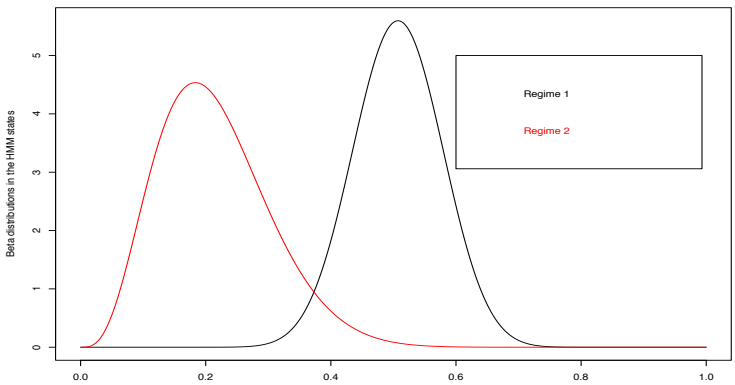

Fig. 3. Beta components in the emission distributions for the zero-or-one inflated HMM model (monthly data)

The a posteriori probabilities of the series being in the second state of the Markov chain were computed using the Viterbi filter and are represented in Figure 4. As it may be seen, the shifts from one regime to the other occur very often, and the two regimes are not at all persistent, although the second regime seems to be more present in the second half of the series. The results are similar to the ones found in [6], but they do not improve them. One of the reasons for this may be linked to the empirical observation above: during almost half of the period, the data contains plenty of zeros and some spikes, the State is generally not legislating and when it does it produces a lot of texts, while during the second half, the activity appears as more regular with less zeros and less spikes. The zero-or-one Beta-inflated or the zero-and-one Beta-inflated HMM models do not seem able to capture this, as least not at a monthly level.

3.2 A zero Beta-inflated HMM for quarterly data

For the quarterly data, the maximum value of the series is 0.6, which means that one-inflated Beta distributions are not fitted. Instead, we shall train a two-state

Fig. 4. Conditional a posteriori probabilities of the second regime - monthly data

hidden-Markov model with zero Beta-inflated distributions in each state. The estimated parameters are

$$\hat{\Pi} = \begin{pmatrix} 0.99 & 0.01 \\ 0.00 & 1.00 \end{pmatrix} \ , \ (\hat{\alpha}_1, \hat{\alpha}_2) = (2.04; 2.47) \ , \ (\hat{\beta}_1, \hat{\beta}_2) = (8.83; 16.72),$$

and $(\hat{\eta}_1, \hat{\eta}_2) = (0.54, 0.26)$. The BIC criterion is equal to 12.01 for this configuration. The corresponding estimated Beta components of the mixed distributions in each state are illustrated in Figure 5. According to the estimated parameters and the graphs in Figure 5, the two regimes are very persistent, the second one being moreover absorbing. The first regime contains a high proportion of zeros, but also a higher probability mass on the large values, while the second regime has a lower proportion of zeros and the probability mass of the Beta component is more concentrated around the smaller values. This appears more consistent with the empirical observations on the time series.

In Figure 6, the probabilities of the time series being in the first regime of the Markov chain are illustrated, after having been computed with the Viterbi filter. The time series switches from one state to the other once only, and the transition lasts about ten years. As anticipated and according to the estimated parameters, the first regime contains more zeros and more spikes, while the second is more regular. Hence, the State appears to have changed its behavior with respect to issuing legislation and also with respect to the importance of military logistics. From the historian perspective, this model brings out a transition from a system yet medieval to a modern State. The transition occurs right before the first War of Monferrat, which started in April 1613 and ended in October 1617. The beginning of the war corresponds to the beginning of the second regime. These results are very consistent with our previous findings in [5], although the transition appears to be shifted in time with about twenty years. The historical

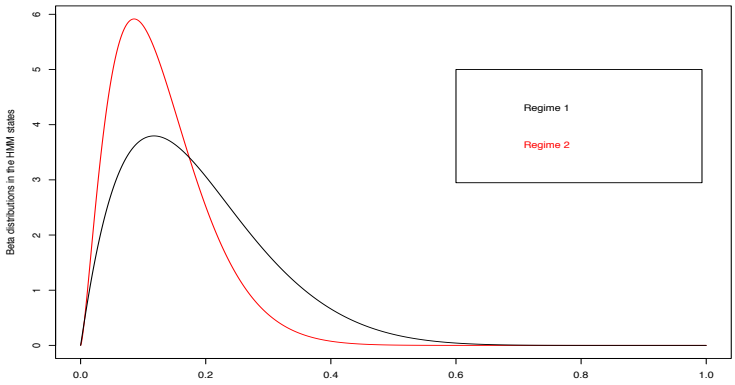

Fig. 5. Beta components in the emission distributions for the zero-inflated HMM model (quarterly data)

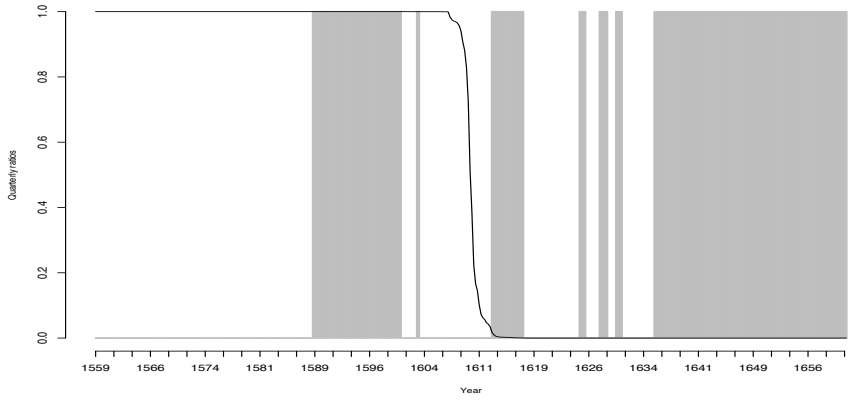

Fig. 6. Conditional a posteriori probabilities of the first regime - quarterly data

reasons and the detailed interpretation of these results are yet beyond the scope of the present manuscript, which is moreover limited in the number of pages, and will not be presented here.

4 Conclusion

Several hidden-Markov models with Beta-inflated distributions in zero or in one were trained on a historical time series of ratios. The performances of the models

were quite uneven, and the difference came mainly from the scale chosen for representing the data. While all models we used for the monthly data appear to fail in capturing the series behavior, the results obtained with quarterly data are very promising, and consistent both with the empirical observations on the data set and with our previous findings [5]. The "zoom level" was crucial here for tracking interesting features from the data. We aim at further investigating this issue during the next months, and also testing change-point detection strategies for the monthly data, although the transitions one may derive from hidden-Markov models were more appealing to the historian in the first instance.

References

1. Baum, L., Petrie, T.: Statistical inference for probabilistic functions of finite state markov chains. The Annals of Mathematical Statistics **37**(6) (1966) 1554–1563
2. Hamilton, J.D.: A new approach to the economic analysis of nonstationary time series and the business cycle. Econometrica **57**(2) (1989) 357–384
3. Simas, A.B., Barreto-Souza, W., Rocha, A.V.: Improved estimators for a general class of beta regression models. Computational Statistics & Data Analysis **54**(2) (2010) 348 – 366
4. Ospina, R., Ferrari, S.L.: A general class of zero-or-one inflated beta regression models. Computational Statistics & Data Analysis **56**(6) (2012) 1609 – 1623
5. Alerini, J., Olteanu, M., Ridgway, J.: Markov and the Duchy of Savoy: segmenting a century with regime-switching models. Journal de la SFdS **158**(2) (2017) 89–117
6. Alerini, J., Cottrell, M., Olteanu, M.: Hidden-markov models for time series of continuous proportions with excess zeros. In: Advances in Computational Intelligence, IWANN 2017, Cadiz, Spain, June 14-16, 2017, Proceedings, Part II. (2017) 198–209
7. Sun, L.: Statistical methods for serially correlated zero-inflated proportions. PhD thesis, Oregon State University (2014)
8. Ospina, R., Ferrari, S.L.P.: Inflated beta distributions. Statistical Papers **51**(1) (2008) 111
9. Dempster, A., Laird, N., Rubin, D.: Maximum likelihood from incomplete data via the em algorithm. Journal of the Royal Statistical Society (B) **39**(1) (1977) 1–38
10. Rabiner, L.R.: A tutorial on hidden markov models and selected applications in speech recognition. Proceedings of the IEEE **77**(2) (Feb 1989) 257–286
11. Duboin, F.A.: Raccoolta per ordine di materie delle leggi cio editti, manifesti, ecc., pubblicati negli stati della Real Casa di Savoia fino all'8 dicembre 1798, Torino (1818-1869)
12. Couzin, T.: Contribution piémontaise à la genèse de l'État italien. L'historicité de la Raccolta per ordine di materie delle leggi (1818-1868). Bolettino Storico-Bibliografico Subalpino **CVI** (2008) 101–120

Comparing Three Time Series Segmentation Methods via Novel Evaluation Criteria

Huynh Thi Thu Thuy[1,2] , Vo Thi Ngoc Chau[3], Duong Tuan Anh[3]

[1] Center for Applied Information Technology, Ton Duc Thang University, Ho Chi Minh City, Vietnam
[2] Faculty of Information Technology, Ton Duc Thang University, Ho Chi Minh City, Vietnam
huynhthithuthuy@tdt.edu.vn
[3] Faculty of Computer Science and Engineering, Ho Chi Minh City University of Technology, Ho Chi Minh City, Vietnam
{dtanh, chauvtn}@cse.hcmut.edu.vn

Abstract. Time series segmentation is a basic task in time series data mining. Time series segmentation is a pre-requisite step for many tasks, such as dimension reduction, representation, classification, clustering, prediction, motif discovery and anomaly detection in time series. Since there have been several segmentation techniques, it is difficult to select a suitable one for a specific application if we do not know how to evaluate the performance of various segmentation methods. This paper focuses on comparing the quality of three well-known segmentation methods: Important Extreme Points, Perceptually Important Points and Polynomial Least Square Approximation by using some existing evaluation criteria for time series segmentation. However, the existing evaluation criteria required prior knowledge about the time series and their segments as external information in their measures. Therefore, we propose one more evaluation criterion for segmentation. Experimental results show that the set of novel evaluation criteria can help to quantify a segmentation result and the quality of each of the three segmentation methods depends on the characteristics of each tested dataset.

Keywords: time series segmentation; important extreme points; perceptually important points; polynomial least square approximation; evaluation criteria

1 Introduction

Time series segmentation is an important task in time series data mining ([10]). In general, time series can consist of hundreds or thousands of observations. The main goal of segmentation is the extraction of time segments with similar observations or different from the rest of the time period. By that way, time series is divided into a small number of homogeneous pieces. In order to perform advanced tasks such as classification, clustering, anomaly detection, motif discovery or forecasting, in time series, segmentation is often a pre-requisite step.

Depending on various applications, segmentation methods can be divided into two categories. The first category is segmentation for time series reconstruction and representation purposes. The algorithms in this category evaluate the approximation error in some form and aim to represent a time series by sequence of linear approximations. The excellent review on this kind of time series segmentation was given by Keogh in 2001 [9]. The approximation of original time series in the form of straight lines is the essence of Piecewise Linear Representation (PLR). The three most common segmentation algorithms, based on the PLR are as follows: Top-down,

Bottom-Up and Sliding Window algorithm [9]. The second category contains algorithms performing time series segmentation based on changes in the characteristics of the time series in a certain way. Some well-known segmentation methods in this category include Important Extreme Points by Fink and Gandhi in 2007 [2], Perceptually Important Points (PIP) by Fu et al. in 2006 [3], and the Polynomial Least-Squares Approximations method by Fuchs et al. in 2010 [5]. The Important Extrema Points method by Fink and Gandhi aims to identify important extrema (maxima and minima) in time series data. The PIP method by Fu et al. searches for the important points in financial time series. The Polynomial Least-Squares Approximations method by Fuchs et. al. aims to identify turning points by using the orthogonal polynomials. Besides, these methods have a characteristic in common such that they are interested in the time point where a state is turned. For the Important Extrema Points method, maxima point marks the status from increase to decrease and minimum point marks the status from decrease to increase. For The PIP method, PIP points are also similar to maximum or minimum points. Turning points in the Polynomial Least-Squares Approximations method are the same as maximum or minimum points. Moreover, these segmentation methods have been applied widely in several applications of time series data mining ([4], [14], [8], [13], [1], [6]). Based on the aforementioned reasons, a choice of these three segmentation methods is made for comparison about their resulting segments.

However, there has been little work in the field of evaluation of time series segmentation methods. It can be observed that most segmentation methods evaluate the performance of a segmentation of a time series by the least-squares construction error that an approximation method makes when approximating the segments of a time series ([3],[5],[9]). The commonly used reconstruction error criterion is not suitable since it only evaluates the quality of the reconstruction rather than the quality of the segmentation points. To address this problem, Gensler and Sick in 2014 [7] proposed a new set of evaluation criteria for time series segmentation methods which are grouped in classification-based criteria and segmentation-zone criteria.

This paper focuses on comparing the quality of three well-known segmentation methods: Important Extreme Points, PIPs and Polynomial Least Square Approximation by using the existing set of evaluation criteria for time series segmentation proposed by Gensler and Sick [7]. These evaluation criteria for segmentation need datasets to be annotated with segmentation-zones in advance by experts. In practice, it is hard for experts to mark all datasets for evaluation. This makes the number of datasets used for experiments significantly reduced. So, we propose one more evaluation criterion for segmentation which is based on the number of segments with the lengths approximately equal to the average length of all segments in the time series. This proposed evaluation criterion does not require any prior knowledge except for the data points themselves. An empirical study on several benchmark datasets shows that the evaluation measures can help to quantify segmentation results. In addition, it is found that the quality of each segmentation method depends on the characteristics of each tested dataset.

The rest of this paper is organized as follows. Section 2 reviews the three segmentation methods: Important Extreme Points, PIP and Polynomial Least Square Approximation. In Section 3 we describe the evaluation criteria for time series

segmentation proposed by Gensler and Sick. In this Section 3, we also present our proposed evaluation criterion which is called Percentage of Average Length Segments (*PALS*) measure. Section 4 reports the experimental results in examining how the criteria perform and comparing the performance of the three time series segmentation methods. Finally, Section 5 gives some concluding remarks.

2 Three Time Series Segmentation Methods

In this section, we briefly review three time series segmentation methods: Important Extreme Points, PIP and Polynomial Least Square Approximation.

2.1 Important Extreme Points

Fink and Gandhi [2] proposed a method for compressing time series which is based on the concept of important extreme points. Important extreme points in a time series contain important features of the time series. The definition of important extreme points is given as follows.

Definition 1. *Important Extreme Points:* A point t_k of a time series $T = t_1, \ldots, t_m$ is an *important minimum* if there are indices i and j, where $i < k < j$, such that t_k is the minimum among $t_i, \ldots, t_j$ and $t_i / t_k \geq R$, and $t_j / t_k \geq R$

Similarly, a point t_k is an *important maximum* if there are indices i and j, where $i < k < j$, such that t_k is the maximum among $t_i, \ldots, t_j$ and $t_k / t_i \geq R$, and $t_k / t_j \geq R$

In the above definition, the parameter R is called *compression rate* which is greater than one. An increase of R leads to selection of fewer important extreme points.

Given a time series T, starting at the beginning of the time series, all important minima and maxima of the time series are computed by using the algorithm given by Fink and Gandhi [2]. The algorithm takes linear time and constant memory.

2.2 Perceptually Important Points

The PIP method is an important point finding method for time series compression, proposed by Fu et al., 2006 [3]. The PIPs extracted from a time series are identified by the following algorithm.

Given a time series $C = \{c_1, \ldots, c_n\}$. The first two PIPs are c_1 and c_n. The third PIP is the point in C with the maximum distance to the first two PIPs. The next PIP is the point in C with the maximum distance to its two adjacent PIPs and so on. The PIPs identified in the earlier iterations are considered to be more important than those points identified later.

Fig. 1.a illustrates the process of identification of 5 PIPs. The distance metric used in the PIP identifying process is the *vertical distance* between the test point and the

line connecting the two adjacent PIPs. To determine the maximum distance to the two adjacent PIPs (x_1, y_1) and (x_2, y_2), as described in Fig. 1.b, is the vertical distance (VD) between the test point p_3 and the line connecting the two adjacent PIPs, i.e., formula (1).

$$VD(p_3, p_c) = |y_c - y_3| = |(y_1 + (y_2 - y_1)(x_c - x_1)/(x_2 - x_1)) - y_3| \quad (1)$$
$$\text{where } x_c = x_3.$$

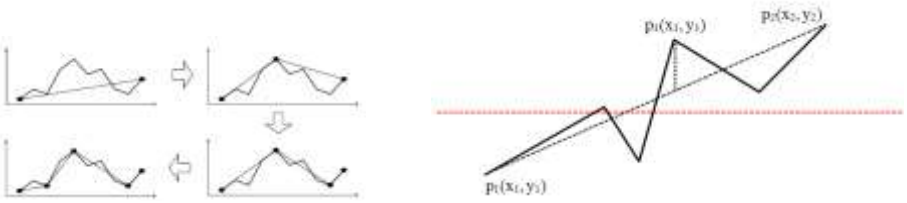

(a) (b)

Fig. 1 (a) PIP identification process (b) Vertical distance measure

The only parameter of PIP segmentation method is the number of perceptually important points (PIPs) used to represent the time series.

2.3 Polynomial Least Square Approximation

In this subsection, we review briefly the time series segmentation method proposed by Fuchs et al. ([5]). This segmentation method is based on a least-squares approximation of time series in sliding windows using a basis of orthogonal polynomials. This allows the definition of fast update steps for the approximation polynomial where the computational effort depends only on the degree of the approximating polynomial and not on the length of the sliding window. The coefficients of the orthogonal expansion of the approximating polynomial can be interpreted as optimal estimators for average, slope, curvature, change of curvature, etc. of the time series in the time window considered.

Fig. 2 shows an example for a time series modeled by polynomials of degree 1, and 2, respectively. The shaded area indicates the least-square error of the polynomial approximation. Due to space limit, here we skip the details of Polynomial Least-Squares Approximation method. Interested reader can refer to [5].

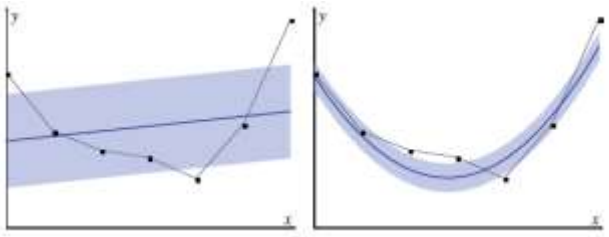

(a) (b)

Fig. 2. Example of a time series modeled by polynomials of various degrees (a) a polynomial of degree 1 and b) a polynomial of degree 2 ([6]).

3 Evaluation Criteria For Time Series Segmentation Methods

3.1 Measures proposed by Gensler and Sick

First, this section presents the set of eight evaluation criteria which was proposed by Gensler and Sick in 2014 [7]. The set consists of two kinds of criteria: classification-based criteria and segmentation-zone criteria. Both kinds of criteria are based on the concepts of *segmentation zone*. The authors model each segment to be determined with the earliest point and the latest point. Such a segment forms an allowed segmentation zone (SZ).

Gensler and Sick proposed an interpretation of the confusion matrix for segmentation problems as follows. When one SZ is assigned exactly one determined segmentation point, it is treated as a *true positive* (TP). If the method does not set a segmentation point in an area where none is expected, it is treated as a *true negative* (TN). If no segmentation point is found in a SZ, it is treated as a *false negative* (FN). False positives (FP) can be created in two situations: (1) An SZ is assigned more than one segmentation point, each segmentation point more than one is treated as a FP, and 2) A segmentation point is found in an area where no SZ exists.

From the defined TP, TN, FN and FP, Gensler and Sick proposed the following criteria for time series segmentation methods: ACC (Accuracy), F_1 (F_1 score [12]), MCC (Matthew correlation coefficient [11]), Prec. (Precision) and Rec. (Recall). The higher values of these criteria, the better segments are found.

The formula for ACC is as follows:

$$ACC = \frac{TP + TN}{TP + FP + TN + FN} \tag{2}$$

The F_1 score describes the harmonic mean of precision and sensitivity and is calculated by the formula:

$$F_1 = \frac{2TP}{(2TP + FP + FN)} \tag{3}$$

The MCC considers all entries of the confusion matrix and is computed by the formula:

$$MCC = \frac{TP.TN - FP.FN}{\sqrt{(TP + FP)(TP + FN)(TN + FP)(TN + FN)}} \tag{4}$$

The MCC takes values from -1 to 1, where +1 represents perfection correlation, 0 a result not better than random guess and -1 absolute disagreement between prediction and ground truth.

Besides ACC, F_1 score and MCC, we can use Precision and Recall which are calculated by formula (5) and (6) as follows:

$$\mathrm{Prec.} = \frac{TP}{TP + FP} \tag{5}$$

$$\mathrm{Rec.} = \frac{TP}{TP + FN} \tag{6}$$

Besides the classification-based criteria for segmentation methods, Gensler and Sick also proposed the three other criteria which are based on segmentation-zones. For the sake of the presentation of these criteria, some important notations are shown in Table 1.

Table 1. Notations in segmentation-zone measures.

Notation	Meaning
SZ	Set of segmentation zones
SP	Set of found segmentation points
p	Segmentation point
$c(p)$	Segmentation zone center of the segmentation point p
|SZ|	Total number of segmentation zones
|SP|	Total number of segmentation points

The first measure in this group is the Average Segmentation Count (ASC), which determines how many times the method creates a segmentation while being inside an SZ in average. The ASC can be calculated by Algorithm 1. The value of ASC closer to 1 is better, a value lower than 1 means too few segments are set inside SZ while a value greater than 1 means too many segments are found.

Algorithm 1 Calculation of Average Segmentation Count (ASC)

```
procedure Cal_ASC(SP, SZ)
Create variable count_z for every segmentation zone z in SZ
ASC := 0
 for each z ∈ SZ do
  for each p∈ SP do
      if  p is inside z then
          count_z := count_z +1
       end if
     end for
     ASC := ASC + count_z
end for
return ASC/|SZ|
end procedure
```

To keep track of how accurately segmentation points hit the target segmentation, Gensler and Sick proposed another measure, called Absolute Segmentation Distance (ASD) which accumulates the distance between target segmentation point and found segmentation point. The ASD can be calculated by the following formula:

$$ASD = \frac{\sum_{p \in SP} \delta(p) dist(p, c(p))}{|SP|} \quad (7)$$

where $\delta(p) = 1$ if p is inside its segmentation zone otherwise, $\delta(p) = 0$; and $dist(p, c(p))$ is the distance between p and its segmentation zone center. Notice that a smaller value of ASD is better.

To keep track of whether an algorithm tends to set its segmentation points too early or too late, Gensler and Sick proposed another measure, called Average Direction Tendency (ADT). ADT describes a quotient of early and late segmentation points. If the segmentation method tends to set its segments too early, the value will be less than 0.5 while a late segmentation will bring out a value greater than 0.5. ADT can be calculated by following formula:

$$ADT = \frac{LateSeg}{LateSeg + EarlySeg} \quad (8)$$

where *LateSeg* and *EarlySeg* are computed by the following formula:

$$LateSeg = \sum_{p \in SP} \delta(p).late(p, c(p)) \quad (9)$$

$$EarlySeg = \sum_{p \in SP} \delta(p).early(p, c(p)) \quad (10)$$

where $\delta(p) = 1$ if p is inside its segmentation zone, otherwise, $\delta(p) = 0$; $late(p, c(p)) = 1$ if p is after its segmentation zone center $c(p)$, otherwise, $late(p, c(p)) = 0$; and $early(p, c(p)) = 1$ if p is before its segmentation zone center $c(p)$, otherwise, $early(p, c(p)) = 0$.

3.2 Our proposed measure

In addition to Gensler and Sick's criteria, we propose one more measure to evaluate the quality of segmentation methods. This measure, called Percentage of Average Length Segments (PALS), focuses on the percentage of the number of segments which have the length approximately equal to the average length of all extracted segments with the range 10% over the total number of extracted segments. The higher percentage indicates a better segmentation. With this measure, we assume that the lengths of extracted segments by a segmentation method have a Gaussian distribution and expect that a better segmentation method will bring out the higher number of segments which have the length approximately equal to the average length of all extracted segments. Given a time series T and the positions $t_1, t_2, \ldots, t_m$ of change points of T, we calculate the average length of all segments. One segment includes points between t_i and t_{i+1}. *PALS* measure is the percentage of number of segments that their length is between 90% * average_length and 110% * average_length.

4 Experimental Evaluations

We compare the performance of the three segmentation algorithms: Important Extreme Points (abbreviated as IEP), Perceptually Important Point method (abbreviated as PIP), Polynomial Least-Squares Approximations method (abbreviated as PLSA) using the set of nine novel evaluation criteria. We used the five selected heart beat datasets downloaded from the website https://www.physionet.org. Each dataset was annotated by an expert. We used these annotations to determine the segmentation zones for each dataset in our experiments. According to these annotations, we sketched the segmentation zones in between ±5% value of positions of the annotated points in the datasets. The test datasets are presented in Table 2. These experimental datasets in Table 2 were annotated in terms of segmentation zones by experts before being tested in the experiments.

Table 2. Descriptions of the test datasets.

No.	Dataset	Length
1	Abdominal and Direct Fetal ECG Database: Record r01	10.000
2	AF Termination Challenge Database: Record learning-set/n01	1.280
3	AHA_Database_ahadb: Record 0001	2.500
4	MIT-BIH ST Change Database: Record 327	3.600
5	PAF Prediction Challenge Database: Record n01-ECG0	1.280

4.1 Experiment 1- How the Criteria Perform

For this experiment, we want to examine how the criteria perform with a specific segmentation method on a given dataset. The dataset used in this experiment is the first one, Abdominal and Direct Fetal ECG Database: Record r01. To show how the criteria behave, we use the PIP segmentation method with two different values for the parameter of the method. In Case I, the number of PIPs is set to 18 and in Case II, 23. We compute the measure values for each case by doing a process consisting of the following steps.criteria

Step 1: Identify the true segmentation points in the dataset using expert-based annotations for the dataset.

Step 2: Apply the PIP segmentation method on the dataset to get the segmentation points.

Step 3: Compare the true segmentation points in Step 1 and the segmentation points found in Step 2 and then build the confusion matrix. Using the confusion matrix, we can obtain the classification-based criteria: *Acc*, *Pre.*, *Rec.*, *F1* and *MCC* for the segmentation results. Notice that the criteria such as *ACC*, F_1, *MCC*, *Prec*., *Rec.* are calculated based on the values of TP (true positives), TN (true negatives), FP (false positives) and FN (false negatives).

Step 4: Also using the true segmentation points and the found segmentation points, we can compute the segmentation-zone criteria: *ASC*, *ASD*, and *ADT*.

Step 5: Using only the found segmentation points, we can compute the *PALS* measure: compute the average length of all the extracted segments and derive the percentage of the number of segments which have the lengths approximately equal to the average length of all extracted segments, with the range 10% over the total number of extracted segments.

Table 3. Confusion matrix resulting from the PIP method (Case I).

		Actual classes	
		Positive	**Negative**
Prediction	**Positive**	3	16
	Negative	16	7798

From our aforesaid evaluation process, we obtain the confusion matrices for the two cases, and report them in Table 3 and Table 4. Next, we compute the evaluation criteria for the two cases, and report them in Table 5. In Table 5, the classification-based criteria are reported on Table 5.a while the segmentation zone criteria and *PALS* are shown in Table 5.b. For most of the criteria, Case I brings out a better segmentation quality than Case II.

Table 4. Confusion matrix for the results in case II.

		Actual classes	
		Positive	**Negative**
Prediction	**Positive**	1	11
	Negative	17	7803

Table 5.a Values of the classification-based criteria of the PIP method in two cases over Dataset 1.

	Acc	*Prec*	*Rec*	F_1	*MCC*
Case I	**0.996**	**0.16**	**0.16**	**0.16**	**0.16**
Case II	0.996	0.08	0.06	0.07	0.07

Table 5.b Values of the other criteria of the PIP method in two cases over Dataset 1.

	ASC	*ASD*	*ADT*	*PALS*
Case I	**0.41**	**33.0**	**0.44**	**27%**
Case II	0.45	32.6	0.70	0%

We can see that *ACC* is unable to distinguish between the results of Case I and Case II. *Precision* remarkably increases from 0.08 to 0.16. *Recall* also increases from 0.06 to 0.16. *F1* increases from 0.07 to 0.16. *ASC*, *ASD*, and *ADT* improve from Case

II to Case I. *ADT* shows a roughly balanced segmentation in Case I (0.5 would be perfectly balanced). The measure *PALS* also improves remarkably from Case II to Case I. This means that the parameter used in Case I is better than the one used in Case II.

In short, these criteria help to evaluate the quality of a segmentation result. Besides, we can observe that PIP method is very sensitive to the specified value of the number of PIPs.

4.2 Experiment 2-Comparing Three Time Series Segmentation Methods

In this experiment, we want to compare the three segmentation methods using the existing evaluation criteria and ours. For each dataset, we executed one segmentation algorithm several times and set different parameters to each test. After that, we calculated the evaluation criteria to find the best set of parameters of a segmentation algorithm. Therefore, for one dataset and each segmentation algorithm, we could find the best set of parameters. We applied the same procedure for all the test datasets. Table 6 reports the best parameters for the three segmentation methods over five datasets. For the Polynomial Least Square Approximation method, we set the degree of the polynomials to 2 and the window size to 10.

Table 6. The best parameters for the three methods over the five datasets.

Dataset	Methods			
	IEP	PIP	PLSA	
	R	**# of PIPs**	**Slope**	**Curve**
1	1.5	22	0.005	-0.005
2	1.5	16	0.005	-0.005
3	1.2	15	0.00105	-0.006
4	1.2	15	0.00106	-0.008
5	1.2	10	0.0001	-0.009

Finally, we report the evaluation results in Table 7 to compare the quality of these methods based on the criteria: *ACC*, F_1, *MCC*, *Prec*., *Rec*. *ASD*, *ASC*, *ADT*, and *PALS*.

In Table 7, for each dataset, if any evaluation measure gets the best value, the result will be printed in bold. We can see from Table 7 that:

- With dataset 1, the IEP method has the criteria ASC, ADT better than those of the other methods. Besides, the IEP method also has the best measure *Acc*., F_1, *MCC*, *Prec*. among the three segmentation methods. Finally, the IEP method has the best value for the *PALS* measure. In sum, for dataset 1, the IEP method can be considered better than the PIP and PLSA methods.
- With the same analysis as above, for dataset 2, the PIP method is better than the IEP and PLSA methods, especially in *Acc*., F_1, *MCC*, *Prec*., *Rec*. and *PALS*.

- For datasets 3 and 5, the PIP method can be considered better than the IEP and PLSA methods in terms of the classification-based criteria.
- Particularly for dataset 4, the PIP and PLSA methods are equivalent to each other and better than the IEP method.

In sum, the results reveal that (i) the quality of each segmentation method depends on the characteristics of each tested dataset and PIPs seems to be more suited to ECG datasets and (ii) a combination of multiple evaluation criteria helps to specify the characteristics of the segmentation method.

Table 7. Values of evaluation measures for the three segmentation methods over the five datasets.

Data set	Methods	*Acc.*	F_1	*MCC*	*Prec.*	*Rec.*	*ASC*	*ASD*	*ADT*	*PALS*
1	**IEP**	**0.997**	**0.270**	**0.269**	**0.263**	0.278	0.591	45.083	0.462	**35%**
	PIP	0.996	0.158	0.156	0.158	0.158	**0.409**	32.609	**0.444**	27%
	PLSA	0.992	0.198	0.230	0.129	**0.421**	0.636	**8.758**	0.615	2%
2	IEP	0.981	0.323	0.379	0.208	**0.714**	1.333	2.226	0.467	0%
	PIP	**0.987**	**0.462**	**0.461**	**0.400**	**0.545**	0.667	2.353	0.375	**13%**
	PLSA	0.985	0.261	0.253	0.273	0.250	**0.250**	**1.000**	**0.333**	9%
3	IEP	0.990	0.154	0.192	0.095	0.400	1.538	4.188	0.800	3%
	PIP	0.991	**0.387**	**0.393**	0.316	**0.500**	0.615	2.238	**0.750**	**5%**
	PLSA	**0.994**	0.125	0.158	**0.333**	0.077	**0.077**	**0.000**	1.000	0%
4	IEP	0.967	0.018	0.024	0.010	0.111	0.300	**0.392**	**1.000**	**3%**
	PIP	0.993	**0.154**	**0.155**	0.125	**0.200**	0.200	1.294	**1.000**	0%
	PLSA	**0.995**	0.118	0.117	**0.143**	0.100	**0.100**	2.250	**1.000**	0%
5	IEP	0.953	0.107	0.178	0.059	**0.600**	2.714	1.705	0.686	0%
	PIP	**0.988**	**0.435**	**0.440**	**0.556**	0.357	0.357	1.100	**0.600**	0%
	PLSA	0.987	0.125	0.186	0.500	0.071	**0.071**	**0.000**	1.000	0%

5 Conclusions

Surprisingly, there has been little work in the field of evaluation of time series segmentation methods. In this paper, we investigated the utility of the evaluation criteria for time series segmentation. The evaluation criteria discussed include the criteria proposed by Gensler and Sick and our proposed measure *PALS*. We conduct the experiments on five benchmark datasets which are annotated by the experts in advance to examine how the criteria perform and compare the effectiveness of the three segmentation algorithms: Important Extreme Points, PIP method and Polynomial Least-Squares Approximations method. Experimental results reveal that a combination of multiple evaluation criteria helps to specify the characteristics of the segmentation method.

In the future, we will utilize the results of the evaluation of the segmentation methods for segmentation-based anomaly detection in time series.

References

1. L. V. Do, and D. T. Anh, "Some Improvements for Time Series Subsequence Join based on Pearson Correlation Coefficients", Proc. of the 7th Int. Symposium on Information and Communication Technology (SoICT), Ho Chi Minh City, Vietnam, Dec. 8-9,pp. 58-65, 2016.
2. E. Fink, & H.S. Gandhi, "Important extrema of time series", Proc. of IEEE International Conference on System, Man and Cybernetics. Montreal, Canada, 366-372, 2007.
3. T.C. Fu, H.P. Chan, F.L. Chung, and C.M. Ng, "Time series subsequence searching in specialized binary tree", Proc. of International Conference on Fuzzy Systems and Knowledge Discovery (FSKD 2006), LNAI 4223, 568-577, 2006.
4. T.C., Fu, F.L.Chung, , R.Luk, and C.M. Ng, "Representing financial time series based on data point importance", Engineering Applications of Artificial Intelligence, vol. 21, no.2, 277-300, 2008.
5. E. Fuchs, T. Gruber, J. Nitschke, and B. Sick, "Online segmentation of time series based on polynomial least-squares approximations", IEEE Transactions on Pattern Analysis and Machine Intelligence, vol. 32, no. 12, 2232-2245, 2010.
6. E. Fuchs, , T.Gruber, , J. Nitschke, and B. Sick, "Online motif detection in time series with SwiftMotif", Pattern Recognition, vol. 42, 3015-3031, 2009.
7. A. Gensler, , and B. Sick, "Novel Criteria to Measure Performance of Time Series Segmentation Techniques", T. Seidl, M. Hassani, C. Beecks (Eds.): Proceedings of the LWA 2014 Workshops: KDML, IR, FGWM, Aachen, Germany, 8-10 September, 2014.
8. C.Gruber, M. Coduro, and B. Sick, "Signature verification with dynamic RBF networks and time series motifs", Proc. of 10th International Workshop on Frontiers in Handwriting Recognition, 2006.
9. E. Keogh, S. Chu, , D. Hart, & M. J. Pazzani, "An online algorithm for segmenting time series", Proceedings of the 2001 IEEE International Conference on Data Mining (ICDM '01), 289–296, 2001.
10. M. Lovric,, M. Milanovic, M. Stamenkovic,: "Algorithmic methods for segmentation of time series: an overview ", JCEBI, Vol. 1, No. 1, 31-53, 2014.
11. B. W. Matthews, "Comparison of the predicted and observed second structure of t4 phase lysozyme", Biochimica et Biophysica Acta (BBA)- Protein Structure, 405 (2), 442-451, 1975.
12. M. Sokolova, , G. Lapalme, " A Systematic analysis of performance measures for classification tasks", Information Processing and Management, vol. 45, no.4, 427-437, 2009.
13. C.D. Truong, H.N. Tin, and D.T. Anh, "Combining motif information and neural network for time series prediction", International Journal of Business Intelligence and Data Mining, vol 7, no.4, 318-339, 2012.
14. P.E. Tsinaslanidis, and D. Kugiumtzis, "A prediction scheme using perceptually important points and dynamic time warping", Expert Systems with Applications, vol 41, no. 15, 6848-6860, 2014.

Eigenvalues distribution limit of covariance matrices with AR processes entries

Zahira Khettab and Tahar Mourid

Department of mathematics, university of Tlemcen, 13000, Algeria
khettab.zahira@yahoo.fr
tmourid@mail.univ-tlemcen.dz

Abstract. *We consider a class of random matrices $B_N = X_N T_N X_N^t$, where X_N is a matrix $(N \times n(N))$ whose rows are independent, the entries X_{ij} in each row satisfy an autoregressive relation AR(1) and T_N is a diagonal matrix independent of X_N. Under some conditions we show that if the empirical distribution function of eigenvalues of T_N converges almost surely to a proper probability distribution as $N \longrightarrow \infty$ and $\frac{n(N)}{N} \longrightarrow c > 0$, then the empirical distribution function of eigenvalues of B_N converges almost surely to a non random limit function given by Marcenko and Pastur. Numerical simulations illustrate the behavior of the estimator.*

Keywords: Large dimensional random matrix; Empirical distribution function of eigenvalues; Covariance matrix; Autoregressive processes; Stieltjes transform.

1 Introduction

Consider a random matrix

$$B_N = X_N T_N X_N^t \tag{1}$$

where $X_N = (\frac{1}{\sqrt{N}} X_{ij}), (i = 1, .., N;\ j = 1, .., n(N))$ is a matrix $(N \times n(N))$ with independent rows with the entries X_{ij} of each row satisfy an autoregressive relation AR(1), and T_N is $(n \times n)$ diagonal matrix with real entries independent of X_N (X_N^t is the transpose matrix of X_N). More precisely, for each $i \geq 1$ we have

$$X_{ij+1} = \rho X_{ij} + \varepsilon_{ij+1}, \qquad j \geq 1 \tag{2}$$

where $(\varepsilon_{ij}, i, j \geq 1)$ are i.i.d. rv's (random values) with mean 0 and variance $\sigma^2 > 0$, such that the rv's ε_{ij} admit a density with respect to Lebesgue measure. The parameter ρ is such that $|\rho| < 1$. The diagonal matrix $T_N = diag\,(\tau_1, ..., \tau_n)$ is independent of X_N and the rv's τ_i are real.

The empirical distribution function $(e.d.f.)$ of the eigenvalues (λ_i) of the symmetric matrix B_N is defined by

$$F^{B_N}(x) = \frac{1}{N} \sum_{i=1}^{N} 1_{(\lambda_i \leq x)},$$

where 1_A denoting the indicator function of the set A.

A large number of papers has dealt with the problem to identify the limit of the empirical distribution function of eigenvalues of random matrices B_N as $N \longrightarrow \infty$ and $\frac{n(N)}{N} \longrightarrow c > 0$. Marcenko and Pastur [9] originally studied this problem for more general forms of random matrices. They establish, under some conditions on moments, that if the empirical distribution function F^{T_N} of T_N converges to a proper distribution function H, then F^{B_N} converges in probability to a proper distribution function. Their method involves the Stieltjes transform, where they shown that the Stieltjes transform of the limiting distribution function satisfies a first order partial differential equation, then via the characteristics they shown that this function is a solution of an algebraic equation identifying hence the limit.

Afterwards, several authors ([6], [7], [10], [12], [13]) extended this result giving the almost sure convergence of the empirical distribution function of eigenvalues under mild conditions on the entries X_{ij}. Most of the papers employ the same transform as [9]. Many domains found out interest of this type of result. We may cite only the case of multivariate statistics where the results are used in the detection problem in signal processing.

In most of the previous works the entries X_{ij} of the matrices are independent random variables, except the paper [4], where dependent entries are considered.

Our goal in this paper is to study, under some assumptions, the limit of the empirical distribution function of eigenvalues F^{B_N} of the random matrix $B_N = X_N T_N X_N^t$, where the entries X_{ij} of the random matrix X_N satisfy an autoregressive relation AR(1) for each i. We follow the approach given in [10], where the authors apply Marcenko and Pastur method to study the Stieltjes transform of the $(e.d.f.)$ of B_N and then to identify the limit law.

The paper is organized as follows. Section 2 provides the main result. Section 3 presents some numerical simulations. The proof of the main result will be postponed to the Appendix.

2 Main result

First, we introduce some rv's and random matrices, truncating and centralizing the entries X_{ij} of the random matrix X_N to obtain new corresponding random matrices as follows: for $i = 1, .., N$; $j = 1, .., n(N)$, let

$$\hat{X}_{ij} = X_{ij} 1_{\left(|X_{ij}| < \sqrt{N}\right)}, \hat{X}_N = \left(\frac{1}{\sqrt{N}} \hat{X}_{ij}\right), \hat{B}_N = \hat{X}_N T_N \hat{X}_N^t, \tag{3}$$

$$\tilde{X}_{ij} = \hat{X}_{ij} - E\left(\hat{X}_{ij}\right), \tilde{X}_N = \left(\frac{1}{\sqrt{N}} \tilde{X}_{ij}\right), \tilde{B}_N = \tilde{X}_N T_N \tilde{X}_N^t, \tag{4}$$

and

$$\begin{cases} \bar{X}_{ij} = \tilde{X}_{ij} 1_{(|X_{ij}| \leq \ln N)} - E\tilde{X}_{ij} 1_{(|X_{ij}| \leq \ln N)}, \\ \bar{X}_N = \left(\frac{1}{\sqrt{N}} \bar{X}_{ij}\right), \bar{B}_N = \bar{X}_N T_N \bar{X}_N^t. \end{cases} \tag{5}$$

We pointed out that the problem described above has been often handled by the method of Stieltjes transform as in [10]. Let $\mathcal{M}(\mathbb{R})$ be the set of distribution functions on $\mathbb{R}$. The Stieltjes transform of a distribution function $F \in \mathcal{M}(\mathbb{R})$ is defined by

$$m_F(z) = \int \frac{1}{\lambda - z} dF(\lambda), \quad z \in \mathbb{C}^+ \equiv \{z \in \mathbb{C} : \Im \mathfrak{m} z > 0\},$$

where $\Im \mathfrak{m}$ is the imaginary part. The inversion formula is given by

$$F([a,b]) = \frac{1}{\pi} \lim_{\epsilon \to 0^+} \int_a^b \Im \mathfrak{m} m_F(x + i\epsilon)\, dx,$$

where a, b are continuity points of F. Recall that weak convergence of probability distribution functions is equivalent to the convergence of Stieltjes transforms (Theorem B.9, [1]) and from the inversion formula, it follows that for any countable set $S \subset \mathbb{C}^+$such that $\mathbb{R} \subset \bar{S}$ the closure of S, and a sequence $(F_N) \in \mathcal{M}(\mathbb{R})$, $F \in \mathcal{M}(\mathbb{R})$, we have the following equivalence

$$\lim_{N \to \infty} m_{F_N}(z) = m_F(z), \forall z \in S \Longleftrightarrow F_N \to F \quad as \quad N \to \infty, \tag{6}$$

where $F_N \to F$ is the vague convergence of distributions functions.

We also consider the following matrices. For $j, l = 1, 2, ..., n(N)$, denote by $\bar{q}_j$ the $j-$th column of $\bar{X}_N$ defined by (5) that is

$$\bar{q}_j = \frac{1}{\sqrt{N}} \left(\bar{X}_{1j}, ..., \bar{X}_{Nj}\right)^t := \frac{1}{\sqrt{N}} V_j$$

and by

$$\bar{B}_{(j)} = \bar{B}^N_{(j)} := \bar{B}_N - \tau_j \bar{q}_j \bar{q}_j^t, \tag{7}$$

where τ_j are the elements of T_N, and define

$$x = x_N := \frac{1}{N} \sum_{j=1}^{n} \frac{\tau_j}{1 + \tau_j m_{F^{\bar{B}_N}}(z)}, x_{(j)} = x^N_{(j)} := \frac{1}{N} \sum_{l=1}^{n} \frac{\tau_l}{1 + \tau_l m_{F^{\bar{B}_{(j)}}}(z)}, \tag{8}$$

where $m_{F^{\bar{B}_N}}$ and $m_{F^{\bar{B}_{(j)}}}$ are Stieltjes transform of the matrices $\bar{B}_N$ and $\bar{B}_{(j)}$ respectively. Finally, set

$$C^1_{(j)} := \left(\bar{B}_{(j)} - zI\right)^{-1}, \quad C^2_{(j)} := \left(x_{(j)} - z\right)^{-1} \left(\bar{B}_{(j)} - zI\right)^{-1} \tag{9}$$

where I is the identity matrix.

Now, we state the main result of this paper giving the almost sure convergence of the empirical distribution function ($e.d.f.$) of the eigenvalues of (1). (tr indicates trace of the matrix).

Theorem *Assume*

(a) *For* $N = 1, 2, ...,$ *let* $X_N = \left(\frac{1}{\sqrt{N}} X_{ij}\right)$ *be a matrix* $(N \times n(N))$ *with independent rows and autoregressive relation* (2) *in each row. The entries* X_{ij} *have all their moments finite and* $\frac{n(N)}{N} \to c > 0$ *as* $N \to \infty$.

(b) $T_N = diag(\tau_1, ..., \tau_n)$, $\tau_i \in \mathbb{R}$, *and the e.d.f. of* T_N *converges almost surely to a distribution function* H *as* $N \to \infty$.

(c) *The matrices* X_N *and* T_N *are independent.*

(d) *For* $k = 1, 2$ *and* $j = 1, 2, ..., n(N)$, *the matrices* $C_{(j)}^k$ *defined in (9) satisfy* $E\left|V_j^t C_{(j)}^k V_j - trC_{(j)}^k\right|^6 \leq KN^3$, *where* K *is a positive constant.*

Then almost surely, the e.d.f. F^{B_N} *of the random matrix* $B_N = X_N T_N X_N^t$ *converges vaguely, to the distribution function* F, *as* $N \longrightarrow \infty$, *whose Stieltjes transform* $m_F(z)$ *satisfies the relation*

$$m_F(z) = -\left(z - c\int \frac{\tau dH(\tau)}{1 + \tau m_F(z)}\right)^{-1}; z \in \mathbb{C}^+. \tag{10}$$

Remark. Assumptions (a) is fulfilled in part if the white noise (ε_{ij}) has all moments (Gaussian white noise). Assumptions (b), (c) are standard and analogous of that existing in [10]. Assumption (d) requires a control of six-th moment of quadratic form of a matrix and its trace by a third power of size N. It is done to handle high order moments of sum of dependent rv's appearing in rows of the matrix X_N. It remains to find sufficient conditions on the entries of the matrix such that Assumption (d) is satisfied. When the entries of X_N are i.i.d. and the corresponding matrices $C_{(j)}^k$ are deterministic (Lemma 3.1 [10]).

3 Numerical Simulations

As practical repercussions of the main result, we illustrate in [8] the behavior of the empirical density estimator of empirical distribution function of eigenvalues of large random matrices B_N, and identify the density function of the limit law by numerical simulations. First, we introduce the formulas giving the empirical estimators and density of limit law. From [11], recall that for all $x \in \mathbb{R} - \{0\}$, and $z = x + iy$, $y > 0$, the distribution function F (limit of the $(e.d.f.)$ F^{B_N}) has a continuous derivative f on $\mathbb{R} - \{0\}$ given by

$$f(x) = (1/\pi)\, \Im m_0(x),$$

where $m_0(x)$ is given by Stieltjes transform $m_F(z)$ as

$$\lim_{z \to x} \; m_F(z) = m_0(x).$$

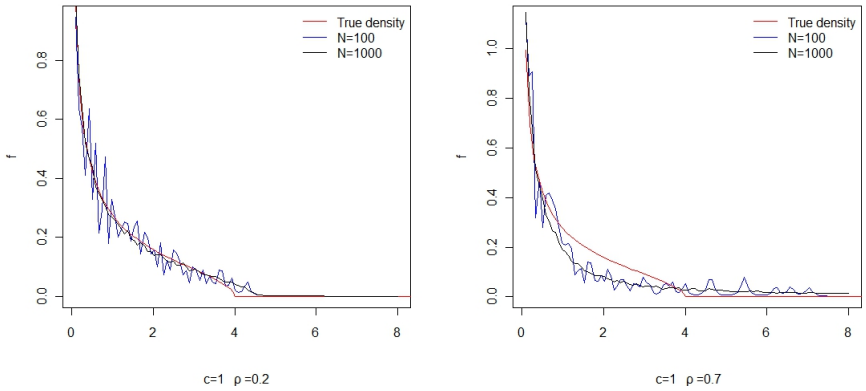

Fig. 1. Densities of the limit law and empirical estimators with T_N identity matrix.

To simulate the empirical density function of the large symmetric random matrices $B_N = X_N T_N X_N^t$ we treat two cases:
Case 1: T_N is the identity matrix $(n \times n)$,
Case 2: T_N is a diagonal matrix: $T_N = diag\,(\tau_1, ..., \tau_n)$, τ_i are real rv's. $(n = n\,(N)\,)$.

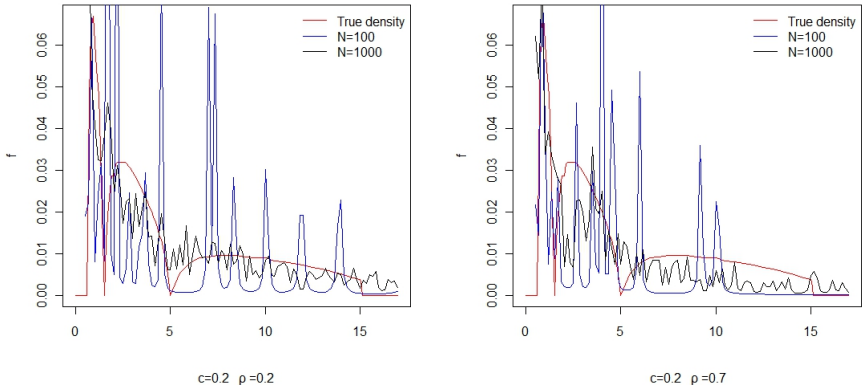

Fig. 2. Densities of the limit law and empirical estimators where matrix T_N has three eigenvalues: 1, 3 and 10.

Conclusion

The performance of estimators strongly depend on the choices of the dimension c, AR parameter ρ and sample size N. We may observe that the variability

of parameters has a direct impact on the stabilization and convergence rate of estimators. Particular choices of parameters confirm a good performance of the estimators and lead to indicate optimal values for these parameters. We also observe marginal influence of the dimension c on density estimator convergence rate. For small values of c ($c < 0.2$), for both weak and strong dependencies ($\rho = 0.2$, $\rho = 0.7$), the estimators perform well from on $N = 100$. However for $c > 1$, we observe the influence of parameter values on the convergence rate. For weak dependence ($\rho = 0.2$) the estimators perform quite well for moderate value $N = 100$, whereas for strong dependence ($\rho = 0.7$) the estimators accurate enough well only for large N (when $N > 1000$). The number of eigenvalues of T_N has an effect on the shape of the estimators as well as on their performance.

Appendix: Proof of Theorem

Recall these well known facts. Let (Z_n) be a stationary sequence of random variables and denote by $\mathcal{F}_0^m$ and $\mathcal{F}_{m+k}^{\infty}$ the $\sigma-$field generated by $\{Z_0, Z_1, ...Z_m\}$ and $\{Z_{m+k}, Z_{m+k+1}, Z_{m+k+2}, ...\}$ respectively. The strong mixing coefficient α_k is defined by

$$\alpha_k = \sup\left\{\left|P\left(A \cap B\right) - P\left(A\right)P\left(B\right)\right|; A \in \mathcal{F}_0^m, B \in \mathcal{F}_{m+k}^{\infty}\right\}.$$

If $\eta \in L^p$ and $\zeta \in L^q$ are $\mathcal{F}_0^m$ and $\mathcal{F}_{m+k}^{\infty}$-measurable respectively, then we have

$$\left|E\left(\eta\xi\right) - E\left(\eta\right)E\left(\xi\right)\right| \leq 12\left\|\eta\right\|_p \left\|\xi\right\|_q \alpha_k^{\frac{1}{r}} \tag{11}$$

for all $1 \leq p, q, r \leq \infty$ with $\frac{1}{p} + \frac{1}{q} + \frac{1}{r} = 1$, and the norm $\left\|.\right\|_p = E^{\frac{1}{p}}\left|.\right|^p$, (see [5]).

On the other hand, for each i the process $(X_{ij},\, j \in \mathbb{Z})$ satisfying relation (2) is a stationary AR(1) process. Then $(X_{ij},\, j \in \mathbb{Z})$ satisfies the geometric strong mixing property (G.S.M) with mixing coefficient : $\alpha_k = O\left(\rho^k\right)$ where $0 < \rho < 1$, whenever ε_{ij} has a strictly positive continuous density (see [3] p 58).

The following distance defines a metric between on the space of $e.d.f.$ of matrices (see [10]). Let $\{f_i\}$ be a sequence of continuous functions taking a constant $\frac{1}{m}$ (m a positive integer) on interval $[a, b]$, where a, b are rational, 0 on $\left(-\infty,\ \ a - \frac{1}{m}\right] \cup \left[b + \frac{1}{m},\ \ +\infty\right)$, and linear over each $\left[a - \frac{1}{m},\ \ a\right]$, $\left[b,\ \ b + \frac{1}{m}\right]$. For F, $G \in \mathcal{M}\left(\mathbb{R}\right)$, the metric

$$D\left(F, G\right) \equiv \sum_{i=1}^{\infty}\left|\int f_i dF - \int f_i dG\right| 2^{-i}$$

induces the topology of vague convergence. Also by Helly selection theorem, for two sequences $(F_N), (G_N) \in \mathcal{M}\left(\mathbb{R}\right)$, we have

$$\lim_{N\to\infty}\left\|F_N - G_N\right\| = 0 \implies \lim_{N\to\infty} D\left(F_N, G_N\right) = 0, \tag{12}$$

where $\|.\|$ denotes the sup-norm of bounded functions from $\mathbb{R}$ to $\mathbb{R}$. Note that for x, $y \in \mathbb{R}$, $|f_i(x) - f_i(y)| \leq |x-y|$ and then for empirical distribution functions F, G over the sets $\{x_1, ..., x_N\}$, $\{y_1, ..., y_N\}$, we have

$$D^2(F,G) \leq \left(\frac{1}{N}\sum_{j=1}^{N}|x_j - y_j|\right)^2 \leq \frac{1}{N}\sum_{j=1}^{N}(x_j - y_j)^2. \tag{13}$$

Now, we replace T by a suitable matrix for further analysis: for $\theta \geq 0$ define, $T_\theta = diag\left(\tau_1 1_{(|\tau_1|\leq\theta)}, ..., \tau_n 1_{(|\tau_n|\leq\theta)}\right)$, and let Q be any $(N \times n)$ matrix. If θ and $(-\theta)$ are continuity points of H, then by Lemma 2.5 of [10] and assumption (b) of the Theorem, as $N \to \infty$ and $\frac{n}{N} \to c > 0$, we have

$$\left\|F^{QTQ^t} - F^{QT_\theta Q^t}\right\| \leq \frac{1}{N}rg(T - T_\theta) = \frac{1}{N}\sum_{j=1}^{n} 1_{(|\tau_j|>\theta)} \to cH\{[-\theta,\theta]^c\} \quad a.s.$$

It follows that if $\theta = \theta_N \to \infty$ then

$$\left\|F^{QTQ^t} - F^{QT_\theta Q^t}\right\| \to 0 \quad a.s. \tag{14}$$

Choose θ such that

$$\theta^4\left[E^{\frac{2}{3}}|X_{11}|^2 1_{(|X_{11}|\geq \ln N)} + \frac{1}{N}\right] \to 0 \tag{15}$$

and

$$\sum_{N=1}^{\infty}\theta^8\left[\frac{1}{N^{7/6}}E^{1/6}|X_{11}|^4 1_{\left(\ln N\leq|X_{11}|<\sqrt{N}\right)} + \frac{1}{N^2}\right] < \infty. \tag{16}$$

For continue, we need the following results.

Lemma 1. *Let the $(N \times n)$ matrices $X = \left(\frac{1}{\sqrt{N}}X_{ij}\right)$ verifying Assumption (a) of Theorem, and $\hat{X} = \left(\frac{1}{\sqrt{N}}\hat{X}_{ij}\right)$ where $\hat{X}_{ij} = X_{ij}1_{\left(|X_{ij}|<\sqrt{N}\right)}$. For $\theta \geq 0$ set $T_\theta = diag\left(\tau_1 1_{(|\tau_1|\leq\theta)}, ..., \tau_n 1_{(|\tau_n|\leq\theta)}\right), \tau_i \in \mathbb{R}$. We have*

$$D\left(F^{XT_\theta X^t}, \quad F^{\hat{X}T_\theta\hat{X}^t}\right) \to 0 \quad a.s.$$

Proof. From Corollary A.42 of [1], we find

$$D^2\left(F^{XT_\theta X^t}, F^{\hat{X}T_\theta\hat{X}^t}\right) \leq \left[\frac{2}{N}tr\left(XX^t - \hat{X}\hat{X}^t\right) + \frac{4}{N}tr\hat{X}\hat{X}^t\right]\left[\frac{\theta^2}{N}tr\left(XX^t - \hat{X}\hat{X}^t\right)\right].$$

In order that this distance tends almost surely to 0, we can show by Borel-Cantelli Lemma, that $\left[\frac{\theta^2}{N}tr\left(XX^t - \hat{X}\hat{X}^t\right)\right]$ tends to 0 and $\left[\frac{4}{N}tr\hat{X}\hat{X}^t\right]$ is bounded almost surely.

Also, for $(N \times n)$ matrix $X = \left(\frac{1}{\sqrt{N}} X_{ij}\right)$ verifying Assumption (a) of Theorem. With help to inequality (11) and the fact that (X_{ij}) satisfies the G.S.M property, we obtain

$$M_1 \leq E\left(tr\left(XX^t\right)^2\right) \leq M_2 \tag{17}$$

where

$$M_1 = \frac{K}{N}\{nE\left|X_{11}\right|^4 + n\left(N+n-2\right)E^2\left|X_{11}\right|^2 - E^{\frac{2}{3}}\left|X_{11}\right|^6\},$$

$$M_2 = \frac{K}{N}\{nE\left|X_{11}\right|^4 + n\left(N+n-2\right)E^2\left|X_{11}\right|^2 + E^{\frac{2}{3}}\left|X_{11}\right|^6 + \left(N-1\right)E^{\frac{4}{3}}\left|X_{11}\right|^3\}.$$

And with the same arguments, we deduce a bound of the variance

$$var\left(tr\left(XX^t\right)^2\right) \leq \frac{K}{N^4}\{N^4 E\left|X_{11}\right|^4 E^2\left|X_{11}\right|^2 \tag{18}$$

$$+N^3[E^{\frac{4}{3}}\left|X_{11}\right|^6 + E^{\frac{1}{2}}\left|X_{11}\right|^4 E^{\frac{1}{3}}\left|X_{11}\right|^6 E^{\frac{1}{3}}\left|X_{11}\right|^{12} + E\left|X_{11}\right|^2 E^{\frac{2}{3}}\left|X_{11}\right|^9]$$
$$+N^2[E^{\frac{2}{3}}\left|X_{11}\right|^6 E^{\frac{1}{6}}\left|X_{11}\right|^{24} + E^{\frac{1}{3}}\left|X_{11}\right|^{15} E\left|X_{11}\right|^3 + E^{\frac{2}{3}}\left|X_{11}\right|^{12} + E^{\frac{5}{12}}\left|X_{11}\right|^{12} E^{\frac{1}{6}}\left|X_{11}\right|^{18}]\}.$$

Using (14) and (12), we may write

$$D\left(F^{XTX^t}, F^{XT_\theta X^t}\right) \to 0 \;\; and \;\; D\left(F^{\hat{X}T_\theta \hat{X}^t}, F^{\hat{X}T\hat{X}^t}\right) \to 0 \;\; a.s.$$

Furthermore by Lemma 1, we get

$$D\left(F^{XTX^t}, F^{\hat{X}T\hat{X}^t}\right) \to 0 \;\; a.s. \tag{19}$$

For $\hat{B}_N$ and $\tilde{B}_N$ defined by relations (3) and (4), we have from Lemma 2.5 of [10]

$$\left\|F^{\hat{B}_N} - F^{\tilde{B}_N}\right\| \to 0. \tag{20}$$

Let $\bar{\tilde{X}}_{ij} = \tilde{X}_{ij} - \bar{X}_{ij}$ or

$$\bar{\tilde{X}}_{ij} = \tilde{X}_{ij} 1_{(|X_{ij}| \geq \ln N)} + E\tilde{X}_{ij} 1_{(|X_{ij}| < \ln N)}, \quad \bar{\tilde{X}} = \left(\frac{1}{\sqrt{N}} \bar{\tilde{X}}_{ij}\right)$$

where $\tilde{X}_{ij}$ and $\bar{X}_{ij}$ are defined by the relations (4), (5) respectively. Then, from (13), and Cauchy-Schwartz inequality, it follows that the squared distance

$$D^2\left(F^{\tilde{X}T_\theta \tilde{X}^t}, F^{\bar{X}T_\theta \bar{X}^t}\right)$$

is bounded by

$$\frac{1}{N}\left\{\theta^2 tr\left(\bar{\tilde{X}}\bar{\tilde{X}}^t\right)^2 \right.$$
$$+4\left[\theta^4 tr\left(\bar{\tilde{X}}\bar{\tilde{X}}^t\right)^2 tr\left(\bar{X}\bar{X}^t\right)^2\right]^{\frac{1}{2}}$$
$$\left. +4\left[\left[\theta^4 tr\left(\bar{\tilde{X}}\bar{\tilde{X}}^t\right)^2 tr\left(\bar{X}\bar{X}^t\right)^2\right]^{\frac{1}{2}} \theta^2 tr\left(\bar{\tilde{X}}\bar{\tilde{X}}^t\right)^2\right]^{\frac{1}{2}}\right\}.$$

Therefore, in order to show that almost surely

$$D\left(F^{\tilde{X}T_\theta\tilde{X}^t}, F^{\bar{X}T_\theta\bar{X}^t}\right) \to 0, \tag{21}$$

it suffices to verify that

$$\theta^4 \frac{1}{N} tr\left(\bar{\bar{X}}\bar{\bar{X}}^t\right)^2 \to 0, \frac{1}{N} tr\left(\bar{X}\bar{X}^t\right)^2 = O(1) \quad a.s. \tag{22}$$

Since $E\left(\bar{\bar{X}}_{11}\right) = 0$ and $\bar{\bar{X}}_{ij} = \tilde{X}_{ij} 1_{(|X_{ij}| \geq \ln N)} + E\tilde{X}_{ij} 1_{(|X_{ij}| < \ln N)}$, we have

$$E\left|\bar{\bar{X}}_{11}\right|^2 \leq KE\left|X_{11}\right|^2 1_{(|X_{11}| \geq \ln N)} \to 0. \tag{23}$$

For $p \geq 4$,

$$E\left|\bar{\bar{X}}_{11}\right|^p \leq K\left(N^{\frac{p-4}{2}} E\left|X_{11}\right|^4 1_{\left(\ln N \leq |X_{11}| < \sqrt{N}\right)} + 1\right). \tag{24}$$

By dominated convergence theorem this yields

$$E\left|\bar{X}_{11}\right|^2 \to E\left|X_{11}\right|^2 = \gamma. \tag{25}$$

For $p \geq 4$ and definition of rv's $\bar{X}_{11}$ we have

$$E\left|\bar{X}_{11}\right|^p \leq K(\ln N)^{p-2}. \tag{26}$$

From (15), (23), (24), $E(|X_{11}|^4 1_{\left(\ln N \leq |X_{11}| < \sqrt{N}\right)}) \leq NE\left|X_{11}\right|^2$ and relation (17), we may write

$$E\left[\frac{1}{N}\theta^4 tr\left(\bar{\bar{X}}\bar{\bar{X}}^t\right)^2\right] \leq K\theta^4\left[E^{\frac{2}{3}}\left|X_{11}\right|^2 1_{(|X_{11}| \geq \ln N)} + \frac{1}{N}\right] \to 0,$$

Also (18) gives

$$var\left(\frac{1}{N}\theta^4 tr\left(\bar{\bar{X}}\bar{\bar{X}}^t\right)^2\right) \leq K\theta^8\left[\frac{1}{N^{7/6}} E^{1/6}\left|X_{11}\right|^4 1_{\left(\ln N \leq |X_{11}| < \sqrt{N}\right)} + \frac{1}{N^2}\right],$$

which is summable by (16). Hence we obtain $\frac{1}{N}\theta^4 tr\left(\bar{\bar{X}}\bar{\bar{X}}^t\right)^2 \to 0$ a.s.

Now it remains to show that $\frac{1}{N} tr\left(\bar{X}\bar{X}^t\right)^2 = O(1)$ a.s. Using (17), (25) and (26), we find

$$\begin{aligned} K\{-\frac{(\ln N)^{\frac{8}{3}}}{N^2}\} &\leq E\left[\frac{1}{N} tr\left(\bar{X}\bar{X}^t\right)^2\right] - \frac{n}{N}\left(\frac{n}{N} + 1 - \frac{2}{N}\right) E^2\left|\bar{X}_{11}\right|^2 \\ &\leq K\{\frac{n}{N}\frac{(\ln N)^2}{N} + \frac{(\ln N)^{\frac{8}{3}}}{N^2} + \frac{(\ln N)^{\frac{4}{3}}}{N}\}. \end{aligned}$$

Consequently

$$E\left[\frac{1}{N}tr\left(\bar{X}\bar{X}^t\right)^2\right]-\frac{n}{N}\left(\frac{n}{N}+1-\frac{2}{N}\right)E^2\left|\bar{X}_{11}\right|^2\to 0,$$

and

$$E\left[\frac{1}{N}tr\left(\bar{X}\bar{X}^t\right)^2\right]\to\gamma^2\left[c\left(c+1\right)\right].$$

Concerning the variance, by (18), (25) and (26), we obtain

$$var\left(\frac{1}{N}tr\left(\bar{X}\bar{X}^t\right)^2\right)\leq K\frac{\left(\ln N\right)^{17/3}}{N^3},$$

which is summable. Then, (22) is verified from which (21) follows. This result with (14) allow us to write

$$D\left(F^{\tilde{X}T\tilde{X}^t},F^{\bar{X}T\bar{X}^t}\right)\to 0\ \ a.s.$$

With (19) and (20), in order to prove $D\left(F^{XTX^t},F\right)\to 0$ a.s, it suffices to verify that

$$D\left(F^{\bar{X}T\bar{X}^t},F\right)\to 0\ \ a.s.$$

For this aim we shall show that for any $z\in\mathbb{C}^+$

$$m_{F^{\bar{X}T\bar{X}^t}}\left(z\right)\to m_F\left(z\right)\ \ a.s.$$

Let $z\in\mathbb{C}^+$ and $\bar{B}_N=\bar{X}T\bar{X}^t$, the sequence $\{F^{\bar{B}_N}\}$ satisfies the assumptions of Lemma 2.8 of [10]. So $\exists m>0$ such that

$$\inf_N F^{\bar{B}_N}\left[-m,m\right]>0,\ \delta=\inf_N\Im\mathfrak{m}\left(m_{F^{\bar{B}_N}}\left(z\right)\right)>0\ \ a.s.$$

Write

$$\bar{B}_N-zI=\left(x-z\right)I+\bar{X}T\bar{X}^t-xI.$$

Then

$$\left(x-z\right)^{-1}-m_{\bar{B}_N}\left(z\right)=\frac{1}{N}\sum_{j=1}^{n}\frac{\tau_j}{1+\tau_j m_{F^{\bar{B}_N}}\left(z\right)}d_j,\tag{27}$$

where

$$\begin{aligned}d_j=d_j^N=&\frac{1+\tau_j m_{F^{\bar{B}_N}}\left(z\right)}{1+\tau_j\bar{q}_j^t\left(\bar{B}_{(j)}-zI\right)^{-1}\bar{q}_j}\bar{q}_j^t\left(\bar{B}_{(j)}-zI\right)^{-1}\left(\left(x-z\right)^{-1}I\right)\bar{q}_j\\&-\frac{1}{N}tr\left(\bar{B}_N-zI\right)^{-1}\left(\left(x-z\right)^{-1}I\right)\end{aligned}$$

with $\bar{q}_j$ denote the $j-$th column of $\bar{X}$, and $\bar{B}_{(j)}$, x, $x_{(j)}$ are defined in relations (7) and (8).

Lemma 3.1 of [10] and assumption (d) of the Theorem permit us to obtain

$$\max_{j\leq n} \max\left[\beta_1, \beta_2, \beta_3\right] \to 0 \quad a.s. \tag{28}$$

Where

$$\begin{aligned}
\beta_1 &= \left| \left\|\bar{q}_j\right\|^2 - 1 \right|, \\
\beta_2 &= \left| \bar{q}_j^t \left(\bar{B}_{(j)} - zI\right)^{-1} \bar{q}_j - \frac{1}{N} tr \left(\bar{B}_{(j)} - zI\right)^{-1} \right|, \\
\beta_3 &= \left| \bar{q}_j^t \left(\bar{B}_{(j)} - zI\right)^{-1} \left(\left(x_{(j)} - z\right) I\right)^{-1} \bar{q}_j \right. \\
&\quad \left. - \frac{1}{N} tr \left(\bar{B}_{(j)} - zI\right)^{-1} \left(\left(x_{(j)} - z\right) I\right)^{-1} \right|.
\end{aligned}$$

Lemma 2.6 of [10] gives us

$$\max_{j\leq n} \max[|\ \gamma_1\ |, |\ \gamma_2\ |] \to 0. \tag{29}$$

Where

$$\begin{aligned}
\gamma_1 &= m_{F^{\bar{B}_{(j)}}}(z) - m_{F^{\bar{B}_N}}(z), \\
\gamma_2 &= m_{F^{\bar{B}_N}}(z) - \bar{q}_j^t \left(\bar{B}_{(j)} - zI\right)^{-1} \bar{q}_j.
\end{aligned}$$

So that for N large enough, we have

$$\max_{j\leq n} \max[|\Im\mathfrak{m}\gamma_1|, |\Im\mathfrak{m}\gamma_2|] < \frac{\delta}{2}.$$

Then for $j, l \leq n$,

$$\left| \frac{1 + \tau_j m_{F^{\bar{B}_N}}(z)}{1 + \tau_j^t \bar{q}_j \left(\bar{B}_{(j)} - zI\right)^{-1} \bar{q}_j} - 1 \right| < \frac{2}{\delta} |\ \gamma_2\ |,$$

and

$$\left| \frac{\tau_l}{1 + \tau_l m_{F^{\bar{B}_N}}(z)} - \frac{\tau_l}{1 + \tau_l m_{F^{\bar{B}_{(j)}}}(z)} \right| \leq \frac{2}{\delta^2} |\ \gamma_1\ |.$$

Therefore

$$\max_{j\leq n} \max[\left| \frac{1 + \tau_j m_{F^{\bar{B}_N}}(z)}{1 + \tau_j^t \bar{q}_j \left(\bar{B}_{(j)} - zI\right)^{-1} \bar{q}_j} - 1 \right|, \left|x - x_{(j)}\right|] \to 0. \tag{30}$$

Using Lemmas 2.6, 2.7 of [10] and (28)–(30), we may have

$$\max_{j\leq n} d_j \to 0.$$

Since

$$\left|\frac{\tau_j}{1+\tau_j m_{F^{\bar{B}_N}}(z)}\right| \leq \frac{1}{\delta},$$

we may conclude from (27) that

$$(x-z)^{-1} - m_{\bar{B}_N}(z) \to 0.$$

Hence, the relation (10) is satisfied.

Finally, using (6) the proof of the Theorem is now complete.

Acknowledgments. The authors would like to sincerely thank anonymous referees for their careful comments on the paper.

References

1. Bai, Z.D., Silverstein, J. W.: Spectral Analysis of Large Dimensional Random Matrices. 2nd Edition, Springer (2010)
2. Billingsley, P.: Convergence of Probability Measures. NewYork: Wiley (1968)
3. Bosq, D.: Linear Processes in Function spaces. Theory and Applications. Lecture Notes in Statistics 149 Springer (2000)
4. Boutet de Monvel, A., Khorunzhy, A.: Limit theorems for random matrices with correlated entries. Markov Process. Related Fields. 4(2), 175-197 (1998)
5. Davydov., Yu, A.: Convergence of distributions generated by stationary stochastic processes. Theor. Probability Appl. 13, 691-696 (1968)
6. Grenander, U., Silverstein, J. W.: Spectral analysis of networks with random topologies. SIAM J. Appl. Math. 32(2), 499-519 (1977)
7. Jonsson, D.: Some limit theorems for the eigenvalues of a sample covariance matrix. J. Multivariate Anal. 12, 1-38 (1982)
8. Khettab, Z., Mourid, T.: Eigenvalues empirical distribution of covariance matrices of AR processes. A simulation study. Annales de l'ISUP, 60, fasc 1-2, 3-22 (2016)
9. Marcenko, V. A., Pastur, L. A.: Distribution of eigenvalues in certain sets of random matrices. Mat. SB (N. S.). 72 (114), 507-536 (1967)
10. Silverstein, J. W., Bai, Z . D.: On the empirical distribution of eigenvalues of a class of large dimensional random matrices. Journal of Multivariate Analysis. 54(2), pp. 175-192 (1995)
11. Silverstein, J. W., Choi, S. I.: Analysis of the limiting spectral distribution of large dimensional Random Matrices. Journal of Multivariate Analysis. 54(2), pp. 295-309 (1995)
12. Wachter, K. W.: The limiting empirical measure of multiple discriminant ratios. Ann. Stat. 8, 937-957 (1980)
13. Yin, Y. Q.: Limiting spectral distribution for a class of random matrices. J. Multivariate Anal. 20, 50-68 (1986)
14. Zhang, T.: Marchenko-Pastur Law for Tyler's and Maronna's M-estimators. ArXiv:1401.3424v3 [math.ST] (2014)

An Incremental von Mises Mixture Framework for Modelling Human Activity Streaming Data

Eris Chinellato[1], Kanti V. Mardia[2], David C. Hogg[2], and Anthony G. Cohn[2]

[1] Middlesex University
The Burroughs, London, NW4 4BT, UK
e.chinellato@mdx.ac.uk
[2] University of Leeds
Leeds, LS2 9JT, UK

Abstract. Modelling the time of occurrence of events from data streams is a challenging task, since the underlying distributions can be both cyclic and multimodal. Moreover, in order to avoid the indefinite growth of data storage, historical streaming data has to be represented only with model parameters, discarding the single values. In this work, we introduce an incremental framework for a mixture of circular von Mises distributions to model the time of occurrence of events. Applying our framework to the time of occurrence of human activities, we show that it is able to represent the relevant information of a cyclic data stream by storing only the distribution parameters, highlighting that its use can extend to a number of applications.

1 Introduction

When analysing information from data streams, modelling efforts have to satisfy conflicting goals, such as representing the data as faithfully as possible while optimising data storage, as saving all data for an indefinitely long period of time is not sustainable. Among the most common data in streams is the time of occurrence of events, the analysis of which is nevertheless particularly challenging, since underlying distributions are usually both cyclic and multimodal.

The distribution of choice for modelling cyclical data is the von Mises distribution, which wraps around over a specified period [13]. Mixtures of von Mises (VMM) have been used before to model cyclical multimodal data, but all existing approaches require the availability of all data to generate the mixture model. By applying core circular statistics concepts to the standard VMM, we have developed IVMM, an *Incremental von Mises Mixture* model. IVMM fits a cyclical, multimodal distribution over the data, and for the first time this is performed incrementally, so that only summary statistics of the model need to be saved, and not all the data as in standard applications.

Incremental model building, here introduced for the first time for circular processes, is in some cases very important, as efficiency can become an issue when considering long term data from multiple sources. Consider for example data from millions of users of a smartphone application coming in continuously,

and having to be merged and processed together, or people passing in front of multiple sensors in public places. In this work we offer a solution to this issue when it refers to cyclic, multimodal events, and apply it to the time of occurrence of human activities.

We next describe the type of data we are dealing with, and existing related works and techniques. We then introduce our new IVMM framework, and show and discuss its experimental evaluation.

2 Background

In this section we describe in detail the type of data we are dealing with, the task, and review current approaches to the problem.

2.1 The problem and data description

Modelling data such as the daily times of occurrence of a human activity is not straightforward, because the data are typically both cyclic and multimodal. This can be appreciated looking at the example activity in Fig. 1, obtained from the Consolidated Human Activity Database (CHAD)[3]. CHAD is a large registry of domestic human activities collected in smart-homes and organised into several datasets. A typical CHAD dataset includes dozens of activities, each with hundreds or thousands of occurrences collected daily, in some cases for more than two years. Each activity instance specifies the location and time of occurrence of the activity, among other information. The time of occurrence is normally rounded to the nearest minute, but some sensors have a one second precision. The plots in Fig. 1 represent the same histogram of the time of occurrence of 515 instances of activity *Converse* (dataset code: CAA, activity code: 17241), plotted in polar (a) and Cartesian (b) spaces.

On the one hand, the activity frequency distribution covers the 24 hours completely, without any time gaps, and there is no easy and correct way to split the data at a certain time (e.g. midnight, as conventionally done, or any other time). This means that any analysis needs to consider the data as wrapped around in a continuous fashion, otherwise there would be a discontinuity in the model at the splitting time. On the other hand, most activities are expected to have a multimodal nature: they cannot be fitted by a single function with only one maximum, but require instead a mixture of functions, like the data in Fig. 1.

Considering that events can have different periodicity T (e.g. 360 for radial directions, 86400 for time of the day in seconds, 366 for days in a year), we express our problem as the following. Let us consider a set X of N points $x_i, i = 1, ..., N$, coming from a data stream of variable x, taking values within the interval $[0, T[$. We want to create and continuously update a model of x using a mixture of distributions, without having to store all data points in memory.

[3] https://www.epa.gov/healthresearch/consolidated-human-activity-database-chad-use-human-exposure-and-health-studies-and

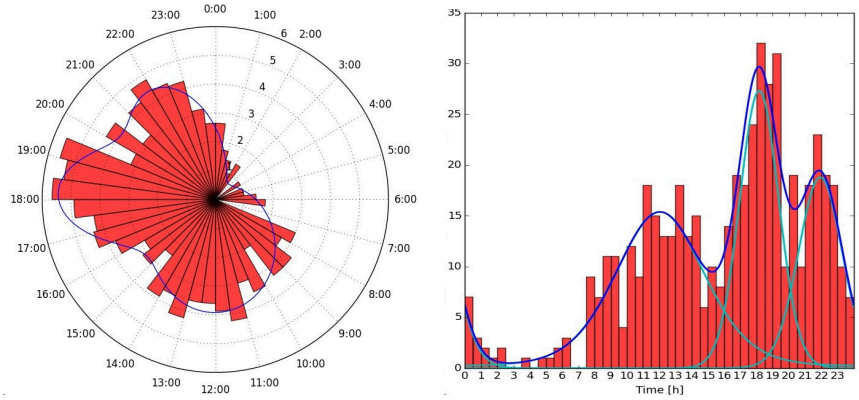

(a) Polar plot (b) Cartesian plot

Fig. 1. Example of activity time data requiring a cyclic, multimodal fitting. To preserve the proportion between frequencies and plot bar surface, bar height in the polar plot is proportional to the square root of the frequency.

2.2 Existing solutions

Circular statistics techniques are typically applied to geographical, meteorological, zoological and biochemical data (see e.g [6, 10, 12, 14]). Their use in human studies, particularly for what concerns time periodicity, is virtually unexplored. Typical methods are non-parametric and require the storage of all datapoints [2, 9], whilst here we are more concerned with parametric and incremental methods.

For what concerns the analysis of time of occurrence of human activities, previous works have often employed non-homogeneous Poisson processes, for classifying and predicting daily patterns and day types [8, 15], or for spatio-temporal identification of people for robotics applications [17]. Works that take into account the cyclic nature of data to avoid discontinuities in the models have recently become more common. They mostly use wrapped Gaussian distributions [4, 3], in one case mixed with von Mises [11]. So far, all of them can only be applied in batch to the whole dataset, and not incrementally, so their models cannot be updated dynamically with the data stream, and they require the storage of every single data point.

Different approaches have been proposed for implementing incremental versions of Gaussian mixture models (see e.g.[16, 5]), but they have not been so far extended to the case of von Mises, or any other circular distribution. An incremental update of a von Mises mixture model is introduced in [1], but only for inserting new points into existing models in the mixture, while in this work we test new data batches against all existing models, and are thus able to add new models to the mixture when necessary. The conceptual complexity of allowing a certain flexibility to the mixture while keeping it parametric is testified by the fact that current split-and-merge methods (see e.g. [18]) are not incremental, and require saving all data in order to add models to the mixture.

2.3 Mixture of von Mises fitting

Cyclic processes are better represented, and fitted, on a circular space, following techniques developed in the field of *directional statistics* [13]. The distribution of choice for fitting circular data is the von Mises, analogue to a normal distribution on the circle. It is typically employed to fit radial directions or periodical events. Multimodal data that cannot be modelled by a single distribution require the fitting of mixtures of von Mises [12, 7]. The blue curves in Fig. 1 show the outcome of fitting a mixture of von Mises distributions over the data, in polar and Cartesian coordinates, respectively. Fig. 1(b) also shows the contribution of each von Mises component.

3 Incremental von Mises Mixture [IVMM]

3.1 The von Mises distribution

A von Mises distribution is described by a preferred direction or mean, μ, and a concentration parameter, κ:

$$f(x|\mu,\kappa) = \frac{e^{\kappa\cos(x-\mu)}}{2\pi I_0(\kappa)}, \tag{1}$$

where $I_0(\kappa)$ is the modified Bessel function of order 0 (the canonical solution of a type of differential equation on purely imaginary numbers). μ is the average of the vectors of all datapoints, and can be estimated by using either angular, or complex number representations. κ is a measure of concentration – reciprocal of dispersion, and thus akin to $1/\sigma^2$ – which cannot be compute analytically, but only estimated by approximation.

Given a dataset of n data points x_i , and a selected period T , all data points can be represented by angles $\theta_i = 2\pi x_i/T$ on the unit circle, $i = 1, ..., n$.

The mean Cartesian coordinates $\bar{C}$ and $\bar{S}$ of all the points are the fundamental descriptors for building the circular statistics.

$$\bar{C} = \frac{1}{n}\sum_{j=1}^{n}\cos\theta_j, \qquad \bar{S} = \frac{1}{n}\sum_{j=1}^{n}\sin\theta_j \tag{2}$$

The mean resultant length $\bar{R}$ and mean direction $\bar{\theta}$ of the dataset can be computed directly from $\bar{C}$ and $\bar{S}$.

$$\bar{R} = \sqrt{\bar{C}^2 + \bar{S}^2} \qquad \bar{\theta} = \arctan\frac{\bar{S}}{\bar{C}} \tag{3}$$

Estimated $\hat{\mu}$ and $\hat{\kappa}$ of a von Mises can be computed through maximum Likelihood Estimation. Considering a samples of n values $\theta_1, ..., \theta_n$ originating from a von Mises distribution $vM(\mu,\kappa)$, the Log-likelihood to maximise is:

$$l(\mu,\kappa;\theta_1,...,\theta_n) = n(-\log 2\pi + \kappa\bar{R}\cos(\bar{\theta}-\mu) - \log I_0(\kappa)) \tag{4}$$

The resultant maximum likelihood estimators are:

$$\hat{\mu} = \bar{\theta} \tag{5}$$

$$A(\kappa) = \frac{I_1(\kappa)}{I_0(\kappa)} = \bar{R} \qquad \rightarrow \qquad \hat{\kappa} = A^{-1}(\bar{R}) \tag{6}$$

where $I_1(\kappa)$ is the modified Bessel function of order 1. The preferred direction $\hat{\mu}$ can thus be computed directly from the sets of θ_i, while the concentration parameter $\hat{\kappa}$ can be estimated numerically from $\bar{R}$ by using one of various existing approximations of the inverse of function $A(\kappa)$ [13, 7].

3.2 Incremental approach

In order to build an incremental mixture of von Mises it is necessary to test if two samples are likely to belong to the same generating distribution or not. A two samples F test on the hypothesis of equality of means is performed for this purpose:

$$H_0 : \mu_1 = \mu_2, \qquad H_1 : \mu_1 \neq \mu_2 \tag{7}$$

The approximated value of the F distribution to check is [13]:

$$\frac{(n-2)(R_1 + R_2 - R)}{n - R_1 - R_2} \approx F_{1,n-2} \tag{8}$$

where R_1, R_2 and R are the resultant lengths of the two samples of size n_1 and n_2, and of the combined sample of size $n = n_1 + n_2$, respectively.

The above formulation allows us to develop a schema for incrementally updating a mixture of von Mises distributions. The only requirement is that each sample has enough datapoints to be suitably modelled by a von Mises function. Our **feature vector** for representing a single von Mises function is composed of only three elements:$(n, SC = n\bar{C}, SS = n\bar{S})$. Let us consider an initial von Mises mixture vMM, composed of N von Mises distributions:

$$vMM = \{vM_i, i = 1, ..., N\}, \qquad vM_i = (n_i, SC_i, SS_i) \tag{9}$$

A new data sample received at time t can again be modelled by a mixture of von Mises:

$$vMM^t = \{vM_j, j = 1, ..., N^t\}, \qquad vM_j = (n_j, SC_j, SS_j) \tag{10}$$

In order to merge the two mixture models, each new vM_j is tested against each existing vM_i. If we can accept the null hypothesis $H_0(\mu_i = \mu_j)$, the current vM_i is updated:

$$vM_i' = (n_i + n_j, SC_i + SC_j, SS_i + SS_j) \tag{11}$$

If, instead, for a certain j we reject the null hypothesis for all existing models, $H_1(\mu_i \neq \mu_j), \forall i$, it means that vM_j cannot be merged with any existing vM_i, and must be added to vMM.

As a last update step, after the model vMM has been modified according to all vM_j, each pair of distributions (vM_i, vM_{i+1}) of vMM (including (vM_N, vM_1)) are tested for equality against each others, and merged if H_0.

3.3 Using IVMM

The new schema introduces the possibility of testing new samples, or whole new datasets, against the current model. An example of how datasets are represented by gradually increasing, but eventually stabilising, number of von Mises distributions is shown in Fig. 2. Clear continuous lines show the evolution of the number of components for eight different example activities, whilst the thicker black line is the average trend.

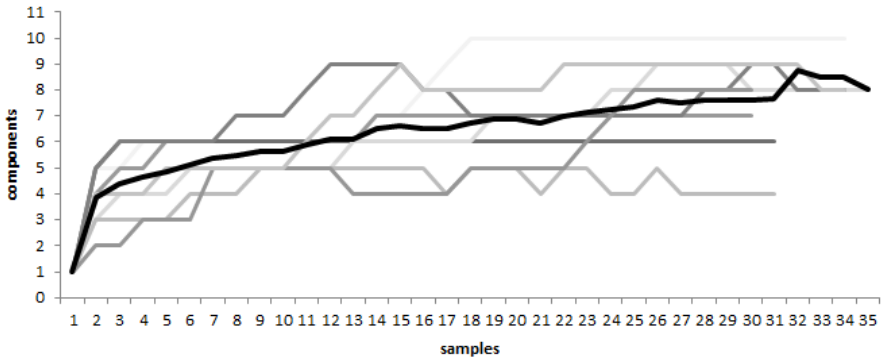

Fig. 2. Evolution of the number of components with number of data samples for eight example von Mises mixtures. Black line is the average trend.

Fig. 3 shows an example of the different outputs obtained by applying the IVMM framework (left) and the standard VMM approach (right). Fitting curves are shown in black, and the contribution of each component in grey. This particular example shows that in some cases the number of components given by IVMM or VMM can be different (here it is 5 and 3, respectively), but there is no implication that either model is better than the other.

4 Experimental validation

The main purpose of the IVMM framework is to produce faithful models of time of occurrence of events when saving all data is not possible or convenient, and standard mixture models cannot thus be applied. The key objective in our experimental validation is then to ensure that information loss in IVMM compared to non incremental methods, particularly standard VMM, is small.

In all experiments we have employed the same values for the fundamental parameters required by the IVMM. The period is in our case always set to 86400, the number of seconds in a day. The maximum number of components allowed for each single VMM is 7 (no limits are set for the total number of components in an incremental model). We have been using the Bayesian Information Criterion

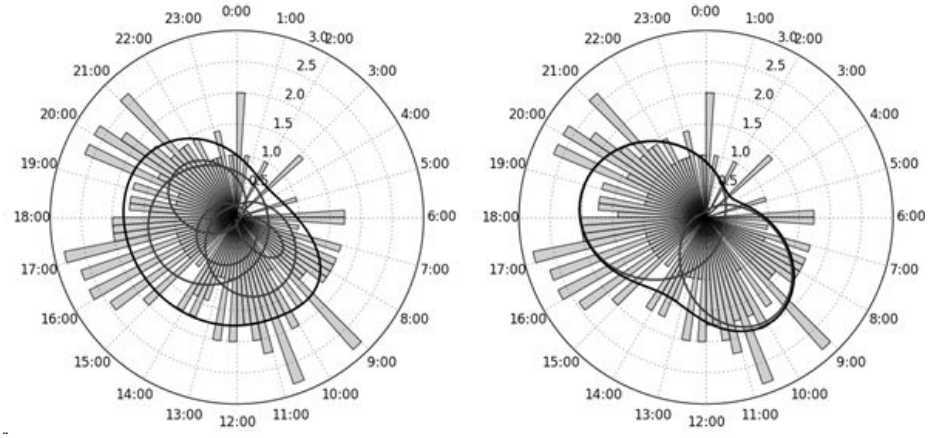

Fig. 3. Comparison between IVMM (left hand side) and VMM (right hand side) fitting (CHAD activity 12100, *care of baby*).

(BIC) for choosing the best number of von Mises components of each mixture, both for IVMM and VMM. The significance level α to compare with F value in equation 8 is set to 0.1. Different datasets and activities achieve better performance for different values of α, but a sensitivity analysis showed that there are no major effects for values between 0.05 and 0.15.

4.1 Testing within a dataset

Even when considering only time of day analysis, the IVMM technique offers a great range of practical applications. For example, it can be used to detect changes in habits, anomalous behaviours or people identities, by assessing the novelty of new data with respect to the accumulated experience.

In order to compare the discrimination capabilities of the models generated by IVMM and VMM, we employed both techniques for identifying atypical data, using only time information, by assessing their response to new samples coming from the same activity or from different ones. We have performed the test on 16 datasets from CHAD, on an average of 13.3 activities per dataset (we omitted all activities with less than 500 points in total, or with less than 3 samples). For each activity in a dataset, we built a full IVMM model, and then tested all samples from all other activities against it, using Equations 7 and 8. We have also tested each activity on its own models, by using a 3-fold validation to avoid testing on data used for building the model.

Fig. 4 shows the percentage of (correctly) passed tests for the same activity (full circles) and that of (wrongly) passed tests for different activities (empty circles). Average passed tests for all activities against themselves was 86.7±8.0%, while average passed tests for other activities was $54.3 \pm 14.9\%$ (experiments (a) and (b), respectively, in Tab. 1). This last figure may appear high as a false

positive, but it is expected, since most activities are consistently overlapping. For example, activities such as *personal hygiene* (code 14120) or *general household* (11000) are typically spread throughout the day and show in many cases very little regularity or clear patterns. These can thus be easily confused with many other activities on the base on pure time information. We also included placeholder activities such as *uncertain* (code U) or *missing* (code X). Moreover, all samples were drawn regularly (one per month) for each activity, with the consequence that, for some activities/datasets there were many points available and precise models could thus be built, whilst for others there were just a few points, resulting in very generic and sparse models.

Finally, tests performed by changing the order of presentation of samples have shown that, while IVMM is sensitive to sample order for small numbers of samples, models obtained from the same set of samples in different sequences are substantially indistinguishable from each others if the number of samples is large enough, as in the CHAD case.

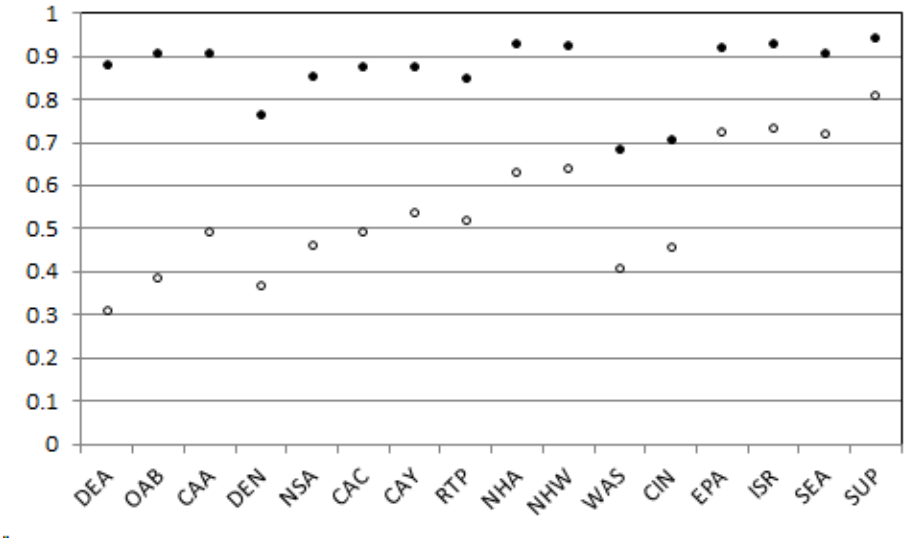

Fig. 4. Cross-activity testing on different datasets from CHAD, identified by their three letter codes. Full dots: passed tests on same activity (true positives); empty dots: average passed tests on other activities (false positives).

4.2 Comparison with standard VMM

To verify if and how much the incremental approach reduced the predictive capabilities of a standard, batch Mixture of von Mises, we performed the same tests as in experiments (a) and (b) in Tab. 1 on standard VMM, computed

Table 1. IVMM experiments, summary of results. Rec Same Act = Recall on target activity, FP Other Act = False Positives on different activities.

Experiment	Mean (%)	Std. Dev. (%)
(a) Rec Same Act, IVMM	86.7	8.0
(b) FP Other Act, IVMM	54.3	14.9
(c) Rec Same Act, VMM	89.8	5.0
(d) FP Other Act, VMM	52.6	20.2
(e) Generalisation, IVMM	80.5	9.2
(e) Generalisation, VMM	82.9	11.9

over all the available data. The results of tests (c) and (d) in Tab. 1 show that recall increased by about 3%, while false positives decreased by almost 2%. The expected performance loss of IVMM with respect to VMM is thus small. Quite importantly, the standard deviation of results is similar in the two cases, indicating that the incremental framework never carries to catastrophic failures in modelling the data. The opportunity of using VMM or IVMM would thus depend on the application, but it can be argued that the observed information loss is compensated by the increased long term usability of the IVMM approach.

4.3 Generalisation test

Sensitivity for a modelled activity is particularly useful if it generalises over datasets. As a validation test, we have thus performed an additional experiment, in which a mixture model created for an activity based on a certain dataset is tested with samples of the same activity obtained from other datasets, thus implementing a *leave-(n-1)-out* validation. The average percentage of successful tests over 37 activities (e) was 80.5 ± 9.2, compared to the same set value (a) 86.7 ± 8.0, showing that IVMM models were indeed able to generalise across datasets. Generalisation capabilities of standard VMM were only slightly better at 82.9, and had a higher variance in performance across activities. The detailed results depicted in Fig. 5 show that only for few particularly difficult activities the generalisation performance was below 0.7. Overall, our results show that faithful modelling of time of occurrence can be used to provide a useful prior to a classifier which combines this and other, non-temporal, features.

5 Conclusions

We have introduced in this work a new incremental von Mises mixture model for analysing and modelling time of occurrence of human activities. We have shown that our IVMM framework allows for both high quality representation of the data and efficient compression, being able to generalise over different datasets, with a small amount of information loss compared to standard VMM.

The gain in processing times and storage requirements of IVMM over VMM can be substantial for big datasets. In fact, space and time complexity of IVMM

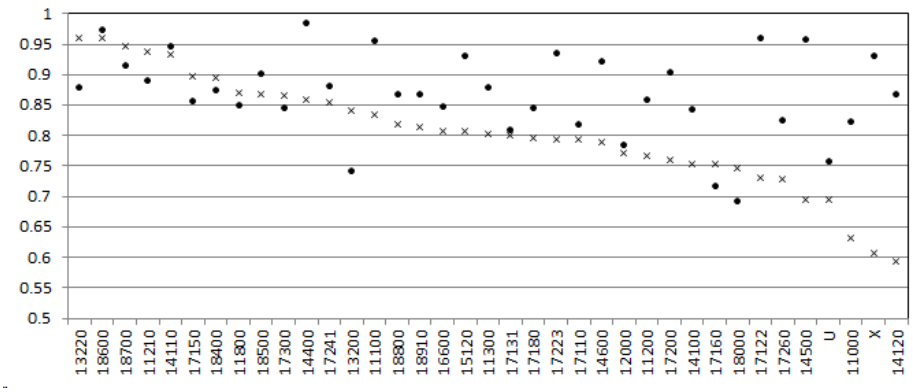

Fig. 5. Generalisation of activity identification across CHAD datasets. Full dots: passed tests on same dataset; crosses: average passed tests on other datasets.

depend only on the number of models in the mixture. Space requirements are negligible, and processing time is always instantaneous for the small number of models expected to compose a mixture (never more than a dozen in all our experiments). For VMM, space requirements increase linearly with data, and this becomes an issue after a sufficiently long time. Computing time also grows linearly with the amount of data, eventually making online updating of models infeasible. Millions of data items are generated daily by increasingly high numbers of sensors, and on our PC applying a standard von Mises Mixture to one million data points (maximum k = 12) took 16 minutes.

The proposed methodology can be applied to a number of different fields, and the fast growth of *big data* technologies and global connectivity suggests that tools such as IVMM, able to represent data in compact and efficient ways will be more and more required in the future. We are currently working on an extension of the IVMM approach in order to make it more dynamic and flexible to changing trends in the data. The plan is to make it *time-aware*, giving higher importance in the model to more recent data. The incremental nature of the approach makes such a goal relatively easy, for example by modifying at each new sampling the importance of each model component according to the last time it has been updated.

References

1. Arindam Banerjee and Sugato Basu. Topic models over text streams: A study of batch and online unsupervised learning. In *Proceedings of the 2007 SIAM International Conference on Data Mining*, pages 431–436, 2007.
2. Chris Brunsdon and Jon Corcoran. Using circular statistics to analyse time patterns in crime incidence. *Computers, Environment and Urban Systems*, 30(3):300 – 319, 2006.

3. Claudio Coppola, Tomas Krajnik, Tom Duckett, and Nicola Bellotto. Learning temporal context for activity recognition. In *European Conference on Artificial Intelligence (ECAI)*, 2016.
4. Tom Diethe, Niall Twomey, and Peter Flach. Bayesian modelling of the temporal aspects of smart home activity with circular statistics. In Annalisa Appice, Pereira Pedro Rodrigues, Vítor Santos Costa, João Gama, Alípio Jorge, and Carlos Soares, editors, *Proceedings of Machine Learning and Knowledge Discovery in Databases: European Conference*, pages 279–294. Springer International Publishing, 2015.
5. Paulo Martins Engel and Milton Roberto Heinen. Incremental learning of multivariate gaussian mixture models. In Antônio Carlos da Rocha Costa, Rosa Maria Vicari, and Flavio Tonidandel, editors, *Advances in Artificial Intelligence – SBIA Proceedings*, pages 82–91. Springer Berlin Heidelberg, 2010.
6. Hajo Holzmann, Axel Munk, Max Suster, and Walter Zucchini. Hidden Markov models for circular and linear-circular time series. *Environmental and Ecological Statistics*, 13(3):325–347, 2006.
7. Kurt Hornik and Bettina Grün. movMF: An R package for fitting mixtures of von mises-fisher distributions. *Journal of Statistical Software*, 58(10):1–31, 2014.
8. Alexander T Ihler and Padhraic Smyth. Learning time-intensity profiles of human activity using non-parametric bayesian models. In *Advances in Neural Information Processing Systems*, pages 625–632, 2006.
9. Thomas Kubiak and Cornelia Jonas. Applying circular statistics to the analysis of monitoring data. *European Journal of Psychological Assessment*, 23(4):227–237, 2007.
10. Alan Lee. Circular data. *Wiley Interdisciplinary Reviews: Computational Statistics*, 2(4):477–486, 2010.
11. S. Luengo-Sanchez, C. Bielza, and P. Larrañaga. Hybrid Gaussian and von Mises model-based clustering. In *European Conference on Artificial Intelligence (ECAI)*, 2016.
12. Kanti V. Mardia. Statistical approaches to three key challenges in protein structural bioinformatics. *Journal of the Royal Statistical Society Series C*, 62(3):487–514, 2013.
13. Kanti V. Mardia and Peter E. Jupp. *Directional Statistics*. John Wiley & Sons, 1999.
14. Antonello Maruotti. Analyzing longitudinal circular data by projected normal models: a semi-parametric approach based on finite mixture models. *Environmental and Ecological Statistics*, pages 1–21, 2016.
15. M. Shimosaka, T. Ishino, H. Noguchi, T. Sato, and T. Mori. Detecting human activity profiles with Dirichlet enhanced inhomogeneous Poisson processes. In *Pattern Recognition (ICPR), 2010 20th International Conference on*, pages 4384–4387, Aug 2010.
16. M. A. Song and H. B. Wang. Highly efficient incremental estimation of gaussian mixture models for online data stream clustering. In *SPIE 5803: Intelligent Computing: Theory and Applications III*, 2005.
17. G. D. Tipaldi and K. O. Arras. I want my coffee hot! learning to find people under spatio-temporal constraints. In *Robotics and Automation (ICRA), 2011 IEEE International Conference on*, pages 1217–1222, May 2011.
18. N. Ueda, R. Nakano, Z. Ghahramani, and G. E. Hinton. SMEM algorithm for mixture models. *Neural Computation*, 12(9):2109–28, 2000.

Simulation of Defect Prediction over Time in Building Façade

Kim, Wooram*, Jeong, Kichang**, Jeon, Yongdeok*, Park, Jinghong*, Jeong, Heeyoung*, Lee, Jaeseob*
*Division of Architectural Engineering, Dongguk University, Seoul, Republic of Korea
**Korea Institute of Construction Management, Seoul, Republic of Korea

Abstract. The purpose of this study is to propose a simulation model to predict the occurrence of defects over time. This simulation model estimates the total amount of defects and the amount of individual defects according to the characteristics of the target building based on past similar cases. It is considered that the prediction of the occurrence of defects over time, which is the result of this model, can be utilized throughout the life cycle of buildings. Especially, it can be used as a key indicator to prevent defects or to establish appropriate management level in the design stage. According to the results obtained by applying the proposed model, it is necessary to reflect the management level of the building and to supplement the defect related data. Therefore, further studies on the above-mentioned additional items will be needed to be practically used in the proposed model.

Keywords: Defect, Life Cycle, Simulation, Prediction, Management Level, Building Façade

1 Introduction

1.1 Background and purpose

Buildings are designed and constructed to meet the various requirements of the client and to produce the best value results. However, after the completion of the construction, the building becomes defective due to environmental and social factors as time passes, and the value of the building is lowered. Since the defects are the main cause of the depreciation of the buildings, appropriate measures are needed to prevent them in advance. The countermeasures against defects include prevention, repair, and replacement. Since these methods have different costs and impacts, each method should be analyzed first. For preliminary analysis of countermeasures, it is important to predict the occurrence of defects according to time and environmental factors.

In this study, the authors propose a simulation model to predict the external wall defects according to time and environmental factors.

1.2 Method

This study is conducted through the following process. First, the authors review the theories related to this study and suggest the need for the results of this study. The concept of simulation and its characteristics are presented. Second, build the database necessary for simulation implementation. Third, a simulation procedure for predicting defects based on a database is presented. Finally, the authors propose a defect prediction simulation technique.

The scope of this study is limited to building exterior walls, and the main focus is to introduce defect prediction simulation model.

2 Theoretical Considerations

2.1 The defect of a building

The defects of a building generally mean defects that reduce the value of its use due to the lack of quality of the finished structure, such as durability and strength, which are required to be provided by the contract. In general, defects are limited to those occurring during design and construction phases and after a certain period of time, and subsequent problems can be judged to be due to deterioration. However, the problems caused by deterioration do not

only occur over time, but can occur in different ways depending on the type of proactive response, because various factors such as use conditions and location conditions are involved in a complex manner.

In this study, the occurrence of defects was extended not only in the design and construction phase, but also in the period until the end of the building life, such as demolition of the building.

2.2 Relationship between defect and building characteristics

There are many factors that affect the defect, and it is rare that one factor acts independently. Factors affecting defects are elapsed years, geographical factors, social factors, conditions of use, design characteristics, construction characteristics, and maintenance neglect. In this regard, Kim(2016) analyzed the relationship between facade elements and defects, and Lourenço, et al. (2006) analyzed the effect of building shape, material, indoor temperature and humidity on defects. In addition, Neto and Brito (2012) analyzed the relationship between exterior walls and stone defects, and Kim(2017) analyzed the relationship between location conditions and defects. Until now, various studies are under way, but there is a limit to focus on relationship analysis.

2.3 Pixelization Method

The pixelization method divides the elevation of a building into sections of a certain size and creates data based on the representativeness of each section(see Figure 1). In other words, it means a method of simplifying the elevation of a building into a mosaic shape, inputting the characteristic of the unit division as data by referring to the unit division as one pixel (Lee, 2016).

This method has the feature that it cannot be applied when the elevation is not plane, and there is a limit that some loss occurs to the elevation factor information, but there is a characteristic that it can intuitively recognize and analyze the position and relation of each unit division. Therefore, in this study, the authors collected the data through the pixelization method and applied it to the simulation implementation.

	X1	X2	X3	X4	X5	X6	X7	X8	X9
Y12	1	1	1	1	1	1	1	1	1
Y11	1	1	1	1	1	1	1	1	1
Y10	1	1	1	1	1	1	1	1	1
Y9	1	1	1	1	1	1	1	1	1
Y8	2	2	2	2	2	2	2	2	2
Y7	2	3	3	3	3	3	3	3	2
Y6	2	3	3	3	3	3	3	3	2
Y5	2	3	3	3	3	3	3	3	2
Y4	2	2	2	2	2	2	2	2	2
Y3	2	3	3	3	3	3	3	3	2
Y2	2	3	3	3	3	3	3	3	2
Y1	2	2	2	2	2	2	2	2	2

Division			X_1Y_1	X_1Y_2	X_1Y_3	···	X_9Y_{12}
Façade elements		Entrance	2	3	3	···	1
		Window	2	2	2	···	1
		Stair	1	1	1	···	1
		Peak	2	3	3	···	1
		Dent	1	1	1	···	1
		Tilting	1	1	1	···	1
		Open	1	1	1	···	1
		Fixture	3	2	1	···	1
		etc	1	1	1	···	1
Defect	Physical damage	Crack	0	0	0	···	0
		Chipping	1	1	0	···	0
		Missing part	0	0	1	···	0
		Scaling	0	0	0	···	0
		Abrasion	0	0	0	···	0
		Glossy	0	0	0	···	0
	Pollution	Soiling	1	1	1	···	1
		Efflorescence	0	0	0	···	0
		Joint	0	0	0	···	1
		Chemical	0	0	0	···	0
		Staining	1	0	0	···	0
		Moisture	1	1	1	···	0
		Biological	0	0	0	···	0
		etc	0	0	0	···	0

*Legend : 1- none of facade element, 2-adjacent of facade element, 3-presence of facade element
*Façade element : Entrance, Window, Stair, Peak, Dent, Tilting, Open, Fixture, Etc
Fig. 1. "Pixelization Method" data collection process

3 Simulation model of defects occurrence over time

3.1 Concept

The authors propose a simulation model of defects occurring over time, which is a model for visually expressing the amount of occurrence and the amount of occurrence region of defects over time. This simulation is applied at the beginning of the life cycle of a building and aims at creating an effective defect response. The simulation process proposed in this study is shown in Figure 2.

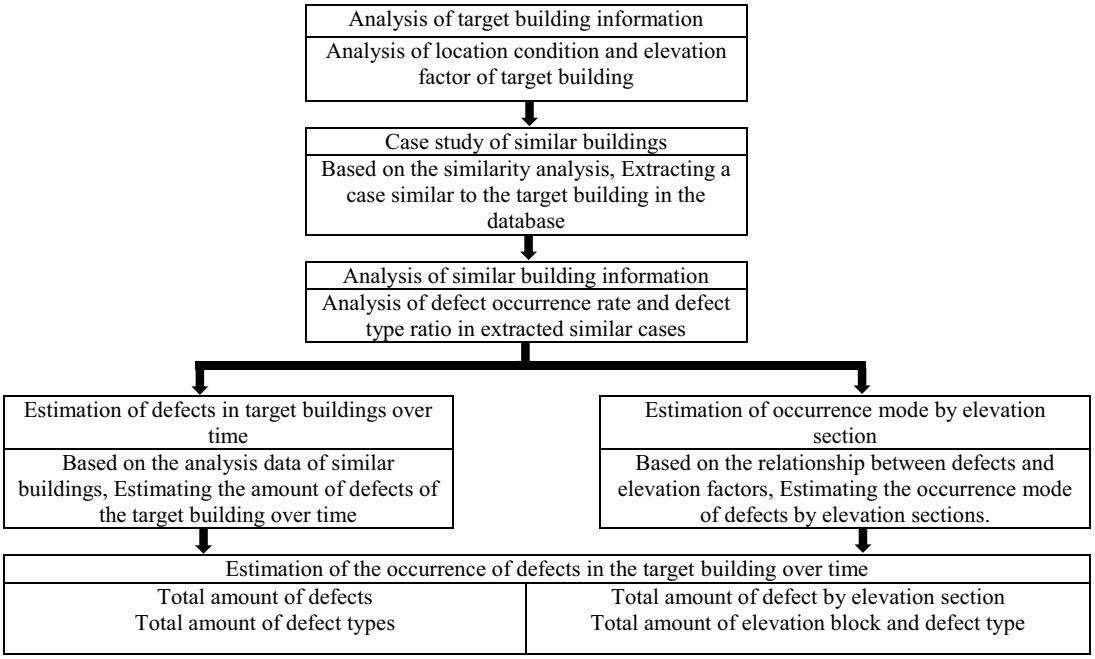

Fig. 2. Simulation process diagram

3.2 Database for simulation implementation

In order to implement the simulation, a database should be built in advance, which consists of variable setting, information collection, and database construction.

3.2.1 Variable setting

Variables are classified into the variables related to buildings and the variables related to defects.

3.2.1.1 Variables related to buildings

The information related to the buildings varies greatly depending on factors such as the shape of the building, the purpose and size of the building, the social environment factors such as the floating population and the size of the adjacent buildings, and natural environmental factors such as the weather, wind and sunshine hours. In this study, Based on the results of the previous research, the variables related to buildings were set as shown in Table 1.

Table 1. Variables related to buildings

Division		Description	Source
Building Factor	Year	Year of New, Extension or Remodeling	Building ledger
	Floor area	Floor area of building	
	Floor	Number of floors	
Façade Factor	Shape	Shape	Pixelization
	Material	Material	
	Entrance	Entrance	
	Window	Window	
	Stair	Stair	
	Peak	Peak	
	Dent	Dent	

	Tilting	Tilting	
	Open	Open	
	Fixture	Fixture	
	Etc.	Etc.	
Natural Factor	Temperature	Weather information of measuring points adjacent to the target building	KMA(2011), 1981~2010 CLIMATOLOGICAL NORMALS OF KOREA
	Humidity		
	Atmospheric Pressure		
	Wind		
	Cloud		
	Rain		
	Evaporation		
	Daylight hour		
	Direction	Façade direction of building	NGII
	Altitude	Altitude of building site	NGII
Social Factor	Population	Population of district	KOSIS
	Population density	Population density of district	KOSIS
	Floating population	Floating population of building	SE&MS
	District area	District area	KOSIS
	Land value	Land value of building site	Onnara Service
	Car amount	Car amount of district	KOSIS
	Road condition	Road condition of building site	Onnara Service
	Building density	Building density of district	KOSIS
	Aging index	Rate of over 30 years building	KOSIS

3.2.1.2 Variables related to defects

Defects appear in different patterns depending on the materials used, but they generally have common characteristics. Theclassification of defects based on common and similar features is shown in Table 2. (Kim Woo-ram, 2016) At this time, the result of collection of individual defects should be presented as an index so that the degree of defects in each case can be compared and analyzed. This study utilizes the method proposed by Kim (2016).

Table 2. Variables related to buildings

Division		Description
Physical damage	Crack	Resulting from separation of one part from another
	Chipping	Local loss of the surface
	Missing part	Local miss of the from wall
	Scaling	Detachment as a scale or stack of scales, not following structure
	Abrasion	Loss of material clearly due to a mechanical action
	Glossy	Aspect of a surface that reflects totally or partially the light
Pollution	Soiling	Deposit of a very thin layer of exogenous particles(e.g. Soot) giving a dirty appearance to the surface
	Efflorescence	Generally whitish, powdery or whisker-like crystals on the surface
	Joint	Contamination on the joint and surrounding due to joint material
	Chemical	Change of the color cause of chemical substance
	Rust	Change of the color cause of rust
	Moisture	Change of the color cause of moisture
	Biological	Colonization by plants and micro-organisms
Etc.	Etc.	Depreciation due to other factors

3.2.2 Information gathering

There is a practical limit to collecting information on variables in this study for all buildings. Therefore, it was considered that it would be reasonable to select the area considering the statistical significance of the characteristics of the building related variables, and to select any building in each area. At this time, consideration was given to the applicability of the simulation, so that commercial buildings less than 10 stories in the area were selected. Figure 3 shows the number of buildings selected and the district of buildings surveyed.

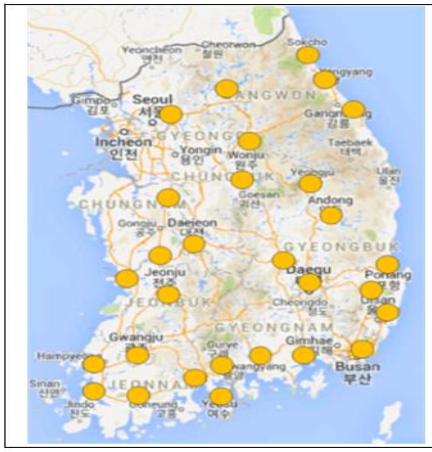

District	Number	District	Number
Namyangju	5	Jinju	5
Cheonan	8	Changwon	8
Daejeon	8	Pusan	5
Nonsan	8	Ulsan	5
Jeonju	7	Gyeongju	7
Gunsan	8	Pohang	8
Hampyeong	7	Daegu	8
Mokpo	8	Gumi	8
Jangheung	8	Andong	5
Suncheon	9	Yeongju	5
Yeosu	4	Gangneung	5
Gwangyang	6	Yangyang	4
Wonju	6	Sokcho	3
Chuncheon	8	Chungju	7

Fig. 3. Building survey area

3.2.3 Database construction

An example of a database constructed based on the above-mentioned process is shown in Figure 4, and the simulation is implemented by using the constructed database.

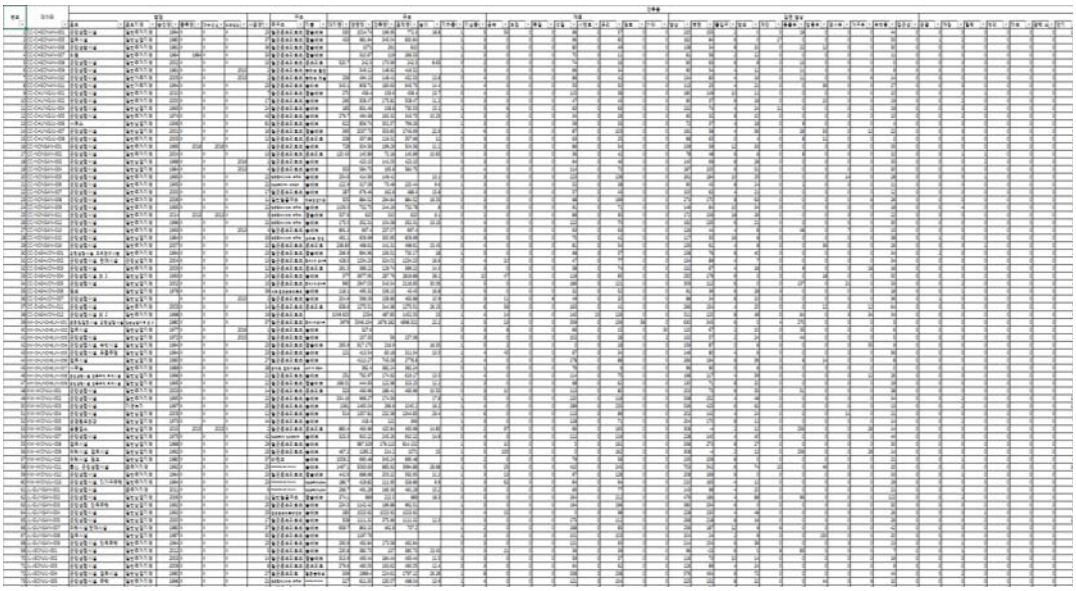

Fig. 4. Example of building a database

3.3 The defect-occurrence-prediction simulation model

Based on the database, the authors propose a simulation model to predict the occurrence of defects. The defect-occurrence-prediction simulation model is a method of estimating the value by case-based reasoning from past cases similar to the object to be analyzed. The model is largely divided into the predicted total amount of defects and the estimated elevation occurrence part according to over time. The explanation of each process is as follows.

3.3.1 Collection of target building information

Since this simulation is based on case-based reasoning, the authors need to collect information of the target building in advance to derive similar cases. In this case, building information collection targets the same variables as the database construction, and when information on some variables is missing due to limitations in the collection process, the information about the items is excluded in the evaluation of similarity. Table 3 summarizes the virtual cases set for the simulation.

Table 3. Virtual case building information

Division	Condition	Remarks
Building Factor	-. Floor area : 1,095.88 ㎡ -. Number of floors : 5 floors above ground, No basement	
Façade Factor	-. Number of elevation shape : 164	Wall, depression, window, and attachment.
Natural Factor	-. Average temperature : 14.3℃ -. Average Relative Humidity : 66.4% -. Average precipitation : 1,439mm -. Average daylight time : 2,321hrs	
Social Factor	-. Population density : 538 people/㎢ -. Official price : 1,830,000won -. Road conditions : Located on a wide road	

3.3.2 Deriving similar cases

Similar cases were derived to estimate the results of the target buildings. Similar case derivation is done by applying GA(Genetic Algorithm) / kNN(k-Nearest Neighbor) algorithm. The kNN algorithm is a method of comparing the cases with new cases by a certain similarity measure among the stored cases and then weighing them together. The similarity is a similarity measure between the input case information and the storage case information (Kim Jong-il, 2009). Because the total amount of defects and the types of defects should be estimated from the extracted cases, 30 cases of similar cases were selected to ensure the reliability of the results. Figure 5 shows the selection example.

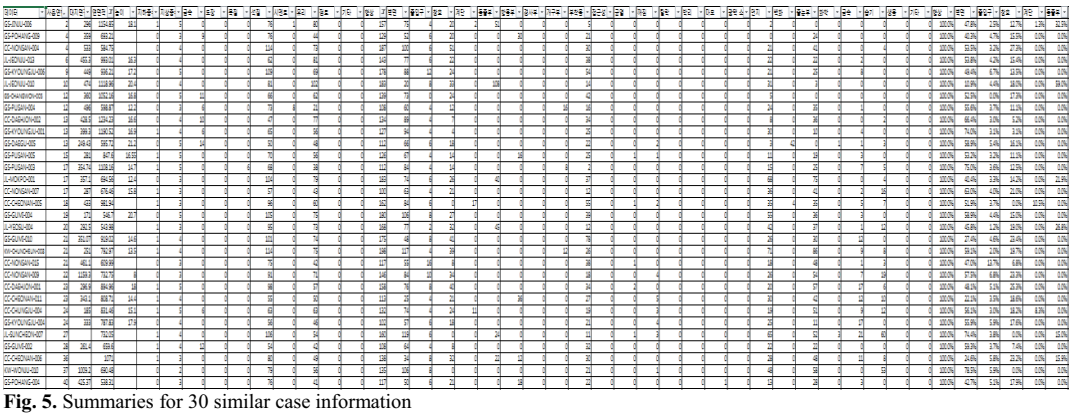

Fig. 5. Summaries for 30 similar case information

3.3.3 Estimation of total amount of defects

Based on the selected similar cases, the defects of the target buildings were estimated over time. Figure 6 shows the total amount of defects in the derived cases. Therefore, Table 4 shows the estimates of the total defects of the target buildings on a 5-year basis.

Table 4. Estimating total amount of defects for every five years

year	5	10	15	20	25	30
defect total amount estimation value	1.777	2.381	2.984	3.588	4.191	4.795

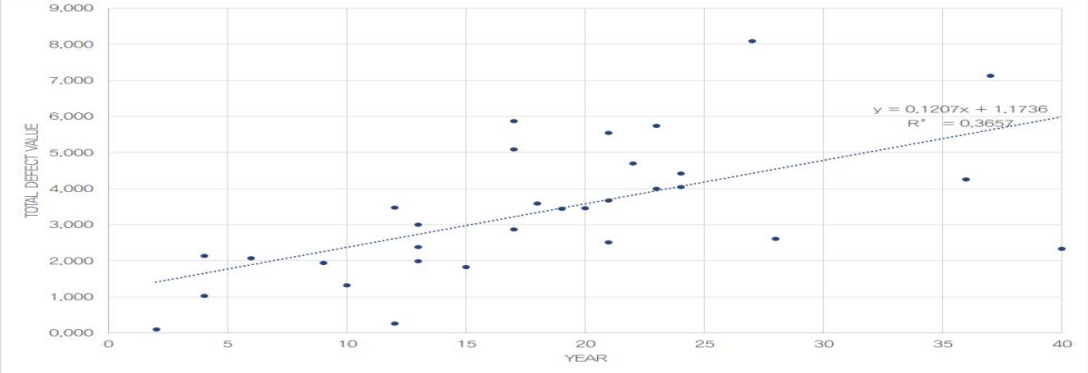

Fig. 6. Regression analysis chart for the defects

3.3.4 Estimation by individual elevation shape

Based on the incidence rate in the defect elevation shape, the amount of occurrence in the individual elevation shape was estimated. The relation between the defects and the elevation shape was referenced by Kim (2016). As for the building to be targeted, the elevation is formed like Figure 7. In case of Soiling, the possibility of occurrence at each elevation is analyzed as shown in Figure 8.

	X1	X2	X3	X4	X5	X6	X7	X8	X9	X10
Y20										
Y19	S	S	S/T	S/T						
Y18	S	S	S	S	S/T	S/T	S/T			
Y17	S	S	S	S	S	S	S	S/T	S/T	
Y16	S	S/W/D	S	S/D	S	S/D	S	S/D	S	
Y15	S	S	S	S	S	S	S	S	S	
Y14	S	S/W/D	S	S/W/D	S	S/W/D	S	S/W/D	S	
Y13	S	S	S	S	S	S	S	S	S	
Y12	S	S/W/D	S	S/W/D	S	S/W/D	S	S/W/D	S	
Y11	S	S	S	S	S	S	S	S	S	
Y10	S	S/W/D	S	S/W/D	S	S/W/D	S	S/W/D	S	
Y9	S	S/F	S/F	S/F	S	S	S	S	S	
Y8	S	S/W/D	S	S/W/D	S	S/W/D	S	S/W/D	S	
Y7	S	S/F	S/F	S/F	S/F	S/F	S/F	S/F	S	
Y6	S	S/W/D	S	S/W/D	S	S/W/D	S	S/W/D	S	
Y5	S	S/F	S/F	S/F	S/F	S/F	S/F	S/F	S	
Y4	S	S/W/D	S	S/W/D	S	S/W/D	S	S/W/D	S	
Y3	S	S/F	S/F	S/F	S/F	S/F	S/F	S/F	S	
Y2	S	S/E	S	S	S	S	S	S	S	
Y1	S	S/E	S	S	S	S	S	S	S	

Fig. 7. Relationship between defect and elevation shape

	X1	X2	X3	X4	X5	X6	X7	X8	X9	X10
Y20										
Y19	8.10%	8.32%	11.81%	12.12%						
Y18	7.68%	7.89%	8.11%	8.33%	11.82%	12.13%	12.45%			
Y17	7.28%	7.48%	7.69%	7.90%	8.12%	8.34%	8.57%	12.14%	12.46%	
Y16	6.90%	7.09%	7.29%	7.49%	7.69%	7.90%	8.12%	8.34%	8.57%	
Y15	6.53%	6.72%	6.90%	7.09%	7.29%	7.49%	7.70%	7.91%	8.13%	
Y14	6.19%	6.36%	6.54%	6.72%	6.91%	7.10%	7.30%	7.50%	7.71%	
Y13	5.86%	6.03%	6.19%	6.37%	6.55%	6.73%	6.91%	7.11%	7.30%	
Y12	5.55%	5.70%	5.87%	6.03%	6.20%	6.37%	6.55%	6.73%	6.92%	
Y11	5.25%	5.40%	5.55%	5.71%	5.87%	6.04%	6.20%	6.38%	6.56%	
Y10	4.97%	5.11%	5.26%	5.41%	5.56%	5.71%	5.88%	6.04%	6.21%	
Y9	4.70%	5.83%	5.99%	6.16%	5.26%	5.41%	5.56%	5.72%	5.88%	
Y8	4.45%	4.58%	4.71%	4.84%	4.98%	5.12%	5.27%	5.41%	5.57%	
Y7	4.21%	5.22%	5.37%	5.52%	5.68%	5.84%	6.00%	6.17%	5.27%	
Y6	3.98%	4.10%	4.21%	4.33%	4.46%	4.59%	4.72%	4.85%	4.99%	
Y5	3.77%	4.68%	4.81%	4.95%	5.09%	5.23%	5.38%	5.53%	4.72%	
Y4	3.56%	3.66%	3.77%	3.88%	3.99%	4.10%	4.22%	4.34%	4.47%	
Y3	3.37%	4.19%	4.31%	4.43%	4.56%	4.69%	4.82%	4.96%	4.22%	
Y2	3.18%	3.28%	3.37%	3.47%	3.57%	3.67%	3.78%	3.88%	4.00%	
Y1	3.01%	3.10%	3.19%	3.28%	3.37%	3.47%	3.57%	3.67%	3.78%	

Fig. 8. Possibility of soiling

As a result of analysis, it can be seen that Soiling occurs with higher probability to the upper layer. Figure 9 shows the estimation of the location with time. As shown in Figure 9, the Soiling can be seen to be enlarged as time elapses, and similar patterns are analyzed for other defects. In this case, the accuracy of the defect occurrence probability of the elevation should be supplemented by additional studies, and the reliability of the simulation of this study should be strengthened.

3.3.5 The defect-occurrence-prediction simulation model assessment

The results obtained from the above simulation process are as follows. First, an estimate of the total defects of the entire building over time. Second, estimates of defects type over time. Third, estimation of total defects by elevation shape. Fourth, an estimate of the occurrence of individual defects by the elevation shape.

The simulation process in this study has the following limitations. First, consideration of management level is excluded. The management level is one of the main indicators in the analysis of defects. Next, it is limited to the occurrence of individual defects. Actual defects differ in intensity and area within the unit area. However, in this study, data were collected by limiting the presence or absence of occurrence. This is an abbreviated data approach to examine the feasibility of the simulation.

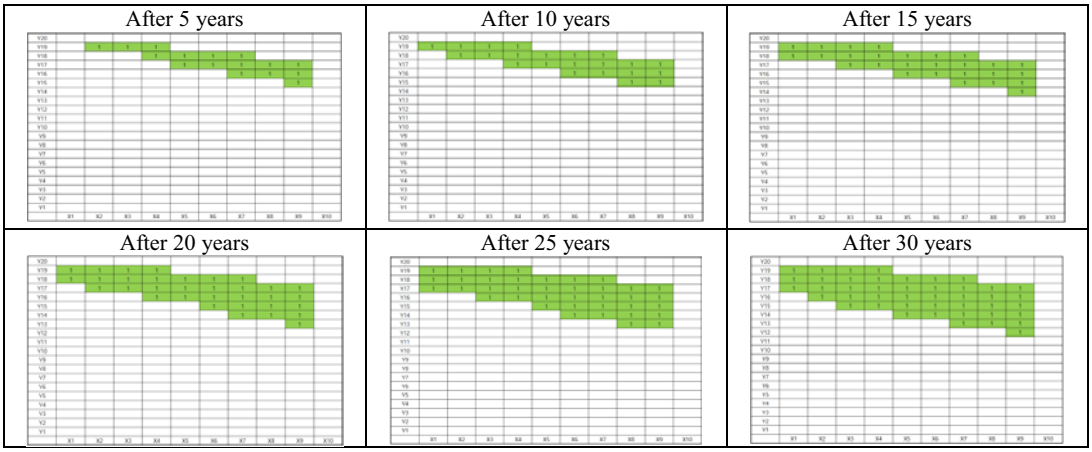

Fig. 9. Location of soiling over time

Considering the above, there is room for some corrections and additions, but considering the feasibility and practical application to be described later, it is considered appropriate to put it into practical use through additional studies related to the simulation.

4 Application of simulation model

The following is a description of how to use the simulation model of defects predicted over time according to the planning, design, construction , maintenance stages of the building.

4.1 Planning and Design Phase

The planning and design phase is a major step in designing the simulation model of this study. It aims at predicting the expected results at the use stage in the process of designing the building. In other words, it is possible to consider the expected maintenance cost or the level of depreciation by estimating the amount of defects over time based on the presented design book and conditions. By analyzing defects occurring in each elevation shape, It is possible to respond in the form of the application of the model at this stage plays a major role in establishing the basis for responding to defects in the building in advance.

4.2 Construction phase

The construction stage is to select a key management subject in consideration of the expected defects in the process of constructing each part of the building, and to establish a basis for actively responding through the change of the construction method. This can be regarded as a somewhat passive application compared to the design stage, but it is necessary to utilize it as a reference material in the construction process since the possibility of the prevention and

minimization of the defect can be additionally expected according to the quality of the construction.

4.3 Maintenance stage

The application at the maintenance stage can be broadly divided into two perspectives. First, estimates of the degree of future maintenance or expected depreciation can be estimated through estimates of the amount of defects that are expected of completed and in-use buildings. Based on this, discussions on whether to maintain or modify existing maintenance plans can be made. Second, it is in laying the foundations for the manual on maintenance measures. This is not limited to a specific building, and suggests a way to optimize the efficiency of maintenance by integrating analysis of existing buildings.

5 Conclusion

The purpose of this study is to propose a simulation model to predict the occurrence of defects over time. This simulation model estimates the total amount of defects and the amount of individual defects according to the characteristics of the target building based on past similar cases. The prediction of the occurrence of defects over time, which is the result of this model, can be considered as a major index to prevent the occurrence of such defects or to set appropriate management levels in the design phase. It is important to note that there are some items that require supplement, such as the estimation result of model application, the reflection of management level, and the supplementation of defect related data. However, considering the result and process, based on the additional study of this simulation model, it is reasonable to establish the foundation of practical use.

Acknowledgments. This research was supported by Basic Science Research Program through the National Research Foundation of Korea (NRF) funded by the Ministry of Science, ICT and Future Planning (No. 2015R1A2A2A01006826)

References

1. A. Silva, J. de Brito, P.L. Gaspar. : Service life prediction model applied to natural stone wall claddings (directly adhered to the substrate). Construction and Building Materials, 25, 9, (2011)
2. B. Lourenco Paulo, Luso Edurada, G. Almeida Manuela. : Defects and moisture problems in buildings form historical city centres: a case study in Portugal. Building and Environment, 41, 2, (2005)
3. Kim, W. R. : Value Analysis Model for Exterior Wall Finishing Material Considering Deterioration. Ph. D. Dissertation, Dongguk Univ., Seoul, (2016)
4. Kim, W. R., Jeon, Y. D., Shin, J. R., Jeong, K. C., Lee, J. S.: Correlation between Building Façade Elements and Defects through Pixelization Method. Korean Journal of Construction Engineering and Management, KICEM, Vol. 17, No.44, pp.40-48 (2016)
5. Lee, J. S., Jeon, Y. D., Jeong, K. C., Shin, Y. W., Kim, W. R.: A Method for Data-mining of Defects on Building Façade Elements. International Journal of Smart Home, 10(12)(2016)
6. Atsushi Takano, et al.: A multidisciplinary approach to sustainable building material selection: A case study in a Finnish context. Building and Environment, 82, pp.526-535(2014)
7. Anthony M, Smith, Glenn R. Hinchcliffe.: RCM-Gateway to World Class Maintenance. Blutterworth-Heinemann(2009).
8. Barletta, R.: An introduction to case-based reasoning. AI EXPERT, Vol.6, No.8, pp.42-49(1991)
9. CIB.: The Performance Concept and its Terminology(CIB Report No. 64). CIB(1982).
10. Daniel Castro-Lacouture, et al.: Optimization model for the selection of materials using a LEED- based green building rating system in Colombia. Building and Environment, 44, pp.1162-1170(2009)
11. Davenport, T. H., DeLong, D. W., Beers, M. C.: Successful Knowledge Management Projects. Sloan Management Review, 39(2), pp. 43-57(1998).
12. Fischer, M. A.: Constructability Input to Preliminary Design of Reinforced Concrete Structures. Technical Report CIFE at Stanford University, 64(1991)
13. George J. Ritz.: Total Construction Project Management. McGraw-Hill, Inc.(1994).
14. Holloway, L.: Materials Selection for Optimal Environmental impact in Mechanical Design. Material & Design,

19(4), pp.133-143(1998)
15. Iqbal Marie.: Perception of darkening of stone façades and the needs for cleaning. International Journal of Sustainable Built Environment, 2, pp.65-72(2013)
16. James R. Evans.: Statistics, Data Analysis, and Decision Modeling. PEARSON(2010)
17. Jee, D. H. and Kang, K. J.: A Method for Optimal Material Selection Aided with Decision Making Theory. Material & Design, 21(3), pp.199-206(2000)
18. Legget R. F.: Testing Building Constructions and The Performance Concept with Special Referents to the Work of ATM Committee E6 on "Performance of Building Construction" DBR Paper No.701 of the Division of Building Research. National Research Council of Canada(1976)
19. Natália Neto, Jorge de Brito.: Validation of and inspection and diagnosis system for anomalies in natural stone cladding. Construction and Building, 30, pp.224-236(2012)
20. Paulo B. Lourenço, et al.: Defects and moisture problems in buildings from historical city centres: a case study in Portugal. Building and Environment, 41, pp.223-234(2006)
21. PeBBu Domains.: Performance Based Design of Building Final Report. PeBBu(2005)
22. Peter Brimblecombe., Carlota M . Grossi.: Aesthetic thresholds and blackening of stone building. Science of the Total, 349, pp.175-189(2005)
23. Ronan Hébert, et al.: Cracks and strains on façade-cladding made of carbonate rock thin panels. Structural Survey, Vol. 30 No. 2, pp. 130~144(2012)
24. Rubistein, R. Y.: Simulation and Monte Carlo Method. John Wiley and Sons, New York(1981)

Signal Classification using Covariance Matrices: A Riemannian Geometry Framework

Shaelyn G. Divins[1], Joshua S. Beard[2], Nenad Mijatovic[3], Rana Haber[3], Anthony O. Smith[3], Adrian M. Peter[3], and Dean A. Clauter[4]

[1] Elizabethtown College, Elizabethtown PA 17022, USA,
[2] Seattle University, Seattle WA 98122, USA,
[3] Florida Institute of Technology, Melbourne FL 32901, USA,
[4] Air Force Technical Applications Center, Melbourne FL, USA
anthonysmith@fit.edu

Abstract. We present a novel framework for time series classification that leverages the geometric structure of covariance matrices when labeling signals. Our method maps each signal to a new multivariate localized feature signal (MLFS) representation, from which we compute a covariance descriptor. This robust MLFS covariance representation handles classification tasks where the sampling rates of the signals vary within a class, and classes. We demonstrate that simply using the k-nearest neighbor classification rule with the Riemannian metric between the MLFS covariance matrices produces state-of-the-art results on a number of standard datasets. Moreover, for the first time, we showcase results on the full Library of Typical Infrasonic Signals dataset which contains four categories of infrasound observations.

Keywords: Signal classification, Riemannian geometry, covariance matrices, infrasound

1 Introduction

Signal classification problems arise in a variety of application domains (e.g. monitoring, security, social media) with differing degrees of complexity. Real-world (one-dimensional) signals are noisy, possibly multi-channel (array observations), and may have differing observation lengths due to varying sampling rates or detection windows. Most often simplifying assumptions are made to facilitate the application of machine learning algorithms that were not originally designed with these real-word issues in mind. The machine learning framework we propose, breaks away from the mold of almost all current automated signal classification techniques [9, 19], and is able to inherently handle the aforementioned processing issues. The basic approach of contemporary methods can be simply summarized (at a high level) by the following two steps: (1) represent each signal as a feature vector, and (2) employ classification algorithms that learn using the feature vectors to decide the category labels. In our development, we jettison the use of feature vectors in favor of the richer descriptive power of covariance matrices

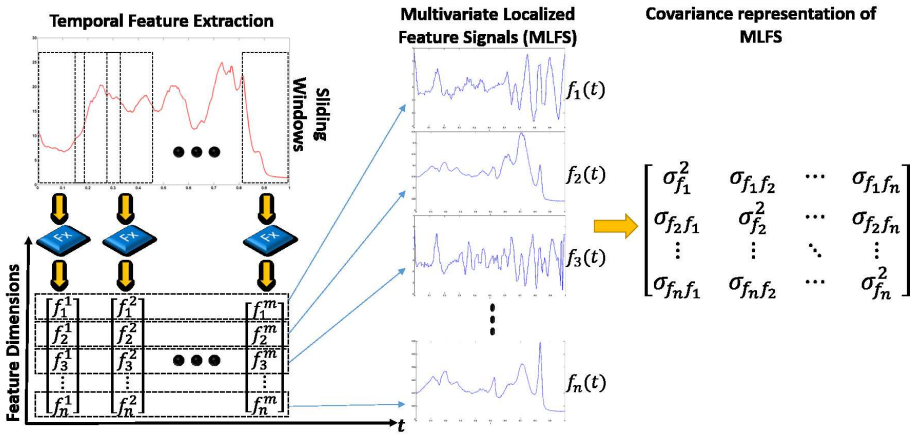

Fig. 1. MLFS Covariance Representation. Our approach maps each input signal (top left) to a multivariate localized feature signal (MLFS) covariance descriptor (far right). The dynamics of a signal are captured by extracting per-window feature vectors and then looking at the temporal signature across each feature dimension. The resulting time series, per feature dimension, are then used to estimate a covariance matrix that encodes all pairwise correlations between feature dimensions. Our k-NN classification algorithm uses the Riemannian metric between covariance matrices to classify the signals.

and follow suit by utilizing classification algorithms that leverage the geometric structure of covariance matrices.

Our classification framework begins by mapping each one-dimensional waveform to a multivariate localized feature signal (MLFS). (Note: We will often use the terms waveform, curve, and time series as all being synonymous with signal.) The MLFS is created by applying a sliding window to the original signal, and extracting various features for each window position. If n features are extracted for each window and there are m windows, then the resulting MLFS is a $n \times m$ matrix. Each row of the matrix can be considered as feature signal that captures the dynamics of how the feature evolves over time t. Next, we create a $n \times n$ covariance descriptor (matrix) using the m samples; see Fig. 1 for an illustration of our overall representation process. Once each signal is mapped to a covariance matrix, we utilize the Riemannian geometry of symmetric positive definite matrices (SPD), which encompasses covariance matrices, to develop our k-nearest neighbor classification rule. The use of covariance matrices as the fundamental object for classification adopts a relational view for classification rather than the independent dimensions approach of the usual feature vectors. Our results will favorably demonstrate the utility of encoding pairwise relationships between feature dimensions and their subsequent use for signal classification.

The remainder of the paper is organized as follows. We begin with a brief discussion of related work in signal classification, Section 2. This is followed

by Section 3 where we provide a detailed description of our MLFS covariance representation. Next, a high-level overview of the geometry of SPD matrices is discussed in Section 4. Experimental results in Section 5 showcase state-of-the-art performance on a number of standard time series datasets as well as an infrasound collection. Section 6 concludes with a summary discussion and potential directions for future research.

2 Related Work

Given the popularity of time series classification, numerous methods to classify them have been investigated. A majority of these techniques incorporate a feature-vector approach, where multiple features are extracted from a signal and then represented as vector in $\mathbb{R}^n$. Recently, Fulcher and Jones [9] investigated over 1,000 feature combinations for time series classification. They used a greedy forward selection method to sequentially search over the various features to obtain the combination that yield the highest accuracies under a linear classifier. Their results on the UCR time-series dataset [3] demonstrated the utility of feature-based methods, obtaining the top scores on many datasets. In [19], the authors gave comprehensive reviews of feature and distance methods for time-series classification, with final comparative analysis on two common methods: Euclidean distance and Dynamic Time Warping (DTW) [18]. Prekopcsk and Lemire[15] learn a Mahalanobis-like distance for signal classification . They claim that these metric learning techniques are comparable or even better than Large Margin Nearest Neighbor (LMNN) [6] and DTW when one nearest neighbor is used to classify time series data. Our experimental results demonstrate state-of-the-art performance on many UCR datasets, achieving a higher accuracy when compared to these methods. Our method only employs 10 features and does not employ a variety of classifiers or greedy feature selection.

Covariance-based signal classification has been previously explored by [11] and [1]. However, both of these methods worked directly on the amplitudes of the signals or their power spectral density curve. In addition, they assumed that all signals are of the same length and did not evaluate their technique on benchmark datasets like UCR. Our method is much more general, generating covariance matrices from multivariate localized feature signals and using the Riemannian covariance distance measure for discrimination between classes. These previous covariance methods are considerably different from what we develop with our MLFS and they provide no performance analysis of their methods. We illustrate the performance of our method on standard benchmarks and also showcase its performance on an infrasound dataset with varying length signals.

3 MLFS Covariance Descriptors

Most feature-based classification approaches extract global features that characterize the entire signal [9, 16]. Hence, any time-dependent feature characteristics are lost during the feature extraction process. We take an alternative approach

of extracting n features within a windowed portion of the signal. As we slide the window over our signal repeating the feature extraction, this process captures the dynamics of how these n features evolve over time. Hence, an original signal $f : \mathbb{R} \to \mathbb{R}$ now becomes a multivariate time series $F : \mathbb{R} \to \mathbb{R}^n$ of time evolving features. We refer to this new time series as a multivariate localized feature signal (MLFS), see Fig 1. It is possible to use any feature extraction technique of choice to construct F. In the present work, we have selected the following features: the identity map (returns the signal), instantaneous frequency (IF) [4], derivatives (first and second order), local statistics (standard deviation, skewness, kurtosis) , local binary pattern (LBP) [13], and stationary wavelet transform (SWT) [12]. The identity map , instantaneous frequency, wavelet, and derivative features do not require windowed samples, and are simply computed at each time index. The identity map and IF are defined as

$$\begin{aligned} \text{identity map:} I[f] &= f(t), \\ \text{IF:} \nu[f] &= \frac{1}{2\pi}\frac{d}{dt}\angle\mathcal{H}[f], \end{aligned}$$

where $\mathcal{H}[f]$ is the Hilbert transform [4] of signal f. The SWT is a time-invariant version of the usual discrete wavelet transform (DWT) and has been shown to be highly effective in noise filtering [5]. We use standard numerical approximations for the derivative order calculations. The local statistics are computed using the standard definitions and applied to only the windowed samples. The LBP was originally defined on images [13] to encode texture properties of local patches. We employ the same coding scheme as the original paper but now apply it to the windowed samples of a one-dimensional signal. For the features that operate on windowed-samples, we use an overlapping sliding strategy, shifting the window a single sample at a time over the signal. We construct a MLFS that is of the same duration as the original signal. Hence, for a signal f with m sample points, the resulting MLFS F will be of dimension $n \times m$. Once the MLFS F is created, it is straightforward to map this to a covariance matrix. We treat each of the m samples as independent and form the $n \times n$ sample covariance.

Notice that regardless of the length of the original signal, the resulting covariance descriptor will always be of the dimension corresponding to the n number of features. This allows us to apply our MLFS covariance descriptor to scenarios where signals may have different sampling rates. Admittedly, having too few samples in the original signal will result in a degenerate covariance estimate (not strictly positive definite). In our empirical evaluations, the shortest duration signals had at least 128 samples producing non-degenerate covariances.

4 Geometry of SPD Matrices

A (non-degenerate) $n \times n$ covariance matrix is identifiable as an element of the set of symmetric positive definite (SPD) matrices, denoted P_n. This space of SPD matrices also has the properties of differential Riemannian manifold [2] and can be proven to be a $n(n+1)/2$ dimensional open cone in the vector space of real

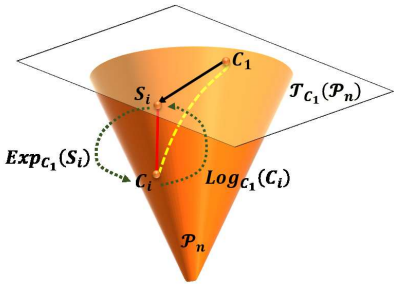

Fig. 2. Cone of Covariance Matrices. A covariance matrix is identifiable as an element on the cone of symmetric positive definite (SPD) matrices P_n. The cone is a differentiable manifold; hence, at a given covariance matrix C_1, a directional derivative (aka tangent vector) S_i is an element of the tangent space of symmetric matrices $T_{C_1}(P_n)$. The exponential (Exp) and log (Log) maps can be used to move back-and-forth between the manifold and the tangent space (locally).

symmetric $n \times n$ matrices, see Fig. 2. This additional structure immediately allows us to carry out familiar operations, like differentiation and integration, directly on the SPD set. In the present context, we are interested in the following intrinsic Riemannian distance [8] between two SPD matrices C_1 and C_2

$$d(C_1, C_2) = \left\| \log\left(C_1^{-1} C_2\right) \right\|_F = \sqrt{\sum_{i=1}^{n} \log^2(\lambda_i)}, \tag{1}$$

where, $\log(\cdot)$ is the principal matrix logarithm, $\|\cdot\|_F$ is the Frobenius norm, and λ_i's are the joint eigenvalues of $C_1^{-1} C_2$. An important property of the Riemannian distance between covariance matrices is that it is invariant under congruent transformations, i.e. $d(A^T C_1 A, A^T C_2 A) = d(C_1, C_2), \forall A \in GL(n)$, where $GL(n)$ represents the set of all $n \times n$ invertible linear transformations. The SPD manifold is also equipped with generalized logarithmic (Log) and exponential maps (Exp) that allow covariance matrices to be projected to the local tangent space and a tangent space element to be projected back to the manifold, respectively. The present work does not employ these maps, strictly focusing on the Riemannian distance measure between two covariance matrices.

In our signal classification framework we directly apply the Riemannian distance measure between MLFS covariance descriptors to determine similarity of signals. Hence, given a dataset of signals consisting of multiple classes, we begin by computing the MLFS covariance matrix of each signal using the features detailed in Section 3. In order to assign a class label to a test signal, we compute the distance between its covariance descriptor and all training data covariances. We then select the top k nearest distances and take the majority vote to assign the test signal an appropriate class label. It is possible to define various other

Table 1. UCR time-series data sets used for MLFS experiments. C presents the number of classes in a data set. N_{train} and N_{test} provides the number of signals in training and testing sets, respectively, while m denotes the number of time samples of each signal in the training and testing sets.

#	Data set	C	N_{train}/N_{test}	m
1	**Beef**	5	30/30	470
2	**Adiac**	37	390/391	176
3	**Lighting-7**	7	70/73	319
4	**50Words**	50	450/455	270
5	**Face (all)**	14	560/1690	131
6	**OSU Leaf**	6	200/242	427
7	**Fish**	7	175/175	463
8	**Swedish Leaf**	15	500/625	128
9	**Yoga**	2	300/3000	426
10	**Lighting-2**	2	60/61	637

distance measures over SPD matrices [7]. We plan to explore the effectiveness of these other measures in future extensions of the present work.

5 Experimental Results

We detail the performance of the MLFS covariance descriptor technique using time series datasets from the "UCR Time Series Data Mining Archive" [3] and the infrasound dataset from [20]. The UCR benchmark, we selected the ten most difficult datasets according to the classification accuracies listed by the repository's owners and in [9]. Details regarding the number of classes, training and test split, and length of the signals are provided in Table 1. Infrasound is a low frequency acoustic signal below audible. Most commonly generated by natural and man-made sources to include atmospheric turbulence, aurora, lightning, bolides, explosions, volcanoes, and rockets. The infrasound library contains four classes (Auroral Infrasonic Waves (AIW), Mountain Associated Waves (MAW), Microbaroms (MB), Volcanic Infrasound (VOL)) (see Figure 3). The number of signals per class, samples per signal are as follows: AIW$\{115, 768\}$, MAW $\{110, 768\}$, MB$\{(44, 512); (14, 480)\}$, VOL $\{65, 768\}$. AIW is generated in the upper atmosphere by the supersonic motions of large scale auroral electrojet during periods of intense geomagnetic disturbances at polar latitudes. MAW are generated by mountain ranges that create atmospheric turbulence when interrupting the tropospheric wind flow. MB are waves that result from the interaction at the surface of the sea during marine storms. VOL are produced by the volcanic eruption which causes a sudden displacement of a very large air mass by the rising cloud of hot gas. Notice that the Microbaroms class has a mix of two different length signals. This is a fairly common situation in infrasound processing due to automatic event detection algorithms producing different length detection windows for the same event observed by a multi-channel array[10, 14].

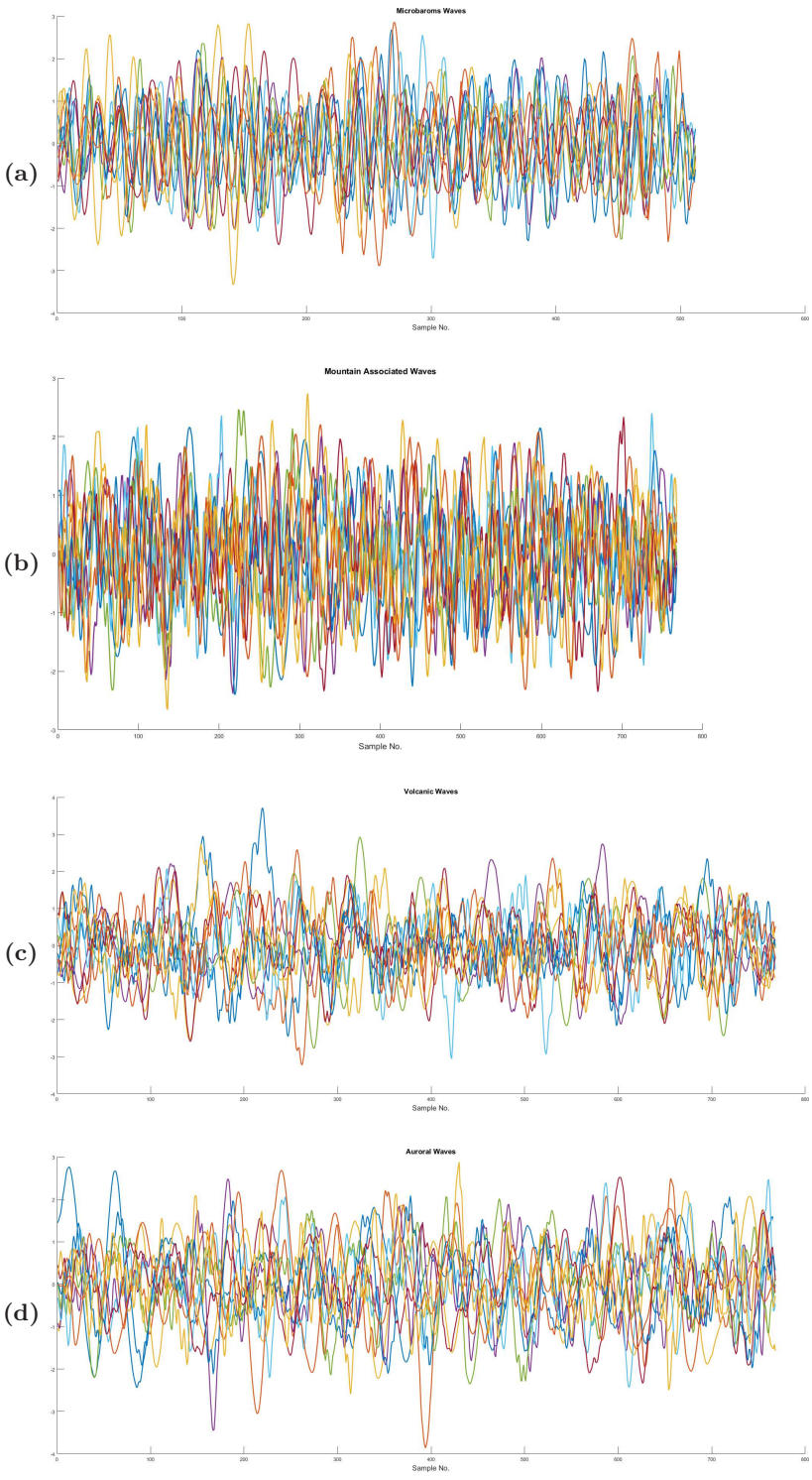

Fig. 3. Infrasound waveforms. Representative time series from each of the four infrasound categories (Library of Typical Infrasonic Signals). **(a)** microbaroms (MB), **(b)** mountain associated waves (MAW), **(c)** volcanic (VOL), **(d)** auroral infrasonic waves (AIW)

This data has been referenced previously [17]; however, they all extracted one or two classes from the entire dataset due to the issue of differing sample rates. Our reported results are a first for the entire collection. We performed a random 70/30 training versus test split of the data for our experiments.

	Dataset *(# classes)*	***Euclidean*** *1-NN(%)*	***DTW 1-NN*** *best WW(%)*	***Feature*** *linear (%)*	***MLFS*** *k-NN (%)*
UCR	**Beef (5)**	53.3	53.3	56.7	**83.3**
	Adiac (37)	61.1	60.9	64.5	**72.6**
	Lightning-7 (15)	57.5	71.2	56.2	61.6
	50 Words (50)	63.1	**75.8**	54.7	43.0
	FaceAll (14)	71.4	**80.8**	70.8	67.9
	OSU Leaf (6)	51.7	61.6	83.5	**87.6**
	Fish (7)	78.3	**84.0**	82.9	77.41
	Swedish Leaf (15)	78.9	84.3	77.3	**91.2**
	Yoga (2)	83.0	**84.5**	77.4	77.8
	Lightning-2 (2)	75.4	86.9	80.3	**88.9**
	Infrasound (4)	NA	NA	NA	**81.6**

Table 2. Classification accuracy on UCR (rows $2-10$) and Infrasound datasets (last row). The first column contains the name of the datasets. For UCR, we picked the ten most difficult. The columns reflect the previous state-of-the-art accuracies as reported in [9]. Results using Euclidean nearest neighbor, dynamic time warping (DTW) , and 'Warping window' which have been abbreviated as 'WW'. Our MLFS covariance descriptor k-NN classifier accuracies are in column five. We outperform the other methods on half of the UCR datasets by significant amounts. These are the first-ever results for the full infrasound collection.

Table 2 has a summary of our classification accuracies and provides comparative analysis to the other leading techniques as reported in [9, 3]. Table 3 provides a list of the parameters used to achieve the comparable results on the datasets. The features used to create the MLFS covariance descriptors and other free parameters are also included. In half of the UCR datasets, our MLFS covariance descriptor approach achieves the highest accuracies—all by significant amounts over the competing methods. It is worth noting that, in the present work, we have only explored the use of 10 localized features. Whereas contemporary methods such as [9] optimized close to 1,000 possible features to produce their classification results. In their experiments, training on larger datasets took over eight hours. The longest run time for any our datasets was on the order of a few minutes, for both training and testing together. The DTW method is able to achieve higher scores on some datasets largely due to the fact it non-linearly warps the signal. Being a strictly feature-based technique, we anticipate that with improved transformation-invariant features, our method can increase its performance on these remaining datasets. The results on the full infrasound li-

	Dataset (#classes)	*MLFS (Parameters)*
UCR	**Beef (5)**	$(1, 1, 9, \{1-10\})$
	Adiac (37)	$(1, 1, 9, \{1-5, 8-10\})$
	Lightning-7 (7)	$(1, 0, 15, \{1, 5, 9\})$
	50 Words (50)	$(1, 1, 9\{1-10\})$
	FaceAll (14)	$(1, 1, 9\{1-10\})$
	OSU Leaf (6)	$(5, 1, 9\{1-10\})$
	Fish (7)	$(1, 1, 15\{1-9\})$
	Swedish Leaf (15)	$(1, 1, 9, \{1-10\})$
	Yoga (2)	$(1, 0, 9, \{1-3, 5-10\})$
	Lightning-2 (2)	$(1, 0, 17, \{2-5, 8-10\})$
	Infrasound (4)	$(1, 0, 17, \{1-3, 5, 9\})$

Table 3. The MLFS free parameter choices are coded as a 4-tuple: (k value for NN, boolean flag for feature normalization, window size, feature coding). The feature coding is as follows: 1-identity map, 2-instaneous frequency, 3-1^{st} order derivative, 4-2^{nd} order derivative, 5-standard deviation, 6-skewness, 7-kurtosis, 8-median, 9-local binary pattern, 10-wavelet transform.

brary are also encouraging. The MLFS covariance descriptor approach produced a very favorable accuracy score on this difficult data; one that we anticipate will improve with better features.

6 Conclusion

In this work, we detailed a new approach to signal classification framework that leverages the relational modeling strengths of covariance descriptors. Specifically, our method transforms each signal to a multivariate localized feature signal (MLFS) from which we obtain our covariance matrix representation. We then perform k-NN classification by utilizing the Riemannian distance measure that leverages the geometric structure of covariance matrices. Our method was evaluated on the UCR time series benchmark and achieved the highest performance to date on several of the datasets. In addition, we demonstrated the robustness of the method in handling a difficult infrasound classification task where the signals were not of the same length, sometimes even within the same class. Our proposed method leverages the power of pairwise relational modeling through the use of covariance matrices, rather than the usual feature vector approach. Our experimental results perform favorably against other state-of-the-art feature based techniques, demonstrating the value of the MLFS covariance descriptor. In the future, we plan to investigate various other localized features and explore the use of other classification techniques like support vector machines that can be reformulated to work directly with covariance matrices.

Acknowledgments

The authors acknowledge partial support from NSF grants Nos. 1263011 and 1560345. Any opinions, findings, and conclusions or recommendations expressed

in this material are those of the authors and do not necessarily reflect the views of the NSF.

References

1. Alexandre Barachant, Stéphane Bonnet, Marco Congedo, and Christian Jutten. Classification of covariance matrices using a Riemannian-based kernel for BCI applications. *Neurocomputing*, 112:172–178, 2013.
2. W. M. Boothby. *An Introduction to Differentiable Manifolds and Riemannian Geometry*. Academic Press, San Diego, 2002.
3. Yanping Chen, Eamonn Keogh, Bing Hu, Nurjahan Begum, Anthony Bagnall, Abdullah Mueen, and Gustavo Batista. The UCR Time Series Classification Archive, July 2015.
4. L. Cohen. *Time Frequency Analysis: Theory and Applications*. Prentice Hall, 1994.
5. R. R. Coifman and D. L. Donoho. *Wavelets and Statistics*, chapter Translation-Invariant De-Noising, pages 125–150. Springer, 1995.
6. C. Domeniconi, D. Gunopulos, and Jing Peng. Large margin nearest neighbor classifiers. *IEEE Transactions on Neural Networks*, 16(4):899–909, July 2005.
7. I. L. Dryden, A. Koloydenko, and D. Zhou. Non-euclidean statistics for covariance matrices, with applications to diffusion tensor imaging. *The Annals of Applied Statistics*, 3(3):1102 – 1123, 2009.
8. Wolfgang Förstner and Boudewijn Moonen. A metric for covariance matrices. In *Geodesy-The Challenge of the 3rd Millennium*, pages 299–309. Springer, 2003.
9. B. D. Fulcher and N. S. Jones. Highly comparative feature-based time-series classification. *IEEE Transactions on Knowledge and Data Engineering*, 26(12):3026–3037, December 2014.
10. F. M. Ham, I. Iyengar, B. M. Hambebo, M. Garces, J. Deaton, A. Perttu, and B. Williams. A neurocomputing approach for monitoring Plinian volcanic eruptions using infrasound. *Procedia Computer Science*, 13:7–17, 2012.
11. Yili Li and KM Wong. Signal classification by power spectral density: An approach via Riemannian geometry. In *2012 IEEE Statistical Signal Processing Workshop (SSP)*, pages 900–903. IEEE, 2012.
12. G. Nason and B. Silverman. *Wavelets and Statistics*, chapter The Stationary Wavelet Transform and some Statistical Applications, pages 281–299. Springer, 1995.
13. T. Ojala, M. Pietikainen, and T. Maenpaa. Multiresolution gray-scale and roation invariant texture classification with local binary patterns. *IEEE Transactions on Pattern Analysis and Machine Intelligence*, 24(7):971–987, July 2002.
14. S. Park, F. M. Ham, and C. G. Lowrie. Discrimination of infrasound events using parallel neural network classification banks. *Nonlinear Analysis: Theory, Methods & Applications*, 63(5):e859–e865, 2005.
15. ZoltÃ¡n Prekopcsák and Daniel Lemire. Time series classification by class-specific Mahalanobis distance measures. *Adv. in Data Analysis and Classification*, 6(3):185–200, 2012.
16. Fabrice Rossi and Nathalie Villa. Support vector machine for functional data classification. *Neurocomputing*, 69(7-9):730–742, 2006.
17. ND Tsybulskaya, SN Kulichkov, and AI Chulichkov. Studying possibilities for the classification of infrasonic signals from different sources. *Izvestiya, Atmospheric and Oceanic Physics*, 48(4):384–390, 2012.

18. Kongming Wang and Theo Gasser. Alignment of curves by dynamic time warping. *Annals of Statistics*, 25(3):1251–1276, 06 1997.
19. Xiaoyue Wang, Abdullah Mueen, Hui Ding, Goce Trajcevski, Peter Scheuermann, and Eamonn J. Keogh. Experimental comparison of representation methods and distance measures for time series data. *Data Mining and Knowledge Discovery*, 26:275–309, February 2012.
20. CR Wilson, JV Olson, and R Richards. Library of typical infrasonic signals. *Report Prepared for ENSCO (subcontract no. 269343-2360.009)*, 1(4), 1996.

Combining Support Vector Regression with Scaling Methods for Highway Tollgates Travel Time and Volume Predictions

Amanda Yan Lin[1,2], Mengcheng Zhang[1,2], and Selpi[1]

Department of Mechanics and Maritime Sciences[1] and
Department of Computer Science and Engineering[2],
Chalmers University of Technology, SE-412 96 Göteborg, Sweden
{yanlin,mezhang}@student.chalmers.se
selpi@chalmers.se

Abstract. Toll roads or controlled-access roads are very commonly used, e.g. in Asia. Drivers expect to drive smoother and faster on the toll roads compared to on regular roads. However, long queues on toll roads, particularly at the tollgates, often happen and create many problems. Being able to accurately predict travel time and volume of the tollgates would allow appropriate measures to improve traffic flow and safety to be taken. This paper describes a novel investigation on the use of scaling methods with Support Vector Regression (SVR) for highway tollgates travel time and volume prediction tasks as well as an investigation of the most important features for these tasks. Experiments were done as part of the Knowledge Discovery and Data Mining (KDD) Cup 2017. Suitability of certain scaling methods for different types of time series and reasoning why certain features are important for these tasks are also discussed.

Keywords: Traffic flow prediction; traffic volume prediction; highway tollgates; time series analysis; SVR with scaling; robust scaling; SVR;

1 Introduction

Transportation problems are increasing along with urbanisation and motorisation. Traffic jams are common scenes in most roads. Toll roads or controlled-access roads are no exception. Highway tollgates, in particular, have been well known as bottleneck in traffic networks, especially during rush hours and holidays. Reliable methods to predict future traffic flow are important for traffic management authorities as well as the road users. With precise predictions, the traffic regulators can decide how to deal with traffic jam or some other problems of highway tollgates (e.g.,to deploy additional toll collectors and/or divert traffic at upstream intersections). Such accurate predictions can also help road users to plan their journey.

In this paper, we address two prediction tasks, travel time prediction and traffic volume prediction, as part of a competition in Knowledge Discovery and Data Mining (KDD) Cup 2017 [7]. The tasks are to predict travel time and

volume for a given road and tollgate during rush hours, knowing the previous two-hour data and some days before. Support Vector Machine for Regression (SVR) with different scaling methods are applied for these prediction tasks.

Travel time is a measurement of time from a designated start point to a designated end point, which is the raw element for a number of performance measures in different transportation analyses [3]. Traffic volume is a record of the number of vehicles at a designated point. Both travel-time and volume calculations depend on many stochastic factors, such as weather conditions, holidays, time of the day, season, etc, making the tasks of predicting travel time and traffic volume become challenging.

SVR is a version of SVM for regression that was proposed in 1996 by Vladimir N. Vapnik, Harris Drucker, Christopher J. C. Burges, Linda Kaufman and Alexander J. Smola [10]. It is an application of SVM (Support Vector Machine) for time-series forecasting [3]. SVR has shown some good performances in different areas, such as financial time series forecasting [4], stock market price forecasting [5] and real-time flood stage forecasting [6]. It was applied for travel-time prediction and achieved good result as well [3]. Those successful results motivate us to use SVR for travel time and volume predictions. However, compared to the previous work, we introduce a novel approach by combining scaling methods with SVR. Furthermore, we also introduce a special approach to fill in the missing data for these tasks.

The rest of this paper is arranged as follows. Section 2 describes the raw data and the two prediction tasks. Section 3 introduces the methods used. We describe and discuss the results of our experiments for travel time prediction and traffic volume prediction in Section 4 and Section 5, respectively. The conclusions are presented in Section 6.

2 Data and tasks description

The data used here was provided by organizers of the KDD Cup 2017. Four different types of data set were provided: road network topology of the area (Fig. 1), vehicle trajectories, traffic volume at tollgates, and weather data for the area.

The road network is represented as a sequence of road links and implemented as a directed graph (Fig. 2). The network includes three intersections (A, B, C) and three tollgates (1, 2, 3). These make up six routes: routes from Intersection A to Tollgates 2 and 3, routes from Intersection B to Tollgates 1 and 3, and routes from Intersection C to Tollgates 1 and 3 (Fig. 1).

Vehicle trajectories data lists time-stamped records of actual vehicles driving from intersections to tollgates. Specifically the data about vehicle trajectories consists of intersection ID, tollgate ID, vehicle ID, date time when the vehicle enters the route, trajectory (sequence of link traces with each trace consists of a link ID, time entering the link, and total travel time (in seconds) passing the link), and total travel time (in seconds) from the intersection to the tollgate. Only data about vehicles using Amap navigation software was included in the

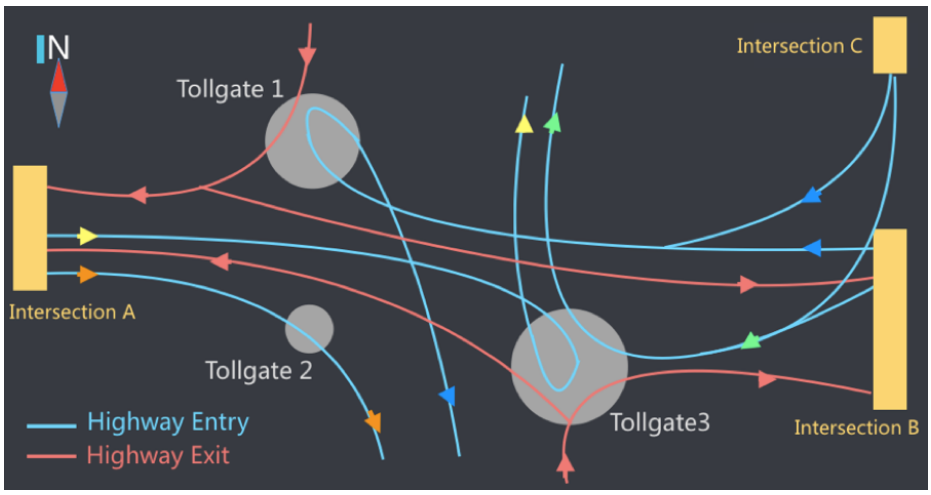

Fig. 1. An overview of road network. This figure is taken from the description of KDD CUP 2017 [7].

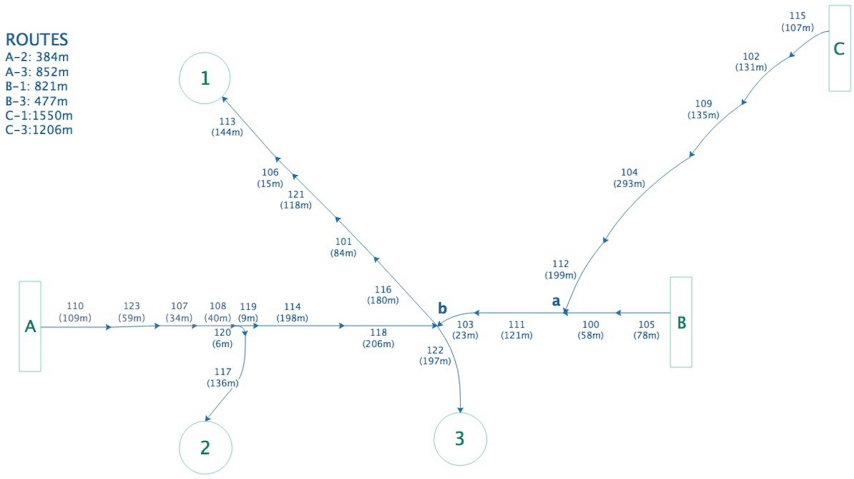

Fig. 2. The link-representation of road network. Each route is composed by a sequence of links, each link is represented by an arrow. The value without parentheses over a link represents the unique id of the link and the value in parentheses represents the length of the link. The total length of each route is presented at the upper left corner.

vehicle trajectories data [7]. Therefore, there was quite a lot of missing data in the provided data set.

The data about traffic volume at tollgates consists of date time when a vehicle passes the tollgate, tollgate ID, direction (0 for entry, 1 for exit), vehicle model (integer 0 to 7 to indicate the capacity of the vehicle), boolean values indicating if the vehicle uses electronic toll collection (ETC) or not, and vehicle type (0 for passenger vehicle, 1 for cargo vehicle).

The weather data consists of weather related measurements collected every three hours in the target area. Specifically the data consists of date, hour, air pressure (in hundred Pa), sea level pressure (in hundred Pa), wind direction (in degrees), wind speed (in m/s), temperature (in Celsius degrees), relative humidity, and precipitation (in mm).

The objectives of this project are to address the following tasks as best we can:

- Task 1 : Travel time prediction. Given training data described above for the period of 19th July to 24th October, estimate the average travel time of vehicles for each route during rush hours (08:00-10:00 and 17:00-19:00), per 20-minute interval, for the period of 25th October to 31st October.
- Task 2: Traffic volume prediction. Given training data described above for the period of 19th September to 24th October, estimate the volume for each of the five tollgate-direction pairs (Tollgate 1-entry, Tollgate 1-exit, Tollgate 2-entry, Tollgate 3-entry, and Tollgate 4-exit) during rush hours, per 20-minute interval, for the period of 25th October to 31st October.

3 Methods

Experiments using SVR with and without scaling methods were conducted. The scaling methods investigated include Standard-scaling, Mix-Max-scaling, and Robust-scaling (Section 3.2). The use of different combinations of features was also tested. Cross-validation was used to measure the predictive performance of each model built using different scaling method and feature set.

3.1 Support Vector Regression

The Support Vector Regression (SVR) uses the same principles as the support vector machine for classification (SVC). The goal of SVR is to find a function, with at most ϵ deviation from the actual target y. The problem can be written as a convex optimization problem

$$\begin{aligned} \text{minimize} \quad & \frac{1}{2}\|w\|^2 \\ \text{subject to} \quad & y_i - \langle w, x_i \rangle - b \leq \epsilon \\ & \langle w, x \rangle + b - y_i \leq \epsilon \end{aligned}$$

If the problem is not feasible, slack variables ξ_i, ξ_i^* are introduced. The formulation becomes

$$\begin{aligned} \text{minimize} \quad & \frac{1}{2}\|w\|^2 + C\sum_{i=1}(\xi_i + \xi_i^*) \\ \text{subject to} \quad & y_i - \langle w, x_i\rangle - b \leq \epsilon + \xi_i \\ & \langle w, x\rangle + b - y_i \leq \epsilon + \xi_i^* \\ & \xi_i, \xi_i^* \geq 0 \end{aligned}$$

where the constant $C > 0$ is penalty parameter. More about SVR can be found in [2][13].

In this project, we used the SVR implementation from Scikit-learn library in Python [12].

3.2 Scaling methods

Scaling is a way to systematically alter all the values in a data set. The simplest method, Min-Max-scaling, is rescaling the data to a fixed range, usually $[0, 1]$ or $[-1, 1]$. For a given data set X, a Min-Max-scaling is typically done via the following equation:

$$lb + \frac{X - min(X)}{max(X) - min(X)}(ub - lb),$$

where lb is a lower bound of the range, ub is an upper bound [15].

One common and widely used scaling method is Standard-scaling. The idea of Standard-scaling is to make the values of each feature in the data have zero-mean and unit-variance, according to

$$\frac{X - mean(X)}{standard\ deviation(X)}.$$

Another scaling method is Robust-scaling, which is based on the median and the interquartile range. If the data set X contains many outliers, Robust-scaling often gives better results [11]. Robust-scaling is defined as

$$\frac{X - median(X)}{IQR},$$

where IQR is interquartile range [11].

3.3 Error measurements and validation method

Mean Absolute Percentage Error (MAPE) has been chosen by KDD cup team to evaluate the predictions.

For Task 1 (travel-time prediction), the MAPE is defined

$$MAPE_{travel-time} = \frac{1}{R}\sum_{r=1}^{R}(\frac{1}{T}\sum_{t=1}^{T}|\frac{d_{rt}-p_{rt}}{d_{rt}}|) \quad (1)$$

In the Eq. 1 above, d_{rt} and p_{rt} are the actual and predicted average travel time for route r during time window t.

For Task 2 (volume prediction), the MAPE is defined:

$$MAPE_{volume} = \frac{1}{M}\sum_{m=1}^{M}(\frac{1}{T}\sum_{t=1}^{T}|\frac{f_{mt}-p_{mt}}{f_{mt}}|). \quad (2)$$

In the Eq. 2, M is the number of tollgate-direction pairs (1-entry, 1-exit, 2-entry, 3-entry and 3-exit), T is the number of time windows in the testing period, and f_{mt} and p_{mt} are the actual and predicted traffic volume for a specific tollgate-direction pair m during time window t.

Cross validation was used to assess the predictive performance of our models.

4 Travel time prediction

In order to build a model that can make good estimations for Task 1, we were given training data for the period of 19th July to 17th October, and was asked to estimate the average travel time, per 20 minutes interval, from designated intersections to tollgates during rush hours (08:00-10:00 and 17:00-19:00) for the period of 18th October to 24th October. For the purpose of testing our models, data from the previous two-hours of the rush hours period to be predicted were used as test-data.

Since there are many missing data, particularly in routes B-1, B-3, C-1 and C-3, the missing data were filled in before experiments were run. In these four routes, the missing data were filled in by applying "complementary" method and then linear interpolation. "Complementary" method means that if there is no data in a 20-minute time window of a route, this missing part will be filled in by the relevant part of other route(s) data. For instance, if the data for a specific time window is missing in route C-3, we gather part of data for that specific time window from route C-1 to get Intersection C to point p (C $\rightarrow$ p) and part of data from route B-3 to get point p to Tollgate 3 (p $\rightarrow$ 3) to fill the missing part in C-3 (see Fig. 2). Similar ways were done for the routes B-1, B-3 and C-1. For the routes A-2 and A-3, the missing data were only filled in by linear interpolation.

As we assumed the travel time of a given route in the morning and afternoon are independent of each other, the same prediction procedure was applied for every route in the morning and afternoon respectively. SVR was used as the main prediction method. After testing with several experiments (with different values chosen randomly), radial basis function (RBF) was chosen as the kernel function, with $\gamma = 0.005$ and $\epsilon = 0.5$. Parameter C was chosen according to

$$max(|\bar{y} + 3\sigma_y|, |\bar{y} - 3\sigma_y|) \quad (3)$$

where $\bar{y}$ and σ_y are the mean and the standard deviation of the y values of training data [9]. SVR with RBF has been found less sensitive to preprocessing of data such as scaling [15].

Many cross-validation experiments were conducted: using different scaling methods, different amount of training data, and different features sets. Two basic features were always included: time window position and the previous two-hour travel time. *Time window position*: The prediction is for every 20-minute time window of the rush hours (rush hours are defined as 08:00-10:00 and 17:00-19:00), therefore the rush hours are split into six 20-minute time windows. For example, for the rush hours in the morning, 08:00-08:20 is the first position, 08:20-08:40 is the second, and so on. *Previous Two-hour travel time*: They are the two-hour travel time data before the rush hours. For instance, the previous two-hour travel time for the rush hours in the morning are the data from 06:00-08:00. They are also split into six 20-minute time windows.

Obviously, the travel-time are a result of dynamic interplay of traffic demand and traffic supply [14]. High traffic flow indicates high traffic demand. Factors influencing traffic demand include temporal effects like daily and weekly pattern, as well as holiday [3]. Factors influencing the traffic supply includes crashes, road works, weather, etc. For this reason, extra features were added one by one and the predictive performance of each resulting model was evaluated by comparing the validation and the prediction result. Additional features that can capture the traffic demand are as follows. *Special days*: working days, weekends, or holidays. *Tollgate volume*: this feature is the volume of the tollgate of the target route. For example, when predicting the travel time of route A-2, the tollgate volume is the volume at tollgate 2 (shown in Fig. 2). *Adjacent tollgate volume*: this feature is the volume of the predicting route's adjacent tollgate. If two routes come from the same intersection and go to different tollgates, one of the two is the predicting route, as a result, another is the adjacent route. The tollgate of the adjacent route is called adjacent tollgate. For example, for route A-2, the adjacent tollgate volume is the volume of tollgate 3.

Table 1. Average MAPE from 13-fold cross-validation experiments with features: time window position and two-hour travel time; Data used for training are from 19/7 to 17/10; Data used to test are from 18/10 to 24/10;

Scaling method	validation result	prediction of test data
Robust-scaling	0.2302	0.1886
Standard-scaling	0.2296	0.1902
Min-Max-scaling, [0,1]	0.2276	0.1935
No scaling	0.2464	0.2081

The predictive performances of using SVR combined with different scaling-methods are presented in Table 1 and Table 2. The results of the experiments using two different amount of training data sets are shown in Table 1 (training

Table 2. Average MAPE from 4-fold cross-validation experiments with features: time window position and two-hour travel time; Data used for training are from 19/9 to 17/10; Data used to test are from 18/10 to 24/10;

Scaling method	validation result	prediction of test data
Robust-scaling	0.1901	0.2073
Standard-scaling	0.1888	0.2083
Min-Max-scaling, [0,1]	0.1811	0.1928
No scaling	0.1977	0.2001

Table 3. Average MAPE from different cross-validation experiments with Min-Max-scaling in range [0,1] and features: time window position and two-hour travel time; Data used for training are from 19/9 to 17/10; Data used to test are from 18/10 to 24/10;

Extra Feature(s)	validation result	prediction of test data
None	0.1811	0.1928
Special days	0.1795	0.1920
Tollgate volume (vol)	0.1770	0.1931
Tollgate volume & special days	0.1773	0.1938
Tollgate vol. & adjacent tollgate vol.	0.1771	0.1900

data from 19/7 to 17/10) and in Table 2 (training data from 19/9 to 17/10). The results of the experiments using different sets of features are shown in Table 3.

Comparing Table 1 and Table 2, one can see that using fewer weeks data for training gives better validation results, but worse prediction results. This also means that our experiments did not show anything conclusive about the influence of season on the travel time prediction (note that the period 19/7 to 18/9 is summer season). Similarly, our experiments (not shown here due to space) suggest that most of the weather-related features did not increase predictive performance of our models. If any, only temperature was worth adding. Based on the experiments with the same amount of training data (data from 19th September to 17th October), adding more features (tollgate volume and adjacent tollgate volume) provides better validation and prediction results (Table 3).

The best experimental result from the travel-time prediction task appears in Table 1 by applying Robust-scaling with the two basic features (the previous two-hour travel time and time window position). From Table 1 and Table 2, using scaling method gives better predictive performance compared to no scaling. Robust-scaling seems to be particularly good for time series with more varying patterns (that include summer season), while Min-Max-scaling seems to be particularly good for time series with more similar patterns.

5 Traffic volume prediction

Similarly to Task 1, in order to build a good model for Task 2, we addressed the following sub-task: given training data for the period of 19th September to 17th October, estimate the average volume for each of the tollgate-direction pairs, per 20 minutes interval, during rush hours (08:00-10:00 and 17:00-19:00) for the period of 18th October to 24th October.

As we assumed the volume of a given tollgate direction pair in the morning and in the afternoon are independent of each other, the same prediction procedure was applied for all tollgate direction pairs in the morning and afternoon respectively. The average error of all tollgate direction pairs was calculated using MAPE defined in Eq. 2. SVR was applied for the volume prediction too. After testing with several experiments (with different values chosen randomly), radial basis function (RBF) was chosen as the kernel function with $\gamma = 0.01$ and $\epsilon = 0.01$. Parameter C was chosen according to Eq. 3.

The feature selection strategy for volume prediction was similar as for travel time prediction (Section 4). The two basic features here were time window position and the previous two-hour volume. The previous two-hour volume means the two hours volume before the rush hours to be predicted and time window position is similar as in Section 4.

The results presented in Table 4 and 5 was obtained by The results of performances by using different scaling-methods combined with SVR are presented in Table 4. In addition, the comparisons of performances for different features are presented in Table 5.

Traffic volume depends on many factors, including time of day, day of week, holiday, weather, etc. For this reason, an additional feature called special days (explained in Section 4) to capture the holidays and weekends effect was added. Moreover, other features (basically extracted from the provided volume data), including the number of vehicles with ETC and the number of vehicles have vehicle model n ($n \in [0, 7]$), were also tested in our experiments (see Table 5).

Table 4. Average MAPE from cross-validation experiments with features: time window position and two-hour volume; Data used for training are from 19/9 to 17/10; Data used to test are from 18/10 to 24/10;

Scaling method	validation result	prediction of test data
Robust-scaling	0.2710	0.1472
Standard-scaling	0.2717	0.1502
Min-Max-scaling, [0,1]	0.3467	0.1526
No scaling	1.0374	0.3128

For the volume prediction, applying SVR combined with a scaling method gives a huge improvement to the result compared with only using SVR, see Table 4. And again, it appears that Robust-scaling is particularly good for time series

Table 5. Average MAPE from cross-validation experiments with Robust-scaling and features: time window position & two-hour volume; Data used for training are from 19/9 to 17/10; Data used to test are from 18/10 to 24/10;

Extra Feature	validation result	prediction of test data
None	0.2710	0.1472
special days	0.2647	0.1470
use ETC	0.3605	0.1705
vehicle model (veh. mod.) 1	0.2854	0.1472
veh. model 2	0.2759	0.1621
veh. model 3	0.3240	0.1531
veh. model 4	0.3138	0.1476
veh. model 5	0.3107	0.1504
veh. model 6	0.2708	0.1476
veh. model 7	0.2738	0.1447
veh. model 7 & special days	0.2682	0.1440
veh. mod. 6 & veh. mod. 7 & special days	0.2691	0.1436

with more varying patterns. Note that the period of 1st October to 7th October is a big holiday period in China and it is widely known that the traffic volume is very different during that period compared to usual days.

The best performance shows up in Table 5, with features: two-hour volume, time window position, vehicle model 6, vehicle model 7, and special days. Table 5 suggests that the feature special days is a very important feature for traffic volume prediction.

6 Conclusion

In this experiment, we demonstrated the application of SVR with scaling methods for travel-time prediction over a very short distance in rush hours and tollgate traffic volume prediction in rush hours. The performances of SVR-predictor combined with three scaling methods (Robust-scaling, Standard-scaling, and Min-Max-scaling) were compared. Our results suggested that SVR with a scaling method performs better compared to without scaling, Robust-scaling is particularly good for time series with varying patterns, and Min-Max-scaling is particularly good for time series with more similar patterns.

Features that capture different travel-time/volume influencing factors were analyzed in the experiments. In general, SVR combined with scaling provides a more accurate prediction than without scaling, especially for volume prediction. Adding extra features (travel-time/volume influencing factors) did not give significant improvement.

When our model was applied to Task 1, the mean absolute percentage error of the travel-time prediction is around 0.19, which differs by only 0.02 from the best result obtained by other contestants (this is a competition task, the best prediction result was announced). Similarly, when our model was applied to

Task 2, the mean absolute percentage error of the volume prediction is around 0.144, which differs by only 0.03 from the best result. We conclude, for the training data containing many outliers (like holiday data) and without deep analysis of the data (no data pruning), SVR combined with a scaling method can still provide reasonable prediction results.

Acknowledgments. S. acknowledges strategic funding support from Chalmers Area of Advance Transport while writing this paper, and thanks "Knut och Alice Wallenbergs Stiftelse - Jubileumsanslaget" for a travel grant to ITISE2017.

References

1. Ding, A., Zhao, X., Jiao, L.: Traffic flow time series prediction based on statistics learning theory. In: Proceedings of the IEEE 5th international conference on intelligent transportation systems, 727-730 (2002)
2. Smola, A. J., Schlkopf, B.: A tutorial on support vector regression. Statistics and computing, 14(3), 199-222 (2004)
3. Wu, C. H., Ho, J. M., Lee, D. T.: Travel-time prediction with support vector regression. IEEE transactions on intelligent transportation systems, 5(4), 276-281 (2004)
4. Lu, C. J., Lee, T. S., Chiu, C. C.: Financial time series forecasting using independent component analysis and support vector regression. Decision Support Systems, 47(2), 115-125 (2009)
5. Yeh, C. Y., Huang, C. W., Lee, S. J.: A multiple-kernel support vector regression approach for stock market price forecasting. Expert Systems with Applications, 38(3), 2177-2186 (2011)
6. Yu, P. S., Chen, S. T., Chang, I. F.: Support vector regression for real-time flood stage forecasting. Journal of Hydrology, 328(3), 704-716 (2006)
7. KDD2017, `https://tianchi.aliyun.com/competition/information.htm?spm=5176.100067.5678.2.ru0ea4&raceId=231597`, accessed on 15 March 2017
8. Müller, K. R., Smola, A. J., Rtsch, G., Schlkopf, B., Kohlmorgen, J., Vapnik, V.: Predicting time series with support vector machines. In: International Conference on Artificial Neural Networks (pp. 999-1004). Springer Berlin Heidelberg (1997, October)
9. Cherkassky, V., Ma, Y.: Practical selection of SVM parameters and noise estimation for SVM regression. Neural networks, 17(1), 113-126 (2004)
10. Drucker, H., Burges, C. J., Kaufman, L., Smola, A., Vapnik, V.: Support vector regression machines. Advances in neural information processing systems, 9, 155-161 (1997)
11. RobustScaler, `http://scikit-learn.org/stable/modules/generated/sklearn.preprocessing.RobustScaler.html`, accessed on 15 March 2017
12. SVR, `http://scikit-learn.org/stable/modules/generated/sklearn.svm.SVR.html`, accessed on 15 March 2017
13. Basak, D., Pal, S., Patranabis, D. C.: Support vector regression. Neural Information Processing-Letters and Reviews, 11(10), 203-224, (2007)
14. van Lint., J. W. C.: Reliable travel time prediction for freeways: bridging artificial neural networks and traffic flow theory. TRAIL Research School, (2004)
15. Crone, S. F., Guajardo, J., & Weber, R.: The impact of preprocessing on support vector regression and neural networks in time series prediction. In: DMIN (pp. 37-44), (2006)

Comparative analysis of criteria for filtering time series of word usage frequencies

Inna A. Belashova, Vladimir V. Bochkarev

Kazan Federal University
420008, Russia, Kazan, Kremlyovstaya 18
inkin91-91@mail.ru, vbochkarev@mail.ru

Keywords: Nonlinear filters, wavelet thresholding, runs test, genetic algorithm

Abstract. This paper describes a method of nonlinear wavelet thresholding of time series. The Ramachandran–Ranganathan runs test is used to assess the quality of approximation. To minimize the objective function, it is proposed to use genetic algorithms - one of the stochastic optimization methods. The suggested method is tested both on the model series and on the word frequency series using the Google Books Ngram data. It is shown that method of filtering which uses the runs criterion shows significantly better results compared with the standard wavelet thresholding. The method can be used when quality of filtering is of primary importance but not the speed of calculations.

1 Introduction

Recently, a new tool for studying the dynamics of languages has become available. The Google Books Ngram corpus was created on the basis of a great number of digitized printed sources which have been published since the 16th century. It contains data on the frequency of words and phrases in different years for 8 languages [1].

Most of the printed materials were drawn from over 40 university libraries around the world. Each page was scanned and then digitized by means of optical character recognition (OCR). Publishers provided additional materials in physical and digital form and along with the libraries provided information describing the date and place of publication. Cultural trends can be quantitatively investigated via computational analysis of this corpus as frequency of word usage depends on various social factors [1]. The corpus is also used for creation of automatic translation systems and investigation of language evolution.

Frequencies of words, especially rare ones, fluctuate strongly. Therefore, it necessary to perform filtering of frequencies series to distinguish significant outbursts of the use of words associated with various social, political, and cultural processes, from random fluctuations.

The Google Books Ngram Viewer service created by the developers of the corpus uses moving average for this purposes. This, however, results in distortion of the

adfa, p. 1, 2011.

series, and impedes the analysis of linguistic changes associated with various historical events. Using linear smoothing filters also shows unsatisfactory results.

Nowadays filtering methods based on statistical significance are wieldy used, in particular wavelet-thresholding. The method of wavelet-thresholding is based on the criterion of the minimum mean square error and is successfully used for the series which fluctuation probability distribution is close to the normal law. This approach can be incorrect in case of the series which distribution differs significantly from the normal one. The maximum-likelihood criterion is more universal than the methods mentioned above but requires knowing the law of time series value distribution. In practice, the distribution law is not always known a priori.

For example, it is often accepted that frequency distribution (at least the distribution of rare words) is governed by Poisson's law [3]. Filtering of time series with Poisson distribution was considered in number of works (see, for example, [4]). Nevertheless, there are a number of reasons to believe that a more complex model is required to describe the frequency distribution of words than the Poisson law. Thus, it is shown in [5] that the average value of the modulus of the relative change in frequency of words over an annual period is well approximated by a power function of the frequency of the words *f*. The following relationship is fulfilled in a wide range of frequencies for the English language corpus of the Google Books Ngram.

$$\left\langle \frac{|\Delta f|}{f} \right\rangle \sim f^{-0.316} \tag{1}$$

Such behaviour of the frequency increments is most likely caused by the mutual influence of the authors on each other, and contradicts the assumption of the Poisson law for the frequency of words.

Thus, the development of filters that use robust quality criteria is an urgent task. In this paper, one of the possibilities of applying runs test is considered.

2 Method

The major challenge is to find a representation of the analysed data as a wavelet series with a small number (compared to the number of samples) of terms.

$$y(t) = \sum_{i \in I} c_i \psi_i(t) \tag{2}$$

Here $y(t)$ is a filtered time series, $\psi_i(t)$ is a wavelet function corresponding to some scale and shift parameters (which are encoded by the multi-index i), c_i is the corresponding coefficient, I is a set of nonzero wavelet coefficients. It is assumed that the size of the set I is much smaller than the length of the approximated time series.

As in the case of standard wavelet-thresholding, it is necessary to choose which terms of the wavelet series will be used for the approximation and estimate the optimum values of the corresponding wavelet coefficients. If the obtained approximation

is good, the approximation errors are weakly correlated and don't form long runs (the sequences of points for which the error has the same sign), thereby allowing us to separate significant details of the times serious from the random ones.

The Ramachandran–Ranganathan runs criterion [6] is used in this paper. In accordance with this criterion, the objective function is written as the sum of the squares of the lengths of the runs l_i:

$$R = \sum_i l_i^2 \tag{3}$$

We have used the Ramachandran–Ranganathan criterion because it is more powerful than other runs criteria, such as the Wald-Wolfowitz criterion. Thus, the calculation of the objective function for a given set of nonzero coefficients I and values of the coefficients c_i is performed in the following order:

- The approximation (2) is calculated and the approximation errors are found;
- Runs are identified and their length is determined for a number of errors.
- Statistics R is calculated by the formula (3).

Since R is a discrete function, determining the value of the coefficients c_i by the criterion (3), only interval estimations can be obtained for them. If it is required to obtain concrete numerical values for c_i, we need to modify expression (3), replacing R by a continuous function with similar properties. It should be note that to do it, the length of the runs $l_{i:}$ can be written as follows:

$$l_i = \left| \sum_{t \in S_i} \operatorname{sign}(\varepsilon_t) \right| \tag{4}$$

Here, S_i is the set of samples forming the i-th runs, and ε_t is the approximation error at instant of time t. We can replace the function sign(x) in a given expression by a monotonically increasing smooth function that takes values from -1 to 1, for example, tanh(x). Thus, we obtain a «soft» runs criterion with statistics.

$$\tilde{R} = \sum_i \left[\sum_{t \in S_i} \tanh \frac{\varepsilon_t}{\lambda} \right]^2 \tag{5}$$

In this case, the value of the scale parameter λ included in this expression can be chosen close to the expected level of additive noise.

To minimize the objective function R it is expedient to use stochastic optimization algorithms. In this paper, a genetic algorithm is used to find the minimum. The positive features of genetic algorithms are their applicability to both continuous and discrete functions (which is especially important in our case), as well as the possibility of finding a global minimum error [7].

Construction of genetic algorithms begins with generation of populations containing a given number of chromosomes. The chromosomes evolve in the process of

many iterations (generations). Similarly, the chromosome is evaluated during each iteration, in other words, the value of the objective function is calculated for the given chromosome. The next generation, called the descendant, is created with the help of two operators - the crossing operator (crossing-over) and the mutation operator. In the first case, the descendant is generated from two chromosomes by crossing the parents according to a given rule (one-point, two-point crossing-over), in the second case, the descendant is obtained by randomly changing the gene of one chromosome. After that, a new offspring is generated from the parental individuals and descendants selected according to the values of the objective function, and the remaining individuals are removed to maintain the population size constant.

The algorithm of filtering using genetic algorithms can be divided into two key blocks:

- Defining a new set of non-zero coefficients;
- Varying values of non-zero coefficients to minimize the statistics of the Ramachandran–Ranganathan runs criterion.

The set of non-zero coefficients of the wavelet decomposition is given by the chromosome. The chromosome is a string of zeros and ones, where «0» corresponds to the coefficients set to zero, and «1» corresponds to non-zero coefficients in formula (1). The genetic algorithm varies the positions of «1» in the chromosome, and there is a set at which the R statistic is minimal.

The most important condition for optimization is the constancy of the number of non-zero coefficients. It should be taken into account when developing the function of crossover and mutation, and also when creating the initial population. A uniform crossover was used in this work. The mutation function was developed taking into account the conservation of the number of non-zero coefficients: if «0» has changed to «1» in the chromosome, an inverse operation occurs in some other locus.

The so-called continuous genetic algorithm is used at the stage of varying the values of non-zero coefficients [7, 8]. Here the chromosome is no longer a bit string, but a vector of non-zero coefficients.

By setting the run of the value of non-zero coefficients, each of these coefficients is modified. Initial population is formed. In this case, crossing-over will occur in a completely different way than it was previously described. Here a mixed crossover is used, in other words, one descendent from the interval is generated by two progenitors:

$$\left[\min(x,y)-\alpha\Delta,\ \max(x,y)+\alpha\Delta\right],\ \ \Delta=\max(x,y)-\min(x,y) \tag{6}$$

Here, x, y are the values of the coefficient of two progenitors, and the parameter α is a small number that determines how much the coefficient of the descendent can go beyond the interval $[x, y]$.

When specifying the mutation function, it is necessary to ensure that the coefficient is not zeroed. After that, calculation of the optimized function is performed. The operation is repeated until the algorithm stop condition is satisfied.

Often, a stop condition is used that stops the algorithm if the average relative change of the best value of the quality function is less than the specified limit accuracy after the specified number of iterations or equals to it. This condition was used in this paper.

3 Testing on model series

The proposed filter was tested on model series with a different law of distribution of variations. To perform testing, we used the example «Bumps» from the Wavelet Toolbox of the MATLAB package. The series with normal, Poisson and stable distributions (with the parameter α equal to 1.3), which mathematical expectation coincided with the selected test signal, were generated. Thus, the noise was additive for normal and stable distribution. For the case of the Poisson law, the numbers *n(t)* were generated for each time *t* in accordance with the distribution.

$$P(n,t)=\frac{\lambda^n(t)}{n!}e^{-\lambda(t)} \tag{7}$$

The parameter of the Poisson law $\lambda(t)$ changed in proportion to the signal from the example «Bumps», but a constant was added to it so that all values were positive. In this case, the minimum and maximum values of $\lambda(t)$ were equal to 0.5 and 15, respectively. The three selected distributions are very different in their properties, which makes it possible to compare the filtering algorithms in different conditions.

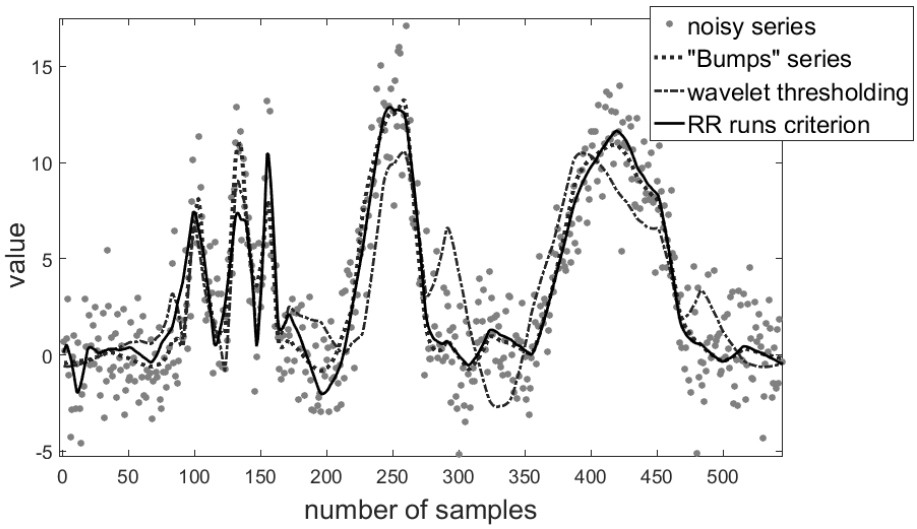

Fig. 1. Filtering of a noisy example «Bumps» (normal distribution). The dashed line shows the original «Bumps» series, the dots represent a noisy row, and the dash-dotted line shows the results of wavelet-thresholding, the solid line shows the results of filtering by the runs criterion

Wavelet-thresholding (by the minimax rule) and filtering by the described algorithm were performed for each generated series. Hereinafter, we used a wavelet basis based on the symlet of the third order, and the maximum possible number of decomposition levels. One of the cases is shown in Figure 1.

In this case, the thresholding algorithm leaves 35 non-zero coefficients out of a total of 1068 (that is, about 3.3%). When filtering using the runs criterion, we leave the same number of non-zero coefficients. It can be seen that the curve obtained by the runs criterion is much closer to the original signal than the curve obtained using wavelet thresholding (in particular, even the number of pulses in the signal is incorrectly determined for the latter curve).

Based on the results of processing of 50 random series (for each of the distributions), root-mean-square deviation of the filtered signal from the original signal «Bumps» was calculated. In this case, the standard deviation of the noise σ for the normal distribution was 2 (Since the standard deviation for the «Bumps» series is 3.77 and the signal-to-noise ratio is 3.56) and the scale parameter of the stable distribution was chosen equal to 1. The results for the three distributions are presented in the Table 1.

Table 1. Comparative RMS values of the filtered source signal for two quality criteria

	Normal distribution	Poisson distribution	Stable Distribution (α=1.3)
Wavelet thtesholding	0.6792	0.7846	1.8670
Runs criterion	0.3944	0.5064	0.8794

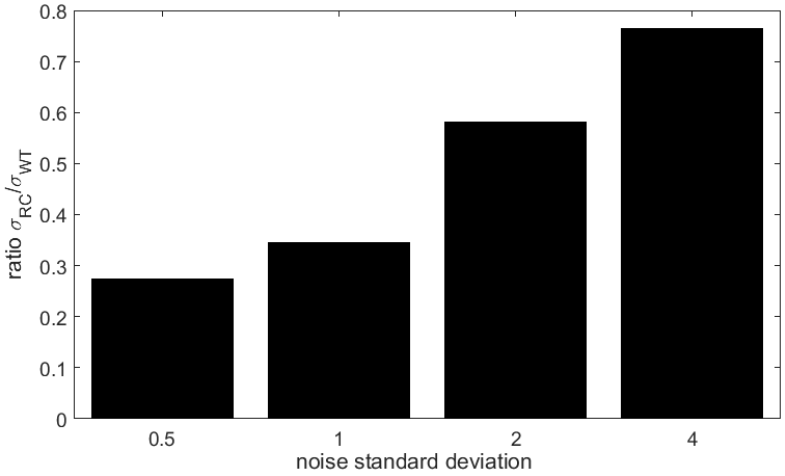

Fig. 2. Ratio of the root-mean-square error obtained after filtering by the runs criterion (RC) to the error obtained after using wavelet-thresholding (WT) for different noise levels

Thus, the results of statistical modelling demonstrate the advantage of filtering by the runs test over the standard wavelet-thresholding. It is particularly interesting that a significant improvement was obtained even for the case of a normal distribution of fluctuations.

The question arises: how the relative efficiency of the two filtration methods changes for the case of a normal distribution for different noise levels. Figure 2 shows how the ratio of filtering errors (i.e., the standard deviation of the filtered series from the original «Bumps» series) depends on the root-mean-square noise level for the compared methods. Error values obtained after filtering by the runs criterion were divided by the error values obtained after wavelet-thresholding, so the smaller values of the ratio mean a more significant advantage of the runs criterion over wavelet-thresholding. As can be seen from the figure, filtering by the runs criterion yields particularly good results at a moderate noise level. As for high noise series, the results obtained using the two methods come close to each other.

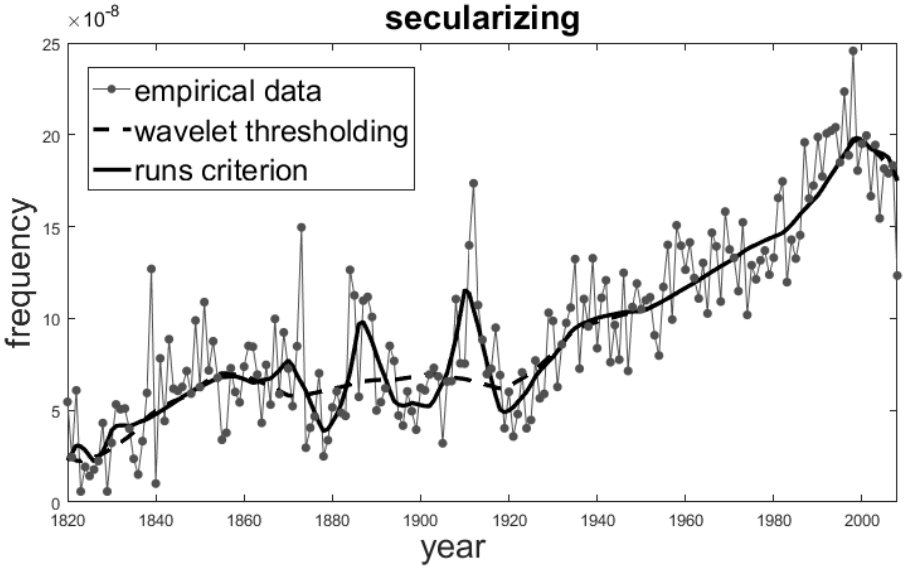

Fig. 3. A series of relative frequencies for the word «secularizing». The solid line shows the results of filtration by the runs criterion, the dashed line shows the series obtained using wavelet-thresholding

4 Filtering of series of words frequencies

Processing of series of words frequencies was also performed using the Google Books Ngram data (the 2009-year version of the corps was used). To carry out the analysis, words were randomly selected from the group of 100 thousand most frequently used words of the English language. We used series of average annual relative frequencies for the period 1800-2008. As in the case of model series, wavelet-thresholding (by the

minimax rule) and filtering according to the runs test were performed (for each series). Figure 3 shows an example of filtering a number of frequencies for a word «secularizing». In this example, the approximating wavelet series contains 19 non-zero coefficients (of the total number 215).

It can be seen that application of the runs criterion allows us to obtain better approximation than wavelet-thresholding. The series obtained using the compared methods mainly diverge between 1880 and 1930. Significant frequency variations of the word «secularizing» are observed during this period. These variations disappear when using wavelet-thresholding, but are clearly seen when filtering by the runs criterion is used.

It should be emphasized once again that both of the compared approximations are wavelet series with the same number of non-zero coefficients.

Figure 4 shows an example of filtering a number of frequencies for the word «Hiibner» (this word can mean a surname, and besides it is used as the name of one of the species of butterflies) This example shows that wavelet-thresholding didn't cope with the task and the method based on the runs criterion reproduces the frequency trends well in the 1840-1970 interval. For example, let us pay attention to the sharp frequency jump in 1855, after which the frequency no longer decrease to the former small values. After conducting wavelet-thresholding, this jump is replaced by a smooth rise, which is a serious qualitative distortion of information. On the contrary, the suggested method correctly approximates the jump region.

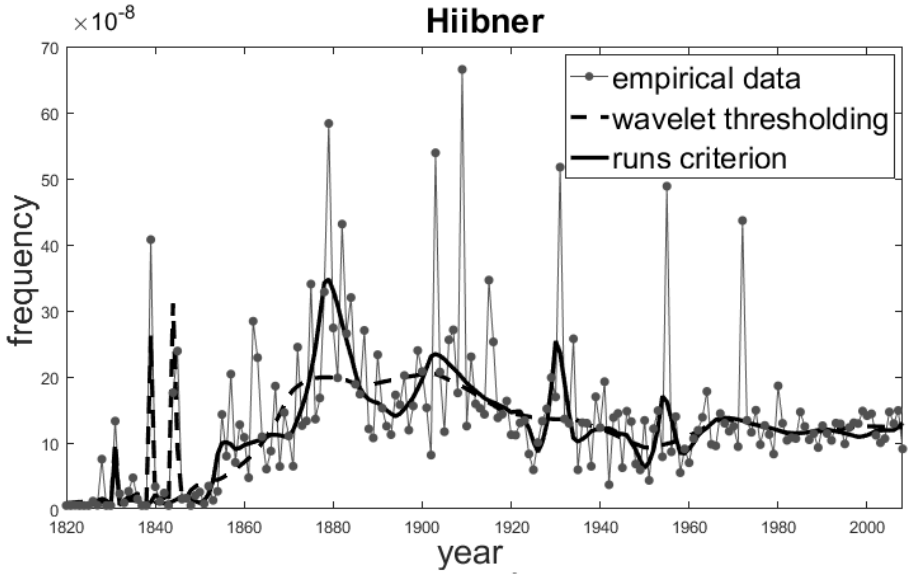

Fig. 4. A series of relative frequencies for the word «Hiibner» The solid line shows the results of filtration by the runs criterion, the dashed line shows the series obtained using wavelet-thresholding

There are some possible reasons why the approximation obtained by the wavelet-thresholding is so regrettable. Sharp peaks are observed in 1839 and 1844-1845 years. If these peaks are not taken into account, they will make a considerable contribution to the quadratic error. Therefore the thresholding algorithm considers them significant, «expending» several wavelet coefficients (out of total number of 19) on their reproduction. On the contrary, dropping such peaks does not contribute to statistics (3) and the method based on the runs criteria removes them quite reasonably. On the other hand, practical tasks are diverse and in some cases peaks can be important to the researcher. In this case, the runs criterion should be combined with a criterion that penalizes the drop of peaks. This can be realized by adding the corresponding term to the formula (3). Due to the universal nature of the genetic algorithm, it will not require sophistication of the calculation scheme.

A total of 70 examples were processed. As contrasted with the model series, in this case, we do not know the true values of the word frequencies in any given year. We only have the values obtained using the books included into the corpus, and therefore containing the error. In such situation, it is difficult to quantify how far one of the methods coped with the filtration task better than other methods. Therefore, the quality of the filtering was assessed visually for each of the examples. Difference in quality of filtering can be assessed as insignificant in 12 cases (17%). Filtering by the runs criterion gives better results than wavelet-thresholding in 31 cases (44%). And the advantage of filtering by the runs criterion can be assessed as very significant in 17 (39%) cases (the example shown in Figure 4 can be included into the latter group).

5 Conclusion

A method of nonlinear wavelet thresholding of time series is proposed in this paper. Signal representation in the form of a wavelet-series and the Ramachandran–Ranganathan runs criterion are used in this method to assess the quality of approximation. To optimize the objective function, the application of genetic algorithms is considered. A comparison of the proposed method with the standard wavelet-thresholding on model time series is performed. At that, the cases when the series are governed by the normal, stable, and Poisson distributions were considered. The de-scribed method was applied to filtering the time series of frequencies of the use of words and phrases (using the Google Books Ngram corpus data). It is shown that the use of a filter based on the runs criterion produces significantly better results than the use of both linear frequency filters and wavelet thresholding. It is clear that this algorithm has no advantage over wavelet-thresholding in the speed of data processing. Thus, this method can be used when quality of filtering is of primary importance but not the speed of calculations.

This work was supported by the Russian Foundation for Basic Research, Grant no. 15-06-07402. The research of the second author was supported by the Russian Government Program of Competitive Growth of Kazan Federal University.

6 References

1. Michel J., Shen Y., Aiden A., Veres A., Gray M., The Google Books Team, Pickett J., Hoiberg D., Clancy D., Norvig P., Orwang J., Pinker S., Nowak M., Aiden E. (2011) Quantitative Analysis of Culture Using Millions of Digitized Books. Science. 331 (6014), pp. 176-182.
2. S. Mallat A Wavelet Tour of Signal Processing, Third Edition: The Sparse Way 3rd Edition. 832 pages, Academic Press. 2008
3. R. H. Baayen Word Frequency Distributions, Kluwer Academic Publishers, 2001
4. Vladimir V Bochkarev and Inna A Belashova Modelling of nonlinear filtering Poisson time series 2016 J. Phys.: Conf. Ser. 738, 012082, doi:10.1088/1742-6596/738/1/012082
5. Bochkarev V, Solovyev V, Wichmann S. 2014 Universals versus historical contingencies in lexical evolution. J. R. Soc. Interface 11: 20140841. doi: 10.1098/rsif.2014.0841
6. David M. Himmelblau Process Analysis by Statistical Methods. John Wiley & Sons Inc, 1970.
7. Riccardo Poli, William B. Langdon, Nicholas Freitag McPhee A Field Guide to Genetic Programming Paperback – 2008, 252 pages, Lulu Enterprises, UK Ltd
8. F. Herrera, M. Lozano, J.L. Verdegay Tackling RealCoded Genetic Algorithms: Operators and Tools for Behavioural Analysis. Artificial Intelligence Review 12: 265–319, 1998. 265.

Educational Data Mining: A Case Study of Data Pre-Processing and Investigation of Students' Academic Achievement with Artificial Intelligence Classifier

Usamah bin Mat, Zainuddin Mohamad, Norlida Buniyamin

Engineering & Technical Education Research Group (EnTER),
Faculty of Electrical Engineering, Universiti Teknologi MARA,
40200 Shah Alam, Selangor, Malaysia
nbuniyamin@salam.uitm.edu.my

Abstract. Educational Data Mining (EDM) researchers are addressing educational related problem of visualizing hidden knowledge available within the huge available collated data from university warehouses. This paper proposed the preliminary preprocessing steps taken from data identification, cleaning, preparation, and visualization to an acceptable format for intelligent predictive classifier model building, for students' academic achievement prediction. Students' academic data from a case study university were preprocessed for analysis, to evaluate the impact of engineering student subject performance in the lower semesters on final cumulative grade achievement. Two core subjects, one elective subject and the students' final Cumulative Grade Point Average (CGPA) were used for this study. Preprocessing procedures on the selected data will help the proposed intelligent predictive classifier model to make accurate and effective decision on the student future achievement, based on the sound preprocessed training knowledge acquired from within the training input data. For future research study, a predictive Adaptive Neuro Fuzzy Inference System (ANFIS) classification model is suggested for effective intelligent model building as established in this research work.

Keywords: Educational data mining, Students' Academic Achievement, Artificial Intelligence Classifier, Linear Regression, Neuro-fuzzy classification, Students' Performance.

1 Introduction

The introduction of data mining approaches for knowledge discovery within huge data warehouse across all field of studies, have also motivated several research work into the areas of educational data mining (EDM). Historically, most researches based on the educational related data mining approaches started in early nineties for the academic, and learning analytic application. The advent of artificial intelligence (AI) approaches, emanated as a necessity tool to eliminate the computational complexity problem faced in solving, and analyzing statistically, the growth in the existing huge educational data warehouse. Thus, increases the advancement in the applied storage

medium, with the introduction of several intelligent based machine learning approaches for the EDM application as proposed [1]. Other proposed supervised machine learning algorithm approaches adopted by several researchers are the Support Vector Machine (SVM), artificial Neural network (ANN), Bayesian Network and others [2]. These proposed methods eliminated the itemized problems faced by the educational institutions of learning, through the bridging of existing gaps in tapping, and discovering hidden correlational knowledge within the huge data warehouse, in order to advance, and improve the educational values, with less computational complexity. The limitations encountered by these earlier proposed intelligent methods in the combination of the learning capability, with decision making ability of individual applied algorithm, warrant the development of a novel technique that could address these limitations. This paper proposed a novel classifier model building for the prediction of student performance evaluation

2 Methodology

Classification algorithm application is one of the known EDM approaches applied for the supervised learning of hidden information within a given educational data of an institution of learning (e.g. students, institutions, and instructors) [3][4]. Researches have established that most predictive models applied in EDM recently are built with the application of classifier algorithm, which helps in the categorization of any given educational data set, on all available features common to different individual class as documented during the data collection processes [5][6]. The classification algorithm harnesses all available features for a particular class as an input for the training of an intelligent algorithm to learn adequate hidden correlations to predict the stated target output class [7]. The error margin between the actual classification and the predicted class is reduced to the barest minimum value, to determine the performance accuracy of such applied built classifier models when presented with new set of data that not applied in the intelligent model training. Overfitting, and under fitting problem must be eliminated to enhance the generalization of the model for effective classification of student education data more effectively [8]. The research objective for this work is to formulated a new knowledge base from existing huge data warehouse of an educational institutions with Malaysia institutions as a case study [9]. Furthermore, classification approach in EDM for information and knowledge discovery within any given set of educational data is executed through these three main steps: data identification, identification of classifier purpose, and classification tool selection as proposed [10].

(i) Data Identification

Most educational data relating to student are usually numeric in nature or categorical as the case maybe. The numeric value comprising the test results across all subjects taken, while the grade points are stored as a discrete or continuous value when considering the time spent in solving test evaluations assessments. Generally, educational data set are stored in different format for easy of accessibility as either notes, text,

video, audio, and students behavioral trait which forms an import aspect of the data base [11]. Educational data for most institutions can be categorized into three:

- Assessment record: Final assessment results, Gross Point Average (GPA), class's attendance, assignment evaluation, tests evaluations, queries, CGPA, laboratory practical assessments, etc.
- Demographics: Age of student, sex, behavior attitude, family background, habit, personality, leadership, teamwork, finance, etc.
- Surrounding environment: study plane, course management, hostels, laboratory, lecturers, classes, hall, campus, etc.

(ii) Identification of classifier purpose

The main goal to be achieved from the proposed predictive or classification model must be identified. This may be for academic performance decision making, to classify students' success in a particular semester, or their achievement in graduation, student's classification in order to predict the number of pass students, and identifying the factors that affected their success as proposed [12]. It may also be as a result of course management and outcomes reasons, where the classification is based on students' performance in course or subject taken, and evaluating the suitability of the study management plan. The analysis, and evaluation of course management via students clustering and feedback proposed [13]. Other factor may be to determine the future Level performance of the student's success in future tasks, to predict what type of students can do better in next level, or how to set next learning level. Some researchers used parents' expectations, students' expectation, and student's previous mathematics ability to predict the future performance in mathematics as proposed [14]. Finally, it may be due to educational environment reasons, to analyze the student's surrounds and the effects of different environment to evaluate instructors, facilities, and services. Ballou and Springe analyzed students' scores to measure teacher performance and showed some vital problems [15].

(iii) Classification tool selection

Selecting algorithm to apply or AI technique, such as Neural Network, or Decision Tree, etc. Prediction and classification algorithm as proposed with the some mentioned proposed parameters [16].

3 EDM case study of engineering student data

The case study presented herewith uses data from a 4 year Bachelor of Engineering (Electrical) degree programme from University Teknologi MARA (UiTM). The programme consists of 50 subjects offering 137 credit units. A minimum Cumulative Grade Point Average (CGPA) score of 2.00 is required for graduation [17]. This research work selected 391 students' academic records, across all the subjects offered, bringing the total value data records to 19,550 from the huge UiTM students' educational data warehouse. The case study proposed two core subjects and one elective

course as selected for this study. Mathematics, alongside with the Signal & Systems students' data were extracted as core courses due to that that, student's strong ability on these fundamental subjects have great influence on students' performance across other subjects. Mathematics is considers as one of the most difficult course by students, and it's a crucial subject that will reflect engineering students performance [18]. On other hand, English language student subject data is also selected as the elective course, from the students' management center. There is no doubt, that the communication skills in English language are most important for knowledge assimilations, good writing skills for all engineering reports writing, and final year students projects[19]. English is essential in workplace for career success development. Graduates with good English language proficiency are valuable manpower to the nation's economy, they are equally of much values in industry [20] [21]. However, some researchers stated that English has less significant in students' academic performance[20]. Nevertheless, this research selected English data from engineering student record for deep evaluation, and comparing its effectiveness to the students' achievement. There are many factors that contribute to students' performance achievement, which include curriculum, teachers, environment, and the students' themselves. This research is proposed to determine features, and factors that affect engineering students' achievements in UiTM. The obtained result will help the school management to provide most effective decision and interventions to improve students' academic achievement at the early stage of their study.

The four steps involved in data preparations in this study are: data collection, data cleaning, data structure, and data pre-processing (visualization). Researchers usually go through these four procedures before modeling and analyzing the system [22] [23].

(a) Data collection and preparation (cleaning)

This research used subjects' data taken from semesters 1 & 3 for the graduation achievement correlation. A sum total of 12,202 records were collected for students admitted from 2005 to 2007, but 3519 complete records for 6 subjects, and CGPA were selected for this study purposes. The selected subject from semester 1 & 3 are English language 1&2 (Eng_1, Eng_2), Mathematics 1 & 2 (Mat_1, Mat_2), and Signal and System 1 & 2 (SS_1, SS_2). Elimination of unwanted noise, and irregular data like incomplete record, students dropped, duplicated grades were removed and data records clean from unwanted information to avoid overfitting during the intelligence system modeling. Four output class labels are as displayed in Table 1. Upon graduation, all grade values will be cumulated and expressed as cumulative grade point average CGPA.

Table 1. SUBJECT CLASSIFICATION LABEL

Grade Value	Classification label	Graduation class
3.50 – 4.00	Excellent	First Class
3.00 – 3.49	Good	Second Upper
2.20 – 2.99	Satisfactory	Second Lower
2.19 ≥	Weak	Third; 2.00 – 2.19*

* Minimum CGPA for graduation is 2.00

(b) Data Preprocessing, visualization, and structuring.

In order to discover hidden knowledge in the selected data , the existing relationships within the academic data record can be visualized with the application of several pre-processing operations to help in the visualization of existing relations based on the following criterial are proposed: Individual performance, linear regression, group achievement, and performance rules.

i) Individual performance evaluation:

Individual subject evaluation was carried out for each student, to determine individual student's classification according to their performance from individual subjects taken, which is applied for class grouping. Every student is classified separately per subject based on their respective achievements by CGPA records. The procedure expressed in pie chart shows the clustered performance for Mat_1, and Mat_2, alongside with students' CGPA records, to visualize the existing relationships with data records and effect as displayed in Fig. 1. The discovered knowledge is tabulated in Tables 2, and 3 in the result and discussion section. The same procedure is repeated across all individual subjects as proposed for this research works, with the results tabulated in Tables 4, 5, 6 and 7.

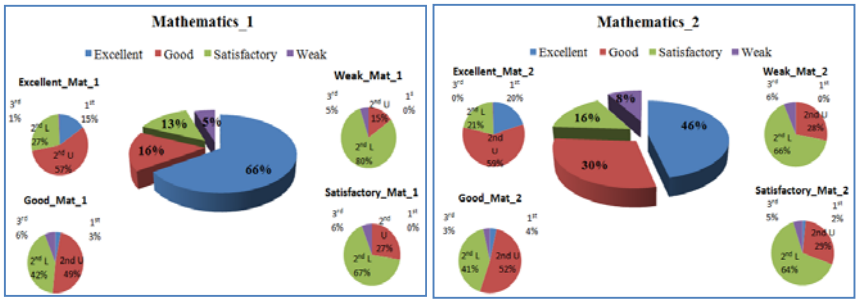

Fig. 1. Performance of (a) Mathematics_1 and (b) Mathematics_2.

ii) Linear Regression per subject:

Next is the determination of existing individual correlation of each selected subject with the corresponding CGPA achieved by each student, and the obtained coefficient from the linear regression equation plot is applied to determine the calculated R^2, which helps to determine how closely related is each subject performance towards archived CGPA. This number falls between 0 and 1, with 0 indicating lack of correlation and 1 indicating high correlation. This indicate that the existence of one variable over the determination of the other. This procedure helps in determining effective correlated variables that can be combination as input variables for the modelling of an intelligent predictive system. The obtained plot from the selected subjects are discussed and displayed in the result and discussion section.

iii) Group Achievement:

Each class in each subject is evaluated, and defines the normalized weight to compare it with normalized average of CGPA. This procedure shows how students perform in group view, and assist the intelligent system modeling in term of range, and parameters in relation with the membership functions of the AI.

iv) Performance Rules formulation:

The individual student subject's performances were analyzed in line with the achieved CGPA, to assist in identifying the major rules needed for the predictive intelligent system modeling with the application of ANFIS, and also avoid overfitting of the given data. As one of the criteria need for the inference system mechanism building, if and then rules similar to those displayed in Table 10 must be built. These rules are formed based on the students' achievement across the 6 selected proposed subjects and as they relate to graduation achievement based on the earlier performance assessments, and linear regression evaluations individually. Major rules were extracted, and can be updated in the future for an enhanced intelligent system building; some generated rules are based on the following criteria:

- Students, who achieved Weak in any of the 6 subjects, did not achieve First Class.
- Students, who achieved Satisfactory in 2 subjects, did not achieve First Class.
- Satisfactory, and Weak students in Mat_1 did not achieve First class.
- Students, who achieved Weak in 3 subjects, achieved Second Lower or Third.
- Students, who did not achieve Excellent or Good, in SS_2, also achieved Second Lower or Third.
- Students, who achieved Weak in Eng_2, also achieved Second Lower or Third.

These rules and the related attributes are applied for the building of the ANFIS reasoning system for future research in term of *IF then format for….* Example are*:*

Rule 1: if *Mat_1* is *E*, and *Mat_2* is *E*, and *Eng_1*is *G*, and, ..., and *SS_2* is *E*, then *f1=p1Mat_1 + q1Mat_2+m1Eng_1+ … + w1SS_2+r1*

Rule n: if *Mat_1* is *n* and *Mat_2* is *n*, and *Eng_1* is *n*, and, ..., and *SS_2* is *n*, then *fn=pnMat_1 + qnMat_2+mnEng_1+ … + wnSS_2+rn*

Example for rules view from Table 10 are also illustrated below:

Rule in raw_1: if *Mat_1* is *E*, and *Mat_2* is *E*, and *Eng_1*is *G*, and *Eng_2* is *E*, and *SS_1* is *E*, and *SS_2* is *E*, then *CGPA=First Class*

Rule in raw_390: if *Mat_1* is *E*, and *Mat_2* is *E*, and *Eng_1*is *G*, and *Eng_2* is *G*, and *SS_1* is *E*, and *SS_2* is *S*, then *CGPA=Second Upper*

(c) Selecting an intelligence classifier tool

Selecting the suitable classification method for a certain task is not easy, as there is no generalized rule in selection. Comparison of tools was done in previous research paper; the research resulted that ANFIS classification is the most suitable technique for this study [2] [15]. ANFIS model will be used to build a multi input and single output

predictive intelligent system (MISO) as displayed in Fig.2. The proposed intelligent predictive system will have six inputs and one output. The input variables for the ANFIS model system are subject results from Mathematics (Mat_1&2), Signal & System (SS_1&2), and English (Eng_1&2), and the output Students Achievement (SA).

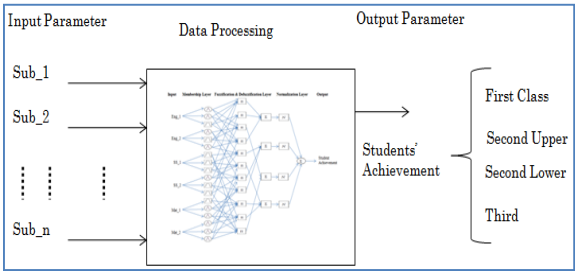

Fig. 2. Block Diagram of the ANFIS model

4 Result and discussion

The result from Fig 1 for individual subject classification, based on the individual students' performance across all subjects as it related to CGPA achievement is displayed in Table 2 and 3. One of the interesting outcome is that students with Weak and Satisfactory achievements in Mat_1& Mat_2 were not able to graduate with First Class grade achievements. However, there is only one student, who achieved Satisfactory in Mat_2, but with excellent achievement in Mat_1, and graduated with First Class. From Fig 1, and Table 2, it can be seen that 66% of the student that achieved Excellent in Mat_1, have chances of graduation, with only 15% achieving First Class, around 57% with Second Upper, 27% achieved Second Lower, and yet some students will end up achieving Third class on graduation as displayed. On the other hand, there were 5% of students that are Weak in Mat_1, and none of them achieved Excellent at graduation as visualized. Also, Fig. 1 shows that there are 46% excellent students in Mat_2, and upon graduation only 20% attained First Class graduation achievements, while 59% achieving Good, 21% achieved satisfactory, and no students had a Weak achievement. This divulged knowledge from the result presented can summarized as: students who achieved Excellent in Mat_2 will never graduate with Third class. Other knowledge outcomes on subjects' performance are stated in Tables 2,3,4,5,6 and 7.

Table 2. Performance of Mathematics_1

Class	Knowledge Discovery
Excellent	Excellent students in Mat_1 have probability to graduate of ;15% First Class, 56.64% Second_Upper, 27.34% Second_Lower, and 0.78% Third
Good	Good students in Mat_1 have probability to graduate of ;3.13% First Class, 48.44% Second Upper, 42.19% Second Lower, and 6.25% Third
Satisfactory	Satisfactory students in Mat_1 have probability to graduate of ;0.00% First Class, 27.45% Second Upper, 66.67% Second Lower, and 5.88% Third
Weak	Weak students in Mat_1 have probability to graduate of ;0.00% First Class, 15.00% Second_Upper, 80.00% Second Lower, and 5.00% Third

Table 3. Performance of Mathematics_1

Class	Knowledge Discovery
Excellent	Excellent students in Mat_2 have probability to graduate of; 20% First Class, 58.89% Second Upper, 21.11% Second Lower, and 0% Third.
Good	Good students in Mat_2 have probability to graduate of; 3.45% First Class , 51.72% Second Upper, 41.38% Second Lower, and 3.45% Third
Satisfactory	Satisfactory students in Mat_2 have probability to graduate; 1.61% First Class, 29.03% Second Upper, 64.52% Second Lower, and 4.84% Third.
Weak	Weak students in Mat_2 have probability to graduate; 0.00% First Class, 28.13% Second Upper, 65.63% Second Lower, and 6.25% Third.

Table 4. Performance of Signal & System_1

Class	Knowledge discovery
Excellent	Excellent students in SS_1, have probability to graduate;32.93% First class, 54.88% Second Upper, 10.98% Second Lower, and 1.22% Third
Good	Good students in SS_1, have probability to graduate;9.30% First class, 63.57% Second Upper, 26.36% Second Lower, and 0.78% Third
Satisfactory	Satisfactory students in SS_1, have probability to graduate;2.20% First class, 47.25% Second Upper, 48.35% Second Lower, and 2.20% Third
Weak	Weak students in SS_1, have probability to graduate;0.00% First class, 25.84% Second Upper, 67.42% Second Lower, and 6.74% Third

Table 5. Performance of Signal And System_2

Class	Knowledge discovery
Excellent	Excellent students in SS_2, have probability to graduate;35.85% First class, 52.83% Second class, 11.32% Second Lower, and 0.00% Third
Good	Good students in SS_2, have probability to graduate;20.73% First class, 57.32% Second class, 21.95% Second Lower, and 0.00% Third
Satisfactory	Satisfactory students in SS_2, have probability to graduate;4.24% First class, 61.86% Second class, 32.20% Second Lower, and 1.69% Third
Weak	Weak students in SS_2, have probability to graduate;0.00% First class, 32.61% Second class, 61.59% Second Lower, and 5.80% Third

Table 6. Performance of English_1

Class	Knowledge discovery
Excellent	Excellent students in Eng_1, have probability to graduate;22.00% First class, 48.00% Second class, 28.00% Second Lower, and 2.00% Third
Good	Good students in Eng_1, have probability to graduate;10.76% First class, 49.78% Second class, 38.57% Second Lower, and 0.90% Third
Satisfactory	Satisfactory students in Eng_1, have probability to graduate;5.26% First class, 50.00% Second class, 39.47% Second Lower, and 5.26% Third
Weak	Weak students in Eng_1, have probability to graduate;0.00% First class, 25.00% Second class, 50.00% Second Lower, and 25.00% Third

Fig. 3 provides the coefficients of the linear regression equation for subjects, SS_1, and SS_2, with respect to CGPA. As shown, SS_2 grades affect CGPA more than SS_1. Table 8 shows the coefficient of best regression line fit of all subjects and is used in selecting the best combination of input variable for the building of the proposed intelligent reasoning system. As shown, Eng_1 & 2 has least influence on CGPA, while Mat_1 & 2, and SS_1 & 2 have considerable influence on CGPA.

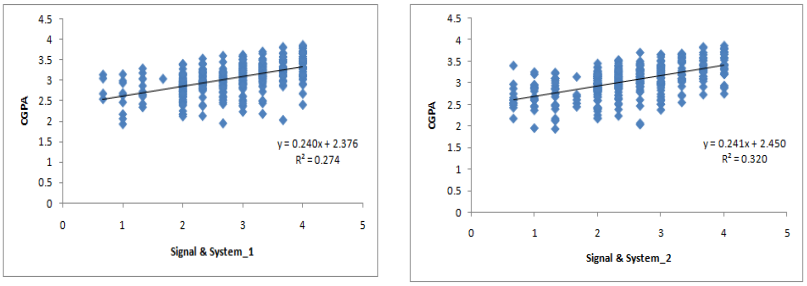

Fig. 3. Linear Regression of SS_1 and SS_2

Table 7. Performance of English_2

Class	Knowledge discovery
Excellent	Excellent students in Eng_2, have probability to graduate;16.06% First class, 56.20% Second class, 27.74% Second Lower, and 0.00% Third
Good	Good students in Eng_2, have probability to graduate;9.23% First class, 48.21% Second class, 40.51% Second Lower, and 2.05% Third
Satisfactory	Satisfactory students in Eng_2, have probability to graduate;1.89% First class, 41.51% Second class, 50.94% Second Lower, and 5.66% Third
Weak	Weak students in Eng_2, have probability to graduate;0.00% First class, 0.00% Second class, 50.00% Second Lower, and 50.00% Third

Table 8**.** Linear regression of selected subjects

Subjects	Linear Regression Equation Line	Coefficient of determination	Correlation Knowledge
Mat_1	y = 0.266x + 2.121	$R^2 = 0.230$	Signal and System_2 is the most influence subject among these six subjects
Mat_2	y = 0.248x + 2.234	$R^2 = 0.224$	
SS_1	y = 0.240x + 2.376	$R^2 = 0.274$	
SS_2	y = 0.241x + 2.450	$R^2 = 0.320$	
Eng_1	y = 0.145x + 2.612	$R^2 = 0.029$	
Eng_2	y = 0.244x + 2.249	$R^2 = 0.117$	

Fig 4 shows that group performance of Eng_1 has no significant change in Good and Satisfactory graduation achievement in (a), while (b) shows a significant change and indication of declined in the students' achievement as the performance declined. Table 9 displayed the group achievement result for all six selected subjects. There is significant decline in Mat_1, Eng_1, and Eng_2 compare to SS_1, SS_2, and Mat_2 as seen in the Figure. 4.

The displayed result of Table 10, contains 391 students with their ID number, and grades; the E acronym represent Excellent achievement with blue shaded background color, G represent Good achievement with red background color, S represent Satisfactory graduation achievement with green shade background, and W represent Weak achievement with purple shade background color.

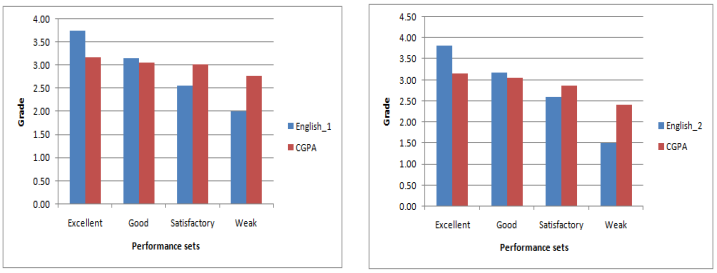

Fig. 4. Group achievement of (a) English_1 and Group achievement of (b) English_2

Table 9. Group Achievement of the Selected Subjects

#	Excellent	Good	Satisfactory	Weak
Mat_1	3.90332	3.20625	2.543333	1.833
CGPA	3.162305	2.950313	2.80451	2.681
Mat_2	3.892431	3.196293	2.5	1.895625
CGPA	3.211492	2.998017	2.838387	2.812188
SS_1	3.851098	3.143256	2.509341	1.752584
CGPA	3.33	3.12907	2.965165	2.79191
SS_2	3.84434	3.175556	2.474068	1.635145
CGPA	3.381887	3.241975	3.066525	2.835725
Eng_1	3.76	3.145022	2.553684	2
CGPA	3.1698	3.052422	3.024386	2.765
Eng_2	3.82	3.179231	2.605849	1.5
CGPA	3.158759	3.057333	2.859811	2.42

Table 10. Subjects' Correlation And Rules

#	Mat_1	Mat_2	Eng_1	Eng_2	SS_1	SS_2	achievement
1	E	E	G	E	E	E	First Class
2	E	E	W	S	S	W	Second Lower
3	E	S	W	S	G	G	Second Upper
⋮	⋮	⋮	⋮	⋮	⋮	⋮	⋮
389	S	S	G	E	S	W	Second Lower
390	E	E	G	G	E	G	Second Upper
391	E	S	S	W	W	W	Third

For example, students' achievements are expressed by four linguistic category indicators; Excellent, Good, Satisfactory, and Weak. Generally, these expressions are used to grade the quality in daily life. If students score in mathamatics_2 is between 50 - 55 points out of 100, and most probably with graduation with CGPA achievement of 2.20 - 3.49. In other words; a student who is Weak in Mathematics will not be Excellent in engineering, and has chances of 25% to be good, 65% to achieve satisfactory performance, and 10% of chances to be weak. In conclusion, some modification of the

analysis will be done; for instance, adding one more class between Good, and Satisfactory classes as students are lumped between 2.50 to 3.30. Moreover, the research will identify and select a desired training data rather than selecting 70% randomly, also reverse view of performance will take a place before system modeling.

5 Conclusion

This research paper presented four procedures for data pre-processing, and investigation of educational data to identify, subject variables, and relevant rules that could be use as input variables to train an intelligent MISO ANFIS model. Four statistical analysis approaches were proven for data visualization, and hidden knowledge discovery during preprocess analysis of the six-proposed selected related subject, based on their impact assessment on CGPA, for the prediction of the student academic achievement. The pre-processing, and investigation procedures on the selected subject data, will help the proposed intelligent predictive classifier model make accurate and effective decision on the student future achievement, based on the sound preprocessed training knowledge acquired from the training input data. This analysis assessment would allow more flexibility in making judgment on single, and group performances which could be more understandable by educators, and parents for further evaluation. For future research study, an ANFIS predictive classification model is suggested for effective intelligent model building, with input variables from the six preprocessed subject data from Mathematics, English, Signal and System discovered knowledge, and one target output from the achievements as established in this research work.

Acknowledgment

The authors would like to acknowledge and thank University Teknologi MARA for the Academic and Research Assimilation (ARAS) Grant. (600-RMI/DANA5/3/ARAS (12/2015)).

References

1. B. U. Mat, N. Buniyamin, P. M. Arsad, and R. Kassim, "An Overview of Using Academic Analytics to Predict and Improve Students' Achievement: A Proposed Proactive Intelligent Intervention," IEEE 5th Conf. Eng. Educ., pp. 126–130, 2013.
2. O. Taylan and B. Karagözoğlu, "An adaptive neuro-fuzzy model for prediction of student's academic performance," Comput. Ind. Eng., vol. 57, no. 3, pp. 732–741, 2009.
3. S. K. Yadav, B. Bharadwaj, and S. Pal, "Mining Education Data to Predict Student ' s Retention : A comparative Study," Int. J. Comput. Sci. Inf. Secur., vol. 10, no. 2, pp. 113–117, 2012.
4. S. K. Yadav, B. Bharadwaj, and S. Pal, "Data Mining Applications : A comparative Study for Predicting Student ' s performance," Int. J. Innov. Technol. Creat. Eng., pp. 13–19, 2012.
5. P. Mara, M. H. Rani, and A. Embong, "Predicting Student Performance in Object Oriented Programming Using Decision Tree : A Case at Kolej," in Conference on Software Engineering & Computer Systems, 2013, pp. 11–8.
6. S. Talebi and A. A. Sayficar, "Using Educational Data Mining (EDM) to Prediction and Classify Students," Int. J. Eng. Comput. Sci., vol. 3, no. 12, pp. 9395–9398, 2014.

7. C. Romero and S. Ventura, “Educational data mining: A survey from 1995 to 2005,” Expert Syst. Appl., vol. 33, no. 1, pp. 135–146, 2007.
8. H. I. Shovon and M. Haque, “An Approach of Improving Student ’ s Academic Performance by using K-means clustering algorithm and Decision tree,” Int. J. Adv. Comput. Sci. Appl., vol. 3, no. 8, pp. 146–149, 2012.
9. S. Khadijah and Z. Tasir, “Educational data mining : A review,” Procedia - Soc. Behav. Sci., vol. 97, pp. 320–324, 2013.
10. P. V. P. Sundar, “A Comparative Study For Predicting Student ’ S Academic Performance Using Bayesian Network Classifiers,” IOSR J. Eng., vol. 3, no. 2, pp. 37–42, 2013.
11. [11] M. Hämäläinen, W., & Vinni, Classifiers for educational data mining. Handbook of Educational Data Mining. 2010.
12. S. Rawat, Sandeep; Reddy, S.; Mishra, Devi; Sultana, “Ascertaining the Factors Influencing Students’ Performance for Engineering Pedagogy,” J. Eng. Educ. Transform., pp. 30–33, 2015.
13. E. Abaidullah, A. M., Ahmed, N., & Ali, “Identifying Hidden Patterns in Students" Feedback through Cluster Analysis,” Int. J. Comput. Theory Eng., vol. 7, no. 1, p. 16, 2015.
14. M. Bravo Sanzana, S. Salvo Garrido, and C. Muñoz Poblete, “Profiles of Chilean students according to academic performance in mathematics: An exploratory study using classification trees and random forests,” Stud. Educ. Eval., vol. 44, pp. 50–59, 2015.
15. M. G. Ballou, D., & Springer, “Using student test scores to measure teacher performance: Some problems in the design and implementation of evaluation systems.,” Educ. Res., vol. 2, no. 44, pp. 77–86, 2015.
16. Usamah Mat, Norlida Buniyamin, and Pauziah Mohd Arshad, “Educational data mining classifier for semester one performance to improve engineering students achievement,” Middle-East J. Sci. Res., vol. 24, no. 2, pp. 338–346, 2016.
17. J. A. Arsad, P. M., Buniyamin, N., & Manan, “Profiling the performance of electrical engineering bachelor degree students based on different entry levels.,” Int. J. Educ. Inf. Technol., vol. 5, no. 2, pp. 267–274, 2011.
18. B. Bognár, G., & Illés, “Mathematics in engineering education. Networking in Engineering and Technology Education,” Netw. Eng. Technol. Educ., no. February, pp. 44–49, 2012.
19. G. K. S. Nair et al., “Malaysian graduates English adequacy in the job sector,” Asian Soc. Sci., vol. 8, no. 4, pp. 143–147, 2012.
20. P. M. Arsad, N. Buniyamin, and J. A. B. Manan, “The Impact of English on students performance based on Neural Network Prediction : A Malaysian Case Study Bachelor of Electrical,” pp. 81–86, 1992.M. S. Sarudin, I., Noor, Z. M., Zubairi, A. M., Ahmad, T. B. T., & Nordin, “Needs assessment of workplace English and Malaysian graduates’ English language competency.,” World Appl. Sci. J., vol. 21, no. 4, pp. 88–94, 2013.
21. I. S. Ahmed, A. B. E. D., & Elaraby, “Data Mining: A prediction for Student’s Performance Using Classification Method.,” World J. Comput. Appl. Technol., vol. 2, no. 2, pp. 43–47, 2014.
22. Q. Zhou, Y. Zheng, and C. Mou, “Predicting students’ performance of an offline course from their online behaviors,” 2015 5th Int. Conf. Digit. Inf. Commun. Technol. Its Appl. DICTAP 2015, pp. 70–73, 2015.

Telescope: A Hybrid Forecast Method for Univariate Time Series

Abstract Paper

Marwin Züfle, André Bauer, Nikolas Herbst, and Samuel Kounev
Julius-Maximilians-University Würzburg

Valentin Curtef
MaxCon Data Science GmbH, Würzburg

Abstract. Forecasting is an important part of the decision-making process and used in many fields like business, economics, finance, science, and engineering. According to the "*No-Free-Lunch-Theorem*" from 1997, there is no general forecasting method, that performs best for all time series. Instead, expert knowledge is needed to decide which forecasting method to choose for a specific time series with its own characteristics. Since a trial and error approach is very inefficient and expert knowledge is useful but a time-consuming task that cannot be fully automated, we present a new hybrid multi-step-ahead forecasting approach based on time series decomposition. Initial evaluations show that this hybrid approach improves the forecast accuracy compared to six existing forecasting methods while maintaining a short runtime.

1 Introduction

Forecasting allows to predict the future by examining past observations. Classical forecasting methods have their benefits and drawbacks depending on the specific use cases. Thus, there is no globally best forecasting technique [19] and further respectively expert knowledge is required for determining the best forecast method. Typically, expert knowledge is needed for two domains, i.e., method selection and feature engineering. The serious problem of expert knowledge is that it can take a long time to deliver results and it cannot be completely automated. In the field of feature engineering, expert knowledge can be replaced by using deep learning [16,12] or random forests [8,2]. To overcome the need of expert knowledge in method selection, a more robust forecasting method compared to the classical forecaster is needed. In this field, robust means that the variance in forecasting results should be reduced, not necessarily improving the forecasting accuracy itself. By reducing the variance of the results, the risk when trusting a bad forecast is lowered. Hybrid forecasting is such a technique since the benefits of multiple forecasting methods can be combined to improve the overall performance. Thus, we introduce a new hybrid, multi-step-ahead forecasting approach for univariate time series. The approach is based on time series decomposition and makes use of existing forecasting methods, i.e., ARIMA, ANN, and XGBoost.

2 Related Work

In 1997, Wolpert and Macready presented the "*No Free Lunch Theorem*" for optimization algorithms [19]. It claims, that there is not a single algorithm that performs best for all scenarios since improving the performance of one aspect normally leads to a degradation in performance for some other aspect. This theorem can also be applied to forecasting methods as there is no single method that outperforms the others for all types of data. To address this issue, many hybrid forecasting approaches have been developed. A hybrid forecasting method makes use of at least two forecasting methods to compensate the limitations of individual forecasting methods. Hybrid methods can be categorized into three groups of approaches each sharing the same basic concept.

The first and historically oldest group is the concept of ensemble forecasting and is the technique of using at least two forecasting methods. While assigning a weight to each method, the forecast result is the weighted sum of each forecast method. This approach was introduced by Bates and Granger in 1969 [1]. The concept of this approach is rather simple, however, the assignment of weights is a crucial part. Thus, many methods for weight estimation have been investigated [4,7,11].

The second group of forecasting methods is based on the concept of forecast recommendation, where the goal is to build a rule set to guess the assumed best forecasting method based on certain time series features. There are two common ways to generate the rule set. One method is using an expert system. Collopy and Armstrong used this approach to create a rule set by hand in 1992 [6]. The other method is using machine learning techniques to automatically generate a rule set. In 2009, Wang et al. proposed clustering and algorithms for rule set learning based on a large variety of time series features [18].

The third group of forecasting methods is based on decomposition of the time series with the goal to leverage the advantages of each method to compensate for the drawbacks of the others. In literature, there are common approaches. The first approach is to apply a single forecasting method on the time series and then apply another method on the residuals of the first one [20,17]. The second forecasting method is intentionally chosen to have different characteristics than the first one, that is, it should have antithetic advantages and drawbacks compared to the first one. An alternative approach is to split the time series into its components trend, seasonality, and noise, applying a different forecasting method on each of them. Liu et al. introduced an approach like this targetted for short-term load forecasting of micro-grids [13]. They used empirical mode decomposition to split the time series and extended Kalman filter, extreme learning machine with kernel, and particle swarm optimization for the forecast.

The hybrid forecasting approach, we propose in this paper, focuses on forecasts based on decomposition. In contrast to Zhang or Pain and Lin [20,17], we use explicit time series decomposition, that is, forecast methods are applied to the individual components of the time series as opposed to the residuals of previous forecasts. Liu et al. introduced a short-term hybrid forecasting method based on an intrinsic mode function. In our approach, the time series is split into trend, seasonality, and noise

components. Additionally, completely different forecasting methods are used as a basis. Furthermore, the hybrid approach of this paper is designed to perform multi-step-ahead forecasting with low overhead and short runtime.

3 Telescope Approach

We call the proposed hybrid forecasting approach *Telescope* according to the analogy with the vision on far-distanced objects. Telescope is developed in *R* to perform multi-step-ahead forecasting while maintaining a short runtime. To this end, only fast and efficient single forecasting methods are used as components of Telescope. A diagram of the forecasting procedure is shown in Fig. 1.

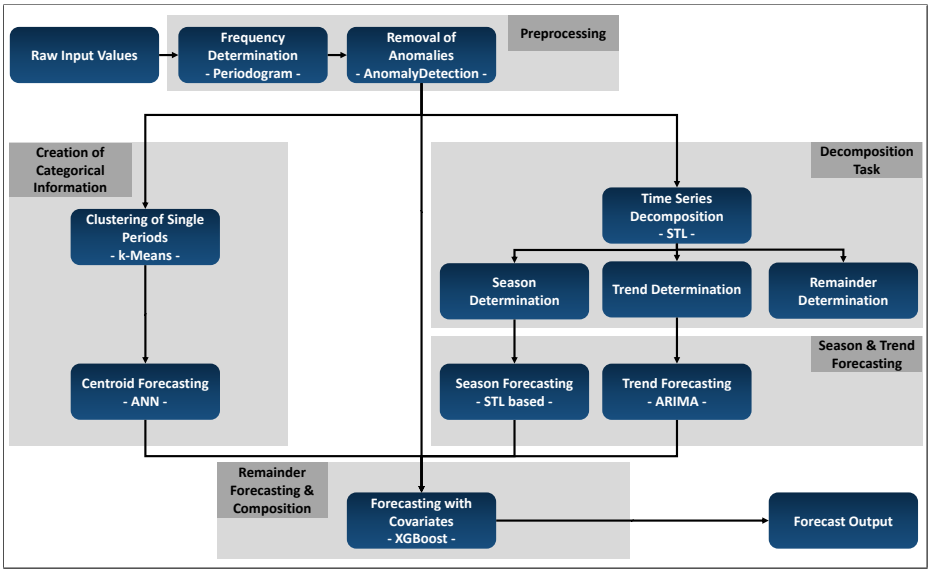

Fig. 1: A simplified illustration of the Telescope approach.

First, a preprocessing step is executed. The frequency of the time series is estimated using periodograms, i.e., applying the *R* function `spec.pgram`. This function uses fast Fourier transformation to estimate the spectral density. The estimated frequency is needed to remove anomalies in the time series by applying the `AnomalyDetection` *R* package [9]. This package uses a modified version of the seasonal and trend decomposition using Loess (STL) [5]. The `STL` decomposition splits the time series into the three components season, trend, and remainder. After the decomposition, `AnomalyDetection` applies generalized extreme studentized deviate test (ESD) with median instead of mean and median absolute deviation instead of standard deviation on the remainder to identify outliers. Furthermore, we use `STL` for an additive decomposition of the revised time series. If the amplitude of the seasonal

pattern increases as the trend increases and vice versa, we assume multiplicative decomposition. Thus, a heuristic testing for such a behavior is implemented. If a multiplicative decomposition is detected, the logarithmized time series is used for the STL decomposition and the components are back-transformed after the decomposition. We apply the STL package because of its short runtime compared to other *R* decomposition functions like `bfast`. Afterwards, the season and trend forecasting is executed. The seasonality determined by STL is simply continued, whereas the trend is forecast using the `auto.arima` function from the `forecast` *R* package by Hyndman [10]. Since there is no seasonal pattern left, seasonality is disabled in `auto.arima` for this purpose. Moreover, this seasonality disabling decreases the runtime of the algorithm. Additionally, the time series with removed anomalies is used to create categorical information. For this purpose, the time series is cut into single periods. Then, the single periods are clustered into two classes using the `kmeans` *R* function. Each class is represented by its centroid. Next, this history of centroids is forecast using an artificial neural network (ANN), i.e., the `nnetar` function of the `forecast` *R* package [10]. If a specific time series is forecast several times, this clustering task does not need to be performed every time. Finally, the last step is the remainder forecast and composition. XGBoost is used [3], which is an implementation of gradient boosted decision trees and it works best when obtaining covariates. XGBoost is applied using the trend, seasonality, and centroid forecasts as covariates and the raw time series history as labels. In addition, 10% of the history data are used for validation in the training phase to prevent XGBoost from overfitting. The sources of the Telescope approach are currently under publication as open-source[1].

4 Preliminary Evaluation

To evaluate the performance of this hybrid forecasting approach, we have conducted some initial experiments presented in this section. As example time series, a trace of completed transactions on an IBM z196 Mainframe during February 2011 and a trace of monthly international airline passengers from 1949 to 1960 are used.

Each observation in the IBM trace contains the quarter-hourly amount of transactions (e.g., bookings or money transfers). The trace contains 2670 observations and is depicted in Fig. 2a. It shows a typical seasonal pattern with a daily and weekly cycle, where the amount of transactions differs completely during weekdays and weekends. The trace exists of about 28 daily periods and 4 weekly periods. Since the approach is designed to perform multi-step-ahead forecasts, the last 20% observations of the time series are chosen as forecast horizon. Thus, the history of the IBM trace incorporates 2136 observations and the forecast horizon is set to 534 observations. The border between history and horizon is shown as vertical purple line in Fig. 2a. The forecast of the IBM trace is shown in Fig. 2b. The original time series is depicted in black, whereas the forecast of Telescope is represented by the red line. As a reference, the second best forecast produced by the tBATS approach [14] is shown as

[1] Telescope: `http://descartes.tools/telescope`

dashed blue line. Besides the good fitting of the observed history, the hybrid approach succeeds in capturing the weekdays and weekends. In contrast to Telescope, tBATS only repeats a single pattern for the whole horizon. For weekdays, the forecast of Telescope and tBATS are very close to each other. However, tBATS misses capturing the weekends.

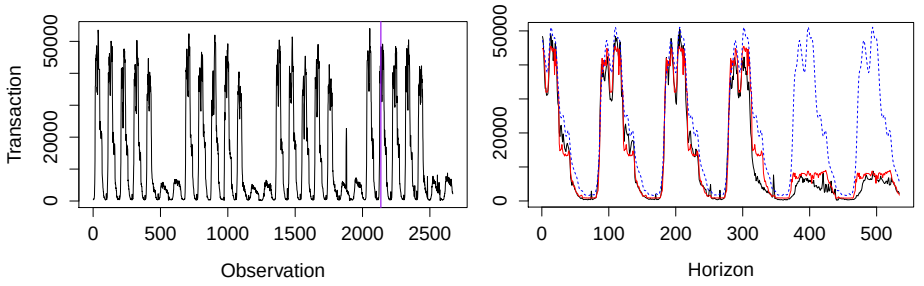

(a) All observations of the history and forecast horizon of the IBM trace.

(b) Telescope (red) and tBATS (dashed blue) forecast of the IBM trace.

Fig. 2: Observations and forecast of the IBM trace.

The airline passengers trace consists of 144 observations and shows an exponential trend pattern as well as a seasonal pattern with yearly cycle. Furthermore, the amplitude of the seasonal pattern increases as the trend rises. The airline passengers trace is shown in Fig. 3a. Since the forecast horizon is set to 20%, the history contains 115 observations and the forecast horizon consists of 29 observations. Again, the border between history and horizon is shown as vertical purple line in Fig. 3a.

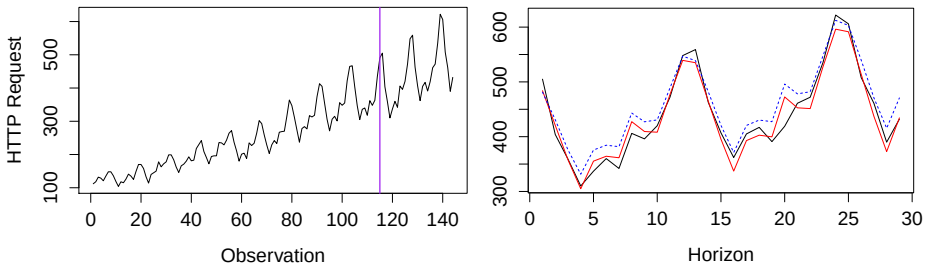

(a) All observations of the history and forecast horizon of the airline passengers trace.

(b) Telescope (red) and tBATS (dashed blue) forecast of the airline passengers trace.

Fig. 3: Observations and forecast of the airline passengers trace.

Fig. 3b shows the forecast of the airline passengers trace. Again, the original time series is depicted as black line, the forecast of Telescope is shown as red line, and the tBATS forecast is depicted as dashed blue line. Both, tBATS and Telescope succeed in capturing the trend and season pattern. Though, besides the first value of the horizon, the tBATS forecast is always greater than the Telescope forecast.

To evaluate the forecasting accuracy in a mathematical way the mean absolute percentage error (MAPE) and mean absolute scaled error (MASE) measures are used. The MAPE is a widely-used measure to assess forecasting accuracy based on the forecasting error normalized with the observations. However, MAPE has some serious limitations, i.e., it cannot be used for time series with zeros in the forecasting horizon and it punishes positive errors harder than negative errors. Thus, we additionally use a second measure called MASE. Both measures are independent of the data scale but in contrast to MAPE, MASE is suitable for almost all situations and the error is based on the in-sample MAE from the random walk forecast. For a 20% forecast, the random walk forecast would forecast the last value of the history for the entire horizon. Thus, the investigated forecast is better than the random walk forecast if the MASE value is less than 1 and worse if the MASE value is greater than 1. The MAPE and MASE values can be calculated as follows:

$$MAPE = 100 \times \frac{1}{n} \sum_{i=1}^{n} |\frac{e_i}{Y_i}| \tag{1}$$

$$MASE = \frac{\frac{1}{n} \sum_{i=1}^{n} |e_i|}{\frac{1}{n-1} \times \sum_{i=2}^{n} |Y_i - Y_l|} \tag{2}$$

Where Y_l is the observation at time l with l being the index of the last observation of the history. Y_i is the observation at time $l+i$. Thus, Y_i is the value of the i-th observation in the forecast horizon. The forecast error at time $l+i$ is calculated as $e_i = Y_i - F_i$ where F_i is the forecast at time $l+i$. The amount of observations in the forecast horizon is represented by n. Another important measure to evaluate the performance of the forecasting approach is the elapsed time for the forecasting process. The total time elapsed for the forecast is measured in seconds. Table 1 shows the MASE and MAPE values and runtime of the hybrid approach for the IBM and airline passengers traces compared to six state-of-the-art forecasting methods:

- **ARIMA**: auto-regressive integrated moving averages (`auto.arima` with seasonality in package `forecast` [10]),
- **ANN**: artificial neural nets (`nnetar` in package `forecast` [10]),
- **ETS**: extended exponential smoothing (`ets` in package `forecast` [10]),
- **tBATS**: trigonometric, Box-Cox transformed, ARMA errors using trend and seasonal components (`tbats` in package `forecast` [10,14]),
- **SVM**: support vector machine (`svm` in package `e1071` [15]),
- **XGBoost**: scalable tree boosting (`xgboost` in package `xgboost` [3]) using only the index of the observation as covariate.

On the one hand, the experiment shows that the hybrid approach reaches the lowest MASE and MAPE values for both time series. The Telescope forecast reaches a MASE value of about 0.064 for the IBM trace and 0.179 for the airline passengers trace. The MAPE values are about 51.628% and 3.382%. The second best MASE values are achieved by tBATS with about 0.191 for the IBM trace and 0.276 for the airline passengers trace. Furthermore, tBATS reaches the second best MAPE value for the airline passengers trace with about 5.472%. However, ANN outperforms tBATS in matters of the MAPE value for the IBM trace, i.e., ANN achieves a MAPE value of about 179.537. On the other hand, the experiment shows that Telescope has a very short runtime with about 8.557 and 2.679 seconds. On the IBM trace, ETS, SVM, and XGBoost itself achieve shorter runtimes compared to Telescope. Though, each of these forecasting methods delivers a bad accuracy. On the airline passengers trace, only tBATS has a longer runtime than Telescope. Since the IBM trace is about 15 times as long as the airline passengers trace, this experiment implies that the runtime of the Telescope approach does not depend as much on the time series length as some state-of-the-art forecasting methods, i.e., ARIMA, ANN, and tBATS, do.

Table 1: Accuracy and runtime of state-of-the-art forecasting methods and Telescope.

Forecasting Method	**IBM Trace**			**Passengers Trace**		
	MASE	MAPE [%]	Time [s]	MASE	MAPE [%]	Time [s]
Telescope	0.064	51.628	8.557	0.179	3.382	2.679
ARIMA	0.343	813.570	12.301	0.358	6.255	1.065
ANN	0.788	179.537	12.172	0.400	7.473	0.801
ETS	0.986	2992.701	0.531	0.358	6.361	2.371
tBATS	0.191	253.243	38.078	0.276	5.472	4.538
SVM	0.276	574.624	2.312	3.711	67.909	0.233
XGBoost	0.736	545.469	0.484	0.692	11.936	0.278

5 Conclusion

In this paper, Telescope, a new hybrid approach for multi-step-ahead forecasting, is introduced. The approach uses clustering for creating categorical information like weekdays and weekends. STL decomposition is used to split the time series into trend, seasonality, and noise. ARIMA without seasonality is used to forecast the trend with low overhead. The seasonal pattern delivered by STL is simply continued. Finally, XGBoost is applied using the trend, season, and cluster forecasts as covariates. Initial evaluations show that the approach achieves good accuracy while maintaining short runtime. As future work, we plan to perform more evaluations and include several extensions to the algorithm like denoising based on wavelet transformations and identification of break points in the trends.

References

1. Bates, J.M., Granger, C.W.: The combination of forecasts. Journal of the Operational Research Society 20(4), 451–468 (1969)
2. Cano, G., Garcia-Rodriguez, J., Garcia-Garcia, A., Perez-Sanchez, H., Benediktsson, J.A., Thapa, A., Barr, A.: Automatic selection of molecular descriptors using random forest: Application to drug discovery. Expert Systems with Applications 72, 151–159 (2017)
3. Chen, T., Guestrin, C.: Xgboost: A scalable tree boosting system. In: ACM SIGKDD 2016. pp. 785–794. ACM (2016)
4. Clemen, R.T.: Combining forecasts: A review and annotated bibliography. International Journal of Forecasting 5(4), 559–583 (1989)
5. Cleveland, R.B., Cleveland, W.S., McRae, J.E., Terpenning, I.: Stl: A seasonal-trend decomposition procedure based on loess. Journal of Official Statistics 6(1), 3–73 (1990)
6. Collopy, F., Armstrong, J.S.: Rule-based forecasting: Development and validation of an expert systems approach to combining time series extrapolations. Management Science 38(10), 1394–1414 (1992)
7. De Menezes, L.M., Bunn, D.W., Taylor, J.W.: Review of guidelines for the use of combined forecasts. European Journal of Operational Research 120(1), 190–204 (2000)
8. El Haouij, N., Poggi, J.M., Ghozi, R., more: Random forest-based approach for physiological functional variable selection: Towards driver's stress level classification (2017)
9. Hochenbaum, J., Vallis, O.S., Kejariwal, A.: Automatic anomaly detection in the cloud via statistical learning. arXiv preprint arXiv:1704.07706 (2017)
10. Hyndman, R.J., Khandakar, Y., et al.: Automatic time series for forecasting: the forecast package for r. Tech. rep., Monash University (2007)
11. Krishnamurti, T.N., Kishtawal, C., Zhang, Z., LaRow, T., Bachiochi, D., Williford, E., Gadgil, S., Surendran, S.: Multimodel ensemble forecasts for weather and seasonal climate. Journal of Climate 13(23), 4196–4216 (2000)
12. LeCun, Y., Bengio, Y., Hinton, G.: Deep learning. nature 521(7553), 436 (2015)
13. Liu, N., Tang, Q., Zhang, J., more: A hybrid forecasting model with parameter optimization for short-term load forecasting of micro-grids. Applied Energy 129, 336–345 (2014)
14. Livera, A.M.D., Hyndman, R.J., Snyder, R.D.: Forecasting time series with complex seasonal patterns using exponential smoothing. Journal of the American Statistical Association 106(496), 1513–1527 (2011)
15. Meyer, D.: Support vector machines (2017), `https://cran.r-project.org/web/packages/e1071/vignettes/svmdoc.pdf`
16. Ngiam, J., Khosla, A., Kim, M., Nam, J., more: Multimodal deep learning. In: ICML 2011. pp. 689–696 (2011)
17. Pai, P.F., Lin, C.S.: A hybrid arima and support vector machines model in stock price forecasting. Omega 33(6), 497–505 (2005)
18. Wang, X., Smith-Miles, K., Hyndman, R.: Rule induction for forecasting method selection: Meta-learning the characteristics of univariate time series. Neurocomputing 72(10 - 12), 2581 – 2594 (2009)
19. Wolpert, D.H., Macready, W.G.: No free lunch theorems for optimization. IEEE Transactions on Evolutionary Computation 1(1), 67–82 (Apr 1997)
20. Zhang, G.P.: Time series forecasting using a hybrid arima and neural network model. Neurocomputing 50, 159–175 (2003)

The analysis of variability of short data sets based on Mahalanobis distance calculation and surrogate time series testing

Teimuraz Matcharashvili[1], Natalya Zhukova[1], Tamaz Chelidze[1],

Evgeni Baratashvili[2], Tamar Matcharashvili[2], Manana Janiashvili[3]

[1] M. Nodia Institute of Geophysics, 1 Alexidze str. Tbilisi, Georgia
[2] Georgian Technical University, 77 Kostava ave, Tbilisi, Georgia
[3] Institute of Clinical Cardiology, 4 Liubliana str. Tbilisi, Georgia

matcharashvili@gtu.ge

Abstract. In this work we present, convenient for short time series, approach which is based on multivariate Mahalanobis distance calculation combined with surrogate time series testing. In order to test ability of this approach to differentiate changes which could occur in complex processes we used data sets of different origin.

We used seismological, meteorological, physiological and economic data sets. Exactly, we analyzed data sets of inter earthquake times (IET), inter earthquake distances (IED) and differences in consecutive magnitudes (DM) compiled from southern Californian earthquake catalogue, data sets of yearly number of warmer and colder days derived from maximal air temperature data bases in Tbilisi, Georgia, arterial systolic and diastolic blood pressure time series of healthy persons, as well as components of Index of Economic Freedom (IEF) and exchange rate time series of three southern Caucasian countries.

It was shown that used approach even in the case of relatively short time series, may effectively be used to quantify dynamical changes occurred in different natural complex processes.

Keywords: short time series, Mahalanobis distance, surrogate time series.

Introduction

Ancient Pythagoreans said: "All things are numbers". Nowadays, in an era of digital technologies, this truth about numbers, through which we explore world around us, has stopped being an abstract philosophical statement and became a part of everyday life. In most cases we manage to do so that these numbers (commonly measured, or calculated somehow) are spaced equally in time and, thus, represent an evenly sampled time series, though often numbers are available to us only in the form of unevenly sampled

data sequences. Anyway time series or data sequences arise as recordings of processes which vary over time. In physical world time series are discrete though in general they can be continuous.

Presently it is well recognized, that natural processes are complex having characteristics, such as: dispersed interaction among locally interacting heterogeneous agents in some space, no global controller that can exploit opportunities arising from these dispersed interactions, cross-cutting hierarchical organization with many tangled interactions, continual learning and adaptation by agents, out of equilibrium dynamics**,** etc. Examples of complexity can be found in very different areas, such as atmosphere (climate and weather change), geophysics (tides, earthquakes, volcanoes, magnetic field variations), social systems (crowd behavior), medicine and biology (rhythms, physiological cycles, epidemics), economy (financial market behavior, exchange rates), engineering (friction, fracturing), communication (electronic networks, internet packet dynamics), etc. Consequently, related time series often are not stationary and complex. The problem arises when we try to get reliable information about behavior of complex process and see that available data set do not allow reliably use existed methods of complex time series analysis; time series from complex processes need to fulfill strong requirements on length, quality, etc. what often is impossible [1, 2].

In such cases we are forced to combine different approaches in order to have understanding on general features of complex process based on existed data sets. In this work we describe results of our analysis of complex time series of different origin based on combination of multivariate analysis and surrogate data testing [1, 2, 3]. Exactly we used multivariate Mahalanobis distance calculation, to assess changes that occurred in the analyzed process as assessed by two or three its main characteristics. After, in order to test whether observed changes are related with internal dynamical structure of process we compared original process with surrogate time series with distorted time structure.

Thus, the objective of this research can be reduced to a problem of classification, having in mind the separation of states of the analyzed complex processes by selected characteristics at original and distorted time structures.

The analysis like that presented in this work is of fundamental scientific importance, but also is the subject of everyday interest for different practical needs.

Data and methods of analysis

In this research, four different types of data sequences have been used to demonstrate how in the case of short data sets multivariate analysis can be used for complex natural processes. We started from the inter earthquake times (IET), inter earthquake distances (IED) and differences in consecutive earthquake magnitudes (DM) compiled from southern California catalogue as presented by Kagan and colleagues [4]. Exactly, we used part of catalogue from 1929 to 2005 at M4.7 representative threshold.

Next data set, we used, was maximum daily temperatures measured in Tbilisi, Georgia from 1915 to 2013. This data set fulfilled all standards of data quality control and homogeneity. From these time series we compiled a daily max temperature anomalies time series consisting of deviations of daily max air temperatures from the long-term average for the same day of the year. From the daily max air temperature anomalies

data sets we compiled sequences of yearly number of days when anomalies of daily max temperatures significantly deviate from the 99-year mean of anomalies for that days. We considered separately sequences of number of days, when anomalies of max daily temperatures were significantly larger (warmer days-WD) or were significantly lower (colder days- CD) than 99-year mean values. These (WD and CD) sequences stronger characterize features of the warm and cold tails of the distribution, and thus are more relevant to characterize aspects of the anomalous changes in max daily temperatures that occurred as a result of temperature increase.

Next we considered arterial blood pressure data sets. The age of 70 participants varied from 30 to 50 years. All subjects gave informed consent to participate in the study. Participants of the study were not given medicines for 2-3 days preceding the examination. The monitoring of blood pressure was carried out from 12.00 a.m. to 12.00 a.m. of the next day, taking into consideration the physiological regime of participants of study. We analyzed systolic (SBP) and diastolic (DBP) arterial blood pressures. These data have been obtained from 24h ambulatory monitoring recordings at 15 min sampling time.

Used in this research economical data sets represented components of Index of Economic Freedom (IEF) as well as daily increments of currency exchange data for three southern Caucasian Countries, Azerbaijan, Georgia and Armenia (2013-2016).

The main goals of our research was akin to a general classification problem, i.e. a problem, regarding changes that occurred in certain process (no matter seismic, climatic, physiological or economical). For this purpose in the present research the Mahalanobis distance (MD) calculation was applied [3] which is a popular method of distinguishing multivariable data groups by using a univariate distance measure that is defined by several performance parameters. Mahalanobis distance can be calculated as following:

$$D^2 = (\bar{x}_1 - \bar{x}_2)^T S^{-1} (\bar{x}_1 - \bar{x}_2)$$

where $\bar{x}_1$ and $\bar{x}_2$ are sample means from sample sets of sizes n1 and n2, The 'T' superscript denotes the transpose operator. S is pooled covariance matrix:

$$S = \frac{((n_1 - 1)S_1 + (n_2 - 1)S_2)}{n_1 + n_2 - 2}$$

where Si are covariance matrices of corresponding groups.

Generally, the two conditions or states of systems are more similar (more probable to belong to the same class or group), if their MD value is smaller. After computation of MD values, in order to assess the significance of separability between compared groups, Hotelings T2 statistics was used, which was then converted into F–value and assessed by F-test. F value was calculated as:

$$F = \frac{n_1 n_2}{n_1 + n_2} \frac{n_1 + n_2 - p - 1}{(n_1 + n_2 - 2)p} D^2$$

where p and (n1+n2 -p-1) are degrees of freedom. Then calculated F values were compared with a critical value, Fc , which, for certain degrees of freedom values, can be easily found in different statistical textbooks. When calculated F>Fc, then null hypothesis, that there is no separation between considered groups, can be rejected and

thus statistically significant difference between groups is established at a specified probability.

Usually MD calculation is preferable for multivariate comparison for two main reasons. First, it reduces a multivariate system to a univariate system, and second, MD is sensitive to inter-variable changes in a multivariate system [3].

In order to assess influence of long- and short-range temporal correlations in considered data sets on separability analysis results, it is necessary to compare with surrogate data sets where original time structure is intentionally distorted in a certain manner [1, 2]. In present research however, we restrict analysis only by shuffled surrogates in which original time structure is completely destroyed. Results of comparison with other surrogates in which original time structure is just partly destroyed will be presented in future. Thus here we completed an analysis on randomized (shuffled) data sets. For 50 of such randomized data sets we compiled sequences necessary for analysis of randomized time series. It is logical that these data sets were much closer to a normal distribution and thus comparison with such data sets was important also for the correctness of interpretation of results of MD calculation.

Results and discussion

As it is said in the previous section, the main goal of research was a classification of changes that occurred in the considered complex system during analyzed period assessed by the specially selected two, three characteristics. Generally, one of the most important steps in such classifications is systems' feature extraction [3]. This implies the transformation of original data sets into new ones, enabling to focus on targeted features of the investigated process.

We have started from the multivariate analysis of seismic process based on Southern California earthquakes catalogue [4]. From this database we compiled IET, IED and DM data sequences. These data sequences are typical examples of unevenly sampled data sets. Thus because of high representative threshold and relatively short catalogue we couldn't analyze systems behavior in equal time intervals and decided to compare similarity or dissimilarity of seismic process in consecutive windows of 40 (IET, IED, DM) data shifted by 10 data. In Fig. 1(left curve), we show results of comparison between the first (starting from 1929) window (containing first 40 data) with other 40 data windows shifted by 10 data. As we see seismic process assessed by the variability of IET, IED, DM sequences in most of these windows looks similar like in the first window. Only two windows (4^{th} and 11^{th}) reveal statistically significant difference comparing to first window. It is important to say that these two windows are quite different by the amount of released seismic energy. Indeed as we see in Fig. 2, in the 4^{th} window almost the maximal amount of seismic energy was released while the 11^{th} window is close to minimal amount of released seismic energy, among all considered 40 data windows. This, apparently, points that the amount of released seismic energy influences features of earthquakes space time and energetic distribution. Here it is necessary to underline that when we compare 2nd, 3rd, etc. windows to other windows we certainly got other results what need to be carefully discussed in future. Again, here we decide to be restricted by comparison with only the first window, in which as it follows from Fig. 2, amount of released seismic energy is close to the maximal amount of energy released in considered 40 data windows.

To make our analysis more independent from space time and energetical dynamical structure of natural seismic process we decided to use shuffling procedure. Exactly, as it was described in methods section, we compared natural seismic process with process in which the original time structure was distorted. In other words, we compared original IED, IET and DM data sets with ones compiled from shuffled catalogues in which temporal structure of original seismic process was destroyed. As we see in Fig. 1(right curve), comparison with data sets compiled from catalogues where natural dynamical structure was distorted, shows that there are windows in which dynamical features of seismic process is close to random process, while in other windows we observe significant difference from randomness. This apparently points that in these windows seismic process behave more regular by the features of space time and energetic distribution. Possible in this case, the coincidence with windows where maximal amount of seismic energy was released is not by chance and the process is influenced by features of aftershocks distribution. It is necessary to underline that we dealt with cleaned catalogue [4] at high magnitude threshold level (M4.7), what definitely decrease possibility of appearance of aftershocks in the catalogue, but to exclude such possibility completely seems is impossible.

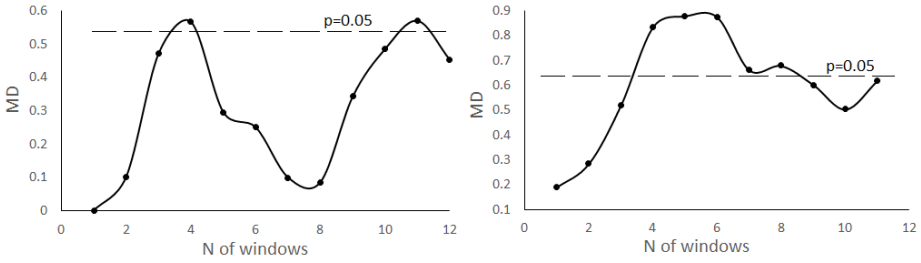

Fig. 1. MD values calculated by IET, IED and DM sequences for consecutive 40 data windows, shifted by 10 data, in Southern California earthquake catalogue, compared to the first window (left curve) as well as compared with randomized IET, IED and DM sequences from the time structure distorted catalogue (right curve). Dotted line corresponds to significant difference between windows at p=0.05.

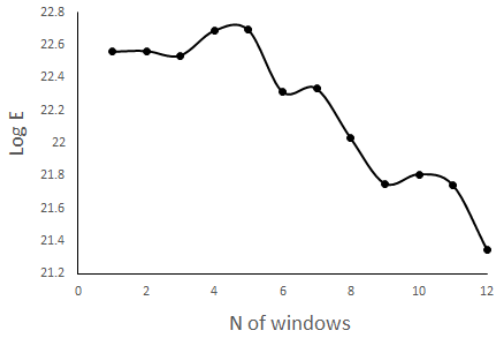

Fig. 2. Seismic energy released in consecutive 40 data windows, shifted by 10 data. Southern California Earthquakes catalogue, 1929-2005.

Anyway presented analysis convinces that even in the case of short data sets for which using of common dynamical data analysis tool is impossible, we may draw important conclusions about dynamical features of complex seismic process based on the procedure of multivariate MD calculation combined with surrogate data testing.

Second type of data sets, for which we tested ability of approach to assess changes in the dynamical features of complex process based on MD calculation of short data sets, came from climatology. Namely, as it was mentioned above we used WD and CD data sequences derived from data bases of daily max air temperatures in Tbilisi, Georgia (1915-2013). We underline again that these sequences of warmer and colder days stem from the same - daily max air temperature data sets. Additional analysis described elsewhere [5] convinces us that changes occurred in the local climate should be much more complicated than a simple shift towards an increase of mean max air temperatures many times described in literature [see e.g. http://www.ipcc.ch/publications_and_data/ar4/wg1/en/ch3s3-8-2.html]. At the same time it becomes clear that a separate analysis of two processes (i.e. variability of warm and cold days), based only on monovariate considerations, will not give a correct view of changes that occurred as a result of increase in max daily air temperatures.

Therefore in order to learn more about changes in the local climate in the sense of variability of warmer and colder days, we accomplished simultaneous multivariate analysis based on both (WD and CD) data sets. We compared two groups, each of which contained sequences of yearly number of warmer days as the first column and colder days as the second column. Analysis was accomplished in the consecutive 33-year windows, shifted by 11 years.

In Fig. 3, we show MD values calculated for different sliding windows; dotted line in these figure corresponds to the level of significant difference ($F > 4$, at critical $Fc=3.14$ for $p=0.05$). According to obtained results, significant separation was observed for mainly distant (in time) windows. Generally significant separation between compared groups means that features of variability of yearly number of warmer and colder days have been strongly changed. Thus assessed by features of the variability of yearly number of warm and cold days the state of the local climate change process in Tbilisi, has significantly changed during last 99 years.

At the same time changes happening with variation of yearly number of warmer and colder days in Tbilisi look regular because they occurred gradually (MD values in later windows compared to the first window almost always increase significantly) during a whole period of observation. MD for windows in the middle of observation period are less different from the first and last window, sometimes the difference is insignificant.

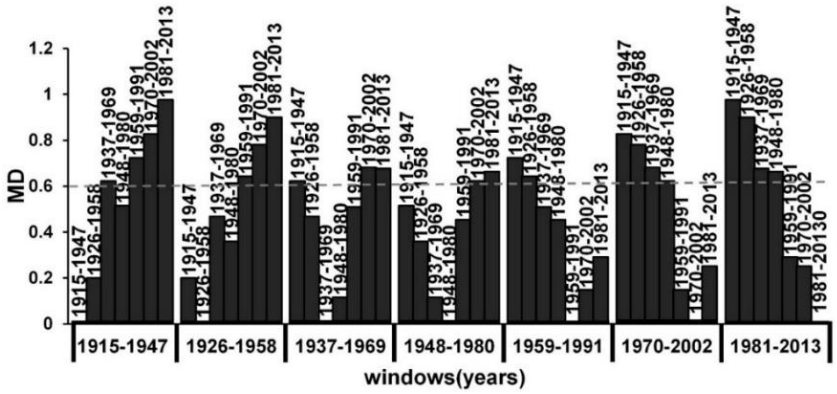

Fig. 3. Mahalanobis distances calculated by sequences of yearly number of warmer and colder days in consecutive 33-year windows. At the bottom are shown sections – windows (of 33year span), to which other 6 windows (in columns) were compared

Thus we can conclude that over the period of our analysis local climate underwent strong changes in the features of variability of yearly number of warmer and colder days. Further we performed analysis of changes in local climate over analyzed period of observation, in sense of time correlation features in variation of yearly number of warmer and colder days. For this, as it was described above, it was necessary to compare original data sets with ones, where original temporal structure was intentionally distorted. In general, time series of daily max air temperature anomalies used in this research, represent a certain type of data sets with removed yearly trends, i.e. the time structure of the original process of daily max air temperature variation is already essentially changed. At the same time, there are different kinds of short- and long-term correlations, which obviously still exist in such data sets even after removal of yearly trends. This is why we further destroyed all internal time structures of the original process by random shuffling. Exactly, we constructed time structure distorted sequences of yearly number of warmer and colder days, based on randomized data sets of anomalies of max daily temperatures, which in turn have been compiled from averaged rows of several tens of shuffled original max air temperature data sets. As it was expected, time structure distorted data sets of number of warmer and colder days almost do not reveal changes in consecutive 33-years windows (not shown here), in contrast to original (WD and CD) sequences (presented in Fig. 3).

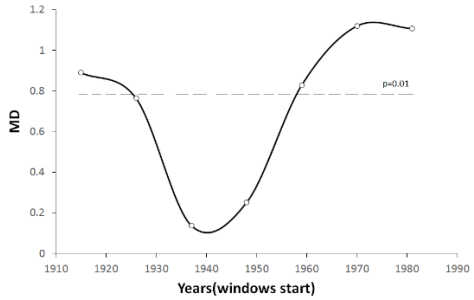

Fig.4. Mahalanobis distance values between original and time structure distorted sequences of yearly number of warmer and colder days in Tbilisi, calculated for consecutive 33-years windows (11-year step, 1915-2013.

Results of Mahalanobis distance calculation when original and time structure data sets have been compared is presented in Fig. 4. From this figure it can be concluded that extent of regularity in the local climate variability, in sense of changes in the amount of warmer and colder days, has significantly changed in different 33 year windows of considered 99 year period. Most dysregulated the situation with climate looked in windows starting from 30^{th} to 70^{th} of last century. What presently can be said for sure is that these changes in the local climate in Tbilisi should be related with changes in large- and small-scale atmospheric dynamics. In the present work we do not go deeper in these discussions, because the main goal was to demonstrate effectiveness of used approach for short data sets from different complex natural processes.

Next for the same purpose we proceeded to the analysis of physiological data sets. Namely we analyzed arterial blood pressure data sets (SBP and DBP) of persons falling into optimal arterial hypertension grade, according to guidelines of European Society of Hypertension (ESH) and the European Society of Cardiology (ESC) [6]. Generally blood pressure variability is one of the most often discussed in special scientific literature questions. Most attention usually is paid to differences in the blood pressure variability of patients from different hypertensive groups [see e.g. 7, 8].

Knowledge of the character of variability of blood pressure characteristics is very important because may provide unique information on human physiological system's behavior and may serve as characteristic fingerprints for health condition identification as well as for comparison with other systems and models. Among others, is very important to further clear up the character of changes in blood pressure typical for certain hypertensive groups (here in the optimal arterial hypertension grade, according to guidelines of European Society of Hypertension (ESH) and the European Society of Cardiology (ESC) [e.g. 6]). Exactly, in this research we aimed to assess changes occurred during different periods of a day in persons falling in optimal arterial hypertension group. We accomplished multivariate analysis of averaged (over whole group) values of systolic and diastolic blood pressures which were measured in each 15 minutes during 24 hour observation period.

We see in Fig.5 (left curve), that all consecutive (8 hour long) windows are indistinguishable from first window (12.00-20.00) excluding two neighbor windows at the beginning of period of observation. Most different from the first window, according to largest MD value, is 12th window. After extent of difference decreases though remain statistically significant comparing to first window (see Fig.5, left curve). It is not shown here but we have carried out comparison between all windows and concluded that in about 60% of considered cases neighboring, 8 hour long, windows are statistically not different. Two windows, started on 16.00 and 18.00, are statistically similar just comparing to one neighbor window. Also, we observed interesting fact that sometimes certain window may reveal kind of long range correlation, when by features of SDP and DBP variability it is statistically different from closer windows but is indistinguishable from farer ones.

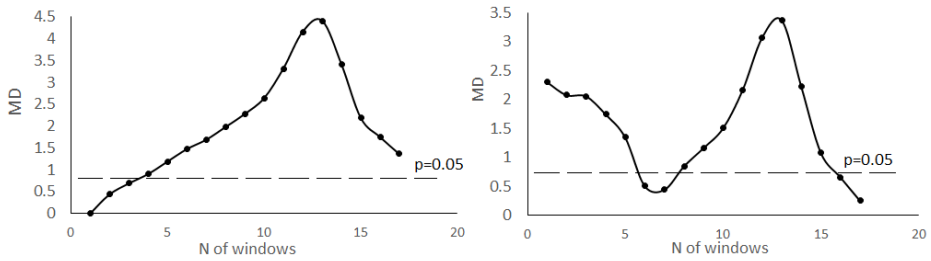

Fig.5. Mahalanobis distance values calculated for consecutive, 8 hour, windows (shifted by 1 hour) of sequences of systolic and diastolic blood pressures of persons in optimal arterial hypertension group comparing to the first window (left curve), comparing to time structure distorted time series (right curve).

This fact inspired us to compare original time series with data sets when original time structure of systolic and diastolic pressure measurements is destroyed by shuffling procedure. In this case as we see in Fig. 5 (right curve), blood pressure variability as compared with sequences of averaged time randomized data sets, reveals interesting features. Exactly, 8 hour windows started on 17.00 and 18.00 as well as 03.00 and 04.00 by features of systolic and diastolic blood pressure variability are indistinguishable from random process.

As we already mentioned above, in this work we did not aimed to provide explanations of found changes. We just wanted to underline that our results clearly show that having just short physiological data sets it is possible to get new information about changes in dynamical features of certain (here healthy) group by the variation of systolic and diastolic blood pressures.

At the next step of our analysis we have targeted to test next example of complex time series - economical data sets. For this purpose we have selected economical data sets for Southern Caucasian Countries: Armenia, Azerbaijan and Georgia. Namely, we started from comparison of economical characteristics of these countries by their Index of Economic Freedom (IEF), as it is presented at Heritage Foundation Report (http://www.heritage.org/index/) for last four years. We have observed that situation in southern Caucasus as whole, according to the yearly IEF components of three countries,

tends to be slightly changed and in 2016 change was rather stronger and close to be significant in comparison with 2013 (left part of Fig. 6).

At the same time comparison with Georgia for four years of analysis indicates, that economical situation as assessed by IEF components is not different from Armenia (MD value 0.45) while situation is close to be significantly different (MD value 0.51, F=2.32 at critical Fc=2.5 for p=0.05) if we compare Georgia with Azerbaijan (not shown here). Because of they are very short and specific, for data sets of yearly components of IEF we could not use surrogate testing. So, we carried out additional multivariate analysis for southern Caucasian countries based on normed increments of daily exchange rates time series. As follows from our results (right part of Fig. 6), by variability of increments of national currencies situation of southern Caucasian countries was significantly different in 2015 comparing to 2013, while in 2014 and 2016 we do not observe significant changes comparing to the 2013.

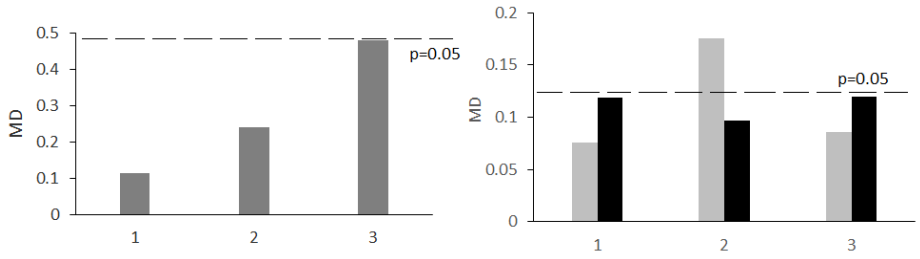

Fig.6. Mahalanobis distance values, calculated for three southern Caucasian countries in 2014(1), 2015(2) and 2016(3) compared with 2013 year: based on yearly components of IEF (left part of figure), based on normed currency exchange rates (grey columns in the right part of figure) compared with time structure distorted data sets of increments of currency exchange (black columns in right part of figure).

Moreover, apparently observed in 2015 change have serious grounds rooted in the processes taking place in domestic economies of these countries as far as are not related with random factors which could be occurred by chance. Indeed when compare with surrogates where original time structure of exchange rate was distorted we did not find significant difference this fact convinces that mentioned changes can not be regarded as random (see black columns in Fig. 6).

Thus in present work, for four data sets of different origin we demonstrated ability of used approach to indicate interesting dynamical features of complex natural processes even in the case of short available data sets.

Summary

In preset work we aimed to test method which was developed for the purpose to assess the character of changes in complex dynamical systems when have short data sets. Approach is based on the Mahalanobis distance calculation combined it with surrogate data testing.

We used approach for analysis of data sets from different natural processes. Exactly we used seismological, meteorological, physiological and economic data sets

For all used data sets it was shown that combination of Mahalanobis distance calculation with the surrogate data testing enables to have new understanding about changes occurred in complex systems even in the case of relatively short time series.

Acknowledgement. This work was supported by Shota Rustaveli National Science Foundation (SRNSF), grant 217838 "Investigation of dynamics of earthquake's temporal distribution".

References

1. Abarbanel, H.D.I., Brown, R., Sidorowich., and Tsimring, L. S. The Analysis of Observed Chaotic Data in Physical Systems, *Rev. Mod. Phys.* 65 (4), 1331–1392 (1993).
2. Matcharashvili T., Chelidze T., Janiashvili M., Identification of Complex Processes Based on Analysis of Phase Space Structures, Imaging for Detection and Identification, Byrnes, J.S. (Ed.) 2007, 207-243, Springer, Dordrecht.
3. McLachlan, G. J. Mahalanobis distance. Resonance, 6, 20–26 (1999).
4. Kagan, Y. Y., D. D. Jackson, and Y. F. Rong, A new catalog of southern California earthquakes, 1800-2005, Seismol. Res. Lett., 77(1), 30-38, 2006.
5. Matcharashvili, T., Zhukova, N., Chelidze, T., Founda, D., Gerasopoulos, E., Analysis of long-term variation of the annual number of warmer and colder days using Mahalanobis distance metrics - A case study for Athens, accepted for publication in Physica A 487, 22-31, (2017).
6. Joint National Committee on the Detection, Evaluation, and Treatment of High Blood Pressure. The sixth report of the Joint National Committee on prevention, detection, evaluation, and treatment of high blood pressure. Arch Intern Med. 157:2413–2446, (1997).
7. Janiashvili, M., Jibladze, N., Matcharashvili, T., Topchishvili, A., Comparison of statistical and distributional characteristics of blood pressure and heart rate variation of patients with different blood pressure categories, Model Assisted Statistics and Applications, 8 177–184, DOI 10.3233/MAS-130262 (2013).
8. Pastor-Barriuso R, Banegas JR, Damian J, Appel LJ, Guallar E. Systolic blood pressure, diastolic blood pressure, and pulse pressure: an evaluation of their joint effect on mortality. Ann Intern Med. 139: 731–739, (2003).

Rainfall Measurements from Commercial Cellular Networks

Reason L. Machete*[1,2] and Leonard A. Smith[2,3] and Nnyaladzi Batisani[1]

[1] Climate Change Div, Botswana Institute for Technology Research and Innovation
[2] Centre for the Analysis of Time Series, London School of Economics
[3] Pembroke College, University of Oxford

Abstract. Weather information is required at various spatial and temporal resolutions for different purposes, including climate studies. If received timely and at relevant time scales and accuracy, such information can be used to issue early warnings. In the case of rainfall, rain-gauges provide the most accurate measurements. In developing countries, however, rain-gauges tend to be few and sparsely distributed. Botswana is a specific example where this is the case. There is access to high-resolution satellite data, but its accuracy is known to be relatively poor. This paper demonstrates how microwave signals from cellphone towers around the country can be used to monitor rainfall to supplement data from other sources. It takes advantage of the nonlinear relationship between signal attenuation and rainfall rate and argues that uncertainty in the rainfall estimates should be modeled by a multiplicative random term. This approach is meant to handle the heteroskedasticity in the noise-free model. Put another way, it is demonstrated that a logarithmic transformation of the power law relation helps deal with heteroskedasticity to improve rainfall estimates.

1 Introduction

A microwave link comprises two towers, one with a transmitter and the other with a receiver. A signal is transmitted between the two towers at a given frequency and power. The power of the signal received at the receiving tower is an index of the quality of the microwave link signal. It is inevitable that the power of the received signal will be lower than that of the transmitted signal, a feature called signal attenuation. Signal attenuation is caused by environmental conditions such as winds, rainfall and humidity. Depending on its magnitude, this attenuation can manifest itself to mobile phone users through an unclear voice signal. Of all environmental conditions, rainfall intensity has the greatest contribution to signal attenuation; higher rainfall intensity results in greater signal attenuation, and the relationship between rainfall intensity and signal attenuation is nonlinear (Hitschfeld and Bordan, 1954; Leijnse *et al.*, 2008). Mobile

* Corresponding author: Email: machete.r.l@gmail.com; rmachete@bitri.co.bw; Tel: +267 3607628

phone companies typically monitor the quality of the signal at each microwave link through devices placed at the towers to transmit information to their respective control centres. An engineer at the control centre can thus log into a computer to see the performance of any microwave link of interest. Any serious problems detected can be addressed as quickly as possible.

Recent studies focusing on some parts of Europe, Asia and some regions of the USA have explored the possibility of estimating rainfall from the attenuation of microwave signals transmitted between mobile phone towers. Some of the studies used the nonlinear model that can be found in Leijnse *et al.* (2008) and Overeem *et al.* (2013), fitting the parameters via the least squares criterion. The model originates from radar technology where microwave signals were originally used to detect aircrafts. An implicit assumption in the rainfall measurement studies is that rainfall intensity has a dominant effect on signal attenuation. Furthermore, several studies (including the ones cited here) use radar rainfall estimates to calibrate the model [4]. In many instances, studies use data obtained under experimental conditions. In particular, rain-gauges have been placed between microwave link towers so as to obtain what is referred to as path-averaged rainfall intensity. This approach can be useful when the distance between the link towers is large. The reason is that it could be raining in some part of the link and not be raining in another part, mainly due to the length of the link. If the link distance is short, it may not be necessary to have several rain-gauges within the link. Despite the link lengths being approximately 3 km long, which is relatively short, Overeem *et al.* (2013) use several rain gauges within the link to then obtain an average value.

The current paper focuses on measuring rainfall intensity using a link situated in Gantsi, a township in Botswana. This study was done in collaboration with Botswana Telecommunications Corporation who provided microwave link data and engineering expertise. The frequency of the link signal lies within one of the two major frequency bands. There is an automatic weather station near the link. Path-averaging is not performed since rainfall information is from the sole automatic weather station near the link. Rainfall data from the automatic weather station and signal data from the nearby microwave link are used to calibrate the model via a least squares approach. There is, however, a problem. Estimation errors are large at large attenuation (and rainfall intensity) values, the so called hetero-skedasticity. This sort of problem was noted in the case of rainfall estimation from radar signal data (Aghakouchak *et al.*, 2010). The signals in question were microwave signals and the rainfall-attenuation model is the same as that used in this paper. Aghakouchak *et al.* (2010) suggested that a way to deal with the problem was to perform maximum likelihood parameter estimation. It is not clear why the maximum likelihood approach would be remedial to this problem. There are traditional approaches to help deal with heteroskedasticity, which include weighted least squares. These approaches are, however, typically appropriate for linear regression. The model here is nonlin-

[4] A limitation of using radar data to calibrate the estimation model is that the resulting estimates cannot outperform the accuracy of the radar estimates.

ear and so requires a different calibration approach to handle heteroskedasticity. This paper suggests that the problem of heteroskedasticity is better dealt with by performing a logarithmic transformation and then doing the least squares fit to calibrate the transformed model. Based on the aforesaid transformation, a stochastic model to account for errors/uncertainties is suggested. An empirical approach that uses the work of Efron and Tishirani (1986) and Efron (1988) is employed to quantify uncertainties in the estimates.

The rainfall retrieval model used in this paper is essentially the same as that for retrieval from radar data as given in Piccolo and Chirico (2005) and Aghakouchak *et al.* (2010). This should not be a surprise because each of these two applications uses microwave signals. Note, however, that a single radar can cost up to a million dollars and currently the sole radar in the country is not functional. Furthermore, the accuracy of retrieval from a weather radar is arguably inferior to that of retrieval from cell phone towers. The country has access to high-resolution satellite data that is received every 15 minutes and at a spatial resolution of 3 km by 3 km. This is from a multi-sensor satellite that uses visible light and infrared, which are known to provide inferior rainfall estimates compared to using microwave signals (Salio *et al.*, 2015).

2 Rainfall-Attenuation Model

The signals within the band of frequencies used for cellular communications are called microwaves and the system of a pair of towers and associated antennas is called a microwave link. Rainfall exacerbates the attenuation of microwave signals. Using an appropriate transfer function, the extent of signal attenuation can be used to infer the amount of rainfall (Leijnse *et al.*, 2008). In earlier work (Overeem *et al.*, 2013), the retrieval algorithm proposed used formulas that depend on the length of a network link that has two antennas (placed on towers), the attenuation due to wet antennas and the minimum and maximum rain-induced attenuation in a 15-minute interval. The maxima and minima were based on network links and not on a single link. These extreme values were then used to compute the path-averaged minimum, maximum and mean rainfall intensities in 15-minute intervals.

In this paper, attenuation due to wet antennas is neglected since discussions with network engineers suggested antenna design is not conducive to film accumulation. Secondly no maxima and minima specific-attenuation values feature because a single link is used in each case. Rainfall data was obtained from the sole automatic station nearest to the link. Assuming that the diameter of raindrops is small compared to signal wavelength, the relationship between signal attenuation and rainfall rate is governed by the power law (Wexler, 1948)

$$R_t = \alpha k_t^{\beta}, \tag{1}$$

where R_t is the rainfall (or rainfall intensity), k_t is the specific attenuation and α and β are parameters that are fixed for a given signal frequency. Under the afore-

mentioned assumption, Rayleigh law of scattering holds [5]. Furthermore, Equation (1) is most accurate at wavelengths approximately equal to 10 cm (Wexler, 1948), at which wavelengths raindrop diameters are comparatively small. More generally, the equation is valid for wavelengths between 3 cm and 10 cm, the accuracy being degraded as the wavelength decreases down to 3 cm (Hitschfeld and Bordan, 1954). Hitschfeld and Bordan (1954) asserted that, at low wavelengths, small errors in the parameters α and β lead to large errors in measured (or estimated) rainfall. Wexler (1948) highlighted that the formula is accurate for raindrops of diameters of up to 2.5 mm when the wavelength is about 3 cm, a raindrop-diameter to signal-wavelength ratio of about 5 %. The maximum raindrop diameter at which Equation (1) yields accurate measurements increases with the wavelength. It has been shown in Gunn and Kinzer (1949) that the largest raindrop diameter is approximately 5 mm. This diameter is approximately 5 % of the 10 cm wavelength; this explains why the formula is accurate at this wavelength regardless of the raindrop-diameter. Errors encountered when the wavelength is low are assessed and quantified in this work. The type of rainfall that is common in Botswana is heavy thundershower and it tends to yield large particle size distribution. For this reason, more accurate rainfall measurements will require signals of long wavelength.

The parameters in Equation (1) are set for a link of length d when attenuation is in the units dB. For a new link of the same frequency but of length d_i, the only parameter that needs to be changed is α. The new parameter to replace α in Equation (1) should then be set to

$$\alpha_i = \alpha \left(\frac{d}{d_i} \right)^{\beta}. \tag{2}$$

Each α_i can then be used in the formula for the ith link of the same frequency (or the same frequency band). On the other hand, if the attenuation is in the units dB/km, then the parameter α should be replaced by $a = \alpha d^{\beta}$ whilst the parameter β remains unchanged. At those parameter values, the formula can then be used for links of the same frequency but different lengths.

It is useful to note that the motion of a signal traveling through a refractive medium is governed by the equation

$$\frac{c}{n} = \lambda f, \tag{3}$$

where c is the speed of light in a vacuum, n is the refractive index of the medium, λ is the wavelength and f is the frequency. Using the refractive index for air, the frequencies corresponding to the wavelengths of 3 cm and 10 cm are approximately 10 GHz and 3 GHz respectively. The assertion of Hitschfeld and Bordan (1954) implies that Equation (1) is valid within these two frequencies, the accuracy getting worse with increasing frequency. These frequencies are well outside

[5] The power of the received signal is proportional to the summation of the sixth powers of the raindrop diameters (Wexler, 1948).

the range of audible frequencies[6], but mobile phone devices have the capacity to demodulate them to the audible range.

As already highlighted, Equation (1) will not hold exactly. It makes sense, therefore, to include a random term that accounts for inaccuracies in the model. One way to include the random term is to modify the power law relation to

$$R_t = \alpha k_t^{\beta} + u_t, \tag{4}$$

where u_t is the random term and α and β are fixed parameters fitted using specific attenuation data and rainfall data from an automatic station. The parameters are fitted as functions of link frequency (Leijnse *et al.*, 2008). Including the random term as in Equation (4) is consistent with fitting the parameters in Equation (1) so as to minimise the root mean square error

$$\mathcal{E}_T^{(1)} = \sqrt{\frac{1}{T}\sum_{t=1}^{T}(\alpha k_t^{\beta} - R_t)^2} \tag{5}$$

as was done in Leijnse *et al.* (2008), where T is the total number of data points used. During the calibration process, only a portion of the data should be used. The rest of the data can then be used to validate the model, i. e. to assess how good the model is. Here, the bootstrap approach proposed by Efron and Tishirani (1986) and Efron (1988) is used to obtain a distribution of errors. The fitting error $\mathcal{E}_T^{(1)}$ can be thought of as a negatively oriented measure of the goodness of the fit. Other measures of goodness of fit are the coefficient of variation, the dispersion of errors and ρ^2 (the explained variance) (Leijnse *et al.*, 2008; Rios-Gaona *et al.*, 2014). In this paper, we contend that fitting the parameters using (5) is ill-advised because of the nature of the regression errors. This point is highlighted further in Section 3 where an alternative approach that is consistent with empirical evidence is suggested.

The received signal level S_t will show fluctuations even on days when there is no rainfall. The fluctuations are due to other environmental effects such as humidity and wind. Humidity can cause fluctuations of 1 dB in amplitude (Ulaby and Moore, 1981). Wind will have a negligible effect on signal level because wind particles are very small relative to signal wavelength. Nonetheless, it is necessary to seave out non-precipitation effects when assessing the impact of rainfall on received signal level. Considering an archive of data, if the minimum received signal level on the days it did not rain is S_c, then specific signal attenuation is given by

$$k_t = (S_c - S_t)H(S_c - S_t), \tag{6}$$

where $H(\cdot)$ is the Heaviside step function. The formula given by Equation (6) gives attenuation due to rainfall, after all other environmental effects have been sieved.

[6] The range of audible frequencies is 300 Hz to 3.4 KH

3 Results and Analysis

The microwave link data was provided by the Botswana Telecommunications Corporation. The data is primarily used to monitor signal performance at the towers to ensure early detection of any signal problems. There is a transceiver placed on each link tower, which means it both transmits and receives a signal, but each recording is unidirectional. The recordings are every 15 minutes. Under normal conditions, signal attenuation is inevitable and the received signal will fluctuate around a certain level. If it rains within the link, then there will be more attenuation of the signal, which results in a greater drop in the received signal level. A good received signal level should lie between -30 dB and -60 dB. When the receiver shows a signal level of around -71 dB, it is an indication of a broken link (or no signal). Rainfall data, sampled every 15 minutes, was obtained from a SASSCAL [7] automatic weather station.

This paper reports results for a links in Gantsi. The transmission frequency for the Gantsi link was 23 GHz. Frequency bands used in cellular communications worldwide typically lie in the range 6 GHz to 40 GHz (Overeem *et al.*, 2013). Since higher frequency signals experience greater attenuation over a given distance, they are used when the link-length is relatively short. The Gantsi link length is about 3.3 km long.

To what extent the power law model presented in the previous section is empirically valid. Consider graphs of Rainfall against signal attenuation given in Figure 1. The left graph in Figure 1 shows a plot on the linear scale whilst the one on the right is shown on the logarithmic scale. In each case, the red line is a mean of bootstrap estimates. According to the graph on the left, larger attenuation values correspond to larger regression errors. It follows that using Equation (5) will suffer from the problem of non-constant variance of regression errors, the so called heteroskedasticity. On the other hand, the graph on the right of Figure 1, which is based on the logarithmic scale, shows regression errors that are homogeneously distributed along the regression line. This suggests that an appropriate model should take the form

$$\log R_t = A + B \log k_t + U_t, \tag{7}$$

where U_t is a random term with $\mathbb{E}[U_t] = 0$ and variance $\mathbb{E}[U_t^2] = \sigma^2$ and $\mathbb{E}[U_t U_\tau] = 0$ whenever $t \neq \tau$. Equation (7) can be obtained from Equation (4) by taking logs on both sides [8] so that $A = \log \alpha$ and $B = \beta$. These parameters can be fitted by minimising the root mean square of errors

$$\mathcal{E}_T^{(2)} = \left\{ \frac{1}{T} \sum_{t=1}^{T} \left(A + B \log k_t - \log R_t \right)^2 \right\}^{1/2}. \tag{8}$$

[7] SASSCAL stands for Southern African Service Centre for Climate Change and Adaptive Land Management. It is a joint initiative of Angola, Botswana, Namibia, South Africa, Zambia and Germany. Data from respective automatic weather stations is provided at www.sasscalweathernet.org.

[8] Provided the noise term u_t is ignored or suppressed.

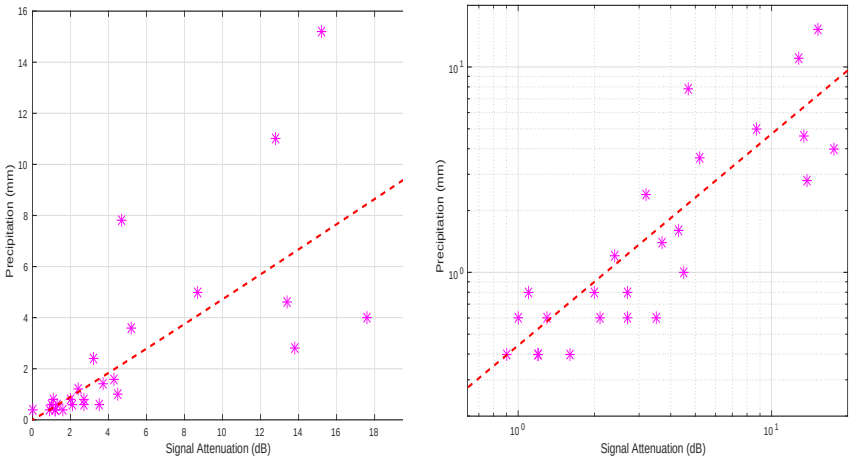

Fig. 1. *Graphs of rainfall (Precipitation) versus signal attenuation for the Gantsi-Khawa Microwave Link. Left: On a linear scale. Right: On a logarithmic scale*

Recasting the problem in the form of Equation (7) reduces it to linear regression, a very well studied problem with established mathematical and statistical properties. The process of fitting the parameters using Equation (8) under the foregoing assumptions is termed ordinary least squares. If the regression errors for the model in (7) are normally distributed, then the resulting parameters are maximum likelihood estimators. Setting $U_t = \log \varepsilon_t$ with $U_t \sim \mathcal{N}(0, \sigma^2)$, then rainfall estimates for a given signal attenuation can be obtained via the formula

$$R_t = \alpha k_t^{\beta} \varepsilon_t. \tag{9}$$

Notice that in this case the multiplicative random term, ε_t, is log-normally distributed and the graph is shown on the right hand of the figure.

Distributions of the parameter estimates for β obtained by the bootstrap method are shown in Figure 2. The distribution of β on the left of Figure 2 was obtained by minimising $\mathcal{E}_T^{(1)}$ whilst the one on the right was obtained by minimising $\mathcal{E}_T^{(2)}$. The distribution on the right is clearly narrower than the one on the left, indicating that there is less uncertainty on estimates of the parameter β when regression errors are homogeneously distributed along the regression line. The homogeneous distribution of regression errors along the regression line is due to the logarithmic transformation of the power law relation. By the logarithmic transformation, a heteroscedastic problem was converted to a homoscedastic one.

Thinking of r_t as the absolute error in rainfall estimates from the regression line, it can be written as $r_t = |\alpha k_t^{\beta} - R_t|$. Distributions of such absolute errors obtained when parameters were estimated using the two measures are shown in Figure 3. Evidently, parameters fitted using the measure for the logarithmic form of the model result in lower estimation errors than those obtained using the

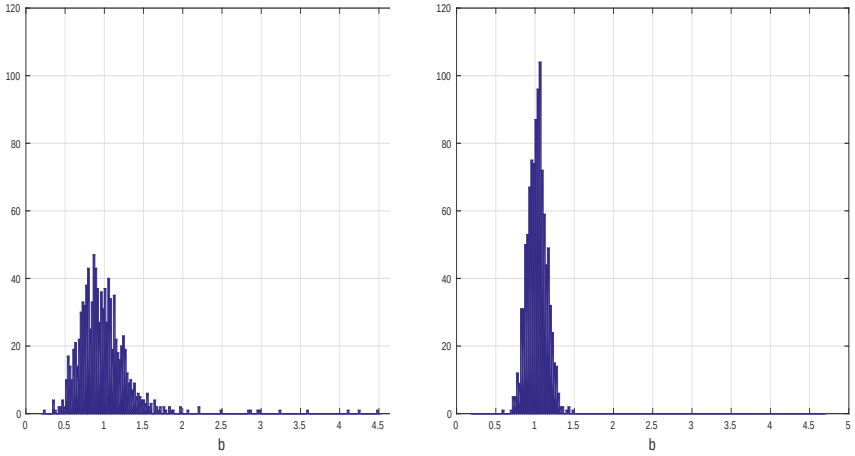

Fig. 2. *Bootstrap distributions of the the parameter β obtained by minimising the measure (Left) in Equation (5) and (Right) in Equation (8).*

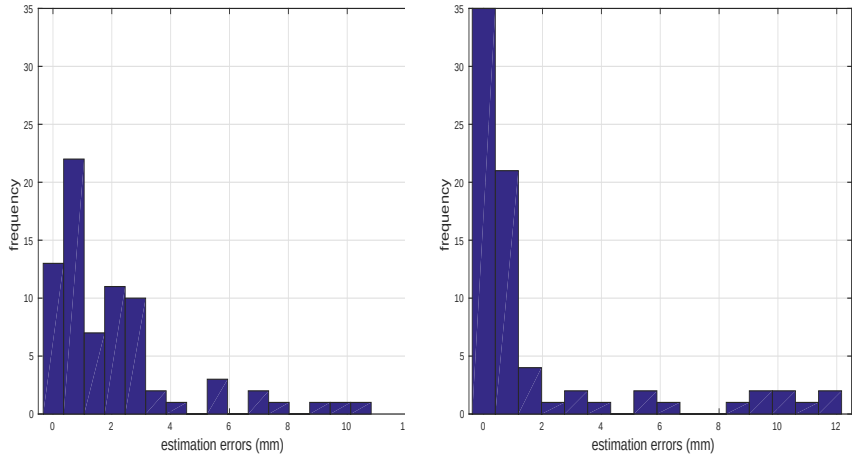

Fig. 3. *Distributions of the absolute errors obtained when the parameters were chosen to minimise the measure (Left) $\mathcal{E}_T^{(1)}$ given in Equation (5) and (Right) $\mathcal{E}_T^{(2)}$ given in Equation (8).*

measure for the power law. In short, transforming the model to its logarithmic form resulted in lower estimation errors. In particular, the logarithmically fitted model yielded only 21% of errors being above 1.5 mm whilst the power-law fitted model yielded 47% of errors above 1.5 mm. The errors are comparable to those obtained in the path-averaged case considered by Leijnse *et al.* (2008) and Aghakouchak *et al.* (2010), yet the parameters in the cited works were event based.

The process of estimating rainfall from signal attenuation can be described as follows: Given an attenuation in the received signal level, one draws a multiplicative random term from the log-normal distribution to compute the corresponding rainfall instead of simply using the original formulation given by Equation (4). In order to further appreciate the effect of the random term in Equation (9), first note that

$$\mathbb{E}[R_t|k_t] = \alpha k_t^{\beta} e^{\sigma^2/2}, \tag{10}$$

where it has been assumed that k_t and ε_t are independent. This assumption is consistent with the graph on the right hand side in Figure 1. Thus an alternative to using Equation (9) is to use the mean curve given by the formula in (10) to estimate rainfall for a given signal attenuation. Equivalently, one can estimate the likely signal attenuation using Equation (10), given a prediction of future rainfall. The implication is that a network company can predict the likely impact of expected rainfall on its network.

4 Discussion

The aim of this paper was to demonstrate how rainfall can be estimated from information used to monitor signal performance of commercial microwave links in Botswana. The area chosen for the study was Gantsi, which lies in the Gantzi districts of Botswana. It contains a microwave link that belongs to Botswana Telecommunications Corporation. There is also a SASSCAL automatic weather station near the link and it provided rainfall data for use in calibrating and validating the retrieval model. The link frequency lies in one of the two major frequency bands that span the country. The link was relatively short.

There was strong empirical evidence in favour of the power law relation between signal attenuation and rainfall intensity. In particular, the logarithmic transformation of the formula fitted the data well and was consistent with a random error distribution that is homogeneous across a range of signal attenuation values. This point helped lay a grasp on the uncertainty in the rainfall estimates. Consequently, a modified version of the power law that appropriately takes uncertainty into account was suggested. It has thus been demonstrated that an appropriate random term to account for uncertainty in the rainfall estimates should be multiplicative. The random term proposed follows a log-normal distribution. Moreover, it has been argued here that the modified formula is better adapted to performing a least squares fit under a logarithmic transformation. A well calibrated model at a given frequency can be used for different link-lengths with an appropriate adjustment of the parameters as suggested in this paper. In earlier studies where there was path averaging, the maximum link length considered was about 22 km (Leijnse *et al.*, 2008; Overeem *et al.*, 2013). In those studies, the majority of the link lengths were less than 6 km. The current study demonstrated that at these short lengths, path-averaging might not be necessary to obtain a well calibrated model.

Leijnse *et al.* (2008) highlighted the effects of frequency and link-length on the accuracy of rainfall estimates, which results were contrary to expectation.

In particular, they suggested that higher (above 22 GHz) frequency links provide more accurate estimates. This contradicts earlier results by Hitschfeld and Bordan (1954). They also argued that the accuracy of the estimates improves with increasing link length. This could be because rainfall intensity estimates are inversely proportional to link length and directly proportional to the logarithm of the link length[9]. Contrary to the argument given by Leijnse *et al.* (2008), the improvement in the accuracy of estimates with link-length is not merely due to path-averaging. The relationship between link frequency and estimation errors, however, needs to be explored further to determine which of the literature strands will be acquitted.

5 Conclusions

This paper demonstrated how rainfall measurements can be estimated from microwave signals, appropriately accounting for uncertainty. Results for a specific frequency band indicated that uncertainty in the estimates should be modeled by a log-normally distributed multiplicative random term. Consequently, high rainfall estimates will be correlated with high errors. The multiplicative random term helps mitigate heteroskedasticity, provided the model parameters are fitted under a logarithmic transformation of the power law. In this paper, it has also been shown how different link lengths at a specific frequency can be accounted for when applying a model calibrated using a specific link. At a given frequency and in the absence of path-averaging, estimation errors need not get better with increasing link length. There is, however, a need to explore the relationship between link frequency and estimation errors in future work to resolve conflicting views in literature.

Acknowledgements

The authors would like to thank the management of Botswana Telecommunications Corporation for permission to access microwave link data and the engineer, Moatshe Nageng, for contributing his time and expertise in the data acquisition. Fruitful discussions with Tiro Nkemelang on remote sensing and with Penny Lesolle on rainfall concepts are appreciated. The authors also thank Khumo Semang for making helpful comments on an earlier version of this manuscript.

[9] The latter part is supported by the path loss model that gives the relationship between signal attenuation and link (or path) length.

Bibliography

Aghakouchak A, Habib E, Bardossy A. 2010. Modeling Radar Rainfall Estimation Uncertainties: Random Error Model. *Journal of Hydrological Engineering* **15**:265–274.

Efron B. 1988. Computer-intensive methods in statistical regression. *SIAM Review* **30**:421–449.

Efron B, Tishirani R. 1986. Bootstrap methods for standard errors, confidence intervals and other measures of statistical accuracy. *Statistical Science* **1**:54–75.

Gunn R, Kinzer GD. 1949. The terminal velocity of fall for water droplets in stagnant air. *Journal of Meteorology* **6**:243–248.

Hitschfeld W, Bordan GW. 1954. Errors inherent in the radar measurement of rainfall at attenuating wavelengnths. *Journal of Meteorology* **11**:58–67.

Leijnse H, Uijlenhoet R, Sticker JNM. 2008. Microwave link rainfall estimation: Effects of link length and frequency, temporal sampling, power resolution, and wet antenna attenuation. *Advances in Water Resources* **31**:1481–1493.

Overeem A, Leijnse H, Uijlenhoet R. 2013. Country-wide rainfall maps from cellular communication networks. *Proceedings of the National Academy of Sciences* **110**.

Piccolo F, Chirico GB. 2005. Sampling errors in rainfall measurements by weather radar. *Advances in Geosciences* **2**:151–155.

Rios-Gaona MF, Overeem A, Leijnse H, Uijlenhoet R. 2014. Space-time quantification of errors in rainfall maps from cellular communication networks. 7th International Scientific Conference on the Global Energy and Water Cycle.

Salio P, Hobouchian MP, Skabar YG, Vila D. 2015. Evaluation of high-resolution satelite precipitation estimates over South America using a dense rain gauge network. *Atmospheric Research* **163**:146–161.

Ulaby FT, Moore RK. 1981. *Microwave remore sensing fundamentals and radiometry. Mocrowave remore sensing: Active and Passive*, volume I. Addison-Wesley, Readong, MA.

Wexler R. 1948. Rain Intensities by Radar. *Journal of Meteorology* **5**:171–173.

Understanding Instantaneous frequency detection: A discussion of Hilbert-Huang Transform versus Wavelet Transform

Maximiliano Bueno-López[1,2], Marta Molinas[2] and Geir Kulia[3]

[1] Facultad de Ingeniería
Universidad de la Salle, Bogotá, Colombia
[2] Department of Engineering Cybernetics
Norwegian University of Science and Technology
Trondheim, Norway
[3] Signal Analysis Lab, Norway

Abstract. *Nonlinear and/or nonstationary properties have been observed in measurements coming from microgrids in modern power systems and biological systems. Generally, signals from these two domains are analyzed separately although they may share many features and can benefit from the use of the same methodology. This paper explores the use of Hilbert-Huang transform (HHT) and Wavelet transform (WT) for instantaneous frequency detection in these two different domains, in the search for a new adaptive algorithm that can be used to analyze signals from these domains without the need to make many a-priory adjustments. Two signals are selected for the investigation: a synthetic signal containing a time varying component and a real EEG signal obtained from The Ecole Polytechnique Federale de Lausanne. The two signals are analyzed with HHT and a discrete WT (DWT). When interpreting the results obtained with the synthetic signal, it is clear that the HHT reproduces the true components, while the DWT does not, making a meaningful interpretation of the modes more challenging. The results obtained when applying HHT to the EEG signal shows 5 modes of oscillations that appear to be well behaved Intrinsic Mode Functions (IMFs), while the results with DWT are harder to interpret in terms of modes. The DWT requires a higher level of decomposition to get closer to the results of the HHT, however multi-frequency bands may be useful depending on the application. The reconstruction of the signal from the approximation and detail coefficients shows a good behavior and this is one application for DWT especially for removing the unwanted noise of a signal.*

Keywords: Electrical signals, EEG signals, Empirical mode decomposition, Hilbert-Huang transform, Hilbert spectral analysis, Wavelets

1 Introduction

1.1 Analysis of modern power systems signals

For many years, Fourier-based analyses was enough to study signals in power systems and the notion of Instantaneous Frequency (IF) has not been previously

explored in such systems. The arrival of new technologies such as distributed generation, nonlinear loads and power electronic devices has increased the network complexity and caused new problems in power quality. This has called for new methodologies for analyzing signals which have different characteristics to previously studied ones [1]. One of the most common techniques used in power systems for signal analysis is the Fast Fourier Transform (FFT) with its intrinsic limitation of frequency resolution. Therefore, new methods that can accurately detect the presence of instantaneous frequency are now necessary. Hilbert-Huang transform (HHT) and Wavelet Transform (WT) have emerged as options to help solve this problem [2], [3], [4]. The disturbance detection method for power systems application has to be capable of dealing with not only harmonic signals but also nonlinear and non-stationary signals. HHT is an adaptive time-frequency analysis method which can deal with this type of signals [2], [5]. Compared with Fourier transform, HHT can analyze and interpret non-stationary and non-periodic signals [6], [7]. WT is a powerful signal-processing tool that has also shown the ability to deal with nonstationary signals and in recent years has taken greater strength in power systems [8]. Usually these techniques are used independently and sometimes combined to provide better performance. In this paper, HHT and WT are applied to two different signals: a synthetic signal that mimics a power system signal and a EEG signal of eye blinks. The observed results and the interpretation from the application of these two methods are discussed in the paper.

1.2 Analysis of Electroencephalography (EEG) signals

The human body has been studied using multiple tools and devices. Nowadays, it is possible to detect diseases, learn about problems and different behaviors using information taken from the body with different types of sensors. Some researchers have focused on analyzing information from the heart [9], [10], [11], but the brain remains one of the organs of greatest interest [12], [13], [14], [15]. Richard Caton discovered electrical currents in the brain in 1875 and Hans Berger recorded these currents and published the first human Electroencephalogram (EEG) in 1924 [16]. The EEG is a measure of neural activity and is used to study cognitive processes, physiology, and complex brain dynamics [17], [18], [19]. EEG signals are nonstationary. In [15] a method is proposed to quantify interaction between nonstationary cerebral blood flow velocity (BFV) and blood pressure (BP) for the assessment of dynamic cerebral autoregulation (CA) using HHT. In [18] an application was presented to detect the emotions of video viewers emotions from electroencephalogram (EEG) signals and facial expressions, while [20] shows the classification of a three-class mental task-based brain-computer interface (BCI) that uses the Hilbert-Huang transform for feature extraction and fuzzy particle swarm optimization with cross-mutated-based artificial neural network (FPSOCM-ANN) for the classifier. In [21] a discrete wavelet transform-based feature extraction scheme for the classification of EEG signals is described. The relative wavelet energy is calculated in terms of detailed coefficients and the approximation coefficients of the last decomposition level. Discrete Wavelet

Transform (DWT) has been widely used to analyze EEG signals. One example of application in [22], refers to providing information related to epilepsy diagnosis.

2 Instantaneous Frequency detection

The notion of Instantaneous Frequency (IF) has been widely studied [23], because in practice, signals are not truly sinusoidal and the concept of frequency must be analyzed in greater depth. Much research has been done on this subject, however it remains an open debate, since some streams of research deny its existence. Generally, signals coming from the physical world have been analyzed using Fourier transform, which gives time invariant amplitude and frequency values. The inherited uncertainty principle associated with the Fourier transform makes the concept of an Instantaneous Frequency hard to define. However, this can be clarified because the uncertainty principle is a consequence of the Fourier transform (or any other type of integral transform). Thus, if we don't apply an integral transform in the frequency computation, we would not be bounded by the uncertainty principle [24]. Historically, IF was computed from analytic signals (AS) through the Hilbert transform. HHT estimates the instantaneous frequency and amplitude of a given signal. To do so, it decomposes any signal down to monocomponents called intrinsic mode function (IMF) by using the Empirical mode decomposition (EMD). With the function $v(t)$ defined as

$$x(t) = r(t) + \sum c_i(t) = r(t) + \sum a_i(t)\cos(\theta_i(t)), \tag{1}$$

where $c_i(t)$ is the IMF number i, $a_i(t)$ and $(\theta_i(t))$ are $c_i(t)'s$ instantaneous amplitude and phase respectively. The residual $r(t)$ is a monotone function. The instantaneous frequency $f_i(t)$ for each IMF $c_i(t)$ is defined by

$$f_i(t) \triangleq \frac{1}{2\pi} \cdot \frac{d\theta_i(t)}{dt}. \tag{2}$$

3 Hilbert-Huang transform

The HHT was created initially to study ocean waves, which are non-stationary and non-linear in nature but over time its application has been spread to other fields. The HHT consits of empirical mode decomposition (EMD) and Hilbert spectral analysis [5]. In this section, we will show some components and properties of HHT. The basic structure of HHT is show in Fig. 1.

The main goal of the development of HHT is to have a tool to manage the time-frequency-energy paradigm of data. The nonlinearity and nonstationarity can be dealt with better than by using the traditional paradigm of constant frequency and amplitude. One way to express the nonstationarity is to find instantaneous frequency and instantaneous amplitude. This was the reason why Hilbert spectrum analysis was included as a part of HHT. Spectral analysis is a powerful tool to analyze the statistical characteristics of stochastic data [23].

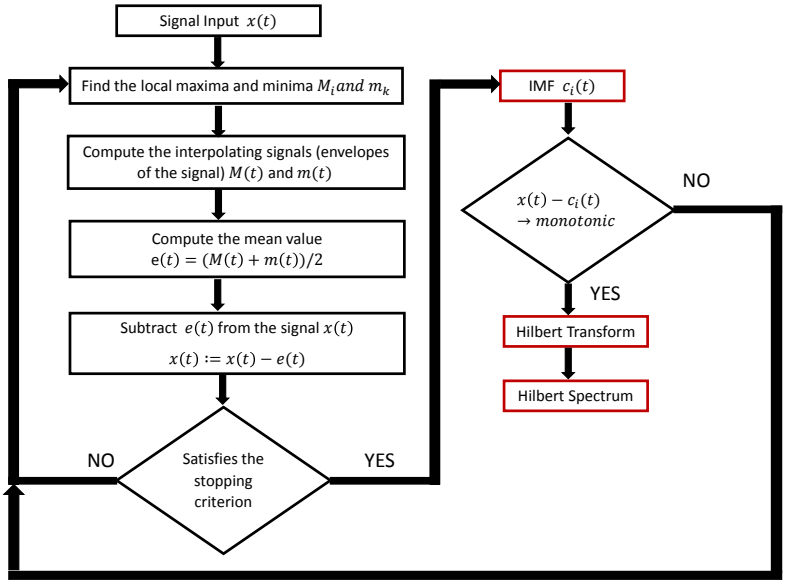

Fig. 1. Flowchart for the Hilbert-Huang transform.

A Hilbert Spectrum (HS) is a 3D representation of the instantaneous amplitude and frequency as a function of time for each Intrinsic Mode Function (IMF).

The HS is defined as

$$H_i(f,t) \triangleq \begin{cases} a_i(t) & \text{for } f = f_i(t) \\ 0 & \text{otherwise} \end{cases} \tag{3}$$

For a general multicomponent signal, the Hilbert Spectrum is defined as the sum of Hilbert Spectra of all the IMFs, as given in

$$H(f,t) \triangleq \sum_{i=1}^{N} H_i(f,t) \tag{4}$$

where N is the total number of IMFs.

4 Wavelet Transform

The concept of wavelets started to appear in the early 1980s. This new concept can be viewed as a synthesis of various ideas originating from different disciplines. In 1982, the idea of wavelet was discovered the by Jean Morlet. The first application was focused on seismic wave analysis [25].

The Wavelet Transform (WT) is a widely used tool in signal processing, it is a quick and efficient way of analyzing transients in voltage and current signals and characterize EEG signals. WT decomposes a signal into frequency bands, which are generated by means of mother wavelet and operations of translation in the time domain. It also responds to the needs of an optimal time-frequency resolution in all frequency ranges.

In order to achieve good time resolution for the high-frequency transients and good frequency resolution for the low-frequency components, the idea of *mother wavelet* was introduced . They are defined by

$$\psi_{a,b}(t) = \frac{1}{\sqrt{|a|}}\psi\left(\frac{t-b}{a}\right), a, b \in \mathbb{R}, a \neq 0, \tag{5}$$

where a is called a scaling parameter which measures the degree of compression or scale, and b a translation parameter which determines the time location of the wavelet [22].

A wavelet is a function $\psi(t) =\in L^2(\mathbb{R})$ with a zero average

$$\int_{-\infty}^{\infty} \psi(t)dt = 0 \tag{6}$$

The discrete wavelet transform (DWT) is obtained by discretizing the parameters a and b. In its most common form, the DWT employs a dyadic sampling with parameters a and b based on powers of two $a = 2^j$ and $b = k2j$, with $j, k \in \mathbb{Z}$. By substituting the discretized parameters into (5), we obtain the dyadic wavelets

$$\psi_{j,k}(t) = \frac{1}{\sqrt{2^j}}\psi\left(\frac{t}{\sqrt{2^j}} - k\right) \tag{7}$$

Therefore, the DWT of a signal s(t) can be written as

$$d_{j,k} = \int_{-\infty}^{\infty} s(t)\psi^*_{j,k}(t)dt = \langle s(t), \psi_{j,k}(t)\rangle \tag{8}$$

where $d_{j,k}$ are known as wavelet (or detail) coefficients at level j and location k. $s(t)$ is the continuous wavelet transform of a signal s(t).

The DWT uses an analysis filter bank to decompose a signal into wavelet coefficients at various frequency bands. The basic structure of DWT for 3 decomposition levels is show in Fig. 2.

5 Illustrative Examples

We have carried out some simulations using HHT and the DWT to analyze two signals whose behavior is easily found in modern power systems and biological signals. In Fig. 3, we show a signal with two frequency components whose model is represented by the equation (9)

$$y(t) = sin(2\pi 50t) + 0.5cos(2\pi 70t^2), \tag{9}$$

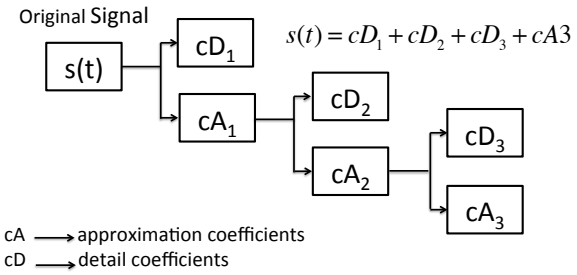

Fig. 2. Discrete wavelet transform

and Fig. 4 shows an EEG signal obtained from The Ecole Polytechnique Federale de Lausanne, Signal Processing Institute [26]. The data matrix used contains the information of 34 electrodes, for our study we used information from one of these. The data were recorded using Biosemi Active Two. The sampling rate is $2048Hz$. EEG signals were recorded from 10 healthy subjects who participated in 2 sessions. Using a speller, subjects can spell characters by focusing their attention on a given character displayed on a computer screen.

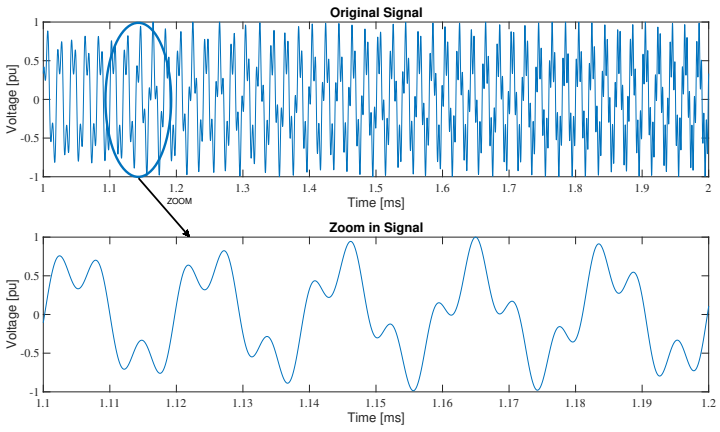

Fig. 3. Synthetic signal with similar behaviour to modern power systems

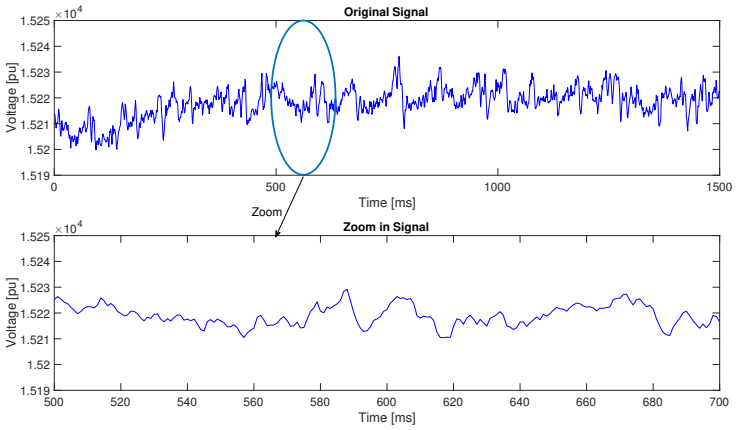

Fig. 4. EEG Signal taken under real-world conditions. This means that the data might contain artifacts coming from eye-blinks, eye-movements, muscle-activity, etc

5.1 Example 1- Modern Power System

In this section, we present the results obtained for the signal in Fig. 3. In Fig. 5 the IMFs and their respective power spectrum are shown, 2 IMFs have been obtained. The Multilevel Wavelet Decomposition using DWT is shown in Fig. 6. For this case we used the Morlet function as mother wavelet. Fig. 7 show the HS. In Fig. 8 the scalogram obtained using Continuous Wavelet Transform (CWT) is shown. The vertical axis is the scale factor, the higher scale factor corresponds to lower frequencies. The time-frequency analysis in wavelet transform, it's a good tool to know the distribution of signal energy of wavelet details coefficient with the change of time. In WT exists a trade-off between the order of the wavelet function and the computation time. Higher order wavelets are better able to distinguish between the various frequencies, but require more computation time.

5.2 Example 2- EEG Signal

In this section, we present the results obtained for the signal in Fig. 4. In Fig. 9 the IMFs and their respective Fast Fourier Transform (FFT) are shown. The Multilevel Wavelet Decomposition using DWT is shown in Fig. 10. For this case we used the Daubechies function as mother wavelet. Finally, in Fig. 11, we show the original signal and the reconstructed signal using the wavelet coefficients.

6 Discussion

We have used HHT and DWT to a synthetic signal and to a real signal, in an attempt to better understand the notion of instantaneous frequency and for

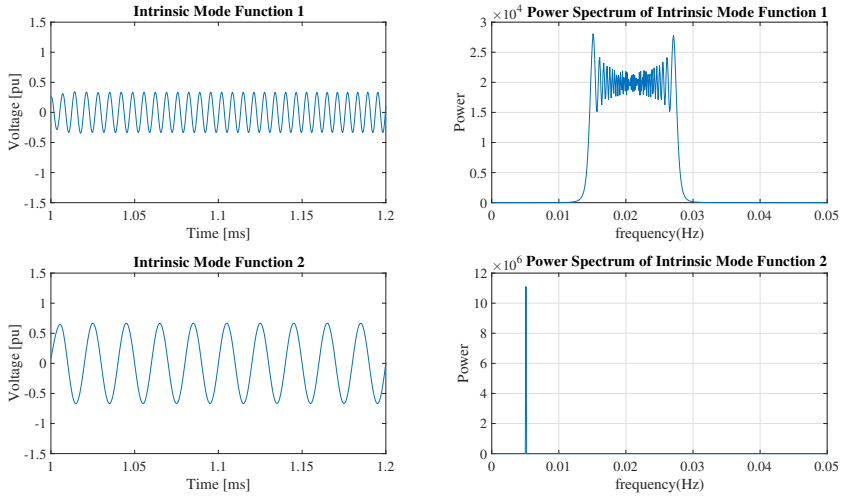

Fig. 5. Intrinsic Mode functions of signal $y(t)$

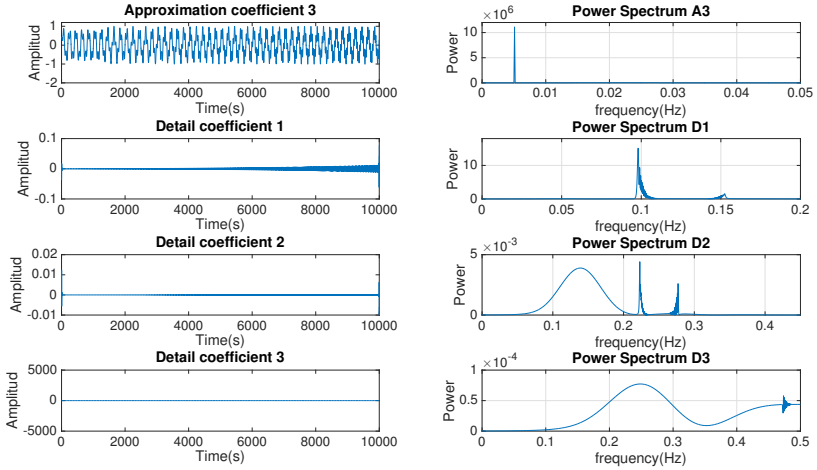

Fig. 6. Multilevel Wavelet Decomposition using DWT for signal $y(t)$

exploring the applicability of these two methods to different applications, that share nonstationary nature. In the case of the synthetic signal, HHT is clearly more suitable for decomposition and meaningful interpretation of the monocomponents. The fast oscillations can be separated from the slow oscillations present in the signal, and this can allow to obtain more information. The HHT has better

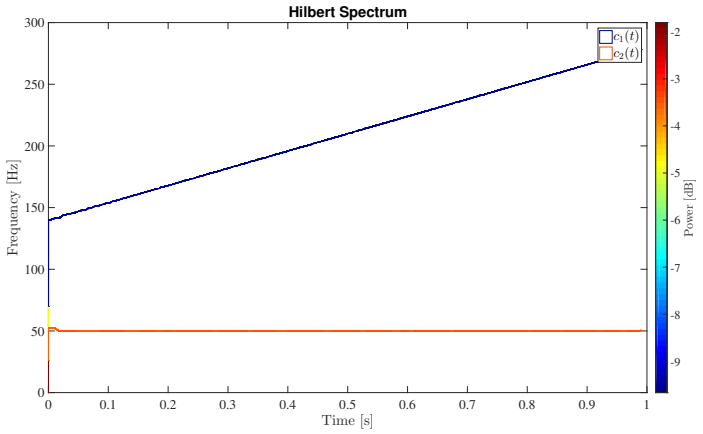

Fig. 7. Hilbert Spectrum for signal $y(t)$

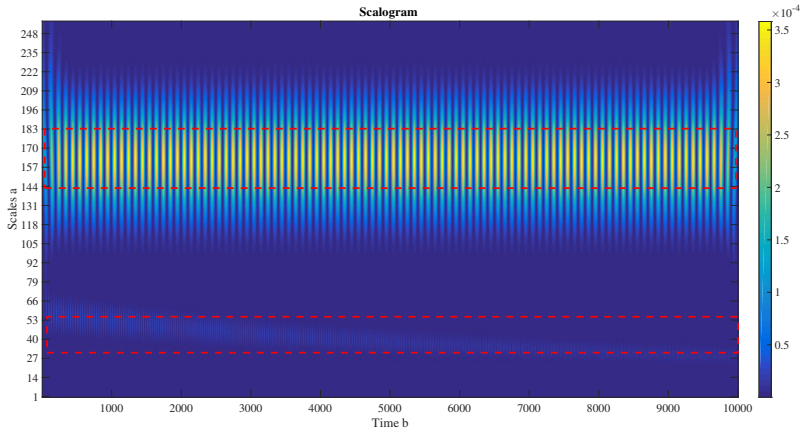

Fig. 8. Scalogram using CWT

resolution in time domain and in frequency domain than the DWT. This makes the HHT more powerful for detecting the impacts of continuous variations in signals. The HHT has better computing efficiency, which means that the HHT is more suitable for large size signal analysis. Fig. 5 shows the different IMFs obtained for a very common signal in modern power systems, in this case we only need 2 IMFs to describe the behavior of the phenomenon. When we compare the IMFs and their respective power spectrum, the IMF1 contains many frequency components and in IMF2 the frequency components are reduced, and the same happens with oscillations. The DWT applied to the same signal has 3 decomposition levels, which is computationally more demanding. The HS often

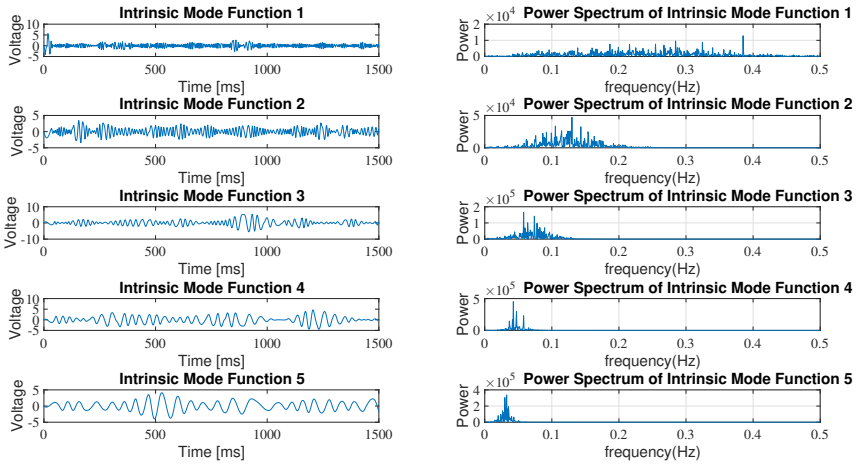

Fig. 9. Intrinsic Mode functions for EEG signal

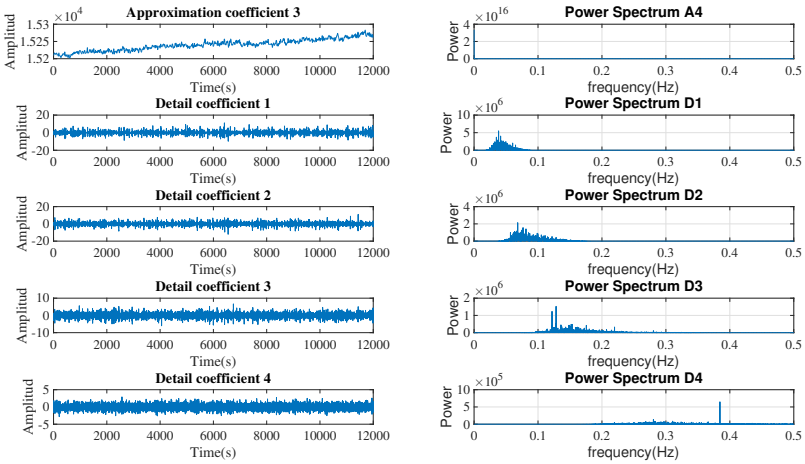

Fig. 10. Multilevel Wavelet Decomposition using DWT

has better resolution than WS, and WS shows a rich distribution of harmonics but does not offer many details about the exact frequency values at which some disturbances may appear. The frequency content of the signal is descomposed into frequency bands (Fig. 6), *Approximation coefficient 3* corresponds to the low frequency component and *Detail coefficient 1* corresponds to the high frequency component. In *Detail coefficient 1*, it is possible to observe the two

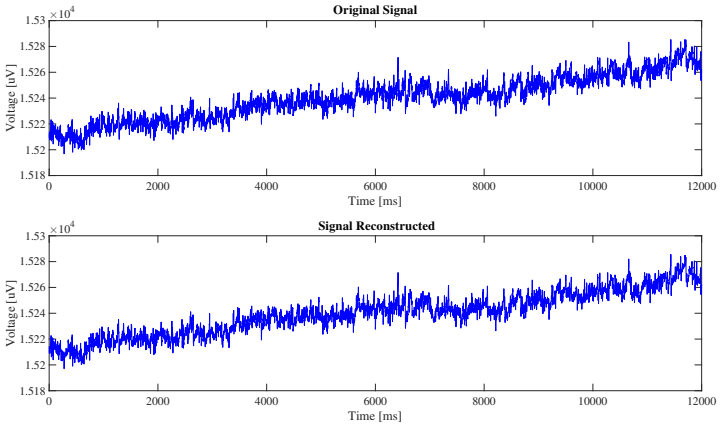

Fig. 11. Signal reconstructed using DWT

frequency components of the signal. In the other frequency bands (*Detail coefficient 2* and *Detail coefficient 3*) also appear frequency components but with lower amplitudes. This behaviour also appears in Fig. 10.

The HS (Fig. 7) reflects the signals instantaneous frequency pattern and allows to observe with greater clarity frequency trends. With the EEG signal, we need more IMFs, but they all appear to be well behaved IMFs. The frequency components are decreasing in each IMF and this is a good approximation for the detection and classification of patterns. When we compare the behavior of HHT in each case, it is possible to affirm that this method works well in both applications. The scalogram (Fig. 8) shows the two frequencies present in the original signal(red rectangle), but the resolution is lower compared wit HS. The frequency component of higher value is difficult to identify in the scalogram.

In Fig. 11, we show the reconstructed signal using the wavelet coefficients, this is one of the great advantages of the DWT. This suggests that a preprocessing signal using DWT and then apply HHT can offer better results than the two tools working separately.

The IMF eliminate the high frequency oscillation (Fig. 5 and 9) and this allows to observe in each component different behaviors. This would allow focus on a specific component and analyze behaviors in power systems and EEG signals according to the application or diagnosis.

In EEG signal analysis one application of HHT and WT can be to detect and characterize sleep spindles (SSs) [12] or Epileptic Focus [22]. The firs step in this process is to mark by an expert in an EEG recording behavior patterns and then decompose the signal to obtain a better resolution. In Fig. 9 is possible to detect changes in the oscillations, for example in *Intrinsic Mode Function 2* we have a strong variation in the envelope. In the DWT is necessary to have more decomposition levels to observe changes in the signal behaviour.

7 Conclusion and further work

In this paper a comparison between the use of HHT and DWT to two different nonstationary signals was presented. The results indicate that for signal decomposition into meaningful modes, the HHT will be a preferable method. One of the advantages of HHT versus DWT is that by being a data driven method, no reference functions are required (mother wavelets) and the adaptability of the method is greater. One of the main challenges of HHT is to improve the calculation process of the IMFs. The best way for this is to optimize the selection method. The reconstruction of the signal from the approximation and detail coefficients shows a good behavior for DWT especially for removing the unwanted noise of a signal. Further investigation is currently being focused on the improvement of the IMFs extraction algorithm in the EMD. The use of black-box optimization is going to be explored as an alternative to the cubic splines used in this paper.

Acknowledgments. This work was carried out during the tenure of an ERCIM 'Alain Bensoussan' Fellowship Programme.

References

1. Kulia, G., Molinas, M., Lundheim, L., Larsen, B.: Towards a Real-time Measurement Platform for Microgrids in Isolated Communities. Procedia Engineering, 159, 94-103 (2016)
2. Huang, N., Shen, S.: Hilbert-Huang Transform and its Applications. World Scientific Publishing, Danvers, MA, USA (2014)
3. Antonino-Daviu, J., Riera-Guasp, M., Pineda-Sanchez, M., Perez, B.: A Critical Comparison Between DWT and Hilbert Huang-Based Methods for the Diagnosis of Rotor Bar Failures in Induction Machines. IEEE Transactions on Industry Applications. 45, 1794-1803 (2009)
4. Toole, J.M., Mesbah, M., Boashash, B.: A New Discrete Analytic Signal for Reducing Aliasing in the Discrete Wigner-Ville Distribution. IEEE Transactions on Signal Processing, 56, 5427-5434 (2008)
5. Huang, N., Shen, Z., Long, S., et al.: The empirical mode decomposition and the Hilbert spectrum for nonlinear and non-stationary time series analysis. Proceedings of the Royal Society, 454, 903-995 (1998)
6. Rilling, G., Flandrin, P.: One or Two Frequencies? The Empirical Mode Decomposition Answers. IEEE Transactions on Signal Processing, 56, 85-95 (2008)
7. Rato, R.T., Ortigueira, M.D., Batista, A.G.: On the HHT, its problems, and some solutions. Mechanical Systems and Signal Processing, 22, 1374-1394 (2008)
8. Barros, J., Diego, R.: Analysis of Harmonics in Power Systems Using the Wavelet-Packet Transform. IEEE Transactions on Instrumentation and Measurement, 57, 63-69 (2008)
9. Li, H., Kwong, S., Yang, L., Huang, D., Xiao, D.: Hilbert-Huang Transform for Analysis of Heart Rate Variability in Cardiac Health. IEEE/ACM Transactions on Computational Biology and Bioinformatics, 8, 1557-1567 (2011)

10. Lin,K.Y., Chen, D.Y., Tsai, W.J.: Face-Based Heart Rate Signal Decomposition and Evaluation Using Multiple Linear Regression. IEEE Sensors Journal, 16, 1351-1360 (2016)
11. Kortelainen, J., et al.: Using Hilbert-Huang Transform to assess EEG slow wave activity during anesthesia in post-cardiac arrest patients. 38th Annual International Conference of the IEEE Engineering in Medicine and Biology Society (EMBC), 1850-1853 (2016)
12. Causa, L., et al.: Automated Sleep–Spindle Detection in Healthy Children Polysomnograms. IEEE Transactions on Biomedical Engineering, 57, 2135-2146 (2010)
13. Lotte F.: A Tutorial on EEG Signal Processing Techniques for Mental State Recognition in Brain-Computer Interfaces. Guide to Brain-Computer Music Interfacing, Springer, Paris, France (2014)
14. Liu, Z., Ying, Q., Luo, Z., Fan, Y.: Analysis and Research on EEG Signals Based on HHT Algorithm. 2016 Sixth International Conference on Instrumentation & Measurement, Computer, Communication and Control (IMCCC), Harbin, 563-566 (2016)
15. Lo, M.-T., Hu, K., Liu, Y., Peng, C.-K., Novak, V.: Multimodal Pressure Flow Analysis: Application of Hilbert Huang Transform in Cerebral Blood Flow Regulation. EURASIP Journal on Advances in Signal Processing, 2008, 1-15 (2008)
16. Im, C., Seo, JM.: A Review of Electrodes for the Electrical Brain Signal Recording. Biomedical Engineering Letters, 6, 104-112 (2016)
17. Dhiman R., Priyanka, J.S.: Wavelet Analysis of Electrical Signals from Brain: The Electroencephalogram. Quality, Reliability, Security and Robustness in Heterogeneous Networks. Lecture Notes of the Institute for Computer Sciences, Social Informatics and Telecommunications Engineering, vol 115. Springer, Berlin (2013)
18. Soleymani, M., Asghari-Esfeden, S., Fu, Y., Pantic, M.: Analysis of EEG Signals and Facial Expressions for Continuous Emotion Detection. IEEE Transactions on Affective Computing, 7, 17-28 (2016)
19. Okcana, k.: Definition of the Instantaneous Frequency of an Electroencephalogram Using the Hilbert Transform. Advances in Bioscience and Bioengineering, 4, 43-50 (2016)
20. Chai, R., Ling, S.H., Hunter, G.P., Tran, Y., Nguyen, H.T.: BrainComputer Interface Classifier for Wheelchair Commands Using Neural Network With Fuzzy Particle Swarm Optimization. IEEE Journal of Biomedical and Health Informatics, 18, 1614-1624 (2014)
21. Amin, H.U., Malik, A.S., Ahmad, R.F. et al.: Feature extraction and classification for EEG signals using wavelet transform and machine learning techniques. Australasian Physical & Engineering Sciences in Medicine, 38, 139-149 (2015)
22. Chen, D., Wan, S., Bao, F.S.: Epileptic Focus Localization Using Discrete Wavelet Transform Based on Interictal Intracranial EEG. IEEE Transactions on Neural Systems and Rehabilitation Engineering, 25, 413-425 (2017)
23. Huang, N., et al.: Holo-Hilbert spectral analysis: a full informational spectral representation for nonlinear and non-stationary data. Phil. Trans. R. Soc. A374 (2016)
24. Huang, N., Wu, Z., Long, S., et al.: On Instantaneous Frequency. Advances in Adaptive Data Analysis, 1, 177-229 (2009)
25. Debnath, L., ShahHuang, F.: Wavelet Transforms and Their Applications. Birkauser, New York, USA (2015)
26. Hoffmann, U., Vesin, J.M., Ebrahimi, T., Diseren, K.: An efficient P300-based brain computer interface for disabled subjects. Journal of Neuroscience Methods, 167, 115-125 (2008)

Deep Learning for Detection of BGP Anomalies

Marijana Cosovic[1], Slobodan Obradovic[1], Emina Junuz[2]

[1]Faculty of Electrical Engineering, University of East Sarajevo, Istocno Sarajevo, BiH
[2]Faculty of Information Technology, Dzemal Bijedic University, Mostar, BiH

marijana.cosovic@etf.unssa.rs.ba, slobo.obradovic@gmail.com, emina@edu.fit.ba

Abstract. The Internet uses Border Gateway Protocol (BGP) for exchange of routes and reachability information between Autonomous Systems (AS). Hence, BGP is subject to anomalous traffic that can cause problems with connectivity and traffic loss. Routing Table Leaks (RTL) are considered anomalous in the sense that they can disrupt Internet routing and cause slowdowns of varying severity, which leads to packet delivery reliability issues. Deep learning, a subfield of machine learning, could be applied in detection of BGP anomalies. Studying RTL events is of interest to network operators and researchers alike. In this paper we consider datasets of several RTL events, all of which caused large-scale Internet outages. We use artificial neural network (ANN) models based on a back-propagation algorithm for RTL event classification.

Keywords: Machine learning·Deep learning·Anomaly detection·BGP·Sampling

1 Introduction

The Internet can be viewed as a graph of nodes in which autonomous systems , collections of routers with same routing policies, are represented by nodes, while the connection between the nodes are data paths used for exchanging reachability information between the ASs. BGP is a protocol that facilitates this exchange [1]. The Routing Information Service (RIS) project initiated by the Réseaux IP Européens Network Coordination Centre (RIPE NCC) is collecting routing data from Remote route collectors (RRC) positioned predominantly at Internet exchange points. RIS raw data come in two different type of files: all BGP packets created every five minutes and a complete BGP routing table that is created every eight hours [2].

By studying BGP packets files and, in particular, by extracting BGP update messages from them as they contain important reachability information, we can study connectivity disruption in the Internet during anomalous events. RTL events are in general initiated by router misconfigurations and, although not malicious in nature, can cause connectivity and traffic loss.

Machine learning techniques have been employed in anomaly classification tasks [3-5]. Deep learning, part of machine learning, has been used extensively in voice and

adfa, p. 1, 2011.

image recognition, language modelling, and information retrieval, amongst others, and has impacted the wide range of information processing tasks [7]. Routing data could be considered as time series data since data points are indexed in time order. Detection of anomalies in time series data has employed deep learning techniques in the past. ANNs are systems that can be trained to recognize patterns in data and classify anomalous from regular data instances [7], [8]. Routing data could be used to analyze past anomalous events and aid in classification of future anomalous events.

The paper is organized as follows. In Section 2, we describe ANNs. Introduction of RTL and particular RTL events are discussed in Section 3. In addition, extraction of BGP features from the datasets concludes Section 3. Classification methodology and used performance measures are discussed in Section 4. We conclude with Section 5.

2 ANN - Deep Learning

Application of Artificial Neural Networks (ANN) is present in the detection of anomalies [7], [8]. ANN are preferably developed to mimic basic biological systems and to learn based on examples in the way humans do. Neural networks learn gradually from the interdependence of data input properties, which can be linear or non-linear in nature. Neural network usage in supervised learning implies that input data are labeled; hence, it is known in advance which class they belong to. Based on a comparison between the output of the neural network and the target function, during the training process, ANN adjusts the weights as shown in Fig. 1.

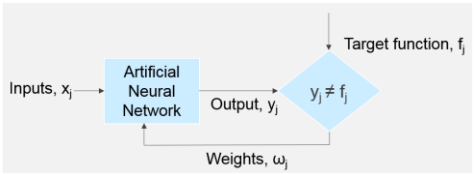

Fig. 1. Artificial Neural Network

Artificial neural networks can be classified as Feedforward or Feedbackward structures, depending on the direction of propagation of the information. The Feedbackward structure of neural networks refers to the spread of information backwards. When the input vector is applied to the input layer of the neural network it propagates through the network throughout all its layers, and it generates output values by using the output layer of the network. The output values are compared with a desired target function, and for each of the neurons in the output layer the difference is calculated. Further information about these differences propagate backwards until all the neurons in the neural network are affected by the difference of the original and the target output value. The value of the weighting factors are determined by the optimization technique (typically a minimizing of the loss function with respect to the weights in the network) which determines the weighting factors such that the loss function is minimized.

ANN are simple mathematical methods made up of basic processing elements called neurons. The structures of neural networks differ in the number of layers used. Between the first and the last layer of neural networks there are hidden layers: usually one hidden layer in simpler networks and more hidden layers in complex neural networks.

The architecture of the neural network is engaged in specific neuronal connectivity in a whole. Usually, the number of neurons in the input layer is equal to the number of features (number of columns in the feature matrix). Each neuron has one input, and all the outputs are connected to all neurons of the next layer, as shown in Fig. 2. When using a neural network for classification the output layer can have one or more neurons, depending on whether it is binary or multi-class classification. The most commonly used functions for the output neuron modeling are sigmoid or normalized exponential [9] functions.

Perceptron is a neuron model type developed in the original neural networks, in which each neuron has a number of inputs (x_j) associated with corresponding weight factors (ω_j), which show the effect of a particular input on the output. Thus, the output neuron classifies information by comparing the value of the sum (1) and the threshold value, which is a parameter of the neuron.

$$\sum_j \omega_j x_j \tag{1}$$

Modeling of neurons with perceptron has the following disadvantage: a small change in the weight factor of any perceptron can lead to a sudden change in its output. This in turn can lead to a complicated change in the rest of the network, which may be difficult to control. The most commonly used artificial neuron model, which solves the afore-mentioned problem, is the sigmoid neuron, shown by the following expression:

$$\frac{1}{1+exp(-\sum_j \omega_j x_j - b)} \tag{2}$$

where ω_j are weighting factors, x_j are input neurons and b is bias. It turns out that a change in the output of sigmoid neurons linear function of changes in weighting factors and bias. In this way it is easier to determine how changes in weighting factors and bias may influence the change of the output neuron; hence, the neural network could be considered more resilient to changes of data and the ability to learn.

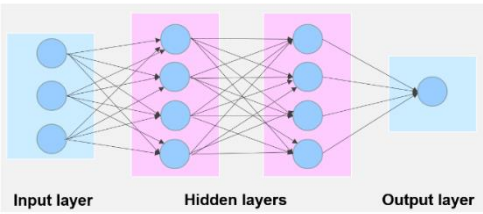

Fig. 2. Architecture of ANN with four layers: one input layer, two hidden layers and one output layer

3 Routing Leaks

The BGP routing system is subject to frequent incidents that result in significant interruptions of Internet connectivity. Many of the events that cause connectivity issues are classified as routing leaks. It is often unclear what is meant by that term. Based on research of actual events on the Internet, which can be of use to network operators and Internet users, the authors in [10] define routing leaks as a propagation of announced paths beyond the intended scope. This means that the BGP path announcement from one AS to another in some way violates the routing agreements between a sending AS, a receiving AS or any transit AS. The consequence of routing leaks is traffic redirection through a path not originally planned, and thus, various malicious attacks from analyzing data to eavesdropping could be performed. The most common reasons why routing leaks occur are errors in the router's configuration [11].

3.1 Routing Table Leak Events

In this paper we consider the following routing table leak events: Routing Leak AS9121 [12], AWS Route Leak [13], Telekom Malaysia AS4788 Route Leak [14], and Indosat Routing Table Leak [15], all of which showed an increased number of announced IP prefixes throughout the duration of the events.

AS9121 Routing Table Leak.

The AS9121 Routing Table Leak took place on December, 24 2004. AS9121 announced to other AS's through BGP sessions that were used to reach almost 70% of all prefixes, which at that time amounted to more than 106k prefixes. As a result, the data of tens of thousands of networks were either lost or diverted. AS9121 started to announce prefixes to its neighbors around 9:20 GMT, and the event lasted until just after 10:00 GMT. AS9121 continued announcing the prefixes for the rest of the day. The prefix announcement rate reached a second peak at 19:47 GMT. The number of announced IP prefixes during the routing leak event is shown in Figure 4.10 (a). Picture 4.10 (b) shows that during the routing leak event, the maximum edit distance (the measure of similarity between two ASPATH attributes) increases within one minute. This could indicate that the choice of the paths differed from the common ones and it was sign of disruption between commonly connected ASs.

AWS Route Leak.

The AWS Route Leak started at 17:10 UTC on April, 22 2016 and affected a large number of ASs and prefixes. Loss of traffic and connectivity were present since networks with high traffic prefixes, such as Google, Amazon, and Twitter, were affected, amongst others. The event occurred due to maintenance issues on Innofield AG (AS 200759) that is connected to Swiss Internet eXchange (SwissIX). Innofield AG normally announces one IPv4 and IPv6 prefix to SwissIX. During maintenance reactiva-

tion of BGP sessions, AS 200759 distributed prefixes belonging to Amazon as belonging to private AS 65021. Prefix announcements were propagated through AS 6939 Hurricane Electric (HE) that peers at SwissIX. This resulted in a redirection of traffic passing through HE to a private AS, and hence, it compromised the reachability of Amazon AS. Since the event was widespread and likely caused by a misconfigured route optimizer, we observed an increase in announced IP prefixes at CIPX, as shown in Fig. 2.

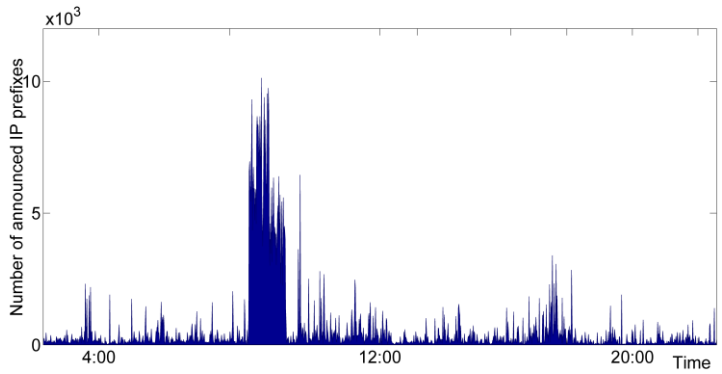

Fig. 3. Number of announced Network Layer Reachability Information (NLRI) prefixes during AS9121 Routing Leak Event as observed on RIPE Route Collector rrc04, CIPX

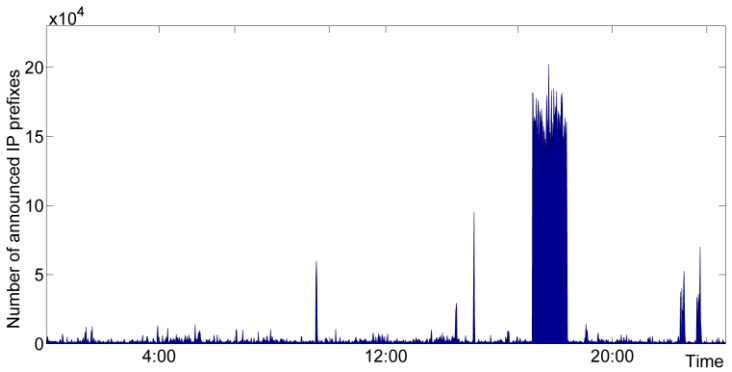

Fig. 4. Number of announced NLRI prefixes during AWS Routing Leak Event as observed on RIPE Route Collector rrc04, CIPX

Telecom Malaysia Route Leak.

The Malaysian Telecom (AS 4788) leaked one third of all IP prefixes in the global routing table to the backbone provider Level3 (AS 3549). The event, triggered by routers misconfiguration at Telecom Malaysia, started on June, 12 2015 at 8:43 UTC and lasted until 11:45 UTC. Level3 (AS 3549) propagated traffic from its peers and customers via Telecom Malaysia, which was not capable of handling traffic volume, re-

sulting in major packet loss and performance degradation. The performance degradation was especially pronounced between the Asia Pacific region and the rest of the Level3 network. Fig. 5 shows an increased number of announced IP prefixes (left) and also an increase of maximum AS-PATH length (right) for the duration of the route leak event.

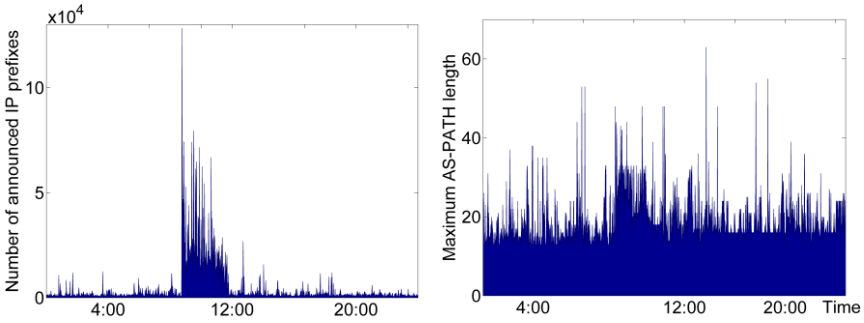

Fig. 5. Number of announced NLRI prefixes (left) and maximum AS-path length (right) during Telecom Malaysia Routing Leak Event as observed on RIPE Route Collector rrc04, CIPX

Indosat Routing Table Leak.

The Indosat routing table leak occurred on April, 2 2014. At the time of the event the global routing table consisted of nearly half a million routes. AS 4761(Indosat) leaked around 320,000 routes, which happened during scheduled maintenance starting at 18:25 UTC. The reason behind Indosat originating prefixes that were not assigned to it is assumed to be that BGP was redistributed with bad upstream filtering. This inadvertent error had an impact that was observed on various route collectors through an increase of announced IP prefixes, as shown in Fig.6 (left). Several hundreds of those prefixes were widely accepted, and services of some networks such as Akamai, a leading content delivery network (CND) and cloud service provider, were disrupted.

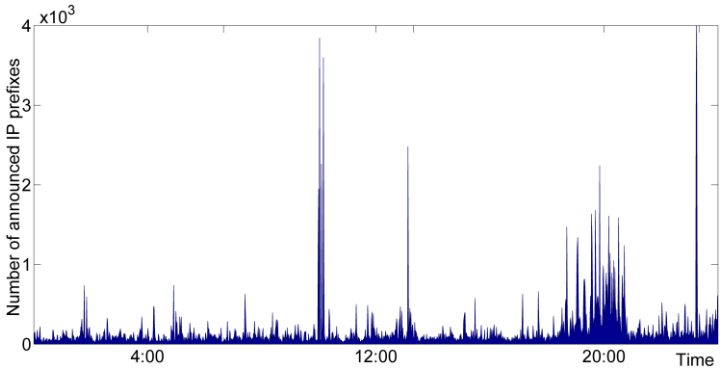

Fig. 6. Number of announced NLRI prefixes during Indosat Routing Leak Event as observed on RIPE Route Collector rrc04, CIPX

3.2 Routing Leak Datasets

We obtain datasets from the RIPE NCC that collects Internet routing data by using Routing Information Service (RIS) Remote Route Collectors (RRC) positioned in various locations throughout the world. Since the effects of all events considered in this paper and presented in Tab. 1 caused globally visible connectivity issues, we have used routing updates collected at RRC located in CIPX, Geneva.

We have used BGP update messages during the occurrence of the routing leak events stored in MRT format described in [16]. We have observed BGP update messages during a five day period, two days before and two days after the actual event. After MRT to ASCII conversion, python code was written in order to extract information from the datasets. We have observed fifteen volume and AS-PATH features on a minute level during five days period, hence producing a feature matrix of 7200x15 size.

The volume features that we have observed are: the number of BGP messages announcing new routes, the number of BGP messages withdrawing already existing routes, the number of announced IP prefixes (Fig. 3, 4, 5, and 6), the number of withdrawn IP prefixes, the number of duplicate announced messages, the number of duplicate withdrawn messages, the number of implicitly withdrawn messages, the number of BGP messages which NLRI originates from Exterior Gateway Protocol (EGP), the number of BGP messages which NLRI originates from Interior Gateway Protocol (IGP), and the number of BGP messages which NLRI originates from unknown sources.

Duplicate announcements and withdrawal messages are defined as BGP update messages that announce the same combination of IP prefix and AS-PATH attribute that has previously been announced. Implicit withdrawal implies that the same IP prefix has been announced with a different AS-PATH attribute, hence it is an implicit withdrawal of a previous announcement (same IP prefix but different AS-PATH).

The features we computed based on AS-PATH attribute are: the average length of AS-PATH attribute, the maximum length of AS-PATH attribute, the average length of unique AS-PATH attribute, the average edit distance, and the maximum edit distance. While extracting information from AS-PATH attribute, we considered regular and unique AS-PATH's. We also considered AS-PATHs as a string of ASNs (autonomous system number) and computed the similarity of two adjacent AS-PATHs by finding their edit distance [17].

Features belong to three types, namely, continuous, categorical and binary. All of the volume features belong to the continuous type since features may have an infinite number of values. On the other hand, features derived from the AS-PATH attribute may have a finite number of values and hence, are categorical. The class feature is of the binary type: given volume and AS-PATH features, we either have anomalous instances or not.

We have labeled all 7200 time instances (described by 15 features) as either belonging to anomalous or regular class in accordance to the information regarding beginning, duration and end of each of the events. We have referred to several sources [18] in order to label our data as correctly as possible.

Considering that global routing tables increase in size from the time of the first event, we needed to normalize feature values to account for Internet size growth. Normalization is done such that each feature vector has a zero mean and a standard deviation of one [17]. We also performed feature discretization for the features of the continuous type prior to training the neural network. We did not encounter any missing data during the four events observed, although we did have an increased number of outliers in the case of Indosat RTL dataset, which can be observed in Fig. 6.

Table 1. RTL events

Dataset	Regular Class	Anomaly Class	Number of features
AS9121 RTL	7121	79	15
AWS RTL	7085	115	15
Malaysian Telecom RTL	7018	182	15
Indosat RTL	7050	150	15

4 Classification of Routing Leaks

4.1 Methodology

We used the Keras Python library with the Theano backend for development and evaluation of deep learning models. Models, based on a backpropagation algorithm for training of fully connected multiplayer perceptron (MLP) neural networks, are defined as sequences of layers: an input layer, hidden layers and an output layer. Only for the first layer in the sequence the shape of the input data needs to be specified. In Keras, using Dense class is one of the ways to define fully connected layers. Network weights can be initialized to random numbers using either uniform or Gaussian distribution. Use of appropriate activation function allows for better training of the network [18]. Traditionally, sigmoid and tanh activation functions are used, but the authors in [18] have shown that better performance can be achieved using a rectifier activation function. In the output layer we use a sigmoid function as we are dealing with binary classification. We use 10-fold cross validation for determining accuracy on the test dataset, and as we increase the number of hidden layers beyond two, classification accuracy decreases. We found that a neural network with two hidden layers is the optimal model for routing table leak datasets. Using either too few or too many neurons in the hidden layers may result in problems of underfitting and overfitting, respectively. General guidelines for determining number of neurons within each hidden layer are used. We selected neural network architecture based on trial and error, but in accordance with the following general guidelines: the number of neurons in hidden layers should be between the sizes of input and output layers, and they should be the sum of 2/3 of the input layer neurons and output layer neurons. Hence, we trained the neural network with two dense hidden layers with 15 and 10 neurons, respectively.

4.2 Performance Measures

The performance measures employed in this paper, needed for comprehensive comparison of different deep learning models, are accuracy, f-measure, the Matthews Correlation Coefficient (MCC), the area under Precision-Recall (PR), and the area under Receiver Operating Characteristics (ROC). Accuracy, considering our datasets are highly imbalanced (Tab. 1), might not be the most accurate performance measure. This is due to the fact that misclassification should have different costs associated with points belonging to either the regular or anomalous class. Accuracy is defined as the ratio of points belonging to the regular/anomalous class that are classified as regular/anomalous and the total number of points in the dataset. In order to define f-measure we first define recall (R) as the ratio of detected anomalous points and all points labeled as anomalous. On the other hand, precision (P) is a ratio of detected anomalous points and all anomalous points. F-measure is given as a double ratio of product of P and R and the sum of P and R. MCC is given by (3) where N is the number of all points and TP is the number of data points classified as anomalous.

$$MCC = \frac{TP / N - PR}{\sqrt{PR(1-P)(1-R)}} \tag{3}$$

4.3 Classification Results

We have used a neural network with two hidden layers and obtained the performance measure values shown in Tab. 2. Accuracy is not the best approach to compare classification of different events, as the datasets are highly imbalanced. Tab. 1 shows that Malaysian Telecom RTL has the largest set of data labeled as anomalous – 182 compared to the AS 9121 RTL event in which only 79 instances are labeled as anomalous. The Indosat RTL event shows the worst performance of all datasets, and we can contribute that to noise in the dataset (Fig. 6).We have used under- and oversampling techniques to balance regular and anomalous instances in the RTL datasets. In the case of oversampled and undersampled datasets, their imbalance ratio is around 1, meaning the classes are balanced; hence, accuracy and f-measure are approximately the same values. Oversampling techniques are algorithms that create additional instances of the class that is represented with a smaller number of instances in the dataset. We used Synthetic Minority Oversampling Technique (SMOTE), Support Vector Machine (SVM)-SMOTE, Borderline1-SMOTE, Borderline2-SMOTE, Adaptive Synthetic Sampling (ADASYN), and Random Oversampling (ROS) algorithms. By using balancing techniques of the datasets, we have achieved better performance measures as shown in Tab. 3. The best results were achieved using the SVM-SMOTE oversampling technique for AS9121 RTL, AWS RTL, and Indosat RTL, while the Malaysian Telecom RTL dataset, when oversampled by ROS algorithm, had the best performance measure that was better by a small margin then when oversampled by the SVM-SMOTE algorithm.
Undersampling techniques are algorithms that remove instances from the dataset that belong to the more represented class. We used ten undersampling algorithms, namely, Near Miss-1, Near Miss-2, Near Miss-3, Tomek Links, Cluster Centroids, One-sided

selection, Random undersampling, Edited Nearest Neighbours, Neighbourhood Cleaning Rule, and Condensed Nearest Neighbours. By using undersampling balancing techniques of the datasets, we have achieved better performance measures as shown in Tab. 4. When comparing Tab. 3 and Tab. 4, the values of performance measures are greater in the case of oversampling techniques, and this is due to possible overfitting. The best results were achieved using the RUS undersampling technique for AS9121 RTL and AWS RTL, while Indosat RTL and Malaysian Telecom RTL datasets, when undersampled by the Near-Miss 1 algorithm, had the best performance measure that was only better by a small margin then when undersampled by the RUS algorithm.

Table 2. Performance measures of the original RTL events

Dataset	Acc	F-measure	MCC	ROC	PR
AS9121 RTL	0.99375	0.945	0.942	0.998	0.946
AWS RTL	0.99431	0.808	0.807	0.961	0.848
Malaysian Telecom RTL	0.9925	0.852	0.848	0.979	0.883
Indosat RTL	0.93056	0.753	0.707	0.897	0.802

Table 3. Performance measures of RTL events using oversampling techniques

Dataset	Acc	F-measure	MCC	ROC	PR
AS9121 RTL	0.99816	0.998	0.996	0.999	0.999
AWS RTL	0.99167	0.992	0.983	0.994	0.984
Malaysian Telecom RTL	0.98953	0.990	0.979	0.995	0.994
Indosat RTL	0.92087	0.923	0.844	0.958	0.940

Table 4. Performance measures of RTL events using undersampling techniques

Dataset	Acc	F-measure	MCC	ROC	PR
92AS9121 RTL	0.98734	0.987	0.975	0.999	0.999
AWS RTL	0.96087	0.960	0.923	0.979	0.986
Malaysian Telecom RTL	0.95055	0.950	0.901	0.975	0.981
Indosat RTL	0.88333	0.878	0.770	0.927	0.948

5 Conclusion

We have developed a model for anomaly detection based on artificial neural networks with two hidden layers, which are optimal since with choosing additional hidden layers performance indices deteriorated. We used a cross-validation technique to determine the number of neurons in each of the layers. Balancing techniques (dataset oversampling and undersampling) were employed as the original datasets are highly imbalanced. Classification of the Indosat RTL dataset achieved the worst performance

measures due to noise in the dataset. We concluded in routing table leak datasets presented in the study that employing volume and AS-PATH features from BGP update messages could lead to reliable classification of RTL events.

References

1. Y. Rekhter, T. Li, S. Hares, "A Border Gateway Protocol 4 (BGP-4)," RFC 4271, IETF, 2006 [Online]. Available: http://ietf.org/rfc/rfc4271
2. RIPE RIS raw data [Online]. Available: http://www.ripe.net/data-tools/stats/ris/ris-raw-data.
3. M. Ćosović, S. Obradović, Lj. Trajković, "Performance evaluation of BGP anomaly classifiers," Proceedings of the International Conference on Digital Information, Networking and Wireless Communication, Moscow, Russia, Feb. 2015, pp. 115–120.
4. M. Cosovic, S. Obradovic, Lj. Trajkovic, "Classifying anomalous events in BGP datasets," in Proceedings of the 29th Annual IEEE Canadian Conference on Electrical and Computer Engineering (CCECE 2016), Vancouver, Canada, May 2016, pp. 697-700.
5. M. Cosovic, S. Obradovic, "Ensemble methods for classifying BGP anomalies," Industrial Technologies, ISSN: 13149911, vol. 4, no. 1, pp. 12-20, June 2017.
6. Li Deng and Dong Yu. 2014. Deep Learning: Methods and Applications. Found. Trends Signal Process. 7, 3–4 (June 2014), 197-387. DOI: http://dx.doi.org/10.1561/2000000039
7. H. A. Dau, V. Ciesielski, A. Song, "Anomaly Detection Using Replicator Neural Networks Trained on Examples of One Class," In Proceedings of the 10th International Conference on Simulated Evolution and Learning (SEAL 2014), vol. 8886, Springer-Verlag New York, Inc., New York, NY, USA, pp. 311-322, 2014.
8. Z. Jadidi, V. Muthukkumarasamy, E. Sithirasenan, M. Sheikhan, "Flow-Based Anomaly Detection Using Neural Network Optimized with GSA Algorithm," In Proceedings of the 33rd IEEE International Conference on Distributed Computing Systems Workshops (ICDCSW '13), Washington, DC, USA, pp. 76-81, 2013.
9. Christopher M. Bishop. 2006. Pattern Recognition and Machine Learning (Information Science and Statistics). Springer-Verlag New York, Inc., Secaucus, NJ, USA.
10. https://tools.ietf.org/html/draft-sriram-route-leak-problem-definition-00 https://www.rfc-editor.org/rfc/rfc7908.txt
11. R. Mahajan, D. Wetherall, T. Anderson, "Understanding BGP misconfiguration," In Proceedings of the Conference on Applications, technologies, architectures, and protocols for computer communications (SIGCOMM '02), New York, NY, USA, pp. 3-16, 2002.
12. A. C. Popescu, B. J. Premore, T. Underwood. (May 19, 2005). Anatomy of a Leak: AS9121. Renesys Corporation. Manchester, NH, USA. [Online]. Available: http://research.dyn.com/content/uploads/2013/05/renesys-nanog34.pdf.
13. (May. 22, 2017) North American Network Operators Group Mailing List – AWS Route Leak [Online]. Available: https://mailman.nanog.org/pipermail/nanog/2016-April/085410.html
14. (May. 22, 2017) North American Network Operators Group Mailing List – Telekom Malaysia AS4788 Route Leak [Online]. Available: https://mailman.nanog.org/pipermail/nanog/2015-June/076187.html
15. (May. 22, 2017) North American Network Operators Group Mailing List – Indosat Routing Table Leak [Online]. Available: https://mailman.nanog.org/pipermail/nanog/2014-April/065920.html
16. T. Manderson, "Multi-threaded routing toolkit (MRT) Border Gateway Protocol (BGP) routing information export format with geo-location extensions," RFC 6397, IETF, [Online]. Available: http://www.ietf.org/rfc/rfc6397.txt.

17. Yann LeCun, Léon Bottou, Genevieve B. Orr, and Klaus-Robert Müller. 1998. Effiicient BackProp. In Neural Networks: Tricks of the Trade, this book is an outgrowth of a 1996 NIPS workshop, Genevieve B. Orr and Klaus-Robert Müller (Eds.). Springer-Verlag, London, UK, UK, 9-50.
18. Vinod Nair and Geoffrey E. Hinton. 2010. Rectified linear units improve restricted Boltzmann machines. In Proceedings of ICML. 807-814.

Abnormal State Prediction based on Deep Learning using Multiple Time Series Process Data

Wen Song[1], Shigeru Fujimura[1]

[1] Graduate School of Information, Production and Systems, Waseda University, Kitakyushu, Fukuoka, 808-0135, Japan
fujimura@waseda.jp

Abstract. In production information systems, many kinds of huge logging time series data are stored. With the current innovation of Artificial Intelligence, how to use these data for supporting production process operation is the most attractive issue in production management field. Until now, many studies were performed in the past for this field. However, these systems need individual consideration or parameter tuning for each production process. In this research, a novel abnormal state prediction approach based on Deep Learning to support operators, which can be applied to any kinds of production process easily, is developed. It is a model to predict future behavior of a production process, which is based on Convolutional Neural Network using accumulated multiple time series data with dependency relationships.

Keywords: Artificial Intelligence, Convolutional Neural Network, Abnormal State Detection, Production Logging Time Series

1 Introduction

Many kinds of information systems are installed into production systems and there is a valuable huge database of production logging time series data. With the current rapid innovation of Artificial Intelligence, expectations to use such a database supporting production operators have increased recently. Although many kinds of approaches in this field have been proposed until now, big amount of cost to install these approaches was taken, because the customized development or parameter tuning for an individual process was necessary. Therefore, the prediction technique of time series data using Deep Learning that is a kind of the Machine Learning is the focus of attention [(1)(2)]. On the other hand, as for Deep Learning, the effectiveness is clarified in fields of character recognition and image recognition. This is because it creates superior models by the learning enormous data prepared beforehand. Applications for automatic operation, operator support, or fault diagnosis are expected in production field, but it is difficult to make a model to distinguish abnormal states because almost prepared past data are for normal states. In this research, a model predicting future behavior based on Deep Learning with time series data for normal states is proposed, and an abnormal state prediction function using the output of this model is implemented.

In production processes, various process values are measured as process variables: temperature, pressure, level and flow. A process variable has a relationship that the other process variable gives influences to it with a dead time lag. In addition, a time series data for a process variable includes various noises, from which actual characteristics have to be extracted except for noise. Therefore, a model predicting the behavior of a process variable which is affected by the other process variables is proposed based on Convolutional Neural Network with multiple related process variables as input information. By using such a behavior prediction model, there is no need to analyze the constitution of a target production process, physical implication or dynamic characteristics of it, and it is available to get started with any multiple process variables related to a target process variable.

In this research, a novel approach to build a model to predict future behavior based on Deep Learning using a target process variable and related multiple process variables from data accumulated in a database.

2 System Configuration

This system consists of three modules: Learning Module creating a suitable model from past data, Prediction Module which predicts future behavior by using the model, and Abnormal Detection Module to judge whether it will be in an abnormal state in the future.

2.1 Learning Module

Firstly, decide a process variable to predict future behavior and choose multiple process variables to affect it. Get started choosing several process variables as the initial setting and it can be selected some of them referring learning result. A process variable which future behavior is predicted and process variables which affect to it are called a predictor variable and explanatory variables respectively. The past time series data of the predictor variable and explanatory variables are inputs of the model. All the sampling time for time series data is the same. The output of the model is time series data of the future behavior of the predictor variable. The number of the data and the time interval from previous data to predict are set beforehand. The details of the model are described in Section 3.

The model produced by Learning Module is used in Prediction Module. In this system, the model is used in real time, and updated using new data in real time.

2.2 Prediction Module

The learned model is used for the prediction of the predictor variable. The input to Prediction Module is time series data of the predictor variable and explanatory variables of a certain fixed period. The output of this module is time series data for predictor future behavior. The time series data of the output is a sequence of values for every time interval that is set beforehand.

2.3 Abnormal Detection Module

A phenomenon caused by the abnormal behavior of the explanatory variable is recognized by time series data of future behavior generated in Predictive Module. For example, there is a case that the change of the value is overlooked because a human process operator doesn't watch a certain process variable. It affects a process variable and may cause a big problem in the future. In this case, this system foresees the abnormality by outputting a predicted value of the future behavior by Prediction Module even if there was the oversight of a human operator. Abnormal Detection Module holds rule group to detect the abnormality of predictor variables and performs abnormal warnings according to rules. These rules are defined by combination with a value itself or a differential value of the predictor variable of predictive variables and the other variables.

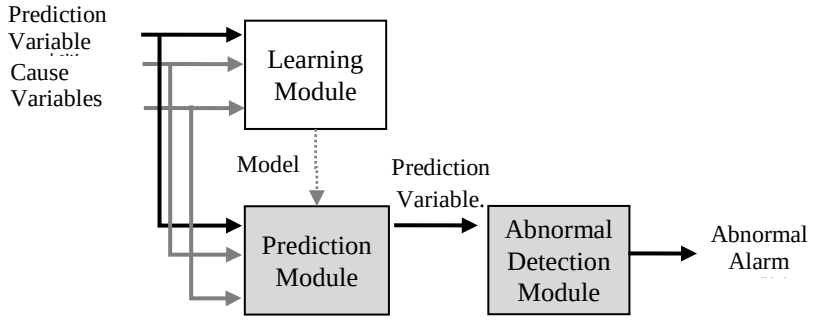

Fig. 1. System Configuration

3 Behavior Prediction Model

Behavior Prediction Model is a model which input is multiple time series data with a constant length of a predictor variable and explanatory variables, and output is one predicted time series data with a constant length of a predictor variable. In the following, the details of this model are explained using Fig. 2.

The input of this model is $N_1 + 1$ time series data which consist of one predictor variable and N_1 explanatory variables, which length is T_1, containing data from the time of the current time – $(T_1 – 1)$ to the current time. The output is a time series data of the predictor variable which contains N_4 data for every T_4 time interval from the current time. For the learning of this model, $N_1 + 1$ time series data with T_1 length as input data, and a time series data for predictor variable which contains N_4 data for every T_4 time interval following to the current time as supervised data to a model. Although it is thought as future data, these data are accumulated data in the past actually. As the learning data, $L - (T_1 + N_4 * T_4) + 1$ data which are moved forward every one time unit from the whole past data which data length is L are used.

The characteristic of time series data is extracted from such an input data with the convolution layer configured by N_2 filters. The filter is a 1-by-T_2 matrix, and T_2 is the length of the time series data which are enough to extract a characteristic. Each weight

in this filter is set so that the sum of them is 1.0. For a matrix of the input layer, it is applied while moving the value of T_2 unit adjacent aside one by one. And a matrix of the size same as a matrix in the input layer is generated, in which cell value is set the total value that multiplied each weight by each value in 1-by-T_2 matrix. With the next pooling layer, values on inside of the range of the 1-by-T_3 matrix designed as a pooling filter are aggregated into one value. The aggregation is the mean of values included in the range of the filter. (N_1+1)-by-T_1 size matrix is compressed in (N_1+1) -by- T_1/ (1-by-T_3) size matrix through this filtering operation. Therefore, the number of nodes in the next layer becomes the number of cells in this matrix multiplied by the number of filters N_2. Furthermore, information is output through the middle layer (N_3 nodes) by the output layer with N_4 nodes. The values of variables: N_1 to N_4 and T_1 to T_4, which are used in the above explanation, are given beforehand.

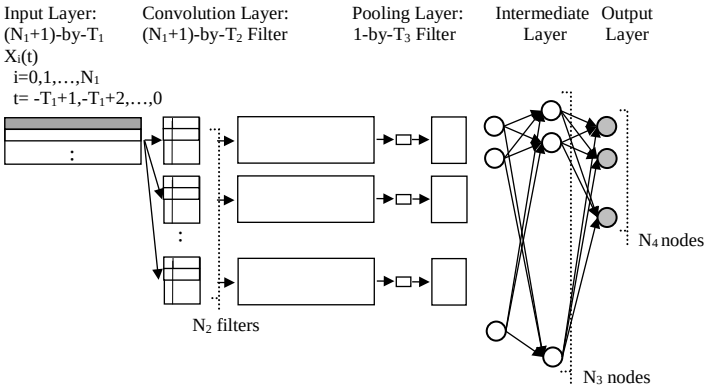

Fig. 1. Behavior Prediction Model

4 Conclusion

In this paper, a convolutional neural network that predicts future behavior of process variables was proposed, and the approach alarming the future abnormality was also shown.

References

1. Lewis, N.D.: DEEP TIME SERIES FORECASTING with PYTHON, An Intuitive Introduction to Deep Learning for Applied Time Series Modeling. www.AusCov.com (2017).
2. Frank, R.J., Davey, N., Hunt, S.P.: Time Series Prediction and Neural Networks. Journal of Intelligent and Robotic Systems (2001).

Human Gait Recognition by Deep Convolutional Activation Feature of Recurrence Plot for Accelerometer Time Series

Yusuke Manabe

Department of Information and Network Science,
Chiba Institute of Technology
Narashino-shi, CHIBA 275-0016 JAPAN
ymanabe@net.it-chiba.ac.jp

Abstract. In this study, to improve the accuracy of the accelerometer-based gait recognition task, we propose an idea of the feature extraction by using a deep neural network and recurrence plots. As the first step, we employ the recurrence plot technique based on delay coordinate embedding for converting a gait time series into an image map. As the second step, we extract the deep convolutional activation feature (DeCAF) from the converted image map by using the pre-trained deep convolutional neural network for ILSVRC2012 data set, as the feature extractor. The gait recognition experiment based on DeCAF have been done to evaluate the proposed method. As the results, we show that the proposed method can improve the recognition accuracy although it depends on embedding parameters.

Keywords: gait recognition, accelerometer, recurrence plot, delay coordinate embedding, deep convolutional activation feature

1 Introduction

Human gait recognition is a most fundamental and important technology for development of a smart home application to recognize human activities of daily living (ADL) under the Internet of Things (IoT) technology. Normaly gait recognition is classified into appearence-based approach[1] and model-based one[2]. These are called MV(Machine Vision)-based approach[3].

On the other hand, accelerometer-based gait recognition researches, which are called WS(Wearable Sensor)-based approach[3], have been increasing in recent years[4][5][6][7]. This approach mainly measures human gait time series by a smartphone with an accelerometer, instead of image processing. In order to recognize persons by using gait-accelerometer time series, we have to extract optimal features to discriminate each person from accelerometer time series based on the human gait movement.

Therefore, this study proposes a novel method to use a trained deep convolutional neural network as a feature extractor from gait-accelerometer time series.

Recently, it is proposed that a pre-trained deep convolutional neural network can be used as a feature extractor of image data[8]. The extracted feature is called a deep convolutional activation feature (DeCAF). Specifically, DeCAF is the feature vector based on the output value of the hidden units in the pre-trained deep convolutional neural network with a lot of image data.

In this study, firstly we convert a gait-accelerometer time series into a visuaized image map by using the recurrence plot method[9][10]. Secondly, we extract the DeCAF from the converted recurrence plot maps. Especially, from the view point of the gait recognition accuracy, we assess the effect of embedding parameters for making recurrence plot maps.

This paper consists of six sections. In the Next section, we explain about a delay coordinate embedding method and a recurrence plot method, as fundamental theoretical aspects. Section 3 shows our proposed method to extract DeCAF from a gait accelerometer time series. Section 4 and 5 show the two experiment tasks, embedding parameter estimation and gait recognition, and their results. Finally, we discuss about the conclusions and future works in section 6.

2 Theoritical Backgrounds

In this section, we explain some theoretical and fundamental elements on our proposed method. Specifically, reconstruction of attractor based on delay coordinate embedding, embedding parameters and their practical estimation methods and recurrence plot are described respectively.

2.1 Embedding Theorem and Delay Coordinate Embedding

Delay coordinate embedding is a sort of analysis method for nonlinear time series based on embedding theorem.

The embedding theorem, proposed by Takens [11] and expanded by Sauer et al. [12] guarantees that the space of time delayed vectors with sufficiently large dimension (actually there is an upper bound provided for the embedding dimension) will capture the structure of the original phase space.

The embedding theorem guarantees that, with a single observed time series $y(t)$, we can obtain the following f which has one-to-one correspondence to the original dynamical system.

$$v(t+1) = f(v(t)), v(t) = (y(t), y(t+\tau), \ldots, y(t+(m-1)\tau)), \qquad (1)$$

where f denotes reconstructed dynamical system, v denotes a delay coordinate vector, m is called embedding dimension and τ is called delay or delay time.

2.2 Embedding parameters Estimation

Unfortunately embedding theorem does not provide any values for the delay τ and embedding dimension m (are called the embedding parameters), a good

choice is needed for correct reconstruction of the attractor. Consequently the reconstructing the attractor is equivalent to making embedding vector with optimal embedding parameters.

m is the embedding dimension or the smallest number of coordinates needed to represent the time series with no overlapping in the state space; and τ is the time lag (time delay) influencing the shape and spread of the reconstructed attractor.

Practically, in the uniform embedding, Average Mutual Information is one of the popular techniques to estimate the optimal τ [13]. Also, the most popular method for estimation of m is False Nearest Neighbor, proposed by Kennel [14].

2.3 Recurrence Plot

After the attractor reconstruction, the characteristics of the attractor are analyzed by recurrence plot proposed by Eckmann et al. [9]. According to [10], the definition of recurrence plot is described as follows:

> *A recurrence plot (RP) is an advanced technique of nonlinear data analysis. It is a visualization (or a graph) of a square matrix, in which the matrix elements correspond to those times at which a state of a dynamical system recurs (columns and rows correspond then to a certain pair of times).*

That is, the recurrence plot method enables us to visualize dynamical features of a nonliner time series as an image map. By using the method, we can convert the gait accelerometer time series into an image data as a recurrence plot while keeping the characteristics of the dynamical system being inherent in the time series.

3 Proposed Method

To improve the accuracy of the accelerometer-based gait recognition task, we propose an idea of the feature extraction by using a deep convolutional neural network and recurrence plots.

Figure 1 shows the processing flow of our proposed method. First, we collect the gait accelerometer time series from many human subjects. Generally accelerometer can measure three dimensional time series data, but in this study we only use the amplitude of three dimensional accelerometer time series. The amplitude is calculated as follows;

$$a(t) = \sqrt{a_x(t)^2 + a_y(t)^2 + a_z(t)^2}, \tag{2}$$

where $a(t)$ denotes the amplitude at time t, $a_x(t)$, $a_y(t)$ and $a_z(t)$ denote three dimensional accelerometer time series.

Second, in order to convert gait time series into recurrence plot, we estimate embedding parameters; delay τ and embedding dimension m. On the basis of

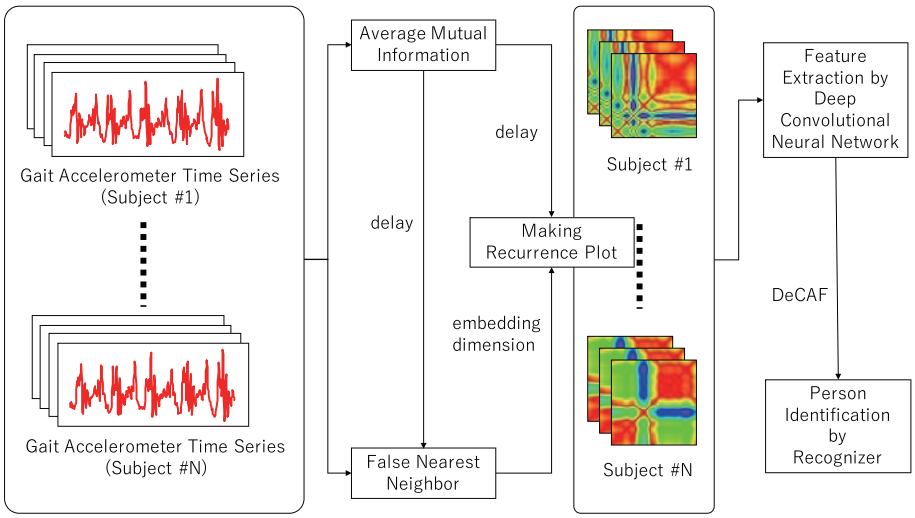

Fig. 1. Processing Diagram for Feature Extraction by Pre-trained Deep Convolutional Neural Network

the conventional analysis strategy, average mutual information are calculated for all of gait time series to estimate an optimal delay τ. The first local minimum point is selected as the optimal delay τ because the correlated relations between each component of embedding vector is eliminated. Subsequently, false nearest neighbor is used for estimating a optimal embedding dimension m.

Although it is necessary to estimate the embedding parameters for making a recurrence plot, Iwanski et al. argued that analysis results of a recurrence plot are unaffected by the embedding parameters[15]. Under this discussion, Wang et al. make recurrence plots without embedding, that is, observed time series are directly converted into recurrence plots[16]. However, bad embedding parameters distort a reconstructed attractor in the phase space and it causes the distortion of characteristics of the recurrence plot. Especially, in this study we extract feature vectors from recurrence plots by using deep convolutional neural network, so the differece of the embedding parameters means the difference of the feature vectors. Therefore we take the embedding strategy so as to reconstruct good attractors and to make good recurrence plot.

After the estimation of the optimal delay τ and dimension m, we create embedding vectors from gait accelerometer time series, and we make recurrence plots by it. Also in this study we create full-colored recurrence plots instead of binary plots.

Finally, the recurrence plots are used as input data for a deep convolutional neural network, which has already trained, the activation value of some of a layer in the neural network is used as feature vectors to identify persons. The feature is called DeCAF (Deep Convolutional Activation Feature). Person identification is done by some sort of a recognizer defined in the DeCAF space.

4 Experiment I: Embedding Parameter Estimation

First of all, we have estimated embedding parameters, embedding dimension m and delay τ.

4.1 Data Preparation

We collect accelerometer time series from 10 human subjects, who put a smartphone（AQUOS PHONE EX SH-04E） in their pants pocket and ordinaly walk on the flat floor in 10 times. The samping frequency is 100 Hz. The total number of collected data is 100 samples (10 subjects $\times$ 10 times). Each data sample is manually arranged in 2 gait cycles (4 steps) data. After that, it is resampled in 256 sample points.

4.2 Results

Figure 2 shows the result of average mutual information (AMI) for all gait data and the histogram of the delay at the first local minimum point of AMI. From these figures, We can estimate optimal delay $\tau = 5, 6, 7, 8, 9$.

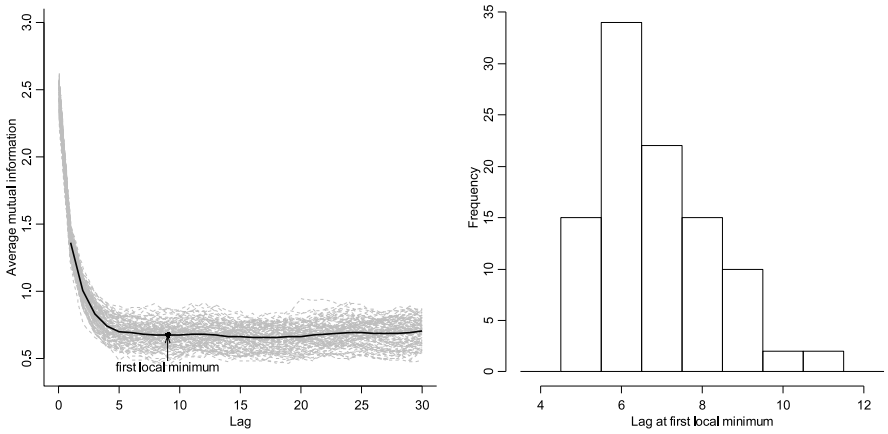

Fig. 2. Average Mutual Information (left) and Histogram of the delay estimated at the first local minimum of AMI (right)

Next, by using the estimated delay, false nearest neighbor (FNN) are calculated for estimating the optimal embedding dimension. Figure 3 shows the result of FNN for each delay. The optimal dimension is estimated when the percentage of the false nearest is equal to or less than 1 %. Figure 4 shows the histogram of the estimated embedding dimension.

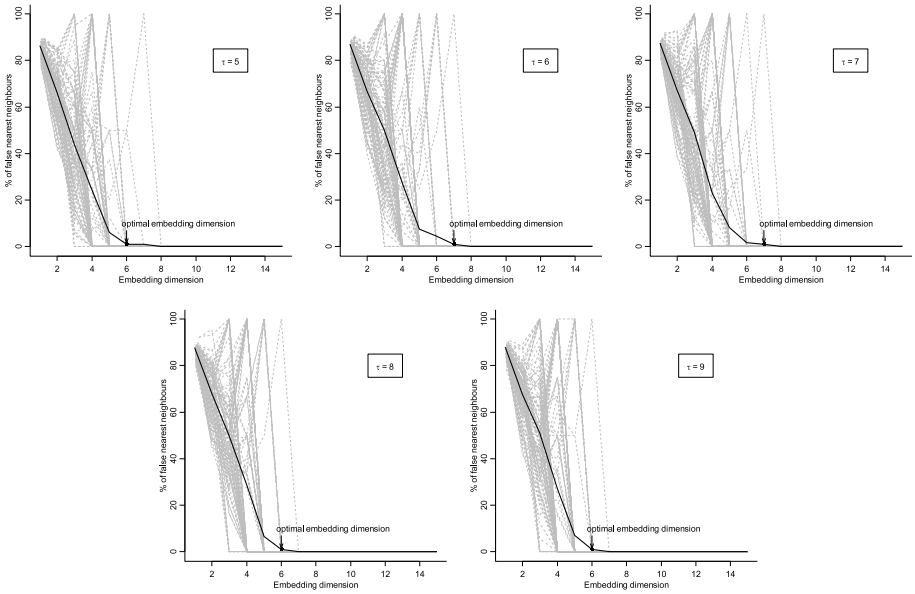

Fig. 3. False Nearest Neighbor

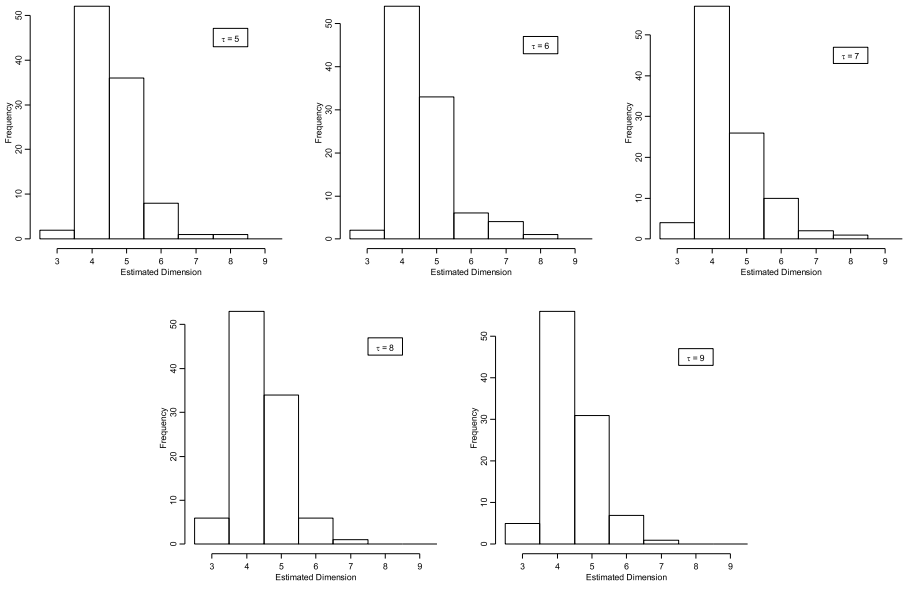

Fig. 4. Histogram of the estimated embedding dimension by FNN

From these figures, We can estimate optimal embedding dimension $m = 4, 5, 6, 7$. Therefore, we can make 20 types of embedding vectors for all of parameter combination ($(\tau = 5, 6, 7, 8, 9) \times$ (m= $4, 5, 6, 7$)).

5 Experiment II: Gait Recognition

5.1 Method

In order to extract the feature vector from each recrrence plot, we adopt a deep learning framework, Caffe[17], which includes a pre-trained deep convolutional neural network model for ILSVRC12 challenge. The network model definition follows the one proposed by Krizhevsky et al.[18]. On the basis of the reference[8], we use the activation of layer 6, DeCAF6, it is the last feature extraction layer before the last three layered neural network. Thus we extract the 4096 dimensional feature vector from a recurrence plot. The size of a recurrence plot depends on embedding parameters, so We resized all of the recurrence plot to 256×256.

As a gait recognizer, we employ a linear deiscriminant analysis (LDA) and evaluation method is leave-one-out validation for each subject.

To compare the effect of embedding parameters, the above feature extraction based on DeCAF6 and the gait recognition based on LDA are done for all recurrence plots with the 20 types of the estimated embedding vector.

5.2 Results

Table 1 shows the recognition accuracy for 20 types of embedding vectors and non- embedding. From this table, we can find that too large embedding parameters value is likely to make recognition accuracy lower.

The best performanceis 91% in (m=4, τ=7) and (m=6, τ=6). This result outperforms 86% of non-embedding. Therefore, this result implies that the delay coordinate embedding can make recognition accuracy high.

Table 1. Recognition Results under Various Embedding Parameters

		dimension (m)				
		non-embed.	4	5	6	7
delay (τ)	non-embed.	86%	—	—	—	—
	5	—	85%	81%	88%	86%
	6	—	89%	90%	**91%**	85%
	7	—	**91%**	87%	85%	83%
	8	—	78%	83%	77%	80%
	9	—	82%	85%	79%	68%

6 Conclusions

In this study, we proposed an idea of the feature extraction by using a deep neural network and recurrence plots for the accelerometer-based gait recognition task. As the result of person identification based on 10 human subjects data, we could obtain a good identification result of 91% at the best. Moreover we could show that the delay coordinate embedding enabled us to improve the identification accuracy.

The most important problem is how to estimate optimal embedding parameters. Especially, the effect of the non-uniform embedding[19] is going to be assessed in the near future.

References

1. H. Murase and R. Sakai, "Moving Object Recognition in Eigenspace Representation: Gait Analysis and Lip Reading," Pattern Recognition Letters, vol. 17, pp. 155-162, 1996.
2. S. Niyogi and E. Adelson, "Analyzing and Recognizing Walking Figures in XYT," Proc. IEEE CS Conf. Computer Vision and Pattern Recognition, pp. 469–474, 1994.
3. D. Gafurov, "A Survey of Biometric Gait Recognition: Approaches, Security and Challenges," Annual Norwegian Computer Science Conference, 2007.
4. M. O. Derawi, "Accelerometer-based gait analysis, a survey," Norwegian Information Security Conference (NISK), pp. 33–44, 2010.
5. Ferrero, R., Gandino, F., Montrucchio, B., Rebaudengo, M., Velasco, A., & Benkhelifa, I. (2015, June). On gait recognition with smartphone accelerometer. In Embedded Computing (MECO), 2015 4th Mediterranean Conference on (pp. 368-373). IEEE.
6. Subramanian, R., Sarkar, S., Labrador, M., Contino, K., Eggert, C., Javed, O., ... & Cheng, H. (2015, March). Orientation invariant gait matching algorithm based on the Kabsch alignment. In Identity, Security and Behavior Analysis (ISBA), 2015 IEEE International Conference on (pp. 1-8). IEEE.
7. Muaaz, M., & Mayrhofer, R. (2017). Smartphone-based Gait Recognition: From Authentication to Imitation. IEEE Transactions on Mobile Computing.
8. J. Donahue, Y. Jia, O. Vinyals, J. Hoffman, N. Zhang, E. Tzeng and T. Darrell, "DeCAF: A deep convolutional activation feature for generic visual recognition," Proceedings of The 31st International Conference on Machine Learning, pp. 647–655 (2014)
9. J. P. Eckmann, S. O. Kamphorst and D. Ruelle, "Recurrence Plots of Dynamical Systems," Europhysics Letters 5 (9), pp. 973–977 (1987)
10. Recurrence Plots and Cross Recurrence Plots, `http://www.recurrence-plot.tk/`
11. F. Takens, "Detecting strange attractors in turbulence," D. A. Rand, L. S. Young (Eds.), Dynamical Systems and Turbulence, Springer, New York, pp. 366–381 (1981)
12. K. Alligood, T. Sauer and J. A. Yorke, "Chaos: An Introduction to Dynamical Systems," Springer, New York (1997)
13. A. M. Fraser and H. L. Swinney, "Independent coordinates for strange attractors from mutual information," Phys. Rev. A, 33, pp. 1134–1140 (1986)

14. M. B. Kennel, "Determining embedding dimension for phase-space reconstruction using a geometrical construction," Phys. Rev. A, 45, pp. 3403–3411 (1992)
15. J. S. Iwanski and E. Bradley, "Recurrence plots of experimental data: To embed or not to embed?," Chaos: An Interdisciplinary Journal of Nonlinear Science, 8(4), pp. 861-871 (1998)
16. Z. Wang and T. Oates, "Imaging time-series to improve classification and imputation," In Proceedings of the 24th International Conference on Artificial Intelligence (IJCAI'15), Q. Yang and M. Wooldridge (Eds.), AAAI Press, pp. 3939–3945 (2015)
17. Caffe, `http://caffe.berkeleyvision.org/`
18. Krizhevsky, A., Sutskever, I.,& Hinton, G. E. . Imagenet classification with deep convolutional neural networks. In Advances in neural information processing systems (pp. 1097-1105).(2012)
19. Y. Manabe and B. Chakraborty, "A Novel Approach for Estimation of Optimal Embedding Parameters of Nonlinear Time Series by Structural Learning of Neural Network," Neurocomputing, Vol. 70, Issue 7-9, pp. 1360-1371 (2007)

Design Aircraft Engine Bivariate Data Phases using Change-Point Detection Method and Self-Organizing Maps

Jean-Marc Bardet, Cynthia Faure, Jérôme Lacaille, and Madalina Olteanu

SAMM, EA 4543
Panthéon-Sorbonne University
90 rue de Tolbiac, 75013 Paris, France
http://samm.univ-paris1.fr
&
Safran Aircraft Engines,
Rond Point René Ravaud, Réau, 77550 Moissy Cramayel, France
https://www.safran-aircraft-engines.com

Abstract. Analyzing multivariate time series created by sensors during a flight represents a challenge for aircraft engineers. Each time series can be decomposed univariately into a series of stabilized phases, well known by the expert, and transient phases, that are merely explored but very informative when the engine is running. Our project aims at converting these time series into a succession of labels, designing transient and stabilized phases in a bivariate context. This transformation of the data will allow several perspectives: tracking similar behaviors or bivariate patterns seen during a flight, detecting frequent or rare sequences of labels during a flight, and discovering hidden multivariate structures. This manuscript proposes a methodology to automatically cluster all engine transient phases. First, the algorithm builds a new database of transient patterns with a change-point detection method. Second, the bivariate transient patterns are clustered into a ranked number of typologies, which will provide the labels. The clustering is implemented with Self-Organizing Maps [SOM]. All algorithms are applied on real flight measurements with a validation of the results from expert knowledge.

1 Introduction

Multiple sensors placed on aircraft engines are daily generating important amounts of data, which are a big concern for engineers. Indeed, experts are interested in extracting patterns, such as, for instance, unusual behaviors or response delays between engine variables. These patterns are almost impossible to detect manually, due to the size and the complexity of the data, hence automatic tools, mixing time series and statistical learning techniques, are needed by the experts so that they may analyse and quickly compare interesting patterns.

Usually, aircraft engine data is provided as a multivariate time series, and it characterizes the behavior of the engine during the flight. One approach for

dealing with this data is to segment it into a succession of stabilized and transient phases. Whereas several methodologies and algorithms (health diagnosis, anomaly detection, and wear patterns) were designed under the stationarity assumption for stabilized phases, [10] and [8], transient phases are poorly mentioned in the literature, although they are of real interest for the engineers. Most of the interesting patterns, for example, occur during transient phases: take-off, landing, ... The aim of the present manuscript is to focus on transient phases, while attempting to identify, isolate, and characterize them. In a previous work, [4], the data was analysed as a univariate time series only, after having extracted one of the signals, suggested by the experts as being of particular interest. In this paper, the adopted point of view is a multivariate one: the time series will be first split into patterns, then the patterns will be clustered into meaningful groups. The eventual goal is to provide a new way of expressing the complex multivariate data as a sequence of labels, making it easier for experts analysis.

The first step of the methodology proposed here is to split the data into stabilized and transient phases. Intuitively, a phase can be considered as stabilized whenever it does not contain any major variation. Using expert knowledge, a major variation for this kind of data is given by a fixed threshold measuring the absolute difference between the first and the last value of the phase (10% in our case). The partitioning is carried out in a univariate framework, similarly to [4], on a signal qualified as "reference variable" by the experts, such as the fan speed. Taking into account the characteristics of the extracted univariate time series which has a piecewise linear behavior, and also the above definition of a transient phase, the partitioning is done by detecting change-points in the slope.

In a previous work devoted to finding the most adequate strategy for segmenting the data [3], several algorithms for change-point detection in offline fashion were tested. Among them, the best trade-off between the computational complexity and the performances in correctly identifying the right number and the right positions of the change-points was achieved by the PELT method [6]. In the present manuscript, this algorithm only was used, with a cost function derived from the sum of squared errors in linear regression and a penalty term similar to that of the BIC criterion.

Once the univariate "reference time series" has been partitioned, the resulting phases or patterns are grouped, according to the definition of transient phases, into stabilized, ascending transient and descending transient. The second step of our methodology is to separately cluster ascending patterns and descending patterns, while also introducing a multivariate aspect in the clustering, as it will be subsequently explained. The clustering step may in turn be divided into several substeps.

First, the univariate transient phases previously identified are clustered. This task is not immediate, since the lengths of the patterns are not identical. Two strategies may at this point be considered: either use specific similarities and/or dissimilarities for time series and a clustering method suited for relational data [1], [9], or extract a fixed number of numerical features characterizing the patterns [5] and use clustering algorithms designed for vector data. As already de-

scribed in [4], after having tested several clustering algorithms and several ways to resume the data, the self-organizing maps (SOM) algorithm [7], trained on a set of numerical features, provides good clustering results, as well as graphical tools for visualizing the groups of patterns.

Second, the clusters obtained on the patterns of the "reference" univariate time series are next divided into subclusters, which take into account a second signal or time series. This step is the main contribution of the present manuscript with respect to our previous work, since we refine the initial univariate clustering proposed in [4] by considering supplementary information. The bivariate framework may allow the observation of interesting phenomena which was not possible in the univariate context such as response time between the signals. The resulting final clustering is eventually validated, using either expert knowledge, or additional variables in the data set and resuming the states of the engine.

The rest of the manuscript is organized as follows: Section 2 contains the detailed methodology on segmenting and clustering bivariate time series, while Section 3 overviews the experimental results on real data. The conclusion as well as the future work tracks are given in Section 4.

2 Segmenting and clustering bivariate time series

Let us now describe the methodology proposed here for extracting and clustering patterns from bivariate time series. Let $(Y^l_{1:N_l,i=1,2})_{l=1,...,L}$ be the available data which corresponds to L flights, each flight l being of length N_l. For each flight, a bivariate time series, corresponding to two signals of interest for the engineers (the "reference variable" and an additional one) is considered.

The first step of the analysis consists in partitioning a univariate time series, the "reference" signal, in order to identify the patterns, while the second step is the bivariate clustering of the patterns. The complete procedure is illustrated in Figure 1.

2.1 Pattern extraction

For each flight l, the univariate "reference" time series $(Y^l_{1:N_l,1}) = (Y^l_{1,1}, ..., Y^l_{N_l,1})$ is optimally partitioned into patterns or phases. As mentioned in the introduction, due to the piecewise linear behavior of the signal, partitioning is achieved through offline change-point detection in the slope.

The partitioning consists in computing the optimal number of change-points $\hat{K}_l$ in the series $Y^l_{1:N_l,1}$, and their optimal positions $(\hat{\tau}^l_j)_{j=1,...,\hat{K}_l}$. This is done by minimizing a penalized cost function which aims at fitting the best number of linear regressions on the data:

$$\left(\hat{K}_l, \hat{\tau}^l_1, ..., \hat{\tau}^l_{\hat{K}_l}\right) = \underset{K_l;1<\tau^l_1<\tau^l_2<\cdots<\tau^l_{K_l}<N_l}{\arg\min} \mathcal{C}(Y^l_{1:N_l,1}, (\hat{\theta}^l_{\tau^l_j+1,\tau^l_{j+1}})_{j=1,...,K_l}) \ ,$$

where

$$\mathcal{C}(Y^l_{1:N_l,1}, (\hat{\theta}^l_{\tau^l_j+1,\tau^l_{j+1}})_{j=1,...,K_l}) = \sum_{j=0}^{K_l} C(Y^l_{\tau^l_j+1:\tau^l_{j+1},1}, \hat{\theta}^l_{\tau^l_j+1,\tau^l_{j+1}}) + \beta \ ,$$

C being a contrast function (least-squares error, -log-likelihood, ...), $\hat{\theta}^l_{\tau^l_j+1,\tau^l_{j+1}}$ being plugged-in as linear-regression estimates

$$\hat{\theta}^l_{\tau^l_j+1,\tau^l_{j+1}} = \underset{\theta_1,\theta_2\in\mathbb{R}}{\arg\min} \sum_{t=\tau^l_j+1}^{\tau^l_{j+1}} \left(Y^l_{t,1} - \theta_1 t - \theta_2\right)^2 \ ,$$

and β being the penalty term, usually that of the BIC ($\beta = cK_l \ln N_l$, c a constant).

In order to simplify the notations hereafter, the estimates $\hat{K}_l$ and $(\hat{\tau}^l_j)_{j=1,...,\hat{K}_l}$ will be confounded with K_l and $(\tau^l_j)_{j=1,...,K_l}$ in the rest of the paper.

For the implementation, the PELT [6] algorithm was preferred, since it provides the best tradeoff between numerical complexity and performances. A detailed discussion about the segmentation of aircraft engine data and the performances of various algorithms is available in our previous work [3].

Once the partitioning algorithm has been trained on all the flights in the data set, one gets the set of all detected phases or patterns, $(Y^{l,j}_{\tau^l_j+1:\tau^l_{j+1},1})_{l=1,...,L\ ;\ j=0:K^l}$ where l is the index of the flight, and j is the index of the pattern within the l-th flight.

2.2 Pattern clustering

Using the empirical definition of transient phases and a fixed threshold of 10%, the extracted patterns are first classified into stabilized, ascending transient and descending transient, as suggested by the experts. Only the results on the ascending phases will be illustrated in the present manuscript, but the same framework could be used for descending phases.

The bivariate framework is progressively introduced in the clustering procedure. First, the ascending univariate patterns previously identified are grouped together. Second, a new variable of interest is taken into account and used during a second clustering step.

In order to simplify the notations, suppose that $(K'_l)_{l=1:L}$ is the number of ascending transient phases previously detected for the l-th flight. The start-point and the end-point of the j-th ascending transient pattern of flight l will be denoted $\tau^{l,s}_j$ and $\tau^{l,e}_j$, where $j = 1, ..., K'_l$. Hence, the data set containing all ascending phases extracted from the "reference" variable is given by $(Y^{l,j}_{\tau^{l,s}_j:\tau^{l,e}_j,1})_{l=1,...,L\ ;\ j=1:K'_l}$. The clustering procedure is to be applied to a set of $P = K'_1 + ... + K'_L$ patterns, with various lengths.

Univariate clustering Since the objects to be clustered are time series with various lengths, the approach chosen here is to summarize each of them as a vector of M_1 numerical features, where the features were chosen with the help of the experts. Hence, the data set of patterns $(Y^{l,j}_{\tau_j^{l,s}:\tau_j^{l,e},1})_{l=1,...,L\ ;\ j=1:K'_l}$ is summarized by the data set of numerical features $(X_k^m)_{k=1,...,P}^{m=1,...,M_1}$, where k indexes the pattern and m indexes the features .

The clustering of the patterns using their numerical features is achieved using self-organizing maps, which are also of interest in this context for their visualization properties. With this in mind, a large map is first trained, providing an exploratory tool for examining the data. Then, the number of clusters is reduced be performing either an hierarchical clustering (AHC) or a K-means algorithm on the prototypes produced by the SOM. The optimal number of clusters is selected using a fixed threshold on the ratio between the within-class variance and the whole variance. Let $(SC_1, ..., SC_\phi)$ be the resulting partition of the P ascending patterns into ϕ clusters. In order to simplify the notations in the subsequent sections, let us suppose that the partition $(SC_1, ..., SC_\phi)$ is expressed in terms of the set of indexes $\{(j,l), j = 1, ..., K'_l, l = 1, ..., L\}$.

Bivariate clustering Once the partition $(SC_1, ..., SC_\phi)$ has been computed, one wants to further split it, by taking into account a second variable and by further investigating the patterns in a bivariate framework. At this point, each cluster $(SC_v)_{1,...,\phi}$ will be divided into subclusters.

As mentioned before, this second clustering allows a more in-depth study of the transient patterns such as comparisons between bivariate patterns, analyses of time-responses between the signals without missing any information,... For instance, if a variation occurs in a transient phase on a signal (temperature, pressure, speed,...), a variation might respond to this change in another variable, but with a certain delay. These phenomena may be brought into light in a bivariate context. However, for carrying out this kind of study, transient patterns with unequal lengths are not suitable. For this reasons, all univariate patterns within a cluster should be first transformed such that they have equal lengths. This consists into re-aligning the patterns within a cluster and, if necessary, lengthening or shortening them.

Re-aligning the patterns within the clusters is done as follows. For each cluster $v = 1, ..., \phi$ and for a given dissimilarity between patterns d, a "reference" curve, minimizing the sum of distances with respect to all patterns in the cluster is chosen:

$$\breve{Y}_v = \underset{(Y^{l,j}_{\tau_j^{l,s}:\tau_j^{l,e},1})_{(j,l)\in SC_v}}{\arg\min} \left(\sum_{(j',l')\in SC_v, j'\neq j, l'\neq l} d(Y^{l,j}_{\tau_j^{l,s}:\tau_j^{l,e},1}, Y^{l',j'}_{\tau_{j'}^{l',s}:\tau_{j'}^{l',e},1}) \right) \quad (1)$$

Next, all patterns of cluster SC_v, for all $v = 1, ..., \phi$, are shifted (or not) so that they are aligned with $\breve{Y}_v$. If the patterns are too short, they are lengthened using the information available from the database. If the patterns are too long,

they are cut at the edges. After this alignement step, all patters within a cluster have the same length.

Within each cluster SC_v, $v = 1, ..., \phi$, the transformed patterns may now be written as $(Y^{l,j}_{\tilde{\tau}^{l,s}_j:\tilde{\tau}^{l,e}_j,1})_{(j,l)\in SC_v}$, where $\tilde{\tau}^{l,s}_j$ are the shifted start-points and $\tilde{\tau}^{l,e}_j$ are the shifted end-points of the j-th ascending pattern for the l-th flight. Given these start-points and end-points, the second signal available in the data set, $(Y^l_{1:N_l,2}) = (Y^l_{1,2}, ..., Y^l_{N_l,2})$, is segmented and the chunks corresponding to the ascending patterns in the "reference signal" are extracted and grouped according to the previously determined clusters for further examination, $(Y^{l,j}_{\tilde{\tau}^{l,s}_j:\tilde{\tau}^{l,e}_j,2})_{(j,l)\in SC_v}$, for all $v = 1, ..., \phi$.

The last step of the bivariate clustering consists in splitting the clusters SC_v, $v = 1, ..., \phi$, by performing independent new clusterings on each of them. The data used for this further partitioning is given by the chunks extracted from the second signal. Here again, the methodological choice is to use self-organizing maps, which are finally reduced to an optimal number of subclusters using a fixed threshold on the ratio of explained variance. Although the time-series to be clustered have the same length in this case, the same approach as previously, summarizing the time series by a vector of numerical features, is preferred, since it reduces the dimensionality of the data and speeds-up the computation time. Hence, for each $v = 1, ..., \phi$, the time series $(Y^{l,j}_{\tilde{\tau}^{l,s}_j:\tilde{\tau}^{l,e}_j,2})_{(j,l)\in SC_v}$ is resumed by a set of numerical vectors $(Z^{l,j}_m)^{(l,j)\in SC_v}_{m=1,...,M_2}$, where M_2 is the number of extracted features.

Once the clustering procedure is applied to the $Z^{l,j}_m$'s, each cluster SC_v is partitioned into ψ_v subclusters, $SC_v = \{SC_{v,w}, w = 1, ..., \psi_v\}$. The final clustering, which will be used for labelling purposes and which will be provided to the experts for further analysis, is thus associated to the partitioning $(SC_{v,w})_{v=1,...,\phi;w=1,...,\psi_v}$ and contains bivariate time-series, of equal lengths within a cluster, corresponding to all ascending patterns extracted from the initial flight data.

3 Applications on flight data

Let us now illustrate the methodology described above on a real dataset. First, the data with the available variables is briefly described. Next, the results of the univariate segmentation and of the bivariate clustering are presented.

3.1 Data information

About 500 flights coming from 8 different engines (with different take-off places and different landing positions) are available. In this database, the sensors present on the engine recorded around 50 variables. Each flight is described by multiple variables (for example the fan speed, the lever of the pilot, temperatures,...) with the same frequency. The mean duration of one flight is around 2,8 hours.

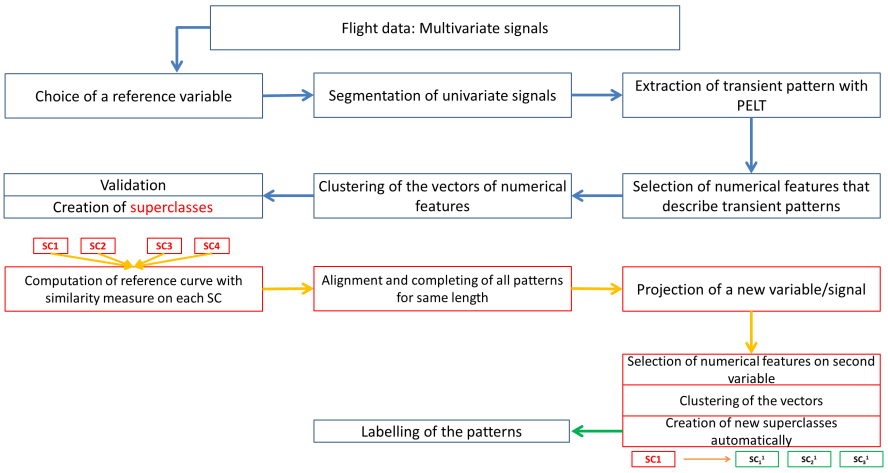

Fig. 1: Procedure of the methodology described step by step

Among all available variables, the fan speed was selected, as suggested by the experts and due to its impact on the functioning of the engine, as the "reference signal" (for examples see Figure 2). Expressed as a percentage (the ratio w.r.t. the maximum value), the fan speed is controlled by the pilot with the lever for the rev up. The behavior of this signal is mainly piecewise linear, hence the approach described in Section 2.1 and consisting in computing change-points in the slope is well adapted. Some of the features of the fan speed as stemming from the available data we used are enumerated in Table 1.

Mean of minima [SD]	0% [±0%]
Mean of maxima [SD]	99% [±1.2%]
Mean of medians [SD]	76% [±21%]
Mean of interquartile ranges [SD]	23% [±22%]

Table 1: Information about the fan speed [SD=Standard deviation]

3.2 Pattern extraction

Segmenting the flights, and more specifically the signals corresponding to the fan speed, in order to extract the patterns is carried out by implementing the PELT algorithm with a cost function corresponding to the minimum description length, [2]. Globally, the change-points are well detected, even the small ones. One may see, for instance, the results for one flight in Figure 2. Overall, around 8,000 transient phases are identified, among which around 4,000 ascending tran-

sient phases, with very different lengths (see Figure 3 for an illustration of the ascending patterns associated to one given engine).

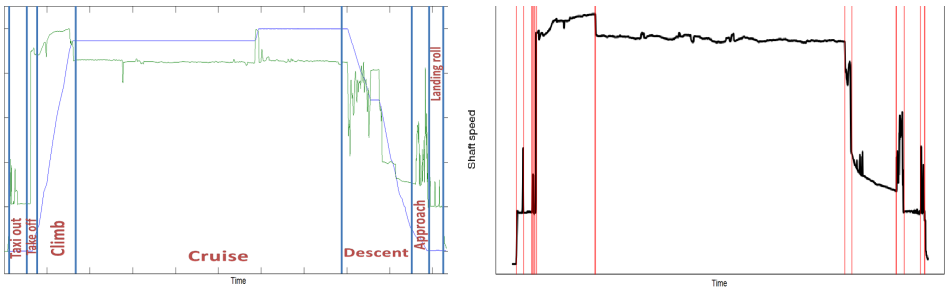

Fig. 2: Fan speed (green) and altitude (blue) during flight [left] & result of PELT on the fan speed [right].

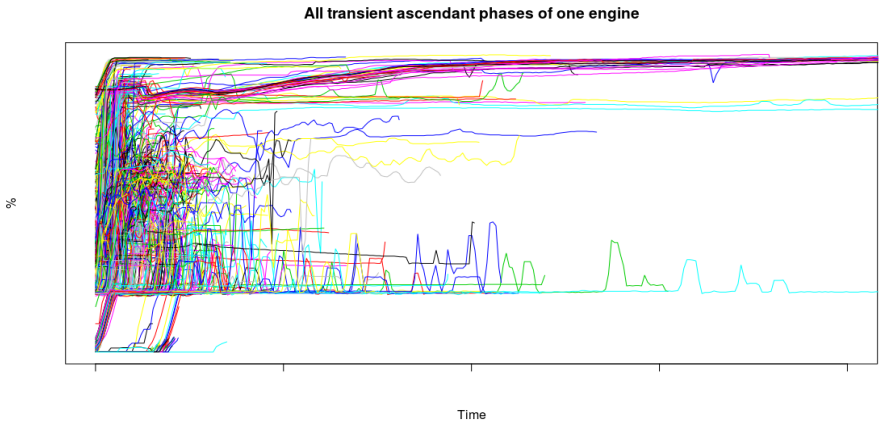

Fig. 3: Visualization of all transient phases for only one engine. The colour is randomly distributed for a better distinction between the curves.

3.3 Pattern clustering

Univariate clustering During this step, the univariate ascending transient patterns previously identified are first summarized by a set of numerical features and then clustered using a self-organizing map. Using the properties of the data and experts' knowledge, the features extracted for each pattern are: start point,

end point, length, mid point, median, variance, variance of first half, variance of second half, mean of first half, mean of second half.

The patterns associated to the fan speed are clustered and mapped onto a 11x11 grid. The grid, which we do not reproduce here due to the limited number of pages, contains homogeneous clusters, well mapped and meaningful to the experts. Next, the number of clusters is further reduced using K-means on the prototypes of the SOM, and finally nine clusters are selected, illustrated in Figure 4.

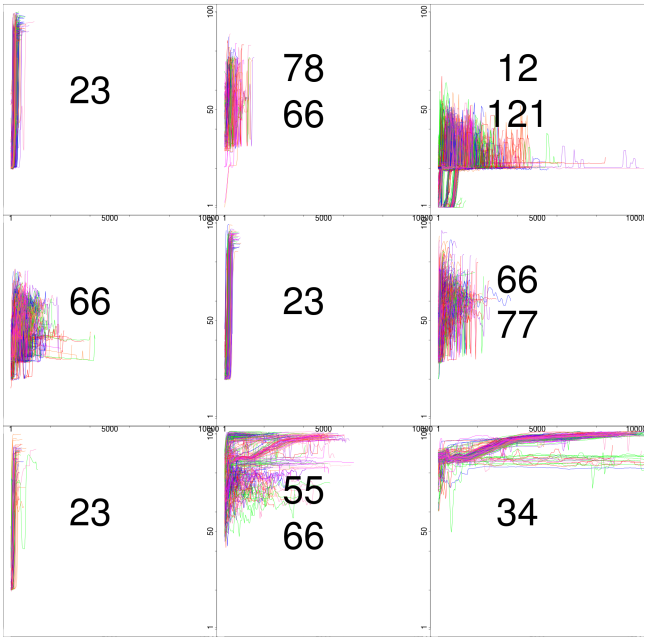

Fig. 4: Fan speed clusters of ascending patterns, crossed with Flight Mode

One way for validating clustering results is to a posteriori cross them with additional information provided by the manufacturer, such as the flight mode (FM). This variable is automatically calculated by the board computer as a combination between the fan speed and other available variables such as the pilot's lever, the altitude, the valve,... Several values, corresponding to different states of the flight, are computed: pre-flight [00], engine start [11], taxi-out [22], take-off [33], climb [44], cruise [55], descent [66], approach [77], landing roll [88] and taxi-in [99].

Since the methodology presented here does not take into account at all this information on the flight-mode, it was interesting for the experts to check whether the extracted patterns and the resulting clusters correspond (at least partially) to the different flight-modes. In Figure 4, two or three digits were used for labelling

each pattern, according to the consecutive flight-modes present in the pattern. For instance, if a pattern contains a take-off state followed by a climb state, it will be labelled [34] and the pattern represents the transition between take-off and climb. As it may be seen in Figure 4, clusters are generally homogeneous and are associated to well identified flight-modes.

Bivariate clustering The next step is to introduce the bivariate framework by adding a second variable to the fan speed. Here, for illustration purposes, we use the temperature, but other variables can be similarly used.

First, each cluster represented in Figure 4 is transformed by re-aligning the patterns within along a "reference" curve. An illustration of this procedure is given in Figure 5, for the cluster in the upper-left corner in Figure 4.

The reference curve (in black in Figure 5) has to be the most similar pattern to all the others in the same cluster. Thus, it is computed by minimizing the criterion introduced in Equation (1). Here, the dissimilarity d is a sliding Euclidean distance, normalized by the length of the patterns.

Once the "reference curves" are identified for each cluster, the patterns are re-aligned along them. If necessary, patterns may be lengthened or shortened, so that all patterns within a cluster have the same length. Upon the recommendation of the experts, all curves are lengthened with 25 seconds to the right so that no delays may affect the clustering. These delays may depend on the conditions of the flight (differences of temperatures, climate, ...).

The modified start-points and end-points of the univariate patterns concerning the fan speed may now be used to extract the corresponding chunks of data in the temperature signals. We obtain, within each cluster, bivariate time-series with equal length.

Next, for each cluster and on the temperature data only, the same set of numerical features (except the length of the time series) are extracted and independent SOMs are trained on each cluster. The self-organizing maps representation may be used for detailed inspection of the results, but we only present here the results after having grouped the prototypes stemming from the SOM into a meaningful number of subclusters, using K-means algorithm and a fixed threshold of 80% for the explained variance. The subclusters corresponding to the cluster in the upper-left corner in Figure 4 are illustrated in Figure 6.

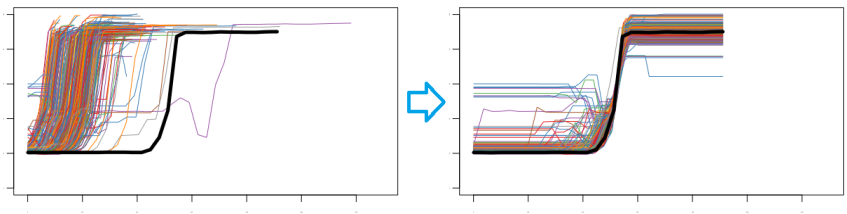

Fig. 5: Alignement of the patterns in Cluster 1 according to the "reference" curve

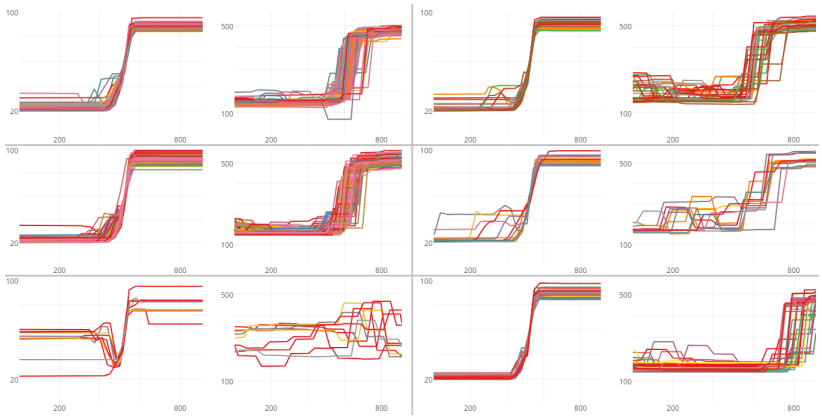

Fig. 6: Bivariate representation fan speed (left) and temperature (right) of the subclusters associated to cluster 1

Figure 6 contains the bivariate representation of the subclusters associated to one of the main univariate clusters (transient patterns between taxi and take-off). Each of the six subclusters illustrates both the fan speed (left) and the temperature (right). The temperature is expected to increase after the take-off, but with a certain delay. Obtaining a meaningful and detailed clustering where different delays may be drawn although the take-off's and the fan speed are very similar is of high interest for the engineers. The bivariate clustering and representation allow to account for various phenomena occuring in the functioning of the engine, which were not visible through a univariate approach only.

4 Conclusion

The present manuscript introduces a global methodology for dealing with bivariate signals related to aircraft-engine flight data. The signals are first analyzed in a univariate fashion, by selecting a "reference variable" which is split into patterns and then clustered. Next, a second variable is added and each cluster previously obtained is partitioned into subclusters by taking into account the information in the second signal. The final clustering on bivariate patterns allows the experts to discover behaviors of the engines never observed so far.

The eventual goal of our work on this data is to use the clustering in order to label the multivariate signal and replace the patterns by the corresponding clusters. This will allow, on the one hand, an easier and less expensive storage for the data, and, on the other hand, a practical representation for carrying out statistical analyses: study the distribution of the engines in the clusters, understand why some patterns are isolated, track a specific pattern,...

References

1. Berndt, D., Clifford, J.: Using dynamic time warping to find patterns in time series. Workshop on Knowledge Knowledge Discovery in Databases 398, 359–370 (1994), http://www.aaai.org/Papers/Workshops/1994/WS-94-03/WS94-03-031.pdf
2. Davis, R.A., Lee, T.C., Rodriguez-Yam, G.A.: Structural break estimation for non-stationary time series models. Journal of the American Statistical Association 101, 223–239 (2006)
3. Faure, C., Bardet, J.M., Olteanu, M., Lacaille: Comparison of three algorithms for parametric change-point detection. In: ESANN. pp. 2–7 (2016)
4. Faure, C., Bardet, J.M., Olteanu, M., Lacaille: Using self-organizing maps for clustering and labelling aircraft engine data phases. In: WSOM (2017)
5. Guyon, I., Elisseeff, A.: An Introduction to Feature Extraction, pp. 1–25. Springer Berlin Heidelberg, Berlin, Heidelberg (2006), https://doi.org/10.1007/978-3-540-35488-8_1
6. Killick R., F.P., Eckley, I.: Optimal detection of changepoints with a linear computational cost. JASA 107(500), 1590–1598 (2012), http://arxiv.org/abs/1101.1438
7. Kohonen, T.: The self-organizing map. Proceedings of the IEEE 78(9), 1464–1480 (1990)
8. Lacaille, J., Gerez, V.: Online Abnormality Diagnosis for real-time Implementation on Turbofan Engines and Test Cells. Phm pp. 1–9 (2011)
9. Olteanu, M., Villa-Vialaneix, N.: On-line relational and multiple relational SOM. Neurocomputing 147(1), 15–30 (2015)
10. Rabenoro, T., Lacaille, J., Cottrell, M., Rossi, F.: Anomaly detection based on indicators aggregation. In: Proceedings of the International Joint Conference on Neural Networks. pp. 2548–2555 (2014)

Linear Trend Filtering via Adaptive Lasso

Matúš Maciak *

Department of Probability and Mathematical Statistics,
Charles University, Sokolovská 82, Prague, 186 75, Czech Republic
maciak@karlin.mff.cuni.cz
http://karlin.mff.cuni.cz/~maciak

Abstract. *Piece-wise linear models are quite popular real applications because of their overall simplicity and straightforward interpretation. In addition, such models are quite flexible in terms of their ability to adapt to existing changes in the trend which usually models the underlying time dependent structure. In this paper we propose an innovative approach to the linear trend filtering which is based on the sparsity principle in atomic pursuit estimation via an adaptive LASSO approach. The proposed method is oracle consistent and the final estimate can be constructed with the same time efficiency as an ordinary linear regression. Moreover, one can take a full advantage of many efficient algorithms used to fit standard LASSO problems. We present some theoretical properties and the finite sample performance is investigated using a comparative simulation study.*

Keywords: trend filtering; adaptive lasso; linear regression; change-points; joinpoint regression; oracle properties;

1 Introduction

Trend filtering is a powerful tool used in statistical modeling approaches to reconstruct the conditional mean structure of some underlying data generating process. A general trend filtering is typically defined in terms of some parametric L_2-based minimization problem, where, in addition, one also penalizes the objective function with respect to the sum of the absolute kth order differences of the unknown parameters. The resulting estimate is then formed by some k degree spline functions defined over a specific mesh of knot points, which are usually preselected in advance. A specific scenario can be obtained for a particular choice of $k = 1$, which leads to the linear trend filtering case. Thus, the resulting estimates are piece-wise linear and, in addition, they are usually required to be continuous. This models are also known as joinpoint regression models (segmented regression, sequential linear models or linear trend models respectively).

* The author would like to express his thanks for a partial support which was provided by the grant of the Ministry of Educations, Youth, and Sports in the Czech Republic (Mobility grant, No. 7AMB17FR030) and the Grant P402/12/G097.

The main advantage of the linear trend filtering models is their overall simplicity. It is also the reason for their huge popularity they gained in last decades – simple and easily interpretable statistical models are the key issue especially in situations where the final conclusions based on them are about to be explained and interpreted to non-statisticians or, more generally, to people with a lack of mathematical skills. On the other hand, the joinpoint models (see, for instance, [8] for an overview) can still offer a quite reasonable flexibility even though the final structure is estimated only by some few linear pieces. These pieces are put together to form a continuous function over the whole domain of interest. The points where the adjacent linear pieces join together are usually called *changepoints* (sometimes also transition points, break-points or joinpoints recpectively). The slopes of the regression lines change at this changepoint locations to adapt for the existing structural changes in the underlying dependence.

There were various methodological approaches proposed to estimate the piece-wise linear model and to perform the linear trend filtering. Beside solving the L_2 based minimization problem one usually needs to decide on the right number of changepoints, or slope breaks respectively. Theoretical results suggest that it might be advantageous to know the number of changepoints in advance; this knowledge can improve the overall performance and it provides a more convenient theoretical background to prove certain statistical properties. In addition, it also yields a better rate of convergence. In practical situations, however, the number of changepoints is rarely known in advance and some model-selection is necessary to choose one final model from a set of all plausible ones. Usually, there is a whole sequence of nested models with different number of changepoints considered; the model selection is then based on either some permutation tests ([1, 7, 9], and [20]), or likelihood ratio tests ([5, 6]) by evaluating some goodness-of-fit criterion (usually BIC), or by adopting the Bayesian framework ([2, 17]) instead. Alternatively, one can use some more recent ideas of the sparse fitting approach via atomic pursuit methods and to adopt the k order differences common for the trend filtering ([10, 24]), the total variation penalty ([16, 21]), or the LASSO regularization ([15, 14]) for the changepoint detection and estimation. These methods based on the sparsity are the same on principle: the idea is to over-parametrize the estimated model and to let the data themselves to choose only relevant parameters while shrinking all other parameters to exactly zero. This is performed exclusively by utilizing the nature of the L_1-norm (see Figure 1 for an illustration), which is applied on the estimated parameters as a penalty, resulting in so called LASSO estimation problem (see [3, 22]).

On the other hand, the standard LASSO problem is well known for having a tendency to choose slightly more parameters in the final model than necessarily needed ([18, 19]). This also implies that the LASSO estimation is not oracle consistent in general scenarios (see, for instance, [26]), but there were some oracle consistent modifications proposed (elastic net by [27] and adaptive LASSO by [26]) to avoid this inconsistency and to improve the selection performance of the LASSO estimated models.

In this paper we use the adaptive LASSO modification and we improve our original idea presented in [14] for the LASSO based changepoint detection and estimation in piece-wise linear models. We introduce the adaptive LASSO trend filtering approach and we show that the final model can be obtained within the same time costs as the standard LASSO based model. The adaptive based trend filtering can be also used to consistently estimate the true slope breaks (i.e., consistent changepoint detection and estimation) in the overall trend and it can be shown to satisfy the oracle properties.

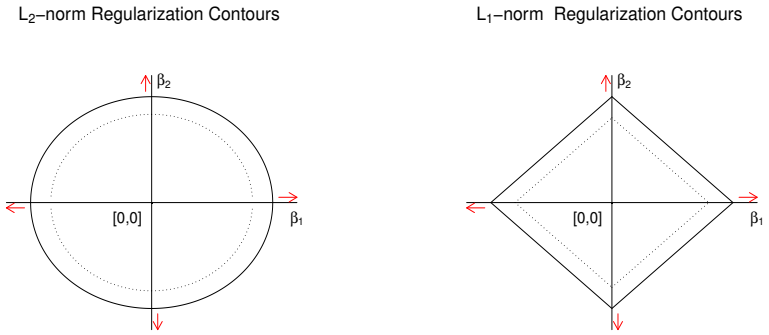

Fig. 1. Standard contours of the L_2-norm penalty and the L_1-norm penalty. The smooth favor of the L_2 norm is responsible for selecting all parameters to be nonzero while the sharp edges of the L_1 norm creates the background for selecting just some nonzero parameters and shrinking remaining one exactly to zero.

In addition, by utilizing the complete solution paths as elucidated by [4] we can, in an easy and straightforward manner, obtain the whole set of all possible models (beginning with a simple linear trend with no breaks up to a perfect linear interpolation over all unique data points), and by using the recent advances in the post-selection inference (see, for instance, [13, 25]) we can test for the significance of the final model. The model selection step is thus performed via the L_1 regularization and both, the changepoint location detection and the changepoint magnitude estimation are performed in a data-driven manner in just one single step. Finally, the proposed modeling approach can be easily extended to handle some qualitative restrictions imposed on the final estimate (in a similar manner as in [15]), which can be easily accounted for by adding some set of straightforward linear constraints. This turns out to be useful especially in economics and econometric modeling.

The paper is organized as follows: in the next section we describe the underlying model and we propose the adaptive LASSO trend filtering approach. Some statistical properties are presented in Section 3 and finite sample properties are investigated in Section 4. The performance of the proposed adaptive LASSO estimation approach is put in contrast with the standard LASSO method and the obtained results are discussed in detail.

2 Adaptive LASSO in Trend Filtering

Let $\{(X_i, Y_i);\ i = 1, \ldots, n\}$ be a random sample drawn from some unknown population, with the join distribution function $F_{(X,Y)}$, such that X_i's are drawn from some compact domain of interest, say, an interval $(0, 1)$, and they are all unique. Without loss of generality we may assume that $X_i < X_{i+1}$, for all $i = 1, \ldots, n-1$. Alternatively, one can also consider the X_i values to be some specific time points in some given period of time, denoting the times when actual observations Y_i's are taking place. In the following, however, we will refer to the general scenario only. Let, moreover, $\{\xi_i\}_{i=1}^{n-1}$ be a sequence of unobserved points from the same domain as the X_i values, such that $X_i < \xi_i \leq X_{i+1}$, for every $i = 1, \ldots, n-1$. We assume that the overall dependence structure between Y and X can be expressed as a piece-wise linear model with the linear pieces joining together at the points ξ_i's only, however, not necessarily all of them. Under these assumptions we can express the underlying piece-wise linear model as

$$Y_i = a_i + b_i X_i + \varepsilon_i, \qquad \text{for } i = 1, \ldots, n, \tag{1}$$

where we assume independent random error terms $\varepsilon_i \sim N(0, \sigma^2)$, for an unknown constant $\sigma^2 > 0$, while the overall continuity condition can be formulated as

$$a_i + b_i \xi_i = a_{i+1} + b_{i+1} \xi_i, \qquad \text{for } i = 1, \ldots, n-1. \tag{2}$$

Considering the model in (1)–(2) we would like to estimate the unknown parameters $a_i, b_i \in \mathbb{R}$, for $i = 1, \ldots, n$, and to find the locations for the existing changepoints (breaks in the overall trend respectively), if there are some. In particular, we need to specify those ξ_i's, for which $b_i \neq b_{i+1}$.

Thus, the sparsity principle is employed throughout the parameters b_i, for $i = 1, \ldots, n$, as we assume that $b_i = b_{i+1}$ holds for all but some small subset of indexes from $\mathcal{I} = \{1, \ldots, n-1\}$. If there is some location ξ_i, for which $b_i \neq b_{i+1}$, then we introduce a changepoint in the model: it holds that $\xi_i = \frac{a_i - a_{i-1}}{b_{i+1} - b_i}$ and the linear trend changes at this location from b_i to b_{i+1} in order to adjust for the underlying structural change in the data. The intercept parameters, values a_i, for $i = 1, \ldots, n$, are then determined by the requirement on the overall continuity over the whole domain of interest (i.e., interval $(0, 1)$).

Using the standard properties of the L_1-based regularization, and LASSO penalty in particular, we can define the corresponding parameter estimates as the solutions of the minimization problem

$$\begin{array}{ll} \underset{a_i, b_i \in \mathbb{R}}{\text{Minimize}} & \frac{1}{n}\sum_{i=1}^{n}\left(Y_i - a_i - b_i X_i\right)^2 + \lambda_n \sum_{i=1}^{n-1}\left|b_{i+1} - b_i\right|, \\ \text{w.r.t.} & X_\ell < \frac{a_\ell - a_{\ell+1}}{b_{\ell+1} - b_\ell} \leq X_{\ell+1}, \text{ for } \ell \in \{i;\ b_{i+1} - b_i \neq 0\}. \end{array} \tag{3}$$

Note, that for $b_{i+1} = b_i$ we are not estimating any location ξ_i, as there is no change in the overall trend at this point. Thus we only minimize (3) with respect to optimal changepoint locations $\xi_i = \frac{a_i - a_{i+1}}{b_{i+1} - b_i}$, for which $b_{i+1} \neq b_i$.

The penalty term in (3) can be interpreted as a penalty of the total variation type ([11, 12, 16]); $\lambda_n > 0$ represents a classical regularization parameter, here controling the number of changepoints in the final estimate. For $\lambda_n \to 0$ we expect changepoints to occur in every ξ_i, for $i = 1, \ldots, n-1$, resulting in an interpolating piecewise linear curve with possible slope changes between every two neighboring observations; for $\lambda_n \to \infty$, on the other hand, an overall linear trend over the whole domain of interest is produced and no changepoints are present, thus $b_i = b_{i+1}$ for all $i = 1, \ldots, n-1$.

The minimization problem in (3) is well defined, but, unfortunately, it is not convex. It can be still solved using some optimization toolboxes though, but it can get quite complicated if the number of observations or changepoints grows. The standard optimization methods may end up in a local instead of the global minimum. The reason of this non-convexity is the assumption we made about the changepoint locations: we assume that $\xi_i \in (X_i, X_{i+1}]$, for $i = 1, \ldots, n-1$, and thus, it can be easily seen that the design matrix of the model depends on these location parameters, which are also subjects to the minimization in (3).

An intuitive way out is to assume that the overall trend can only change in the actual observational points X_i's. We can define $\xi_i = X_{i+1}$, for $i = 1, \ldots, n-1$, which now simplifies the initial minimization problem and brings it back to a standard convex optimization scenario. The potential regression segments are now only determined by two neighboring observations, possibly having $n-1$ segments at most joining together at the design points $X_2, \ldots, X_{n-1}$. This scenario was already proposed in [14] and futher investigated in [15]. As the authors pointed out, this restriction might be slightly limiting in some finite sample cases, but this limitation becomes negligible and vanishes as the sample size increases. Once we assume that the possible changepoint locations can only occur at the observational points X_i's, then the minimization problem in (3) can be expressed as a classical LASSO problem

$$\underset{\boldsymbol{\beta} \in \mathbb{R}^n}{\text{Minimize}} \quad \frac{1}{n}\left\|\boldsymbol{Y} - \mathbb{X}\boldsymbol{\beta}\right\|_2^2 + \lambda_n \sum_{j=2}^{n-1}|\beta_j|, \tag{4}$$

where $\boldsymbol{Y} = (Y_1, \ldots, Y_n)^\top$ is the response vector, for the parameter vector we have $\boldsymbol{\beta} = (\beta_0, \ldots, \beta_{n-1})^\top = (a_1, b_1, (b_2 - b_1), \ldots, (b_{n-1} - b_{n-2}))^\top \in \mathbb{R}^n$, and the

design matrix takes the form

$$\mathbb{X} = \begin{pmatrix} 1 & X_1 & 0 & 0 & \dots & 0 \\ 1 & X_2 & 0 & 0 & \dots & 0 \\ 1 & X_3 & (X_3 - X_2) & 0 & \dots & 0 \\ \vdots & \vdots & \vdots & \ddots & \ddots & \vdots \\ 1 & X_n & (X_3 - X_2) & (X_4 - X_3) & \dots & (X_n - X_{n-1}) \end{pmatrix}, \tag{5}$$

The regularization parameter $\lambda_n > 0$ is, as we already mentioned, used to control the number of changepoints appearing in the final model. The design matrix $\mathbb{X}$ can be decomposed into two parts: the first two columns corresponds with a standard design matrix used for an ordinary linear regression with $(a_1, b_1) \in \mathbb{R}^2$ being the corresponding intercept and slope parameters and the remaining columns of $\mathbb{X}$ are used to model the existing trend breaks in the final model.

The minimization problem in (4) is convex, and thus, it can be easily solved using some standard optimization tools. An effective approach, for example, is to use the LARS algorithm proposed in [4], and to obtain the whole solution paths for all $\lambda_n > 0$. On the other hand, this problem also has some limitations, which are evident especially when it comes to the theoretical properties of the estimates obtained by (4). The standard LASSO penalty in (4) is well known for selecting slightly more non-zero parameters in the final model than actually needed and the model, which yields the optimal consistency rate in terms of the L_2 loss sense, does not provide a consistent selection in terms of the sparsity, but it rather results in a slightly over-parametrized model (see [18] for details).

In order to improve the selection performance of the model we adopt the idea presented in [26], and we introduce an analogous minimization problem where the estimate for $\boldsymbol{\beta} = (\beta_0, \dots, \beta_{n-1})^\top$ is now defined as

$$\widehat{\boldsymbol{\beta}} = \underset{\boldsymbol{\beta} \in \mathbb{R}^n}{\text{Argmin}} \ \frac{1}{n} \|\boldsymbol{Y} - \mathbb{X}\boldsymbol{\beta}\|_2^2 + \lambda_n \sum_{j=2}^{n-1} \frac{|\beta_j|}{|\widehat{\beta}_j^{(LS)}|}, \tag{6}$$

where, in addition to (4), we are using a specific scaling factor for each parameter β_j, $j = 2, \dots, n-1$, in order to make the shrinkage effect (in terms of the relative magnitude) same for all elements. The scaling factor is given by the corresponding ordinary least squares estimate $\widehat{\beta}_j^{(LS)}$ of β_j, for each $j = 2, \dots, n-1$. Recall, that we again do not penalize for the overall intercept and slope parameters, which are $\beta_0, \beta_1 \in \mathbb{R}$. The ordinary least squares estimates are well defined and they are unique. Indeed, the total number of parameters used in the estimation is the same as the overall number of observations, and thus, the ordinary least squares lead to a perfect data interpolating fit.

2.1 Computational Aspects

As already pointed out, the minimization formulated in (6) is a convex optimization problem and therefore, a global minimum can be efficiently found. Moreover,

the same efficient algorithms, which are used to solve the standard LASSO problems, can be also employed to deal with the adaptive LASSO modification.

From the practical point of view, it is also possible to use some other scaling factors in the penalty term in (6). Especially in situations, where the standard least squares estimates can not be calculated (for instance, if the number of observations is less than the number of parameters in the model, or the data matrix is not regular), it might be suitable to use some alternative techniques instead. From the theoretical point of view, the adaptive LASSO can be proved to preserve its oracle properties and the selection consistency property once the scaling factors are some $\sqrt{n}$-consistent estimates of the unknown parameters (which can be obtained, for instance, by the elastic net approach if the system is over-parametrized). The $\sqrt{n}$-consistency can be even weakened (see the technical details in [26]).

In the following we propose a straightforward algorithm to perform the adaptive LASSO trend filtering as defined in (6).

1. Calculate the ordinary least squares estimate for $\boldsymbol{\beta} = (\beta_0, \ldots, \beta_{n-1})^\top \in \mathbb{R}^n$ as $\widehat{\boldsymbol{\beta}}^{(LS)} = \left(\mathbb{X}^\top \mathbb{X}\right)^{-1} \mathbb{X} \boldsymbol{Y}$, where $\mathbb{X}$ is defined in (5).
2. Define a new design matrix $\widetilde{\mathbb{X}} = (w_0 \boldsymbol{X}_0, \ldots, w_{n-1} \boldsymbol{X}_{n-1})$, where $w_j = |\widehat{\beta}_j^{(LS)}|$, for $j = 0, \ldots, n-1$, and $\boldsymbol{X}_0, \ldots, \boldsymbol{X}_{n-1}$ are the columns of $\mathbb{X}$.
3. Solve the standard LASSO minimization formulated as

$$\widetilde{\boldsymbol{\beta}} = \underset{\boldsymbol{\beta} \in \mathbb{R}^n}{\operatorname{Argmin}} \ \frac{1}{n} \left\| \boldsymbol{Y} - \widetilde{\mathbb{X}} \boldsymbol{\beta} \right\|_2^2 + \lambda_n \sum_{j=2}^{n-1} |\beta_j|, \tag{7}$$

   and obtain the whole solution paths provided by the LARS algorithm.
4. Calculate the final estimates for $\beta = (\beta_0, \ldots, \beta_{n-1})^\top$ as $\widehat{\beta}_j = \widetilde{\beta}_j w_j$, for $j = 0, \ldots, n-1$.

The minimization in (7) doest not yet fully correspond with the standard LASSO problem as defined in [22], where the author considered the same vector of parameters in the objective function and also in the penalty term. In our situation, we do not want to penalize for the first two parameters (the overall intercept and slope) and thus, only a subvector of $\boldsymbol{\beta} \in \mathbb{R}^n$ plays the role in the penalty term in (7). The problem can be, however, easily transformed to exactly correspond with the LASSO problem in [22]. Indeed, if we split the design matrix into two parts as $\widetilde{\mathbb{X}} = (\widetilde{\mathbb{X}}_1, \widetilde{\mathbb{X}}_2)$, where $\widetilde{\mathbb{X}}_1$ consists of the first two columns of $\widetilde{\mathbb{X}}$, and the corresponding vector of parameters is split accordingly, $\boldsymbol{\beta} = (\boldsymbol{\beta}_{(1)}^\top, \boldsymbol{\beta}_{(2)}^\top)^\top$, such that $\boldsymbol{\beta}_{(1)} = (a_1, b_1)^\top = (\beta_0, \beta_1)^\top$, then it only needs some basic algebra calculations to show that $\widetilde{\mathbb{X}} \widetilde{\boldsymbol{\beta}} = \widetilde{\mathbb{X}}_1 \widetilde{\boldsymbol{\beta}}_1 + \widetilde{\mathbb{X}}_2 \widetilde{\boldsymbol{\beta}}_2$, for $\widetilde{\boldsymbol{\beta}} = (\widetilde{\boldsymbol{\beta}}_{(1)}^\top, \widetilde{\boldsymbol{\beta}}_{(2)}^\top)$ being the solution of (7), can be equivalently expressed as $\mathbb{H} \boldsymbol{Y} + (\mathbb{I} - \mathbb{H}) \widetilde{\mathbb{X}}_2 \widetilde{\boldsymbol{\beta}}_{(2)}$, where $\mathbb{H} = \widetilde{\mathbb{X}}_1 \left(\widetilde{\mathbb{X}}_1^\top \widetilde{\mathbb{X}}_1\right)^{-1} \widetilde{\mathbb{X}}_1$, and $\widetilde{\boldsymbol{\beta}}_{(2)}$ is now the solution of the minimization problem

$$\widetilde{\boldsymbol{\beta}}_2 = \underset{\boldsymbol{\beta}\,\in\,\mathbb{R}^{n-2}}{\text{Argmin}} \;\; \frac{1}{n}\,\|(\mathbb{I}-\mathbb{H})\boldsymbol{Y} - (\mathbb{I}-\mathbb{H})\mathbb{X}_2\boldsymbol{\beta}_2\|_2^2 + \lambda_n\|\boldsymbol{\beta}_2\|_1,$$

which now fully corresponds with the standard LASSO problem introduced in [22]. Technical details can be found in [14].

3 Theoretical Properties

The theoretical properties of the adaptive LASSO are mostly well known and most of the details can be found in [26]. Some theoretical results related to the changepoint detection and estimation can be also found in [23]. In this session we summarize some important and useful facts and we provide some technical details, which are not found elsewhere.

Let us recall, that $\boldsymbol{X}_j$, for $j = 0, \ldots, n-1$, denote the corresponding columns of the designs matrix $\mathbb{X}$, defined in (5). For the vector of parameter estimates $\widehat{\boldsymbol{\beta}}$ given by (6), and the vector of the corresponding signs $\hat{\boldsymbol{s}} \in [-1,1]^{n-2}$, with $\hat{s}_j = sign(\widehat{\beta}_{j+1})$, for $j = 1, \ldots, n-2$, the KKT optimality conditions can be expressed in a straightforward way as

$$\begin{aligned}
&\boldsymbol{X}_j^\top(\mathbb{X}\widehat{\boldsymbol{\beta}} - \boldsymbol{Y}) = 0, && \text{for } j = 0, 1; \\
&\boldsymbol{X}_j^\top(\mathbb{X}\widehat{\boldsymbol{\beta}} - \boldsymbol{Y}) + \frac{\lambda_n}{|\widehat{\beta}_j^{(LS)}|}\hat{s}_{j-1} = 0, && \text{for } j = 2, \ldots, n-1; \\
&\hat{s}_{j-1} = sign(\widehat{\beta}_j), && \text{if } \widehat{\beta}_j \neq 0, \text{ for } j = 2, \ldots, n-1; \\
&\hat{s}_{j-1} \in [-1, 1], && \text{if } \widehat{\beta}_j = 0.
\end{aligned} \tag{8}$$

Using the KKT conditions above and applying the same idea as we used in Theorem 1 in [14] we can prove the consistency property of the adaptive LASSO estimate of the underlying linear trend in a classical L_2-norm sense. In addition, inheriting the properties of the adaptive LASSO approach we can also show that the obtained estimates preserve the oracle properties, which, beside the asymptotic normality property of the nonzero estimates, means that the consistent selection is achieved, meaning that

$$P\big[\forall j \in \{0, \ldots, n-1\};\; \widehat{\beta}_j = 0 \Leftrightarrow \beta_j^o = 0\big] \to 1, \quad \text{for } n \to \infty,$$

for some vector of the true parameters $\boldsymbol{\beta}^o = (\beta_0^o, \ldots, \beta_{n-1}^o)^\top \in \mathbb{R}^n$, and the optimal choice of the regularization parameter $\lambda_n > 0$, which needs to fulfill $\lambda_n \to \infty$ and $\lambda_n/\sqrt{n} \to 0$, both for $n \to \infty$.

Reflecting this selection consistency property and the mean consistency in the L_2-norm sense back onto the initial model scenario defined in (1) and (2) we can conclude that the changepoints in the model (i.e. breaks in the overall linear trend) are truly estimated as the sample size tends to infinity. The theoretical properties guarantee both – the consistent estimation of the true number of changepoints in the model and also, their actual positions and the overall trend estimation too.

4 Simulations

For the simulation purposes we only considered a simple situation for a linear trend model with two existing breaks: the first changepoint occurs at the point $x_1 = 0.2$ and the second at the point $x_2 = 0.7$. The magnitudes of the both breaks are proportional to the variance parameter $\sigma^2 = 1$. The underlying function, which is estimated, is given by the expression

$$f(x) = 2x\mathbb{I}_{\{x\in(0,0.2)\}} + (0.6 - x)\mathbb{I}_{\{x\in[0.2,0.7)\}} + (x/2 - 0.45)\mathbb{I}_{\{x\in[0.7,1)\}},$$

where for the domain of interest we take the unit interval $(0, 1)$. There were four sample sizes considered ($n \in \{50, 100, 500, 1000\}$) and for each we simulated 100 Monte Carlo simulations according to the model above. The random error terms were assumed to be independent with the Gaussian distribution $N(0, 1)$.

n	λ_{AS}	$\lambda_{(2)}$		LASSO with $\lambda_{(2)}$	LASSO with λ_{AS}		ALASSO with λ_{AS}	
	Value	Mean	Std.Err.	MSE (St.Err)	MSE (St.Err)	Breaks	MSE (St.Err)	Breaks
50	7.04	0.21	*(0.10)*	0.021 *(0.027)*	0.021 *(0.029)*	0 [0–2]	0.022 *(0.030)*	0 [0–2]
100	9.95	0.36	*(0.18)*	0.013 *(0.017)*	0.013 *(0.018)*	2 [0–5]	0.015 *(0.020)*	1 [0–2]
500	22.22	1.81	*(0.83)*	0.007 *(0.010)*	0.003 *(0.004)*	7 [3–13]	0.006 *(0.009)*	2 [0–4]
1000	31.41	3.96	*(1.65)*	0.007 *(0.008)*	0.002 *(0.003)*	10 [5–22]	0.003 *(0.004)*	2 [1–5]

Table 1. Simulation results for three different models: the first model is fitted with a standard LASSO penalty using a prior knowledge, that there are only two breaks in the overall trend. The corresponding regularization parameter is denoted as $\lambda_{(2)}$ and it is different for each Monte Carlo repetition. The other two models (standard LASSO and adaptive LASSO) are fitted using the asymptotically optimal value of the regularization parameter denoted as λ_{AS}. The Monte Carlo repetitions vary with respect to the number of the estimated breaks. The mean squared error quantity with the corresponding standard error values are provided as a goodness of fit measure and the median number of estimated breaks with the corresponding range over all repetitions is given to compare the models with respect to the selection consistency.

For each random sample we estimated three different models: firstly, the standard LASSO penalty was used together with a prior knowledge that there are only two slope breaks in the true model – the corresponding regularization parameter denoted as $\lambda_{(2)}$ was selected from the LASSO path (obtained by the LARS algorithm), such that two changepoints are nonzero in the final model; In the second model we again considered the standard LASSO penalty, however, the regularization parameter, denoted as λ_{AS}, was taken as an asymptotically optimal value satisfying $\lambda_n = o(\sqrt{n})$ and $\lambda_n \to \infty$, for $n \to \infty$. The same optimal value (λ_{AS}) was also used to fit the adaptive LASSO model proposed in this paper. The fitted models are then compared with respect to two quantitative qualities: the mean squared error of the model (MSE) was used to judge the mean

consistency of the given model and the number of estimated breaks was used as a meaningful tool to check the selection consistency. The results on all three models are summarized in Table 4.

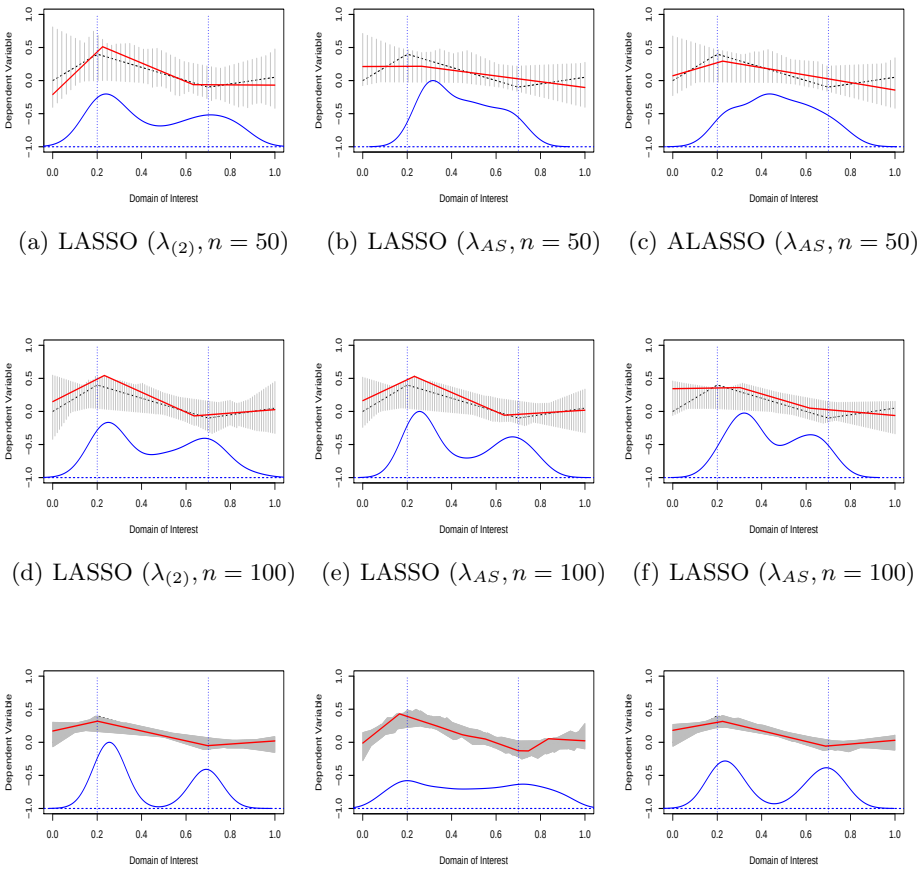

(a) LASSO ($\lambda_{(2)}, n = 50$) (b) LASSO ($\lambda_{AS}, n = 50$) (c) ALASSO ($\lambda_{AS}, n = 50$)

(d) LASSO ($\lambda_{(2)}, n = 100$) (e) LASSO ($\lambda_{AS}, n = 100$) (f) LASSO ($\lambda_{AS}, n = 100$)

(g) LASSO ($\lambda_{(2)}, n = 1000$) (h) LASSO ($\lambda_{AS}, n = 1000$) (i) LASSO ($\lambda_{AS}, n = 1000$)

Fig. 2. Finite sample performance for three different models: the standard LASSO model fitted with a prior knowledge that there are only two breaks in the slope is always provided in the first figure column (the corresponding regularization parameter is denoted as $\lambda_{(2)}$). In the middle column, there is again the standard LASSO model, however, with the asymptotically optimal value of the regularization parameter ($\lambda_{AS} = o(\sqrt{n})$), and finally, in the last column, there is the adaptive LASSO model with the same value of the optimal parameter – λ_{AS}. The point-wise range for the estimated models over 100 Monte Carlo repetitions is given by the gray regions and the blue solid lines represent a scaled density of the estimated changepoint locations.)

From Table 4 it is quite obvious that the models based on the optimal parameter λ_{AS} perform slightly better (in terms of the MSE value) than the model which uses the prior knowledge about the true number of breaks, and thus, the regularization parameter $\lambda_{(2)}$. The best mean consistency is observed for the standard LASSO model, however, the price being paid for this is the selection inconsistency – the model indeed selects more nonzero parameters than actually needed. On the other hand, the adaptive LASSO seems to correct for this inconsistency and the number of the nonzero parameters being selected in the final model seems to correspond with the reality. The estimated changepoint locations seem to be consistent as well for the sample size increasing. For a visualization of the behavior of these three models we also refer to Figure 2.

5 Conclusion

In this paper we proposed a new approach to fit linear trend models. The idea is based on the sparse fitting modeling approach where we adopted the adaptive LASSO approach in order to achieve the model selection consistency in terms of the true number of changepoints being estimated in the final model. As a simple extension of the proposed model we can also incorporate some qualitative restrictions like monotonicity or isotonic properties. This can be convenient especially in finance and econometric modeling where one expects the final model to have some specific monotonic/isotonic properties. Unlike the classical LASSO estimation the adaptive LASSO yields a consistent selection and the constructed estimates are known to have the oracle properties. Therefore, the proposed methodology is especially suitable in situations where no prior knowledge on the true number of changepoints in the model is given in advance.

Acknowledgments.
This work was partially supported by the grant of the Ministry of Education, Youth, and Sports in the Czech Republic (Mobility grant, No. 7AMB17FR030) and the Grant P402/12/G097.

References

1. Bosetti, C., Bertuccio, P., Levi, F., Lucchini, F., Negri, E. and La Vecchia, C. (2008). "Cancer Mortality in the European Union, 1970 - 2003, with a Joinpoint Analysis." *Annals of Oncology, 16*, 631–640.
2. Carlin, B.P., Gelfand, A.E. and Smith, A.F.M. (1992). "Hierarchical Bayesian Analysis of Changepoint Problems." *Applied Statistics 41*, 389–405.
3. Chen, S.S., Donoho, D.L., and Saunders, M..A. (2001). "Atomic decomposition by basis pursuit." *SIAM Reviews 43*, No.1, 129–159.
4. Efron, B., Hastie, T. and Tibshirani, R. (2004), "Least Angle Regression." *The Annals of Statistics, 32*, 407–499.
5. Feder, P. (1975). "The Log Likelihood Ratio in Segmented Regression." *The Annals of Statistics, 3*, 84–97.

6. Hinkley, D.V. (1971). "Inference in Two-Phase Regression." *Journal of American Statistical Association, 66*, No.336, 736–743.
7. Kim, H.J., Yu, B. and Feuer, E.J. (2009). "Selecting the Number of Change-Points in Segmented Line Regression." *Statistica Sinica, 19*, 597–609.
8. Kim, H.J., Fay,, M.P., and Yu, B. (2004). "Comparability of Segmented Line Regression Models." *Biometrics, 60*, No.4, 1005–1014.
9. Kim, H.J., Fay, M.P., Feuer, E.J. and Midthune, D.N. (2000). "Permutation Tests for Joinpoint Regression with Application to Cancer Rates." *Stat. Med., 19*, 335–351.
10. Kim, S.J., Koh, K., Boyd, S., and Gorinevsky, D. (2009). "l_1 Trend Filtering." *SIAM Rev.*, 51, 339–360.
11. Koenker, R., Ng, P. and Portnoy, S. (1994), "Quantile Smoothing Splines." *Biometrika, 81*, 673–680.
12. Koenker, R. and Mizera, I. (2004), "Penalized Triograms: Total Variation Regularization for Bivariate Smoothing" *Journal of the Royal Statistical Society, Series B, 66*, 1681–1736.
13. Lockhart, R., Taylor, J., Tibshirani, R.J., Tibshirani, R. (2014). "A Significance Test for LASSO." *Annals of statistics, 42*, No.(2), 413–468.
14. Maciak, M. and Mizera, I. (2016). "Regularization Techniques in Joinpoint Regression." *Statistical Papers, 57*, No.4, 939–955.
15. Maciak, M. (2016). "Testing Shape Constrains in Lasso Regularized Joinpoint Regression." *In Antoch, J., Jurečková, J., Maciak, M., Pešta, M., editors, Analytical Methods in Statistics, AMISTAT*, Prague, November 2015, 105–122.
16. Mammen, E. and Van De Geer, S. (1997). "Locally Adaptive Regression Splines." *Annals of Statistics, 25(1)*, 387–413.
17. Martinez-Beneito, M., García-Donato, G. and Salmerón, D. (2011), "A Bayesian Joinpoint Regression Model with an Unknown Number of Break-Points." *The Annals of Applied Statistics, 5*, No.3, 2150–2168.
18. Meinshausen, N., and Bhlmann, P. (2004), "Variable Selection and High- Dimensional Graphs With the Lasso." *Technical report*, ETH Zrich.
19. Meinshausen, N., and Yu, B. (2009), "Lasso-type Recovery of Sparse Representations for High-dimensional Data." *Annals of Statistics, 37*, No.1, 246–270.
20. Qui, D., Katanoda, K., Tomomi, M. and Tomotaka, S. (2009). "A Joinpoint Regression Analysis of Long-term Trends in Cancer Mortality in Japan (1958 - 2004)." *International Journal of Cancer, 24*, 443–448.
21. Rudin, L.I., Osher, S., and Faterni, E. (1992). "Nonlinear Total Variation Based Noise Removal Algorithm" *Physics D: Applied Physics, 60*, 259–268.
22. Tibshirani, R.(1996). "Regression Shrinkage and Selection via the LASSO" *Journal of the Royal Statistical Society, Series B 58(1)*, 267–288.
23. Shen, J., Gallagher, C.M., amd Lu, Q. (2014). "Detection of Multiple Undocumented Change-points Using Adaptive Lasso", *Journal of Applied Statistics, 46*, No.6, 1161–1173.
24. Tibshirani, R.J. (2014). "Adaptive Piecewise Polynomial Estimation via Trend Filtering" *Annals of Statistics, 42*, No.1, 285–323.
25. Tibshirani, R., Taylor, J., Lockhart, R., and Tibshirani. R. (2016). "Exact Post-selection Inference for Sequential Regression Procedures." *Journal of the American Statistical Association, 111*, No. 514, 600–620.
26. Zou, H. (2006). "The Adaptive Lasso and Its Oracle Properties." *Journal of the American Statistical Association, 101*, No. 476, 1418–1429.
27. Zou, H. and Hastie, T. (2005) "Regularization and Variable Selection via the Elastic Net." *Journal of the Royal Statistical Society B, 67*, No.2, 301–320.

A novel genetic algorithm based similarity measure for time series classification

Basabi Chakraborty and Sho Yoshida

Faculty of Software and Information Science
Iwate Prefectural University
152-52 Sugo, Takizawa, Japan 020-0693

Abstract. Practical pattern recognition or data mining problems often encounter time series data. Choice of a proper representation method and a similarity measure is essential for classification or clustering of time series data. Though there are various representation methods and similarity measures proposed so far, dynamic time warping (DTW) seems to be the most popular measure for comparison of two time series. Though classification accuracy with DTW measure is quite high, it imposes a heavy computational cost. In this work a novel algorithm DTW-GA, a combination of DTW and Genetic Algorithm (GA), is proposed in which an evolutionary approach using genetic algorithm is used to identify the most important portion of the time series by masking the time series with the optimum gene code which reduces the time of similarity computation by DTW. The simulation experiments with 43 publicly available bench mark data sets from different areas show that an increased computational speed by 7 times on average over normal DTW can be achieved without considerable degradation in recognition accuracy for time series classification problems. The proposed measure is particularly effective for longer time series.

Keywords: Similarity measure, time series classification, dynamic time warping, genetic algorithm

1 Introduction

Now-a-days time series data is abundant in nature and real life. Thus the need for analysis of time series data has becoming more and more important [1]. Time series data is defined as the data which varies with time and the observed value over a period of time is collected for its acquisition. Some examples are human gait data, online signature data in biometric authentication, EEG, ECG like biosignals in medical field or stock price, exchange rate in financial analysis. For pattern classification or data mining problems with time series data, similarity computation between two time series is essential. Unlike static data where the dissimilarity measure is straightforward with euclidean distance, distance metric between time series need to be carefully defined to capture dissimilarity between them. Another main challange for time series analysis is the use of proper

representation method. Raw time series has large number of points leading to expensive processing and storage.

The most popular method to compare two time series is warping the time axis in order to achieve an alignment between the data points of the series.The Dynamic Time Warping (DTW) algorithm, first being used in speech recognition [2], has been shown to be an effective solution for measuring the distance between time series [3]. Unlike euclidean distance which is easier to compute, DTW allows a time series to be stretched or compressed to provide a better match with another time series and can handle time series with local time shifting and different lengths. Despite the effectiveness of DTW algorithm, it has a computational cost of $O(N^2)$ which makes it computationally difficult to use for longer time series. Several measures have been introduced to speed up DTW computations as well as to better control the possible routes of the warping path [4], [5], [6].

In this work, a new similarity measure based on dynamic time warping (DTW) and genetic algorithm has been proposed in which the computational cost of DTW is reduced by using a mask over time series which facilitates the comparison of the most important points of the timeseries, skipping irrelevat points. The optimum mask is determined by an evolutionary approach using genetic algorithm. Genetic algorithm (GA) [7], a randomized heuristic and adaptive search technique based on the principal of natural selection and the most popular evolutionary approach, is a good candidate for solving optimization problems where the search space is large [8].In genetic algorithm, a population of possible solutions, encoded as a binary string of n bits, are maintained through several generations. In each generation, genetic operators such as crossover and mutation are used to generate new population from the most elite pairs of the current generation and the good ones are retained after evaluation by a fitness function. Through the generations, the population is led to the better solution space and finally produces the near optimal solution in the final generation. GA requires no domain knowledge and quite robust than other random or local search methods.

Simulation experiments are done with 43 publicly available bench markdata sets from UCR repository [9] for time series classification problems using proposed similarity measure DTW-GA as well as other wellknown similarity measures including original DTW. The next section represents approaches for time series classification and other popular similarity measures. Section 3 presents our proposed similarity measure followed by simulation experiments and results in the next section. The last section contains the summarization and conclusion.

2 Time Series Classification

Time series classification is an important task in real world applications and lots of work have been done on recent times. In this section, approaches for time series classification and some popular similarity measures are discussed. Current approaches for time series classification techniques can be broadly classified into three categories [10].

2.1 Feature based classification

In this approach a multidimensional time series is transformed into a feature vector and then classified by traditional classification algorithms.The choice of appropriate features plays an important role in this approach. A number of techniques has been proposed for compact representation of high dimensional time series into one row to facilitate application of traditional feature selection algorithms like recursive feature elimination (RFE), zero norm optimization etc. [11] [12]. Time series shapelets, characteristic subsequences of the original series, are recently proposed as the features for time series classification [13]. Lesh et al. [14] proposed a pattern based feature selection method in which short segments of time series are considered to be features when they appear frequently in a class. Ji et.al [15] introduced a pattern-extraction algorithm called Minimal Distinguishing Subsequence, more appropriate for classifying biological sequences.

Another group of techniques extract features from the original time series by using various transformation techniques like Fourier, Wavelet etc. In [16], a family of techniques have been introduced to perform unsupervised feature selection on multidimensional time series data based on common principal component analysis (CPCA), a generalization of PCA for multivariate data items where all the data items have the same number of dimensions. Any distance metric is used for classification of the feature based representation of the time series data.

2.2 Model based classification

In model based classification approaches, a model is constructed from the data and the new data is classified according to the model that best fits it. Models used in time series classification are mainly statistical, such as Gaussian, Poisson, Markov and Hidden Markov Model (HMM) or based on neural networks. Naive Bayes is the simplest model and is used in text classification [17]. Hidden Markov models (HMM) are successfully used for biological sequence classifications. Some neural network models such as recurrent neural network (RNN) are suitable for temporal data classification. Probabilistic distance measures are generally suitable for model based classification of time series.

2.3 Distance based classification

In this approach, a distance function which measures the similarity between two time series is used for classification. Similarity or dissimilarity measures are the most important component of this approach. Euclidean distance is the most widely used measure with 1NN classifier for time series classification. Though computationally simple, it requires two series to be of equal length and is sensitive to time distortion. Elastic similarity measures such as Dynamic Time Warping (DTW) [18] and its variants overcome the above problems and seem to be the most successful similarity measure for time series classification in spite of

high computational cost. The present work is related to the proposal of a new similarity measure to be used with distance based classification techniques for time series. In the next subsection some of the popular similarity measures are presented in brief.

2.4 Similarity measures

The list of time series similarity measures proposed so far is quite long and none of them proved to be the best one in all time series classification tasks. Here we present several representative examples which we use in our work for comparison with the proposed new measure. Similarity measures popularly used for multivariate time series analysis from different categories listed below are Euclidean distance (lock step measure), Fourier coefficient (feature based measure), DTW (elastic measure) and autoregressive AR as model based measure.

Euclidean distance Euclidean measure is the simplest and the most popular dissimilarity measure.

The dissimilarity $D(x, y)$ between two time series x and y using any L_n norm is defined as

$$D_{ec}(x, y) = \left(\Sigma_{i=1}^{M}(x_i - y_i)^n\right)^{\frac{1}{n}} \tag{1}$$

where n is a positive integer, M is the length of the time series, x_i and y_i are the i th elements of x and y time series respectively. For $n = 2$, we obtain Euclidean distance. This measure is difficult to use for time series of different lengths and having a time lag.

Fourier Coefficient measure Instead of comparing the raw time series, comparison can be done between the ith Fourier coefficients of the time series pair after the Discrete Fourier Transform. This measure falls under the category of feature based classification. The equation is given as:

$$D_{fc}(x, y) = \left(\Sigma_{i=1}^{\theta}(\hat{x}_i - \hat{y}_i)^2\right)^{\frac{1}{2}} \tag{2}$$

where $\hat{x}_i$ and $\hat{y}_i$ represent ith Fourier coefficients of x and y time series and $\theta = \frac{M}{2}$,M is the length of the time series.

Auto Regression coefficient measure This distance measure falls under the category of model based classification and uses the model parameters for calculating similarity values. Auto regression coefficients of two time series are calculated beforehand from AR(Auto Regressive) models and the distance between corresponding coefficients is taken as the dissimilarity measure. The number of AR coefficients is controlled by a parameter in this model and directly affects the speed of the similarity calculation.

Dynamic Time Warping (DTW) distance measure Dynamic Time Warping (DTW) is a classic approach for computing dissimilarity between two time series. DTW belongs to the group of elastic measures and works by optimally aligning the time series in temporal domain so that the accumulated cost of the alignment is minimal.The accumulated cost can be calculated by dynamic programming, recursively applying

$$D_{i,j} = f(x_i, y_j) + \min\left(D_{i,j-1}, D_{i-1,j}, D_{i-1,j-1}\right) \tag{3}$$

for $i = 1 \ldots M$ and $j = 1 \ldots N$ where M and N are the length of the time series x and y respectively and $f(x_i, y_j) = \sqrt{(x_i - y_j)^2}$.

Currently DTW is the main benchmark against any promising new similarity measure, though its computational cost is quite high.

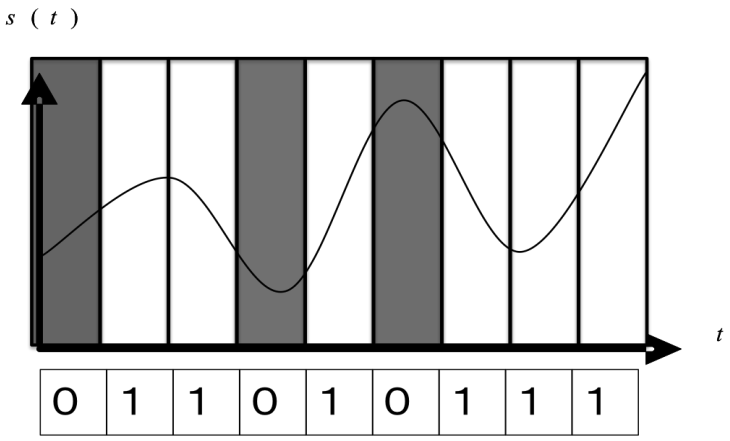

Fig. 1. Representation using gene masking.

3 Proposed New Similarity Measure DTW-GA

The new similarity measure DTW-GA proposed here is a combination of dynamic time warping (DTW) with genetic algorithm (GA). DTW-GA use masking of time series with the optimum gene of GA as the representation method of time series and DTW as the comparison method of two time series. The main concept behind this new measure is that GA searches the best(optimum) gene for masking so that the most important points of the time series is used for comparison instead of the whole series to reduce the computational cost. The whole procedure is explained below.

3.1 Time series representation using masking with gene

Figure 1 shows the idea of time series representation by masking with gene. The length of the gene/ chromosome is set beforehand. The time series is sliced into portions by the length of the optimum gene as the slicing window. In this figure, the bit string shows the optimum gene code generated by genetic algorithm. The time series points corresponding to 1 is used for comparison while the points corresponding to zero are discarded. The distance between two time series are computed as shown in Figure 2 and average is taken as the distance between two time series.

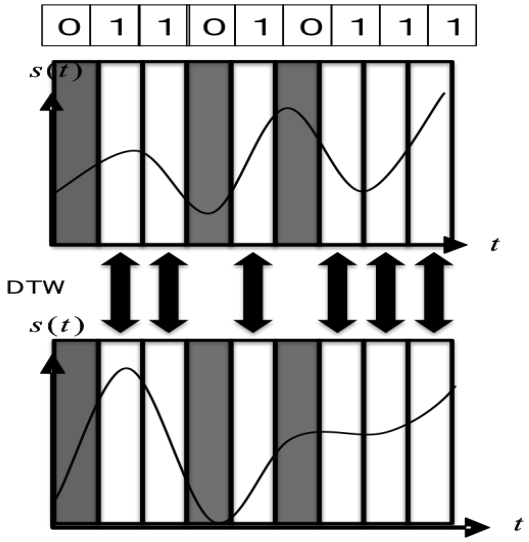

Fig. 2. Distance computation by DTW-GA

3.2 Proposed algorithm of DTW-GA for time series classification

As the most important points of the time series (which can be called feature pattern of the time series) is different for different classes, the optimum gene code is different for different classes. So at the first step GA is used to find out the optimum gene code of each class from the training samples of the class. Minimum intra class distance is used as the fitness function of the genetic algorithm. So the gene code is considered optimum for the specific class for which the average of the pairwise distance of the training samples is minimum. In the second step 1NN classifier is used to find out the class of the unknown test time series using class specific gene codes of each class for comparison of the unknown time series and training time series of the class.

The details of the genetic algorithm process is as follows:

1. Generation of initial solution group (shown in Figure 3)
   - Generate N searching genes having cells stored 0 or 1 randomly
   - Generate C comparison genes stored 0 where C is number of class
   - Initialize evaluation value of comparison genes to infinity
2. Fitness evaluation (shown in Figure 4)

```
for each Searching genes n
   for each Comparison genes c
     for M (parameter for stabilization)
 get two c class time series from
   training data randomly
  compare two time series using
      gene n
   if distance is less than d_c, store
        distance in d_c
 if d_c is lower than evaluation value of
  class c,comparison gene and evaluation
   value of class c are overwritten by gene
     n and d_c
store minimum value d_1 to d_ c in
  evaluation value of gene n
```

3. Genetic operation (selection, crossover and mutation as in ordinary GA)
4. Repeat step 2 and 3 until stopping criterion is fulfilled

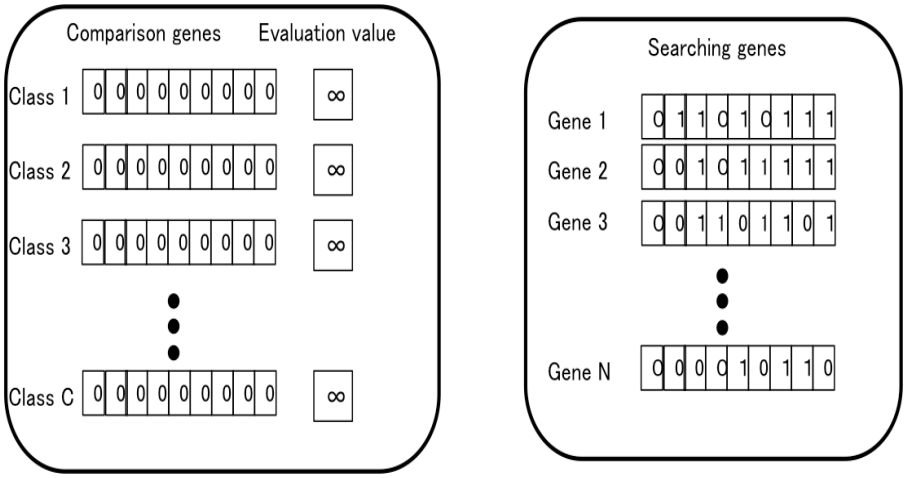

Fig. 3. Generating intitial solution group

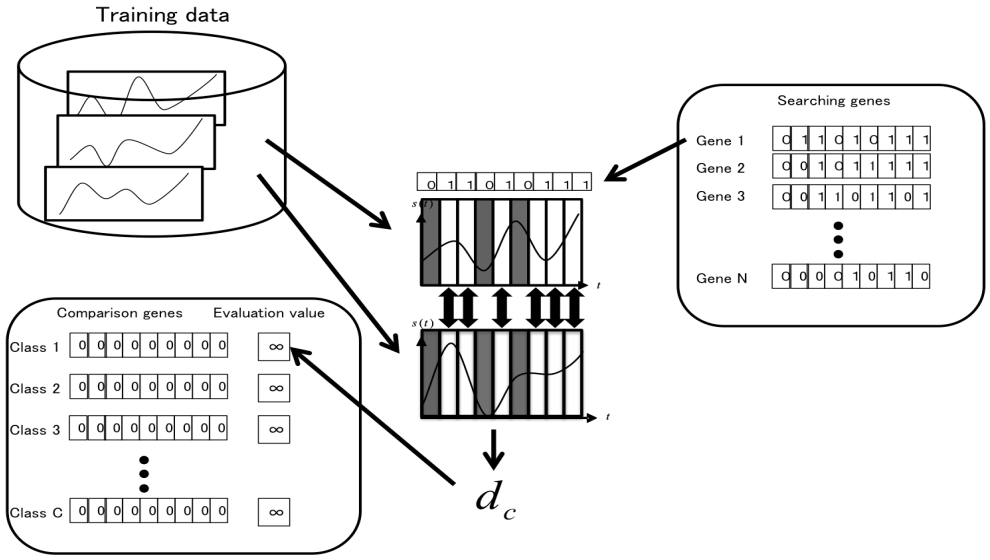

Fig. 4. The evaluation process in GA

The classification process is shown in Figure 5. 1NN classifier is used for classification, The optimum gene code for the specific class is used with the training sample of the same class and the test sample for similarity checking with DTW.

4 Simulation Experiment and Results

The efficiency of the proposed similarity measure DTW-GA is evaluated by comparing it with original DTW and other similarity measures using the computational cost and classification accuracy of 1NN classifier. Nearest neighbour classifier is supposed to achieve the best classification accuracy for time series classification suggested by many researchers [19].

4.1 Data set

The benchmark data sets consisting of 43 different time series data from University of California, Riverside (UCR) time series repository [9] are used for the simulation experiments. The training data is used as labeled data for classifier and classification accuracy is calculated on the test set. The average classification accuracy for twenty trials on different partitions of training and test data are noted for all the data sets.

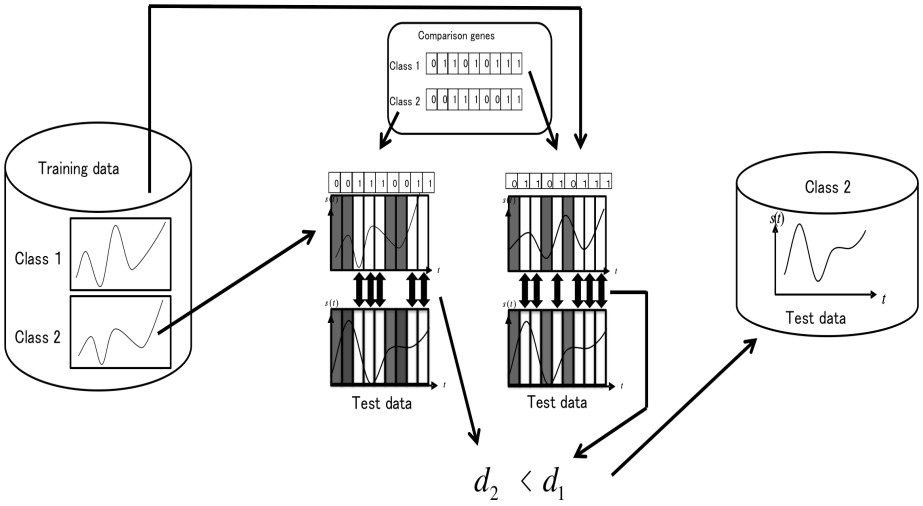

Fig. 5. The process of time series classification

4.2 Parameter setting of GA

Parameter setting of GA is as follows:

- Iteration: 50
- Population size: 32
- Elite population: 2
- Superior population: 6
- Gene length: 5 to 30 at intervals of 5
- Crossover method: Two points crossover
- Mutation rate: 0.02
- Selection method: Rank selection

Experiments are also done to find out proper gene length by changing from 5 to 30 at intervals of 5.

4.3 Evaluation results of DTW-GA

Table 1 shows classification accuracy of all the benchmark data sets with each similarity measure. This result of DTW-GA is calculated using suitable parameter for each dataset. In the average accuracy, DTW-GA is better than general similarity measure Euclidean distance. However DTW-GA is lower than DTW. In the statistical test, DTW-GA is not inferior to DTW because Wilcoxon signed-rank test showed that there is no significant difference between DTW-GA and DTW in the 95 % confidence intervals. From the view point of computational cost, DTW-GA is better than DTW as it is found that the average computational time for DTW and DTW -GA is 1.15 ms and 0.14 ms respectively (average

Table 1. Classification accuracy for different measures

Data Set Name	No. of class	Classification accuracy with				
		Euclidean	Fourier	AR	DTW	DTW-GA
50Words	50	0.668	0.626	0.213	**0.709**	0.681
Adiac	37	0.598	**0.652**	0.286	0.586	0.547
Beef	5	0.500	0.600	0.533	0.500	**0.633**
CBF	3	0.888	0.752	0.537	**0.997**	0.959
ChlorineConc.	3	0.627	0.663	**0.683**	0.626	0.670
Cinc_ECG_torso	4	0.944	0.880	0.535	0.689	**0.920**
Coffee	2	0.750	**0.928**	0.857	0.821	0.785
CricketX	12	0.592	0.510	0.302	**0.777**	0.636
CricketY	12	0.674	0.492	0.220	**0.764**	0.744
CricketZ	12	0.641	0.530	0.279	**0.779**	0.685
DiatomSR	4	0.928	0.934	0.771	**0.960**	0.948
ECG200	2	0.890	**0.9**	0.79	0.79	0.87
ECG5days	2	0.785	0.741	0.736	0.786	**0.872**
FaceAll	14	0.721	**0.796**	0.359	0.772	0.722
Face4	4	0.840	0.727	0.420	0.841	**0.909**
FacesUCR	14	0.801	0.717	0.341	**0.938**	0.813
Fish	7	0.794	0.788	0.354	**0.857**	0.783
GunPt	2	0.953	0.920	0.787	0.880	**0.913**
Haptics	5	0.361	0.377	0.302	0.360	**0.399**
InlineSkate	7	0.352	0.307	0.352	**0.369**	0.365
ItalyPD	2	0.962	0.959	0.610	0.947	**0.967**
Lighting2	2	**0.819**	0.655	0.672	0.803	0.787
Lighting7	7	0.712	0.534	0.369	**0.767**	0.671
MALLAT	8	**0.924**	0.909	0.487	0.915	0.908
MedImage	10	0.706	0.689	0.500	**0.764**	0.697
MoteStrain	2	0.865	0.860	0.568	**0.891**	0.866
Oliveoil	4	0.833	0.833	0.500	**0.867**	0.833
OSULeaf	6	0.549	0.523	0.446	**0.636**	0.549
SonyAiboRS	2	0.687	0.698	**0.930**	0.730	0.688
SonyAiboRS2	2	**0.867**	0.839	0.861	0.844	0.796
StarLightC	3	0.852	0.822	0.829	0.886	**0.914**
SwedishLeaf	15	0.788	0.752	0.600	0.797	**0.816**
Symbols	6	0.903	0.873	0.738	**0.951**	0.927
Syncontl	6	0.880	0.793	0.513	**0.986**	0.870
Trace	4	0.760	0.800	0.840	**0.990**	0.870
TwoPattern	4	0.961	0.778	0.277	**1.00**	0.933
TwoLeadECG	2	0.734	0.777	0.672	**0.946**	0.754
uWGLX	8	0.741	0.731	0.265	0.731	**0.747**
uWGLY	8	0.667	0.635	0.294	0.645	**0.690**
uWGLZ	8	0.650	0.640	0.271	**0.660**	0.639
Wafer	2	**0.995**	**0.995**	0.990	0.983	**0.995**
WordsSyn	25	0.635	0.594	0.215	**0.674**	0.630
yoga	2	0.829	0.834	0.608	0.839	**0.847**
Average		0.759	0.730	0.528	0.792	0.773

over all the benchmark data sets). It is found that in the shortest dataset ItalyPowerDemand, there is less difference between DTW-GA and DTW. However computational speed of DTW-GA is 9 times as of DTW in the longest dataset CinC_ECG_torso. On average, computational speed of DTW-GA is about 7 times as DTW. DTW-GA can decrease computational cost significantly for the longer time series.

5 Conclusion

Classification of time series data is very important for practical data processing and has growing applications in various areas. As time series data is generated in huge quantity, its analysis and processing needs faster algorithms. Traditional machine learning algorithms for static data become unsuitable for large temporal data. For classification or clustering of time series data, similarity measure is the most important component. Though there are many similarity measures already developed, none of them are the best match for all possible time series classification problems. Euclid distance is the simplest one, but it cannot be used for camparing two time series of unequal length. DTW and its variants are the most popularly used measure but their computational cost is high.

In this work, to reduce the computational cost of DTW, without considerably sacrificing the classification accuracy, a new similarity measure DTW-GA has been proposed. The core idea of DTW-GA is to select the most informative class specific pattern from the raw training time series by using genetic algorithm and then to use the selected part of the time series for similarity computation with DTW. The simulation results indicate that the computational time is reduced compared to original DTW and the classification accuracy has not degraded much according to the results of statistical significance tests. The most prominent effect is noticed for the data sets having longer time series. Though for DTW-GA, GA takes some time for initial selection of the optimum gene for a particular class before actual classification, the total computation time is lesser than original DTW. On the average over 43 data sets, computational speed of DTW-GA is 7 times higher than original DTW. Further experiments reveal that there is a suitable gene length to be set for each data set. The experiments on the percentage of reduction of time series data points has also been done, though the detail results are not presented here. It has been found that minimum 60% retention of time series data is enough to produce maximum possible classification accuracy for most of the data sets.

Acknowledgment

The authors would like to thank all the donors as well as the maintainer of the benchmark data sets for providing us the access for downloading the data from The UCR Time Series Classification/Clustering Homepage:

www.cs.ucr.edu/~eamonn/time_series_data/

References

1. H. Kantz, T. Schreiber, *Nonlinear Time Series Analysis*, Cambridge University Press, Cambridge, UK, 2004.
2. L. Rabiner and B.H. Juang, *Fundamentals of Speech Recognition*, Englewoods Cliffs, N. J.,1993.
3. D. J. Berndt and J. Clifford, "Using dynamic time warping to find patterns in time series",*Proc. AAAI Workshop on Knowledge Discovery in Databases*, pp. 359–370, 1994.
4. S. Chu, E. Keogh, D. Hart and M. Pazzani, "Iterative deepening dynamic time warping for Time series", *Proc. 2nd SIAM International Conference on Data Mining*, 2002
5. S. Salvador and P. Chan, "Toward accurate dynamic time warping in linear time and space", *Intelligent Data Analysis.*, Vol.11, No.5, pp. 561–580, 2007.
6. E. Keogh and M. Pazzani, "Derivative dynamic time warping", *Proc. SIAM International Conference on Data Mining*, 2001.
7. D. E. Goldberg, *Genetic Algorithms in Search, Optimization and Machine Learning*, Addison-Wesley, 1989.
8. B. Chakraborty, " Genetic Algorithm with Fuzzy Operators for Feature Subset Selection", *IEICE Trans. on Fundamentals of Electronics , Communications and Computer Sciences*, E85-A, No.9, 2089–2092, 2002.
9. Keogh, E., Zhu, Q., Hu, B., Hao. Y., Xi, X., Wei, L. & Ratanamahatana, C. A. (2011). The UCR Time Series Classification/Clustering Homepage: www.cs.ucr.edu/ eamonn/time_series_data/
10. Xing, Z., Pei, J., Keogh, E.: A brief survey on sequence classification. *ACM SIGKDD Explorations Newsletter*. 12. No.1, 40–48 (2010)
11. T. N. Lal et al., "Support Vector Channel Selection in BCI".,*IEEE Trans. on Biomedical Engineering,*. Vol. 51, No.6, pp. 1003–1010 ,2004.
12. B. Chakraborty, ." Feature selection and classification techniques for multivariate time series", *Proc. of ICICIC 2007*, September, 2007.
13. L. Ye., E. Keogh, "Time series shapelets: A new primitive for data mining", *Proc.ACM SIGKDD International Conference of Knowledge Discovery and Data Mining* ,2009.
14. N. Lesh., M. J. Zaki, and M. Ogihara, "Mining Features for Sequence Classification", *Proc. of 5th ACM SIGKDD International Conference on Knowledge Discovery and Data Mining*. pp. 342–346, 1999.
15. X. Ji, J. Baily, and G. Dong," Mining minimal distinguishing subsequence patterns with gap constraints" *Knowledge and Information Systems*, Vol. 11, No. 3, pp. 259–286, 2007.
16. H. Yoon., K. Yang., C. Sahabi, " Feature subset selection and feature ranking for multivariate time series"¡ *IEEE Trans. on Knowledge and Data engneering,*, Vol. 17. No 9, pp. 1186–1198, 2005.
17. S. B. Kim, K. S.. Han, et.al.,. "Some effective techniques for naive bayes text classification", *IEEE Trans. on Knowledge and Data Engineering*, Vol.18, No.11, pp. 1457–1466, 2006.
18. X. Wang, A. Mueen, H. Ding, G. Trajcevski, P. Scheuermann, E. Keogh, "Experimental comparison of representation methods and distance measures for time series data", *Data Mining and Knowledge Discovery*, Vol. 26, pp. 275–309 ,2013.
19. J. Serra., J. Arcios, "An empirical evaluation of similarity measures for time series classification"¡ *Knowledge based systems*, Vol. 67, pp. 305–314, 2014.

A time series clustering technique to analyze the stock market movement after the budget announcement

Abstract. Analyzing stock price movement has been of great interest to diverse communities. These movements are quite sensitive to different events like budget announcement, monetary policy change, poll results or any other macroeconomic event. Not every stock reacts similarly and sometime even if they are from the same sector, their price movements are quite different. A tool, which can analyze the time series and then partition them into different clusters, can really be beneficial to summarize and understand the broad nature of these movements. In this paper, a simple correlation based clustering technique for stocks (TSCCS) has been proposed to group stocks based on their time series. The period considered is 1 month from the day of the announcement of union budget in 2017. Stocks included in the Nifty-50, has been considered in the scope of the study. The clustering technique (TSCCS), produces results which can give practitioners significant insight to the movement of the market. After clustering of the stocks, an industry specific volatility analysis followed by outlier detection are performed to generate additional insights.

Keywords: Time Series, Clustering, Stock Market, Correlation

1 Introduction:

Often, the quantities or the characteristics we are interested at are measured over a period of time. Collection of such observations over a time period gives rise to a time series data. Time series are prevalent across various domains. Some of the examples where time series plays an important role are the rainfall data for weather forecasting [1], the EEG data for medical domain [2] or the mutual funds returns in banking and financial sector [3]. In, traditional data i.e. non time series data, each observation is represented as an entity and is treated as a vector. On the contrary, time series data is represented in a matrix form. Consequently, usual data mining techniques like classification or clustering cannot be applied as is to the time series data.

Banking and financial services is a functional area where time series data is frequently occurring and is of immense interest. Stock market is an important subfield where there is an abundance of time series data. Bombay stock exchange and National Stock exchange are flagship share exchanges of

adfa, p. 1, 2011.

India. With more than 1.5 trillion-dollar market capitalization, they figure among the top 10 share exchanges across the world. Founded in 1875, BSE the oldest stock exchange of Asia has more than 5000 companies listed in it. The prices of each stock is refreshed in every 4 seconds based on current supply and demand. This generates huge amount of time series data. Traditionally, fundamental analysis and technical analysis are used for a suitable investment strategy. Technical analysis deals with the price chart which is nothing but a time series representation of the stock prices. In Technical analysis, numerous aspects of the charts like trend lines, Bollinger bands, and various other patterns (Head and Shoulder, Triangle etc.) are studied along with different indicators (Relative Strength Index, Stochastics etc.). The leading charting software tools like MetaStiock, eSignal reduce the effort of data extraction and storage and prepare the charts with several annotations. However, the study and identification of such patterns are mostly a manual process and is done for individual stocks. These tools lack the capability of discovering unobserved patterns by processing large amount of data available. Also, it lacks capability of exploratory analysis like grouping different stocks, sectors etc. for better summarization and understanding. This motivates the use of data mining / machine learning techniques.

Time series clustering technique is quite important because grouping of similar time series may be important for many domains. Particularly as noted in [10], summarization and visualization of different phenomenon is one of the most important problems to handle in modern finance. The clustering techniques that can be applied, for time series data are varied based on the representation scheme and the similarity measure that are adopted [4]. The raw time series can be used or alternatively various transformations can be applied on the same. This varied options often works as an impediment to the end users.

In this paper, we have proposed a simple time series clustering technique based on correlation for stocks (TSCCS). The said algorithm has been used to cluster 51 stocks included in the Nifty index. The period of study is 1 month after the announcement of the union budget in 2017. The prototype stocks of the clusters have been used to summarize and understand the clusters behavior. An industry specific study has also been presented to relate the movement of the stocks, with that of the index (Nifty). Finally, an analysis

with respect to the k-outlier stocks in each cluster is also performed. The proposed algorithm demonstrates

- How clustering can be used to better investigate stock market movements, especially after an event?
- It visually represents the similarity of stocks with in an industry and with the index, highlighting the variability and degree of such similarity.
- It visually presents the similarity between the movements between different stocks, which can be helpful for portfolio management.
- Finally, an outlier analysis is performed, which can also potentially generate valuable insight for the investors.

Rest of the paper is organized as follows: - Section 2, outlines about related works in this area. Section 3, discusses about the proposed algorithm. Section 4, presents different parameters and configurations used for the experiment. Section 5 has the results with a critical analysis. Section 6, contains the conclusion of the work.

2 Related Works:

As pointed out by Aghabozorgi et. al. [4-5], time series clustering can be classified in broad three categories namely Whole time series clustering, Subsequence time series clustering and Time point clustering. TSCCS can work equally adeptly for whole as well as subsequence time series clustering. We have divided the subsequent discussion in two parts. In the first part, we have given a focused discussion on clustering techniques and correlation analysis on stock market data. In the second part, we have briefly discussed about other important works in stock market modeling.

2.1 Works using clustering or correlation analysis in stock market:

Nanda et. al [6] used clustering for an optimal portfolio selection. They have used percentage return and valuation of the stocks and applied k-means. Finally, internal validity measures have been used to test the quality of the clusters. The period of time considered was 2007 – 2008. The proposed approach produced better return than sensex, however the paper does not deal with explicit time series data. Dorr et. al. [7] used a technique to establish relationship among a sequence and a subsequence. The proposed technique allows

finding similar patterns over unequal length time series. Their techniques were tested over stock market data. Guo et al. [8] in their work has first applied independent component analysis (ICA) and then subsequently has modified k-means algorithm for clustering the time series data. Shapira et. al. [9] studied the effect of index correlation on other stocks and how this acts as an additional factor in time series movement of a stock. This study was conducted on New York Stock Exchange and Istanbul Stock exchange. Liao et. al. has worked on Taiwan stock market [10]. They have applied a two stage approach, in the first step apriori algorithm is used for finding the association rules in the second step k-means have been applied.

2.2 Some other notable works in stock market modeling:

Apart from clustering, the most common use of time series analysis has been in forecasting of prices of the stock. Banerjee et al [11], Mondal et al [12] have used auto regressive integrated moving average (ARIMA) models to predict the stock prices for Indian market. There has been also a trend where multiple models have been combined for better result. Yakup et. al. [13] has combined support vector machine with artificial neural network where as Kazem et. al. [14] has effectively used support vector machine in conjunction with a variant of firefly algorithm. Few research groups have also investigated correlation of sentiment expressed in social media with the stock market movement [15-16].

3 Proposed Method:

The proposed algorithm, compares the closing price of selected stocks for a given time period. Based on their similarity, the stocks are grouped into different clusters. Apart from clustering, an outlier analysis is also performed in this paper. An outlier can be defined as an observation; whose variation is quite significant with respect to the other observations of the population. It is often felt that outliers are generated by a different mechanism [18].

Algorithm: TSCCS (Time Series Clustering using Correlation for Stocks)

Input: A portfolio of stocks closing time series [STK], Indices Values [IND], Number of Clusters (NC), Number of Outliers (k)
Output: $PAM_{results}$, $PAM_{outlier}$

Begin:

Step 1 Smoothing the Time Series

// The closing price/value time series of each stock and indices is replaced by a simple moving average.

// TS_i indicates the i th the time series and SMA returns the simple moving average of a time series for given period p

TS_i = SMA [TS_i, p]

Step 2 Similarity Matrix

// A similarity matrix is constructed using the Pearson's product moment correlation matrix

// Number of Stocks in Portfolio as |STK|

```
For (i in 1 to |STK|)
{
  For (j in 1 to |STK|)
  {
      Sim [i, j] = Correlation (TSi, TSj)
  }
}
```

Step 3 Dissimilarity Matrix

```
For (i in 1 to |STK|)
{
    DSIM [i, j] = 1 -  Sim [i, j]
}
```

Step 4 Create clusters

// Partitioning around Medoid

```
PAM results =    PAM ( DSIM, NC)
```

Step 5 Find correlation with the index

```
For (i in 1 to |STK|)
{
```

```
Simind [i] = Correlation (TS ind, TSi)
}
```

Step 6 Find k outlier points with respect to each cluster

// outlier (Cluster $_1$, k) :- Identifies 'k' outliers furthest from the cluster medoid

$$PAM_{outlier} = outlier(Cluster_1, k) \cup outlier(Cluster_2, k) \ldots \cup outlier(Cluster_{NC}, k)$$

Step 7 Visualization

// sector(STK) gives the sectoral information of the stocks

```
TimeSeriesPlot (TS nc ) for all TS ∈ Mediods (PAM)
// Useful for investing the nature of the cluster
Boxplot (Simind with respect to sector)
Clusterplot (DSIM)
OutlierPlot (PAM outlier)
```

4 Materials and Methods:

In this section, we have provided the details about experimental setting which can be used to reproduce the results.

The stocks included in the stock are from the popular NIFTY50 index, which has 51 shares from 12 industry sectors, namely Cement & Cement Products, Services, Consumer Goods, Construction Pharma, Automobile, Financial Services, Energy, Telecom, Metal, IT, Media & Entertainment. The different stocks which are included industry wise are as follows

- Cement & Cement Products: - ACC Ltd, Ambuja Cements Ltd., UltraTech Cement Ltd.
- Services: - Adani Ports and Special Economic Zone Ltd.
- Consumer Goods: - Asian Paints Ltd., Hindustan Unilever Ltd., I T C Ltd.
- Pharma: - Aurobindo Pharma Ltd., Cipla Ltd., Dr. Reddy's Laboratories Ltd., Lupin Ltd., Sun Pharmaceutical Industries Ltd.,
- Financial Services: - Axis Bank Ltd., Bank of Baroda, HDFC Bank Ltd., Housing Development Finance Corporation Ltd., ICICI Bank Ltd., Indiabulls

Housing Finance Ltd., IndusInd Bank Ltd., Kotak Mahindra Bank Ltd., State Bank of India, Yes Bank Ltd.

- Automobile: - Bajaj Auto Ltd., Bosch Ltd., Eicher Motors Ltd, Hero MotoCorp Ltd., Mahindra & Mahindra Ltd., Maruti Suzuki India Ltd., Tata Motors Ltd DVR, Tata Motors Ltd.
- Energy: - Bharat Petroleum Corporation Ltd., GAIL (India) Ltd., Indian Oil Corporation Ltd., NTPC Ltd., Oil & Natural Gas Corporation Ltd., Power Grid Corporation of India Ltd., Reliance Industries Ltd., Tata Power Co. Ltd.
- Telecom: - Bharti Airtel Ltd., Bharti Infratel Ltd,
- Metals: - Coal India Ltd., Hindalco Industries Ltd., Tata Steel Ltd.,
- IT: - HCL Technologies Ltd., Infosys Ltd., Tata Consultancy Services Ltd., Tech Mahindra Ltd.
- Construction: - Larsen & Toubro Ltd.,
- Media & entertainment: - Zee Entertainment Enterprises Ltd.

The budget was announced on 1st February 2017. The time period considered in the experiment is from 1st of February to 28th February. The daily closing prices have been used to construct the time series. A simple moving average of 3 days has been used to smooth out the daily fluctuations. Partitioning around medoid (PAM) is used as the clustering algorithm in this experiment. The computational environment used is R [17]. Some of the important libraries that have been used are stat, qgraph, zoo, ggplot2 etc. The index that we have compared with is Nifty 50. Number of clusters has been taken as 3 and number of outliers per cluster is 2.

5 Results:

In this section, we have presented and critically discussed about the results obtained from applying time series clustering on Nifty 50 Stocks.

5.1 Analysis of the clusters:

Three has been taken as the cluster count. The description of the clusters and their analysis as per the prototype stock has been presented in Table 1.

Table 1. Analysis of the clusters

Clusters	Cluster Details	Prototype Time Series	Trend
Cluster 1	24 Stocks are in cluster 1. The representative stock of the cluster is State bank of India.	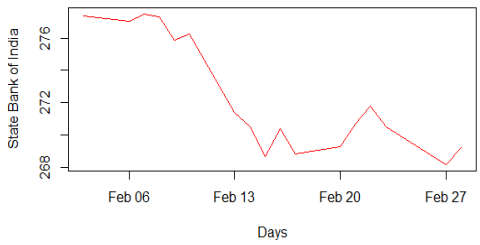	This cluster would mostly consist of stocks going southward.
Cluster 2	10 stocks are in cluster 2. The representative stock is Axis Bank	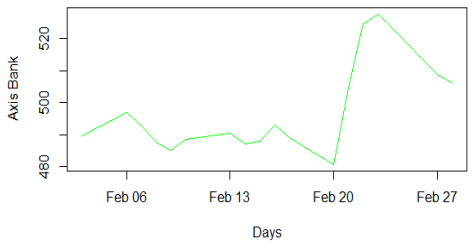	This cluster would mostly consistent of stocks showing moderate upside.

Cluster 3	17 Stocks are present in cluster 3. The representative stock is Infosys.	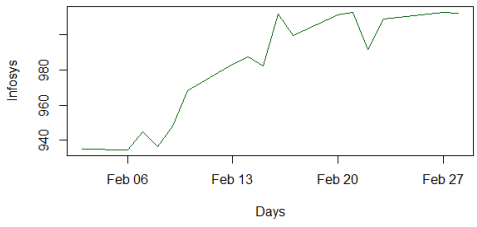	This cluster would mostly consistent of stocks showing strong rally.

The below figure gives a visualization representation of the similarity between the stocks.

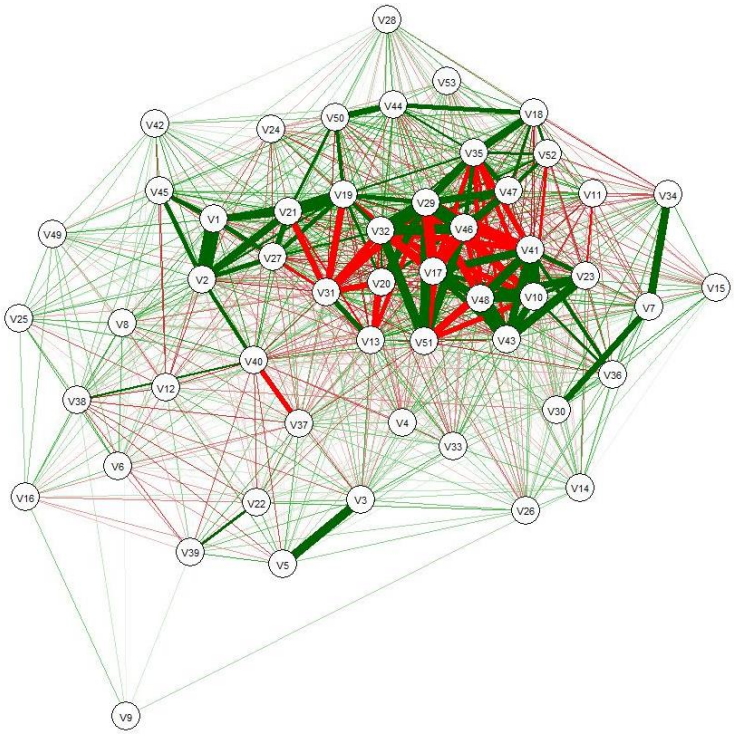

Fig. 1. Similarity graph with Nifty 50 stock

The above figure, attaches a color scheme commensurate with the similarity. The red color represents negative correlation and green color indicates positive correlation.

It can be observed that,

- V17 (Dr. Reddy) and V46 (TCS), has a negative correlation of 0.93 and it has been annotated with dark red color.
- V29 (Infosys) and V41(State bank of India) has similar negative correlation of 0.91.
- Same sector stocks like ACC and Ambuja exhibit high correlation of 0.91 which is expected.
- However, Gail and HDFC back, which are from different sector demonstrate high correlation of 0.94 and Sun pharma and Dr. Reddy, which are from the same sector display a negative correlation of 0.24.

An ideal portfolio should be well diversified. Hence, those stocks which show similar price movement should be avoided. The above similarity graph can be helpful for the same.

5.2 Analysis of the outliers:

In this experiment, 2 most outlying points from each cluster has been found out and investigated for potential insight useful in investment. The similarity graph for those 9 stocks is shown in figure 2. The intensity of the color and thickness of the edges is proportional to the degree of the correlation.

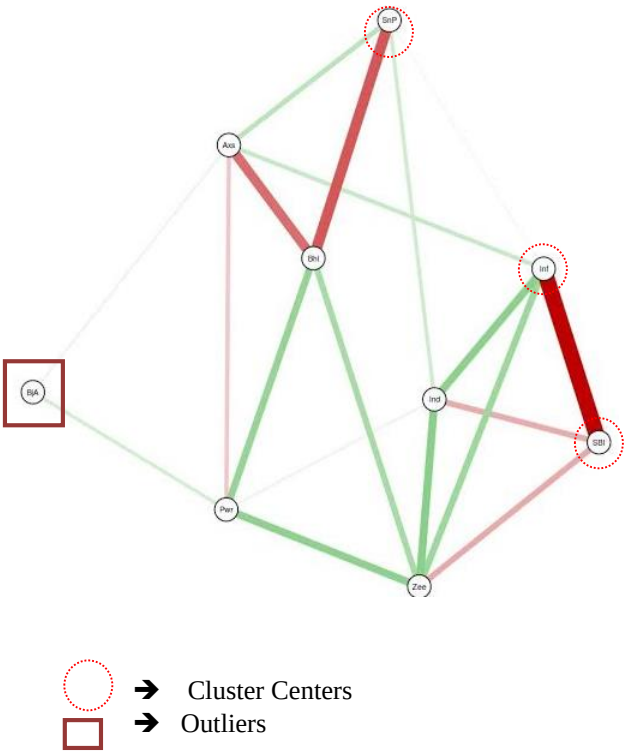

Fig. 2. Cluster center with 2 outlying stocks of each cluster

Upon inspection we have found Bajaj Auto's stock to be the farthest from all the centers. Below, is a snapshot of the time series in Figure 3.

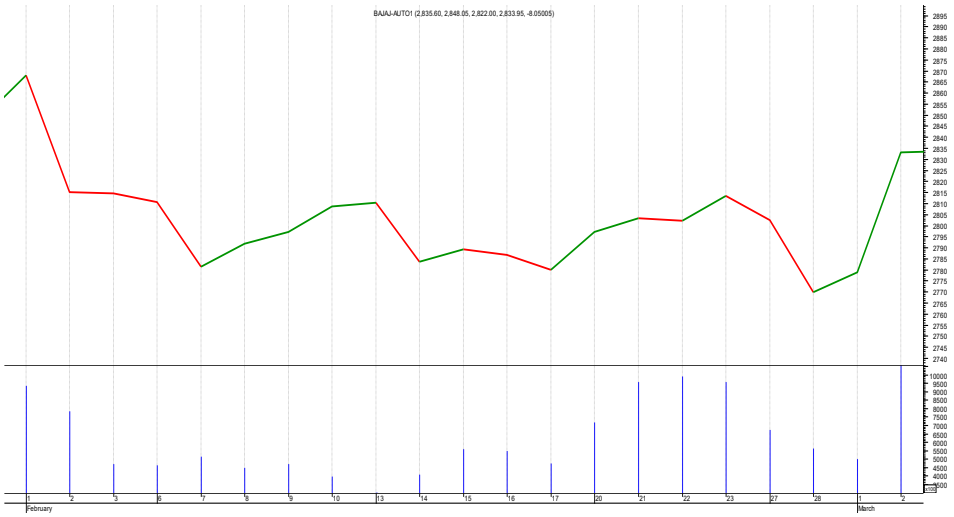

Fig. 3. Bajaj Auto time series during February 1st to February 28th

It can be well observed that Bajaj Auto displayed quite random movement during the said period and hence may be a stock not to be invested in. So the outlier analysis also generates some insight to the investors.

5.3 Comparison with the index

In this section, we have compared the sectoral variations with changes with respect to index. Figure 4, shows the correlation of the individual stock time series with the index time series using a box plot.

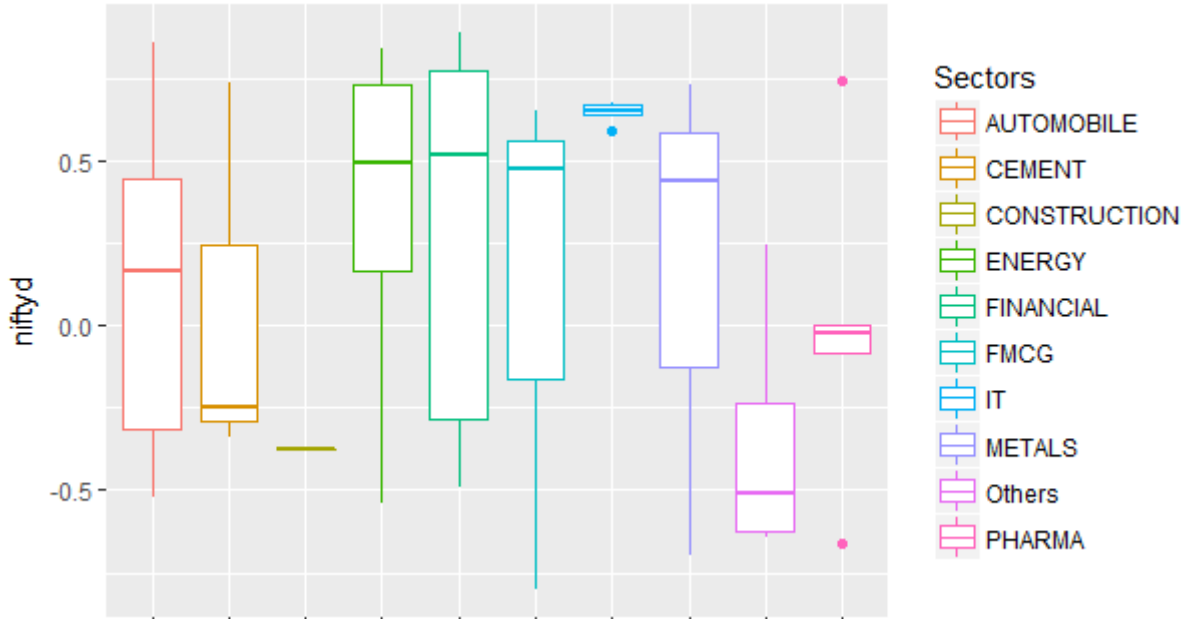

Fig. 4. Boxplot showing correlation of the stocks across sectors.

It can be observed from Figure 4, that

- Most of the sectors especially financial, automobile and metal sectors show a wide range of variation. IT as a sector shows minimal variation
- IT, Energy and Metal stocks have shown positive correlation with NIFTY
- Other sector stocks which include Media, Telecom and Services show a negative correlation with the index

6 Conclusion:

In this paper, we have analyzed stock price movement of 51 stocks included in the Nifty 50 index after announcement of union budget in 2017. For the same, a simple time series clustering has been applied. The three clusters clearly presented downward trend, moderate uptrend and strong uptrend. The visualization of the similarity graph and the subsequent inferences can be useful for an optimal portfolio strategy. An analysis with respect to similarity of the different industries with the index is also performed, which can work as a cue to the investors. Finally, an outlier analysis is applied, which proves to be effec-

tive as far as investment decisions are concerned. The simple clustering technique based on correlation (TSCCS) is found to be quite effective in finding some useful patterns. This can be further extended for a longer term association, a broader range stocks and an inter-event comparison

7 Reference:

1. Di Piazza, A., et al. "Comparative analysis of different techniques for spatial interpolation of rainfall data to create a serially complete monthly time series of precipitation for Sicily, Italy." International Journal of Applied Earth Observation and Geoinformation 13.3 (2011): 396-408.
2. Lehnertz K. Non-linear time series analysis of intracranial EEG recordings in patients with epilepsy—an overview. International Journal of Psychophysiology. 1999 Oct 1;34(1):45-52.
3. Chevalier, Judith, and Glenn Ellison. "Risk taking by mutual funds as a response to incentives." *Journal of Political Economy* 105.6 (1997): 1167-1200.
4. A Review of Subsequence Time Series Clustering, Seyedjamal Zolhavarieh, Saeed Aghabozorgi, and Ying Wah The, Department of Information Systems, Faculty of Computer Science and Information Technology, University of Malaya (UM), 50603 Kuala Lumpur, Malaysia.
5. Time series clustering – A decade review, Saeed Aghabozorgi, Ali Seyed Shirkhorshidi n, TehYingWah, Department of Information System, Faculty of Computer Science and Information Technology, University of Malaya (UM), 50603 Kuala Lumpur, Malaysia.
6. Nanda SR, Mahanty B, Tiwari MK. Clustering Indian stock market data for portfolio management. Expert Systems with Applications. 2010 Dec 31;37(12):8793-8.
7. Dorr DH, Denton AM. Establishing relationships among patterns in stock market data. Data & Knowledge Engineering. 2009 Mar 31;68(3):318-37.
8. Guo C, Jia H, Zhang N. Time series clustering based on ICA for stock data analysis. In Wireless Communications, Networking and Mobile Computing, 2008. WiCOM'08. 4th International Conference on 2008 Oct 12 (pp. 1-4). IEEE.
9. Shapira Y, Kenett DY, Ben-Jacob E. The index cohesive effect on stock market correlations. The European Physical Journal B-Condensed Matter and Complex Systems. 2009 Dec 1;72(4):657-69.
10. Liao SH, Ho HH, Lin HW. Mining stock category association and cluster on Taiwan stock market. Expert Systems with Applications. 2008 Aug 31;35(1):19-29.
11. Banerjee D. Forecasting of Indian stock market using time-series ARIMA model. In Business and Information Management (ICBIM), 2014 2nd International Conference on 2014 Jan 9 (pp. 131-135). IEEE.

12. Mondal P, Shit L, Goswami S. Study of effectiveness of time series modeling (ARIMA) in forecasting stock prices. International Journal of Computer Science, Engineering and Applications. 2014 Apr 1;4(2):13.

13. Kara, Yakup, Melek Acar Boyacioglu, and Ömer Kaan Baykan. "Predicting direction of stock price index movement using artificial neural networks and support vector machines: The sample of the Istanbul Stock Exchange." Expert systems with Applications 38.5 (2011): 5311-5319.

14. Kazem A, Sharifi E, Hussain FK, Saberi M, Hussain OK. Support vector regression with chaos-based firefly algorithm for stock market price forecasting. Applied soft computing. 2013 Feb 28;13(2):947-58.

15. Bollen J, Mao H, Zeng X. Twitter mood predicts the stock market. Journal of computational science. 2011 Mar 31;2(1):1-8.

16. Kumar S, Maskara S, Chandak N, Goswami S. Empirical Study of Relationship between Twitter Mood and Stock Market from an Indian Context. International Journal of Applied Information Systems (IJJAISS). 2015;8:1-5.

17. R Core Team (2016). R: A language and environment for statistical computing. R Foundation for Statistical Computing, Vienna, Austria. URL https://www.R-project.org/.

18. Ghosh S, Goswami S, Chakrabarti A. Outlier detection from ETL Execution trace. InElectronics Computer Technology (ICECT), 2011 3rd International Conference on 2011 Apr 8 (Vol. 6, pp. 343-347). IEEE.

An Efficient Anomaly Detection in Quasi Periodic Time-series Data - A Case Study with ECG

Goutam Chakraborty[1], Takuya Kamiyama[1], Hideyuki Takahashi[2], and Tetsuo Kinoshita[2]

[1]Grad. School of Software & Information Science.
Iwate Prefectural University, Takisawa, Iwate, Japan
goutam@iwate-pu.ac.jp, takuya@gmail.com
[2]Research Institute of Electrical Communication
Tohoku University, Sendai, Miyagi, Japan
hideyuki@riec.tohoku.ac.jp, kino@riec.tohoku.ac.jp

Abstract. Anomaly detection from a time-series is an important problem with applications to find or predict development of a fault in a system. Depending on the source of the data, it could be non-periodic, quasi-periodic and periodic. Modeling an a-periodic data to detect anomaly is difficult. A pure periodic data seldom happens in nature. Finding anomaly in quasi periodic time series signals, for example bio-signals like ECG, heart rate (pulse) data, are important. But, the analysis is computationally complex, because of the need of proper window size selection and comparison of every pair of sub-sequences of windoe-size duration. This makes real-time anomaly detection of bio-signals difficult. In this paper, we proposed an efficient algorithm for anomaly detection of quasi-periodic time-series data. We introduced a new concept *"mother signal"*, which is the average of normal sub-sequences. Creation of the *mother signal* is the first step in the process. Finding deviations of sub-sequences of varied duration (due to quasi-periodicity) from *mother signal*, the second step. When this distance crosses a threshold, it is declared as a discord. The algorithm is light enough to work in real-time on computationally weak platforms like a mobile phone. Experiments were done with ECG signals to evaluate the performance. It is shown to be computationally more efficient compared to existing works, and could identify discords with higher rate.

Keywords: Quasi Periodic Time series, Anomaly detection, Fundamental period, Clustering

1 Introduction

The health of any running system is monitored by a set of sensors, the collected data from which is analyzed to ensure safety and/or predict malfunctioning.

Depending on the system, the data could be aperiodic or periodic. There are studies on anomaly detection, both on periodic and non-periodic signals. Various techniques are used, such as HMM based [2], prediction based [3], similarity based [4], window based [7] and segmentation based [12]. For aperiodic signals, piecewise regression [5] [6] and model-based clustering methods [1] are proposed. These models need a lot of training data to optimize the model parameters. They require long training using computationally hwavy algorithms like expectation maximization.

For many systems, the data collected are quasi-periodic, where the period varies slightly over an average. Important bio-signals to monitor health, like ECG, pulse rate are quasi periodic. Recently, systematic collection, storing and analysis of bio-signals is widely adapted for personalized health-care, medical informatics, drug testing and a plethora of applications. Anomalies in bio-signal can detect/predict heart disease, pulse failure or other kinds of life-threatening situations. Present health-care systems installed on mobile devices collect data continuously, to get analyzed at the end of the day on a different platform. A real-time analysis to create alarms for people vulnerable to heart-related problems, could save lives, avoid driving accidents etc. This is not realized yet.

The main motivation of this work is to detect anomaly in quasi periodic time-series signals in real-time, on computationally weak platforms like smart phones. We did experiment on ECG data, because there are many works done, and labeled data available on the web. The approach is from the signal point of view. No physiological or medical knowledge is used.

1.1 Definition of Time Series Discords

The anomaly subsequences in a quasi periodic signal are called discords. In quasi periodic signals, as the period randomly varies over the average, to find anomaly, one needs to compare every possible pair of subsequences. Usually, from the domain knowledge one fixes the subsequence window length. Time series discords are subsequences, which are maximally different to all the rest of the subsequences of the whole sequence. Discords could be detected by comparing every pair of sub-sequences, and identifying and ordering them, with the largest distance from its nearest (least distant) neighbor heading the list. Usually, we are interested to find the set of discords for which the distance from the normal subsequence is above some predefined threshold. We can find discords using brute force method which is computationally heavy with time complexity of $O(n^2)$, where n is the total number of subsequences possible out of the whole time series.

Let us consider a discrete time series consisting of T time-slots. Let us also consider that the subsequence length is m time-slots, where $m \ll T$. Thus, the original signal consists of $n = (T - m + 1)$ such subsequences. The i^{th} subsequence starts at i^{th} slot, where $0 \leq i \leq (T - m)$. If all possible pairs are to be compared, we need $n^2 \approx T^2$ comparisons, because $m \ll T$ and therefore $n \approx T$. In previous works, the length of the subsequence was user defined [7]. In

our work, the length m is computed from the signal, and is equal the average of the fundamental period of the quasi-periodic time series [13].

1.2 Related Works

As the time-series length gets longer, comparing all pairs to find discords is computationally complex. Related works are proposals of how to find discords efficiently. As ECG data is one of the most popular quasi periodic signal, many of the works are with ECG signals. One of the early work was by Keogh [7]. They discretize the data value into 3 levels, assigning alphabets "A", "B", "C", and proposed a heuristic algorithm to find maximal distance subsequences. In Keogh's work one need to fix parameters, and the result depends on them. Subsequently, parameter free discord search algorithm for quasi periodic signals were reported in [8] and [9]. Recently, anomaly detection in ECG artifacts using Motif was proposed in [10].

Of quasi-periodic signals, ECG is one most investigated and recently finds applications in many mobile devices. It is now common to attach wearable sensors to collect bio-signal and transfer to mobile device by Blue-tooth communication. Simple analysis, like instantaneous pulse rate are available. Real analysis of the recorded data is done off-line after uploading the data on a PC. For example, the device would collect ECG data over a day, and then it is analyzed for detecting discords.

Existing algorithms to find anomaly in quasi-periodic signals like ECG are computationally heavy. Yet, it is important to identify anomaly in bio-signals in real-time, especially for those who have medical history. A real-time identification and warning could avoid fatality. The aim of this work is to propose an algorithm which can run on a weak computational platform, with low memory requirement - for example a smart phone.

Depending on the algorithm used, anomaly location and frequency would vary. The ground truth could be understood and identified only by the domain expert, in case of bio-signals by a health professional. Anomaly detected on the basis of algorithmic analysis may not tell the ground truth. In fact, some signal anomaly could be of no health concern, whereas the algorithm may miss some subtle problems. Yet, a warning is important even when there could be an occasional false-alarm.

The rest of the paper is as follows. In Section 2, the core idea behind the algorithm, creation of *mother signal* is explained. How it is actually done for ECG data is also explained. In section 3, the algorithm to find discords is explained. Experimental data set and their results are elaborated. The paper is concluded in section 4.

2 Proposed Idea - Mother Signal

2.1 What is *Mother Signal*?

We proposed a new concept [11] we named *"mother signal"*. As a first step we set m equal to the fundamental period, average of most frequently occurring pe-

riodic signals. The fundamental assumption here is that normal (not discords) subsequences overwhelmingly outnumber subsequences with discords, which is true for any running system. *Mother signal* is the average of those normal subsequences. Once mother signal is known discords are detected more efficiently. Even if we use exhaustive comparison with mother signal, the complexity is $O(mn)$ much less than $O(n^2)$. In other words, comparisons with mother signal will be much more efficient compared to brute force comparison of every possible pairs. The largest discord is the one whose distance is highest from the mother signal. Multiple discords can be detected as subsequences whose distances with mother signal exceed a pre-defined threshold. Otherwise, we can identify and list the first pre-defined number of discords in order of their distances from the mother signal.

From a given quasi-periodic time series, first its fundamental period is determined. For that the slowly moving baseline is shifted to a constant level of zero, as shown in Fig. 1. Next, the peaks of the signal are identified, to find the span of different subsequences. This procedue is explained in Fig. 2. The time-series signal, shown in Fig. 1 and Fig. 2, is an ECG signal. One peak to the next is one subsequence. The time-duration of these sub-sequences vary over an average, except at places where there is a discord. We took a large number of samples to verify their distribution, and found that to be normal. The average of these periods is set as the value of m, the time duraiton of the so called *mother signal*. For any two normal subsequences, though their durations may differ a little from m, if we normalize the durations to m and shift-and-rotate for maximum match (minimum Euclidean distance), their distance will be small. Only in case of discords the distance from *mother signal* would be large even when all possible shifts and rotations are tried.

2.2 Creation of the *Mother Signal*

In this section, we describe how the mother signal is created. As shown in Fig. 2, local minimum points are marked, and subsequences from one to its next are identified. The basic idea is to cluster those subsequences. The cluster with the maximum cardinality is considered to be consisting of normal subsequences. Their mean will form the *mother signal*.

For clustering, we need to measure distance between any pair of subsequences. As they are of different length in time, ideally the distance measured by dynamic time warping (DTW), should be considered. We too did clustering using distances measured by DTW. But, DTW is computationally heavy. We proposed a faster solution. All subsequences are scaled to the same length, the average length of all subsequences. For length normalization algorithms used for image compression and enlargement, are tried. Euclidean Distance between two subsequences were calculated after scaling them to same time duration by using, (a) Lanczos, (b) Bilinear, (c) Nearest Neighbor, (d) Piecewise Aggregate Approximation, (e) Bicubic algorithms. The total computation time for clustering, using DTW to measure distance and Euclidean distance after scaling using different scaling algorithms, are shown in Fig. 3. Euclidean distance after scaling takes

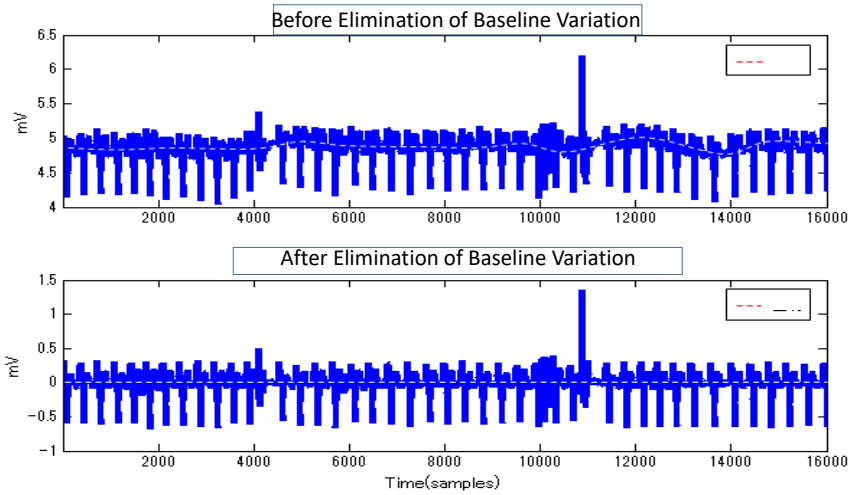

Fig. 1. The slowly moving baseline is shifted to constant zero.

almost the same time, using different scaling algorithms. DTW requires nearly 100 times more computation time.

Clustering of subsequences The number of clusters are not known a-priori. As the motivation is to find the cluster with highest cardinality, the result is not affected much on the setting of the number of clusters. We tried different clustering algorithms as listed here: agglomerative clustering; k-means with K=2, 3, 4, 5; X-means, SOM, DBSCAN. Both DBSCAN, X-means, where optimum cluster number are automatically set, resulted in 4 clusters. Those four clusters are shown in Fig. 4. the result when only 40 subsequences were used for clustering. We included some discord portion. As shown in the figure, majority of signals fall in cluster 2, which we conclude is the ensemble of normal subsequences. The average of all members of this highest cardinality cluster is the *mother signal*. In case of ECG data, *mother signal* may change with time. In fact, with the same person, it will change with the person's activity. While we experimented with ECG data, we updated *mother signal* using latest ν subsequences, where $\nu = 40$. Once *mother signal* is ready, it is used for next incoming signal.

3 Proposed Algorithm, Experimental data and Results

The computational complexity for anomaly detection using brute force method is $O(n^2)$. Even all possible comparisons with mother signal will reduce the complexity to $O(mn)$. As $n \gg m$, comparison using mother signal is much more

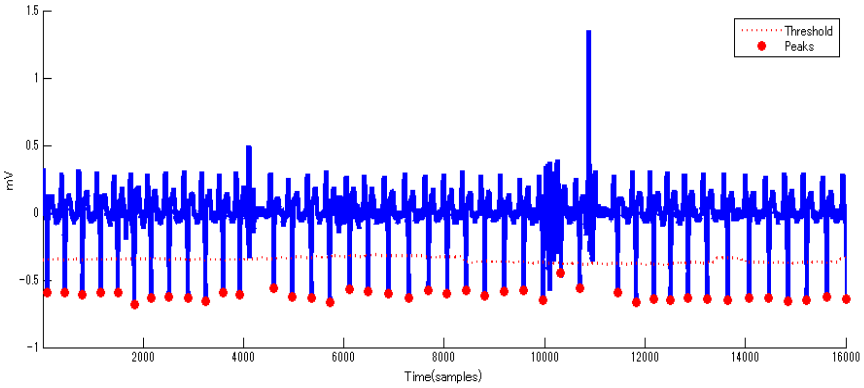

Fig. 2. Identifying the peaks to determin the periods.

efficient. In this section, we propose a heuristic algorithm which will improve the efficiency even further.

The basic idea of proposed heuristic for reducing computation is as follows. Suppose, for i^{th} subsequence, to find the minimum distance (i.e., maximum match) with mother signal, we need to shift-and-rotate the i^{th} signal by p slots. We already found that by using step-by-step shift-and-rotate comparions. In that case, for comparing $(i+1)^{th}$ subsequence with the mother signal, we need to shift-and-rotate $(i+1)^{th}$ subsequence by $(p+1)$ slots, because $(i+1)^{th}$ subsequence is only 1-slot shifted from the i^{th} subsequence. In that way, for $(i+1)^{th}$ subsequence, the number of shift-rotate-compare will be reduced from m to 1. We can reduce the computation for distance comparison by m times. Through experiment, we found that 97% of times, this 1-slot shift gave best match. But, it does not always happen, especially for discord subsequence. First, we shift $(i+1)^{th}$ subsequence by p-slots, $(p+1)$-slots and $(p+2)$-slots, and calculate the distance with mother signal. Ideally, $(p+1)$-slots shift will give the best match. If that does not happen, we need more elaborate searching for proper shift that would achieve maximum match with the mother signal. An efficient heuristic algorithm for this elaborate searching is proposed and explained below.

In Fig. 5, we show the distance when a normal signal is compared with the mother signal. The x-axis represents the shift and the y-axis is the distance. The change of distance with shift is smooth, with a prominent minimum at shift around 100 slots. The distance is symmetric on two sides of the minimum. Because of this shape, it is easy to find the minimum without comparing distances for all possible m shifts. We calculate distances for a few equally spaced shifts,

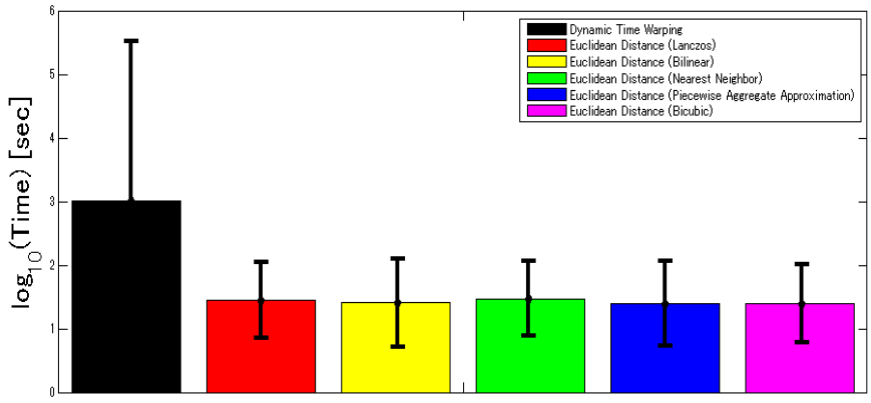

Fig. 3. Time required for clustering when different algorithms were used for measurement of distance between a pair of subsequences

and can easily converge to the minimum point (maximum match) in a few trials. The heuristic search algorithm to find minimum distance is explained in [11].

4 Experimental Data and Results

We used data from MIT-BIH Database [15], the detail of which is shown in Table. 1. The algorithm complexity to find anomaly is basically the number of times we need to calculate distance between two subsequences. Distance function calculates Euclidean distance between two subsequences. Computation time for the proposed algorithm is at fourth column, and for other competitive algorithms, are shown in the last three columns of Table 1. For the proposed algorithm, time to generate mother signal is also included. We can see that the proposed algorithm is almost 8 times faster compared to [16] (with parameter s=100) and [7]. Though, [16] (s=20) is faster compared to [16] (s=100), in Table. 2 we can see that its performance (F-score) is not good.

In Table. 2, we show the average of F-measure for all 8 data sets using our proposed algorithm and related works reported in [16] [7]. This table verifies that, in spite of our algorithm being faster, its identification of discords (both precision and recall) are either the best, or very near to the best. In the last coulmn, we show how F-score of our algorithm differs from the best result. Out of 8, for 4 data sets, it gave the best result. For the rest, it was near the best.

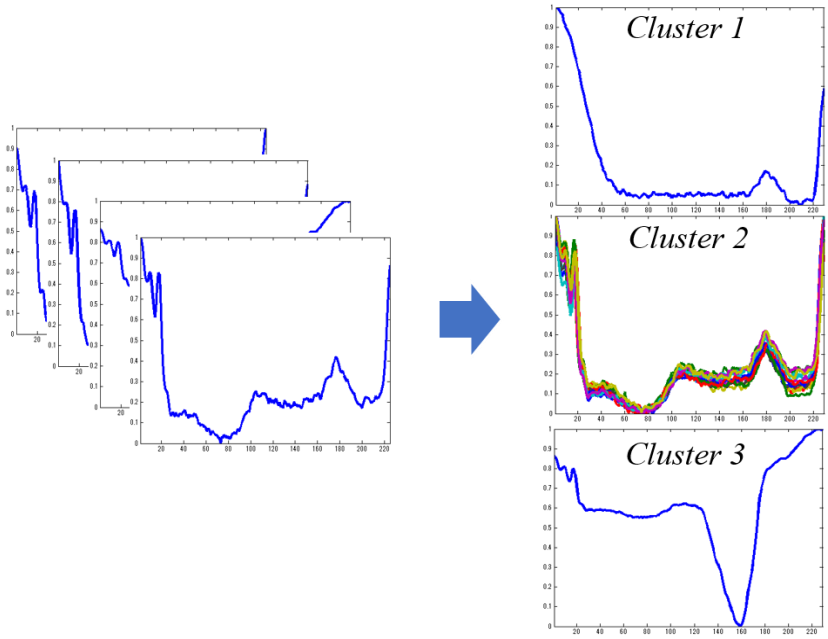

Fig. 4. Three clusters from 40 subsequences. Cardinality of cluster 2, which consists of normal subsequences, is the highest.

It is usual to evaluate any pattern recognition algorithm by precision and recall. In our case, the ground truth is not known. The decision of anomaly is solely based on the distance from the normal trend - both for the proposed method as well as brute force method. All the results in Table.2 are from signal shape perspective. The medical interpretation of discords could differ.

To evaluate the significance of our result in medical perspective, we did experiment with a different (much longer) data set. The data parameters and the result are shown in Table. 3. These are labeled data, with two types of discords, PVC (Premature Ventricular Contractions and SVPC (Supraventricular Premature Contraction). The distance of subsequences, from mother signal is shown in Fig. 6. PVC discords are more prominent, and we could detect with very high accuracy. But, most of the SVPC discords were missed. It is also evident from Fig. 6 that though prominent discords form sharp spikes, setting proper threshold value to identify all discords, is difficult.

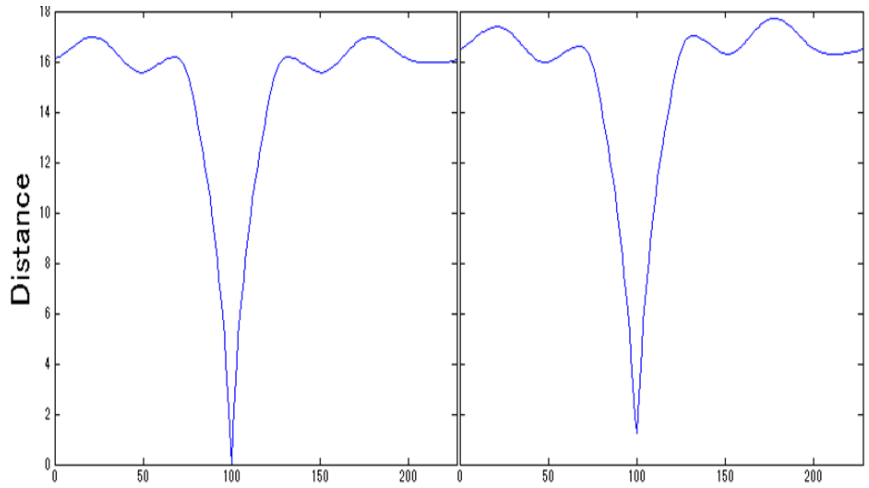

Fig. 5. Distance of two subsequences from mother, shown at different shifts. The graph is symmetrical on both sides of minimum. The one on the left is a closer match to mother signal, as distance minimum is almost zero.

5 Conclusion

We could improve the efficiency of discord detection in periodic signals. We compared our algorithm to other kind of algorithms [16] proposed recently. Comparison with [10] is underway. The memory requirement is not analyzed. The parameters used in our algorithm, determine both the efficiency as well as the quality of the result. To find their optimum values for maximum efficiency without sacrificing quality is a challenge. We will investigate how the result changes with parameter values, for certain type of bio-signals. Finally, the most important aspect is to compare the results with ground truth. We hope to obtain more labelled data with discords, identified by health experts. Our algorithm works for quasi periodic signals. The period changes over time, like pulse rate varies with the level of exhaustion or emotional state. We took care by using a window of $40 \times m$ (the last m) to find new m and the new *mother signal*. Selecting this window size is critical and application dependent. Discords with different waveforms have different meanings. For practical application we need to analyze the discords to provide the user with their level of emergency and suggestions for action to be taken.

Acknowledgment

Part of this work was carried out under the cooperative research project program of the research institute of electrical communication, Tohoku University.

Table 1. Data used for experiments and Computation time

Data set	T	m	Proposed Algo	[16](s=20)	[16](s=100)	[7]
1	3751	228	**1.14**	2.48	6.9	8.8
2	3750	163	**0.85**	2.01	5.73	8.6
3	3750	251	**1.09**	2.06	5.77	9.03
4	3750	143	**0.95**	3.06	8.94	8.47
5	5400	351	**2.43**	4.77	12.67	15.46
6	5401	292	**1.56**	3.16	8.76	14.74
7	5400	399	**2.23**	2.84	8.55	16.85
8	16500	370	**8.28**	21.33	60.92	67.01

Table 2. Comparison of F-score for all eight Data sets

Data set	Proposed Algo	[16](s=20)	[16](s=100)	[7]	Difference with best
1	0.92	0.89	0.91	**0.94**	0.02
2	0.54	0.35	**0.58**	0.44	0.04
3	**0.88**	0.51	0.59	0.51	0.00
4	**0.95**	0.72	0.85	0.71	0.00
5	0.91	0.87	0.93	**0.95**	0.04
6	**0.76**	0.52	0.61	0.34	0.00
7	**0.72**	0.34	0.65	0.52	0.00
8	0.83	0.73	**0.84**	0.81	0.01

References

1. F. Chamroukhi, "Piecewise regression mixture for simultaneous functional data clustering and optimal segmentation" , Journal of Classification - Springer, 33(3):374–411, 2016.
2. Wenyao Sha, Yongxin Zhu, Tian Huang, Meikang Qiu , Zhong Ming , Yan Zhu, Qiannan Zhang; Shanghai Jiao Tong, "A Multi-order Markov Chain Based Scheme for Anomaly Detection," Computer Software and Applications Conference Workshops (COMPSACW). Pages: 83–88. 2013.
3. Junshui Ma, Simon Perkins, "Online novelty detection on temporal sequences," In KDD'03, Proceedings of the ninth ACM SIGKDD international conference on Knowledge discovery and data mining. Pages: 613–618. 2003.
4. U. Rebbapragada, P. Protopapas, C. E. Brodley, and C. Alcock, "Finding anomalous periodic time series," Vol 74, Issue 3, pp: 281–313, 2009.
5. V. L. Brailovsky and Y. Kempner, "Application of Piece-wise regression to detecting internal structure of signal," Pattern Recognition, 25(11), pp: 1361 – 1370, November 1992.
6. G. Ferrari-Trecate and M. Muselli, "A new learning method for piecewise linear regrassion," ICANN, 28-30, Spain, August 2002.

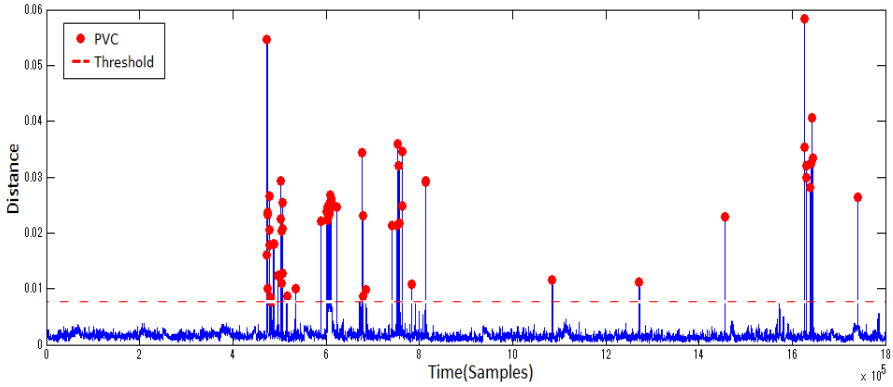

Fig. 6. Distance from mother signal and Discords for certain threshold value.

7. Keogh. E, Lin. J, Ada Waichee Fu, Van Herle. H: Finding the Unusual Medical Time Series, Algorithms and Applications. Information Technology in Biomedicine, IEEE Transactions on (Volume:10 , Issue: 3), Pages:429–439. 2006.
8. Wei Luo and Marcus Gallangher, "Faster and Parameter Free Discord Search in Quasi-Periodic Time Series," J. Z. Huang, L. Cao, and J. Srivastave (Eds.): PAKDD 2011, Part II, LNAI 6635, pp. 135–145, Springer, 2011.
9. Wei Luo, Marcus Gallangher, Janet Wiles "Parameter Free Search of Time Series Discord," Journal of Computer Science and Technology, 28(2), pp: 300-310, Mar, 2013.
10. Haemwaan Sivaraks and Chotirat Ann Ratanamahantana, "Robust and Accurate Anomaly Detection in ECG Artifacts Using Time Series Motif Discovery," Computational and Mathematical Methods in Medicine, Vol 2015, Article ID 453214, 20 papges. http://dx.doi.org/10.1155/2015/453214.
11. Takuya Kamiyama and Goutam Chakraborty, "Real-Time Anomaly Detection of Continuously Monitored Periodic Bio-Signals Like ECG," M. Otak et. al.(Eds.): Springer LNAI 10091, pp: 418 – 427, 2017.
12. Stan Salvador, Philip Chan: Learning states and rules for detecting anomalies in time series. Applied Intelligence, 23(3). Pages: 241–255. 2005.
13. Basha R, Ameen JRM: Unusual sub-sequence identifications in time series with periodicity. In IJICIC f07: International Journal on Innovative Computing, Information and Control, volume 3. 2007.
14. Korkmaz S, Goksuluk D, Zararsiz G. MVN: An R Package for Assessing Multivariate Normality. The R Journal. 2014 6(2):151-162.
15. Goldberger AL, Amaral LAN, Glass L, Hausdorff JM, Ivanov PCh, Mark RG, Mietus JE, Moody GB, Peng C-K, Stanley HE. PhysioBank, PhysioToolkit, and PhysioNet: Components of a New Research Resource for Complex Physiologic Signals. Circulation 101(23), pp215–220.

Table 3. Detection of PCV and SPVC discords

Data set	T	m	PVC count	SPVC count	PVC detection	SPVC Detection	Error Rate
1	1000500	210	18	4	78%	0%	14%
2	1000500	220	9	4	89%	0%	10%
3	1000500	270	12	2	75%	50%	9%
4	1000500	250	23	7	87%	14%	5%
5	1000500	270	10	13	80%	25%	23%
6	1800000	253	86	0	100%	-	0%
7	1800000	279	9	16	90%	8%	9%
8	1800000	268	8	5	80%	20%	1%

16. Sugiyama, M., Borgwardt, K.M.: Rapid Distance-Based Outlier Detection via Sampling, NIPS 2013.

New Hybrid Feature Selection Algorithm based on Consistency Measures and Simulated Annealing Search

Adrian Pino Angulo[1], Kilho Shin[1], and Takako Hashimoto[2]

[1] Graduate School of Applied Informatics: University of Hyogo, Hyogo, Kobe, Japan.
{apinoa85,kilhoshin314}@gmail.com
[2] Chiba University of Commerce, Chiva, Japan
takako@cuc.ac.jp

Abstract. Hybrid feature selection is an special issue in machine learning because in many cases they can find better sets than the filter algorithms and are faster than wrapper algorithms. However, to the best of our knowledge, most of hybrid algorithms only take into account individual relevance of features and redundancy score to create the search space for the wrapper search. This may lead to loss of valuable features that could increase the accuracy of classifiers. In this paper we deal with this problem by proposing a new hybrid algorithm that reduces the search space of the wrapper search to a set of features with high interaction score and high individual relevance. To relieve the wrapper search we use the *Simulated Annealing* algorithm. Experiments on sixteen datasets reveals the new algorithm can effectively detect feature sets with high *auc-roc* values with small number of evaluations.

1 Introduction

Feature selection plays an essential role in supervised classification since its main goal is to identify and remove irrelevant and redundant features that do not contribute to minimize the error of subsequent classification [1]. Basically, given a dataset $\mathbf{D}$, the advantages of feature selection include selecting a set of features $\tilde{F} = \{f_{i_1}, \ldots, f_{i_k}\} \subsetneq F$ with:

$$Err(\ell, \mathbf{D}_{\tilde{F}}) \leq Err(\ell, \mathbf{D}),$$

where $\mathbf{D}_{\tilde{F}}$ is the result of projecting $\tilde{F}$ over $\mathbf{D}$ and $Err(\ell, \mathbf{D})$ represents the error rate of a classifier ℓ when trained and tested on $\mathbf{D}$. The process of selecting features is composed of two basic components: an evaluation function and a search engine [2]. The evaluation function is a metric that evaluates quantitatively how good is a set of features to discriminate among class labels. The search engine generates potential sets that will be evaluated by the evaluator. According to the way sets are evaluated, feature selection can be classified as: feature ranking, pairwise comparison and subset comparison methods. Feature ranking algorithms rank all features according to their correlation to the class

and then select the top features. These algorithms are prone to select redundant features. On the contrary, pair-wise comparison methods detect and remove redundancy features by evaluating pair of features. Although they are fast and accurate they cannot detect feature interaction [3].

Multiple features interact with each other, when the set composed by all of them is more relevant to classes than any of its proper subsets. Since feature ranking and pairwise comparison algorithms cannot detect interacting features, subset comparison methods are often more accurate [3]. Within the subset comparison methods, *consistency-based* algorithms can detect interacting features by evaluating collective relevance (correlation) of a feature set to the class. In section 2 we explain more in detail the definition of consistency measures and some of their properties.

We first introduce the *Bayesian risk* as a consistency measure, which is used by most of the *consistency-based* feature selection algorithms. For a dataset $\mathbf{D}$, we view a feature of $\mathbf{D}$ as a random variable and a feature set $\tilde{F}$ as a joint variable. Then, we let $\Omega_{\tilde{F}}$ denote the sample space of $\tilde{F}$, C denotes a variable that describes classes and $\Pr_{\mathbf{D}}$ denotes the empirical probability distribution of $\mathbf{D}$. With these notations, the Bayesian risk is defined by

$$\mathfrak{Br}(\tilde{F}) = 1 - \sum_{\boldsymbol{x} \in \Omega_{\tilde{F}}} \max\{ \Pr_{\mathbf{D}}[\tilde{F} = \boldsymbol{x}, C = y] \mid y \in \Omega_C \}. \tag{1}$$

This function is also referred to as the *inconsistency rate* in [4].

To the best of our knowledge, LCC [5] and its fastest version SUPER-LCC [6] have the most practical performance in both time efficiency and prediction accuracy in the consistency-based feature selection field. In the first step, LCC sorts the features in F into $(f_1, \ldots, f_{|\mathcal{F}|})$ in the increasing order of the *Symmetric Uncertainty* $\mathrm{SU}(f_i, \mathrm{C})$ and then fixes $\tilde{F}$, a variable that represents a subset of F, to F. In the second step, starting from $i = 1$, LCC lets $\tilde{F} = \tilde{F} \setminus \{f_i\}$ and computes $\mathfrak{Br}(\tilde{F} \setminus \{f_i\})$. If $\mathfrak{Br}(\tilde{F}) \setminus \{f_i\} \leq \delta$, LCC judges that the feature f_i is not important and eliminates it from $\tilde{F}$. This procedure is repeated until no features left untested. SUPER-LCC outputs the same set as LCC, but uses the *binary search* instead of *linear search* to significantly reduce the number of sets evaluated [6]. The parameter δ defines the upper-bound *bayesian risk* of the selected set. Therefore, we may think that the lower the value of δ is, the more classification accuracy the selected set can yield. However, we have investigated that in terms of classification accuracy, the minimum *bayesian risk* not necessarily conducts to a maximal accuracy of classifiers in practice. As an instance, Figure 1 depicts the resulted AUC-ROC values of *C4.5* classifier for different values of δ. However, the maximum AUC-ROC value is not reached with the minimum δ in many cases. This phenomena occurs probably because LCC/SUPER-LCC are prone to select features with low individual relevance when δ is small [7].

The main contribution of this paper is to present a new feature selection algorithm that uses LCC/SUPERLCC, a wrapper search and the *Simulated Annealing* search to efficiently find a suboptimal set with high prediction accuracy.

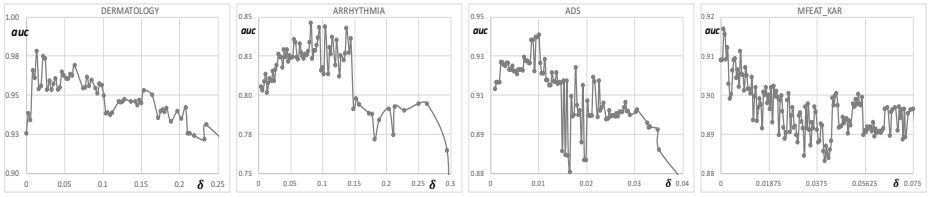

(a) dermatology (b) arrhythmia (c) ads (d) pixel

Fig. 1: AUC-ROC values of *c4.5* classifier for the outputed value of LCC/SUPER-LCC when varying δ. Five-fold cross validation was used to compute AUC-ROC values.

In section 2, we briefly review some methods based on consistency measures and show some important properties of LCC/SUPERLCC that allow us to efficiently look for feature sets with small *bayesian risk*. In section 3, we explain how to combine the *simulated annealing* algorithm to LCC for an optimal search. Finally, in section 4 we present and discuss the results of experiments conducted on sixteen datasets.

2 Consistency measures and Lcc/SuperLcc

The Bayesian risk has two important properties, that is, *determinacy* and *monotonicity*, and we first introduce the notion of *consistent feature sets* to explain the properties.

Definition 1. *For a dataset* $\boldsymbol{D}$ *described by a feature set* F*, a feature set* $\tilde{F} \subseteqq F$ *is* consistent*, iff,* $\Pr_{\boldsymbol{D}}[C = y \mid \tilde{F} = \boldsymbol{x}] = 0$ *or* 1 *for all* $\boldsymbol{x} \in \Omega_{\tilde{F}}$ *and* $y \in \Omega_C$*.*

Then, the determinacy and monotonicity properties are described as follows.

Determinacy. $\mathfrak{Br}(\tilde{F}) = 0$, if, and only if, $\tilde{F}$ is consistent in $\mathbf{D}$.
Monotonicity. $\mathfrak{Br}(\tilde{F}) \geq \mathfrak{Br}(G)$, if $\tilde{F} \subseteqq G \subseteqq F$.

Formally, a consistency measure is defined as a function that returns real numbers on input of feature sets and has the determinacy and monotonicity properties. The *consistency-based feature selection*, on the other hand, is characterized by use of consistency measures as the evaluation function.

To the best of our knowledge, SUPER-LCC is one of the fastest and accurate feature selection algorithm based on consistency measures. SUPER-LCC works under the assumption that high-dimensional datasets are abundant in irrelevant features that can be removed in mass. By the first to the $(i-1)$-th iterations of the algorithm, SUPER-LCC determines a sequence of indices of features $l_1 < l_2 < \cdots < l_{i-1}$, and defines $\tilde{F} = (F \setminus \{f_1, \ldots, f_{l_{i-1}}\}) \cup \{f_{l_1}, \ldots, f_{l_{i-1}}\}$. In the i-th iteration, the algorithm finds l_i such that

$$l_i = \underset{j=l_{i-1}+1,\ldots,n}{\operatorname{argmin}} \mathfrak{Br}(\tilde{F} \setminus \{f_{l_{i-1}+1}, \ldots, f_j\}) \leq \delta,$$

by *binary search* due to the monotonicity property of the bayesian risk. SUPER-LCC outputs the same set as LCC but on average has a computational complexity of $O(nm(\log n + \log m))$, where n is the number of features that describes the m instances in $\mathbf{D}$. To the best of our knowledge, SUPER-LCC is the algorithm with better practical performance in both of efficiency and accuracy in the field of feature selection. According to the authors of [6], for data with more than hundred thousand features, SUPER-LCC needs some seconds to give a response in an ordinary personal computer. In the remaining of this paper, we show how to incorporate SUPERLCC and LCC to our approach, but first we present some important properties of LCC/SUPERLCC.

Theorem 1. *Let $\tilde{F}$ be a subset with $\mathfrak{Br}(\tilde{F}; C) = \beta$, with $\delta = \beta - \epsilon$. For $\epsilon > 0$,* LCC *outputs a different feature set from $\tilde{F}$. For the output of the i-th iteration of* LCC*, $F_i = (F \setminus \{f_1, \ldots, f_{l_i}\}) \setminus \{f_{l_1}, \ldots, f_{l_i}\}, \mathfrak{Br}(F_i; C) \leq \delta$ holds.*

Theorem 1 suggests that, if we run LCC multiple times increasing δ, then the smaller δ is, the smaller the index of the first feature selected by LCC in $F = \{f_n, \ldots, f_1\}$ is. Therefore, if we want to run LCC twice with δ_1 and δ_2 (being $\delta_1 < \delta_2$) over F, and assuming f_{l_1} is the first feature selected by LCC with δ_1, it is reasonable to run LCC with δ_2 not over F, but over $\{f_{l_1}, \ldots, f_1\} \in F$. This is a very important property of LCC to save computational time. In the next section we state how to use it in our new algorithm.

Another important property of LCC/SUPERLCC is as follows. Being br and $\tilde{F}$ the *Bayesian risk* and the outputted set obtained when we run LCC/SUPERLCC with δ, if we let $\delta = br - \alpha$ then LCC/SUPERLCC output a set $\tilde{F}'$ different from $\tilde{F}$. This property suggests that if we perform multiple running of LCC using different and sorted thresholds $\{\delta_m, \delta_{m-1}, \ldots, \delta_0\}$ with $\delta_i > \delta_{i-1}$ and $\mathfrak{Br}(\emptyset; C) \leq \delta_i \leq \mathfrak{Br}(\tilde{F}; C)$ then we obtain $\{F_{\delta_m}, F_{\delta_{m-1}}, \ldots, F_{\delta_0}\}$ different sets. Moreover, if we compute the AUC-ROC values with a given classifier for all these sets then we can see the AUC-ROC function defined by the interval $[\delta_{min}, \delta_{max}]$.

Furthermore, given the entire feature set F of a dataset, if we fix $\delta^- = \mathfrak{Br}(F; C)$ and $\delta^+ = \mathfrak{Br}(F; C) + \epsilon$ and let be $\Delta = \{\delta^+, \delta^+ - \alpha, \delta^+ - 2\alpha, \ldots, \delta^-\}$, then for a relatively small value of ϵ, if we run LCC with the ordered δ values in Δ, then we may expect to obtain m subsets, which *bayesian risk* are close to $\mathfrak{Br}(F; C)$. Under the assumption these sets may have very low *bayesian risk*, they can be used as the search space for the wrapper search. In the next section we propose a new algorithm that take advantage of Theorem 1 to efficiently generate a space of high-quality features given δ^- and δ^+.

3 Our Proposal

3.1 Simulated Annealing

Simulated Annealing is a stochastic technique used in optimization problems to efficiently scape from local optima. Given a current state of the problem cs, the algorithm generates a candidate (or next) state ns and stochastically

decides whether or not the current state is updated to the candidate state. The probability of passing from one state to another is called the transition probability p and often is defined as $p = exp(nf - cf)/T$ where nf and cf are the values of the target function for ns and cs respectively, and T is the temperature variable. In simulated annealing we keep the temperature variable T to simulate the heating process on metal.

We initially fix a high temperature, for example: $T = 0.1/(\log(t+1))$ with $t = 1$, and then allow it to slowly decrease as the algorithm runs. That is, we can increase t in each iteration. The higher the temperature the more likely to accept solutions that are worse than the current solution. This gives the algorithm the ability to jump out of any local optimums found in early iterations. As the temperature is reduced the algorithm gradually focus on the area of the search space in which hopefully, a close to optimum solution can be found. This gradual cooling process is what makes the simulated annealing algorithm remarkably effective when dealing with large problems which contain numerous local optimums such as the depicted in Figure 1. Figure 2 depicts the general scheme of *Simulated Annealing* we will use for our feature selection algorithm where $rnd(0,1)$ returns a random number between zero and one according to a uniform distribution and k is an arbitrary constant. Moreover, *continue* defines the stopping criterion and can be: a) $T > T_{min}$ or/and b) $t < t_{max}$, where T_{min} and t_{max} are predefined constants.

Algorithm 1: *Simulated Annealing*

Terminology: cs: current state
ns: next state
$next(cs)$: a function that returns a neighbour state of cs
$f(cs)$: the target function

```
1  cs = cs_0
2  cf = f(cs_o)
3  t = 1
4  while continue do
5  |   ns = next(cs)
6  |   nf = f(ns)
7  |   T = k/(log(t + 1))
8  |   p = exp(nf − cf)/T
9  |   if rnd(0, 1) < p then
10 |   |   cs = ns
11 |   |   cf = nf
12 |   |   t = t + 1
13 |   end
14 end
15 return cs
```

Fig. 2: The algorithm of *Simulated Annealing*

3.2 Target Function

Now we only need to define the function $next(\delta_c)$ to generate a neighbour state δ_n of the current state δ_c and the target function $f(\delta_c)$. In our problem we state the parameter δ of LCC algorithm as the space of all possible states. In particular, we generate some of the values of δ in the interval of $\delta^+ \leq \delta \leq \delta^-$ to run LCC and obtain a set of feature subsets $\tilde{F}_\delta$ that can be evaluated by the AUC-ROC function across a fold-cross validation process. We let $\text{AUC}(\mathbf{D}_{\tilde{F}_\delta}, \ell)$ be the target

function for the current state δ. $\tilde{F}$ represents the subset of features selected by LCC with δ and $\mathbf{D}_{\tilde{F}}$ represents the the dataset resulted from projecting the set $\tilde{F}$ over $\mathbf{D}$. ℓ is the classifier used in the training and testing process of the cross validation.

3.3 Neighbour generator function

The neighbour generation function is crucial in the *Simulated Annealing* algorithm to scape from local optima. Given a current value δ_c of δ, we intend generate a neighbour b of δ_c such that $\text{AUC}(\mathbf{D}_{\tilde{F}_b}, \ell) > \text{AUC}(\mathbf{D}_{\tilde{F}_{\delta_c}}, \ell)$. However, since the target function AUC is unknown this is difficult to achieve.

Another issue in the neighbour generation function is that two different values of δ can lead to the same output of LCC. In this case we may have duplication of candidate sets in the search space of the feature selection problem, which lead to compute the same operations more than once. One way to avoid this is by performing a downward search over the space of δ-values. That is, we generate the search space of feature subsets for the wrapper evaluator by running $\text{LCC}(\delta_t)$ with different values of δ in decreasing order. As an instance, given δ^- and a predefined constant ϵ we run LCC with $\delta^- \leq \delta_t \leq (\delta^- + \epsilon) = \delta^+$ such that:

$$\delta_t = \begin{cases} \delta^+ - \beta_t & \text{if } br_{t-1} \geq (\delta^+ - \beta_t) \\ br_{t-1} - \alpha & \text{if } br_{t-1} < (\delta^+ - \beta_t) \end{cases},$$

where β_t is a propagation function with respect to t such as: $k * t$ or $k/2^t$ (with k as a constant), α is a value as small as required and br_t represents the *bayesian risk* of the set obtained by $\text{LCC}(\delta_t)$ with δ_t. t is a counter variable that increase in one in each iteration. According to the property of LCC exposed in section 2, when we run LCC with different δ_t always obtain a different set. Therefore, the problem of duplication of sets is solved by this procedure. However, iterating downward may lead to miss the global optima behind. Therefore, we need a mechanism to make a bi-directional search over δ and minimize the number of sets duplicated. Figure 3 depicts the proposed function $next(\delta_c)$ to generate a neighbour b given the current

Algorithm 2: *next(δ_c)*

Terminology:
δ_c: current δ
step: a given constant to determine the upper limit of the next state

```
1 mv = step * (rnd(0,1) − 0.5)
2 br_closest = closestSBrComputed(δ_c + mv)
3 if (δ_c + mv) − br_closest > α then
4 |   (F, b) = LCC(δ_c + mv)
5 |   list.add((F, b))
6 |   return b
7 end
8 return br_closest
```

Fig. 3: Algorithm to generate the next candidate *Bayesian risk*

state δ_c. In this function, we move δ_c in the space of δ by mv, which is a number generated randomly in the interval $[step + 0.5, step - 0.5]$ (line 1). To minimize the duplicity of feature sets when running LCC with similar values of δ: $br_{closest}$ and $\delta_c + mv$, we fix a threshold α, such that, if $(\delta_c + mv) - br_{closest} > \alpha$ holds, then we consider $\text{LCC}(\delta_c + mv) = \text{LCC}(br_{closest})$ (line 3), where $br_{closest}$ is the closest and smaller *Bayesian risk* computed so far ($closestSBrComputed(\delta)$) stored in *list* (line 5).

3.4 SALCC: A new Algorithm

Now that we have defined some properties of LCC and our scheme for the *Simulated Annealing* algorithm, we propose a new feature selection algorithm namely *Simulated Annealing for Linear-Consistency-Constrained-based feature selection*(SALCC) as follows.
1. First, we rank the features in F in increasing order of *Symmetrical Uncertainty* (SU) values.
2. Second, we find the *border feature* f_l such that l is maximum and

$$\mathfrak{Br}(\{f_l, \ldots, f_n\}; C) = \mathfrak{Br}(F; C)$$

and fix $\tilde{F} = \{f_{l+1}, \ldots, f_n\}$. This is easily and efficiently achieved by running the first iteration of SUPERLCC described in [6].
At this point, we reduce the search space from $F = \{f_1, \ldots, f_n\}$ to $\tilde{F} = \{f_l, \ldots, f_n\}$. Note that this does not affect the final solution of our algorithm because of Theorem 1. This step will make our algorithm scalable for high-dimensional datasets. To make sure this expectation is true, we picked 44 datasets from the *UCI machine learning repository* [8] and determine the percentage of features removed in the first iteration of SUPERLCC. Results are depicted in Figure 4.

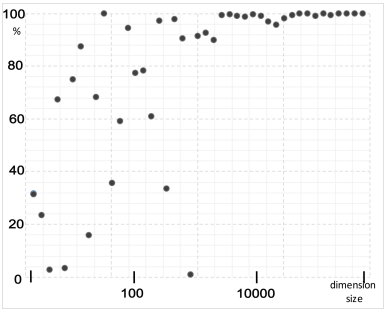

Fig. 4: Percentage of the first consecutive features $\{f_1, \ldots, f_l\}$ such that $\mathfrak{Br}(F; C) = \mathfrak{Br}(F \setminus \{f_1, \ldots, f_l\}; C)$ to the entire feature set F.

3. We run the *Simulated Annealing* algorithm shown in section 3.1 by using the proposed target and neighbour generator functions.

4 Experiments

We empirically evaluate the performance of the proposed algorithm in terms of accuracy, and number of times the classifier is used and number of features selected. For the experiments we use the following parameters: $\delta_{max} = 0.4$,

$T_{min} = 0.2$, $step = 0.1$, $\alpha = 0.001$ and we use *C4.5* as classifier. Datasets were selected from the *UCI Machine learning repository* and they represent several areas of current researches [8].

Figure 5 shows part of the entire search space of sixteen datasets and the suboptimal set reached by our algorithm depicted with a black cross. In datasets a, b, f, h, i, j, k and l, the algorithm found the global optima and in datasets c, d, e, g, m, o and p, the sets found are very close to the optimal solution in terms of AUC-ROC values.

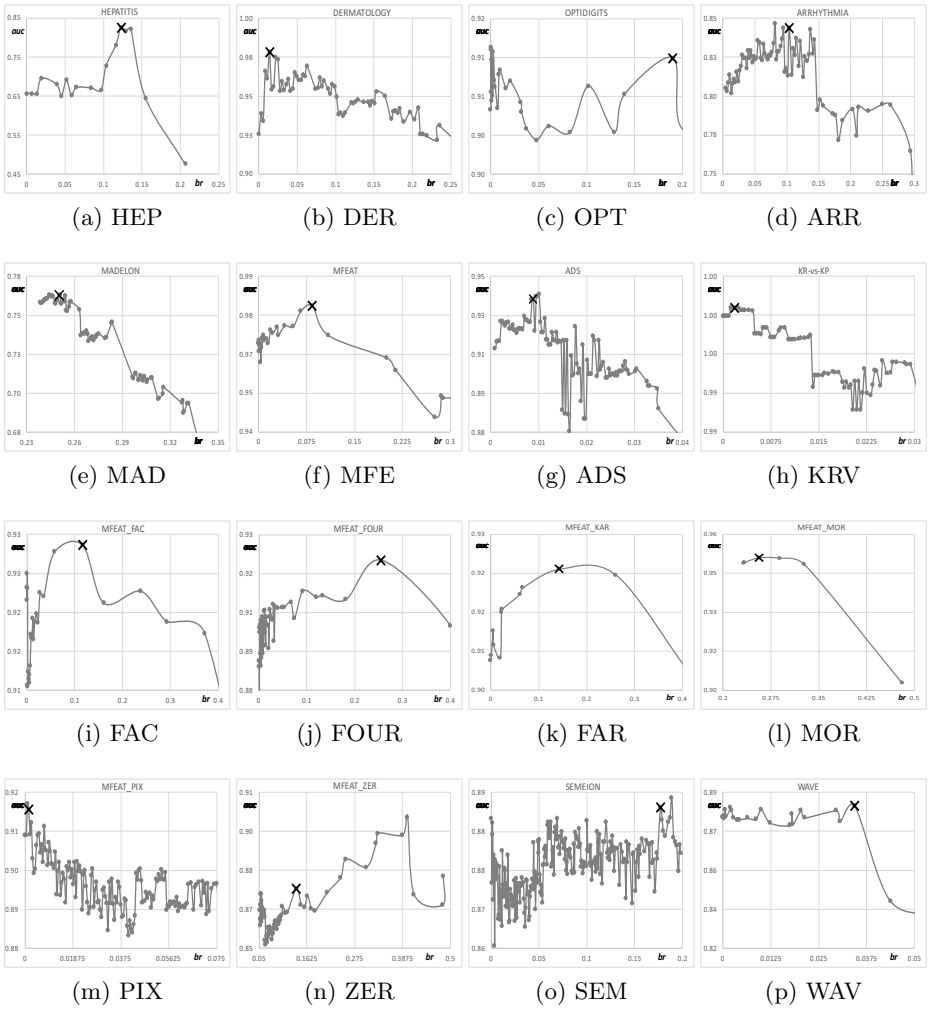

(a) HEP (b) DER (c) OPT (d) ARR

(e) MAD (f) MFE (g) ADS (h) KRV

(i) FAC (j) FOUR (k) FAR (l) MOR

(m) PIX (n) ZER (o) SEM (p) WAV

Fig. 5: search space and set found by the proposed algorithm

Table 1: AUC values comparison among some of the state-of-the-art algorithms and SALCC.

	NB-AUC values					C4.5-AUC values				
dataset	RF	Cfs	Fcbf	SLcc	SaLcc	RF	Cfs	Fcbf	SLcc	SaLcc
tr21	.807	.829	.833	.834	.871	.732	.824	.821	.825	.827
tr41	.612	.721	.794	.748	.748	.587	.741	.788	.714	.714
tr45	.827	.822	.834	.843	.847	.700	.798	.818	.821	.821
wap	.902	.963	.945	.945	.948	.932	.981	.961	.962	.974
tr31	.832	.821	.809	.819	.831	.847	.882	.856	.856	.875
fbis	.709	.722	.734	.729	.741	.776	.742	.739	.747	.747
la2s	.825	.881	.846	.867	.881	.624	.708	.725	.724	.724
la1s	.863	.869	.868	.865	.865	.833	.869	.849	.847	.901
AVG.	.797	.829	.833	.831	.842	.754	.818	.820	.812	.823

Althoug these datasets are abundant in local optima, we can conclude that SALCC can approximately find the optimal set in many cases. We also conclude that *Simulated Annealing* works very well in these data and can easily scape from local optima.

To evaluate in a more appropiate way SALCC algorithm we perform a ten-fold cross validation comparison with some of the state-of-the-art algorithm in eight text-classification datasets[1]. The algorithms selected for the comparison are: RELIEFF[9], CFS[10], FCBF[11] and SLCC. Table 1 shows that SALCC performs well in most of the datasets when compared with the state-of-the-art algorithms. Table 2 shows the number of times SALCC use the classifier to evaluate a set (ESets), the total number of sets in the range of $[\delta^-, \delta^+]$ (TSets), number of features selected by LCC ($\text{LCC}_{\#f}$) and SALCC ($\text{SALCC}_{\#f}$). As the table depicts, the number of evaluations is relatively small respect to the total number of sets. Also, the number of features selected by SALCC is very small when compared with the number of features selected by LCC. I general we state that SALCC significantly improves the accuracy and size of solutions of LCC.

Table 2: Number of times the classifier is used versus the number of all possible sets and the number of features selected by LCC and SALCC.

DATA	ESets	TSets	$\text{LCC}_{\#f}$	$\text{SALCC}_{\#f}$
HEP	10	18	10	3
DER	31	69	10	9
OPT	14	29	13	5
ARR	35	78	23	11
MAD	31	76	15	11
MFE	13	31	8	4
ADS	46	107	39	21
KRV	28	94	29	23
FAC	12	27	12	4
FOU	19	44	14	6
KAR	8	12	9	4
MOR	5	6	5	4
PIX	37	298	16	21
ZER	24	62	12	7
SEM	33	319	29	23
WAV	20	39	12	8

5 Conclusion and Future Works

Feature selection is a central issue in machine learning. In this paper, we have improved the accuracy of LCC/SUPERLCC, one of the best feature selection algorithms in the literature, by incorporating

[1] http://tunedit.org/repo/Data/Text-wc

the wrapper approach to the search. The meta-heuristic of *Simulated Annealing* is used in this approach to reduce the probability to be trapped by local optima. In the proposed algorithm we use generate sets by simply decreasing or increasing the value of δ for LCC/SUPERLCC. In future work, we will extend the experiments to high-dimensional data.

References

1. Kohavi, R., John, G.H.: Wrappers for feature subset selection. Artif. Intell.,(1997)
2. L. C. Molina, L. Belanche, A. Nebot,: Feature Selection Algorithms: A Survey and Eperimental Evaluations. Proceedings of the 2002 IEEE International Conference on Data Mining (ICDM 2002), 9-12 December 2002, Maebashi City, Japan, (2002)
3. A. Jakulin, I. Bratko,: Testing the significance of attribute interactions. In ICML, (2004)
4. Z. Zhao, H. Liu.: Searching for interacting features. In Proceedings of the 20th international joint conference on Artifical intelligence (IJCAI'07), (2007)
5. K. Shin and X.M. Xu.: Consistency-based feature selection. In 13th International Conferece on Knowledge-Based and Intelligent Information and Engineering System, (2009)
6. K. Shin, T. Kuboyama, T. Hashimoto, D. Shepard.: Super-CWC and super-LCC: Super fast feature selection algorithms. Proc. 2015 IEEE International Conference on Big Data (Big Data) pp. 1-7, (2015)
7. A. Pino, K. Shin,: Fast and Accurate Steepest-Descent Consistency-Constrained Algorithms for Feature Selection. First International Workshop on Machine Learning, Optimization, and Big Data, Vol. 9432. Springer-Verlag, 293-305, (2015)
8. M. Lichman,: UCI Machine Learning Repository [http://archive.ics.uci.edu/ml]. Irvine, CA: University of California, School of Information and Computer Science, (2013)
9. K. Kira, L. A. Rendell.: A practical approach to feature selection. In Proceedings of the ninth international workshop on Machine Learning, pp. 249-256. Morgan Kaufman Publishers Inc., (1992)
10. M. A. Hall and L. A. Smith.: Feature Selection for Machine Learning: Comparing a Correlation-Based Filter Approach to the Wrapper. In Proceedings of the Twelfth International. AAAI Press 235-239, (1999)
11. L. Yu, H. Liu,: Feature Selection for High-Dimensional Data: A Fast Correlation-Based Filter Solution. In Proceedings of the Twentieth International Conference on Machine Learning (ICML-2003), (2003).

On methods to assess the significance of community structure in networks of financial time series

Argimiro Arratia and Martí Renedo

Universitat Politècnica de Catalunya, Barcelona, SPAIN
argimiro@cs.upc.edu, marti.renedo@estudiant.upc.edu

Abstract. We consider the problem of determining whether the community structure found by a clustering algorithm applied to financial time series is statistically significant, or is due to pure chance, when no other information than the observed values and a similarity measure among time series are available. As a subsidiary problem we also analyse the influence of the choice of similarity measure in the accuracy of the clustering method.
We propose two raw-data based methods for assessing robustness of clustering algorithms on time-dependent data linked by a relation of similarity: One based on community scoring functions that quantify some topological property that characterises ground-truth communities, and another based on random perturbations and quantification of the variation in the community structure. These methodologies are well-established in the realm of unweighted networks; our contribution are versions of these methodologies properly adapted to complete weighted networks.

Keywords: clustering time series, ground-truth communities, similarity measures, Forex network

1 Introduction

We treat in this work the problem of determining the intrinsic structure of clustered data, where the clusters are based on some measure of similarity affecting all pairs of data points. From a network analysis perspective we are concerned with assessing the significance of communities formed by some unsupervised classification algorithm (i.e. clustering procedure) applied to fully-connected weighted networks.

We are motivated by research in community structure and their dynamics in financial market networks, which are characterise by a fixed number of nodes, each representing a financial time series, and links among all pairs of nodes weighted by the values of a measure of similarity, commonly based on pairwise correlation, between pairs of time series (see, e.g., [3],[5],[9],[12],[11]). In our previous work [14] we presented empirical evidence of the impact of the chosen similarity measure on the clustering results: In a foreign exchange (FX) network, and clustering based on the Girvan-Newman modularity maximisation

algorithm [10, 2], we analysed the qualitative differences in the clusterings obtained under three different correlation measures: Pearson, Kendall and the most recent distance correlation [4]. As an application of the statistical and topological criteria that we developed and present here to assess robustness of clustering on weighted networks, we shall give quantitative measures of the nature of the clustering obtained by considering similarity either based on Pearson or on distance correlation.

To assess the significance of communities structure in complete weighted networks, we developed a collection of cluster scoring functions that measure some topological characteristic of the ground-truth communities as defined by Yang and Leskovec in [15] for unweighted networks. Our scoring functions are proper extensions of theirs to weighted networks. We then combined these topological measures of robustness of clusters with an analysis of the variation of successive random perturbations of the original network. The perturbations consist on changing the weights distribution and degenerate the original network, the cluster variation is measured in terms of the change of information (in the sense of Shannon's Theory of Information [7]). The idea is that a robust community should differ in its structural properties from the random perturbations inasmuch as these affect greater proportions of the network. Additional clustering robustness tests and fine details of the ones presented here can be read in the extended report [13].

2 Basic definitions

2.1 The Forex Network

The networks of exchange rates studied in [14][3] are built by considering the exchange rates as vertices and drawing edges between these vertices, weighted by the similarity between the returns of the pair of chosen exchange rates. We will focus on two possible similarity measures: one based on the Pearson correlation and the other based on the distance correlation[4][1].

For the Pearson similarity network, the adjacency matrix is defined as

$$A^{\rho}_{ij} = \frac{1}{2}(\rho(r^i, r^j) + 1) - \delta_{ij}. \tag{1}$$

This scales the Pearson correlation $\rho(\cdot, \cdot)$ from $[-1, 1]$ to $[0, 1]$, while the Kronecker delta δ_{ij} removes self-edges. In the graph with adjacency matrix A^{ρ} exchange rates with positively linearly correlated returns will be connected by edges of weight close to 1, and weight near 0 if the correlation is negative. Edges connecting non correlated exchanges will have weights closer to the center of the interval $[0, 1]$.

[1] In previous work [14] we considered in addition Kendall correlation measure. We omit it in this study since our main purpose here is to put to test the clustering performance measures, as opposed to compare clustering methods.

In the case of the distance correlation $\mathcal{R}(\cdot,\cdot)$, the network is simply built from the matrix of distance correlations, $A^{\mathcal{R}}$ by removing self edges. For each pair of exchange rate returns r^i, r^j,

$$A^{\mathcal{R}}_{ij} = \mathcal{R}(r^i, r^j) - \delta_{ij} \tag{2}$$

2.2 Community Detection

The partition of the networks into communities is done using the Potts method. It consists on minimising an objective function, the Potts Hamiltonian, which evaluates the strength[2] of a partition of the graph. This can be seen as a generalisation of the modularity function[10].

Definition 1. *The modularity of the partition $\mathcal{P}$ of a weighted undirected graph with adjacency matrix A is given by*

$$Q(\mathcal{P}) = \frac{1}{2m}\sum_{ij}[A_{ij} - P_{ij}]\delta(c_i, c_j) \tag{3}$$

where c_i is the community of the node i in the partition $\mathcal{P}$ (so $\delta(c_i, c_j)$ is 1 when i and j are in the same community and 0 otherwise), P_{ij} is the expected weight of the edge ij in a null model and m is the sum of the weights of all edges in the graph.

Definition 2. *The Hamiltonian of the Potts system of the partition $\mathcal{P}$ of a weighted undirected graph with adjacency matrix A is given by*

$$H(\mathcal{P}) = -\sum_{ij}[A_{ij} - \gamma P_{ij}]\delta(c_i, c_j)$$

where γ is a parameter which determines how likely vertices are to form communities.

The algorithm used to minimise the Potts Hamiltonian has been adapted from the modularity maximisation algorithm in [2] to suit weighted networks and this objective function.

3 Cluster scoring functions

Here we will provide functions which will evaluate the division of networks into clusters, specifically when the edges have weights. Using the scoring functions for communities in unweighted networks given in [15] as a reference, we propose generalisations of some of them to the weighted case.

[2] Considering a strong partition one that has strong links inside the communities and weak links between them.

Basic definitions. Let $G(V, E)$ be an undirected graph of order $n = |V|$ and size $m = |E|$. In the case of a weighted graph $\tilde{G}(V, \tilde{E})$[3], we will denote $\tilde{m} = \sum_{e \in \tilde{E}} w(e)$ the sum of all edge weights. Given $S \subset G$ a subset of vertices of the graph, we have $n_S = |S|$, $m_S = |\{(u, v) \in E : u \in S, v \in S\}|$, and in the weighted case $\tilde{m}_S = \sum_{(u,v) \in \tilde{E}: u,v \in S} w((u, v))$. Note that if we treat an unweighted graph as a weighted graph with weights 0 and 1 (1 if two vertices are connected by an edge, 0 otherwise), then $m = \tilde{m}$ and $m_S = \tilde{m}_S$ for all $S \subset V$.

The following definitions will also be needed later on:

- $c_S = |\{(u, v) \in E : u \in S, v \notin S\}|$ is the number of edges connecting S to the rest of the graph.
- $\tilde{c}_S = \sum_{(u,v) \in E: u \in S, v \notin S} w_{uv}$ is the natural extension of c_S to weighted graphs; the sum of weights of all edges connecting S to $G \setminus S$.
- $\tilde{d}(u) = \sum_{v \neq u} w_{uv}$ is the natural extension of the vertex degree $d(u)$ to weighted graphs; the sum of weights of edges incident to u.
- $d_S(u) = |\{v \in S : (u, v) \in E\}|$ and $\tilde{d}_S(u) = \sum_{v \in S} w_{uv}$ are the (unweighted and weighted, respectively) degrees[4]restricted to the subgraph S.
- d_m and $\tilde{d}_m$ are the median values of $d(u)$, $u \in V$.[5]

Scoring functions. The left column in Table 1 shows the community scoring functions for unweighted networks defined in [15]. These functions characterise some of the properties that are expected in networks with a strong community structure, with more ties between nodes in the same community than connecting them to the exterior. There are scoring functions based on internal connectivity (internal density, edges inside, average degree), external connectivity (expansion, cut ratio) or a combination of both (conductance, normalised cut, and maximum and average out degree fractions)

On the right column we propose generalisations to the scoring functions which are suitable for weighted graphs while most closely resembling their unweighted counterparts. Note that for graphs which only have weights 0 and 1 (1 indicates that an edge exists, 0 that it doesn't) each pair of functions is equivalent (any definition that didn't satisfy this wouldn't be a generalisation at all).

- **Internal density, edges inside, average degree:** These definitions are easily and naturally extended by replacing the number of edges by the sum of their weights.
- **Expansion:** Average number of edges connected to the outside of the community, per node. For weighted graphs, average sum of edges connected to the outside, per node.

[3] For every variable or function defined over the unweighted graph, will use a "$\sim$" to denote its weighted counterpart

[4] We assume the weight function w_{uv} is defined for every pair of vertices u,v of the weighted graph, with $w_{uv} = 0$ if there is no edge between them.

[5] To prevent confusion between the function $d_S(\cdot)$ and the median value (which only depends on G) d_m we will always refer to subgraphs of G with uppercase letters.

Table 1. Community scoring functions for weighted and unweighted networks.

	unweighted	weighted
Internal density	$f(S) = \frac{m_S}{n_S(n_S-1)/2}$	$f(S) = \frac{\tilde{m}_s}{n_S(n_S-1)/2}$
Edges Inside	$f(S) = m_S$	$f(S) = \tilde{m}_S$
Average Degree	$f(S) = \frac{2m_S}{n_S}$	$f(S) = \frac{2\tilde{m}_S}{n_S}$
Expansion	$f(S) = \frac{c_s}{n_s}$	$f(S) = \frac{\tilde{c}_s}{n_s}$
Cut Ratio	$f(S) = \frac{c_s}{n_s(n-n_s)}$	$f(S) = \frac{\tilde{c}_s}{n_s(n-n_s)}$
Conductance	$f(S) = \frac{c_s}{2m_s+c_s}$	$f(S) = \frac{\tilde{c}_s}{2\tilde{m}_s+\tilde{c}_s}$
Normalised Cut	$f(S) = \frac{c_s}{2m_s+c_s}$	$f(S) = \frac{\tilde{c}_s}{2\tilde{m}_s+\tilde{c}_s}$
Maximum ODF	$f(S) = \max_{u\in S} \frac{\lvert\{(u,v)\in E : v\notin S\}\rvert}{d(u)}$	$f(S) = \max_{u\in S} \frac{\sum_{v\notin S} w_{uv}}{\tilde{d}(u)}$
Average ODF	$f(S) = \frac{1}{n_s}\sum_{u\in S} \frac{\lvert\{(u,v)\in E : v\notin S\}\rvert}{d(u)}$	$f(S) = \frac{1}{n_s}\sum_{u\in S} \frac{\sum_{v\notin S} w_{uv}}{\tilde{d}(u)}$

- **Cut Ratio:** Fraction of edges leaving the cluster, over all possible edges. The proposed generalisation is reasonable because edge weights are upper bounded by 1 and therefore relate easily to the unweighted case. In more general weigthed networks, however, this could take values well over 1 while lacking many "potential" edges (as edges with higher weights would distort the measure). In general bounded networks (with bound other than 1) it would be reasonable to divide the result by the bound, which would result in the function taking values between 0 and 1 (0 with all possible edges being 0 and 1 when all possible edges reached the bound).
- **Conductance and normalised cut:** Again, these definitions are easily extended using the methods described above.
- **Maximum and average Out Degree Fraction:** Maximum and average fractions of edges leaving the cluster over the degree of the node. Again, in the weighted case the number of edges is replaced by the sum of edge weights.

Clustering coefficient. Another possible scoring function for communities is the clustering coefficient or transitivity: the fraction of closed triplets over the number of connected triplets of vertices. A high internal clustering coefficient (computed on the graph induced by the vertices of a community) matches the intuition of a well connected and cohesive community inside a network, but its generalisation to weighted networks is not trivial.

There have been several attempts to come up with a definition of the clustering coefficient for weighted networks. One is proposed in [1] and is given by $c_i = \frac{1}{\tilde{d}(i)(d(i)-1)}\sum_{j,h}\frac{w_{ij}+w_{ih}}{2}a_{ij}a_{jh}a_{ih}$. Note that this gives a local (*i.e.* defined for each vertex) clustering coefficient.

While this may work well on some weighted networks, in the case of complete networks, such as those built from correlation of time series,

$$c_i = \frac{1}{\tilde{d}(i)(d(i)-1)} \sum_{i,j} \frac{w_{ij}+w_{ih}}{2} = \frac{\sum_j w_{ij} + \sum_h w_{ih}}{\tilde{d}(i)(n-2)\cdot 2} = \frac{2\tilde{d}(i)}{\tilde{d}(i)(n-2)\cdot 2} = \frac{1}{n-2} \tag{4}$$

is constant on all edges and doesn't give any information about the network.

An alternative was proposed in [6] with complete weighted networks (with weights in the interval $[0,1]$) in mind, which makes it more adequate for our case:

- For $t \in [0,1]$ let A_t be the adjacency matrix with elements $a^t_{ij} = 1$ if $w_{ij} \geq t$ and 0 otherwise.
- Let C_t the clustering coefficient of the graph defined by A_t.
- The resulting weighted clustering coefficient is defined as

$$\tilde{C} = \int_0^1 C_t \; dt \tag{5}$$

Since C_t can only take as many different values as the number of different edge weights in the network, the integral is actually a finite sum. However, computing C_t (which is not computationally trivial) potentially as many as $n(n-1)$ times would be very costly for large values of n , so this function has been implemented by approximating the integral dividing the interval [0,1] into `n_step` parts (where `n_step`[6]is much smaller than $n(n-1)$).

It is worth noting that some of the introduced functions (internal density, edges inside, average degree, clustering coefficient) take higher values the stronger the clusterings are, while the others (expansion, cut ratio, conductance and normalised cut) do the opposite.

3.1 Variation of information

To compare and measure how similar two clusterings of the same network are, we will use the variation of information; a criterion introduced in [7] and which is based on information theory.

Definition 3. *The entropy of a partition $\mathcal{P} = \{\mathcal{P}_1, ..., \mathcal{P}_K\}$ of a set is given by:*

$$\mathcal{H}(\mathcal{P}) = -\sum_{k=1}^{K} \frac{|\mathcal{P}_k|}{n} \log\left(\frac{|\mathcal{P}_k|}{n}\right), \tag{6}$$

where n is the size of the set and $\mathcal{P}_k$ is the k-th cluster of the partition.

[6] In this case we set `n_step`=100. This gives a reasonable resolution while keeping computations fast.

Definition 4. *Given* $P(k,k') = \frac{|\mathcal{P}_k \cap \mathcal{P}'_{k'}|}{n}$ *the joint probability distribution of elements belonging to clusters* $\mathcal{P}_k$ *and* $\mathcal{P}_{k'}$*, the mutual information is defined as:*

$$I(\mathcal{P},\mathcal{P}') = \sum_{k=1}^{K}\sum_{k'=1}^{K'} P(k,k')\log\frac{P(k,k')}{P(k)P'(k')} \tag{7}$$

Definition 5. *The variation of information between partitions* $\mathcal{P}$ *and* $\mathcal{P}'$ *is given by:*

$$VI(\mathcal{P},\mathcal{P}') = \mathcal{H}(\mathcal{P}) + \mathcal{H}(\mathcal{P}') - 2I(\mathcal{P},\mathcal{P}') \tag{8}$$

Intuitively, the mutual information measures how much knowing the membership of an element of the set in partition $\mathcal{P}$ reduces the uncertainty of its membership in $\mathcal{P}'$. This is consistent with the fact that the mutual information is bounded between zero and the individual partition entropies

$$0 \leq I(\mathcal{P},\mathcal{P}') \leq \min\{\mathcal{P},\mathcal{P}'\}, \tag{9}$$

and the right side equality holds if and only if one of the partitions is a refinement of the other. Consequently, the variation of information will be 0 if and only if the partitions are equal (up to permutations of indices of the parts), and will get bigger the more the partitions differ. It also satisfies the triangle inequality, so it is a metric in the space of clusterings of any given set.

4 Generating a random graph

The algorithm proposed here to generate a random graph which will serve as a null model is a modification of the switching algorithm described in [8]. Each step of this algorithm involves randomly selecting two edges AC and BD and replacing them with the new edges AD and BC (provided they didn't exist already). This leaves the degrees of each vertex A, B, C and D unchanged while shuffling the edges of the graph.

One way to adapt this algorithm to our weighted graphs (more specifically, complete weighted graphs, with weights in $[0,1]$) is, given vertices A,B,C and D, transfer a certain weight $\bar{w}$ from w_{AC} to w_{AD}, and from w_{BD} to w_{BC}[7]. We will select only sets of vertices A, B, C, D such that $w_{AC} > w_{AD}$ and $w_{BD} > w_{BC}$, that is, we will be transferring weight from "heavy" edges to "weak" edges. For any value of $\bar{w}$, the weighted degree of the vertices remains constant, but if it is not chosen carefully there could be undesirable consequences.

4.1 Selection of $\bar{w}$

Choosing large values of $\bar{w}$ could result in edge weights falling outside of the $[0,1]$ interval in which all of our original values are contained, but small values will hardly have similarly small effects on the network. Restricting $\bar{w}$ to be as

[7] Here, w_{ij} refers to the weight of the edge between vertices i and j

large as possible without edge weights falling out of $[0, 1]$, however, will favour a degenerate network in which most of the edge weights are either 0 or 1, which is also undesirable and unlike any network that could be obtained from correlations of time series.

If we bound the transferred weight to the difference between the strong and weak edges, the new weights will be upper and lower bounded by the initial strong and weak weights, respectively, which would avoid this issue entirely. In this case, the maximum transferred weight would have to be $\bar{w} = \min(w_{AC} - w_{AD}, w_{BD} - w_{BC})$. This results in one of the pairs of edges being exchanged, while in the other a certain weight equal or smaller than their difference is transferred. In this second case, it is important to note that the difference between the new edge weights will be smaller than the difference of the original weights (strictly smaller if $w_{AC} - w_{AD} \neq w_{BD} - w_{BC}$).

The effect this has on the variance of the weights of the network can be seen in Figure 1. Unfortunately, as soon as the network starts to be significantly shuffled, the variance starts to fall. If we iterate the algorithm until the variation of information stops increasing, the variance has more than halved in our sample network.

As an alternative, we can impose the sample variance (i.e. $\frac{1}{n-1}\sum_{i,j=1}^{n}(w_i j - m)^2$, where m is the mean) to remain invariant after applying the transformation, and find the appropriate value of $\bar{w}$. The variance remains constant if and only if the following equality holds:

$$\begin{aligned} & (w_{AC} - m)^2 + (w_{BD} - m)^2 + (w_{AD} - m)^2 + (w_{BC} - m)^2 \\ = \quad & (w_{AC} - \bar{w} - m)^2 + (w_{BD} - \bar{w} - m)^2 + (w_{AD} + \bar{w} - m)^2 + (w_{BC} + \bar{w} - m)^2 \\ \iff \quad & 4\bar{w}^2 + 2\bar{w}(-(w_{AC} - m) - (w_{BD} - m) + (w_{AD} - m) + (w_{BC} - m) = 0 \\ \iff \quad & 2\bar{w}^2 + \bar{w}(-w_{AC} - w_{BD} + w_{AD} + w_{BC}) = 0. \end{aligned} \tag{10}$$

The solutions to this equation are $\bar{w} = 0$ (which is trivial and corresponds to not applying any transformation to the edge weights) and $\bar{w} = \frac{w_{AC} + w_{BD} - w_{AD} - w_{BC}}{2}$.

While this alternative can result in some weights falling outside of the interval $[0, 1]$, in the networks we studied it is very rare, so it is enough to discard these few steps to obtain the desired results.

Note that if all edge weights are either 0 or 1, in both cases this algorithm is equivalent to the original switching algorithm for discrete graphs, as in every step the transferred weight will be one if the switch can be made without creating double edges, or zero otherwise (which corresponds to the case in which the switch cannot be made).

4.2 Number of iterations

To determine how many iterations of the algorithm are enough to sufficiently "shuffle" the network, we study the variation of information of the resulting clustering respect to the initial one (Figure 1). As the algorithm transfers weight between the edges, the variation of information increases, until it stabilises roughly

after 10^4 iterations. Then, running 10^5 iterations to generate each random graph will be more than enough (there will be no improvement by iterating further) while still being very fast to compute. This is also consistent with the number of iterations found to be enough for the discrete case in [8].

Fig. 1. Normalised variance, Potts Hamiltonian and variation of information after applying the proposed algorithm with the minimum difference method. Horizontal axis is on logarithmic scale.

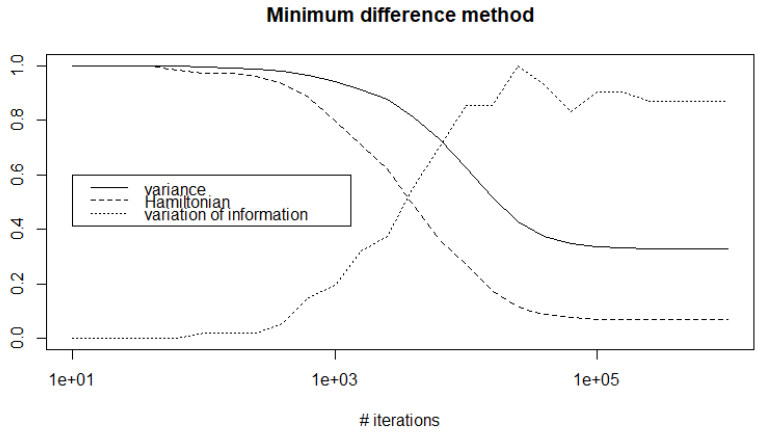

5 Clustering validation

To check that the results given by the clustering algorithm when applied to our FX networks are significant, we generate a random network using the method described in Section 4 for every month in the 2009-2016 period. Ideally, we would expect to see that the clusters found in the real networks are much stronger than those in the randomised networks, which shouldn't have any meaningful community structure. And indeed, we found that the clusterings of the randomised networks have many isolated vertices, and those that are grouped together are in smaller clusters than those we find in the original networks. (Nice pictures of these clusterings can be seen in the full report [13].)

In Figure 2 we verify that, across the entire observed period, the studied FX networks form larger communities than their randomised counterparts, and the number of nodes which are isolated or on very small communities is much smaller. Moreover, the value of the FX network Hamiltonian is consistently at least four times that of its corresponding randomised network using the distance correlation (Figure 3). With the Pearson correlation, the Hamiltonian varies

Fig. 2. Distribution of vertices grouped by the size of their communities, across the entire 2009-2016 period, for both the original and randomized networks.

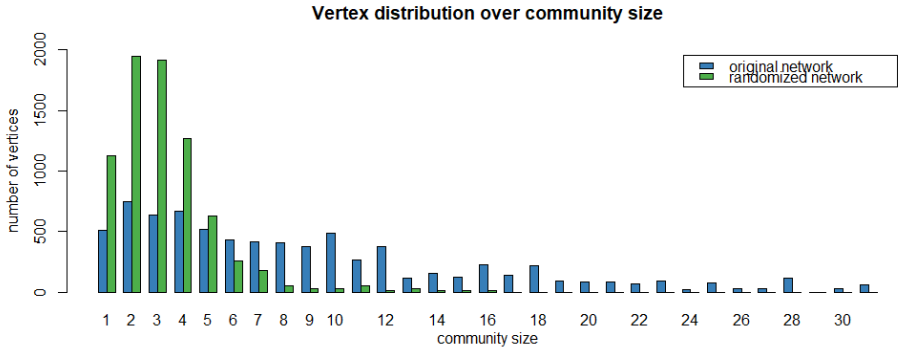

Fig. 3. Hamiltonians for the original and randomised networks (solid and dashed lines, respectively), for both the distance and Pearson correlation methods.

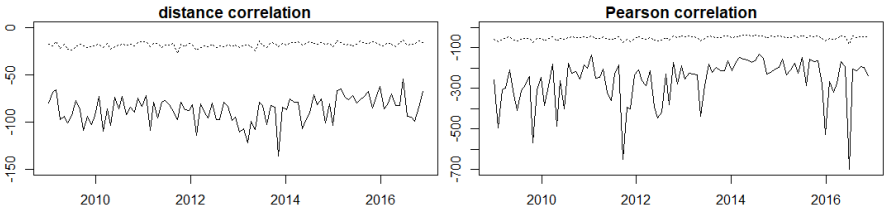

more but is also much lower than in the randomised network. Note though that the Hamiltonians cannot be compared across the different clustering methods, because with the Pearson correlation we need to take the inverses of each time series, resulting in a graph twice the order and four times the size.

Regarding the evolution of the scoring functions introduced in Section 3, in all cases the values of the original networks are better than those of their corresponding randomised ones[8]. We note that not only are the average scores better, but the results are consistent across all functions and periods of time. This, together with the much lower values achieved for the Hamiltonian, the objective function of the clustering algorithms, suggests that the observed community structure on our networks is significant and consistent.

While most of the values given by the scoring functions cannot be compared across the two clustering methods due to differences in the networks (their size, for example), Table 2 gives the percentage of increase of the real networks respect to the randomised models. We have observed the most dramatic increases on

[8] We omit the tables showing these explicit values due to space restrictions. Details can be seen in the full report [13]

the internal connectivity based functions on the Pearson correlation networks (probably related to the inclusion of inverse exchange rates in the network), but the decreases in external connectivity (expansion, cut ratio) are better in the distance correlation networks. The distance correlation method also performs better according to the clustering coefficient measure, with an increase that almost doubles that of the Pearson correlation.

As for the improvements in the hamiltonian, the rates of increase for both methods are very similar, but the consistency observed by the distance correlation as opposed to the highs and lows observed over time with the Pearson correlation Hamiltonian (Figure 3) could make it preferable.

Table 2. Means of the scoring functions over the 2009-2016 period for the randomised and observed networks, as well as the percentage of increase of the latter respect to the former.

	distance correlation			Pearson correlation		
	original	randomised	variation	original	randomised	variation
internal.density	0.83	0.81	1.90 %	0.85	0.91	-6.33%
edges.inside	24.02	3.00	701.49%	89.21	3.70	2313.02%
av.degree	4.44	1.62	174.37%	8.87	2.07	329.50%
expansion	16.97	18.70	-9.24%	35.46	37.96	-6.57 %
cut.ratio.	0.23	0.25	-6.87%	0.24	0.25	-3.74%
conductance	0.89	0.95	-6.24%	0.87	0.95	-8.53%
norm.cut	0.91	0.97	-5.37%	0.89	0.96	-7.32%
max.ODF	0.94	0.97	-3.84%	0.92	0.97	-5.41%
average.ODF	0.94	0.97	-3.84%	0.92	0.97	-5.40%
clustering.coef	0.89	0.75	17.82%	0.91	0.83	9.72 %
hamiltonian	-79.49	-18.24	335.79%	-259.35	-57.89	348.02 %

6 Conclusions

The clustering analysis in FX networks with appropriate scoring functions allow us to conclude that the community structure formed by the modularity maximisation algorithm is statistically significant as it is not present in random networks.

As for the comparison between clusterings relying on the distance or the Pearson correlations, the results obtained here back up the soundness of both methods, but there are slight quantitative differences worth mentioning. The distance correlation does offer some improvements in the clustering coefficient, one of the most relevant scoring functions, and the values of its Hamiltonian achieved by the optimisation algorithm, while similar on average to those of the Pearson correlation, are more consistent. Additionally, the fact that it runs the optimisation algorithm on networks of half the number of nodes greatly reduces the computation time.

It is also worth noting that while this work focused on financial networks, the methods proposed here are valid for evaluating the results of clustering algorithms on weighted networks in general.

Acknowledgments. A. Arratia acknowledge support of MINECO project APCOM (TIN2014-57226-P), and Gen. Cat. SGR2014-890 (MACDA).

References

1. Barrat, A., Barthélemy, M., Pastor-Satorras, R., Vespignani, A.: The architecture of complex weighted networks. Proceedings of the National Academy of Sciences of the United States of America 101(11), 3747–3752 (2004)
2. Blondel, V.D., Guillaume, J., Lambiotte, R., Lefebvre, E.: Fast unfolding of communities in large networks. J. of Stats. Mechanics: Theory and Experiment (2008)
3. Fenn, D.J., Porter, M.A., Mucha, P.J., McDonald, M., Williams, S., Johnson, N.F., Jones, N.S.: Dynamical clustering of exchange rates. Quantitative Finance 12(10), 1493–1520 (2012)
4. G. J. Székely, M. L. Rizzo, N.K.B.: Measuring and testing dependency by correlation of distances. The Annals of Statistics 35(6), 2769–2794 (2007)
5. Mantegna, R.N.: Hierarchical structure in financial markets. Eur. Phys. J. B. 11, 193–197 (1999)
6. McAssey, M.P., Bijma, F.: A clustering coefficient for complete weighted networks. Network Science 3(2), 183–195 (2015)
7. Meilă, M.: Comparing clusterings - an information based distance. Journal of Multivariate Analysis 98(5), 873 – 895 (2007)
8. Milo, R., Kashtan, N., Itzkovitz, S., Newman, M.E.J., Alon, U.: On the uniform generation of random graphs with prescribed degree sequences. Arxiv preprint cond-mat/0312028 (2003)
9. Mucha, P.J., Richardson, T., Macon, K., Porter, M.A., Onnela, J.P.: Community structure in time-dependent, multiscale, and multiplex networks. Science 328(5980), 876–878 (2010)
10. Newman, M.E.J., Girvan, M.: Finding and evaluating community structure in networks. Phys. Rev. E 69, 026113 (2004)
11. Onnela, J.P., Kaski, K., Kertész, J.: Clustering and information in correlation based financial networks. The European Physical Journal B-Condensed Matter and Complex Systems 38(2), 353–362 (2004)
12. Otranto, E.: Clustering heteroskedastic time series by model-based procedures. Computational Statistics & Data Analysis 52(10), 4685–4698 (2008)
13. Renedo, M.: On methods to assess the significance of community structure in networks of financial time series. Master's thesis, FME, Universitat Politècnica de Catalunya (2017), http://www.lsi.upc.edu/∼argimiro/mystudents/TFM_MartiRenedo.pdf
14. Renedo, M., Arratia, A.: Clustering of exchange rates and their dynamics under different dependence measures. In: Proc. of the First Workshop on MIning DAta for financial applicationS (MIDAS 2016), collocated ECML-PKDD. pp. 17–28 (2016)
15. Yang, J., Leskovec, J.: Defining and evaluating network communities based on ground-truth. Knowledge and Information Systems 42(1), 181–213 (2015)

Minimizing the Number of Probes and Maximizing Classification Performance for P300 BCI speller

Weilun Wang[1], Horie Shigeki[1] and Goutam Chakraborty[1]

[1]Faculty of Software and Information Science
Iwate Prefectural University
152-52 Sugo, Takizawa, Japan 020-0693

Abstract. To decipher human intentions by analyzing her brain wave is the basis for Brain Machine Interface (BMI) applications. Recently, with advancement of low noise probes, and fast signal processing software and hardware, brain signals generated by excitations of neurons, could be correctly classified for useful purpose. Conventional BCI speller uses 8 probes at pre-defined locations on the skull. In P300 BCI speller, an event related potential (ERP), called ERP-P300, is to be detected. Though it is strong in the parietal region of the brain, exact location of the strongest signal varies from person to person. The idea is that, if we optimize probe locations for an individual, we could reduce the number of probes required. Searching for optimum location of probes is done in two steps. First, we cluster the probe signals and select one representative from each cluster. Next, we find the optimum combination of those representative probes. Optimization criterion is two fold: minimizing the number of probes and maximizing classification accuracy. We use Pareto Genetic Algorithm for this Multi-Objective Optimization. We achieved over 75% classification accuracy even with as low as 2 probes, and from single P300 signal.

Keywords: Event Related Potential(ERP) P300, Reduction of Probes, Multi-objective Optimization, Pareto Genetic Algorithm

1 Introduction

In 1929, physiologist Berger demonstrated that it is possible to record the electrical activity of the brain by placing electrodes on the surface of the scalp [1]. The brainwave called Event Related Potential (ERP), which is regarded as neural manifestations of specific psychological functions, became popular several decades ago. This work is related to the ERP called P300 which is identified by Sutton in 1964 [2]. P denotes a positive potential, and 300 means the signal will appear 300ms after the stimuli. It is elicited by task relevant oddball stimuli and is most prominent at a parietal scalp location. In 1988, Farwell and Donchin designed a system called P300 BCI speller for the people who cannot use human motor system for communication [3]. P300 BCI speller is a communication

support to Systemic paralysis person, such as spinal cord injury patients and Amyotrophic Lateral Sclerosis patients, whose brain is working normally, but communication by speech and gestures are impossible due to damaged nervous system. Furthermore, the P300 BCI speller can help Virtual Reality (VR) user to do text input in the VR world. Helping communication by using P300 BCI Speller is one important area of research and development. Its working principle is simple. The subject chooses a letter from the word he intends to spell. Different characters flash on display at random intervals. When the chosen letter flashes, the subject's brain is stimulated to generate P300 signal. The signal is strong as it happens occasionally at random intervals, and the subject has to concentrate so that he does not miss it.

The system has two problems. The data we get from probes have noise and other spurious brain signals. High frequency noise is removed by band pass filter (BPF) and spurious brain signals are eliminated by averaging multiple samples. Second, the strength of ERP300 will be different depending on the probes' location. We have to select the locations where P300 is most prominent.

In 2007, Hoffmann et.al. did a comparison of accuracy using signals from 4 channels, 8 channels and 32 channels. In 2014, Yokoha [5] reduced the number of probes from 21 channels to 4 channels by clustering signals from 21 channels to 4 clusters, and selecting one member from each cluster. Compared to Hoffmann et.al., with the same number of 4 probes the classification accuracy was increased by 3-5% [5]. In 2015, Horie reduced the number of probes by analyzing signals from 21 channels, and reduced required probes to 2 or 3 channels (depending on the subject) with even improved accuracy [6]. Both Yokoha [5] and Horie [6] searched for best channels from 21 probes, referred in international 10-20 system. In this work, our search expands to net-station 128 probes. We achieved even better classification results, and sometime with less number of probes.

The paper is organized as follows. Following introduction, in section 2, we describe the experimental set-up and its details. In section 3 we will explain the basic idea and procedure. Section 4 includes experimental results and comparison with previous works. Finally we conclude the paper in section 5.

2 Experimental Set-up and details of the experiment

2.1 Experimental Set-up

The specifications of the BCI equipment used in our experiments are as follow. It is Netstation System 300 for Dense array EEG from Electrical Geodesics, Inc. (EGI) [9]. It is equipped with 128 channels. The specified noise level is 0.7uV RMS. A/D conversion resolution is 24bit. Maximum sampling rate is 2000Hz. Input impedance is 200MΩ. In our experiments, we used a sampling rate of 1000Hz i.e., 1000 samples per second. To train our classifier, we need signals with and without ERP-P300. For generating such signals, we used P300 BCI speller interface, as shown in Fig 1. We collected data from healthy young subjects (students of age around 22). The experimental set-up is explained below.

Our aim is to classify EEG signals into two classes, to identify whether the signal contains P300 signals or not [10]. In the experiment we have two targets: minimizing probes and maximizing classification performance.

Fig. 1. P300 BCI Speller

The interface of BCI speller is a 6×6 matrix, consisting of 26 characters and 10 numerals. They are organized in 6-rows and 6-columns, as shown in Fig.1. All elements of a row or a column flash simultaneously. The subject targets one character at a time. When the array containing the presented character flashed, the subject needs to perform a task, like count up. Flashing of rows and columns are random. The subject needs to concentrate, so as not to miss the target character. When the target character flashes, the brain responds strongly to the match. In the experiment, there is a training phase for the participants, called the *Copy Spell Phase*. We use signals that received from this phase to train the classifier. Next is the *free spell phase*, the subject counts the target character in his mind when the intended character flashes. The BCI speller identifies this unknown character by analyzing when P300 signals are present. Our equipment provides 128 probes as shown in Fig.2.

In conventional BCI speller [7] [8], 8 probes on the central parietal region of the brain are used. Our motivation is to find the location for the strongest P300 signal for an individual, so that one can design personalized BCI Speller with less number of probes.

2.2 Experimental details

To communicate a single character or numeral, all the 6 rows and 6 columns flash for 10 times. The flashing occurs with random uniform probability distribution. The duration of the flash is 600ms. Thus, to communicate a single target character or numeral will take $(6 + 6) \times 10 \times 600$ ms=72 Sec. Every time the target character is included in the row or column which is flashed, the subject is to count up. At the end, the total count should be 20, i.e., for a character

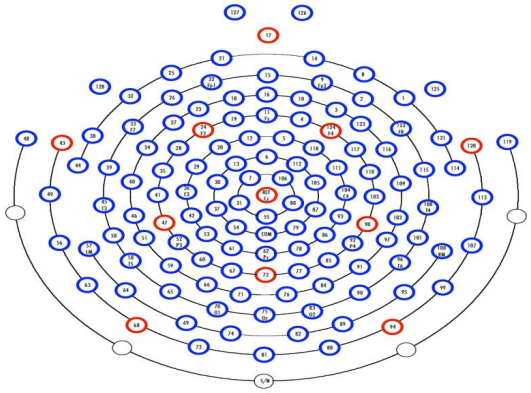

Fig. 2. Probe locations In Net Station System 300

presented we get 20 signals with P300 and 100 without. As the subjects need to concentrate, and as the chosen character row/column flashes with low probability(1/6), a strong P300 signal is generated. If we can get clearer P300 signal in one flash, we don't need repeat the flash so many times.

3 Algorithm Description

3.1 Basic Idea

The basic idea for reducing the number of probes is divided into two steps. In step I, we cluster the signals received from different probes. Signals in one cluster are similar. Instead of all members, if we select one prominent member for each cluster, we can reduce the number of probes to the number of clusters.

Next, the goal is to find the smallest subset of probes that could give the largest classification result. This is possible, because some of the clusters do not represent the target signal. In fact, by eliminating them we can improve classification result for classifying P300.

We collected EEG data from 128 probes and did 3 experiments. In Experiment I, we used data from 21 probes, the locations of which are specified by International 10-20 system [11]. This is the preliminary experiment to see the efficacy of clustering and reducing the number of channels. We grouped probe signals into 8 clusters. Dynamic Time Warping (DTW) was used to calculate distances, to group signals of similar shape in the same group, even if there is a time delay. Finally, Pareto GA is used to reduce the numbers of probes.

In Experiment II, we used data from all the 21 probes, and used Pareto GA to reduce the number of probes. If we can achieve similar results as in Experiment I, it would confirm that the clustering idea worked. As clustering is much faster compared to searching by GA, it is more efficient to first reduce the probes by clustering and then use GA for final probe selection. That way, search space of GA will be reduced and could deliver better searching results in shorter time.

In Experiment III, we clustered signals from all the 128 probes. Agglomerative clustering is used to ensure that the individual clusters have high clustering index. The number of clusters therefore varied from individual to individual. Finally, multi-objective optimization is performed with two objectives, (1) to reduce probe numbers and (2) to achieve higher classification performance. In the next section, the details of the algorithm is described.

3.2 First Reduction

Data collected from the probes have induced and spurious noises. As ERP300 is of low frequency, we used bandpass filter with frequency band of 0.1HZ to 13HZ to clean the high frequency and DC components. Then, we calculated the average of these 20 times of em copy spell data, and get clean signal free of high frequency noise and spurious brain signals). Most spurious signals are eliminated due to averaging. Thus 20 signals become to 1 signal for every individual probe. The amplitude of signals varies over probes. For normalization, necessary for clustering, we used pulse code modulation (PCM), with 8 levels (3bit) [12]. After normalization, the signals are clustered (both in Experiment I and Experiment III). Distances between signals after pre-processing and normalization are calculated by using dynamic time warping (DTW) algorithm. This ensures that signals of similar shape, though with certain time delay, will have low distance and would be clustered in the same group.

Next, the signals are clustered by Ward's algorithm. This is a top-down agglomerative clustering algorithm. The purpose of choosing top-down algorithm is that, we can set a threshold of the inter cluster distance and tune the number of cluster visually, using Dendrogram. In Experiment I, we divided these signals into 8 clusters. In Experiment III, the cluster number varied from individual to individual, ensuring that every cluster has high clusterin index. Next, step is to select a representative from each cluster. We select the one for which the change in potential is highest. This is explained in Fig.3. Member with maximum value of (max-min) is selected from every cluster. In conventional BCI speller [7] [8], 8 probes on the central parietal region of the brain are used. Our motivation is to find the location for the strongest P300 signal, which is different for different subjects.

3.3 Second Reduction

Our aim is to select minimum number of probes that would give the highest classification accuracy. After selecting representatives from each cluster, suppose we have N EEG signals, N is equal to the cluster number. We need to find the minimum subset of these N-probes which would give the highest recognition. This is a multi-objective optimization problem. We used Multi-Objective Genetic Algorithm (MOGA) suitable for such problem.

Chromosomes with N binary units are used. A gene with 1 represents that the corresponding probe is selected and 0 represents that the signal is not selected. For crossover, 2-point crossover is used, with crossover probability 0.5. Mutation

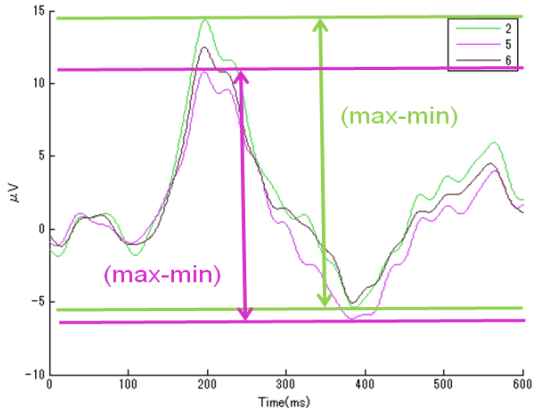

Fig. 3. Select Electrodes

is used with 0.01 probability. Tournament selection is used. To calculate the fitness of a chromosome with respect to its classification fitness, we used back-propagation training algorithm to find classification accuracy. For every signal, we used 2 features, the maximum difference of the potential and the difference of time between the occurrences, *max T* and *min T*. This is explained in Fig. 4. The classification result is one criterion of a chromosome's fitness. The other criterion is the number of probes, which we want to minimize. Using these two criteria, rankings of all the chromosomes in the population are calculated according to multi-objective optimization algorithm.

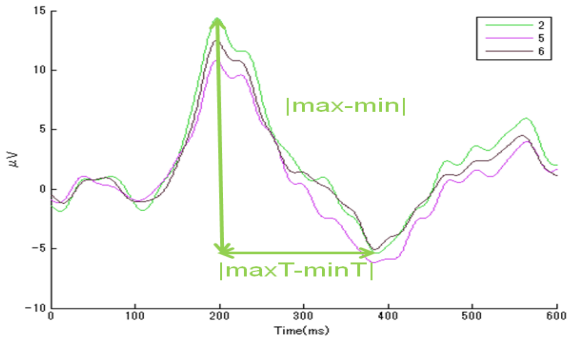

Fig. 4. Feature Extraction

This ranking is different from traditional MOGA. We use the summation of two criteria. The minimum is the fittest sample and will be ranked 1. We

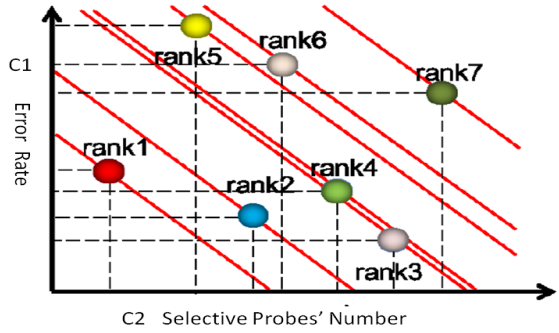

Fig. 5. Ranking for multi-objective genetic algorithm

normalize the two criteria for equal weight. Ranking is pictorially explained in Fig. 5.

3.4 Procedure of each Experiment

Experiment I

Here we used signals from 21 probes, as specified in international 10-20 system. Signals are Band Pass Filtered, Averaged, Normalized by PCM, Distance measured by DTW and then clustered in 8 groups. One representative probe is selected from each cluster. Feature is extracted, as described in previous section. Pareto GA selects the optimum probe set (minimum number of probes with minimum classification error.)

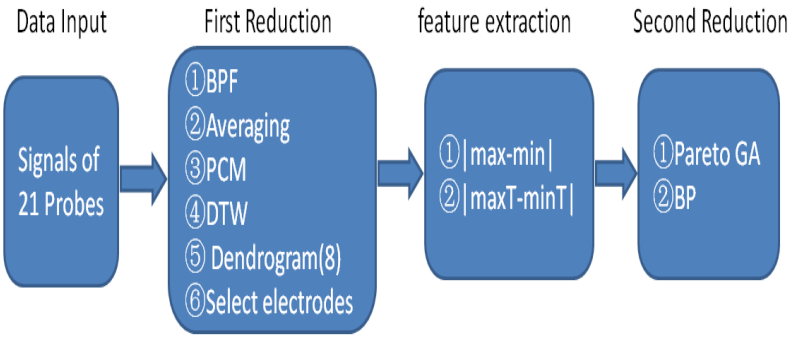

Fig. 6. Procedure of Experiment I

Experiment II Similar to **Experiment I**, except that we do not reduce the number of probes by clustering. Pareto GA is run with signals from all 21 probes. Naturally, GA searching took longer time. We compared the results from **Experiment I** and **Experiment II** in Section 4.

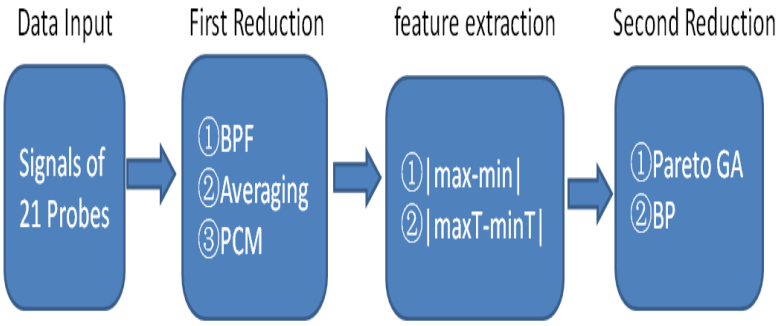

Fig. 7. Procedure of Experiment II

Experiment III
The steps of this experiment is similar to **Experiment I**. **Experiment I** started with 21 probe data. Here we take all 128 probe data. In addition, in **Experiment I** we always had 8 clusters. Here, the number of clusters varies from subject to subject, to ensure that clusters are compact. Higher number of clusters is better, as then the clusters are more compact. But, then GA search takes longer time. We need to compromise these two aspects.

4 Experimental Results

4.1 Experiment I

Pareto GA details:
-Population size: 20
-Length of the chromosome: 8
-Number of generation: 200
-Crossover: 2 point crossover with 0.5 crossover probability
-Selection rule: Tournament selection

In Table 1, we compared results with [5], because experimental condition are similar. **Experiment I** and [5], both used 21 probes. In [5], data from 21 probes are grouped into 4 clusters, and representative from each cluster was used for

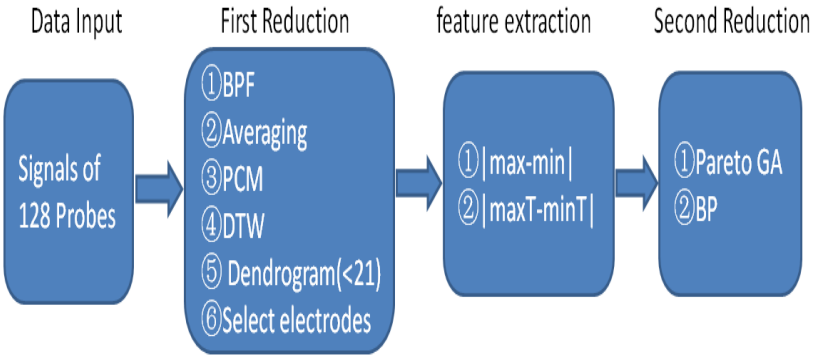

Fig. 8. Procedure of Experiment III

classification. In **Experiment I**, after clustering into 8 groups MOGA is used to find minimum set of probes with minimum error of classification. In Table 1, the first row is results from **Experiment I** and the second row is from [5]. We can see, **Experiment I** delivers much better classification result using even less number of probes.

Table 1. Result of Experiment I

	Subject1	Subject2	Subject3	Subject4	Subject5	Subject6
Experiment I						
Number of probes	2	2	3	2	2	2
Recognition rate	71 %	73%	76%	75%	63%	70%
Results of [5]						
Number of probes	4	4	4	4	4	4
Recognition rate	56%	67%	76 %	65 %	49 %	70%

4.2 Experiment II

Pareto GA details:
-Population size: 20
-Length of the chromosome: 21
-Number of generation: 40 60
-Crossover: 2 point crossover with 0.5 crossover probability
-Selection rule: Tournament selection

Here we compare results from **Experiment I** and **Experiment II**, to verify the efficacy of clustering. In both the experiments, we use the same signals from 21 probes. For **Experiment I**, we cluster to 8 groups and then run GA on 8 representative probes. In **Experiment II**, we use all 21 signals and run GA. If the results are similar, we can ensure that by clustering we are not missing any information, and we can select important probes more efficiently. In fact, the results are very similar. For subject 1, subject 5 and subject 6, there is a slight increase in classification accuracy at the cost of one increased probe. From this result, we conclude that clustering was and effective way to reduce the overall search time.

Table 2. Result of Experiment II

	Subject1	Subject2	Subject3	Subject4	Subject5	Subject6
Experiment I						
Number of probes	2	2	3	2	2	2
Recognition rate	71 %	73%	76%	75%	63%	70%
Experiment II						
Number of probes	3	2	3	2	3	3
Recognition rate	74%	73%	76 %	75 %	65 %	72%

4.3 Experiment III

Pareto GA details:
-Population size: 20
-Length of the chromosome:
Subject1-10, Subject2-13, Subject3-15, Subject4-13, Subject5-13, Subject6-14
-Number of generation: 100
-Crossover: 2 point crossover with 0.5 crossover probability
-Selection rule: Tournament selection

In this section we compare results from **Experiment I** and **Experiment III**. The experimental procedure are same, but in **Experiment I** the search is from the set of 21-probe data, whereas in **Experiment III** it is from the set of 128-probe data. The steps are same, clustering, representative signal selection and then MOGA search. We can see a further improveent in classification result. For subject 3, even with one less probe, we got better classification. On the other hand, for subject 5 and subject 6, we got much better classification with one extra probe.

5 Conclusion

In this work, we used 2 steps to reduce the number of probes. In step I, we cluster the signals received from different probes. Signals belonging to the same

Table 3. Result of Experiment III

	Subject1	Subject2	Subject3	Subject4	Subject5	Subject6
Experiment I						
Number of probes	2	2	3	2	2	2
Recognition rate	71 %	73%	76%	75%	63%	70%
Experiment III						
Number of probes	2	2	2	2	3	3
Recognition rate	75%	74%	79 %	77 %	70 %	78%

cluster are similar. Instead of all members, if we select one prominent member from each cluster, we can reduce the number of probes equal to the number of clusters. In the next step, we aim to further reduce the number of probes. Here, the goal is to find the smallest subset of probes that could give the largest classification result. This is possible, because some of the clusters do not contain the target ERP300 signal. By eliminating them, we reduce the number of probes and at the same time improve classification. To confirm that this idea does work, we performed **Experiment I** and **Experiment II**. Comparing results which are almost similar, we verified that reducing our GA search space, by clustering and taking one probe from each cluster, do work as expected. Finally, when we take data from all 128 probes, we could achieve very good classification results. It should be mentioned that in testing phase (all the results in Table. 1 to Table. 3) we used only one signal, i.e., the signals collected when all 6 rows and 6 columns are flashed only once. Thus, we did not eliminate spurious brain signals by averaging, for the test signals. In other words, our spelling time for a letter was 7.2 seconds.

Many industrial systems are monitored by several sensors. The proposed method can be used to reduce the number of probes in any general situation, where sensors are used to detect a particular type of perturbation of the system which would be reflected in the time-series data collected by various sensors. The idea introduced in this work could be extended to any such monitoring system to reduce the number of sensors.

Acknowledgment

This project was partially supported by research grant from Iwate Prefectural University, iMOS research center, and cooperative research project program of the research institute of electrical communication, Tohoku University.

References

1. Berger, Hans. "Uber das Elektrenkephalogramm des Menschen." European Archives of Psychiatry and Clinical Neuroscience 94.1 (1931): 16-60.1.

2. Sutton, Samuel, et al. "Evoked-potential correlates of stimulus uncertainty." Science 150.3700 (1965): 1187-1188.
3. Farwell, Lawrence Ashley, and Emanuel Donchin. "Talking off the top of your head: toward a mental prosthesis utilizing event-related brain potentials." Electroencephalography and clinical Neurophysiology 70.6 (1988): 510-523.
4. Hoffmann, Ulrich, et al. "An efficient P300-based brain?computer interface for disabled subjects." Journal of Neuroscience methods 167.1 (2008): 115-125.
5. Yokoha, Hikaru, Goutam Chakraborty, and Daigo Kikuchi. "Clustering of eeg signal to optimize number of electrodes in bci applications." Proceedings of the International Conference on Complex Medical Engineering (ICME). 2014.
6. Horie Shigeki,Goutam Chakraborty. gUser Specific EEG Probe Minimization for BCI Speller by Eliminating Irrelevant Ones using pareto GAh. JSAI International Symposia on AI(JSAI). 2015.
7. Kikuchi, Daigo, et al. "Analysis of EEG signal to investigate the influence of intoxication in perception delay." Awareness Science and Technology and Ubi-Media Computing (iCAST-UMEDIA), 2013 International Joint Conference on. IEEE, 2013.
8. Mizuno, Yuji, et al. "Clustering of EEG data using maximum entropy method and LVQ." Proceedings of the 10th WSEAS international conference on Systems theory and scientific computation. World Scientific and Engineering Academy and Society (WSEAS), 2010.
9. Electrical Geodesics Incorporated: https://www.egi.com/research-division
10. Polich, John. "Updating P300: an integrative theory of P3a and P3b." Clinical neurophysiology 118.10 (2007): 2128-2148.
11. Klem, George H., et al. "The ten-twenty electrode system of the International Federation." Electroencephalogr Clin Neurophysiol 52.3 (1999): 3-6.
12. Goodall, William M. "Telephony by pulse code modulation." The Bell System Technical Journal 26.3 (1947): 395-409.

Author Index